Impacts of drought on biomass and carbon fluxes in the Amazon rainforest : a modeling approach

Yitong Yao

université PARIS-SACLAY

Impacts of drought on biomass and carbon fluxes in the Amazon rainforest : a modeling approach

Impacts des sécheresses sur la biomasse et les flux de carbone dans la forêt amazonienne : une approche de modélisation

Thèse de doctorat de l'université Paris-Saclay

École doctorale n° 129 : Sciences de l'environnement d'Ile-de-France (SEIF)
Spécialité de doctorat : Surfaces continentales
Graduate school : Géosciences, climat, environnement et planètes
Référent : Université de Versailles -Saint-Quentin-en-Yvelines

Thèse préparée dans la unité de recherche **LSCE (Université Paris-Saclay, CNRS, CEA, UVSQ)**, sous la direction de **M. Nicolas Viovy**, directeur de recherche, la co-direction de **M. Philippe Ciais**, directeur de recherche, le co-encadrement de **Mme. Emilie Joetzjer,** chargée de recherche

Thèse présentée et soutenue à Paris-Saclay, le 28 Avril 2022, par

Yitong YAO

Composition du Jury

Mme. Agnès DUCHARNE Professeur, Sorbonne Université	Présidente
Mme. Anja RAMMIG Professeur, Technical University of Munich	Rapporteur et examinateur
M. Stephen SITCH Professeur, University of Exeter	Rapporteur et examinateur
M. Nicolas DELPIERRE Professeur, Université Paris Saclay	Examinateur
M. Nicolas VIOVY Directeur de recherche, LSCE	Directeur de thèse

THESE DE DOCTORAT

NNT : 2022UPASJ010

ÉCOLE DOCTORALE
Sciences de l'Environnement d'Île-de-France (SEIF)

Titre : Impacts des sécheresses sur la biomasse et les flux de carbone dans la forêt amazonienne : une approche de modélisation

Mots clés : mortalité des arbres due à la sécheresse, défaillance hydraulique, forêt amazonienne, modèle mécanistes, dynamique de la biomasse, flux de carbone

Résumé: Les sécheresses ont eu un impact récurrent sur les forêts tropicales amazoniennes, amenuisant la capacité de puits de carbone de la biomasse forestière. La plupart des modèles globaux de surface terrestre utilisés pour les évaluations du budget mondial du carbone et les projections climatiques futures, n'intègrent pas la mortalité des arbres induite par la sécheresse. Leurs prévisions de la dynamique de la biomasse sont donc sujettes à de grandes incertitudes. Les faiblesses des modèles globaux sont liés à : (1) l'absence de la représentation explicite du transport hydraulique; (2) le manque d'équations basées sur les processus à travers la description de la façon dont une altération du système de transport hydraulique des arbres conduit à la mortalité ; (3) le manque de représentation de la mortalitéà travers les tailles des arbres.

Tout d'abord, j'ai implémenté une architecture hydraulique mécaniste qui a été conçue par E. Joetzjer, et un module de mortalité des arbres que j'ai conçu dans l'ORCHIDEE-CAN-NHA. Notre modèle a produit des taux annuels de mortalité des arbres comparables à ceux observés et a capturé la dynamique de la biomasse. Ce travail fournit une base pour des recherches ultérieures sur l'assimilation des données d'observation expérimentales afin de paramétrer la mortalité des arbres induite par la défaillance hydraulique.

Deuxièmement, j'ai appliqué ORCHIDEE-CAN-NHA sur la forêt tropicale intacte de l'Amazonie. Le modèle a reproduit la sensibilité à la sécheresse de la croissance et de la mortalité de la biomasse aérienne (AGB) observée sur des réseaux de placettes d'inventaire forestier dans les forêts intactes d'Amazonie pour les deux récentes méga-sécheresses de 2005 et 2010. Dans le modèle, même si le changement climatique, avec des sécheresses devenant plus sévères, a eu tendance à intensifier la mortalité des arbres, l'augmentation de la concentration de CO_2 a contribué à atténuer la perte de carbone due à la mortalité en supprimant la transpiration.

Enfin, j'ai utilisé le modèle ORCHIDEE-CAN-NHA afin de simuler le futur du stockage du carbone dans la biomasse en Amazonie. La plupart des modèles climatiques (ISIMIP-2) projettent néanmoins de manière cohérente une tendance plus sèche dans le nord-est de l'Amazonie. La simulation forcée par le modèle climatique HadGEM dans le scénario RCP8.5 montre un assèchement plus prononcé dans l'est et le nord-est de l'Amazonie, avec un point d'intersection où le puits de carbone se transforme en source de carbone dans le bouclier guyanais et le centre-est de l'Amazonie, au milieu du 21e siècle. Cette étude permet de prédire l'évolution future de la dynamique de la biomasse de la forêt amazonienne avec un modèle amélioré basé sur les processus, capable de reproduire la mortalité induite par le changement climatique.

Dans les sections conclusion et perspectives, des développements futurs et des priorités de recherche sont proposés, qui amélioreraient la fiabilité et les performances du modèle basé sur les processus présentés dans cette thèse, permettant de mieux capturer les mécanismes qui contrôlent l'évolution de la dynamique de la biomasse forestière face à des risques de sécheresse plus fréquents.

ÉCOLE DOCTORALE
Sciences de l'Environnement d'Île-de-France (SEIF)

Title : Impacts of drought on biomass and carbon fluxes in the Amazon rainforest: a modeling approach

Keywords : drought-induced tree mortality, hydraulic failure, Amazon rainforest, process-based model, biomass dynamics, carbon flux

Abstract: Droughts have recurrently impacted the Amazon rainforests, undermining the forest biomass carbon sink capacity due to a quicker increase of biomass mortality compared to growth. Most global land surface models used for assessments of the Global Carbon Budget and future climate projections have not incorporated drought-induced tree mortality. Their prediction of biomass dynamics are therefore subject to large uncertainties, as a result of (1) lack of explicit simulation of hydraulic transport in the continuum from soil to leaves; (2) lack of process-based equations connecting the impairment of the hydraulic transport system of trees to mortality; (3) lack of representation of mortality across trees sizes. To address these critical research gaps, I improved plant hydraulic representation in ORCHIDEE-CAN. This model was re-calibrated and evaluated over rainforests in Amazon basin, and applied to simulate the future evolution of biomass dynamics facing droughts.

Firstly, I implemented a mechanistic hydraulic architecture that was designed by E. Joetzjer, and a hydraulic-failure related tree mortality module that I designed into ORCHIDEE-CAN. The model was calibrated against the world's longest running drought manipulation experiment of Caxiuana in the eastern Amazon. Our model produced comparable annual tree mortality rates than the observation and captured biomass dynamics. This work provides a basis for further research in assimilating experimental observation data to parameterize the hydraulic failure induced tree mortality.

Secondly, I applied ORCHIDEE-CAN-NHA over the Amazon intact rainforest. The model reproduced the drought sensitivity of aboveground biomass (AGB) growth and mortality observed at networks of forest inventory plots across Amazon intact forests for the two recent mega-droughts of 2005 and 2010. We predicted a more negative sensitivity of the net biomass carbon sink to water deficits for the recent 2015/16 El Nino, which was the most severe drought in the historical record. In the model, even if climate change with droughts becoming more severe tended to intensify tree mortality, increased CO_2 concentration contributed to attenuate the C loss due to mortality by suppressing transpiration.

Lastly, I used the ORCHIDEE-CAN-NHA model for future simulations of biomass carbon dynamics. Most climate models (ISIMIP2 program) consistently predict a drier trend in northeastern Amazon. The simulation forced by the HadGEM climate model in the RCP8.5 scenario shows the most pronounced drying in eastern and northeastern Amazon, with a cross-over point at which the carbon sink turned to a carbon source in the Guiana Shield and East-central Amazon in the middle of the 21st century. This study sheds light on predicting the future evolution of Amazon rainforest biomass dynamics with an improved process-based model able to reproduce climate-change induced mortality.

In the conclusion and outlook sections, future developments and research priorities are proposed, which would improve the reliability and performances of the process-based model presented in this dissertation, allowing to better capture mechanisms that control the evolution of forest biomass dynamics in the face of more frequent drought risks.

Résumé

Les forêts tropicales amazoniennes jouent un rôle clé dans la séquestration du carbone et le cycle de l'eau. Les sécheresses ont eu un impact récurrent sur les forêts tropicales amazoniennes, amenuisant la capacité de puits de carbone de la biomasse forestière via une augmentation plus rapide de la mortalité des arbres par rapport à l'augmentation de la croissance. La plupart des modèles globaux de surface terrestre utilisés pour les évaluations du budget mondial du carbone et les projections climatiques futures, n'intègrent pas la mortalité des arbres induite par la sécheresse. Leurs prévisions de la dynamique de la biomasse sont donc sujettes à de grandes incertitudes. Les faiblesses des modèles globaux sont liés à : (1) l'absence de la représentation explicite du transport hydraulique dans le continuum du sol aux feuilles; (2) le manque d'équations basées sur les processus à travers la description de la façon dont une altération du système de transport hydraulique des arbres conduit à la mortalité ; (3) le manque de représentation de la mortalitéà travers les tailles des arbres.

Tout d'abord, j'ai implémenté une architecture hydraulique mécaniste qui a été conçue par E. Joetzjer, et un module de mortalité des arbres que j'ai conçu dans l'ORCHIDEE-CAN-NHA. L'implémentation de l'architecture hydraulique reproduit le flux d'eau de la plante à travers les gradients de potentiel d'eau le long du continuum du sol aux feuilles, une perte de conductance de la tige (PLC) et le changement du stockage d'eau régulé par la capacité d'eau pendant les saisons sèches périodiques ou les années de sécheresse. Le modèle a été calibré à l'aide d'expérience de sécheresse artificielle la plus longue au monde à Caxiuana dans l'est de l'Amazonie (Fisher et al., 2007) pour le flux de sève à l'échelle du peuplement, l'humidité du sol et les changements de productivité dans des conditions de contrôle et d'exclusion des chutes. Notre modèle a produit des taux annuels de mortalité des arbres comparables à ceux observés et a capturé la dynamique de la biomasse, en particulier l'augmentation de la mortalité des grands arbres en 2005 suite à quatre années de sécheresse. Ce travail fournit une base pour des recherches ultérieures sur l'assimilation des données d'observation expérimentales afin de paramétrer la mortalité des arbres induite par la défaillance hydraulique.

Deuxièmement, j'ai appliqué ORCHIDEE-CAN-NHA sur la forêt tropicale intacte de l'Amazonie. Le modèle a reproduit la sensibilité à la sécheresse de la croissance et de la mortalité de la biomasse aérienne (AGB) observée sur des réseaux de placettes d'inventaire forestier dans les forêts intactes d'Amazonie pour les deux récentes méga-sécheresses de 2005 et 2010, ainsi que l'équilibre net entre ces deux flux de carbone. Nous avons prédit une sensibilité plus négative du puits net de carbone de la biomasse aux déficits hydriques pour le récent El Nino 2015/16, par rapport aux anciennes sécheresses de 2005 et 2010. Lorsque tous les épisodes de sécheresse du siècle dernier ont été classés en fonction de leur gravité, à partir des anomalies maximales cumulées du déficit hydrique, j'ai constaté que 2015/16 était la sécheresse la plus grave de l'histoire en termes d'intensité, de perte d'AGB et de zone subissant une grave perte de carbone. Les simulations factorielles nous ont permis de séparer la contribution individuelle du changement climatique et de l'augmentation du CO2 sur la dynamique de l'AGB. Dans le modèle, même si le changement climatique, avec des sécheresses devenant plus sévères, a eu tendance à intensifier la mortalité des arbres, l'augmentation de la concentration de CO2 a contribué à atténuer la perte de carbone due à la mortalité en supprimant la transpiration.

Enfin, j'ai utilisé le modèle ORCHIDEE-CAN-NHA afin de simuler le passé et le futur du stockage du carbone dans la biomasse en Amazonie. La reconstruction du climat historique et les données de forçage climatique futur corrigées du biais ont été sélectionnées dans le programme ISIMIP-2. La plupart des modèles climatiques projettent néanmoins de manière cohérente une tendance plus sèche dans le nord-est de l'Amazonie. La simulation forcée par le modèle climatique HadGEM dans le scénario RCP8.5 montre un assèchement plus prononcé dans l'est et le nord-est de l'Amazonie, avec un point d'intersection où le puits de carbone se transforme en source de carbone dans le bouclier

guyanais et le centre-est de l'Amazonie, au milieu du 21e siècle. Cette étude permet de prédire l'évolution future de la dynamique de la biomasse de la forêt amazonienne avec un modèle amélioré basé sur les processus, capable de reproduire la mortalité induite par le changement climatique.

Dans les sections conclusion et perspectives, des développements futurs et des priorités de recherche sont proposés, qui amélioreraient la fiabilité et les performances du modèle basé sur les processus présentés dans cette thèse, permettant de mieux capturer les mécanismes qui contrôlent l'évolution de la dynamique de la biomasse forestière face à des risques de sécheresse plus fréquents. L'introduction d'une variation spatiale des traits hydrauliques et une calibration systématique des paramètres sont discutées.

Remerciement
Il est difficile de croire que ça fait plus de 3 ans depuis mon arrivée en France. Depuis la fin d'année 2018, je commençais mon étude doctorale. Ces trois ans sont les moments les plus remarquables dans ma vie. Quand je rencontrais des problèmes dans ma vie, je me suis demandée si je pouvais les tous surmonter. Heureusement, j'ai réussi à finir mon travail et à faire la défense. Durant un peu plus de trois ans de mon étude, Je tiens à remercier les nombreuses personnes qui m'ont aidé, encouragé et soutenu.

Mes premiers et les plus sincères remerciements vont à mes deux superviseurs, Prof. Philippe Ciais et Prof. Nicolas Viovy, qui m'ont fourni de l'opportunité d'étude au LSCE et ont encadré cette thèse. C'est une grand honneur de pourvoir faire mes travaux de doctorale avec eux. Je n'aurais pas réussi à faire cette thèse sans eux. Merci à Philippe, qui m'a donné beaucoup d'idées pour résoudre les problèmes scientifiques et m'a donné beaucoup d'aide en corrigeant mes écrits anglais avec son grand patience. Il m'a aussi enseigné la philosophie de recherche à part des connaissances scientifiques et des méthodes techniques. Son attitude professionnelle et son passion des sciences m'ont inspiré à poursuivre ma carrière de recherche. Merci à Nicolas, qui m'a donné beaucoup des conseils en manière de programmer et de déboguer. Quand j'essayais de faire des travaux sur les paramètres, je ne savais pas comment les réaliser rapidement et proprement. C'est Nicolas qui m'a donné des suggestions et m'a enseigné très patiemment. Merci aussi à mon superviseur pendant mes études de master à Université de Peking, Prof. Shilong Piao, qui m'a aidé à lancer ma carrière de recherche, m'a encouragé de solliciter une opportunité et m'a recommandé d'étudier ici. C'est une opportunité très précieuse. Sans son enseignement, je ne serais pas capable d'avoir des bonnes habitudes de recherche, comme rester logique pendant la rédaction d'un article ou suivre les derniers progrès de la recherche.

Merci aux membres de comité, Prof. Jerome Chave et Prof. Nicolas Delpierre, qui ont fourni les suggestions très utilisées pour mon progrès académique et ma présentation.

Merci aux programmes de MOPGA et CLand, qui ont fourni le financement pour ma contrat doctoral. C'est le programme MOPGA qui m'a fourni la opportunité de participer au Banquet d'État à l'Élysée en March 2019 ainsi que l'opportunité de présentation académique à Mr. Président et Ministre de l'Éducation en Décembre 2019.

Ensuite, je voudrais remercier aux Emilie Joetzjer et Fabio Cresto Aleina, qui sont mes demi-superviseurs pendant la première année. Fabio, merci pour ta compréhension et ton encouragement quand j'étais contrarié. Même si tu as quitté France depuis la fin d'année 2019, le lien entre nous serons persister. Emilie, merci pour ton aide sur mon travail en manière de modèle et ta participation de notre discussion chaque vendredi. Merci aussi pour ton aide sur la recommandation lettre.

Merci à mes collègues du Group de Biogeo : Fabienne Maignan et Daniel Goll, qui ont participé à ma réunion sur les progrès de mon étude et m'a donné des suggestions très utilisés pour ma présentation. Merci aussi à Albert Jornet, qui m'aidé à résoudre des problèmes techniques.

Merci à mes professeurs de français : Daniel Lejard et Philippe Houdbine, qui m'ont enseigné le français pendant trois semestres. Merci à mes camarades dans la classe de français, Aditya, Elissa, Vidissha, Yossef, Fernando, David et Lucia. Ce sont aussi les expériences pour lesquelles j'ai été reconnaissant.

Merci à mes collègues Chinoise en France, qui m'ont offert un grand soutien et m'ont partagé des bon moments. Remerciements particuliers à Wenfang Xu, qui se souciait de moi comme une famille.

Merci aussi aux Hui Yang, Jinghui Lian, Bo Zheng, Yuan Zhang, Zheng Fu, Qinwei Ran, Liyang Liu, Yidi Xu, Haicheng Zhang, et Yunjiang Zhang.

Un merci particulier à tous ceux qui font le badminton avec moi. Depuis le juin d'année 2021, je me suis fait trois nouveaux amis, Bo Qin, Weiwei Xiong, et Siteng Fan, avec lesquels je suis sortie jouer au badminton deux fois par semaine, pour rester en forme avec plaisir. Bien que je ne jouasse pas bien au badminton, mon coéquipier toujours m'encourageait et m'emmenait à gagner les matchs sans effort. Bien que mon coéquipier, Siteng, m'ait donné beaucoup de pression, je voudrais quand même le remercier pour m'avait poussé à avancer et à poursuivre des réalisations plus importantes. Ma gratitude sincère pour son aide lorsque j'ai postulé pour l'opportunité de postdoc à caltech, soit l'encouragement, soit les conseils. J'espère qu'il passera avec succès l'application du projet "National Overseas excellent youth".

La vie est un peu dure pendant l'épidémie. Merci en particulier aux Yang Xu, Yunsong Liu et Shangyu Yao, qui m'accompagnaient quand j'ai connu la solitude la plus durement. Merci à mes amies en Chine, Yue He, Ling Huang, et Songbai Hong, qui m'ont partagé des histoires drôles et ont discuté des questions scientifiques avec moi. Merci à mon amie aux États-Unis, Donghai Wu, qui m'encourageait pendant ma carrière doctorale et me communiquaient les progrès de la recherche scientifique.

Enfin, merci beaucoup à mes parents, pour votre confiance, votre soutien inconditionnel et votre amour tout au long de ma vie. C'est dommage que vous ne puissiez pas venir à Paris pour assister à ma défense. Merci à Yanwei Cao, qui m'a consolé lorsque j'étais dans l'anxiété. Bon courage pour son défense et je le félicite d'avoir réussi ses examens pour devenir un médecin à l'hôpital de Jishuitan.

Table of contents

1 GENERAL INTROUDCTION

1.1 THE STATE OF AMAZON RAINFOREST

Amazon rainforests, accounting for approximately half of global rainforest area (Qin *et al.*, 2021), half of tropical forest biomass carbon stock (Malhi *et al.*, 2006; Saatchi *et al.*, 2011), and a quarter of residual terrestrial carbon sink (Pan *et al.*, 2011), plays an important role in conservation of biodiversity, carbon sequestration, hydrological resources and environmental services. Deforestation and degradation heavily affect vegetation biomass and forest area. Drought is a main driver of forest degradation (Qin *et al.*, 2021). During the periods of severe drought, degradation and natural disturbances affected similar forest area than deforestation over the past two decades (Bullock *et al.*, 2020). Recent studies indicated that the Amazon rainforest is very sensitive to the variability of climate state like shift in precipitation pattern (Ciemer *et al.*, 2019), and it is becoming under threat due to more frequent and more intense drought events, which increases the possibility of stepping over 'tipping points' beyond which forest dieback may occur (Machado-Silva *et al.*, 2021). The forest loss caused by the extreme events would significantly and persistently affect global water and carbon cycles, and feedback on global climate change. Such threat has prompted a strong research interest in understanding the internal mechanisms of forests' responses to droughts.

Forest inventory data shows a slow-down of wood growth trends and a quicker increase of tree mortality and corresponding carbon loss trends reduces the carbon accumulation rate over the past three decades, with a 1/3 decrease in the biomass carbon sink, that is, a decelerating sink rate of 0.017 MgC $ha^{-1}yr^{-2}$ (Brienen *et al.*, 2015). The strong El Niño in 2015/16 resulted in substantial loss of forest biomass over both intact and secondary forests, covering ~63% of the Brazilian Amazon (Qin *et al.*, 2021). Aircraft sampling measurements used in a regional inversion by Gatti *et al.* (2021) found that the southeastern Amazon acts as carbon source to the atmosphere, with increased fire emissions due to intensification of dry periods and deforestation. Remotely sensed vegetation data suggests that Amazon rainforest has decreased its resilience since 2003, a process likely to persist given the intensification of dry season and drought frequency (Boulton *et al.*, 2021). The combination of deforestation and drought induce higher risks than each factor separately in the southeastern Amazon (Staal *et al.*, 2020). These multiple lines of evidences indicate a vulnerable state of Amazon rainforests, at least in the South-east, which requires careful assessment of current dynamics and sensitivity therein as well as its future evolution under possibly more severe climate regimes with regional warming trend that may press the forest ecosystem over the tipping point.

The Amazon rainforest was hit by multiple drought events in the past. The drought events since last century can be categorized as two types according to the reason of their occurrence: tropical Atlantic positive sea surface temperature anomalies (1916, 1963, 2005, 2010) and strong El Niño events (1926, 1983, 1997/98, 2015/16). These two types of drought have different drought timing. For example, the 2005 tropical Atlantic warmer temperature mainly impacted the western and southern Amazon in the dry season. The 2015/16 El Niño drought was the most severe from the end of 2015 to early 2016 in the wet season. With regard to these past drought events, the comparison of drought coverage and intensity has been carried out through drought indices, like self-calibrated palmer drought severity index (scPDSI) and maximum climate water deficit (MCWD). Jiménez-Muñoz *et al.* (2016) found that regional warming trend and the El Niño event together made 2015/16 more severe than other earlier drought events. Papastefanou *et al.* (2020a) classified drought affected areas by different levels of MCWD. Xu *et al.* (2011) compared the vegetation greenness change from satellite measurement during the 2005 and 2010 droughts and found that the 2010 event led to more stressed forests. Furthermore, the new generation of models, CMIP6, predicts that most area in

Amazon basin will receive less rainfall in the future, with a drying trend in eastern and western Amazon (Parsons, 2020). Given the similarity between the intense 2015/16 El Niño and future anticipated climate change (Chadwick *et al.*, 2016), there is a pressing need to understand the tree mortality in response to heavy drought events and improve simulation for further forest dynamics.

1.2 THE STARTING POINT FOR THIS PHD PROJECT

The starting point for my PhD study is ORCHIDEE-CAN. ORCHIDEE is a physical process-based model, which can simulate the energy, water, and carbon fluxes between land surfaces and the atmosphere. The development of this branch of the ORCHIDEE model focuses on improving the capability of the ORCHIDEE model to simulate the biogeochemical and biophysical effects of forest management and includes allometric-based allocations of carbon to different pools, a simple plant hydraulic structure (see below) as well as an albedo scheme that in part depends on canopy structure (Naudts *et al*., 2015). One of its new features is the way the vegetation is discretized; a dynamic canopy structure is simulated by considering an user-defined number of circumference classes (n=20 in this study) and an empirical rule reflecting intra-tree competition that downscales canopy level gross primary productivity (GPP) into different circumference classes, which feedbacks on light interception and mortality through self-thinning. Background mortality comes from the reciprocal of a constant residence time. Climate based mortality, e.g. from drought has not been modeled yet using this system. The hydraulic architecture in ORCHIDEE-CAN tried to track the vertical water flow but used some fixed variables (e.g. leaf water potential) to represent the water transport in a very simple way that impedes the further connection with tree mortality in detail.

Based on the ORCHIDEE-CAN, I implemented a new mechanistic hydraulic architecture, and a tree mortality scheme linked to this hydraulic module, from which we can track the plant water transport and quantify the extent of hydraulic damage – induced tree mortality.

1.3 THE DRIVERS AND OCCURRENCE OF TREE MORTALITY

Tree mortality affects ecosystem carbon and water fluxes, functioning, biodiversity and possibly stability. Tree mortality controls the spatial pattern of carbon storage and greatly affects the carbon sequestration capacity in Amazon forests (Johnson *et al.*, 2016). In other word, the degree to which forest will continue to act as carbon sink depends not only on the trend of growth, but also on tree mortality that cause carbon release to the atmosphere. Tree mortality accelerates tree turnover, and this variation in turnover regulates the net carbon balance during drought years (Leitold *et al.*, 2018). Malhi *et al.* (2015) found that it is the variation of residence time affected by mortality that affects spatial biomass dynamics more than tree growth.

The drivers of tree mortality across spatial scales include water stress (regionally), disturbances from wind-thrown, flood, lightning and fire, pest, insect outbreak, and shading (locally). Tree mortality is classified into three processes, a background mortality caused by light competition between individuals (self-thinning as mentioned above), climate-induced mortality, and mortality from other agents like fire, pest, insect, and wind storm. These processes are not independent from each other. Among them, self-thinning embeds in the concept that the product of tree density and tree size determines the forest resource usage, like competition for light and/or water sources, which regulates the forest demography structure. From long-term demography data in French Guiana, Pillet *et al.* (2018) found U-shaped size-specific mortality, with higher mortality rate in both smaller and very big trees. A suppressed power-law size structure is also confirmed in tropical forests as forests recover from disturbance (Farrior *et al.*, 2016). The structural overshoot from favorable preceding climate and management condition, and subsequent mismatch between water demand and supply can modify the self-thinning relationship (Jump *et al.*, 2017). Similarly, it should be noted that enhanced growth from rising CO_2 exacerbates competition and could also increase self-thinning (McDowell *et*

al., 2018). Climate-induced mortality, especially from drought, is becoming widespread given the increased frequency of these extreme events (Choat *et al.*, 2018). Rising temperature and vapor pressure deficit (VPD) as well as soil moisture stress exacerbate the risk of hydraulic failure and carbon starvation (described in detail in next section). Other mortality processes like biotic agents or disturbances like storms are also found to occur frequently in central Amazonia (Fontes *et al.*, 2018). Biotic agents also can enhance the climate-induced mortality itself. The enhanced growth towards large tree size strengthens the risk of upper canopy trees to wind or lightning (McDowell *et al.*, 2018). The drivers or causes of the tree mortality also control how tree die, including standing dead trees and broken/up-rooted (Esquivel-Muelbert *et al.*, 2020). During storms, from high wind and rain events, trees would fall, and both trees uprooted and snapped were found (Fontes *et al.*, 2018). During or after drought events, trees died in standing state, showing leaf senescence and partial dieback. Tree die-back can also occur as a consequence of two or more different factors that appear concurrently or sequentially. For example, dry climate conditions could be followed by other tree-killing process like more frequent and intense fire activity and also insects. Thus drought and dryness events may also enhance fire and pest risk.

Tree mortality drives the forest structure dynamics or variation in demography. A small fraction of large trees determines the forest dominance in global carbon budget in terms of biomass carbon stocks (Bennett *et al.*, 2015). The above-mentioned three types of tree mortality processes impose different effects on tree demographic distribution. Regarding the self-thinning mortality, smaller trees are less competitive than the larger canopy one in acquiring light and water sources. In contrast, for the relationship between drought-induced tree mortality and tree size, debates still persist. On the one hand, the taller the tree, the longer the water transport pipeline would be, under which there would be higher embolism cavitation risk while facing water stress. On the other hand, taller trees tend to have deeper roots that access to deeper soil water. Trugman *et al.* (2021) found that taller trees are apt to distribute in well-watered condition relative to small trees or saplings with constrained access to resources. Under drought risk, besides the tree size, Esquivel-Muelbert *et al.* (2017) found that water affiliation (a general adaptation of mortality being lower in regions with a larger long term exposure to water stress) also affects the tree mortality. The wet-affiliated genera (which very rarely experience drought) appear to be more vulnerable thus bear more risk than the dry-affiliated ones, although this relationship was only demonstrated empirically in the southern Amazon, from spatial regression (Esquivel-Muelbert *et al.*, 2020). Thirdly, other natural disturbances, like windstorm, within the blowdown, the mortality risk would be greater with higher tree size and the uproot of big trees may also hit the smaller ones (Rifai *et al.*, 2016). The threat priority from biotic agents on tree survival differs among host-tree selection, tree size and other traits (Stephenson *et al.*, 2019).

With respect to rainforests in the Amazon basin, the increasing tree mortality rate over the past decade was attributed to greater climate variability and also possibly from feedbacks from faster growth that may induce a shorter life span (Dalagnol *et al.*, 2021), whereas the driving factors for the spatial pattern are not universal. The annual mortality rate is higher in the southeastern Amazon from long-term forest plots of the RAINFOR network (Esquivel-Muelbert *et al.*, 2020), where the dead trees in standing state accounts for more than 50% compared to other dead trees categories. In the western Amazon, broken/uprooted trees is a more prevalent death mode, suggesting wind a key driver (Negrón-Juárez *et al.*, 2018). The higher vulnerability of trees in the northwestern Amazon forests to winds was also found in Rifai *et al.* (2016). Based on Cox proportional hazard models, the mean growth rate was found to be the most powerful predictor of tree death, which verifies the growth-risk trade-off that is able to neutralize the enhanced vegetation growth by the lagged tree mortality increase (Brienen *et al.*, 2020), or simply, fast growth – fast dieback. Species tolerance also affects the mortality risk especially in the driest part of the Southern Amazon where the drought-adapted trees are at lower risk than vulnerable ones. The tree mortality-size relationship is not consistent over the entire Amazon, since different risk factors may add up to the other where both linear and U-shaped risk factors exist and affect the mortality pattern.

Despite our knowledge on tree die-back drivers and mortality categories, there is a strong gap between the observed die-off pattern and our predictive capability. Tree mortality is hard to predict solely based on earlier behavior of trees or change in productivity (Meir *et al.*, 2018), not to mention the mismatch between the fast changing climate condition and the lagged demography response in trees (Jump *et al.*, 2017). Researchers tried to identify feasible early warning metrics for the tree mortality risk. Anderegg *et al.* (2019) proposed satellite-derived 'non-physiologically active vegetation' as an efficient warning indicator that is spatially related to lagged tree mortality pattern following drought. Tree mortality can also be preceded by the temporal loss of resilience, which was assessed by the increased lag-1 temporal autocorrelation of NDVI anomalies, with lead time of 6-19 months before mortality (Liu *et al.*, 2019). Besides these early warning metrics, other opportunities from remote-sensing also provide easily-monitored indicator for tree mortality, e.g. LiDAR-tracked dynamic gap fraction, which is greatly associated with the field-based stem mortality rate but also partly fails in explicitly detecting the standing dead trees due to drought (Dalagnol *et al.*, 2021).

1.4 MECHANISMS RELATED TO TREE MORTALITY

The drivers for the tree mortality including drought, wind, biotic agents, rising temperature and VPD, self-thinning (enhanced growth related risk) have been described in Section 1.3. The mechanisms by which trees would die after the appearance of those factors have long been explored and reviewed. Two mechanisms were proposed to be mainly responsible for the tree mortality, hydraulic failure, and carbon starvation. Hydraulic failure relates to the gradual loss of xylem water conductance then the dysfunction of water transport. Specifically, when atmospheric water demand is quite high and soil water declines, the water loss due to transpiration can be even greater than root water uptake from soil. Then the high up-ward tension within the xylem would strain the water transport pathways and embolism cavitation would progressively happen later, although partial stomatal closure would happen to slow such dehydration process (Sevanto *et al.*, 2014) and partial cavitation can occur when plant tends to maximize the transpiration (Manzoni *et al.*, 2013). Carbon starvation results from the gradual exhaustion of the available non-structural carbohydrates (NSC) due to the stomatal closure in response to the water stress that hampers the carbon accumulation (McDowell & Sevanto, 2010). After either of these two mechanisms sets in, the vulnerability to biotic agents of pest and insect is also aggravated. Many manipulation experiments and field measurement after natural drought events were used to distinguish the relative importance of these two mechanisms in pushing the occurrence of tree mortality. For example, the world's longest-running tropical drought manipulation experiment in Caxiuana provides good reference on inferring drought impacts on carbon and water dynamics. At the Caxiuana site, Rowland *et al.* (2015) found that the growth rate as well as sugar and starch content of surviving trees did not differ under drought manipulation compared to the control setup, then the high tree mortality rate observed was attributed to the hydraulic dysfunction rather than the carbon starvation. The carbon accumulation rate also did not change in surviving trees after the El Niño drought (Berenguer *et al.*, 2018). Although many studies showed that the amount of NSC does not vary during the drought period, it should be noticed that depletion of NSC can hinder the hydraulic recovery (Tomasella *et al.*, 2021), since the recovery requires the regrowth of xylem (Choat *et al.*, 2018).

Regarding the hydraulic failure process, the xylem vulnerability to the cavitation is often assessed by Ψ_{50}, the tree water potential at which 50% loss of conductance happens, or Ψ_{88}. Xylem resistance to embolism cavitation is a great determinant for tree survival during drought. Genera associated with low embolism resistance showed higher drought-induced mortality. In the plant hydraulics framework, the safety-efficiency tradeoff reflects the complementary relationship between water transport conductance (or water transport efficiency) and the sensitivity to water stress, namely, Ψ_{50}, although it appears less frequently than expected (Gleason *et al.*, 2016). The plasticity in hydraulic traits reflects the ability of plant adaptation to drier climate, e.g. to which extent the plant can avoid the hydraulic damage, where the plasticity would benefit the resistance and resilience but we still

need more measurement evidence to prove its existence and performance. Experiments found structural acclimation in the response to drought to be related to the leaf to sapwood area (Huber value), which could explain the vulnerability to cavitation in plant itself (Choat *et al.*, 2018).

1.5 THE PERFORMANCE OF PROCESS-BASED MODELS IN SIMULATING PLANT HYDRAULICS

The tree mortality risk can be predicted from empirical relationship with climate metrics reflecting the extremes, like cumulated water deficit (Anderegg *et al.*, 2015). However, such relationship may not hold if the plant sensitivity changes. Since there is decoupling between tree vulnerability and aridity, it is not an ideal solution to just use spatial climate metrics to infer temporal tree mortality changes (Choat *et al.*, 2018). Meir *et al.* (2018) demonstrated that the short-term drought experiments may be inadequate to infer the long-term behavior given the unpredictable varying carbon allocation in response to stress condition, although transpiration seems predictable as it would be maximized. Furthermore, earlier tree mortality events than the 2005 drought cannot be tracked by inventories and instead be either predicted by process-based model or inferred from statistical reconstruction (Csilléry *et al.*, 2013). Compared with traditional field observation and experiments that have limitation in time length and spatial coverage, process-based models can simulate large spatial scales as well as both long and short time scales. Process-based models were developed to simulate the ecosystem carbon, water and energy cycles, like photosynthesis, carbon allocation, competition and mortality, transpiration, evaporation, … using generalized concepts. However, mortality is still not well-represented in such models, due to the knowledge gap in our understanding of the physiological mechanisms and possible thresholds.

Amongst the mechanisms underlying the drought-induced tree mortality, hydraulic failure is the one that is best observed and holds the great promise to be represented in process-based models (Rowland *et al.*, 2015). Many vegetation models use empirical formulations to regulate plant photosynthesis under water stress, which adds to uncertainties in simulating terrestrial carbon balance changes. Prioritized improvements should target soil hydraulic processes, plant transport and how water stress limits plant functions (Trugman *et al.*, 2018). The empirical soil water stress function used in current earth system models has been demonstrated to overestimate the sensitivity of evapotranspiration to soil moisture while it underestimates the hydrological sensitivity to the atmospheric water demand (VPD). Incorporating the full representation of plant hydraulics in models should help to better separate the role of soil moisture and VPD (Liu *et al.*, 2020b). Reducing the uncertainty of the response to drought is indispensable for improving the long-term predictability of the water, carbon and energy budgets.

How models represent plant water stress evolved from empirical soil water stress factors imposed on stomatal conductance and / or carboxylation rates, to the explicit simulation of plant leaf water potential impacting stomatal closure. Soil water content was firstly simulated from the mass balance of a soil bucket in simple models, where no soil depth discretization was imposed. Root water uptake cannot be simulated explicitly without accounting for vertical soil water potential profile and soil to root resistances. Later, soil moisture profiles were simulated, with water movement between soil layers. The soil water potential in the root zone is closer to the real water stress that can be perceived by a plant. The contribution of each soil layer to root zone soil water potential depends on the soil moisture and root biomass in each layer (Naudts *et al*., 2015), the soil-root conductance, following Darcy's law (Xu *et al*., 2016). Variability of soil moisture content indeed affects the vegetation growth. However, it may not completely reflect all the water stress that is experienced by a plant given various plant water use strategies and the decoupling of soil moisture and VPD to some extent (Liu *et al.*, 2020a).

The simulation of plant hydraulic failure caused by soil droughts requires a mechanistic model

of plant hydraulic architecture since classical models without hydraulic architecture consider only the demand term assuming that supply is never limiting. Supply-demand theory is the most commonly-used framework in water flow simulation, that is, the water supply and demand must balance out each other (Figure 1.1). Darcy's law is used in approximation of water supply, coming from the water flow proportional to vertical water potential differences and hydraulic conductance along the transport pathway. The water demand is regulated by leaf-level transpiration. Water potential is coupled to the calculation of both water supply and water demand, thus matching the water supply and demand constrains the corresponding water potential, after which the conductance can be derived based on nonlinear relationship with water potential.

Process-based model attempted to implement plant hydraulic processes but they differed in the specific realization therein, e.g., the formula of the conductance, whether the capacitance, the internal water storage are considered or not, whether the sunlit leave and shade leaves are separately simulated or not (Kennedy *et al*., 2019), the modeling of scales of isohydricity to anisohydricity, the inclusion of complete hydraulic segmentation, etc. Table 1.1 summarizes recent model progress in advancing our knowledge on simulation of plant hydrodynamics, where the stomatal optimization and supply-demand theory are involved mostly. In Xu *et al* (2016), the water storage in each organ is considered, where the water supply comes not only from the vertical water potential gradient, but can also be charged from water storage pool regulated by capacitance traits. A high capacitance can reduce the decline in water potential caused by transpiration demand. In other words, the water storage pool of each organ acts as a buffer for the decrease in water potential under water stress condition. However, such model cannot be applied to the whole Amazon basin. Besides such complex modeling approaches, Papastefanou *et al.* (2020b) found that a more parsimonious model with two parameters, one used to scale leaf water potential with soil water potential, manifesting the different water regulation strategies, the other defining the minimum negative leaf water potential under well-watered condition, can successfully reproduce the plant hydraulic response to drought in terms of the change in leaf water potential. Research also focused on stomata scale, namely, the stomatal conductance optimization, where the target evolves quite a lot. Rather than traditional stomatal conductance optimization assuming to maximize the marginal increase of photosynthesis per unit water cost, Eller *et al* (2020) improved the optimization target to the product of leaf photosynthesis and xylem hydraulic conductance, reflecting xylem-stomata coordination. Wang *et al.* (2021) calculated the steady state stomatal conductance by maximizing the difference between leaf level carbon gains and the risk from leaf hydraulics and photosynthesis, which performed better than the empirical formula from Ball *et al.* (1987) and Medlyn *et al.* (2011). Such optimization theories reduce the dependence of models on empirical parameters that are laborious to constrain and hard to interpret. Nevertheless, instantaneous optimization cannot reproduce long-term optimal strategies as plants would not be able to operate optimally at any time. Feng *et al.* (2021) demonstrated that the traditional stomatal optimization behavior is not always applicable due to the legacy effect and a dynamic framework tracking the preceding feedback should be further tested for more realistic simulation of stomatal behavior. Despite different attempts and validations in process-based model or demography model, we think it is too early to sort the most ideal representation of plant hydrodynamics until the completion of more comprehensive data validation and the fill of more knowledge gap especially the characteristics relating to the threshold-type response.

We can therefore justify that ORCHIDEE-CAN-NHA is superior to other models in terms of its performance at regional scale and the improvement in hydraulic transport. For instance, models like ED can be calibrated at site level and include detailed demographic processes, but to the best of our knowledge, it has not been applied to the whole Amazon basin. Models like FORMIND can describe individual-based stand growth processes but remain very simple for hydraulic processes and energy / water budgets thus is inadequate to represent tree mortality in more mechanistic way (Rödig *et al.*, 2017).

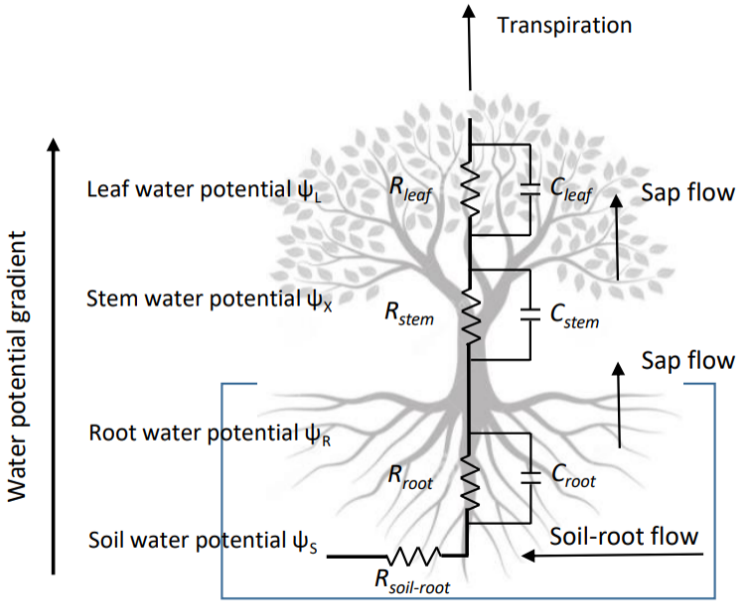

Figure 1.1 Schematic diagram of rationale of plant water transport. *R* denotes the resistance. *C* denotes the capacitance. Water flow is based on the water potential difference between two adjacent organs.

Table 1.1 Plant hydraulics in major vegetation models. The column of validation indicates how the model performance be validated against observation.

Model	Framework for modeling hydrodynamics	Validation	Reference
CLM v5	Stomata optimization and supply-demand theory	Caxiuana site	Kennedy *et al.* (2019)
JULES-SOX	Optimization of stomatal conductance by maximizing the product of leaf photosynthesis and xylem hydraulic conductance	70 global eddy flux sites	Eller *et al.* (2020)
CliMA	Optimization-based stomatal model by maximizing the difference between leaf level carbon gain and risk	Two flux sites in US	Wang *et al.* (2021)
CABLE	Supply-demand theory	Garden dry-down experiment across south-east Australia	De Kauwe *et al.* (2020)
ORCHIDEE-CAN	Water supply via Darcy's law without dynamics in stem water potential	Europe	Naudts *et al.* (2015)
Ecosystem Demography Model 2	Stomata optimization and supply-demand theory	Costa Rican field	Xu *et al.* (2016)
TRIPLEX	Loss of stem conductivity is related to soil water potential	Canada boreal forests	Liu et al (2021)
SPAC	Stomata optimization and supply-demand theory	13 temperate and tropical forest biomes across the globe	Liu *et al.* (2017)
One hydraulic module	Two parameters: isohydricity factor and well-	Leaf- and soil water potentials of 66 species under drought and non-	Papastefanou *et al.* (2020b)

	watered forcing pressure	drought conditions	
SurEau	Water mass conservation law	One forest site in east France	Cochard *et al.* (2021)
TFS v.1-Hydro	Continuous porous approach with pressure-volume formula	Caxiuana site	Christoffersen *et al.* (2016)
SPA	Stomata optimization and supply-demand theory	Caxiuana site	Fisher *et al.* (2007)

Hydraulic traits reflect water use strategies that need to be parameterized in model for simulation of plant water dynamics. It has been highly recognized that plant hydraulic traits mediates the ecosystem response to drought, the land-atmosphere feedback, and corresponding hydro-climatic feedbacks (Liu *et al.*, 2021b). Important hydraulic traits required for models include Ψ_{50} like we mentioned in last section, the sensitivity of water conductance to water potential, minimum leaf water potential or turgor loss point, and capacitance. These hydraulic traits and states are poorly constrained currently. One simple way is tuning the parameter against the observation data, but overfit could occur. Christoffersen *et al.* (2016) tried to parameterize the hydraulic traits as function of easily-measurable leaf and stem traits like wood density and leaf mass per area. Konings and Gentine (2017) used microwave-based vegetation optical depth (VOD) to calculate the effective ecosystem-scale isohydricity since the diurnal variation in VOD is directly related to leaf water potential. However, xylem traits are less well constrained by VOD (Liu *et al.*, 2021b). Markov Chain Monte Carlo (MCMC) also helps identify the most likely traits related to model simulated properties that are closer to the observation and is often used in parameters retrieval, which can give the distribution of the expected parameters rather than a single value estimate (Liu *et al.*, 2021b). However, the efficiency and accuracy of such parameters retrieval also depend on the data used as constraints and the scale mismatch between modeling unit and plant species level, since intra-species variability in hydraulic traits is comparable with the inter-species difference. Besides, an optimization routine by a target that is related e.g. to two trade-off processes is a great alternative. Such optimization-based parameters retrieval alleviates the need on tuning of empirical parameters against different observation data, and thus can favor the generalization of model to large-scale. Safety-efficiency trade-off has been involved in the design of modeling plant hydraulics, although the optimization target differs from marginal water cost of productivity (Xu *et al*., 2016), to the product of photosynthesis and xylem hydraulic conductance (Eller *et al.*, 2020). Wang *et al.* (2020) reviewed different stomatal optimization formulations and found that taking stress-related hydraulic failure as the risk penalty function is highly skillful. Meir *et al.* (2018) also suggested that parameters retrieval from a trade-off framework or probabilistic inference approaches are more efficient ways than hands-on addition of empirical parameterization. Another trade-off of hydraulic safety margin – growth rate is also proposed and works well in reproducing the observed biomass dynamics pattern (Oliveira *et al.*, 2021). Although growth-storage trade-off, reflecting different allocation rules, is not directly related to the hydraulics, such strategy also affects the species resilience to drought (Signori-Müller *et al.*, 2021).

Recently, a hybrid model, that is, the fusion of a process-based model and machine learning techniques, was proposed, since machine learning or deep learning, can be an alternative to replace the uncertain process within the physics-based model (Kraft *et al.*, 2021). Such paradigm has been attempted in global hydrological models and is able to reproduce the observed water cycle variations very well with dynamic neural network and a conceptual water balance model (Kraft *et al.*, 2020). To enable the addition of machine learning into the process-based model, observation is required to train the missing or uncertain process, e.g., the link between the soil moisture content and real water stress perceived by the plant xylem. This approach can maximize the usage of environmental observations and learn data-driven clues therein. We acknowledge that such synergistic combination of machine learning and process-based model is still in early development stages and whether it can work well to solve the problems of missing representation of explicit and detailed plant hydraulics process still requires further test and validation.

1.6 SIMULATING TREE MORTALITY

The simulation of tree mortality firstly requires the representation of demography structure. Until

recently, in each grid cell, process-based models regard plant communities as area-averaged representation for each plant functional type (PFT). To have a better approximation of vegetation structure and composition, some vegetation models strive to represent the demographic processes (Fisher *et al.*, 2018). For example, ORCHIDEE-CAN applied cohort-based scheme, which means multiple size-classes in same PFT (Naudts *et al*., 2015) and a self-thinning module with a cohort-based equation to distribute growth. Other schemes used in vegetation representation are individual-based competition, like in the ED model. Such individual model can simulate canopy vertical structure following the size distribution observed in the field. Although inclusion of such process also introduces additional uncertainty to some extent, it allows model to approximate the real-world demographic dynamics. Nevertheless, it is very time consuming and difficult to apply on large scale compared to cohort approach. Our starting point ORCHIDEE-CAN thus satisfies the requirement of cohorts distribution.

Given the complexity of forest ecosystems, and uncertainties in representing the related processes, it is hard to accurately simulate mortality (Liu *et al.*, 2017). Efforts for modeling tree mortality with process-based models are summarized in Table 1.2. Initially, a background mortality was parameterized as the inverse of a PFT-specific longevity parameter (e.g. 40 yr in tropics). Such parameterization is used in most global dynamic vegetation models, whereas such approach is only valid for an equilibrium forest state thus can constitute a problem in representing forest dynamics. Growth vigor, or growth efficiency was considered to constitute a dynamic mortality formulation (Sitch *et al.*, 2003). Threshold-type response was also employed by taking increasing mortality rate as a function of daily minimum temperature in ORCHIDEE-MICT (Zhu *et al.*, 2015). However, high uncertainties reside in mortality predictions if it is solely based on age or climate related metrics. How to efficiently parameterize tree mortality has also been highlighted as a critical challenge between complex effects including weather extreme on tree growth and simplified formulations in process-based models. With the above-mentioned several significant causes for tree mortality, many attempts have been made. Liu *et al.* (2017) formulated duration-based mortality indicator via two parts in SPAC model: hydraulic failure risk by the fraction of days with minimum xylem water potential below Ψ_{50} and stomatal closure risk by fraction of days with stomata closed completely. Liu *et al* (2021) used non-linear regression to parameterize the relationship between annual mortality rate and percentage loss of stem conductance (PLC). In the ED2 model, Xu *et al* (2021) included both hydraulic failure-induced mortality risk in relation to PLC and carbon starvation-related mortality risk via a function of annual diameter growth rates. In reality, tree mortality corresponds to an accumulation of exposure to stress, either water stress or carbon stress. Memory effects are critically important, and their outcome may be tracked for example from a higher autocorrelation / low resilience detected from NDVI anomalies (Liu *et al.*, 2019), although such relationship can also be regulated by water use strategies, since isohydric species experienced more mortality as they are subject to stomatal closure (Mrad *et al.*, 2019). The translation of early warning signal to mortality also depends on the species type (Liu *et al.*, 2019). Threshold-type response of tree mortality was observed along climate water deficit gradient or soil volume water content, although threshold-type formula needs to balance false alarm and false negative (Anderegg *et al.*, 2015). Knowledge of the specific thresholds of water stress above which mortality is triggered is still lacking and more field measurement evidence is highly required. My PhD study thus attempts to incorporate the threshold-type behavior in ORCHIDEE-CAN-NHA to track the water stress related tree mortality.

Table 1.2 Representation of tree mortality in vegetation models.

Model	Type	Formula	Reference
TRIPLEX-mortality	Nonlinear regression between PLC and mortality rate	Nonlinear regression between mortality rate and PLC	Liu *et al.* (2021a)
ORCHIDEE-MICT	Loss of vigor	-	Zhu *et al.* (2015)
ED2	Carbon balance related per capita mortality term (like carbon starvation)	c0*exp(c1*GR) GR: annual diameter growth rate	Xu *et al.* (2021)
ED2_hydro	Hydraulic failure (related to PLC)	h0*PLC^h1	
SPAC	Hydraulic failure risk and stomatal closure risk	Fraction of days with minimum xylem water potential below P50; fraction of days with stomata closed	Liu *et al.* (2017)
Bayesian dynamic linear model (not process-based)	Temporal loss of resilience	High autocorrelation of NDVI anomaly exceeding the threshold	Liu *et al.* (2019)

1.7 THE PAST DROUGHT EFFECTS ON FOREST BIOMASS DYNAMICS

For recent drought events, inventory, remote sensing and process-based models have all been used to assess the drought impacts. Forest inventories monitor the biomass growth and loss between two censuses, e.g. RAINFOR network spanning across tropical regions. Phillips *et al.* (2009) found that the 2005 drought led to a biomass carbon loss of 1.2-1.6PgC. Feldpausch *et al.* (2016) found the 2010 drought resulted in a reduction in biomass carbon uptake of 1.1PgC and the effect of this repeated drought is not affected by the previous one. In-situ observations provide evidence for forest biomass carbon dynamics, although it is hard to isolate the factor effects unless manipulation experiments are carried out explicitly and consecutively. Satellite datasets, such as LiDAR-observed tree height, has been also used to investigate post-drought forest dynamics (Yang *et al.*, 2018). VOD measured by passive microwave remote sensing, is also demonstrated to scale with changes in aboveground biomass (Liu *et al.*, 2013), although its temporal variation is modulated by changes of vegetation water content (Konings *et al.*, 2021). Qin *et al* (2021) used VOD-AGB (aboveground biomass) data to detect climate-induced tree mortality in intact forests after the last El Niño. Indeed, satellites data have broader coverage and higher temporal frequency than the inventory, but they are still unable to cover periods before 1980. Currently, these two data-streams, forest inventories and satellite data, mainly focus on past two decades. To resolve for long-term forest dynamics, process-based models can be used to both trace back to the past and anticipate the future. Powell *et al.* (2013) found that terrestrial biosphere models are able to successfully reproduce the ecosystem carbon fluxes under present climate condition but the poor representation of drought-induced mortality necessitated more efforts on refining physiological response since only ED model produces biomass loss under drought manipulation. As we mentioned in section 1.5 and 1.6, more concrete formulation of plant hydraulics and reasonable tree mortality scheme should be attempted to present better simulation of drought impacts. The model ORCHIDEE-CAN-NHA used in my PhD project improved by more mechanistic hydraulic architecture and tree mortality scheme in related to the hydraulic damage under water stress can be an ideal tool for detecting the past drought impacts.

1.8 THE EFFECT OF ELEVATED CO2 DURING DROUGHT

CO_2 fertilization effect has long been discussed and reviewed. The expected benefits from the elevated CO_2 concentration on forest productivity holds in both experimental observation and process-based models (Keenan *et al.*, 2021). Increased CO_2 concentration benefits the vegetation growth like higher leaf area index (LAI) then higher transpiration. The following decrease of leaf transpiration due to partial closure of stomata would appear and can help alleviate the water stress (Liu *et al.*, 2017). Since such stimulation effects on LAI are not very significant in tropics, the latter effect could take a dominant role in the response of forest dynamics. Through factorial simulation, Liu *et al.* (2017) found alleviation effect of elevated CO_2 on mortality risk due to partial closure of stomata. Wang *et al.* (2019) used CO_2 treatment of a series of CO_2 concentration experiment for birch and found that leaf xylem pressure is more negative when CO_2 concentration decreased a lot. The physiological CO_2 effect helps reduce future water stress, evidenced by metric of precipitation minus evapotranspiration (Swann *et al.*, 2016). The counteracting CO_2 effects between stomatal closure (leaf level) and the possible increase of transpiration (canopy level) during the drought and the impacts on forest biomass mortality have not been analyzed clearly in Amazon basin rainforest. The model ORCHIDEE-CAN-NHA thus offers us such an opportunity to carry out the factorial simulation to infer the elevated CO_2 effects.

1.9 THE FUTURE FOREST BIOMASS CARBON DYNAMICS IN AMAZONIAN RAINFOREST

Since extreme drought events will appear more frequently in the future, our knowledge on how Amazon rainforest will evolve is crucial for further policy formulation on forest management and related climate mitigation target. Current prediction on the fate of Amazon rainforest is still limited and far from reaching consensus. Hubau *et al.* (2020) built statistical models with CO_2 change, mean annual temperature, mean annual temperature change, MCWD, wood density and carbon residence time as explanatory variables to fit the forest inventory data and then applied the fitted model to predict future evolution of net carbon sink. The predicted Amazon rainforest carbon sink will disappear around 2035, but the estimation is very sensitive to the ongoing CO_2 emission pathways (Hubau *et al*., 2020). Zhang *et al.* (2015) showed that HadCM3 climate change trajectory causes region-wide AGB loss in Amazonian rainforest under modeling framework of ED2, IBIS and JULES, and up to 2100, JULES simulation shows that AGB can be 30MgC ha^{-1} less than that in 2009 despite JULES only presented mortality as background wood biomass turnover rate. However, Huntingford *et al.* (2013) used MOSES-TRIFFID land surface model forced by 22 climate models and found that only one simulation predicts a biomass loss by the end of 21st century. For the future, there is no consensus on whether the Amazon rainforest biomass carbon sink capacity will persist or when the collapse risk is the highest given a specific carbon emission pathway.

1.10 THE AIM AND RESEARCH QUESTIONS OF THIS PHD PROJECT

The main research questions of my thesis are:

(1) How does tropical soil heterotrophic respiration respond to climate variability?

(2) how to simulate the plant hydraulics and estimate the tree mortality rate in process-based models ?

(3) to what extent the model that I developed can capture the long-term net forest biomass carbon trends over Amazon basin and how drought impacts biomass growth and mortality ?

(4) is there a tipping point of net forest biomass carbon sink and when would it occur over the Amazonian intact rainforest?

Therefore, we need an ideal model tool that allows us to address these above-mentioned research questions, specifically, a model that can represent drought-induced tree mortality, and can be run over a large area and for long time periods.

My PhD thesis is formulated as below described (work flow please see Figure 1.2):

In chapter 2, the question to be solved is: **how does the tropical soil heterotrophic respiration (SHR) respond to climate variability?** I produced spatially-gridded soil heterotrophic respiration (SHR) dataset and identify the climatic driver for its inter-annual variability.

In chapter 3, the question to be solved is: **how to simulate the plant hydraulics and estimate the tree mortality rate in process-based models?** I described the improved hydraulic architecture in ORCHIDEE-CAN-NHA and calibrated it against the drought manipulation experiment at Caxiuana site in aspects of water fluxes like transpiration, soil moisture content and carbon fluxes like GPP and net biomass change. A simple but efficient tree mortality scheme is added in relation to hydraulic module and calibrated against the observed annual tree mortality rate and also validated at another throughfall exclusion site at Tapajos.

In chapter 4, the question to be solved is: **to what extent the model that I developed can capture the long-term net forest biomass carbon trends over Amazon basin and how drought impacts**

biomass growth and mortality? I applied the well-calibrated ORCHIDEE-CAN-NHA (from Chapter 3) to simulate the impacts of past drought events over Amazon rainforest. The long-term trend of forest biomass carbon gains, carbon losses and net carbon sink were simulated. The simulated drought sensitivity of three mega drought events over the last two decades was compared against the forest inventory statistics. The timing, coverage and intensity of eight past severe drought events since last century were compared. The effects of climate change and increased CO_2 concentration on forest biomass carbon dynamics were also separated through factorial simulations.

In chapter 5, the question to be solved is: **is there a tipping point of net forest biomass carbon sink and when would it occur over the Amazonian intact rainforest?** I applied the well-calibrated ORCHIDEE-CAN-NHA (from Chapter 3) to simulate the future forest vegetation carbon dynamics over Amazon rainforest using ISIMIP forcing data. For the future (2006-2099), two carbon emission scenarios RCP2.6 and RCP8.5 were considered. A quasi-emergent constraint method was used to calibrate the mean value and inter-annual variability of ISIMIP precipitation forcing data firstly. Then the process-based model simulated the long-term trend of forest carbon gains, carbon losses and net carbon balance until the end of the 21st century, where the tipping point from biomass carbon sink to carbon source was also identified. The regions subjected to the highest tree mortality risk was also detected.

Finally, in Chapter 6, the conclusion for Chapter 2 to 5 is given and perspective of potential direction is also discussed.

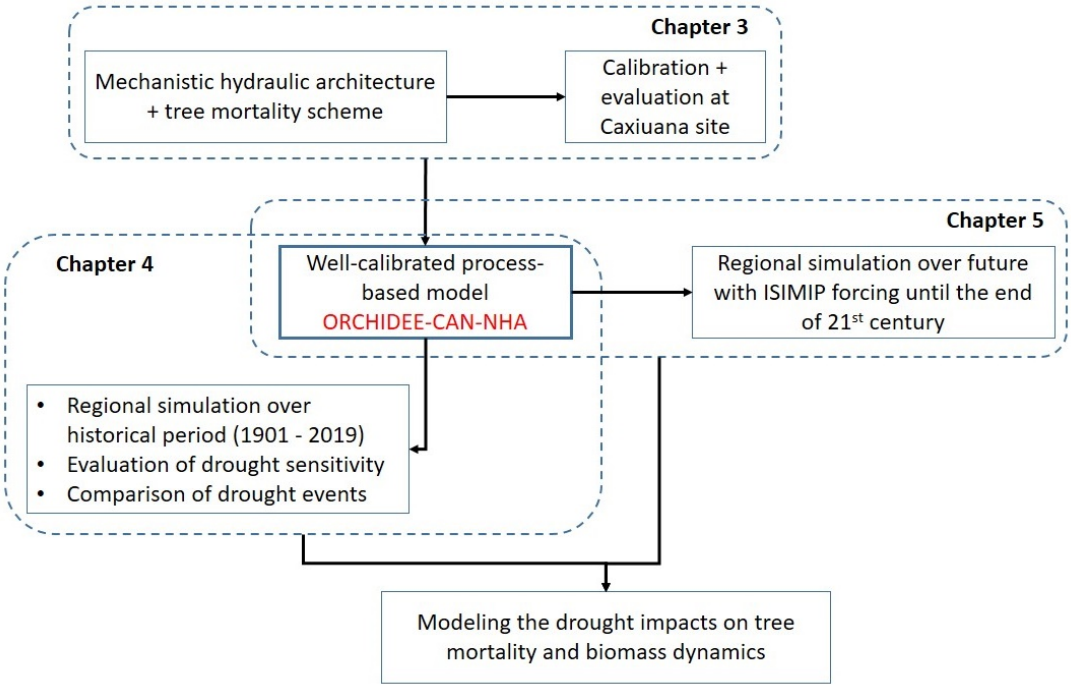

Figure 1.2 The work flow illustration of this PhD thesis (chapter 3 to 5) with the target of modeling the drought impacts on tree mortality and biomass dynamics.

1.11 REFERENCES

Anderegg, W.R., Flint, A., Huang, C.-y., Flint, L., Berry, J.A., Davis, F.W., Sperry, J.S. & Field, C.B. Tree mortality predicted from drought-induced vascular damage. *Nature Geoscience*, **8**, 367-371, 2015.

Anderegg, W.R., Anderegg, L.D. & Huang, C.y. Testing early warning metrics for drought-induced tree physiological stress and mortality. *Global change biology*, **25**, 2459-2469, 2019.

Ball, J.T., Woodrow, I.E. & Berry, J.A. (1987) A model predicting stomatal conductance and its contribution to the control of photosynthesis under different environmental conditions. *Progress in photosynthesis research*, pp. 221-224. Springer.

Bennett, A.C., McDowell, N.G., Allen, C.D. & Anderson-Teixeira, K.J. Larger trees suffer most during drought in forests worldwide. *Nature Plants*, **1**, 15139, 2015.

Berenguer, E., Malhi, Y., Brando, P., Cardoso Nunes Cordeiro, A., Ferreira, J., França, F., Chesini Rossi, L., Maria Moraes de Seixas, M. & Barlow, J. Tree growth and stem carbon accumulation in human-modified Amazonian forests following drought and fire. *Philosophical Transactions of the Royal Society B: Biological Sciences*, **373**, 20170308, 2018.

Boulton, C., Lenton, T. & Boers, N. Pronounced loss of Amazon rainforest resilience since the early 2000s. 2021.

Brienen, R.J., Phillips, O.L., Feldpausch, T.R., Gloor, E., Baker, T.R., Lloyd, J., Lopez-Gonzalez, G., Monteagudo-Mendoza, A., Malhi, Y. & Lewis, S.L. Long-term decline of the Amazon carbon sink. *Nature*, **519**, 344-348, 2015.

Brienen, R.J., Caldwell, L., Duchesne, L., Voelker, S., Barichivich, J., Baliva, M., Ceccantini, G., Di Filippo, A., Helama, S. & Locosselli, G.M. Forest carbon sink neutralized by pervasive growth-lifespan trade-offs. *Nature communications*, **11**, 1-10, 2020.

Bullock, E.L., Woodcock, C.E., Souza Jr, C. & Olofsson, P. Satellite-based estimates reveal widespread forest degradation in the Amazon. *Global change biology*, **26**, 2956-2969, 2020.

Chadwick, R., Good, P., Martin, G. & Rowell, D.P. Large rainfall changes consistently projected over substantial areas of tropical land. *Nature Climate Change*, **6**, 177-181, 2016.

Choat, B., Brodribb, T.J., Brodersen, C.R., Duursma, R.A., López, R. & Medlyn, B.E. Triggers of tree mortality under drought. *Nature*, **558**, 531-539, 2018.

Christoffersen, B.O., Gloor, M., Fauset, S., Fyllas, N.M., Galbraith, D.R., Baker, T.R., Kruijt, B., Rowland, L., Fisher, R.A. & Binks, O.J. Linking hydraulic traits to tropical forest function in a size-structured and trait-driven model (TFS v. 1-Hydro). *Geoscientific Model Development*, **9**, 4227-4255, 2016.

Ciemer, C., Boers, N., Hirota, M., Kurths, J., Müller-Hansen, F., Oliveira, R.S. & Winkelmann, R. Higher resilience to climatic disturbances in tropical vegetation exposed to more variable rainfall. *Nature Geoscience*, **12**, 174-179, 2019.

Cochard, H., Pimont, F., Ruffault, J. & Martin-StPaul, N. SurEau: a mechanistic model of plant water relations under extreme drought. *Annals of Forest Science*, **78**, 1-23, 2021.

Csilléry, K., Seignobosc, M., Lafond, V., Kunstler, G. & Courbaud, B. Estimating long-term tree mortality rate time series by combining data from periodic inventories and harvest reports in a Bayesian state-space model. *Forest ecology and management*, **292**, 64-74, 2013.

Dalagnol, R., Wagner, F.H., Galvão, L.S., Streher, A.S., Phillips, O.L., Gloor, E., Pugh, T.A., Ometto, J.P. & Aragão, L.E. Large-scale variations in the dynamics of Amazon forest canopy gaps

from airborne lidar data and opportunities for tree mortality estimates. *Scientific reports*, **11**, 1-14, 2021.

De Kauwe, M.G., Medlyn, B.E., Ukkola, A.M., Mu, M., Sabot, M.E., Pitman, A.J., Meir, P., Cernusak, L., Rifai, S.W. & Choat, B. Identifying areas at risk of drought-induced tree mortality across South-Eastern Australia. *Global Change Biology*, 2020.

Eller, C.B., Rowland, L., Mencuccini, M., Rosas, T., Williams, K., Harper, A., Medlyn, B.E., Wagner, Y., Klein, T. & Teodoro, G.S. Stomatal optimization based on xylem hydraulics (SOX) improves land surface model simulation of vegetation responses to climate. *New Phytologist*, **226**, 1622-1637, 2020.

Esquivel-Muelbert, A., Galbraith, D., Dexter, K.G., Baker, T.R., Lewis, S.L., Meir, P., Rowland, L., da Costa, A.C.L., Nepstad, D. & Phillips, O.L. Biogeographic distributions of neotropical trees reflect their directly measured drought tolerances. *Scientific reports*, **7**, 1-11, 2017.

Esquivel-Muelbert, A., Phillips, O.L., Brienen, R.J., Fauset, S., Sullivan, M.J., Baker, T.R., Chao, K.-J., Feldpausch, T.R., Gloor, E. & Higuchi, N. Tree mode of death and mortality risk factors across Amazon forests. *Nature communications*, **11**, 1-11, 2020.

Farrior, C., Bohlman, S., Hubbell, S. & Pacala, S.W. Dominance of the suppressed: Power-law size structure in tropical forests. *Science*, **351**, 155-157, 2016.

Feldpausch, T., Phillips, O., Brienen, R., Gloor, E., Lloyd, J., Lopez-Gonzalez, G., Monteagudo-Mendoza, A., Malhi, Y., Alarcón, A. & Dávila, E.Á. Amazon forest response to repeated droughts. *Global Biogeochemical Cycles*, **30**, 964-982, 2016.

Feng, X., Lu, Y., Manzoni, S., Vico, G., Katul, G., Mrad, A. & Jiang, M. Revisiting stomatal optimization: a new dynamic-feedback approach highlights the importance of memory effects. *AGU abstract*, 2021.

Fisher, R., Williams, M., Da Costa, A.L., Malhi, Y., Da Costa, R., Almeida, S. & Meir, P. The response of an Eastern Amazonian rain forest to drought stress: results and modelling analyses from a throughfall exclusion experiment. *Global Change Biology*, **13**, 2361-2378, 2007.

Fisher, R.A., Koven, C.D., Anderegg, W.R., Christoffersen, B.O., Dietze, M.C., Farrior, C.E., Holm, J.A., Hurtt, G.C., Knox, R.G. & Lawrence, P.J. Vegetation demographics in Earth System Models: A review of progress and priorities. *Global change biology*, **24**, 35-54, 2018.

Fontes, C.G., Chambers, J.Q. & Higuchi, N. Revealing the causes and temporal distribution of tree mortality in Central Amazonia. *Forest ecology and management*, **424**, 177-183, 2018.

Gatti, L.V., Basso, L.S., Miller, J.B., Gloor, M., Domingues, L.G., Cassol, H.L., Tejada, G., Aragão, L.E., Nobre, C. & Peters, W. Amazonia as a carbon source linked to deforestation and climate change. *Nature*, **595**, 388-393, 2021.

Gleason, S.M., Westoby, M., Jansen, S., Choat, B., Hacke, U.G., Pratt, R.B., Bhaskar, R., Brodribb, T.J., Bucci, S.J. & Cao, K.F. Weak tradeoff between xylem safety and xylem-specific hydraulic efficiency across the world's woody plant species. *New Phytologist*, **209**, 123-136, 2016.

Hubau, W., Lewis, S.L., Phillips, O.L., Affum-Baffoe, K., Beeckman, H., Cuní-Sanchez, A., Daniels, A.K., Ewango, C.E., Fauset, S. & Mukinzi, J.M. Asynchronous carbon sink saturation in African and Amazonian tropical forests. *Nature*, **579**, 80-87, 2020.

Huntingford, C., Zelazowski, P., Galbraith, D., Mercado, L.M., Sitch, S., Fisher, R., Lomas, M., Walker, A.P., Jones, C.D. & Booth, B.B. Simulated resilience of tropical rainforests to CO 2-induced climate change. *Nature Geoscience*, **6**, 268-273, 2013.

Jiménez-Muñoz, J.C., Mattar, C., Barichivich, J., Santamaría-Artigas, A., Takahashi, K., Malhi, Y., Sobrino, J.A. & Van Der Schrier, G. Record-breaking warming and extreme drought in the Amazon rainforest during the course of El Niño 2015–2016. *Scientific reports*, **6**, 1-7, 2016.

Johnson, M.O., Galbraith, D., Gloor, M., De Deurwaerder, H., Guimberteau, M., Rammig, A., Thonicke, K., Verbeeck, H., Von Randow, C. & Monteagudo, A. Variation in stem mortality rates determines patterns of above-ground biomass in A mazonian forests: implications for dynamic global vegetation models. *Global change biology*, **22**, 3996-4013, 2016.

Jump, A.S., Ruiz-Benito, P., Greenwood, S., Allen, C.D., Kitzberger, T., Fensham, R., Martínez-Vilalta, J. & Lloret, F. Structural overshoot of tree growth with climate variability and the global spectrum of drought-induced forest dieback. *Global change biology*, **23**, 3742-3757, 2017.

Keenan, T., Luo, X., De Kauwe, M., Medlyn, B., Prentice, I., Stocker, B., Smith, N., Terrer, C., Wang, H. & Zhang, Y. A constraint on historic growth in global photosynthesis due to increasing CO2. *Nature*, **600**, 253-258, 2021.

Kennedy, D., Swenson, S., Oleson, K.W., Lawrence, D.M., Fisher, R., Lola da Costa, A.C. & Gentine, P. Implementing plant hydraulics in the community land model, version 5. *Journal of Advances in Modeling Earth Systems*, **11**, 485-513, 2019.

Konings, A.G. & Gentine, P. Global variations in ecosystem-scale isohydricity. *Global change biology*, **23**, 891-905, 2017.

Konings, A.G., Holtzman, N.M., Rao, K., Xu, L. & Saatchi, S.S. Interannual variations of vegetation optical depth are due to both water stress and biomass changes. *Geophysical Research Letters*, **48**, e2021GL095267, 2021.

Kraft, B., Jung, M., Körner, M. & Reichstein, M. Hybrid modeling: Fusion of a deep approach and physics-based model for global hydrological modeling. *The International Archives of Photogrammetry, Remote Sensing and Spatial Information Sciences*, **43**, 1537-1544, 2020.

Kraft, B., Jung, M., Körner, M., Koirala, S. & Reichstein, M. Towards hybrid modeling of the global hydrological cycle. *Hydrology and Earth System Sciences Discussions*, 1-40, 2021.

Leitold, V., Morton, D.C., Longo, M., dos-Santos, M.N., Keller, M. & Scaranello, M. El Niño drought increased canopy turnover in Amazon forests. *New Phytologist*, **219**, 959-971, 2018.

Liu, L., Gudmundsson, L., Hauser, M., Qin, D., Li, S. & Seneviratne, S.I. Soil moisture dominates dryness stress on ecosystem production globally. *Nature communications*, **11**, 1-9, 2020a.

Liu, Q., Peng, C., Schneider, R., Cyr, D., Liu, Z., Zhou, X. & Kneeshaw, D. TRIPLEX-Mortality model for simulating drought-induced tree mortality in boreal forests: Model development and evaluation. *Ecological Modelling*, **455**, 109652, 2021a.

Liu, Y., Parolari, A.J., Kumar, M., Huang, C.-W., Katul, G.G. & Porporato, A. Increasing atmospheric humidity and CO2 concentration alleviate forest mortality risk. *Proceedings of the National Academy of Sciences*, **114**, 9918-9923, 2017.

Liu, Y., Kumar, M., Katul, G.G. & Porporato, A. Reduced resilience as an early warning signal of forest mortality. *Nature Climate Change*, **9**, 880-885, 2019.

Liu, Y., Kumar, M., Katul, G.G., Feng, X. & Konings, A.G. Plant hydraulics accentuates the effect of atmospheric moisture stress on transpiration. *Nature Climate Change*, **10**, 691-695, 2020b.

Liu, Y., Holtzman, N.M. & Konings, A.G. Global ecosystem-scale plant hydraulic traits retrieved using model–data fusion. *Hydrology and Earth System Sciences*, **25**, 2399-2417, 2021b.

Liu, Y.Y., van Dijk, A.I., McCabe, M.F., Evans, J.P. & de Jeu, R.A. Global vegetation biomass change (1988–2008) and attribution to environmental and human drivers. *Global Ecology and Biogeography*, **22**, 692-705, 2013.

Machado-Silva, F., Peres, L.F., Gouveia, C.M., Enrich-Prast, A., Peixoto, R.B., Pereira, J.M., Marotta, H., Fernandes, P.J. & Libonati, R. Drought resilience debt drives NPP decline in the Amazon Forest. *Global Biogeochemical Cycles*, **35**, e2021GB007004, 2021.

Malhi, Y., Wood, D., Baker, T.R., Wright, J., Phillips, O.L., Cochrane, T., Meir, P., Chave, J., Almeida, S. & Arroyo, L. The regional variation of aboveground live biomass in old-growth Amazonian forests. *Global Change Biology*, **12**, 1107-1138, 2006.

Malhi, Y., Doughty, C.E., Goldsmith, G.R., Metcalfe, D.B., Girardin, C.A., Marthews, T.R., del Aguila-Pasquel, J., Aragão, L.E., Araujo-Murakami, A. & Brando, P. The linkages between photosynthesis, productivity, growth and biomass in lowland Amazonian forests. *Global Change Biology*, **21**, 2283-2295, 2015.

Manzoni, S., Vico, G., Katul, G., Palmroth, S., Jackson, R.B. & Porporato, A. Hydraulic limits on maximum plant transpiration and the emergence of the safety–efficiency trade-off. *New Phytologist*, **198**, 169-178, 2013.

McDowell, N., Allen, C.D., Anderson-Teixeira, K., Brando, P., Brienen, R., Chambers, J., Christoffersen, B., Davies, S., Doughty, C. & Duque, A. Drivers and mechanisms of tree mortality in moist tropical forests. *New Phytologist*, **219**, 851-869, 2018.

McDowell, N.G. & Sevanto, S. The mechanisms of carbon starvation: how, when, or does it even occur at all? *New Phytologist*, **186**, 264-266, 2010.

Medlyn, B.E., Duursma, R.A., Eamus, D., Ellsworth, D.S., Prentice, I.C., Barton, C.V., Crous, K.Y., De Angelis, P., Freeman, M. & Wingate, L. Reconciling the optimal and empirical approaches to modelling stomatal conductance. *Global Change Biology*, **17**, 2134-2144, 2011.

Meir, P., Mencuccini, M., Binks, O., da Costa, A.L., Ferreira, L. & Rowland, L. Short-term effects of drought on tropical forest do not fully predict impacts of repeated or long-term drought: gas exchange versus growth. *Philosophical Transactions of the Royal Society B: Biological Sciences*, **373**, 20170311, 2018.

Mrad, A., Sevanto, S., Domec, J.-C., Liu, Y., Nakad, M. & Katul, G. A dynamic optimality principle for water use strategies explains isohydric to anisohydric plant responses to drought. *Frontiers in Forests and Global Change*, **2**, 49, 2019.

Naudts, K., Ryder, J., McGrath, M., Otto, J., Chen, Y., Valade, A., Bellasen, V., Berhongaray, G., Bönisch, G. & Campioli, M. A vertically discretised canopy description for ORCHIDEE

(SVN r2290) and the modifications to the energy, water and carbon fluxes. *Geoscientific Model Development*, **8**, 2035-2065, 2015.

Negrón-Juárez, R.I., Holm, J.A., Marra, D.M., Rifai, S.W., Riley, W.J., Chambers, J.Q., Koven, C.D., Knox, R.G., McGroddy, M.E. & Di Vittorio, A.V. Vulnerability of Amazon forests to storm-driven tree mortality. *Environmental Research Letters*, **13**, 054021, 2018.

Oliveira, R.S., Eller, C.B., Barros, F.d.V., Hirota, M., Brum, M. & Bittencourt, P. Linking plant hydraulics and the fast–slow continuum to understand resilience to drought in tropical ecosystems. *New Phytologist*, **230**, 904-923, 2021.

Pan, Y., Birdsey, R.A., Fang, J., Houghton, R., Kauppi, P.E., Kurz, W.A., Phillips, O.L., Shvidenko, A., Lewis, S.L. & Canadell, J.G. A large and persistent carbon sink in the world's forests. *Science*, **333**, 988-993, 2011.

Papastefanou, P., Zang, C.S., Angelov, Z., de Castro, A.A., Jimenez, J.C., De Rezende, L.F.C., Ruscica, R., Sakschewski, B., Sörensson, A. & Thonicke, K. Quantifying the spatial extent and intensity of recent extreme drought events in the Amazon rainforest and their impacts on the carbon cycle. *Biogeosciences Discussions*, 1-37, 2020a.

Papastefanou, P., Zang, C.S., Pugh, T.A., Liu, D., Grams, T.E., Hickler, T. & Rammig, A. A dynamic model for strategies and dynamics of plant water-potential regulation under drought conditions. *Frontiers in Plant Science*, **11**, 373, 2020b.

Parsons, L. Implications of CMIP6 projected drying trends for 21st century Amazonian drought risk. *Earth's Future*, **8**, e2020EF001608, 2020.

Phillips, O.L., Aragão, L.E., Lewis, S.L., Fisher, J.B., Lloyd, J., López-González, G., Malhi, Y., Monteagudo, A., Peacock, J. & Quesada, C.A. Drought sensitivity of the Amazon rainforest. *Science*, **323**, 1344-1347, 2009.

Pillet, M., Joetzjer, E., Belmin, C., Chave, J., Ciais, P., Dourdain, A., Evans, M., Hérault, B., Luyssaert, S. & Poulter, B. Disentangling competitive vs. climatic drivers of tropical forest mortality. *Journal of Ecology*, **106**, 1165-1179, 2018.

Powell, T.L., Galbraith, D.R., Christoffersen, B.O., Harper, A., Imbuzeiro, H.M., Rowland, L., Almeida, S., Brando, P.M., da Costa, A.C.L. & Costa, M.H. Confronting model predictions of carbon fluxes with measurements of Amazon forests subjected to experimental drought. *New Phytologist*, **200**, 350-365, 2013.

Qin, Y., Xiao, X., Wigneron, J.-P., Ciais, P., Brandt, M., Fan, L., Li, X., Crowell, S., Wu, X. & Doughty, R. Carbon loss from forest degradation exceeds that from deforestation in the Brazilian Amazon. *Nature Climate Change*, **11**, 442-448, 2021.

Rödig, E., Cuntz, M., Heinke, J., Rammig, A. & Huth, A. Spatial heterogeneity of biomass and forest structure of the Amazon rain forest: Linking remote sensing, forest modelling and field inventory. *Global ecology and biogeography*, **26**, 1292-1302, 2017.

Rifai, S.W., Urquiza Muñoz, J.D., Negrón-Juárez, R.I., Ramírez Arévalo, F.R., Tello-Espinoza, R., Vanderwel, M.C., Lichstein, J.W., Chambers, J.Q. & Bohlman, S.A. Landscape-scale consequences of differential tree mortality from catastrophic wind disturbance in the Amazon. *Ecological Applications*, **26**, 2225-2237, 2016.

Rowland, L., da Costa, A.C.L., Galbraith, D.R., Oliveira, R., Binks, O.J., Oliveira, A., Pullen, A., Doughty, C., Metcalfe, D. & Vasconcelos, S. Death from drought in tropical forests is triggered by hydraulics not carbon starvation. *Nature*, **528**, 119-122, 2015.

Saatchi, S.S., Harris, N.L., Brown, S., Lefsky, M., Mitchard, E.T., Salas, W., Zutta, B.R., Buermann, W., Lewis, S.L. & Hagen, S. Benchmark map of forest carbon stocks in tropical regions across three continents. *Proceedings of the national academy of sciences*, **108**, 9899-9904, 2011.

Sevanto, S., Mcdowell, N.G., Dickman, L.T., Pangle, R. & Pockman, W.T. How do trees die? A test of the hydraulic failure and carbon starvation hypotheses. *Plant, cell & environment*, **37**, 153-161, 2014.

Signori-Müller, C., Oliveira, R.S., Valentim Tavares, J., Carvalho Diniz, F., Gilpin, M., de V. Barros, F., Marca Zevallos, M.J., Salas Yupayccana, C.A., Nina, A. & Brum, M. Variation of non-structural carbohydrates across the fast–slow continuum in Amazon Forest canopy trees. *Functional Ecology*, 2021.

Sitch, S., Smith, B., Prentice, I.C., Arneth, A., Bondeau, A., Cramer, W., Kaplan, J.O., Levis, S., Lucht, W. & Sykes, M.T. Evaluation of ecosystem dynamics, plant geography and terrestrial carbon cycling in the LPJ dynamic global vegetation model. *Global change biology*, **9**, 161-185, 2003.

Staal, A., Tuinenburg, O.A., Bosmans, J.H., Holmgren, M., van Nes, E.H., Scheffer, M., Zemp, D.C. & Dekker, S.C. Forest-rainfall cascades buffer against drought across the Amazon. *Nature Climate Change*, **8**, 539-543, 2018.

Staal, A., Flores, B.M., Aguiar, A.P.D., Bosmans, J.H., Fetzer, I. & Tuinenburg, O.A. Feedback between drought and deforestation in the Amazon. *Environmental Research Letters*, **15**, 044024, 2020.

Stephenson, N.L., Das, A.J., Ampersee, N.J., Bulaon, B.M. & Yee, J.L. Which trees die during drought? The key role of insect host-tree selection. *Journal of Ecology*, **107**, 2383-2401, 2019.

Swann, A.L., Hoffman, F.M., Koven, C.D. & Randerson, J.T. Plant responses to increasing CO2 reduce estimates of climate impacts on drought severity. *Proceedings of the National Academy of Sciences*, **113**, 10019-10024, 2016.

Tomasella, M., Casolo, V., Natale, S., Petruzzellis, F., Kofler, W., Beikircher, B., Mayr, S. & Nardini, A. Shade-induced reduction of stem nonstructural carbohydrates increases xylem vulnerability to embolism and impedes hydraulic recovery in Populus nigra. *New Phytologist*, 2021.

Trugman, A., Medvigy, D., Mankin, J. & Anderegg, W. Soil moisture stress as a major driver of carbon cycle uncertainty. *Geophysical Research Letters*, **45**, 6495-6503, 2018.

Trugman, A.T., Anderegg, L.D., Anderegg, W.R., Das, A.J. & Stephenson, N.L. Why is tree drought mortality so hard to predict? *Trends in Ecology & Evolution*, 2021.

Wang, Y., Sperry, J.S., Venturas, M.D., Trugman, A.T., Love, D.M. & Anderegg, W.R. The stomatal response to rising CO2 concentration and drought is predicted by a hydraulic trait-based optimization model. *Tree physiology*, **39**, 1416-1427, 2019.

Wang, Y., Sperry, J.S., Anderegg, W.R., Venturas, M.D. & Trugman, A.T. A theoretical and empirical assessment of stomatal optimization modeling. *New Phytologist*, **227**, 311-325, 2020.

Wang, Y., Köhler, P., He, L., Doughty, R., Braghiere, R.K., Wood, J.D. & Frankenberg, C. Testing stomatal models at stand level in deciduous angiosperm and evergreen gymnosperm forests using CliMA Land (v0. 1). *Geoscientific Model Development Discussions*, 1-35, 2021.

Xu, L., Samanta, A., Costa, M.H., Ganguly, S., Nemani, R.R. & Myneni, R.B. Widespread decline in greenness of Amazonian vegetation due to the 2010 drought. *Geophysical Research Letters*, **38**, 2011.

Xu, X., Medvigy, D., Powers, J.S., Becknell, J.M. & Guan, K. Diversity in plant hydraulic traits explains seasonal and inter-annual variations of vegetation dynamics in seasonally dry tropical forests. *New Phytologist*, **212**, 80-95, 2016.

Xu, X., Konings, A.G., Longo, M., Feldman, A., Xu, L., Saatchi, S., Wu, D., Wu, J. & Moorcroft, P. Leaf surface water, not plant water stress, drives diurnal variation in tropical forest canopy water content. *New Phytologist*, 2021.

Yang, Y., Saatchi, S.S., Xu, L., Yu, Y., Choi, S., Phillips, N., Kennedy, R., Keller, M., Knyazikhin, Y. & Myneni, R.B. Post-drought decline of the Amazon carbon sink. *Nature communications*, **9**, 1-9, 2018.

Zhang, K., de Almeida Castanho, A.D., Galbraith, D.R., Moghim, S., Levine, N.M., Bras, R.L., Coe, M.T., Costa, M.H., Malhi, Y. & Longo, M. The fate of Amazonian ecosystems over the coming century arising from changes in climate, atmospheric CO 2, and land use. *Global change biology*, **21**, 2569-2587, 2015.

Zhu, D., Peng, S., Ciais, P., Viovy, N., Druel, A., Kageyama, M., Krinner, G., Peylin, P., Ottlé, C. & Piao, S. Improving the dynamics of Northern Hemisphere high-latitude vegetation in the ORCHIDEE ecosystem model. 2015.

2 SPATIAL DISTRIBUTION OF TROPICAL SOIL HETEROTROPHIC RESPIRATION AND THE CLIMATIC DRIVER ON ITS INTER-ANNUAL VARIABILITY

2.1 SUMMARY

Soil heterotrophic respiration (SHR), represents a large component of soil-atmosphere carbon exchange fluxes, the magnitude of which greatly affects the soil carbon dynamics and net change of atmospheric CO_2 concentration. The sensitivity of SHR to climate variability constitutes one of the largest uncertainty underlying land-atmosphere feedback. Regarding the fact that current available SHR datasets have either a very coarse spatial resolution like from atmospheric inversions, or are based on simpler upscaling formula or lacking evaluation of uncertainty, a long-time SHR dataset in higher spatial resolution with explicit uncertainty measure is highly necessary for carbon cycle research. In this chapter, we produced a new ensemble of global gridded SHR datasets by upscaling the 455 observations from Global Soil Respiration Database (SRDB 4.0) using Random Forest with inputs of climatic, edaphic and productivity variables. Then the dominant drivers of SHR inter-annual variability (IAV) are also analyzed.

Tropical forests account for almost one fifth of global SHR, with a regional total flux to the atmosphere of $8.5^{8.9}_{8.0}$ PgC yr^{-1} over 1985-2013, and a trend of 0.003 PgC yr^{-2} (P = 0.1). To quantify the uncertainty due to the explanatory gridded datasets, six climate datasets (temperature and precipitation), three soil moisture datasets and seven productivity datasets are used to constitute a 126 SHR members ensemble. We find that the choice of soil moisture datasets leads to the largest difference of SHR estimates. Temperature strongly controls the SHR IAV in tropical forests, and short-wave radiation is the second most important factor, while the TRENDY process-based models show that the SHR IAV is driven instead by precipitation or soil moisture variability, although ensemble members exhibit different SHR IAV drivers in tropical forest. Positive temperature sensitivity and negative precipitation sensitivity of SHR are found in tropical forests, especially in the Amazon basin, which suggests that future warming and local drying may induce more soil carbon loss if we accept the hypothesis that our observation-derived sensitivity persists in the future. Soil carbon pools thus face a risk of depletion from climate change if there is no significant enhancement of productivity-driven inputs.

This study provided spatially-gridded maps of annual SHR and identified the most influential climatic drivers of its inter-annual variability. Regarding further improvement for SHR mapping tasks, we emphasize the value of more SHR observations, particularly in tropical regions, and the possible use of deep-learning methods that could maximize the use of observation data, including the time dimension.

This chapter has been published as Yao, Y., Ciais, P., Viovy, N., Li, W., Cresto-Aleina, F., Yang, H., ... & Bond-Lamberty, B. (2021). A data-driven global soil heterotrophic respiration dataset and the drivers of its inter-annual variability. Global Biogeochemical Cycles, 35(8), e2020GB006918 (see Appendix A)

2.2 ABSTRACT

Soil heterotrophic respiration (SHR) is important for carbon-climate feedbacks because of its sensitivity to soil carbon, climatic conditions and nutrient availability. However, available global SHR estimates have either a coarse spatial resolution or rely on simple upscaling formulations. To better quantify the global distribution of SHR and its response to climate variability, we produced a new global SHR dataset using Random Forest, up-scaling 455 point data from the Global Soil Respiration Database (SRDB 4.0) with gridded fields of climatic, edaphic and productivity. We estimated a global total SHR of $46.8^{56.3}_{38.6}$ PgC yr^{-1} over 1985-2013 with a significant increasing trend of 0.03 Pg C yr^{-2}. Among the inputs to generate SHR products, the choice of soil moisture datasets contributes more to the difference among SHR ensemble. Water availability dominates SHR inter-annual variability (IAV) at the global scale; more precisely, temperature strongly controls the SHR IAV in tropical forests, while water availability dominates in extra-tropical forest and semi-arid regions. Our machine-learning SHR ensemble of data-driven gridded estimates and outputs from process-based models (TRENDYv6) shows agreement for a strong association between water variability and SHR IAV at the global scale, but ensemble members exhibit different ecosystem-level SHR IAV controllers. The important role of water availability in driving SHR suggests both a direct effect limiting decomposition and an indirect effect on litter available from productivity. Considering potential uncertainties remaining in our data-driven SHR datasets, we call for more scientifically-designed SHR observation network and deep-learning methods making maximum use of observation data.

2.3 INTRODUCTION

Soil heterotrophic respiration (SHR), the CO_2 flux produced by free-living microbial heterotrophs and soil fauna feeding on soil organic matter (Carbone et al., 2016; Hanson et al., 2000), constitutes a key ecosystem-to-atmosphere carbon flux that affects soil carbon storage and carbon-climate feedbacks. Since the magnitude of SHR is roughly four times of global annual anthropogenic fossil fuel emission (Le Quéré et al., 2018) and SHR can regulate the net ecosystem carbon exchange variability in some regions (Liu et al., 2018c), even small changes in this flux can cause carbon redistribution between soil and atmosphere, and modify the carbon sink. Enhanced microbial dynamics in soil organic matter decomposition have been detected as the dominant factor in an increasing imbalance between higher CO_2 loss rate and CO_2 uptake by plants (Bond-Lamberty et al., 2018). Therefore, a detailed understanding of the SHR spatial and temporal dynamics under changing climate conditions is pivotal to improve projections of the carbon–climate feedback (Ballantyne et al., 2017; Bradford et al., 2019).

However, unlike other components of the terrestrial carbon cycle like gross primary productivity (GPP) that can be measured through eddy covariance flux tower at plot scale, SHR observations mainly come from small-scale chambers, combined with intrusive methods (trenching, root exclusion, root extraction), or non-intrusive methods of isotope labelling with uncertainty in ^{14}C measurements (Bond-Lamberty et al., 2004; Hanson et al., 2000) to partition the heterotrophic and autotrophic soil fluxes. Due to the considerable uncertainty underlying these measurements, SHR is the most poorly constrained ecosystem and global carbon flux (Ciais et al., 2020; Konings et al., 2019).

Most existing SHR-related research has focused on testing the sensitivities of SHR to environmental variations through multi-factorial manipulation experiments at small scales like soil warming (Noh et al., 2016; Schindlbacher et al., 2009), rainfall exclusion (Hinko-Najera et al., 2015; Huang et al., 2018), water addition (Liu et al., 2018a; Zou et al., 2018), and nitrogen fertilization experiments (Chen et al., 2018; Peng et al., 2018). Although these studies enable us to understand

local SHR responses under different environmental conditions, large-scale spatial information of SHR is still limited, and contains large uncertainty. For example, global SHR estimates from Earth System Models (ESMs) range from 40 to 70 PgC yr^{-1} during 1965 to 2004 (Hashimoto et al., 2015; Shao et al., 2013) with large inter-model differences. Apart from these ESM estimates, we know of only four global SHR maps available at present (Table 2.1). The first data-driven SHR map was generated by Hashimoto et al. (2015) who upscaled *in situ* measurements of soil respiration with a modified version of functional relations from Raich & Potter (1995) and Raich et al (2002) to calculate total soil respiration using monthly temperature and precipitation, and then used a constant partitioning ratio to scale down total soil respiration to SHR. One limitation acknowledged by this study is that only 53 sites from Bond-Lamberty et al (2004) were used to derive that coarse ratio. Warner et al (2019) used a similar approach, first computing total soil respiration and then SHR from a partitioning ratio, to generate a static high resolution global SHR map. Tang et al (2020) used Random Forest model to produce a data-driven global SHR dataset but this lacked uncertainty evaluation. Finally, Konings et al. (2019) employed a constrained carbon balance framework using atmospheric inversion based on net ecosystem productivity, solar-induced fluorescence based GPP, and modeled carbon use efficiency to produce a top-down global SHR estimation; this is available at relatively coarse spatial resolution ($4^o \times 5^o$) and for a short time period (2010-2012), which limits its validation against *in situ* measurements. Considering the limitations of the above-mentioned datasets, there is a clear need for spatially explicit data-driven global-scale SHR maps at a finer resolution and for a longer time period with full uncertainty accounting, which can be used for evaluation and optimization of process-based models (Li et al., 2016; Huang et al., 2020).

Table 2.1 Comparison with previously-published respiration datasets. Rs: soil respiration.

Data type	Reference	Target variable	Number of site data	Method	Period	Spatial resolution	Uncertainty
Site-level data	Bond-Lamberty & Thomson (2010)	Rs, SHR	3379 records of Rs; 333 records of SHR (if we use same filtering criterion)	Collecting published studies	1961-2007	-	-
Global map	Hashimoto et al (2015)	Rs, SHR	1638 records of Rs	Monthly Rs=f(monthly temperature, monthly precipitation, precipitation of the previous month) A globally constant coarse ratio is used to transform Rs to SHR: ln(annual SHR)=1.22+0.73*ln(annual Rs)	1965-2012	0.5°×0.5°	-
	Tang et al (2020)	SHR	504 records of SHR (with update from Chinese publications)	Random Forest	1980-2016	0.5 °×0.5°	-
	Warner et al (2019)	Rs; SHR	2657 records of Rs	Quantile Regression Forest on Rs, and empirical equation on SHR.	-	1km	Sampling bias uncertainty
	Adachi et al (2017)	Rs	Only 5 sites were used in validation	Empirical equation	2001-2009	4km	-

	Konings et al (2019) – top-down	SHR	-	Inverting land surface carbon balance	2010-2012	4°×5°	Inversion uncertainty
	This study	SHR	455 records of SHR (after filtering)	Random Forest	1985-2013 (overlapped period affected by the explanatory variables)	0.5°×0.5°	Extrapolation uncertainty and uncertainty from alternative gridded input datasets

A decade ago, Bond-Lamberty & Thomson (2010) compiled a large soil respiration database — the Global Soil Respiration Database (SRDB), with soil respiration observations from peer-reviewed literature studies. The number of soil respiration records has reached 6,634 (4,111 valid values) in the latest SRDB 4.0 (Bond-Lamberty & Thomson, 2018) although SHR observations are far fewer (674 valid values before filtering); very recently, the SRDB 5.0 (Jian et al. 2021, not used here) was released with 1,147 annual SHR values. A data-driven SHR estimate from site to regional even global scale is thereby becoming feasible now, and Bond-Lamberty et al. (2016) suggested that machine learning could be an ideal tool towards the large-scale data-driven SHR estimation. Machine learning algorithms are powerful tools for data-driven up-scaling estimation of a target variable in ecological studies (Jung et al., 2011; Steidinger et al., 2019; Yao et al., 2018). Research on predictions of carbon or water flux (Jung et al., 2010; Zeng et al., 2014) and crop yield (Cai et al., 2019; Feng et al., 2019) have affirmed the utility of those algorithms. Estimation with such data-oriented techniques gives us a new opportunity to evaluate SHR and its dynamics in response to environmental variations globally.

In this study, we apply Random Forest (RF) algorithms to estimate global annual SHR at 0.5°×0.5° spatial resolution over the period 1985-2013 with meteorological, edaphic factors and GPP as explanatory variables. With this method, we can produce an ensemble of different data-driven SHR gridded dataset at global scale over last three decades, and we are also able to examine the contribution of dynamic climate drivers to SHR inter-annual variability (IAV), including annual temperature, precipitation or soil moisture, and radiation.

2.4 Materials and Methods

2.4.1 Soil respiration database

The Global Soil Respiration Database (SRDB), is composed of soil respiration measurements from peer-reviewed studies. It was first released in Bond-Lamberty & Thomson (2010) and updated in Bond-Lamberty & Thomson (2018) as SRDB version 4.0. We used 455 site-year observations after data filtering. There are 290 sites in total and most sites have records less than 3. Our data filtering criteria included: 1) removing records without detailed temporal, coordinates and annual SHR information, and 2) excluding observations from manipulation experiments and soda lime measurements, which tend to underestimate soil CO_2 fluxes (Haynes & Gower, 1995). Records using isotope, gas chromatography or other measurements were retained. Figure 2.1 shows that current SHR observations after filtering mainly distributed in temperate zones, with higher sample density in East Asia, Europe and North America. These available observations belong to seven ecosystem types (Friedl et al., 2010).

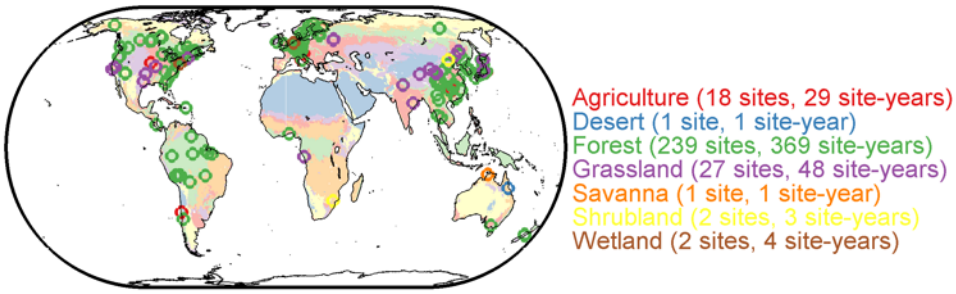

Figure 2.1 The spatial distribution of selected soil heterotrophic respiration observation sites (bold circles) by ecosystem type. The land cover used to define ecosystems from MCD12Q1 is shown in a color lighter than the circles in same category. Numbers in brackets denote the available sites and records for a given ecosystem.

Here we introduce different climatic, soil moisture and GPP datasets that are used to produce large ensemble global SHR datasets by upscaling SRDB point data, which improves on previous studies with only few available SHR members resulting in incomplete uncertainty accounting.

2.4.2 Climatic datasets

2.4.2.1 Temperature, precipitation and radiation

CRUNCEP

The climatic variables of annual temperature, annual precipitation and annual short-wave radiation used in this study are obtained from the CRUNCEP v6.1 (Viovy, 2015) covering the period 1901 to 2015. CRUNCEP is a combination of two existing datasets: the Climate Research Unit (CRU) TS3.2 observation-based monthly climatological data in spatial resolution of 0.5°×0.5°, and the National Center for Environmental Prediction (NCEP) reanalysis product in 2.5°×2.5° and 6-hour temporal step. The latter is used to define the diurnal and daily variation of the climate forcing.

CRUJRA

CRUJRA v1.1 is based on the same methodology as CRUNCEP but uses the Japanese Reanalysis Data (JRA) produced by the Japanese Meteorological Agency (JMA) with a spatial resolution of 0.5°×0.5°adjusted to match the CRU TS 3.26 data (Harris et al., 2014; Kobayashi et al., 2015). These data are available at a 6-hour time-step from 01/1901 to 12/2017. The annual temperature, annual precipitation and annual short-wave radiation from CRUJRA are also used in this study.

Princeton climate dataset

This global meteorological forcing dataset is a blend of NCEP/NCAR reanalysis data and a series of global observations to form global 0.25°×0.25° daily temperature and precipitation datasets from 1948 to 2016 (Sheffield et al., 2006). We aggregate daily data to annual values first.

WFDEI meteorological forcing dataset

This WFDEI meteorological forcing dataset is a combination of ERA-interim re-analysis data with daily variability and monthly in-situ observation. There are two precipitation products available from WFDEI: one is corrected using CRU observations, and the other using the Global Precipitation Climatology Centre (GPCC) dataset (Weedon et al., 2014). WFDEI-CRU and WFDEI-GPCC are both used in this study. These two datasets span from 1979 to 2016 and are provided at 0.5°×0.5° spatial resolution.

Climate Prediction Center (CPC)

This CPC climatological dataset includes daily maximum and minimum temperature (t_{max} and t_{min}) and daily precipitation. Daily average temperature is generated by averaging t_{max} and t_{min}. Then the daily temperature and daily precipitation are aggregated to annual values. This dataset starts from 1979, has been updated through 2021, and is available at 0.5°×0.5°.

2.4.2.2 Soil moisture datasets

CPC soil moisture

The CPC monthly soil moisture dataset is estimated by a one-layer leaky-bucket model (Huang et al., 1996; Van den Dool et al., 2003). The driving fields for the model include temperature and precipitation from CPC precipitation reconstruction over Land (Chen et al., 2002) and CPC Global Land Surface Air Temperature Analysis (Fan & Van den Dool, 2008). This dataset starts from 1948 and updates in real time (currently to 2021), with a spatial resolution of 0.5°×0.5° (Fan & van den Dool, 2004). The CPC moisture is calculated with a soil depth of 1.6 m.

Gravity Recovery and Climate Experiment terrestrial water storage reconstruction (GRACE-rec TWS)

Humphrey et al. (2017) constructed a statistical model by linking the anomalies of the main meteorological drivers to the terrestrial water storage (TWS) anomalies observed by the GRACE satellite after 2002. The pre-2002 TWS anomalies are reconstructed based on this calibrated statistical model, driven by precipitation and temperature. This reconstructed TWS dataset covers 1985-2015 and is provided at a spatial resolution of 0.5°×0.5°. It should be noted that this variable is not equal to soil moisture but also includes change in land ice, and free water (Humphrey et al., 2017). In the results section below, "GRACE-rec" is used as an abbreviation for GRACE reconstruction.

Global Land Data Assimilation System (GLDAS) version 2

GLDAS version 2 data is composed by GLDAS 2.0, which uses the Princeton meteorological data as forcing data for 1948-2010, and GLDAS 2.1, which is forced by a combination of model and observation based datasets from 2000 to present (Beaudoing & Rodell, 2016; Rodell et al., 2004). The output soil moisture is at 0.25°×0.25° and has four soil layers, 0-0.1m, 0.1-0.4m, 0.4-1.0m, and 1.0-2.0m. We take the sum of soil moisture in these four layers.

2.4.3 Soil properties datasets

Soil carbon content

Soil carbon content is extracted from Harmonized World Soil Database (HWSD), which is produced by FAO and IIASA by combining existing global regional and national inventories for soil information in over 15000 different soil mapping units (Nachtergaele et al., 2010; Wieder et al., 2014). Top-soil (0-0.3m) and sub-soil (0.3-1.0m) organic carbon content are provided and employed.

Soil nitrogen density

We also used a soil nitrogen density dataset (unit: g N m^{-2}) from Global Gridded Surfaces of Selected Soil Characteristics developed by the International Geosphere-Biosphere Program Data and Information System (IGBP-DIS). A statistical bootstrapping approach is applied by the SoilData System to link the global pedon records to the FAO/UNCESCO digital soil map. The total soil nitrogen content is for a soil depth of 0-1.0m. Soil nitrogen density was treated as explanatory variable for SHR estimate.

2.4.4 Land cover dataset

The MODIS land cover type product (MCD12Q1) is derived using a supervised decision tree classification algorithm (Friedl et al., 2010). We group land cover types in the MODIS product to correspond with the classification in SRDB following Table S1. In this study, we do not consider the effect of land use/cover change (cf. Huang et al. 2020), and we use a static land cover map in 2001 as input for the estimation model.

2.4.5 Gross primary productivity datasets

FLUXCOM

GPP drives net primary production and litterfall, thus it is used as a predictor of SHR. We used an ensemble of gridded GPP products generated by training three machine learning algorithms (Random Forest, Multivariate Adaptive Regression Spline, and Artificial Neural Network) on daily GPP estimates from 224 flux towers (Jung et al., 2017; Tramontana et al., 2016). The combinations between three available algorithms and two GPP estimates (due to two partitioning methods) produce 6 GPP ensembles spanning 1980-2013 in monthly intervals. Each GPP member is used as one GPP data source for SHR estimation.

P-model GPP

P-model is a Light Use Efficiency (LUE) model (Wang et al., 2017), in which monthly LUE is predicted on the basis of changing environmental conditions and an optimality criterion with respect to stomatal behaviors and other related traits (Prentice et al., 2014). Daily GPP, which is then calculated by monthly LUE and daily varying absorbed photosynthetically active radiation, can be further aggregated to annual time step. This product is released at a spatial resolution of 0.25×0.25°and over a time span of 1982-2016 (Stocker et al., 2019). This GPP dataset includes the soil moisture effects on LUE.

2.4.6 Random Forest algorithm and its performance

To generate a data-driven SHR estimation, we implemented a Random Forest ensemble machine learning algorithm, as in former carbon research studies (Baccini et al., 2012; Buermann et al., 2018; Jung et al., 2017; Schwalm et al., 2017; Zhu et al., 2017). Random Forest, as one of the widely used and fast running algorithms, is suited for handling non-linear relationship between the target and the corresponded independent variables, without requiring predefined functional forms or a normal sample distribution (Breiman, 2001). A RF model consists of multiple uncorrelated regression trees, each of which uses a subset of all the training samples with replacement (~63%) to reach the same total sample size and random subset of explanatory variables (Breiman, 2001). This bootstrapping procedure can decrease the influence of noise and outliers, and raise the stability of model predictions, by averaging over all constructed trees. In our study, the number of trees is set to be 1,000. In addition to the mean value output from 1,000 trees, we also obtain 95% confidence interval of outputs from these trees. The feature importance is provided by assessing the difference in prediction error (Mean Squared Error for this study) on out-of-bag data before and after variable permutation.

To get a robust evaluation of model performance, we use Leave-One-Out Cross Validation (hereinafter LOOCV). The goal of cross-validation is to test the model's ability to work on independent samples, in order to identify problems like over-fitting. Each time a sample is excluded and the remaining samples are used to train a RF model, the predicted value of the excluded one is estimated by that fitted model. Instead of taking average of out-of-bag R^2 from all trained RF models,

we use the LOOCV-based predicted value of each observation to get R^2 as metric. LOOCV is used both at the sample and site levels.

Since the observed SHR data are provided at annual timescale, we need to aggregate the high temporal resolution to coarser time scale (annual) as inputs to the RF model. The RF model was first fitted on our filtered 455 site-year observation dataset, and then applied to predict annual SHR for each 0.5°×0.5° grid cell driven by meteorological factors and other environmental indicators (Table 2.2). We obtain 126 (6*7*3=126) global SHR members in total derived from crossing combinations of six climate datasets, seven GPP datasets (six members from FLUXCOM and one member from P-model) and three soil moisture / TWS datasets (CPC, GRACE-rec and GLDAS) used as gridded inputs to RF model. Considering that different climate datasets (temperature and precipitation), soil moisture datasets, and GPP datasets served as our efficient explanatory variables and their different time period coverage, we choose 1985-2013 as the common time length for estimation.

Table 2.2 Explanatory variables used for soil heterotrophic respiration upscaling and their data access.

Variable name	Variable variability state	Data access
Annual temperature	Inter-annual	CPC: https://www.esrl.noaa.gov/psd/data/gridded/data.cpc.globaltemp.html https://www.esrl.noaa.gov/psd/data/gridded/data.cpc.globalprecip.html CRUNCEP: http://dods.extra.cea.fr/store/p529viov/cruncep/ CRUJRA: http://dx.doi.org/10.5285/13f3635174794bb98cf8ac4b0ee8f4ed Princeton: http://hydrology.princeton.edu/data.pgf.php WFDEI: http://www.eu-watch.org/data_availability
Annual precipitation	Inter-annual	
Annual short-wave radiation	Inter-annual	
Annual soil moisture	Inter-annual	CPC: https://www.esrl.noaa.gov/psd/data/gridded/data.cpcsoil.html. GRACE reconstruction: http://doi.org/10.5905/ethz-1007-85

		GLDAS: https://disc.gsfc.nasa.gov/datasets/GLDAS_NOAH025_M_V2.1/summary
Annual gross primary productivity	Inter-annual	FLUXCOM: https://www.bgc-jena.mpg.de/geodb/projects/Home.php P-model: https://doi.org/10.5281/zenodo.1423484
Annual nitrogen deposition	Inter-annual	https://daac.ornl.gov/NACP/guides/NACP_MsTMIP_Model_Driver.html
Soil carbon content	Static	https://daac.ornl.gov/cgi-bin/dsviewer.pl?ds_id=1247
Total nitrogen density	Static	https://daac.ornl.gov/SOILS/guides/igbp-surfaces.html
Land cover classification	Static	https://modis.gsfc.nasa.gov/data/dataprod/mod12.php

2.4.7 Soil heterotrophic respiration datasets used for comparison

Soil respiration dataset from Hashimoto et al (2015)

Hashimoto et al. (2015) applied climate-driven functions modified from Raich et al (2002) to fit soil respiration from 1638 data points. The soil respiration was solely driven by temperature and precipitation, and the partitioning between its autotrophic and heterotrophic part followed two fixed parameters summarized from the data in Bond-Lamberty et al. (2004) (an approach also used by Warner et al. 2019). Two parameters in the model were assumed to be globally constant, so that the spatial heterogeneity in the Hashimoto et al. (2015) dataset is provided only by variations in climatic drivers. This data-driven model was extrapolated to 1901-2012. We downloaded this dataset from http://cse.ffpri.affrc.go.jp/shojih/data/index.html.

Soil heterotrophic respiration data from Tang et al (2020)

Tang et al (2020) upscaled site-level observations in SRDB4.0 using Random Forest model to produce an annual global SHR dataset spanning 1980-2016 in spatial resolution of $0.5^{o}\times0.5^{o}$. The explanatory variables include mean annual temperature, mean annual precipitation, diurnal temperature range, nitrogen deposition, Palmer Drought Severity Index, shortwave radiation, soil carbon content, soil nitrogen content and soil water content. We downloaded this dataset from https://doi.org/10.6084/m9.figshare.8882567.

Top-down SHR dataset from Konings et al (2019)

Konings *et al* (2019) produced a top-down SHR estimate from 2010 to 2012 in spatial resolution of $4^{o}\times5^{o}$. Total ecosystem respiration was first derived from carbon balance method by the difference between GPP and net ecosystem productivity (NEP) and carbon use efficiency from model-data fusion framework was used to partition the autotrophic and heterotrophic respiration. NEP is from atmospheric inversion of NASA Carbon Monitoring System-Flux. GPP is based on satellite-observed solar-induced fluorescence. Monthly top-down SHR data was aggregated to an annual time step.

TRENDY global models

We use simulations of 12 dynamic global vegetation models from the project "Trends and drivers of the regional scale sources and sinks of carbon dioxide" (TRENDY) v6 for the period of 1985-2013. These models used a common set of observed climate, atmospheric CO_2 concentration, land-use change, and experimental protocols. Our analysis uses model SHR outputs (named as Rh in models) under the TRENDY "S3" experiment (which included the effects of time-varying CO_2 concentrations, climate change, and land use change). The 12 models are CABLE (Haverd et al., 2018), CLASS-CTEM (Melton & Arora, 2016), CLM4.5 (Oleson et al., 2013), ISAM (Jain et al., 2013), JSBACH (Reick et al., 2013), JULES (Clark et al., 2011), LPX (Keller et al., 2017), OCN (Zaehle & Friend, 2010), ORCHIDEE-MICT (Guimberteau et al., 2018), ORCHIDEE (Krinner et al., 2005), VEGAS (Zeng et al., 2005) and VISIT (Kato et al., 2013).

2.4.8 Attribution analysis for SHR inter-annual variability (IAV)

We apply the carbon flux anomaly decomposition approach proposed in Jung et al. (2017) to diagnose the contribution of different climate variables on SHR IAV, including annual temperature (TEMP), annual water availability proxies (precipitation or soil moisture, PREC or SMC) and annual short-wave radiation (RAD). We first obtain detrended annual SHR anomalies and climate indicators

anomalies in each pixel by removing their linear trend on annual basis (least-squares fitting). Then we implement multiple linear regressions with zero-intercept between anomalies in SHR and all variables to separate their contribution. The estimated SHR sensitivity to climate anomaly (shown as the linear regression slopes a_s^{var} in Equation 1) multiplied by the corresponding forcing anomaly (shown as $\Delta var_{s,y}$ in Equation 1) defines the SHR anomaly component $\Delta SHR_{s,y}^{var}$ driven by each forcing variable. These components can be added together to form a reconstructed SHR anomaly ($\Delta SHR^*_{s,y}$ in Equation 2). A correlation coefficient is calculated to demonstrate the consistency between the climate-reconstructed SHR anomalies ($\Delta SHR^*_{s,y}$) and the detrended estimates ($\Delta SHR_{s,y}$).We also implement similar procedures on SHR from the Hashimoto and Tang datasets and TRENDY models. In all attribution analyses (except Hashimoto), both precipitation and soil moisture are considered as water-related proxies in the regression processes (Equation 1 - 4).

$$\Delta SHR_{s,y,e} = a_{s,e}^{TEMP} \times \Delta TEMP_{s,y,e} + a_{s,e}^{PREC} \times \Delta PREC_{s,y,e} + a_{s,e}^{RAD} \times \Delta RAD_{s,y,e} + \in_{s,y,e} \quad (1)$$

$$\Delta SHR^*_{s,y,e} = \Delta SHR_{s,y,e}^{TEMP} + \Delta SHR_{s,y,e}^{PREC} + \Delta SHR_{s,y,e}^{RAD} \quad (2)$$

$$\Delta SHR_{s,y,e} = a_{s,e}^{TEMP} \times \Delta TEMP_{s,y,e} + a_{s,e}^{SMC} \times \Delta SMC_{s,y,e} + a_{s,e}^{RAD} \times \Delta RAD_{s,y,e} + \in_{s,y,e} \quad (3)$$

$$\Delta SHR^*_{s,y,e} = \Delta SHR_{s,y,e}^{TEMP} + \Delta SHR_{s,y,e}^{SMC} + \Delta SHR_{s,y,e}^{RAD} \quad (4)$$

Subscripts s, y and e refer to index of grid cells, every year from 1985 to 2013, and one member from the SHR ensemble, respectively.

2.4.9 Factorial analysis for SHR trend

To understand the controlling variables for the regional variation in SHR trend map, we performed factorial estimation by removing the inter-annual variation of each dynamic explanatory variable, that is, keeping each variable static during 1985-2013. Dynamic explanatory variables of annual temperature, annual precipitation, annual radiation, annual GPP, annual soil moisture and annual nitrogen deposition were tested.

2.4.10 Statistical software

All data processing and statistical analysis were performed in R statistical software (R Development Core Team, 2019) version 3.5.0 using packages “randomForest” version 4.6-14 (Liaw & Wiener, 2018), “raster” version 3.0-7 (Hijmans et al., 2019), “pracma” version 2.2.5 (Borchers, 2019).

2.5 RESULTS

2.5.1 Performance of Random Forest via cross validation

After testing on all combinations of these temperature and precipitation datasets, soil moisture and GPP choices, we derived the LOOCV R^2 of these RF models, which is 0.57 ± 0.01 (0.01 is the standard deviation of LOOCV R^2 from all combinations). We can see that at least at site-level, different climate datasets sources, soil moisture and GPP variable choices do not result in any R^2 or RMSE difference (Figure 2.2a). We also try leave-one-site-out evaluation, which resulted in a lower R^2 (Figure 2.2b). Tests of model performance with more input explanatory variables are shown in Supplementary Figures S1-S3. We show the importance of different variables in Figure 2.2c. Annual precipitation and annual temperature are the two most important variables, whereas static variables such as land cover type, soil carbon and nitrogen content contribute relatively less to model performance.

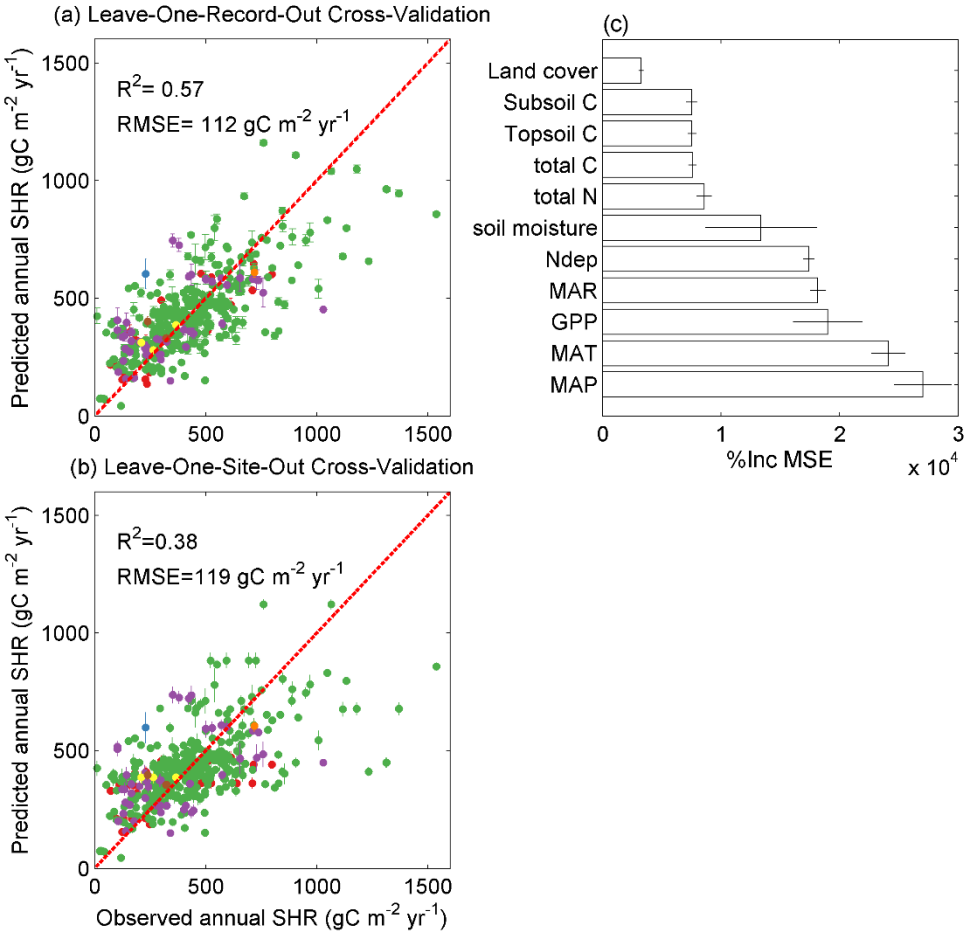

Figure 2.2 The performance of Random Forest evaluated by (a) Leave-One-Record-Out Cross Validation and (b) Leave-One-Site-Out Cross Validation. The error bar on each point denotes the standard deviation of soil heterotrophic respiration (SHR) predictions estimated on the basis of different temperature and precipitation, soil moisture and GPP datasets combinations. Different colors show the land cover types of the observation data (same color setting as Figure 2.1). (c) Feature importance scores ranking deduced from increase of mean squared error (MSE) after permuting variable. MAT (annual temperature), MAP (annual precipitation), MAR (annual radiation), Ndep (nitrogen deposition), GPP, soil moisture are time specific values depending on the observation year.

2.5.2 Spatiotemporal pattern of global SHR

The spatial pattern of mean annual SHR at 0.5°×0.5° spatial resolution during 1985-2013 is shown in Figure 2.3a, and follows the geographic GPP variations to a large degree (see Figure S4). Annual SHR decreases from tropics to high-latitude area, with the highest values in wet tropics of exceeding 800 gC m^{-2} yr^{-1} and the lowest in northern boreal area including Alaska, northern Canada and Siberia area (less than 200 gC m^{-2} yr^{-1}). Such a latitudinal SHR gradient particularly appears in Australia (from coastal area to inland), Africa and South America. Similar spatial gradients appear among all members of our data-driven SHR estimates.

The global mean of our data-driven SHR is 46.8 Pg C yr^{-1} over 1985-2013, (95% confidence interval: 38.6-56.3 Pg C yr^{-1} based on the estimates of 1000 Random Forest model trees), with an increasing trend of 0.03 Pg C yr^{-2} (0.015-0.044 Pg C yr^{-2}, $P < 0.01$), which is similar to the 1.2% increase of SHR detected in Bond-Lamberty et al (2018) over a similar timespan. The global total SHR is close to global total NPP (48.8 Pg C yr^{-1} during 2001-2015, Table S2) when we applied the same spatial mask. We do expect SHR to be globally smaller than NPP, because of lateral export by ecosystems that reduce considerably the fraction of NPP given to soil as litter for SHR (Ciais *et al*., 2020).

The choice of soil moisture variables contributes more to the difference among these data-driven SHR members rather than that of GPP, temperature and precipitation data sources (Figure S5). For example, using CPC soil moisture data produces an almost 1 Pg C yr^{-1} lower global SHR value than other data-driven estimates using GLDAS soil moisture (Figure S5c). In spite of these differences, the total amount of all our data-driven SHR members consistently displays a drop in 1992 and a peak in 2010 across all members (Figure S5).

2.5.3 Comparison with previous data products and models

Our data-driven SHR estimation is close to that of Hashimoto et al (2015), who predicted a global flux of 46.5 Pg C yr^{-1} and temporal trend of 0.05 Pg C yr^{-2} (Figure 2.4). These two sets of gridded SHR products also show similar frequency distributions, although the spatial variation of Hashimoto et al. (2015) as smoother, as SHR in that dataset depends only on climate (Figure 2.3b). Compared to our data-driven estimate, Hashimoto *et al* (2015) presented higher SHR values in boreal area and lower values in tropics (Figure S6a, S6b, S7). Conversely, Tang et al (2020) found lower values in Amazon and central Africa and higher values in temperate areas; their global total SHR amount of 46.9 Pg C yr^{-1} after applying same land mask was similar (Figure S6c, S6d). Global total amount of top-down SHR was about 40.8 Pg C yr^{-1} during 2010-2012 (Konings *et al*., 2019). The top-down SHR shows more distinct spatial gradients (Figure 2.3d) and larger values than this study in both tropics and boreal area (Figure S6e, S6f).

The ensemble mean SHR over all TRENDY models is larger than empirically-estimated SHR products, increasing from 49.9 Pg C yr^{-1} to 53.8 Pg C yr^{-1} during our studied period, due to a four times larger temporal trend (0.14 Pg C yr^{-2} versus 0.03 Pg C yr^{-2} in our data-driven products) (Figure 2.4). The TRENDY multi-model ensemble mean shows more drastic geographic contrasts across the globe (Figure 2.3e), with a different frequency distribution of SHR from our data-oriented estimate (Figure 2.3a, 2.3e). Large inter-model discrepancies are present among TRENDY models both for global totals and spatial details; the standard deviation can be as high as 8~9 Pg C yr^{-1} in each year and both underestimation and overestimation of SHR appear in different models in comparison to our data-oriented products (Figures S6g, S6h, S8-S9).

With respect to the spatial distribution of temporal trend of SHR, we can find that there is no uniform trend in our data-driven products (Figure S10a). To understand the controlling variables for

the regional variation in SHR trend map, here we ran factorial estimation for one SHR member only for efficiency (see Methods 2.4.9). Through comparison between Figure S11 and S12 we can see that change in soil moisture dominates the negative SHR trend in South America and central Africa, as well as the positive trend in Arctic tundra, and the increase in atmospheric nitrogen deposition contributes to patterns of positive SHR trend in Asia near urbanized areas. Tang et al (2020) found clearly positive SHR trends in Arctic tundra areas (Figure S10c). Hashimoto et al (2015) and TRENDY ensemble mean also produced positive trends in most areas, matching their increasing global trends (Figure 2.4, S10b, S10d).

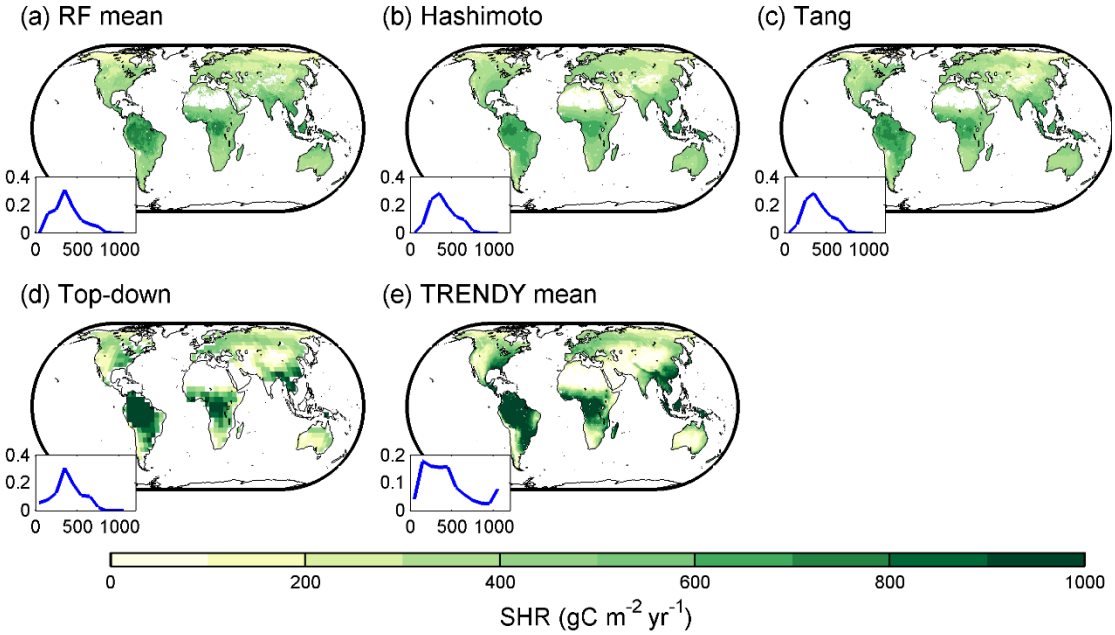

Figure 2.3 Spatial pattern of (a) ensemble mean of our data-driven soil heterotrophic respiration (SHR) members, (b) Hashimoto et al (2015), (c) Tang et al (2020), (d) top-down and (e) TRENDY model ensemble mean. Frequency distribution of SHR in different levels for each SHR dataset is shown in the bottom left of each panel. It should be noted that the studied period of Hashimoto product is up to 2012 and the studied period of top-down SHR dataset is between 2010-2012.

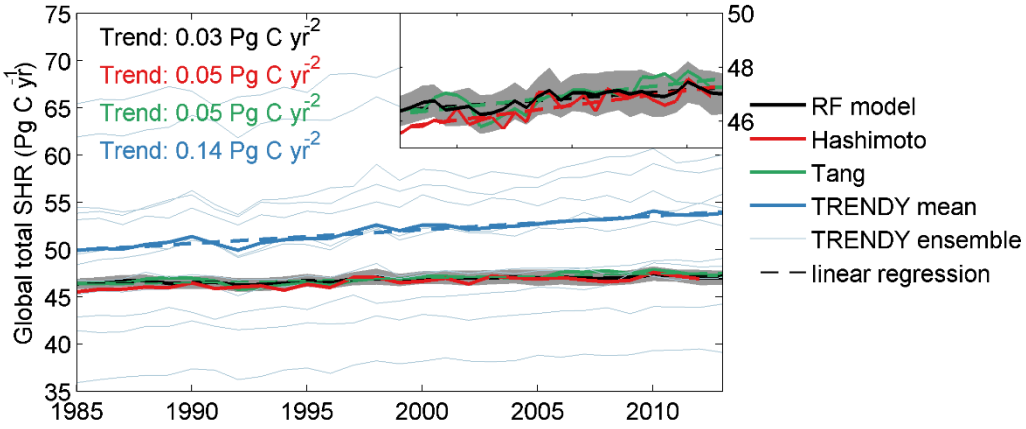

Figure 2.4 Global total amount of soil heterotrophic respiration (SHR) over 1985-2013. The shaded area in gray indicates the spread over all members from Random Forest models (RF). The zoomed plot in the top right shows the global mean of our data-driven ("RF"), Tang and Hashimoto SHR estimates more clearly. The dashed lines refer to fitted global total SHR time series against time. The global total amount of SHR in each TRENDY model is shown as thin blue line.

2.5.4 SHR anomalies in relation to meteorological factors

We attribute the factors contributing to SHR inter-annual variability (IAV) using a linear decomposition approach described in section 2.4.8. We first verified that the SHR anomaly reconstructed with climate factors can correctly reproduce the detrended SHR time series spatially (evaluated by the correlation coefficients as shown in Figure S13). It should be noted that both soil moisture and precipitation are used in upscaling of SHR but only one water proxy is used in the reconstruction of SHR anomalies. The quality of the reconstruction is impacted by the choice of water-related variables in linear decomposition process. For example, when CPC soil moisture is employed in the up-scaling of SHR, including it allows for better reconstruction of the SHR IAV than when using precipitation (Figure S13). Conversely, when using GLDAS soil moisture as input, precipitation has better performance in reconstructing SHR anomaly than the soil moisture variable. When the reconstructed anomalies are integrated to the global scale, we find that the correlation coefficient between reconstructed and detrended SHR anomalies can reach 0.9 when annual precipitation is used as a predictor, and 0.94 when soil moisture is used.

In general, we can see from Figure 2.5 that the globally integrated SHR IAV is mainly controlled by water availability, with higher correlation coefficients between reconstructed SHR and the water related SHR anomalies (SHR^{PREC} or SHR^{SMC}). However, the strength of this control varies depending on the water availability variables that are used in the SHR estimation and subsequent regression. For SHR up-scaled using GRACE-rec TWS, the correlation coefficient between SHR^{SMC} and SHR IAV is two times higher than when using precipitation as a regressor, although the overall reconstruction efficiency does not differ greatly (Figure S14). This should be expected since terrestrial water storage anomaly is not always comparable to soil moisture and precipitation. Specifically, there are two most prominent anomalies in all data-driven SHR estimation members in 1992 and 2010 consistently (Figure S15). According to the similarity between SHR IAV driven by each climatic factor and the detrended series locally, we found that the negative SHR anomaly in 1992 is particularly driven by water-related proxies under cooler and drier climate after the Mount Pinatubo eruption (Figures S16 - S18). The contribution of precipitation variability to the positive SHR anomaly in 2010 is larger than the one from temperature anomaly (Figure 2.5). We also identified the climatic drivers for the Tang et al (2020) SHR product, and found that, similarly, precipitation or soil moisture anomaly dominate its SHR IAV (Figure S19).

We analyzed the drivers for SHR IAV from TRENDY model ensembles using the same approach. For TRENDY models, their simulated soil moisture is also used in the regression. In general, climate variables had a good capacity for reconstructing TRENDY SHR anomalies (Figures S20-S21). SHR IAV from TRENDY ensemble mean displays dominance by water availability at global scale (Figures 2.5b and 2.5d). The driving factors for SHR IAV differ widely among TRENDY models (Figure S22), with six models showing dominance of water availability fluctuation on SHR IAV at the global scale, and five exhibiting dominance by temperature. The TRENDY models capture the negative SHR anomaly in 1992 and precipitation variability can better account for that. With regard to the distinctly positive anomaly in 2010, TRENDY ensemble mean also shows an apparent dominance of precipitation variability (Figure 2.5b). We repeated the analysis on the Hashimoto dataset and we show the result in the Supplementary Information section of this paper (Text S1).

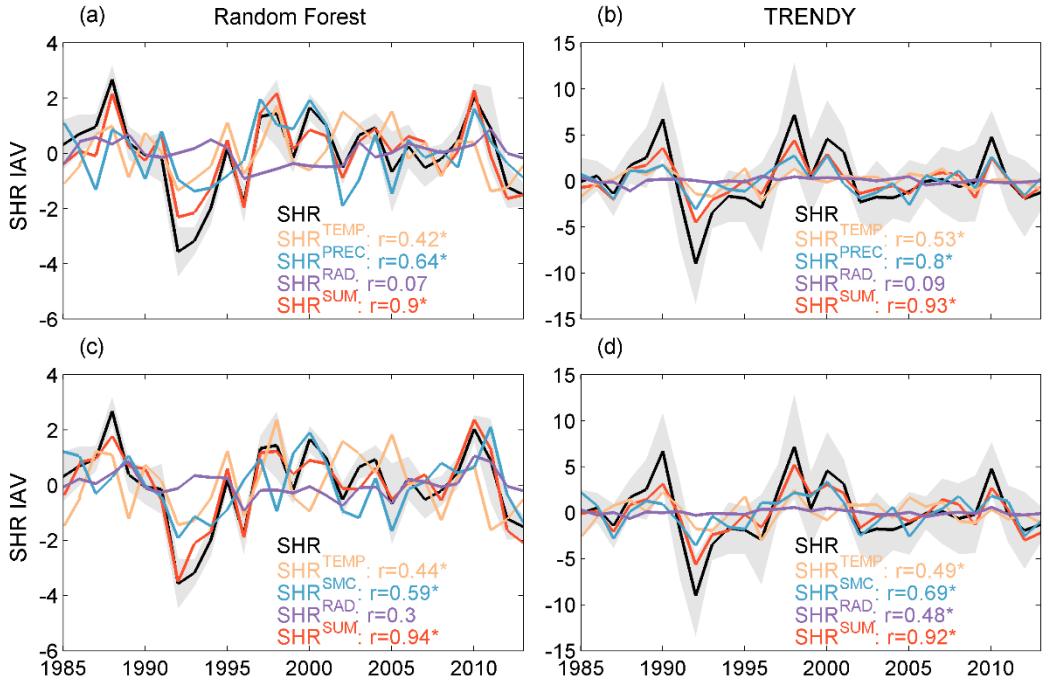

Figure 2.5 Climatic variables controls on soil heterotrophic respiration (SHR) inter-annual variability at global scale. The black lines indicate detrended SHR anomalies. The colored lines indicate SHR anomalies driven by different climate factors. 'SUM' means the sum of SHR IAV driven by three climatic factors. The top panels include regressions using precipitation as a water proxy; in the bottom panels, the water proxy is soil moisture. The correlation coefficient between SHR anomaly and the component driven by a forcing is labeled. An asterisk denotes the significance of the corresponding correlation coefficient ($P < 0.05$). Shaded areas represent the spread among ensembles of Random Forest or TRENDY products. Due to the difference between soil moisture and water storage variables, only SHR estimated using soil moisture (CPC and GLDAS) is shown here. Regression for SHR estimated from GRACE-rec TWS is shown in Figure S14.

2.5.5 Biome-scale SHR anomalies attribution

To check whether the dominance of water availability on SHR IAV differs between biome types and regions, we aggregate SHR anomalies to tropical forest, extra-tropical forest, semi-arid region, Arctic tundra, grass and crop area (Figure S23, adapted from Ahlström et al. (2015)). To confirm whether the uncertainty affects the relationship between SHR and climatic factors, here we show the pattern of correlation between SHR anomaly driven by each climatic factor and SHR anomaly in Figure S24. We can find that precipitation and soil moisture significantly control the SHR IAV in Arctic tundra, semi-arid regions and extra-tropical forests. In tropical forests, as well as grass and cropland, fluctuations in both temperature and precipitation show significant effects on SHR IAV in more than half of our SHR ensembles (63 of 126 members). Such a statistically significant response to climatic factors across multiple members allows us to analyze the regional drivers of SHR IAV.

In tropical forests, SHR IAV is mainly driven by temperature variability, whereas in extra-tropical forests and semi-arid areas, precipitation variability plays a dominant role (Figure S25). Precipitation variability is comparable to temperature in driving SHR anomalies in grass and crop areas. In Arctic tundra, the dominant factor for SHR IAV is the fluctuation in soil water content, regardless of the moisture variable being used, while fluctuation in temperature seems to be less important (Figures 2.6, S25-S26). When considering regression against soil moisture, we notice that the ranking of factors is shuffled to some extent (Figures 2.6 and S25), which may be due to the difference between variability in precipitation and soil moisture regionally (Figures S17-S18). For

example, in extra-tropical areas, the importance of water availability increases greatly when regression is carried out against soil moisture (CPC or GLDAS, Figures 2.6 and S25). For the Tang dataset, we found that a dominance of precipitation or soil moisture also appears in tropical and extra-tropical forests, semi-arid areas, and Arctic tundra (Figure S27). In grass and cropland, temperature is also important for SHR IAV regionally (Figure S27). Our attribution of climatic drivers for SHR IAV differs from Tang et al (2020) mainly in tropical forests (temperature is dominant in our study vs. precipitation in Tang et al., 2020).

Attribution of the TRENDY ensemble shows consistent water-driven estimation in semi-arid areas but differs from our data-driven results mainly in the tropical forest (Figure 2.6): in these regions, TRENDY SHR IAV is mainly driven by precipitation or soil moisture variability rather than temperature variability (Figures 2.6 and S28). In extra-tropical forest and Arctic tundra, the controlling effect of temperature on TRENDY SHR anomaly is also non-negligible compared to that of water availability (Figure 2.6). In grass and crop area, TRENDY ensemble mean shows that both precipitation and soil water effects outbalance temperature effects, which does not perfectly match our estimation. Furthermore, it also should be noted that the different TRENDY models disagree on the attribution of SHR anomalies between water vs. temperature across different ecosystems (Figures S28-S29).

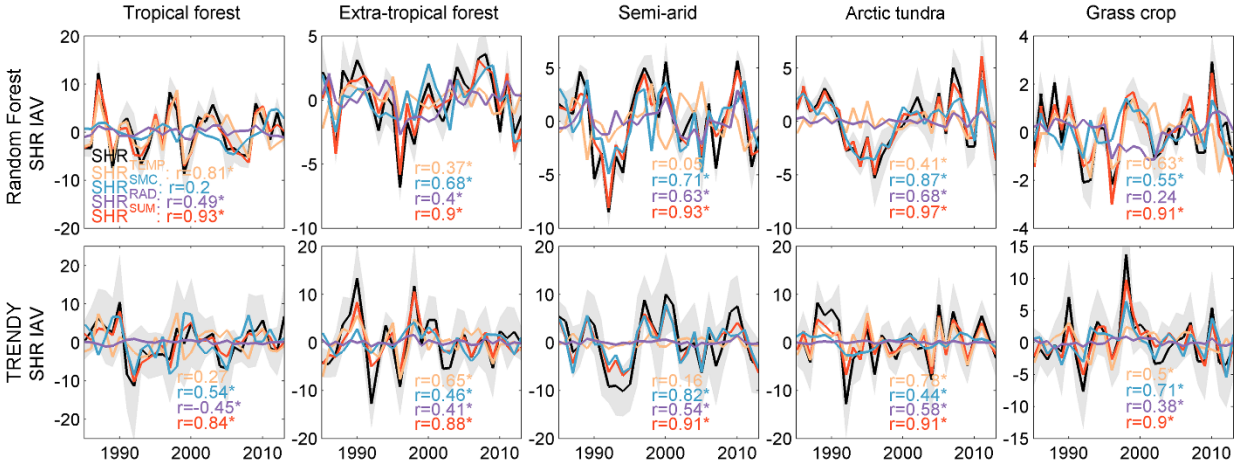

Figure 2.6 Environmental controls on soil heterotrophic respiration (SHR) inter-annual variability (IAV) in different ecosystems. Panels in top row are derived using our data-driven SHR products. Panels in the bottom row are derived using TRENDY multi-ensemble mean. The correlation coefficients between SHR IAV and SHR anomalies driven by a given factor are labeled in each panel. An asterisk denotes the significance of the corresponding correlation coefficient ($P < 0.05$). The decomposition using precipitation anomaly is shown in supplementary as Figure S25.

During the reconstruction process, we also computed the distinct sensitivities of SHR to climate factors, especially temperature and water availability (Figures 2.7 and S30). Regional heterogeneity of the sensitivity of SHR to temperature and precipitation / soil moisture may alter the overall trajectory of SHR because of coexistence of regional deceleration and acceleration of SHR and/or compensatory effects of temperature and precipitation. For our data-driven SHR members, for example, in the tropics, positive temperature sensitivity in Amazon, central Africa, as well as negative sensitivity to precipitation in these areas lead to opposite temperature and precipitation driven SHR anomalies in the cooler and drier year of 1992. In Siberia, negative SHR sensitivity to temperature and positive sensitivity to precipitation contribute to additive climate driven sub-components in IAV under warm but dry condition. The sensitivity of SHR to soil moisture depends on the dataset used, especially in boreal regions and central Africa (Figure S30). More negative sensitivity to soil moisture availability was found in wet tropics areas when using GLDAS soil moisture (0-2.0m) as a predictor

than when using CPC (0-1.6m), indicating that soil moisture increases in deeper layers can be more negatively related to SHR than changes in shallow layers if we assume little difference of soil moisture in their common depth intervals.

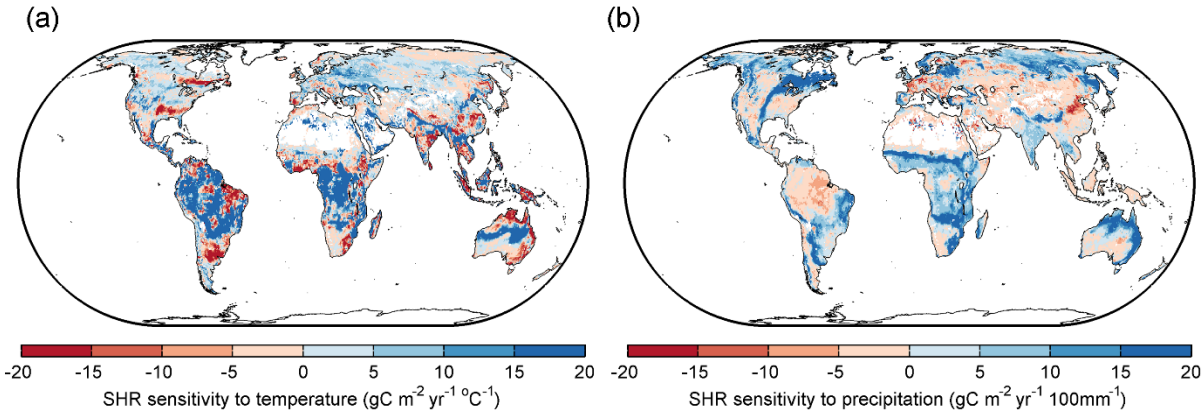

Figure 2.7 Spatial distribution of the sensitivities of our data-oriented soil heterotrophic respiration to anomalies in (a) temperature and (b) precipitation. A negative temperature sensitivity means that when temperature increases, SHR decreases.

2.6 DISCUSSION

2.6.1 Implications and future directions of data-driven SHR estimation

In this study, we generated a newly up-scaled SHR dataset using a Random Forest algorithm and explanatory variables of climatological indicators, GPP as well as soil properties. We carefully evaluated the model performance with cross-validation and assessed the estimated uncertainty, which has generally not been done in previous studies. Our products can be utilized to evaluate the sensitivities of process-based models and constrain their performances in both spatial and temporal scales (Ichii et al., 2017).

Our results exhibited both similarities and differences compared to results from previous analyses. The similarities in spatial distribution with Hashimoto et al (2015) could be due to two reasons. First, both studies used observation records from SRDB, which ensured their similar SHR range (although a more recent version of SRDB, with much more data, was used here). Second, both two studies are vulnerable to uneven sampling and potential extrapolation problem to some extent. In terms of the Tang SHR data, both differences in explanatory variables selection and sample dataset affect regional SHR variation between Tang et al (2020) and our SHR datasets, and the inclusion of records with annual SHR above 1100 gC m^{-2} yr^{-1} influences the magnitude of SHR in tropical regions (Figure S31a, d). When we exclude GPP from explanatory variables sets, SHR differs especially in central Africa and India, where inclusion of GPP helps produce higher SHR in central Africa and lower SHR in India (Figure S31a, c). It also should be noted that Tang et al (2020) included more sample data in China, which also contributes to the difference of their SHR estimation in temperate climate regions like China and Europe. RMSE from leave-one-out cross validation was 20% smaller in our study (112 gC m^{-2} yr^{-1}) compared to Tang et al (2020), with RMSE of 143 gC m^{-2} yr^{-1}.

We found that TRENDY models underestimate boreal region SHR, and overestimate SHR especially in tropics, with a conspicuous spatial contrast along latitudes (Figure S8). A misrepresentation of nitrogen constraints, and oversimplified treatment of processes like microbial dynamics and the climatological dependence of decomposition in different soil texture types, may be

responsible for this tendency to produce unrealistic SHR values compared to observations, in turn suggesting areas for focused model research and improvement (Shao et al., 2013; Yan et al., 2018). Our newly derived estimation can thus help improve model ability to accurately predict response of soil carbon to future climate change scenarios.

Nevertheless, limitations undoubtedly remain in our data-driven products, which we suggest can be split into uncertainties in the (i) underlying soil respiration observation data, (ii) the driving climate and GPP gridded data, and (iii) the up-scaling process. First of all, the uncertainty introduced by partitioning of autotrophic and heterotrophic (i.e. SHR) components of the measured soil respiration flux is poorly understood but potentially large. Approaches such as isotope labeling bring less disturbance to the root-soil system, but introduce their own uncertainties from e.g. mixing model assumptions. Root extraction methods neglect the contribution of priming mechanism (Kuzyakov & Larionova, 2005), the amplified effect of which is ~12% in permafrost ecosystem (Keuper et al., 2020). Trenching approaches feature significant disturbance but subsequent simpler inference. Better partitioning will reduce uncertainties entered into the estimation model (Carbone et al., 2016), and we suggest that it is the right time for a meta-analysis examining the potential biases of these different approaches.

Second, observation data of SHR is provided at coarse temporal resolution of a year. Our upscaled SHR dataset thus incorporates responses to environmental variations only annually, which mask different sensitivities (possibly different signs of sensitivities as well) at the seasonal scales (Shao et al., 2013). More SHR observations at daily, monthly, and seasonal measurements will help us understand more of its responses to varying environmental conditions like seasonal lagged responses (Vargas et al., 2010) and also benefit model evaluations.

Third, the biased sampling of observations at the global scale (Xu & Shang 2016, Schimel et al. 2015) forces up-scaling approaches to extrapolate to under-sampled area, affecting the accuracy of model prediction. For example, the tropics are predicted to have the largest SHR fluxes, but are greatly under-sampled, leading to the largest uncertainty in our data-driven SHR dataset. The climate space sampled by all filtered observations ranges from 11.5 mm to 5302 mm in mean annual precipitation and from -10 ℃ to 31.5 ℃ in mean annual temperature. Relatively few reported data exist from cold areas, warm dry areas, and warm humid areas (Figure S32). The space of GPP, soil moisture, soil carbon content and annual nitrogen deposition under-sampled by measurement records are shown in Figure S33. The spread of 1000 trees in Random Forest can reflect the uncertainty from such extrapolation to under-sampled domain, from which the 95% CI is 38.6-56.3 Pg C yr^{-1}. This uncertainty measure has also been used in Zeng et al (2020) for net ecosystem productivity and Warner et al (2019) as well as Stell et al (2021) for soil respiration. Through the comparison of two sources of uncertainties (alternative gridded explanatory data and uncertainty from extrapolation to under-sampled domain by spread of trees), we find that uncertainty from individual trees in Random Forest model is far larger than that from different explanatory variables datasets. Our similarity with Hashimoto dataset in spatial gradient could also be partly explained by the under-sampling issue in both studies. In the Hashimoto work, the two globally fixed parameters to derive SHR from soil respiration can possibly narrow the real range of SHR compared to broader coverage of soil respiration point data in climate space. Therefore, the priority should be more data collection in under-sampled areas to constrain the current wider prediction distributions, as an optimized network design has been demonstrated to decrease uncertainty in global estimates (Stell et al., 2021).

In addition, unlike eddy-covariance records extending more than 20 years, most available SHR observations are of short duration (the longest continuous observation lasted 6 years in SRDB 4.0). The "space substitution for time" concept is common under such circumstances but should be treated with caution since the prediction accuracy of such substitution requires consistency between temporal and spatial variation in climate space (Blois et al., 2013). Therefore, we call for more valid sub-

sampling, which can be indispensable to fill the gap between spatial and temporal climatic gradients. Further data compilation and integration are extremely valuable for upscaling and improving performances of SHR estimation models (Bond-Lamberty, 2018; Harden et al., 2018).

With regard to uncertainty emerged during the up-scaling process, it is worth noting that some variables are poorly represented within our procedure. For example, land cover is found to contribute the least to change in model error as shown in Figure 2.2c. Although our way of handling this categorical variable, one-hot encoding (Lantz, 2013), is good at tackling discrete variables, land cover's effect may covary with other environmental gradients and climatic proxies. In addition, climatological and other physiological inputs are less certain, especially in the tropics. Besides, some key explanatory variables remain unavailable currently, e.g. other nutrients like phosphorus availability, microbial activity, mycorrhizal types (Crowther et al., 2019), as well as disturbance information including land use / cover change (LUCC). The uncertainties in inputs and the lack of consideration of other potential factors can be responsible for the underestimation in prediction for observed SHR exceeding 1000gC m^{-2} yr^{-1} in tropics (Figure 2.2a). Disturbances affect how SHR varies over vegetation succession and then lead to changes of ecosystem soil carbon pools (Harmon et al., 2011), but limited mapping of this information, and the highly uncertain consequences of SHR responses to LUCC, impede our careful consideration of its effect. The treatment of disturbance history has been attempted in the case of taking stand age to account for disturbance effects on forest carbon dynamics (Xiao et al., 2014), and a similar approach could be used to extend our estimation framework toward better SHR prediction.

Recently, scientists have started to explore the application of deep-learning in data-driven earth system science (Reichstein et al., 2019). Recurrent Neural Network (RNN) may have great potential in modeling dynamic time series like net ecosystem productivity, with advantages over other regression methods in considering legacy effects or lagged indicators (Reichstein et al., 2018). Considering that time-lag responses of SHR to climate anomalies are important in evaluating terrestrial carbon cycle feedbacks to climate warming (Zhou et al., 2010), and photosynthesis can also influence soil respiration with hysteresis regionally (Kuzyakov & Gavrichkova, 2010), deep learning frameworks like RNN are ideal tools for improving our SHR estimation. Given the large demand for observation samples in deep learning neural networks, we highlight again that more SHR observations should be implemented and compiled. Since eddy covariance data provides ecosystem respiration records (auto- plus heterotrophic respiration) as well, a reasonable model as partition tool from autotrophic parts can also be an ideal solution for collecting more available SHR data (Koerber et al., 2016).

2.6.2 Climatic drivers of SHR anomalies

Since many studies emphasize the controls of water availability on ecosystem carbon fluxes (Humphrey et al., 2018; Jung et al., 2017), it is not surprising that we found that global SHR IAV is mainly controlled by the fluctuation in water condition. The dominance of water variation exists, yet the sensitivity of SHR IAV to water depends on the choice of proxy for water content (using soil moisture or precipitation in linear decomposition of SHR anomalies). Similar findings have been identified in Ballantyne et al. (2017) and Yan et al. (2018). This can be expected since SHR depends on soil water content (Skopp *et al.*, 1990), although this relationship can be influenced by soil property (Moyano et al., 2013; Moyano et al., 2012), microbial diversity (Zhang & Zhang, 2016), historical rainfall condition (Hawkes et al., 2017), and background water condition (Hinko-Najera et al., 2015; Matteucci et al., 2015). In addition, water content also affects the microbial community composition (Zhao et al., 2016), substrates availability, activities of extracellular enzymes (Schindlbacher et al., 2012), and even temperature sensitivity to SHR (Suseela et al., 2012).

Regionally speaking, our result of dominant water controls of SHR in extra-tropical forest and

semi-arid regions are consistent with plot-scale experimental tests (Hursh et al., 2017; Liu et al., 2009). In semi-arid areas, a small response to temperature fluctuation is possibly restrained by soil moisture and substrate availability (Zhang et al., 2013). As for Arctic tundra, such colder high-latitude areas can be more responsive to warming (Carey et al., 2016) and warmer temperature can cause shifts from heterotrophic to autotrophic respiration (Hicks Pries et al., 2015). Nevertheless, our diagnosed soil moisture control on tundra SHR IAV is not unrealistic, as some researchers have also reported that soil moisture affects ground thaw and the magnitudes of carbon loss is driven by soil moisture (Natali et al., 2015). There are also few records from Arctic tundra, meaning that incorrect spatial extrapolation might explain this particular positive response of tundra SHR to water availability.

Given that large-scale droughts will likely to happen by the end of the 21st century (Lu et al., 2019), our examined response of SHR to variability in water condition is a first step towards making reliable projections of soil carbon loss. However, we only consider the non-lag (yearly) response of SHR to environmental variability in current year; in the real world, lagged or adapted responses are non-negligible (Arnone Iii et al., 2008; de Nijs et al., 2019; Göransson et al., 2013). As noted above, applying deep learning techniques such as RNN (Kraft et al., 2019) hold great promise to robustly deal with such dynamics.

Despite the prevalent positive water controlling effects of SHR in most ecosystems, we also note that our ecosystem-level IAV attribution found that temperature anomalies dominate tropical forest SHR variability. Warming stimulating soil respiration has been demonstrated in many previous studies (Hursh et al., 2017; O'Connell et al., 2018), although thermal acclimation of heterotrophic microbes occurs (Carey et al., 2016; Crowther & Bradford, 2013). Since warming could also lead to soil water loss, primary positive effects of temperature mainly distribute in non-water-limited areas. Tropical forests account for the largest fraction of global SHR, and current tropical temperatures seem still lower than the physiological optima for respiration (Liu et al., 2018b; Huang et al., 2019). In other words, a stimulation effect from warming to SHR still exists, which may greatly affect the local soil-atmospheric carbon fluxes fluctuations and place tropical soil carbon storage at risk given the positive sensitivity to temperature. In addition, any interplay among different factors is not accounted for in our multiple linear regression formula. Therefore, further research is required to clarify the interaction effects between two associated factors of temperature and water availability.

The responses of SHR from TRENDY models to climatic variability differ among models at biome and global scales (Figures S22 and S28). This could be due to different specific formula forms of SHR parameterizations with climatic factors among models, like Arrhenius, hill or monotonic type (Todd-Brown et al., 2013) and to different degrees of couplings between productivity and respiration. For example, CABLE, ISAM and VEGAS exhibit dominant temperature controls on SHR IAV, which are different from the water effects identified in nearly all data-driven products in our study. The underestimation of water effects on year-to-year fluctuations of net carbon fluxes in process-based models has already been highlighted (Green et al., 2017; Humphrey et al., 2018; Liu et al., 2018c). Therefore, the internal parameterization schemes should be rigorously constrained and improved with the aid of causal perspectives in sensitivities of SHR to climate variability from our data-driven estimation. Using such causal statistics as a benchmark can better constrain the modelled carbon cycle feedback (Claessen et al., 2019), reducing the uncertainties in climate projections (Friedlingstein et al., 2014).

2.6.3 Effects of other environmental factors on SHR

Apart from the climate variables that have been used in our attribution analyses, other explanatory variables like GPP (affected by climate) and nitrogen availability are non-negligible factors affecting SHR through substrate availability and / or microbial activity (Figure 2.2c). The spatial gradient reflected in our data-driven SHR resembles that of GPP. This is expected, as

decomposition of fresh or recent organic matter like leaves and fine roots contributes to the main component of SHR (Janssens et al., 2001). However, the association between productivity and substrate availability is not constant or always predictable (Peterson & Lajtha, 2013), and the dependence of SHR on productivity can be confounded by temperature effects (Li et al., 2013).

We also found that nitrogen deposition influences the change in mean squared error of predicted SHR (Figure 2.2c). Nitrogen content may exert a major control on soil microbial activity (Janssens et al., 2010), indirectly expressed as soil acidification (Wang et al., 2019), limitation on substrate sources supply through harm on specific enzymes (Li et al., 2015), and functional changes in the microbial community (Allison et al., 2008). Higher carbon to nitrogen ratio in soil organic matter decreases decomposer carbon use efficiency and often impedes decomposition (Manzoni et al., 2017; Zhang et al., 2018), but not always (Bowden et al., 2004; Guo et al., 2017; Olsson et al., 2005). Controversy still exists on the stimulatory or suppressive effects of nitrogen addition on SHR (Chen et al., 2018), which also vary depending on original nitrogen availability (Liu et al., 2017; Sun et al., 2014), the amount of addition (Gao et al., 2014) and even ecosystem types (Cusack et al., 2010; Maaroufi et al., 2019; Mo et al., 2008; Zhou et al., 2014). Since any SHR reduction caused by nitrogen addition could reach the same order of magnitude of forest carbon sink (Janssens et al., 2010), further fundamental research is needed to understand how SHR responds to nitrogen deposition in different ecosystems, and whether possible negative effect on SHR could offset the warming induced increase in carbon loss, to better predict SHR changes given increasing nitrogen deposition in the future.

2.7 CONCLUSION

Our study integrates a large number of in-situ SHR measurements, satellite and meteorological observations using Random Forest models to produce an ensemble of data-driven global soil heterotrophic respiration (SHR) products. This ensemble dataset is independent of process-based model outputs and is expected to be beneficial for the model sensitivity parameter calibration. Our attribution analysis provides evidence for an important role of water availability in impacting year-to-year fluctuations of carbon fluxes, although of which can be mediated to some extent by choice of water content proxies in attribution process. To reduce SHR uncertainty and advance our ability to diagnose the state of SHR, we argue that more evenly-distributed SHR observations—especially from cold, warm dry and warm humid areas—and more powerful deep learning methods should be considered in further global SHR mapping tasks.

2.8 REFERENCES

Adachi, M., Ito, A., Yonemura, S., et al. (2017) Estimation of global soil respiration by accounting for land-use changes derived from remote sensing data. Journal of Environmental Management, 200, 97-104.

Ahlström, A., Raupach, M.R., Schurgers, G., et al. (2015). The dominant role of semi-arid ecosystems in the trend and variability of the land CO2 sink. Science, 348, 895-899.

Allison, S.D., Czimczik, C.I. & Treseder, K.K. (2008). Microbial activity and soil respiration under nitrogen addition in Alaskan boreal forest. Global Change Biology, 14, 1156-1168.

Arnone Iii, J.A., Verburg, P.S., Johnson, D.W., et al. (2008). Prolonged suppression of ecosystem carbon dioxide uptake after an anomalously warm year. Nature, 455, 383-386.

Baccini, A., Goetz, S., Walker, W., et al. (2012) Estimated carbon dioxide emissions from tropical

deforestation improved by carbon-density maps. Nature Climate Change, 2, 182-185.

Ballantyne, A., Smith, W., Anderegg, W., et al. (2017) Accelerating net terrestrial carbon uptake during the warming hiatus due to reduced respiration. Nature Climate Change, 7, 148-152.

Beaudoing, H. & Rodell, M. (2016) GLDAS Noah Land Surface Model L4 monthly 0.25 x 0.25 degree V2. 1. In. NASA/GSFC/HSL: Greenbelt, Maryland, USA, Goddard Earth Sciences Data and Information Services Center (GES DISC).

Blois, J.L., Williams, J.W., Fitzpatrick, M.C., et al. (2013) Space can substitute for time in predicting climate-change effects on biodiversity. Proceedings of the National Academy of Science of the United States of America, 110, 9374-9379.

Bond-Lamberty, B. & Thomson, A. (2010) A global database of soil respiration data. Biogeosciences, 7, 1915-1926.

Bond-Lamberty, B., Bailey, V.L., Chen, M., et al. (2018) Globally rising soil heterotrophic respiration over recent decades. Nature, 560, 80-83.

Bond-Lamberty, B. & Thomson, A. (2018) A Global Database of Soil Respiration Data, Version 4.0. ORNL DAAC,.

Bond-Lamberty, B., Wang, C. & Gower, S.T. (2004) A global relationship between the heterotrophic and autotrophic components of soil respiration? Global Change Biology, 10, 1756-1766.

Bond-Lamberty, B., Epron, D., Harden, J., et al. (2016) Estimating heterotrophic respiration at large scales: Challenges, approaches, and next steps. Ecosphere, 7, e01380, doi: 10.1002/ecs2.1380.

Bond-Lamberty, B. (2018) New techniques and data for understanding the global soil respiration flux. Earth's Future, 6, 1176-1180, doi: 10.1029/2018EF000866.

Borchers, H.W. (2019) pracma: Practical Numerical Math Functions. R package version 2.2.5. https://cran.r-project.org/web/packages/pracma/ (8 April 2019)

Bowden, R.D., Davidson, E., Savage, K., et al. (2004) Chronic nitrogen additions reduce total soil respiration and microbial respiration in temperate forest soils at the Harvard Forest. Forest Ecology and Management, 196, 43-56.

Bradford, M.A., McCulley, R.L., Crowther, T.W., et al. (2019) Cross-biome patterns in soil microbial respiration predictable from evolutionary theory on thermal adaptation. Nature Ecology & Evolution, 3, 223-231.

Breiman, L. Random forests. (2001) Machine learning, 45, 5-32.

Buermann, W., Forkel, M., O'Sullivan, M., et al. (2018) Widespread seasonal compensation effects of spring warming on northern plant productivity. Nature, 562, 110-114.

Cai, Y., Guan, K., Lobell, D., et al. (2019) Integrating satellite and climate data to predict wheat yield in Australia using machine learning approaches. Agricutural and Forest Meteorology, 274, 144-159.

Carbone, M.S., Richardson, A.D., Chen, M., et al. (2016) Constrained partitioning of autotrophic and heterotrophic respiration reduces model uncertainties of forest ecosystem carbon fluxes but

not stocks. Journal of Geophysical Research - Biogeosciences, 121, 2476-2492.

Carey, J.C., Tang, J., Templer, P.H., et al. (2016) Temperature response of soil respiration largely unaltered with experimental warming. Proceedings of the National Academy of Science of the United States of America, 113, 13797-13802.

Chen, M., Xie, P., Janowiak, J.E., et al. (2002) Global land precipitation: A 50-yr monthly analysis based on gauge observations. Journal of Hydrometeorology, 3, 249-266.

Chen, Z., Xu, Y., He, Y., et al. (2018) Nitrogen fertilization stimulated soil heterotrophic but not autotrophic respiration in cropland soils: a greater role of organic over inorganic fertilizer. Soil Biology and Biochemistry, 116, 253-264.

Ciais, P., Yao, Y., Gasser, T., et al. (2020) Empirical estimates of regional carbon budgets imply reduced global soil heterotrophic respiration. National Science Review, doi: 10.1093/nsr/nwaa145.

Claessen, J., Molini, A., Martens, B., et al. (2019) Global biosphere–climate interaction: a multi-scale appraisal of observations and models. Biogeosciences Discussions, https://doi.org/10.5194/bg-2019-212, in review.

Clark, D.B., Mercado, L.M., Sitch, S., et al. (2011) The Joint UK Land Environment Simulator (JULES), model description–Part 2: carbon fluxes and vegetation dynamics. Geoscientific Model Development, 4, 701-722.

Crowther, T.W. & Bradford, M.A. (2013) Thermal acclimation in widespread heterotrophic soil microbes. Ecology Letters, 16, 469-477.

Crowther, T., Van Den Hoogen, J., Wan, J., et al. (2019) The global soil community and its influence on biogeochemistry. Science, 365, eaav0550, doi: 10.1126/science.aav0550.

Cusack, D.F., Torn, M.S., McDOWELL, W.H., et al. (2010) The response of heterotrophic activity and carbon cycling to nitrogen additions and warming in two tropical soils. Global Change Biology, 16, 2555-2572.

de Nijs, E.A., Hicks, L.C., Leizeaga, A., et al. (2019) Soil microbial moisture dependences and responses to drying–rewetting: The legacy of 18 years drought. Global Change Biology, 25, 1005-1015.

Fan, Y. & van den Dool, H. (2004) Climate Prediction Center global monthly soil moisture data set at 0.5 resolution for 1948 to present. Journal of Geophysical Research - Atmospheres, 109, D10102, doi: 10.1029/2003JD004345.

Fan, Y. & Van den Dool, H. (2008) A global monthly land surface air temperature analysis for 1948–present. Journal of Geophysical Research - Atmospheres, 113, D01103, doi:10.1029/2007JD008470.

Feng, P., Wang, B., Li Liu, D., et al. (2019) Incorporating machine learning with biophysical model can improve the evaluation of climate extremes impacts on wheat yield in south-eastern Australia. Agricultural and Forest Meteorology, 275, 100-113.

Friedl, M.A., Sulla-Menashe, D., Tan, B., et al. (2010) MODIS Collection 5 global land cover: Algorithm refinements and characterization of new datasets. Remote Sensing of Environment,

114, 168-182.

Friedlingstein, P., Meinshausen, M., Arora, V.K., et al. (2014) Uncertainties in CMIP5 climate projections due to carbon cycle feedbacks. Journal of Climate, 27, 511-526.

Göransson, H., Godbold, D.L., Jones, D.L., et al. (2013) Bacterial growth and respiration responses upon rewetting dry forest soils: impact of drought-legacy. Soil Biology and Biochemistry, 57, 477-486.

Gao, Q., Hasselquist, N.J., Palmroth, S., et al. (2014) Short-term response of soil respiration to nitrogen fertilization in a subtropical evergreen forest. Soil Biology and Biochemistry, 76, 297-300.

Green, J.K., Konings, A.G., Alemohammad, S.H., et al. (2017) Regionally strong feedbacks between the atmosphere and terrestrial biosphere. Nature Geoscience, 10, 410-414.

Guimberteau, M., Zhu, D., Maignan, F., et al. (2018) ORCHIDEE-MICT (v8. 4.1), a land surface model for the high latitudes: model description and validation. Geoscientific Model Development, 11, 121-163.

Guo, H., Ye, C., Zhang, H., et al. (2017) Long-term nitrogen & phosphorus additions reduce soil microbial respiration but increase its temperature sensitivity in a Tibetan alpine meadow. Soil Biology and Biochemistry, 113, 26-34.

Hanson, P., Edwards, N., Garten, C.T., et al. (2000) Separating root and soil microbial contributions to soil respiration: a review of methods and observations. Biogeochemistry, 48, 115-146.

Harden, J.W., Hugelius, G., Ahlström, A., et al. (2018) Networking our science to characterize the state, vulnerabilities, and management opportunities of soil organic matter. Global Change Biology, 24, e705-e718.

Harmon, M.E., Bond-Lamberty, B., Tang, J., et al. (2011) Heterotrophic respiration in disturbed forests: A review with examples from North America. Journal of Geophysical Research - Biogeosciences, 116, G00K04, doi:10.1029/2010JG001495.

Harris, I., Jones, P.D., Osborn, T.J., et al. (2014) Updated high-resolution grids of monthly climatic observations–the CRU TS3. 10 Dataset. International Journal of Climatology, 34, 623-642.

Hashimoto, S., Carvalhais, N., Ito, A., et al. (2015) Global spatiotemporal distribution of soil respiration modeled using a global database. Biogeosciences, 12, 4121-4132.

Haverd, V., Smith, B., Nieradzik, L., et al. (2018) A new version of the CABLE land surface model (Subversion revision r4601) incorporating land use and land cover change, woody vegetation demography, and a novel optimisation-based approach to plant coordination of photosynthesis. Geoscientific Model Development, 11, 2995-3026.

Hawkes, C.V., Waring, B.G., Rocca, J.D., et al. (2017) Historical climate controls soil respiration responses to current soil moisture. Proceedings of the National Academy of Science of the United States of America, 114, 6322-6327.

Haynes, B.E. & Gower, S.T. (1995) Belowground carbon allocation in unfertilized and fertilized red pine plantations in northern Wisconsin. Tree Physiology, 15, 317-325.

Hicks Pries, C.E., van Logtestijn, R.S., Schuur, E.A., et al. (2015) Decadal warming causes a consistent and persistent shift from heterotrophic to autotrophic respiration in contrasting permafrost ecosystems. Global Change Biology, 21, 4508-4519.

Hijmans, RJ., van Etten, J., Sumner, M., et al. (2019) raster: Geographic Data Analysis and Modeling. R package version 3.0-7 https://CRAN.R-project.org/package=raster (22 September 2019)

Hinko-Najera, N., Fest, B., Livesley, S.J., et al. (2015) Reduced throughfall decreases autotrophic respiration, but not heterotrophic respiration in a dry temperate broadleaved evergreen forest. Agricultural and Forest Meteorology, 200, 66-77.

Huang, J., van den Dool, H.M. & Georgarakos, K.P. (1996) Analysis of model-calculated soil moisture over the United States (1931–1993) and applications to long-range temperature forecasts. Journal of Climate, 9, 1350-1362.

Huang, M., Piao, S., Ciais, P., et al. (2019) Air temperature optima of vegetation productivity across global biomes. Nature Ecology & Evolution, 3, 772-779.

Huang N, Wang L, Song X P, et al. (2020) Spatial and temporal variations in global soil respiration and their relationships with climate and land cover. Science advances, 6, eabb8508, doi: 10.1126/sciadv.abb8508.

Huang, S., Ye, G., Lin, J., et al. (2018) Autotrophic and heterotrophic soil respiration responds asymmetrically to drought in a subtropical forest in the Southeast China. Soil Biology and Biochemistry, 123, 242-249.

Humphrey, V., Gudmundsson, L. & Seneviratne, S.I. (2017) A global reconstruction of climate-driven subdecadal water storage variability. Geophysical Research Letters, 44, 2300-2309.

Humphrey, V., Zscheischler, J., Ciais, P., et al. (2018) Sensitivity of atmospheric CO 2 growth rate to observed changes in terrestrial water storage. Nature, 560, 628-631.

Hursh, A., Ballantyne, A., Cooper, L., et al. (2017) The sensitivity of soil respiration to soil temperature, moisture, and carbon supply at the global scale. Global Change Biology, 23, 2090-2103.

Ichii, K., Ueyama, M., Kondo, M., et al. (2017) New data-driven estimation of terrestrial CO2 fluxes in Asia using a standardized database of eddy covariance measurements, remote sensing data, and support vector regression. Journal of Geophysical Research - Biogeosciences, 122, 767-795.

Janssens, I., Lankreijer, H., Matteucci, G., et al. (2001) Productivity overshadows temperature in determining soil and ecosystem respiration across European forests. Global Change Biology, 7, 269-278.

Janssens, I., Dieleman, W., Luyssaert, S., et al. (2010) Reduction of forest soil respiration in response to nitrogen deposition. Nature Geoscience, 3, 315-322.

Jian, J., Vargas, R., Anderson-Teixeira, K., et al. (2021). A restructured and updated global soil respiration database (SRDB-V5). Earth System Science Data, 13, 255-267.

Jung, M., Reichstein, M., Ciais, P., et al. (2010) Recent decline in the global land evapotranspiration trend due to limited moisture supply. Nature, 467, 951-954.

Jung, M., Reichstein, M., Margolis, H.A., et al. (2011) Global patterns of land-atmosphere fluxes of carbon dioxide, latent heat, and sensible heat derived from eddy covariance, satellite, and meteorological observations. Journal of Geophysical Research - Biogeosciences, 116, G00J07,doi:10.1029/2010JG001566.

Jung, M., Reichstein, M., Schwalm, C.R., et al. (2017) Compensatory water effects link yearly global land CO2 sink changes to temperature. Nature, 541, 516-520, doi: 10.1038/nature20780.

Kato, E., Kinoshita, T., Ito, A., et al. (2013) Evaluation of spatially explicit emission scenario of land-use change and biomass burning using a process-based biogeochemical model. Journal of Land Use Science, 8, 104-122.

Keller, K., Lienert, S., Bozbiyik, A., et al. (2017) 20th century changes in carbon isotopes and water-use efficiency: tree-ring-based evaluation of the CLM4. 5 and LPX-Bern models. Biogeosciences, 14, 2641-2673.

Keuper, F., Wild, B., Kummu, M., et al. (2020) Carbon loss from northern circumpolar permafrost soils amplified by rhizosphere priming. Nature Geoscience, 13, 560-565.

Kobayashi, S., Ota, Y., Harada, Y., et al. (2015) The JRA-55 reanalysis: General specifications and basic characteristics. Journal of the Meteorological Society of Japan Ser. II, 93, 5-48.

Koerber, GR., Meyer, WS., SUN, Q., et al. (2016) Under a new light: validation of eddy covariance flux with light response functions of assimilation and estimates of heterotrophic soil respiration. Biogeosciences Discussions, 1-28, doi:10.5194/bg-2016-182.

Konings, A.G., Bloom, A.A., Liu, J., et al. (2019) Global satellite-driven estimates of heterotrophic respiration. Biogeosciences, 16, 2269-2284.

Kraft, B., Jung, M., Körner, M., Requena, Mesa. C., Cortés, J., and Reichstein, M. (2019) Identifying Dynamic Memory Effects on Vegetation State Using Recurrent Neural Networks. Frontiers in Big Data, 2, 31, doi:10.3389/fdata.2019.0003.

Krinner, G., Viovy, N., de Noblet-Ducoudré, N., et al. (2005) A dynamic global vegetation model for studies of the coupled atmosphere-biosphere system. Global Biogeochemical Cycles, 19, GB1015, doi:10.1029/2003GB002199.

Kuzyakov, Y. & Larionova, A.A. (2005) Root and rhizomicrobial respiration: a review of approaches to estimate respiration by autotrophic and heterotrophic organisms in soil. Journal of Plant Nutrition and Soil Science, 168, 503-520.

Jain, A.K., Meiyappan, P., Song, Y., et al. (2013) CO2 emissions from land-use change affected more by nitrogen cycle, than by the choice of land-cover data. Global Change Biology, 19, 2893-2906.

Kuzyakov, Y. & Gavrichkova, O. (2010) Time lag between photosynthesis and carbon dioxide efflux from soil: a review of mechanisms and controls. Global Change Biology, 16, 3386-3406.

Lantz, B. (2013) Machine learning with R. Packt Publishing Ltd.

Le Quéré, C., Andrew, R.M., Friedlingstein, P., et al. (2018) Global carbon budget 2018. Earth System Science Data, 10, 2141-2194.

Li, J., Wang, Y.P., Duan, Q., et al. (2016) Quantification and attribution of errors in the simulated annual gross primary production and latent heat fluxes by two global land surface models. Journal of Advances in Modeling Earth Systems, 8, 1270-1288.

Li, P., Yang, Y. & Fang, J. (2013) Variations of root and heterotrophic respiration along environmental gradients in China's forests. Journal of Plant Ecology, 6, 358-367.

Li, Y., Liu, Y., Wu, S., et al. (2015) Microbial properties explain temporal variation in soil respiration in a grassland subjected to nitrogen addition. Scientific Reports, 5, 18496, doi:10.1038/srep18496.

Liaw, A., & Wiener, M. (2018) Classification and regression based on a forest of trees using random inputs, based on Breiman (2001) R package version 4.6-14 https://www.stat.berkeley.edu/~breiman/RandomForests/ (22 March 2018)

Liu, W., Zhang, Z. & Wan, S. (2009) Predominant role of water in regulating soil and microbial respiration and their responses to climate change in a semiarid grassland. Global Change Biology, 15, 184-195.

Liu, W., Lü, X., Xu, W., et al. (2018a) Effects of water and nitrogen addition on ecosystem respiration across three types of steppe: The role of plant and microbial biomass. Science of the Total Environment, 619, 103-111.

Liu, X., Yang, Z., Lin, C., et al. (2017) Will nitrogen deposition mitigate warming-increased soil respiration in a young subtropical plantation? Agricultural and Forest Meteorology, 246, 78-85.

Liu, Y., He, N., Wen, X., et al. (2018b) The optimum temperature of soil microbial respiration: Patterns and controls. Soil Biology and Biochemistry, 121, 35-42.

Liu, Z., Ballantyne, A.P., Poulter, B., et al. (2018c) Precipitation thresholds regulate net carbon exchange at the continental scale. Nature Communications, 9, 3596, doi:10.1038/s41467-018-05948-1.

Lu, J., Carbone, G.J. & Grego, J.M. (2019) Uncertainty and hotspots in 21st century projections of agricultural drought from CMIP5 models. Scientific Reports, 9, 4922, doi:10.1038/s41598-019-41196-z.

Maaroufi, N.I., Nordin, A., Palmqvist, K., et al. (2019) Anthropogenic nitrogen enrichment enhances soil carbon accumulation by impacting saprotrophs rather than ectomycorrhizal fungal activity. Global Change Biology, doi: 10.1111/gcb.14722

Manzoni, S., Čapek, P., Mooshammer, M., et al. (2017) Optimal metabolic regulation along resource stoichiometry gradients. Ecology Letters, 20, 1182-1191.

Matteucci, M., Gruening, C., Ballarin, I.G., et al. (2015) Components, drivers and temporal dynamics of ecosystem respiration in a Mediterranean pine forest. Soil Biology and Biochemistry, 88, 224-235.

Melton, J.R., & Arora, V.K. (2016) Competition between plant functional types in the Canadian Terrestrial Ecosystem Model (CTEM) v. 2.0. Geoscientific Model Development, 9, 323-361.

Mo, J., Zhang, W., Zhu, W., et al. (2008) Nitrogen addition reduces soil respiration in a mature tropical forest in southern China. Global Change Biology, 14, 403-412.

Moyano, F.E., Vasilyeva, N.A., Bouckaert, L., et al. (2012) The moisture response of soil heterotrophic respiration: interaction with soil properties. Biogeosciences, 9, 1173-1182.

Moyano, F.E., Manzoni, S. & Chenu, C. (2013) Responses of soil heterotrophic respiration to moisture availability: An exploration of processes and models. Soil Biology and Biochemistry, 59, 72-85.

Nachtergaele, F., van Velthuizen, H., Verelst, L., et al. (2010) The harmonized world soil database. Proceedings of the 19th World Congress of Soil Science, Soil Solutions for a Changing World, Brisbane, Australia, 1-6 August 2010 (ed by, pp. 34-37.

Natali, S.M., Schuur, E.A., Mauritz, M., et al. (2015) Permafrost thaw and soil moisture driving CO2 and CH4 release from upland tundra. Journal of Geophysical Research - Biogeosciences, 120, 525-537.

Noh, N.-J., Kuribayashi, M., Saitoh, T.M., et al. (2016) Responses of soil, heterotrophic, and autotrophic respiration to experimental open-field soil warming in a cool-temperate deciduous forest. Ecosystems, 19, 504-520.

O'Connell, C.S., Ruan, L. & Silver, W.L. (2018) Drought drives rapid shifts in tropical rainforest soil biogeochemistry and greenhouse gas emissions. Nature Communications, 9, 1348, doi:10.1038/s41467-018-03352-3.

Oleson, K., Lawrence, DM., Bonan, GB., & Drewniak, B. (2013) Technical description of version 4.5 of the Community Land Model (CLM). Boulder, CO: NCAR.

Olsson, P., Linder, S., Giesler, R., et al. (2005) Fertilization of boreal forest reduces both autotrophic and heterotrophic soil respiration. Global Change Biology, 11, 1745-1753.

Peng, Y., Chen, G.-t., Li, S., et al. (2018) Nitrogen additions reduce rhizospheric and heterotrophic respiration in a subtropical evergreen broad-leaved forest. Plant Soil, 431, 449-463.

Peterson, F.S. & Lajtha, K.J. (2013) Linking aboveground net primary productivity to soil carbon and dissolved organic carbon in complex terrain. Journal of Geophysical Research - Biogeosciences, 118, 1225-1236.

Prentice, I.C., Dong, N., Gleason, S.M., et al. (2014) Balancing the costs of carbon gain and water transport: testing a new theoretical framework for plant functional ecology. Ecology Letters, 17, 82-91.

R Development Core Team. (2019) R: A language and environment for statistical computing. Vienna, Austria: R Foundation for Statistical Computing, available at http://www.R-project.org/

Raich, J.W. & Potter, C.S. (1995) Global patterns of carbon dioxide emissions from soils. Global Biogeochemical Cycles, 9, 23-36.

Raich, J.W., Potter, C.S. & Bhagawati, D. (2002) Interannual variability in global soil respiration, 1980–94. Global Change Biology, 8, 800-812.

Reichstein, M., Besnard, S., Carvalhais, N., et al. (2018) Modelling Landsurface Time-Series with

Recurrent Neural Nets. IGARSS 2018-2018 IEEE International Geoscience and Remote Sensing Symposium, pp. 7640-7643.

Reichstein, M., Camps-Valls, G., Stevens, B., et al. (2019) Deep learning and process understanding for data-driven Earth system science. Nature, 566, 195-204.

Reick, C.H., Raddatz, T., Brovkin, V., et al. (2013) Representation of natural and anthropogenic land cover change in MPI-ESM. Journal of Advances in Modeling Earth Systems, 5, 459-482.

Rodell, M., Houser, P., Jambor, U., et al. (2004) The global land data assimilation system. Bulletin of the American Meteorological Society, 85, 381-394.

Schimel, D., Stephens, B.B., Fisher, J.B. (2015) Effect of increasing CO2 on the terrestrial carbon cycle. Proceedings of the National Academy of Science of the United States of America, 112, 436-441.

Schindlbacher, A., ZECHMEISTER-BOLTENSTERN, S. & Jandl, R. (2009) Carbon losses due to soil warming: do autotrophic and heterotrophic soil respiration respond equally? Global Change Biology, 15, 901-913.

Schindlbacher, A., Wunderlich, S., Borken, W., et al. (2012) Soil respiration under climate change: prolonged summer drought offsets soil warming effects. Global Change Biology, 18, 2270-2279.

Schwalm, C.R., Anderegg, W.R., Michalak, A.M., et al. (2017) Global patterns of drought recovery. Nature, 548, 202-205.

Shao, P., Zeng, X., Moore, D.J., et al. (2013) Soil microbial respiration from observations and Earth System Models. Environmental Research Letters, 8, 034034, doi: 10.1088/1748-9326/8/3/034034.

Sheffield, J., Goteti, G., Wood, E.F. (2006) Development of a 50-year high-resolution global dataset of meteorological forcings for land surface modeling. Journal of Climate, 19, 3088-3111.

Skopp, J., Jawson, M. & Doran, J. (1990) Steady-state aerobic microbial activity as a function of soil water content. Soil Science Society of America Journal, 54, 1619-1625.

Steidinger, B.S., Crowther, T.W., Liang, J., et al. (2019) Climatic controls of decomposition drive the global biogeography of forest-tree symbioses. Nature, 569, 404-408.

Stell, E., Warner, D., Jian, J., Bond-Lamberty, B., & Vargas, R. (2021). Spatial biases of information influence global estimates of soil respiration: how can we improve global predictions? Global Change Biology. doi: 10.1111/GCB.15666.

Stocker, B.D., Zscheischler, J., Keenan, T.F., et al. (2019) Drought impacts on terrestrial primary production underestimated by satellite monitoring. Nature Geoscience, 12, 264-270.

Sun, Z., Liu, L., Ma, Y., et al. (2014) The effect of nitrogen addition on soil respiration from a nitrogen-limited forest soil. Agricultural and Forest Meteorology, 197, 103-110.

Suseela, V., Conant, R.T., Wallenstein, M.D., et al. (2012) Effects of soil moisture on the temperature sensitivity of heterotrophic respiration vary seasonally in an old-field climate change experiment. Global Change Biology, 18, 336-348.

Tang, X., Fan, S., Du, M., et al. (2020). Spatial and temporal patterns of global soil heterotrophic respiration in terrestrial ecosystems. Earth System Science Data, 12, 1037-1051.

Todd-Brown, K., Randerson, J., Post, W., et al. (2013) Causes of variation in soil carbon simulations from CMIP5 Earth system models and comparison with observations. Biogeosciences, 10, 1717-1736.

Tramontana, G., Jung, M., Camps-Valls, G., et al. (2016) Predicting carbon dioxide and energy fluxes across global FLUXNET sites with regression algorithms. Biogeosciences Discussions, doi:10.5194/bg-2015-661.

Van den Dool, H., Huang, J. & Fan, Y. (2003) Performance and analysis of the constructed analogue method applied to US soil moisture over 1981–2001. Journal of Geophysical Research - Atmospheres, 108 (D16), 8617, doi: 10.1029/2002JD003114.

Vargas, R., Baldocchi, D.D., Allen, M.F., et al. (2010) Looking deeper into the soil: biophysical controls and seasonal lags of soil CO2 production and efflux. Ecological Applications, 20, 1569-1582.

Viovy, N. (2015) CRU-NCEP v6.1 Dataset. http://dods.extra.cea.fr/store/p529viov/cruncep/

Wang, H., Prentice, I.C., Keenan, T.F., et al. (2017) Towards a universal model for carbon dioxide uptake by plants. Nature Plants, 3, 734-741.

Wang, J., Fu, X., Zhang, Z., et al. (2019) Responses of soil respiration to nitrogen addition in the Sanjiang Plain wetland, northeastern China. PloS ONE, 14, e0211456, doi: 10.1371/journal.pone.0211456.

Warner, D. L., Bond-Lamberty, B., Jian, J., Stell, E., & Vargas, R. (2019). Spatial predictions and associated uncertainty of annual soil respiration at the global scale. Global Biogeochemical Cycles, 33, 1733-1745.

Weedon, G.P., Balsamo, G., Bellouin, N., et al. (2014) The WFDEI meteorological forcing data set: WATCH Forcing Data methodology applied to ERA-Interim reanalysis data. Water Resources Research, 50, 7505-7514.

Wieder, W., Boehnert, J., Bonan, G., et al. (2014) Regridded harmonized world soil database v1. 2. ORNL DAAC.

Xiao, J., Ollinger, S.V., Frolking, S., et al. (2014) Data-driven diagnostics of terrestrial carbon dynamics over North America. Agricultural and Forest Meteorology, 197, 142-157.

Xu, M., & Shang, H. (2016) Contribution of soil respiration to the global carbon equation. Journal of Plant Physiology, 203, 16-28.

Yan, Z., Bond-Lamberty, B., Todd-Brown, K.E., et al. (2018) A moisture function of soil heterotrophic respiration that incorporates microscale processes. Nature Communications, 9, 2562, doi:10.1038/s41467-018-04971-6.

Yao, Y., Wang, X., Li, Y., et al. (2018) Spatiotemporal pattern of gross primary productivity and its covariation with climate in China over the last thirty years. Global Change Biology, 24, 184-196.

Zaehle, S., & Friend, A.D. (2010) Carbon and nitrogen cycle dynamics in the O-CN land surface model: 1. Model description, site-scale evaluation, and sensitivity to parameter estimates. Global Biogeochemical Cycles, 24, doi:10.1029/2009GB003522..

Zeng, J., Matsunaga, T., Tan, Z. H., et al. (2020). Global terrestrial carbon fluxes of 1999–2019 estimated by upscaling eddy covariance data with a random forest. Scientific data, 7, 1-11.

Zeng, N., Mariotti, A., Wetzel, P.. (2005) Terrestrial mechanisms of interannual CO2 variability. Global Biogeochemical Cycles, 19, GB1016, doi:10.1029/2004GB002273.

Zeng, Z., Wang, T., Zhou, F., et al. (2014) A worldwide analysis of spatiotemporal changes in water balance-based evapotranspiration from 1982 to 2009. Journal of Geophysical Research - Atmospheres, 119, 1186-1202.

Zhang, F.G., & Zhang, Q.G. (2016) Microbial diversity limits soil heterotrophic respiration and mitigates the respiration response to moisture increase. Soil Biology and Biochemistry, 98, 180-185.

Zhang, H., Goll, D.S., Manzoni, S., et al. (2018) Modeling the effects of litter stoichiometry and soil mineral N availability on soil organic matter formation using CENTURY-CUE (v1. 0). Geoscientific Model Development, 11, 4779-4796.

Zhang, N., Liu, W., Yang, H., et al. (2013) Soil microbial responses to warming and increased precipitation and their implications for ecosystem C cycling. Oecologia, 173, 1125-1142.

Zhao, C., Miao, Y., Yu, C., et al. (2016) Soil microbial community composition and respiration along an experimental precipitation gradient in a semiarid steppe. Scientific Reports, 6, 24317, doi:10.1038/srep24317.

Zhou, L., Zhou, X., Zhang, B., et al. (2014) Different responses of soil respiration and its components to nitrogen addition among biomes: a meta-analysis. Global Change Biology, 20, 2332-2343.

Zhou, X., Luo, Y., Gao, C., et al. (2010) Concurrent and lagged impacts of an anomalously warm year on autotrophic and heterotrophic components of soil respiration: a deconvolution analysis. New Phytology, 187, 184-198.

Zhu, J., Hu, H., Tao, S., et al. (2017) Carbon stocks and changes of dead organic matter in China's forests. Nature Communications, 8, 151, doi:10.1038/s41467-017-00207-1.

Zou, J., Tobin, B., Luo, Y., et al. (2018) Response of soil respiration and its components to experimental warming and water addition in a temperate Sitka spruce forest ecosystem. Agricultural and Forest Meteorology, 260, 204-215.

2.9 SUPPORTING INFORMATION

A data-driven global soil heterotrophic respiration dataset and the drivers of its inter-annual variability

Yitong Yao[1], Philippe Ciais[1], Nicolas Viovy[1], Wei Li[2], Fabio Cresto-Aleina[1], Hui Yang[1], Emilie Joetzjer[3], Ben Bond-Lamberty[4]

[1] Laboratoire des Sciences du Climat et de l'Environnement, LSCE/IPSL, CEA-CNRS-UVSQ, Université Paris-Saclay, Gif-sur-Yvette, 91191, France

[2] Department of Earth System Science, Tsinghua University, Beijing, 100084, China

[3] CNRM, Université de Toulouse, Météo-France, CNRS, Toulouse, 31057, France

[4] Pacific Northwest National Laboratory, Joint Global Change Research Institute at the University of Maryland-College Park, College Park, Maryland, MA 20740, USA

Contents of this file

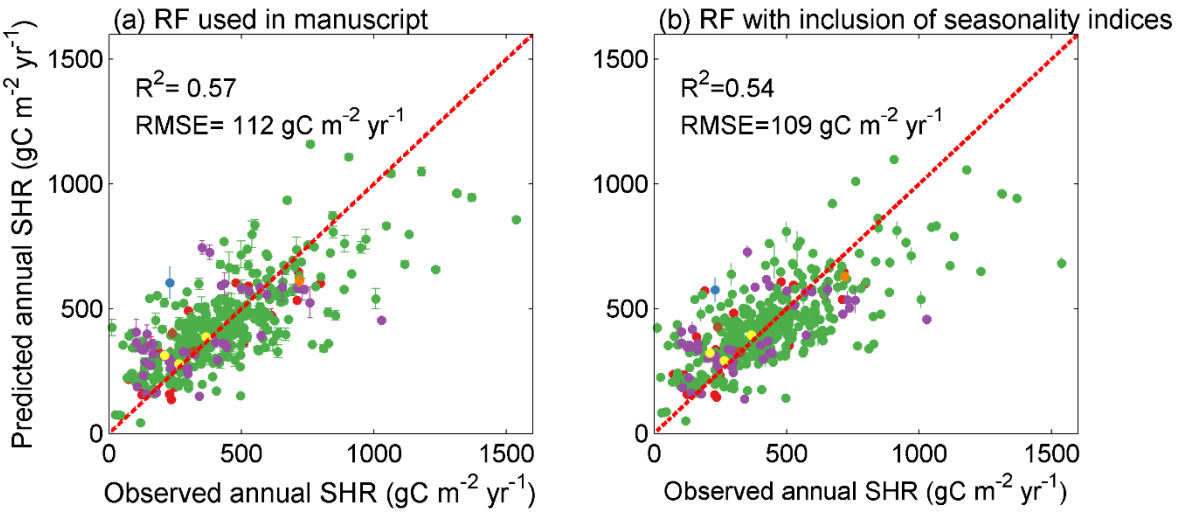

Figure S1 The performance of Random Forest model (a) used in the main text and (b) with inclusion of three seasonality indices: temperature difference between the hottest and coldest month, precipitation difference between the wettest month and driest month and precipitation seasonality index derived from Walsh and Lawler (1981).

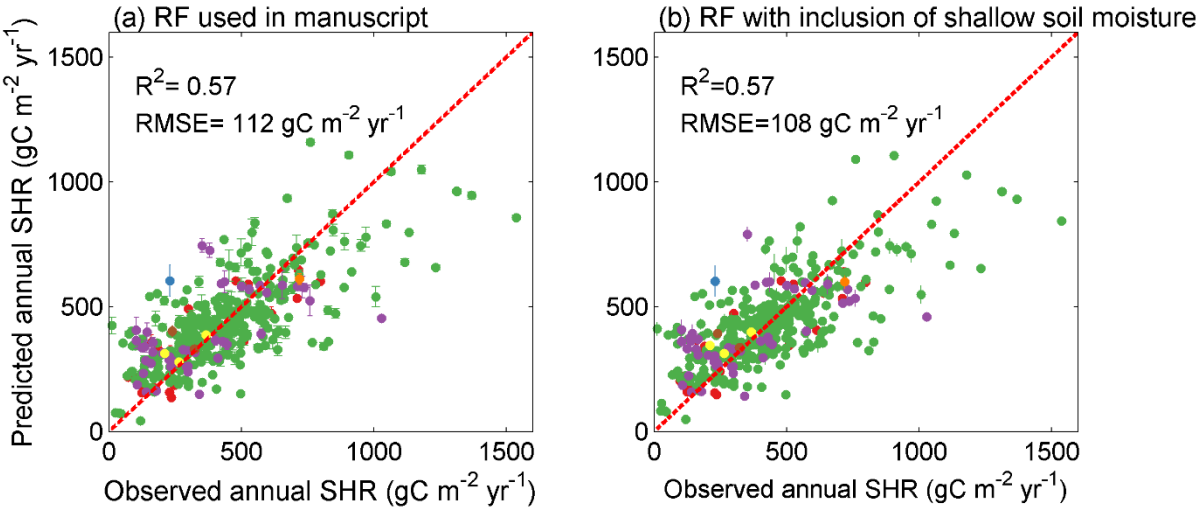

Figure S2 The performance of Random Forest model (a) used in the main text and (b) with inclusion of soil moisture in shallow layer (0-0.1m, 0.1-0.4m).

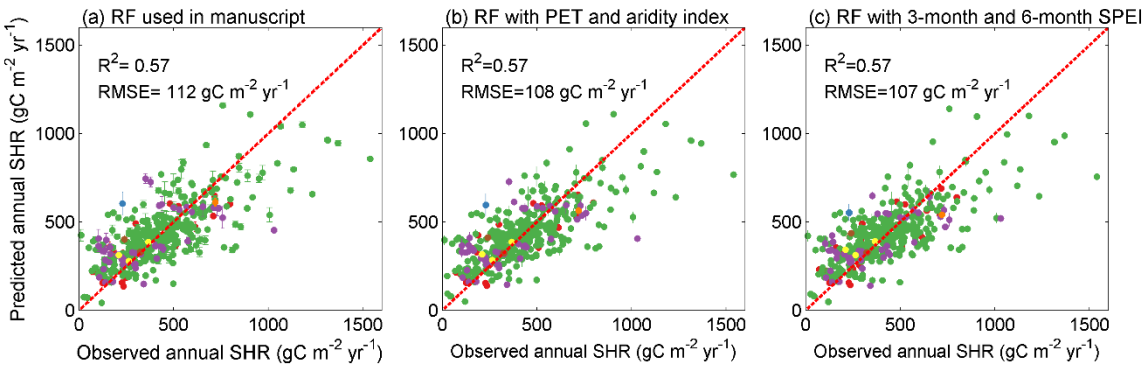

Figure S3 The performance of Random Forest model (a) used in the main text, with inclusion of (b) PET and aridity index and (c) 3-month and 6-month SPEI index. We download the PET and aridity index from https://cgiarcsi.community/2019/01/24/global-aridity-index-and-potential-evapotranspiration-climate-database-v2/. They are static indices for the period 1970-2000. We also try to use a dynamic aridity-related index like SPEI as explanatory variable. We download SPEI dataset from https://spei.csic.es/database.html. Here we added 3-month and 6-month SPEI index into Random Forest model.

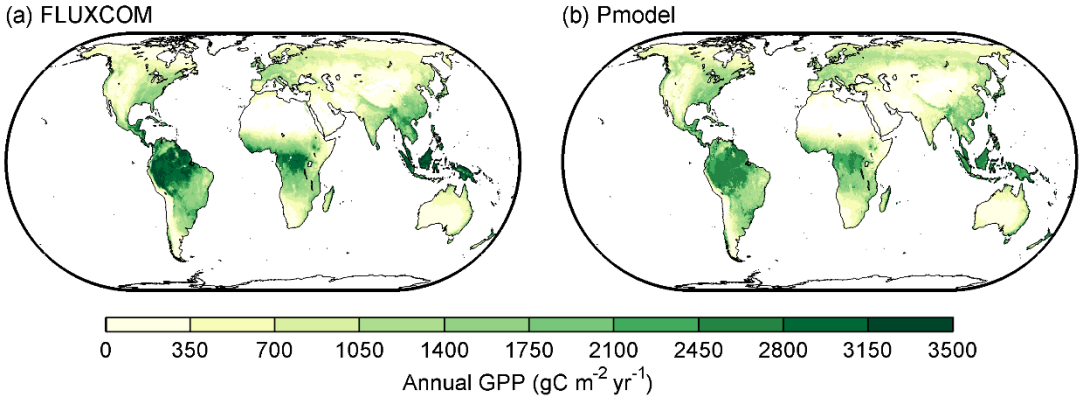

Figure S4 Spatial distribution of annual gross primary productivity averaged over 1985-2013.

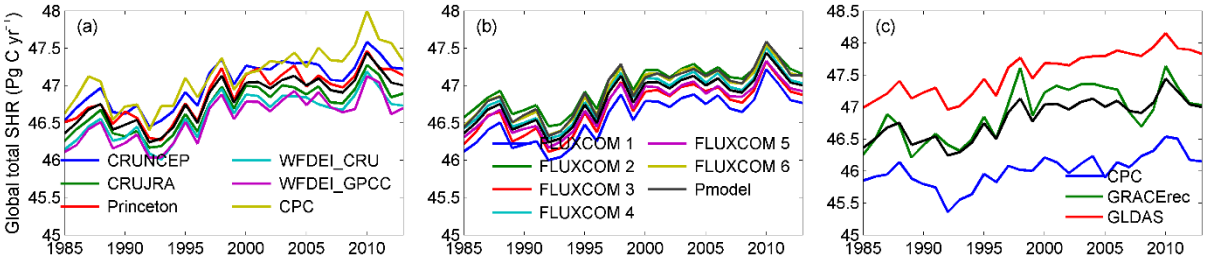

Figure S5 Global total amount of soil heterotrophic respiration grouped by the enrolled (a) temperature and precipitation (n=6), (b) GPP (n=7) and (c) soil moisture (n=3) data sources. The black line in each panel is the average over all ensembles.

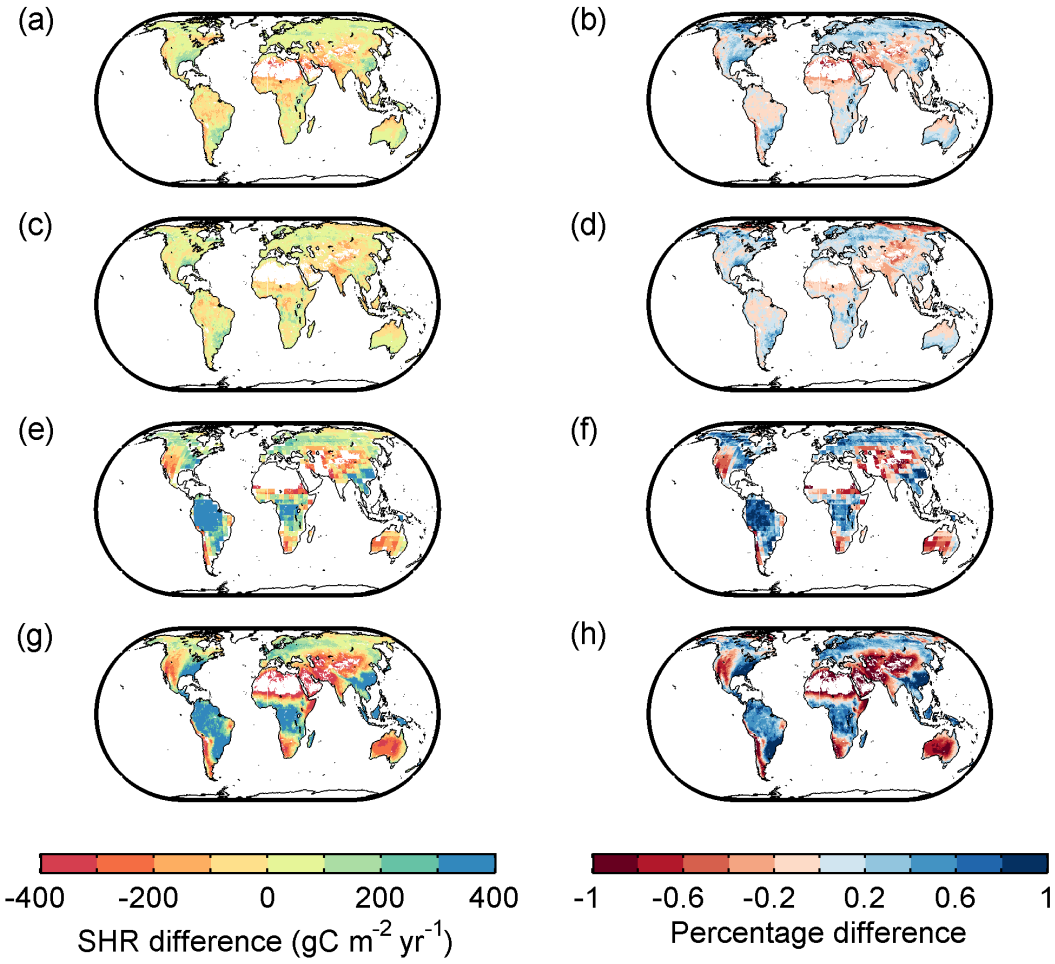

Figure S6 (a, c, e, g) Absolute values and (b, d, f, h) percentage difference between our data-driven SHR and (a,b) Hashimoto et al (2015), (c, d), Tang et al (2020), (e, f) top-down estimate from Konings et al (2019) and (g, h) TRENDY mean.

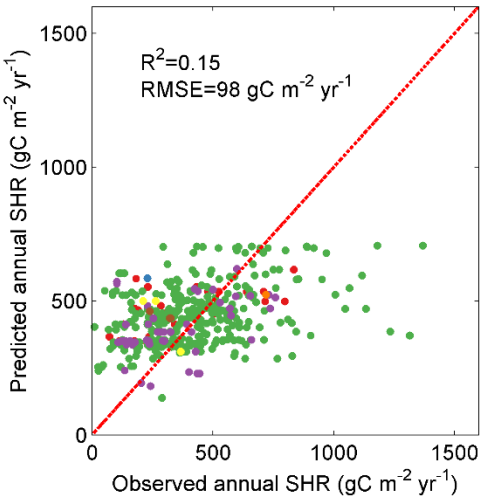

Figure S7 Comparison of observed annual SHR v.s. bottom-up estimate at the same sites in Hashimoto et al (2015).

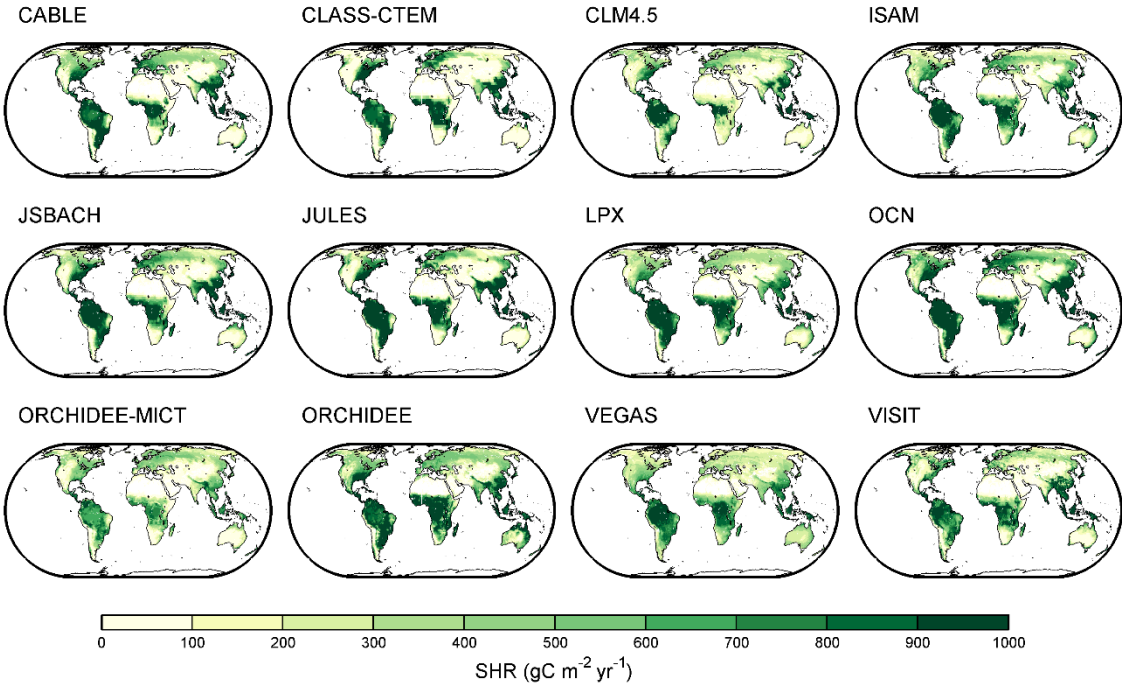

Figure S8 Spatial distribution of mean annual soil heterotrophic respiration averaged over 1985-2013 from TRENDY model ensembles.

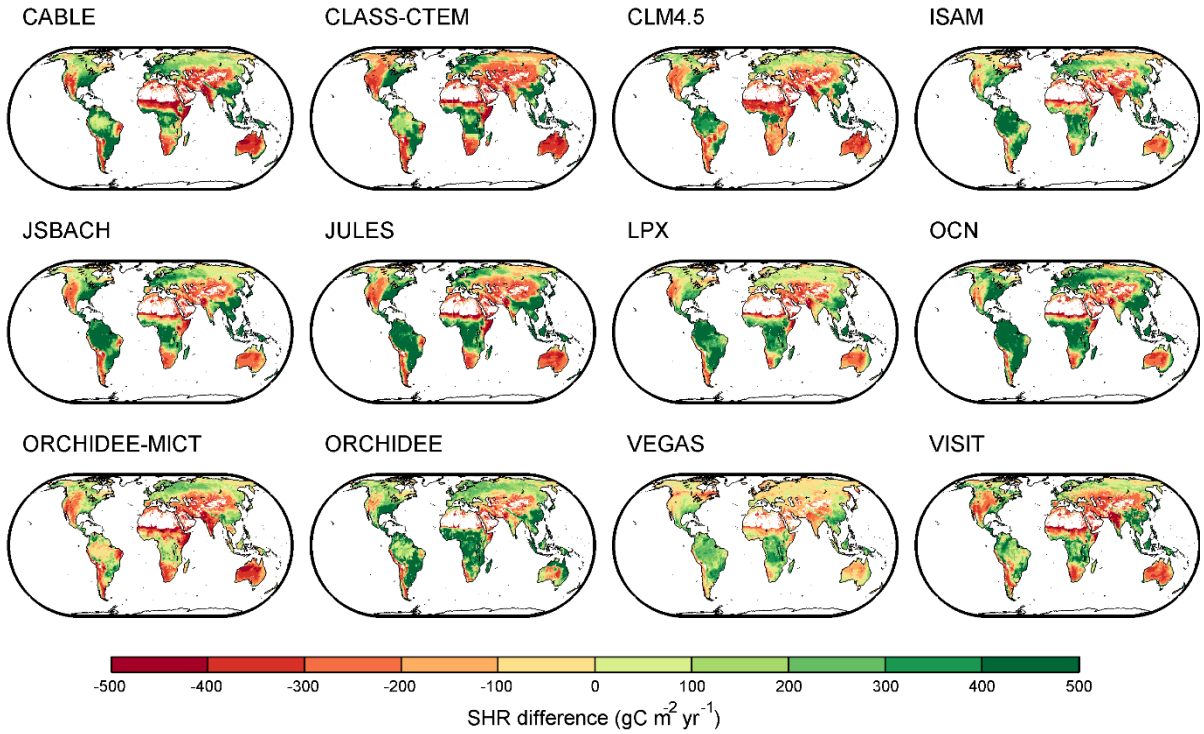

Figure S9 The absolute difference between TRENDY SHR and our data-driven product.

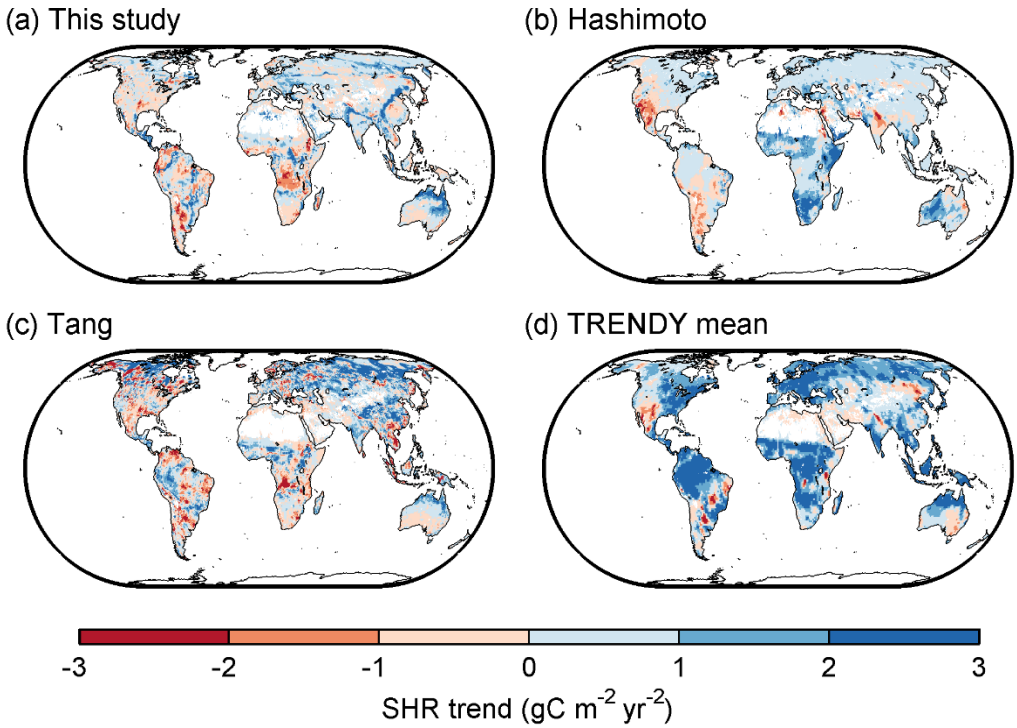

Figure S10 Spatial distribution of SHR trend during 1985-2013 for (a) our data-driven product, (b) Hashimoto et al (2015), (c) Tang et al (2020), and (d) TRENDY mean.

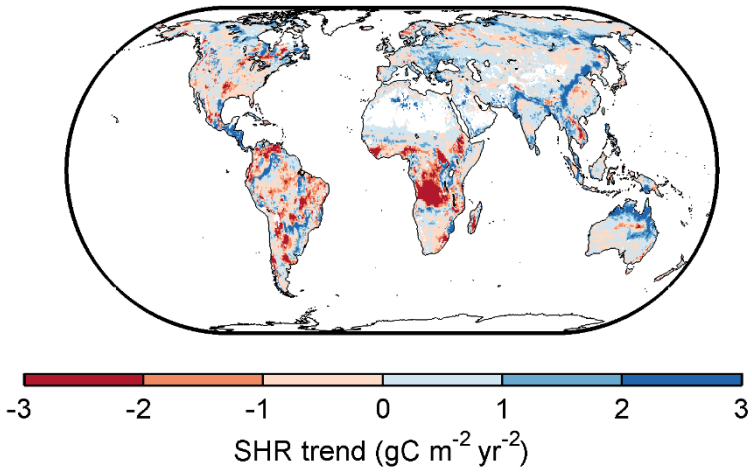

Figure S11 Spatial pattern of SHR trend from one SHR member in our study. This SHR member is estimated by using CRUNCEP climate data, FLUXCOM GPP data and CPC soil moisture data.

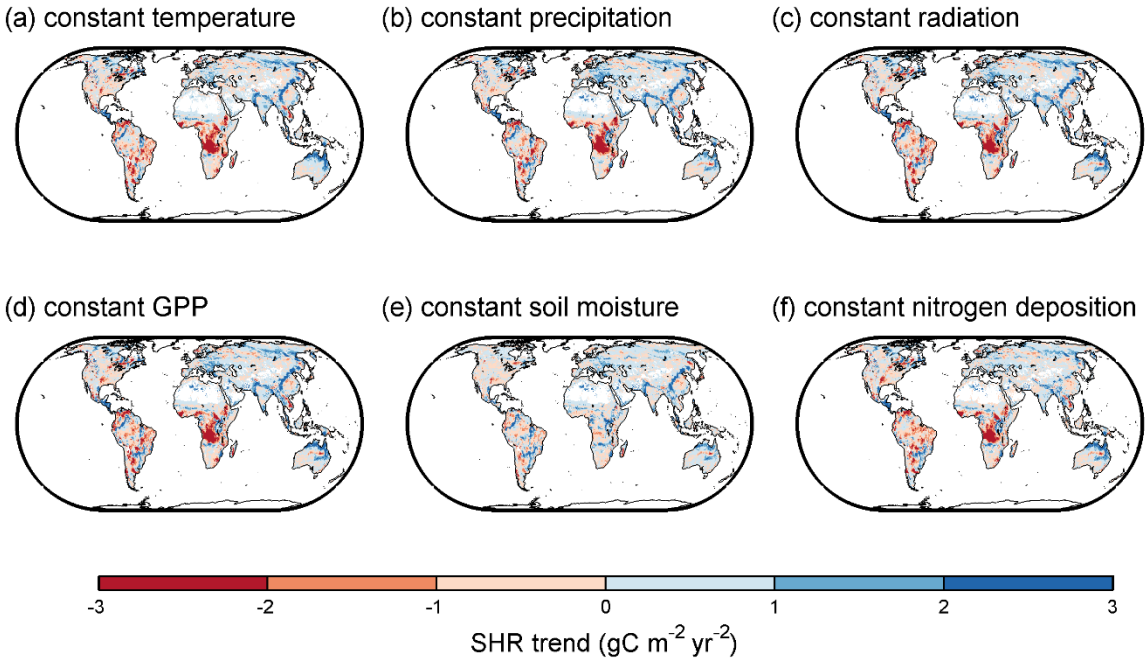

Figure S12 Spatial pattern of SHR trend from one SHR member in our study when one explanatory variable is set to static with values in 1985 as replacement. (a) Temperature, (b) Precipitation, (c) Radiation, (d) GPP, (e) Soil moisture and (f) Nitrogen deposition.

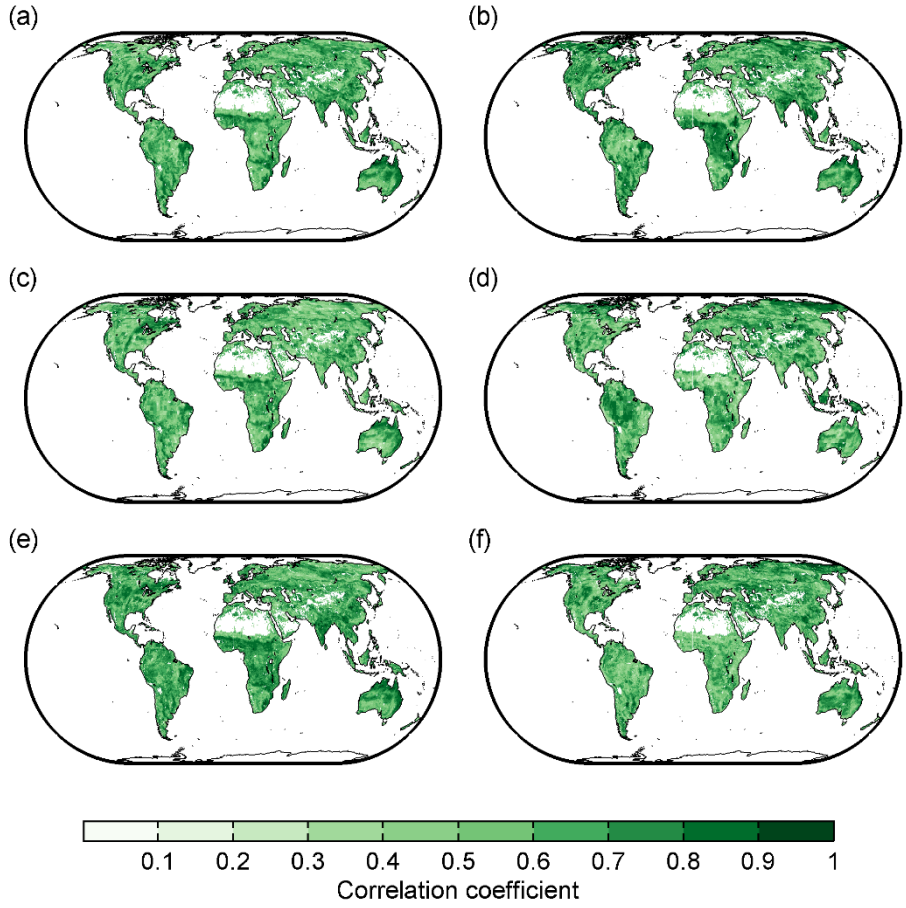

Figure S13 The correlation coefficient between reconstructed soil heterotrophic respiration (SHR) anomaly and original detrended anomaly. SHR estimation in these panels use (a, b) CPC soil moisture, (c, d) GRACE-rec TWS and (e, f) GLDAS soil moisture as explanatory variable, respectively. Panels in the left column show the reconstruction efficiency using precipitation as water proxy and right columns of corresponding soil moisture variable.

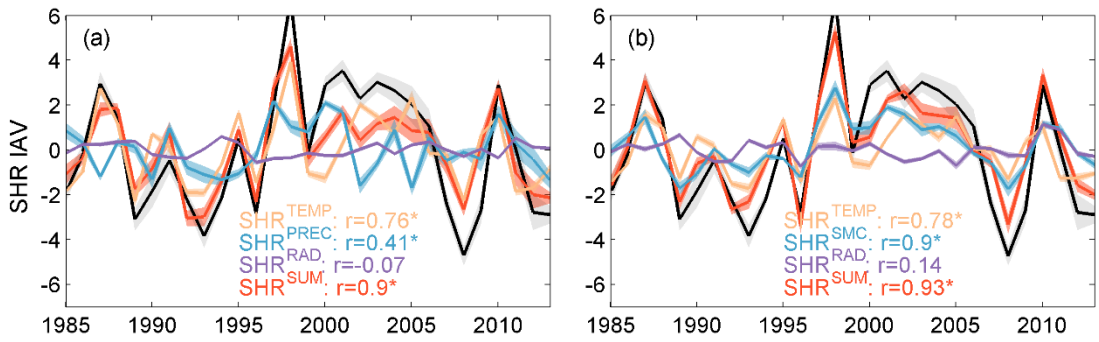

Figure S14 Similar to Figure 5. Only soil heterotrophic respiration (SHR) estimated from GRACE-rec TWS is shown here. The left panel indicates regression against precipitation and the right panel of water storage. The correlation coefficient between SHR anomaly and the component driven by a forcing is labeled. The asterisk denotes the significance of corresponding correlation coefficient (P <

0.05). Shading area represents the spread among ensembles.

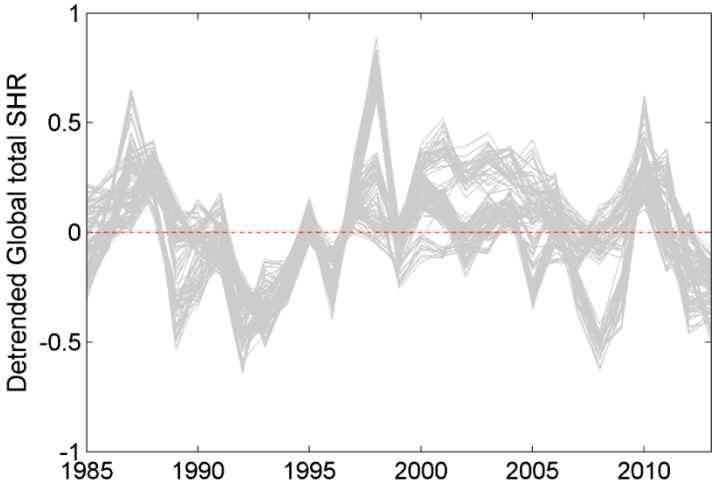

Figure S15 Ensembles of detrended global total soil heterotrophic respiration.

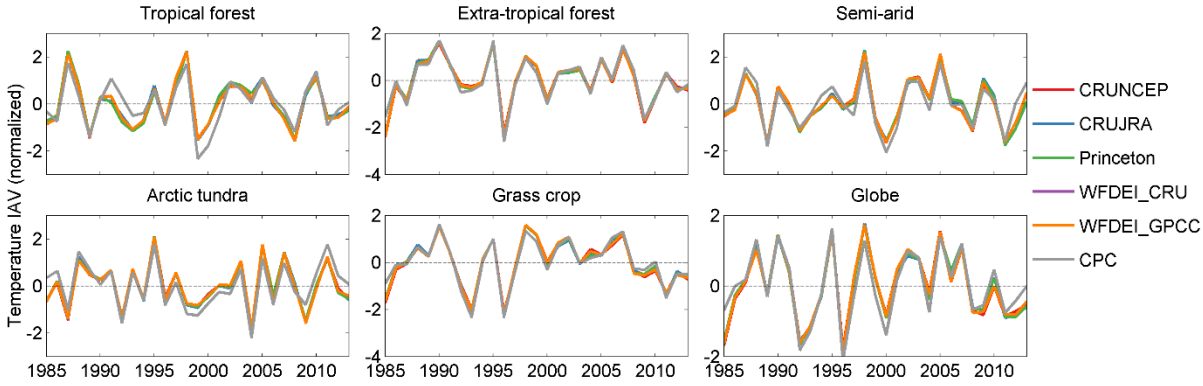

Figure S16 Temperature anomalies in different ecosystems and globe. All these variables are detrended and normalized by their individual standard deviation over 1985-2013.

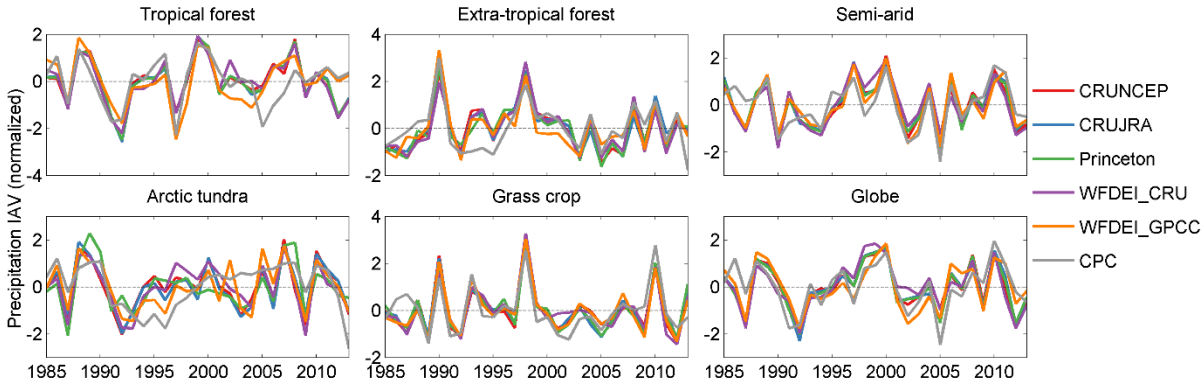

Figure S17 Precipitation anomalies in different ecosystems and globe. All these variables are detrended and normalized by their individual standard deviation over 1985-2013.

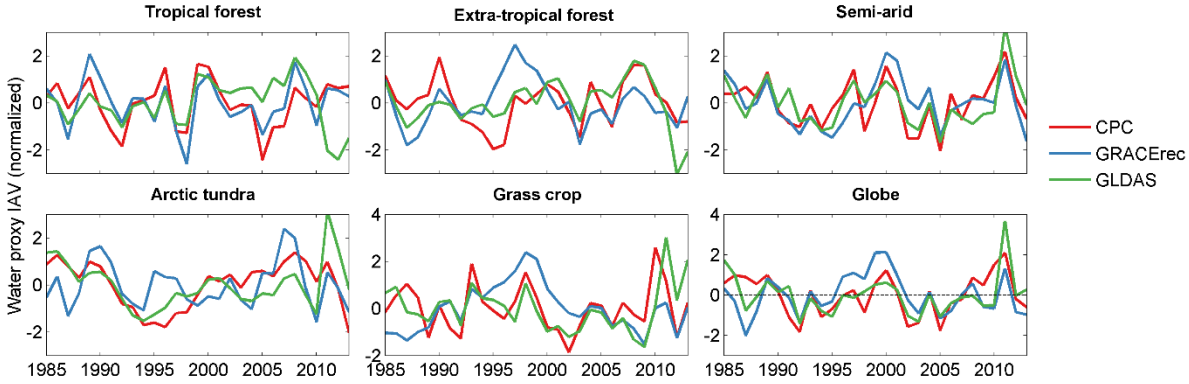

Figure S18 Soil moisture anomalies in different ecosystems and globe. All these variables are detrended and normalized by their individual standard deviation over 1985-2013.

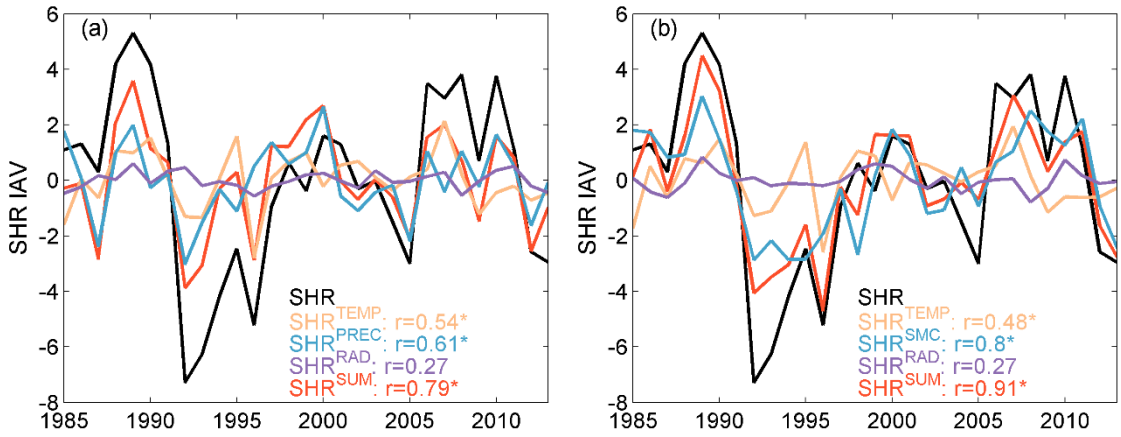

Figure S19 Similar to Figure 5 but for SHR data in Tang et al (2020).

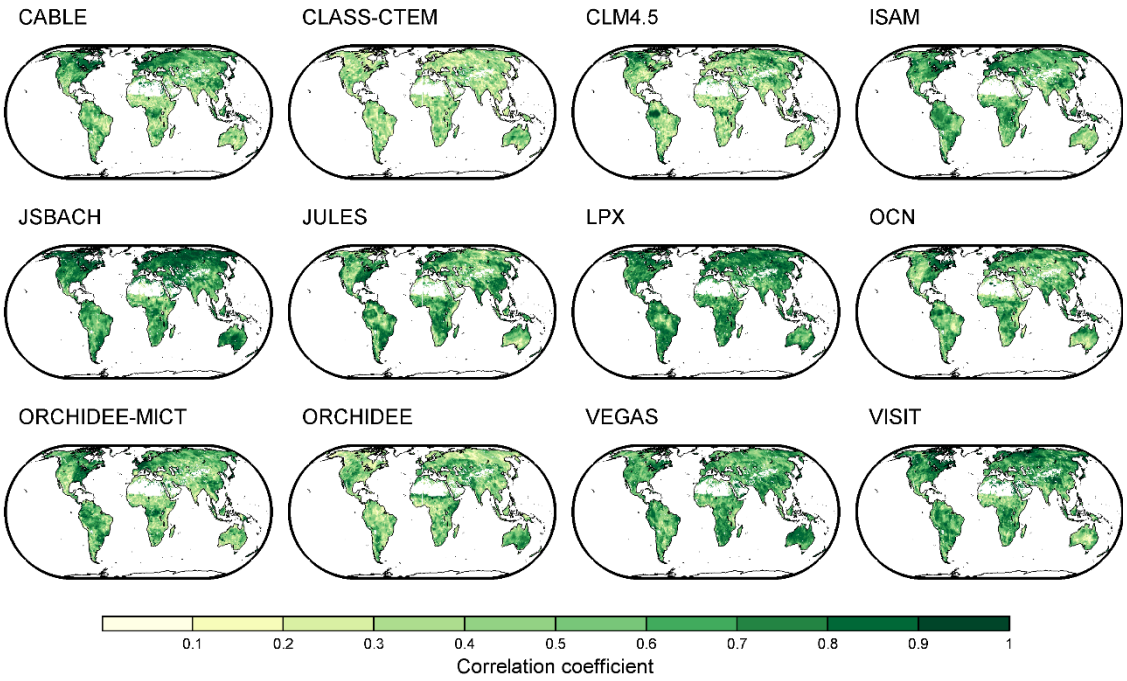

Figure S20 The spatial distribution of correlation coefficient between reconstructed soil heterotrophic respiration (SHR) anomalies and original detrended anomalies in TRENDY model ensembles. The reconstructed SHR anomalies is driven by variability in temperature, precipitation and radiation.

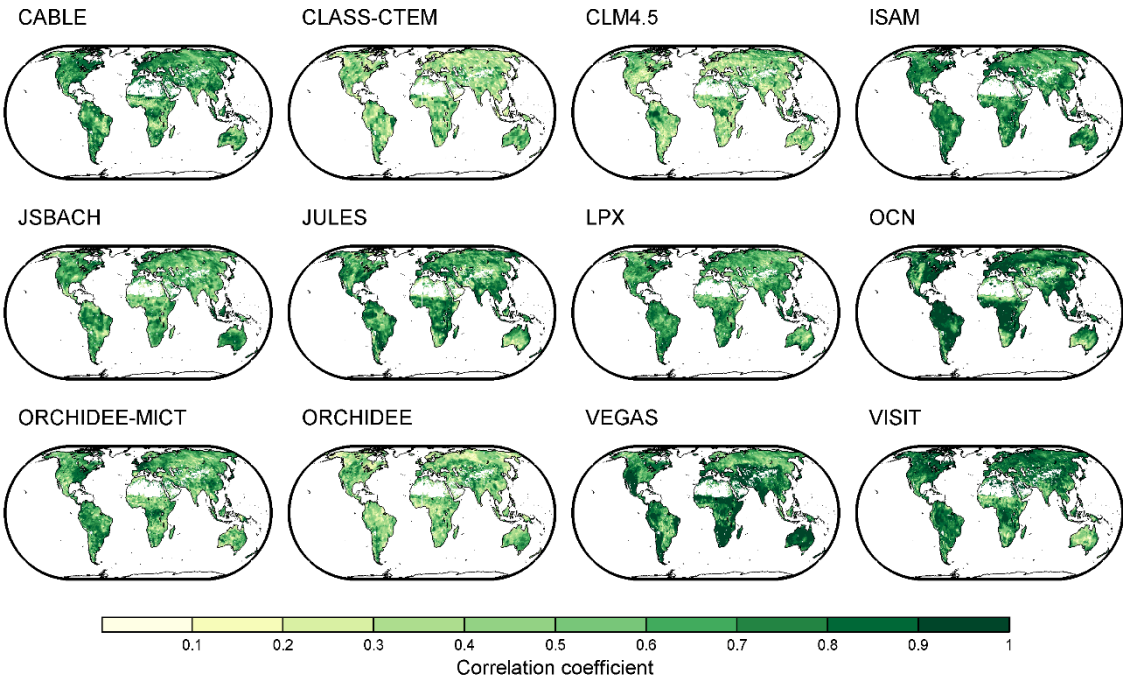

Figure S21 Similar to Figure S20 but using variability in soil moisture as water proxy in regression processes.

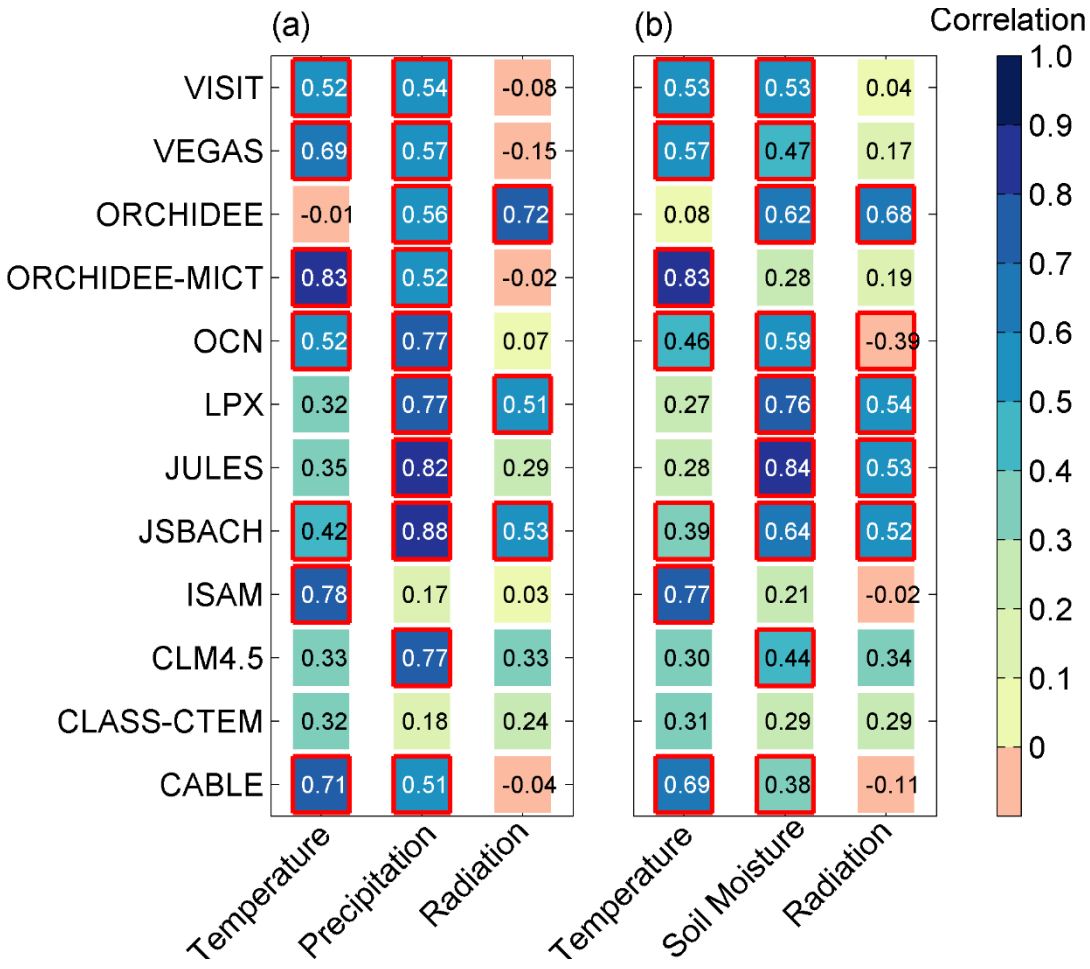

Figure S22 Climatic controls on soil heterotrophic respiration (SHR) inter-annual variability in TRENDY model ensembles. The correlation coefficient between SHR anomaly and the component driven by a forcing is labeled. The red bold frame denotes the significance of corresponding correlation coefficient ($P < 0.05$).

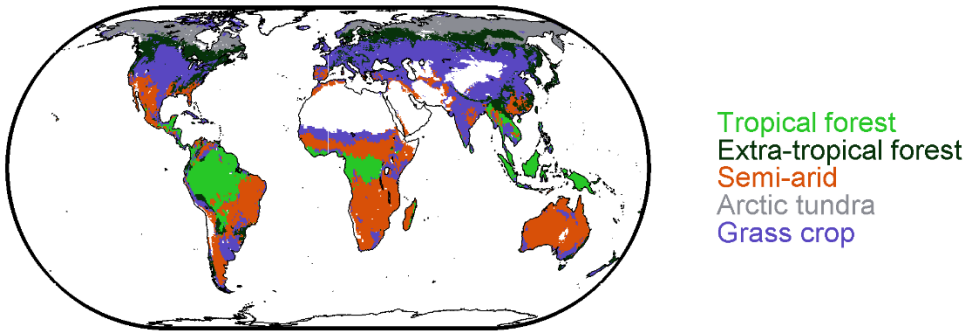

Figure S23 Spatial classification system following Ahlstrom *et al* (2015), which is derived from MCD12Q1 land cover classification. This is only used for ecosystem-scale attribution analysis.

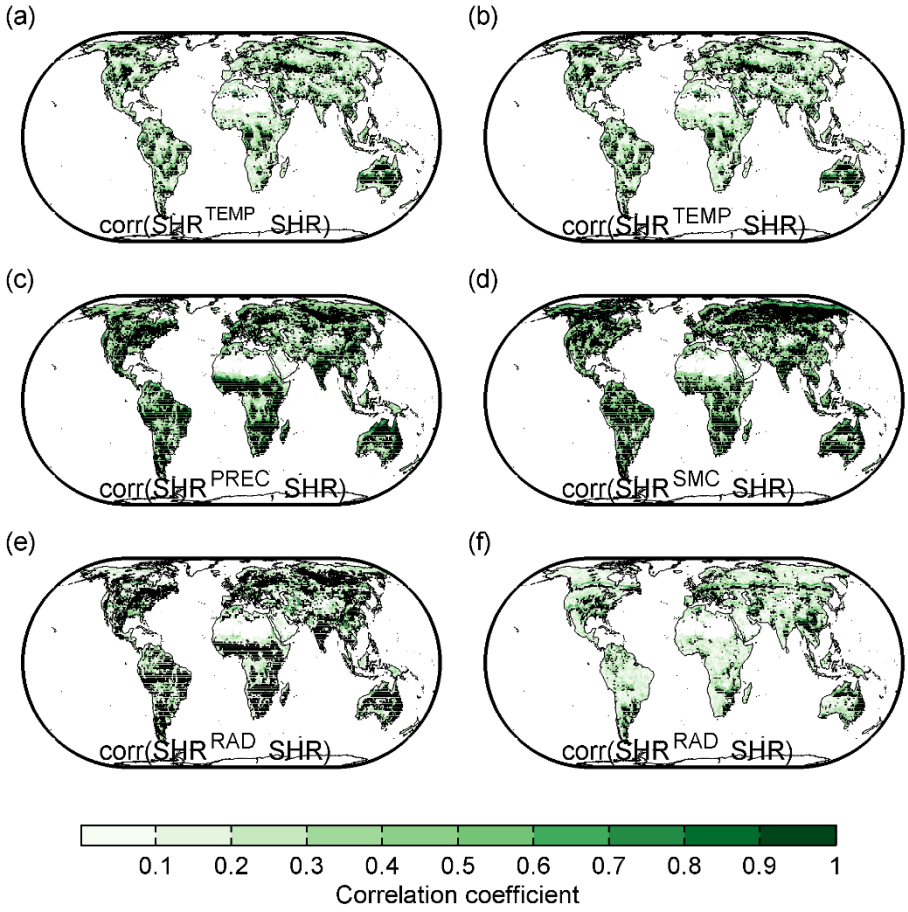

Figure S24 Spatial pattern of correlation coefficient between SHR anomaly driven by one climatic factor and detrended SHR anomaly. The left panels use precipitation as water proxy in regression and soil moisture is used in regression for SHR IAV attribution in right panels. The stippling on the map means more than 63 members (that is, 1/2 of ensembles) showing significant relationship at grid level.

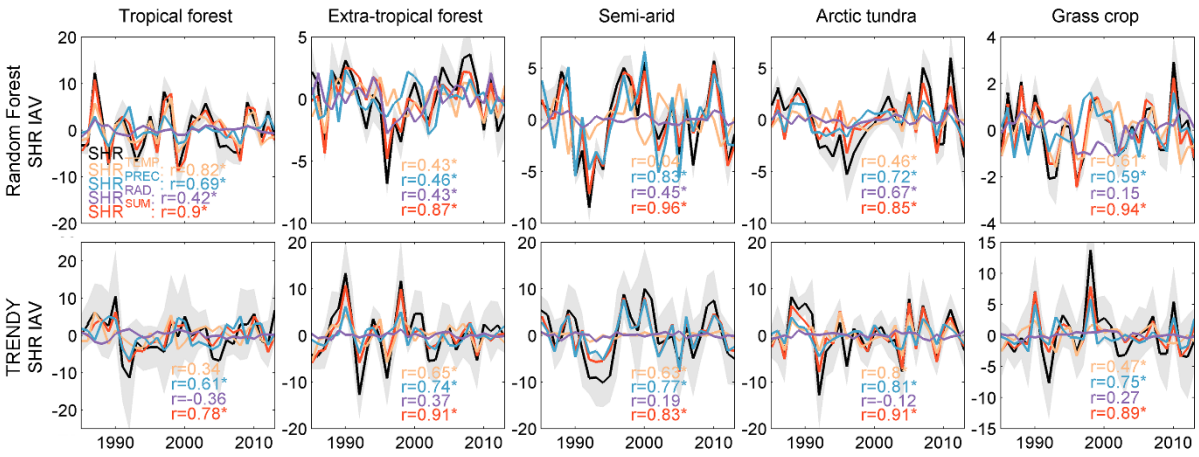

Figure S25 Similar to Figure 6 but using precipitation as water proxy in linear decomposition of SHR anomaly.

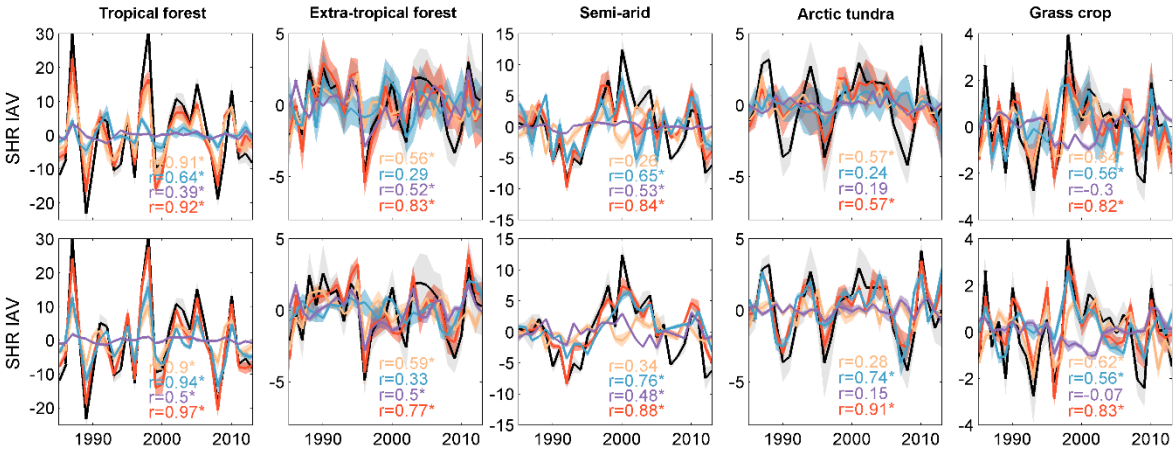

Figure S26 Environmental controls on soil heterotrophic respiration (SHR) inter-annual variability (IAV) in different ecosystems. Here, SHR is estimated using GRACE-rec TWS. The correlation coefficients between aggregated SHR IAV and SHR anomalies driven by a given factor in different ecosystems are labeled. Top panels are derived by using precipitation as water proxy in regression and bottom panels use water storage in regression.

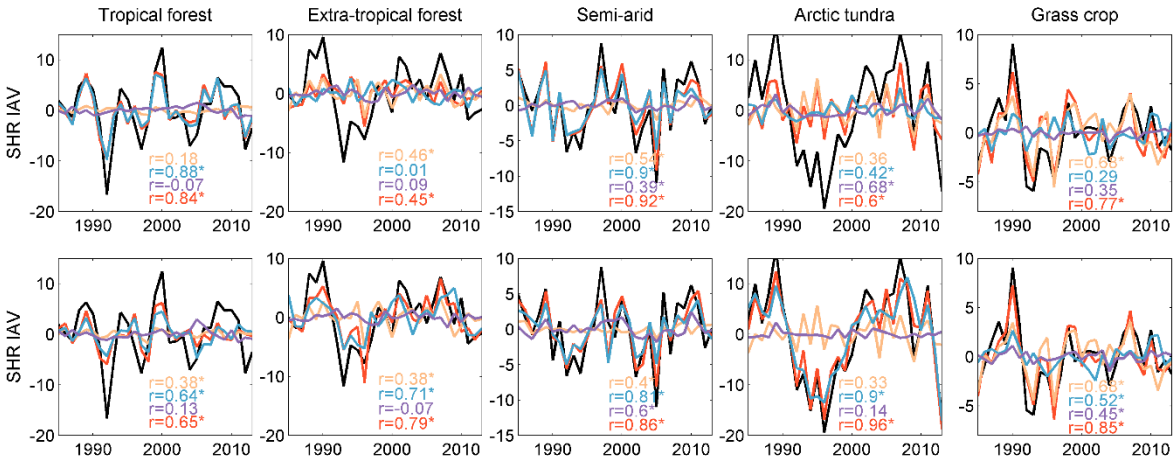

Figure S27 Similar to Figure 6 but for SHR data in Tang et al (2020). Top panels are derived by using precipitation as water proxy in regression and bottom panels use CPC soil moisture in regression.

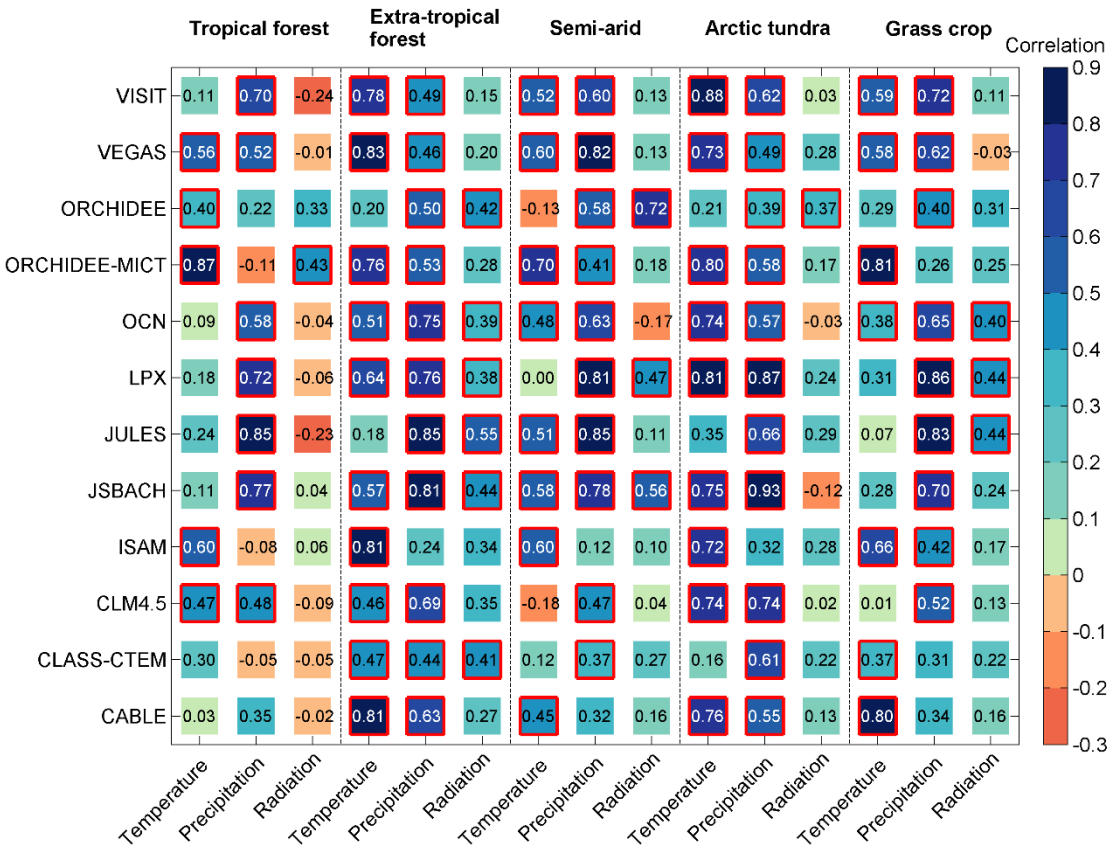

Figure S28 Climatic controls on soil heterotrophic respiration inter-annual variability in different ecosystems in TRENDY model ensembles. The significant correlation coefficient has been marked by red bold frame.

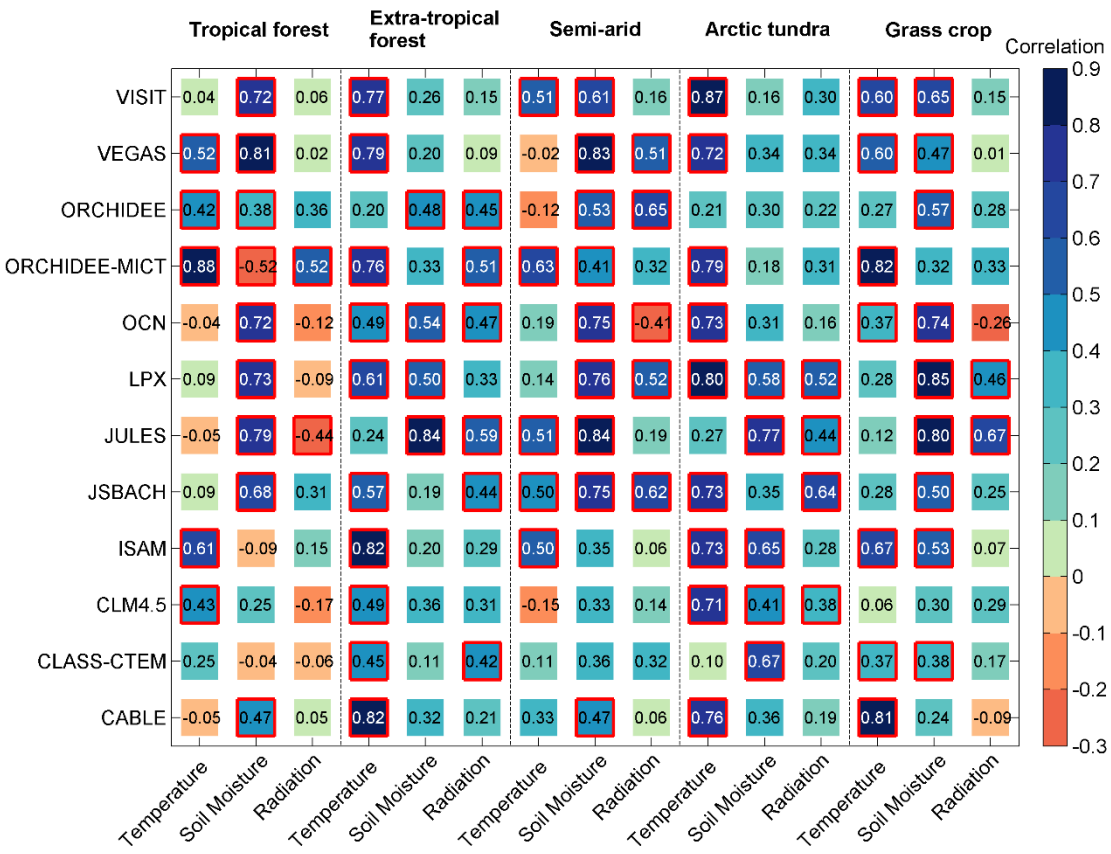

Figure S29 Similar to Figure S28 but using modelled diagnostic soil moisture as water proxy in regression.

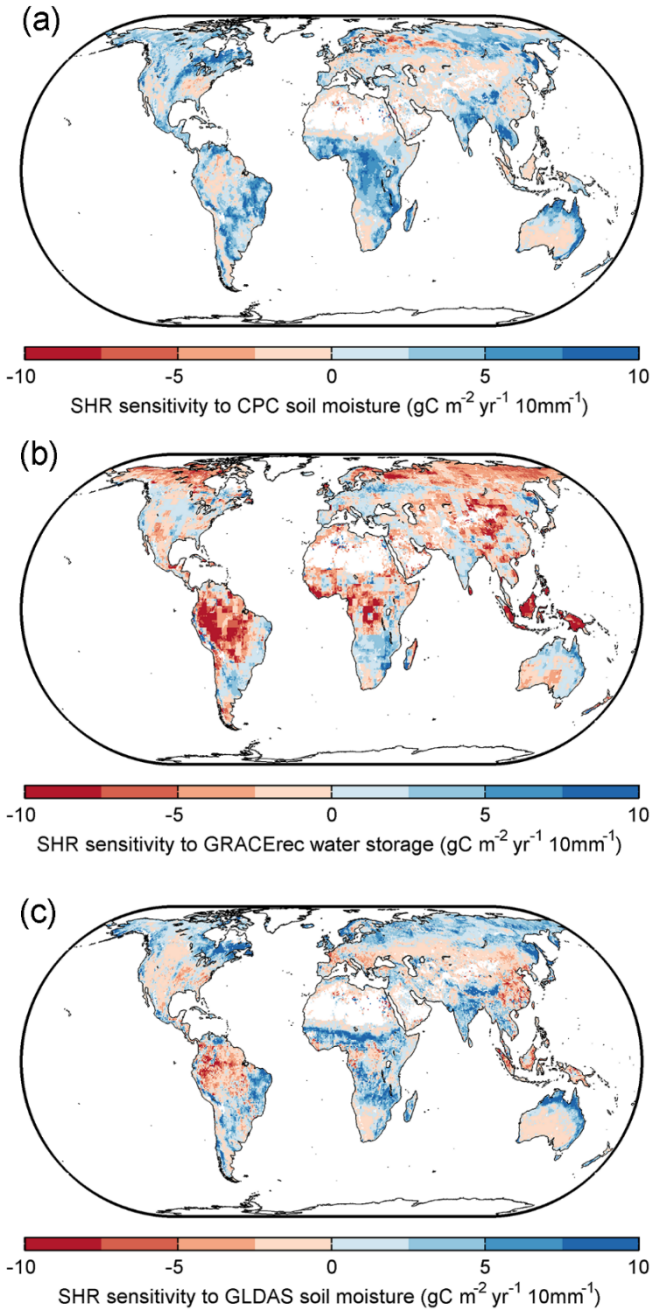

Figure S30 The sensitivity of our data-driven soil heterotrophic respiration to enrolled soil moisture gridded datasets (a) CPC soil moisture, (b) GRACE-rec TWS and (c) GLDAS soil moisture.

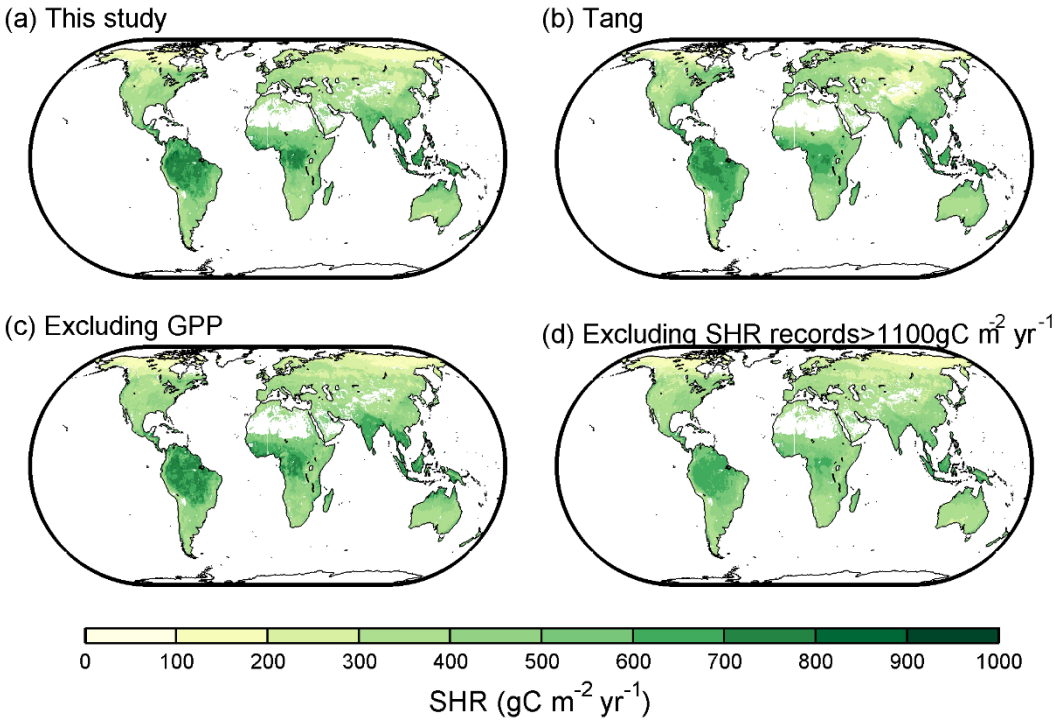

Figure S31 Spatial pattern of (a) SHR in our study, (b) SHR in Tang et al (2020), (c) SHR estimation without using GPP and (d) SHR estimation removing the largest SHR records (>1100gCm^{-2}yr^{-1}).

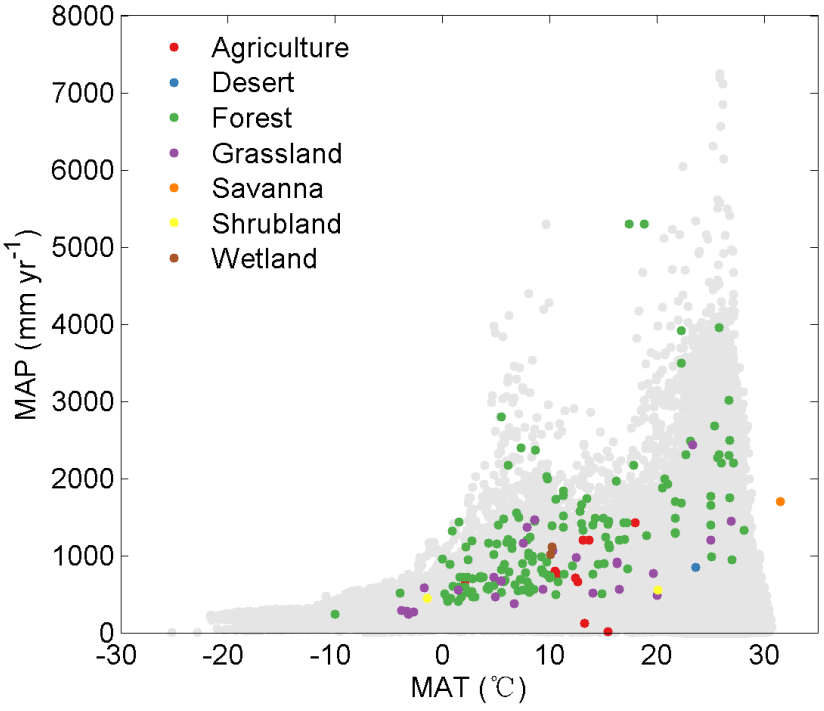

Figure S32 Climate space sampled by our filtered soil heterotrophic respiration observations. The gray points in this plot represents the global climate distribution.

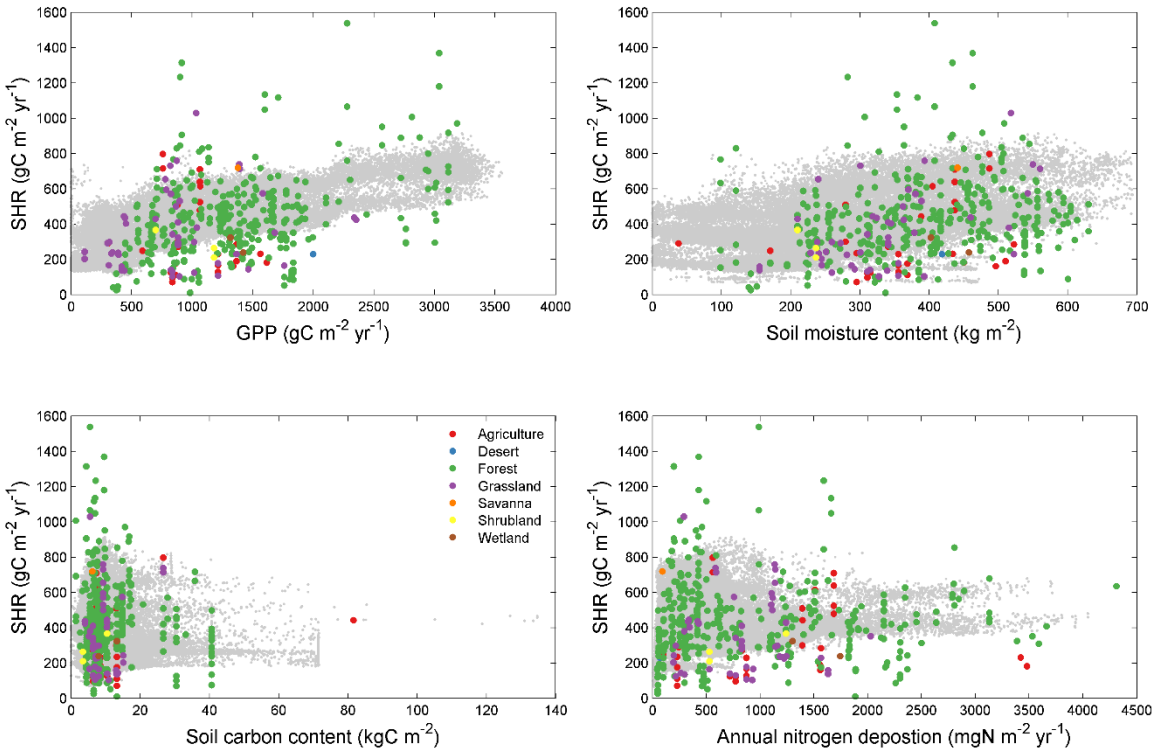

Figure S33 Space sampled by our filtered soil heterotrophic respiration observations. The gray points in this plot represents the global distribution of one explanatory variable.

Text S1 Attribution for soil heterotrophic respiration fluctuation in Hashimoto's product

For Hashimoto's dataset, the reconstructed soil heterotrophic respiration (SHR) inter-annual variability (IAV) from climatic factors can reproduce the year-to-year fluctuation in SHR well in boreal area and North America, but not in East Asia and most area of South America and Africa (Figure S34). Although the Hashimoto's dataset shows a similar spatial pattern of annual SHR as our data-driven estimation, the attribution of the variations in annual SHR reveals discrepancies (Figure S35), especially for tropical forest, in which the local importance of temperature is not detected in Hashimoto's product (Figure S36). In addition, the controlling effect of temperature on Hashimoto's SHR anomalies is more prominent than that of precipitation, especially in extra-tropical forests as well as Arctic tundra areas (Figure S36).

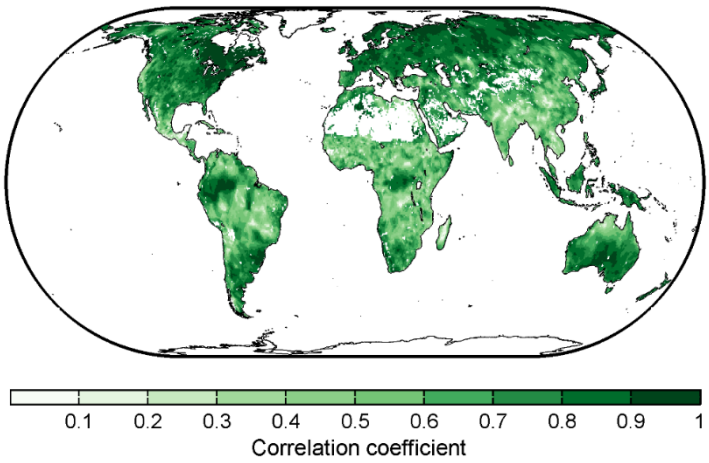

Figure S34 The spatial distribution of correlation coefficient between reconstructed soil heterotrophic respiration (SHR) anomalies and original detrended SHR anomalies in Hashimoto's dataset.

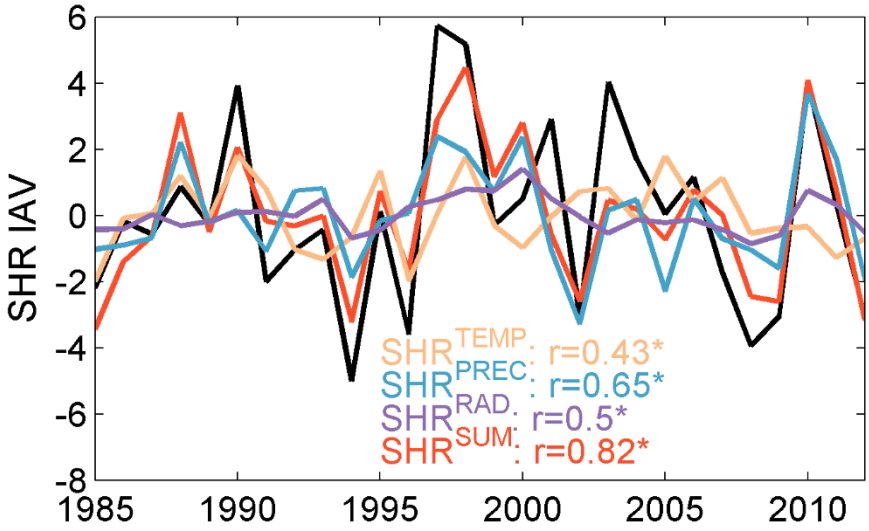

Figure S35 Environmental controls on Hashimoto's soil heterotrophic respiration inter-annual variability at global scale.

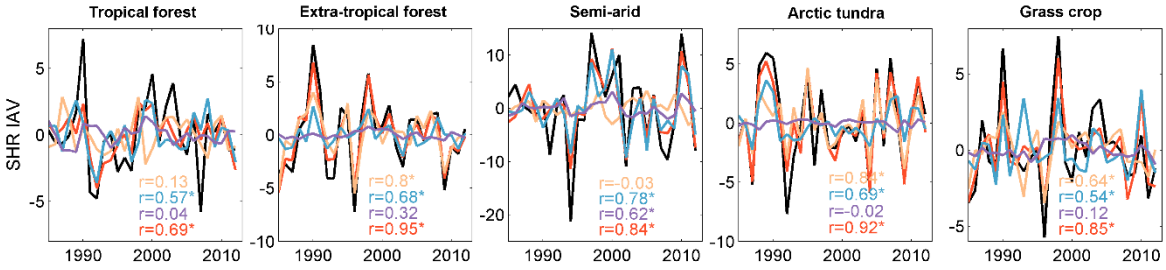

Figure S36 Environmental controls on Hashimoto's soil heterotrophic respiration (SHR) inter-annual variability (IAV) in different ecosystems. The correlation coefficients between aggregated SHR IAV and SHR anomalies driven by a given factor in different ecosystems are labeled.

Table S1 Land cover types in MODIS and SRDB.

Land cover type in MODIS	Land cover type in SRDB
Evergreen Needleleaf forest	Forest
Evergreen Broadleaf forest	
Deciduous Needleleaf forest	
Deciduous Broadleaf forest	
Mixed forest	
Closed shrublands	Shrubland
Open shrublands	
Woody savannas	Savanna
Savannas	
Grasslands	Grassland
Permanent wetlands	Wetland
Croplands	Cropland
Cropland/Natural vegetation mosaic	
Barren or sparsely vegetated	Bare

Table S2 Global total NPP during 2001 to 2015. We download NPP data from http://files.ntsg.umt.edu/data/NTSG_Products/MOD17/GeoTIFF/MOD17A3/GeoTIFF_30arcsec/. We apply the land mask derived from the overlapped area of GPP and climatic data used in this study on MODIS NPP data.

Year	Global NPP (PgC yr^{-1})
2001	49.0
2002	47.8
2003	48.6
2004	49.6
2005	46.9
2006	48.7
2007	48.4
2008	48.9
2009	49.1
2010	48.5
2011	50.4
2012	48.7
2013	49.4
2014	49.9
2015	48.1
2001-2015 average	48.8

3 FOREST FLUXES AND MORTALITY RESPONSE TO DROUGHT: MODEL DESCRIPTION (ORCHIDEE-CAN-NHA) AND EVALUATION AT THE CAXIUANÃ DROUGHT EXPERIMENT

3.1 SUMMARY

Severe drought events frequently hit the Amazon rainforest over last two decades, threatening its carbon sequestration capacity and ecosystem functions. There is a debate on whether those shocks could lead to a more vulnerable state inducing a possible 'tipping point' for larger carbon losses. For the forest resilience to drought, understanding plants hydrodynamics is required since hydraulic failure, disruption of xylem water transport culminating to embolism cavitation can be triggered by high transpiration demand. This mechanism has been demonstrated to be a major cause for tree dieback during drought (both natural and manipulated one). However, current process-based models still perform poorly in estimating the drought-induced tree mortality and biomass loss, using either assumption of constant turnover rate as substitution for tree mortality or carbon balance-based metrics for approximating tree vigor, which is far from a mechanistic representation of tree death and biomass losses during drought event. Therefore, a critical need emerged to incorporate into models a mechanistic hydraulic architecture that can represent the plant water transport, and tree mortality parameterizations linked to the state of plant hydrodynamics.

In this chapter, I evaluated the performance of a mechanistic hydraulic architecture model in ORCHIDEE-CAN for the seasonality of transpiration, soil moisture content and carbon fluxes against the world's longest running drought manipulation experiment at Caxiuana. This site is located in eastern Amazon, with a control (CTL) and a through-fall exclusion experiment (TFE) covering an area of 1ha. This new hydraulic module was pre-developed by E. Joetzger and I made it work in ORCHIDEE-CAN after a lot of debugging and tests. The module enables the simulation of dynamics of water potential and water conductance considering the vertical water transport following Darcy's law, where both water supply and water demand coupled to change in water potential, and water charge/discharge from organ water pool regulated by water capacitance. I proposed a simple tree mortality sub-model connecting the loss of stem conductance and tree mortality rate by two parameters: a cumulated drought exposure threshold and tree mortality rate once the exposure threshold is surpassed. From tests against the field measurements of Caxiuana, we found that the model performs well in simulating both water and carbon fluxes and even in reproducing the observed biomass drop in year 2005 after 4 years of rain-out manipulation. Our model captures the average mortality rate observed at the site, especially the higher tree mortality rate in larger cohorts, although the underestimation of tree mortality rate in smaller cohorts contributes the most to a residual model-observation misfit.

The hydraulic modeling framework and tree mortality scheme could benefit from improvements to enhance the prediction of forest mortality risk. With variability and plasticity of key hydraulic traits in the model, like water potentials when 50% of stem conductance is lost and the sensitivity of water conductance to change in water potential, our model could be given regional parameterizations for the simulation of plant hydrodynamics.

This chapter is published in the journal *Geoscientific Model Development* (GMD):

Yao, Y., Joetzjer, E., Ciais, P., Viovy, N., Cresto Aleina, F., Chave, J., Sack, L., Bartlett, M., Meir, P., Fisher, R., and Luyssaert, S.: Forest fluxes and mortality response to drought: model description (ORCHIDEE-CAN-NHA r7236) and evaluation at the Caxiuanã drought experiment, Geosci. Model Dev., 15, 7809–7833, https://doi.org/10.5194/gmd-15-7809-2022, 2022. (see Appendix B)

3.2 ABSTRACT

Extreme drought events in Amazon forests are expected to become more frequent and more intense with climate change, threatening ecosystem function and carbon balance. Yet large uncertainties exist on the resilience of this ecosystem to drought. A better quantification of tree hydraulics and mortality processes is needed to anticipate future drought effects on Amazon forests. Most state-of-the-art dynamic global vegetation models are relatively poor in their mechanistic description of these complex processes. Here, we implement a mechanistic plant hydraulic module within the ORCHIDEE-CAN-NHA r7236 land surface model to simulate the percentage loss of conductance (PLC) and changes in water storage among organs via a representation of the water potentials and vertical water flows along the continuum from soil to roots, stems and leaves. The model was evaluated against observed seasonal variability in stand-scale sap flow, soil moisture and productivity under both control and drought setups at the Caxiuanã throughfall exclusion field experiment in eastern Amazonia between 2001 and 2008. A relationship between PLC and tree mortality is built in the model from two empirical parameters, the cumulated drought exposure duration that triggers mortality, and the mortality fraction in each day exceeding the exposure. Our model captures the large biomass drop in the year 2005 observed four years after throughfall reduction, and produces comparable annual tree mortality rates with observation over the study period. Our hydraulic architecture module provides promising avenues for future research in assimilating experimental data to parameterize mortality due to drought-induced xylem dysfunction. We also highlight that species-based (isohydric or anisohydric) hydraulic traits should be further tested to generalize the model performance in predicting the drought risks.

3.3 INTRODUCTION

Drought-induced forest mortality events are projected to become more frequent and intense under current climate trends (Allen *et al*., 2015) and may threaten vegetation carbon sinks, as well as bio-physical climate regulation by forests (Allen *et al*., 2010;McDowell *et al*., 2018). Amazonian rainforests hold the largest forest biomass carbon stock on Earth as one of the most important components of the global carbon balance. In the last 15-20 years Amazonia has been heavily affected by concurrent drought at intervals of 5-6 years (Lewis *et al*., 2011;Phillips *et al*., 2009;Yang *et al*., 2018). A persistent increase of biomass mortality and levelling-off of stand-level growth rate from forest inventory plots suggest a decrease of net biomass accumulation rate over the past 30 years (Brienen *et al*., 2015). The predicted intensification of droughts for future climate change scenarios may continue to cause increased tree mortality across large areas (Duffy *et al*., 2015), and exacerbate the likelihood of exceeding a tipping point for regional carbon stocks (Nobre and Borma, 2009). Yet, great uncertainties prevent understanding and quantification of tree mortality, given the high diversity of tree species with different resistance and resilience to drought. Ecosystem models are especially challenged to simulate climate induced mortality at individual and stand level, given the lack of field studies providing long-term data for both biometric measurements and observations of soil and canopy physical climate variables leading to water stress and impairment of tree function. Local ecosystem models with a simulation of individual tree growth and death are computationally expensive, require a large number of parameters per species, and are generally less developed for simulating the soil water dynamics and surface energy budget. Upscaling of these models is also challenging (Maréchaux *et al*., 2021) and to our knowledge, few land surface models have included climate induced mortality beyond that arising from crowding and tree longevity related mortality for large regions (Adams *et al*., 2017;Delbart *et al*., 2010; Powell *et al*., 2013). On the other hand, land surface models, part of Earth System Models, have advanced capabilities to simulate water and energy fluxes between forests and the atmosphere, but usually have rather simple representations of biomass carbon

dynamics, and many of them do not explicitly resolve climate-induced mortality processes. A mechanistic representation and prediction of the Amazon forest response to drought in global land surface models is thus an important priority for research.

Early vegetation models parameterized mortality through indicators of competition-induced self-thinning and /or threshold of growth vigor (Adams *et al*., 2013;Zhu *et al*., 2015;McDowell *et al*., 2011), which ignored the mortality related to extreme events such as drought. Improving mortality representation requires more robust physiological processes embedded in models that couple water, carbon and energy fluxes (Gustafson and Sturtevant, 2013). Recent advances have been made for improved resolution of the mechanisms by which trees die from drought. Two non-exclusive physiological mechanisms have been proposed: hydraulic failure and carbon starvation (Choat *et al*., 2018;McDowell *et al*., 2018;Meir *et al*., 2015). Hydraulic failure occurs when the tension within the xylem vessels is so high that it causes air-seeded embolism, which impedes water transport. If embolism exceeds a tree dependent survival threshold (Cochard and Delzon, 2013), individual tree dieback may occur, possibly with some lag in case of insufficient repair capabilities to restore upward water transport. Carbon starvation during drought is expected to occur from prolonged stomatal closure causing reduced photosynthetic assimilation, resulting in a drawdown and possible exhaustion of nonstructural carbohydrate reserves (NSC) (Hartmann, 2015;Signori-Müller *et al*., 2021). Also, embolized vessels may be detrimental to the carbon assimilation processes, so that hydraulic failure and carbon starvation are coupled together (McDowell *et al*., 2018). Many studies have tried to discern the respective contributions of the two mechanisms in tree wilting during drought (Rowland *et al*., 2015;Yoshimura *et al*., 2016). After 15-years of experimental throughfall exclusion in a forest in the Amazon, Rowland *et al*. (2015) found that hydraulic failure was most closely associated with tree mortality under the drier condition, and that there was no distinct difference in NSC concentration between droughted and non-droughted trees, although seasonal differences were observed. Here, we will build on this early understanding of drought-induced impacts in the Amazon and present a model where hydraulic failure is considered to be the dominant risk factor for tree mortality, but we recognize the importance of carbon starvation and also investigate primary production and labile carbon changes in the simulations.

Efforts have been made toward accounting for physically-based water transport in land surface models, implemented through regulation of stomatal behavior, and the explicit simulation of water transport across the soil, root, stem, leaves and atmosphere continuum following a gradient of water potential and organ-specific conductivity parameters. The Ecosystem Demography model optimized the marginal increase of net carbon assimilation per unit of water loss within the soil-plant-atmosphere continuum to simulate a realistic stomatal conductance (Xu *et al*., 2016). Given the benefit-cost tradeoff between photosynthetic carbon gain and hydraulics uplift of water, Sperry *et al*. (2017) modeled stomatal behavior by maximizing the instantaneous difference between photosynthetic gain and the proximity to hydraulic failure. The target of such stomatal optimization schemes varies from carbon gains (Dewar *et al*., 2018), water use efficiency (Bonan *et al*., 2014) to profit maximization of the difference between carbon gain and hydraulic cost (Sabot *et al*., 2020), or optimization was performed using a linear function of water potential (Eller *et al*., 2018) or xylem conductance (Eller *et al*., 2020). In addition to the optimization of stomatal control, key features of water potential along the soil-plant-atmosphere continuum are also introduced in some models to describe plant hydraulic responses. Papastefanou *et al*. (2020) modeled plant hydraulics starting from leaf water potential in consideration of iso-hydricity among different hydraulics strategies. De Kauwe *et al*. (2020) incorporated the plant hydraulic module 'Desica' into the CABLE land surface model, which simulated water flows and water potential through the soil-plant-atmosphere continuum following Xu *et al*. (2016). Kennedy *et al*. (2019) generated new configurations of prognostic vegetation water potential at the root, stem and leaf levels and based plant water stress on the metrics of leaf water potential in the community land model version 5a. Explicit representations of plant hydraulics in process-based models advance our knowledge of the plant responses to drought (Hendrik and Maxime, 2017). However,

in terms of how tree mortality responds to future climate scenarios, research gaps still remain in the specific thresholds of hydraulics failure beyond which drought stress induces tree mortality (Anderegg, 2015;Choat, 2013;Hammond *et al*., 2019), which limits the development and testing of hydraulic failure mechanisms coupled to mortality in Amazonian rainforests.

Identifying a specific threshold for hydraulic failure associated with a given mortality likelihood remains challenging (Choat *et al*., 2018). Drought indices related to climate have already been tested in this context and were found to be species and trait dependent. Anderegg *et al*. (2015) found that hydraulic conductivity of aspen dropped rapidly when accumulated climatic water deficit from 2000-2013 exceeds almost 5300 mm from break-point regression analysis. Relative water content derived from vegetation optical depth also contains the signal of such a threshold relationship with drought-driven mortality rates (Rao *et al*., 2019). The percentage of loss in conductivity (PLC) has also been found to be an appropriate metric for assessment of hydraulic dysfunction (Adams *et al*., 2017), and has been linked experimentally to plant mortality (Brodribb and Cochard, 2009;Liu *et al*., 2021a;Urli *et al*., 2013). Liu *et al*. (2021a) fitted relationships between simulated PLC and observed mortality rate across investigated sites via multiple regression, and used this formula for the prediction of mortality. Brodribb and Cochard (2009) found that the maximum survivable water stress in conifer species was a 95% loss in leaf conductance. For five angiosperm tree species in Europe, Urli *et al*. (2013) found that the embolism threshold was closer to the water potential at 88% of conductance loss. Plant volumetric water content also shows a threshold-type response empirically related to mortality risk, with an inflection point at 47% of volumetric content (Sapes *et al*., 2019). Thus, the lethal point can differ among tree species, and presumably strongly in tropical forests in which different species vary widely over hydraulic traits (Bittencourt *et al*., 2020;Rowland *et al*., 2015). This variation needs to be considered in hydraulic modelling.

Currently, only a few studies have integrated plant hydraulic failure as a process in a global land surface model and parameterized mortality as a consequence. In this study, we implement a mechanistic hydraulic architecture modeling of the water transport in the continuum from soil to atmosphere in the ORCHIDEE-CAN model. We refer to this New Hydraulic Architecture module as "NHA" that is, ORCHIDEE-CAN-NHA. We describe three developments and their evaluation against field measurements for control and experimental throughfall conditions, in aspects of soil and plant water variables, and biometric variables such as tree growth and mortality, at the Amazon tropical forest site of Caxiuanã (Fisher *et al*., 2006; Meir *et al*., 2018). Firstly, we describe the development of the new hydraulic architecture model. Then we carry out site-level simulations and evaluate the model performance in aspects of seasonal variability in transpiration, soil moisture and productivity against experimental control and drought observations. Thirdly with the simulation of dynamic water potential, water transport, and conductance, the model is extended to define a mortality risk from continuous high loss of stem conductance from cavitation. In this part, we bridge the gap between reaching a stem conductance threshold corresponding to a high loss of conductance and mortality risk. Finally, we compare the modeled mortality in different circumference classes to verify whether our improved model can capture the observed size-related mortality distribution, with trees being first rather insensitive to drought during the first years, after which larger trees are affected by dieback.

3.4 METHODS

3.4.1 Model description and simulation protocols

The starting point: ORCHIDEE-CAN r2290

The model version taken as the starting point for development in this study is ORCHIDEE-CAN (r2290), a branch of the ORCHIDEE land surface model. ORCHIDEE is a physical process-based

model, which can simulate the energy, water, and carbon fluxes between land surfaces and the atmosphere. The SECHIBA module corresponds to faster processes, such as exchange of water and energy as well as photosynthesis between land and the atmosphere in half hour time interval. The carbon module (STOMATE) simulates soil processes (soil decomposition, heterotrophic respiration, soil organic carbon dynamics) at the half-hourly time step and vegetation carbon cycle processes at daily intervals, including carbon allocation, vegetation mortality and recruitment, phenology, litter fall. The development of this branch of the ORCHIDEE model focuses on improving the capability of the ORCHIDEE model to simulate the biogeochemical and biophysical effects of forest management and includes allometric-based allocations of carbon to different pools, a simple plant hydraulic structure (see below) as well as an albedo scheme that in part depends on canopy structure (Naudts *et al*., 2015). One of its new features is the way the vegetation is discretized; a dynamic canopy structure is simulated by considering a user-defined number of circumference classes (n=20 in this study) and an empirical rule reflecting intra-tree competition that downscales canopy level GPP into the different circumference classes, which feedback on light interception and mortality through self-thinning. Background mortality comes from the reciprocal of a constant residence time. Climate based mortality, e.g. from drought has not been modeled yet using this system.

Hydraulic architecture representation in ORCHIDEE-CAN

In ORCHIDEE-CAN r2290 (Naudts *et al*., 2015), the representation of water stress is realized through a constraint based on the amount of water that plants can transport from soil to their leaves. This constrained transpiration supply equals the quotient between the water potential gradient from soil to leaves, and a total hydraulic resistance of leaf, stem and root. In this framework, the leaf water potential is fixed to a constant value for each plant functional type (PFT), with specific minimum value (-2.2 MPa for tropical evergreen forests, Hickler *et al.* (2006). The soil water potential in the root zone is calculated by adding a tuned scaling factor, accounting for soil-root resistance and other missing processes, to the sum of the soil water potential (calculated from soil moisture and van Genuchten parameters, Van Genuchten (1980) weighted by a proportion of root mass in each soil layer. Such hard modulator can sometimes lead to unrealistic soil water potential in the root zone (Joetzjer *et al*., under review). The prescribed vegetation distribution is used to constrain this modulator to minimize model bias (Naudts *et al*., 2015). During the simulation, transpiration is co-limited by the energy budget providing a transpiration demand, and the transpiration water supply limited by transport from soil to leaves. When the potential transpiration constrained by the energy budget is higher than the transpiration supply, real transpiration is limited to the physically plausible water supply. Then the energy budget and photosynthesis-related processes are recalculated. It should be noted that the root and leaf resistance parameters in ORCHIDEE-CAN depend only on conductivity and biomass (root mass for root, LAI for leaf) and do not respond to hydrological conditions directly. Only the stem resistance related to xylem conductivity is dynamic and changes as a function of the soil water potential in the root zone. The schematic framework of the ORCHIDEE-CAN model is illustrated in Figure 3.1a. This architecture is not completely mechanistic, given the tuned factor on top of soil water potential, the fixed leaf water potential values and the conductivities affected solely by organ mass. Therefore, further developments of the hydraulic architecture scheme were performed and presented here.

Dynamic root scheme in ORCHIDEE-CAN-RS

To increase the reliability of soil water potential simulations in root zone ($\Psi_{soil\text{-}root}$), Joetzjer *et al* (under review) improved this part of the model (flowchart in Figure 3.1b, ORCHIDEE-CAN-RS). $\Psi_{soil\text{-}root}$ integrated Ψ_{soil} in the root zone vertically, i.e. Ψ_{soil} in the root zone is now weighted by the maximum amount of water that can be absorbed by roots in each soil layer (E_{max}), which depends on a soil-to-root resistance and on a prescribed minimum root water potential (-3 MPa in this study)

below which no more water in a given soil layer can be drawn into the plant. The soil-to-root resistance accounts for the water transport path from soil to root surface. With this scheme, the plant will dynamically use deep layer soil moisture when the surface soil desiccates, so that this process allows to sustain more transpiration from deeper layers during dry periods. Although Joetzjer *et al* (under review) solved the problem of tuned modulator imposed on $\Psi_{soil\text{-}root}$ by adding a parameterization of the soil-to-root resistance, a more integral mechanistic structure of water transport from soil to leaf remains to be done to enable a dynamic connection between soil and leaf as well as corresponded simulations during drought events. $\Psi_{soil\text{-}root}$ is calculated separately for different cohorts, since we assume taller trees have deeper roots and can reach water stored in deeper layers. For example, we assume that the largest cohort can take water from all 12 soil layers while the smallest cohort can only take water in shallow layer.

Hydraulic scheme development and implementation in ORCHIDEE-CAN-NHA r7236

Figure 3.1c presents the schematic diagram of the new hydraulic architecture in ORCHIDEE-CAN-NHA. Besides the water transport driven by vertical water pressure difference, the water flow to / from organ-specific water storage at time t is explicitly modeled based on capacitances and water potential differences between time t and t-1. For each organ, the water supply should meet its water demand. For example, water demand at leaf level is parameterized as the transpiration supply. Water supply to leaf is composed by water transport from stem minus the water charge or plus the discharge from the leaf water storage pool. The water budget of the leaves is calculated first, in order to determine how much water has to be drawn up from the other connected upstream organs. It should be noted that the new hydraulic mechanism is imposed on 20 circumference classes, separately. The detailed description of new mechanistic hydraulic processes is given below. This water transport module does not affect assimilation directly but relates to the water supply for transpiration. Normally, when there is no water limitation, GPP is calculated by FvCB model that is the minimum of the Rubisco-limited rate of CO_2 assimilation and the electron transport-limited rate of CO_2 assimilation (Yin & Struik, 2009). If transpiration exceeds the estimated water supply, then the transpiration is recalculated to meet the water supply part. The canopy resistance is also re-calculated and so does the GPP.

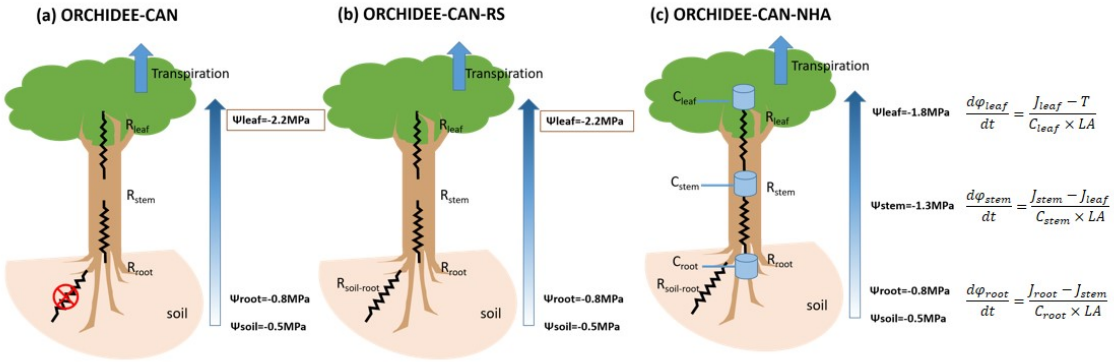

Figure 3.1 Schematic framework for hydraulic architecture in (a) ORCHIDEE-CAN, (b) ORCHIDEE-CAN-RS and (c) ORCHIDEE-CAN-NHA. The framed rectangles represent fixed values during the simulation. In ORCHIDEE-CAN and ORCHIDEE-CAN-RS, R_{leaf} is related to leaf conductivity and leaf area. R_{stem} is related to sapwood conductivity that can vary with cavitation and sapwood area. R_{root} is related to fine root conductivity and root biomass. In ORCHIDEE-CAN-NHA, transport conductance of each organ is a function of their organ-specific water potential, maximum conductance and water potential when loss of 50% conductance occurred. C_{leaf}, C_{stem} and C_{root} represent water storage capacitance. J_{leaf}, J_{stem} and J_{root} are vertical water transport to leaf, stem and root, respectively. LA is total leaf area.

Water storage calculation

The Supply-Demand framework is solved at leaf, stem and root, separately. We assume that during the first time step, all water potentials in different organs are the same (Eq. 1).

$$\Psi_{leaf,\,t} = \Psi_{stem,\,t} = \Psi_{root,\,t} = \Psi_{soil\text{-}root,\,t} \quad (1)$$

Water storage in the different organs is calculated with organ-specific capacitance values (unit: mmol):

$$m_{leaf,max} = \frac{b_{leaf}}{LDMC} - b_{leaf} \quad (2)$$

$$m_{leaf,t} = m_{leaf,max} + C_{leaf}\psi_{leaf,t}LA \quad (3)$$

Where C_{leaf} is relative leaf capacitance in unit of mmol m^{-2} MPa^{-1}, *LDMC* the leaf dry matter content, b_{leaf} is the dry leaf biomass. *LA* is total leaf area. Maximum water storage in leaf ($m_{leaf,max}$) is generated by leaf fresh mass minus dry mass. $m_{leaf,t}$ is leaf water storage at time t.

$$m_{sap,max} = v_{stem}WC \quad (4)$$

$$m_{sap,t} = m_{sap,max} + C_{stem}\psi_{stem,t}v_{stem} \quad (5)$$

$$v_{stem} = \pi\left(\frac{dbh}{2}\right)^2 h \quad (6)$$

Where C_{stem} is sapwood capacitance, h tree height in m, v_{stem} is proportional to the volume of tree stem in m^3. *WC* is the amount of water (mmol) per unit volume of sapwood. $m_{sap,max}$ and $m_{sap,t}$ are maximum sapwood water storage and sapwood water storage at time t, respectively. *dbh* is the diameter at breast height.

$$m_{root,max} = b_{root}root_{wc} \quad (7)$$

$$b_{root} = v_{stem} \times WD \times ratio_{root:shoot} \quad (8)$$

$$v_{root} = \frac{b_{root}}{\rho_{root}} \quad (9)$$

$$m_{root,t} = m_{root,max} + c_{root}\psi_{root,t}v_{root} \quad (10)$$

Where $root_{wc}$ indicates the amount of water (mmol) stored in per gram of root mass. *WD* is aboveground wood density. v_{root} is root volume. $ratio_{root:shoot}$ is root to shoot ratio. b_{root} is root mass. ρ_{root} is root density. $m_{root,max}$ and $m_{root,t}$ are maximum root water storage and root water storage at time t, respectively. c_{root} is root capacitance.

Hydraulic conductance calculation

Hydraulic conductance per unit of leaf area in leaf, sapwood and root at time t ($k_{leaf,t}$, $k_{stem,t}$, $k_{root,t}$) are calculated with sigmoidal relationships, based on their real-time water potential and a maximum conductance. $\psi_{50,organ}$ denotes the water potential when 50% conductance lost. $e^{a_{organ}}$ describes the sensitivity of conductance to changes in water potential around $\psi_{50,organ}$. An example for how these two shape parameters affecting sapwood conductance is shown in Figure 3.2 for the stem organ.

$$k_{leaf,t} = \frac{k_{leaf,max}}{1+exp\left(a_{leaf}\times\left(\varphi_{leaf,t}-\varphi_{50,leaf}\right)\right)} \quad (11)$$

where $k_{leaf,t}$ and $k_{leaf,max}$ are leaf conductance at time t and maximum leaf conductance, respectively.

$$k_{stem,t} = \frac{k_{stem,max}}{1+exp\left(a_{stem}\times(\varphi_{stem,t}-\varphi_{50,stem})\right)} \quad (12)$$

where $k_{stem,t}$ and $k_{stem,max}$ are stem sapwood conductance at time t and maximum stem sapwood conductance, respectively.

$$k_{root,t} = \frac{k_{root,max}}{1+exp\left(a_{root}\times(\varphi_{root,t}-\varphi_{50,root})\right)} \quad (13)$$

where $k_{root,t}$ and $k_{root,max}$ are root conductance at time t and maximum root conductance, respectively.

The conductance of the upper part of the tree (leaf plus upper part of stem) and lower part of the tree (lower part of stem plus root) are calculated following Eq. 14-15. These two conductances will be used to calculate the water flow from stem to leaf, and root to stem later separately.

$$k_{upper,t} = \frac{1}{\frac{1}{k_{leaf,t}}+\frac{1}{2k_{stem,t}}} \quad (14)$$

$$k_{trunk,t} = \frac{1}{\frac{1}{2k_{root,t}}+\frac{1}{2k_{stem,t}}} \quad (15)$$

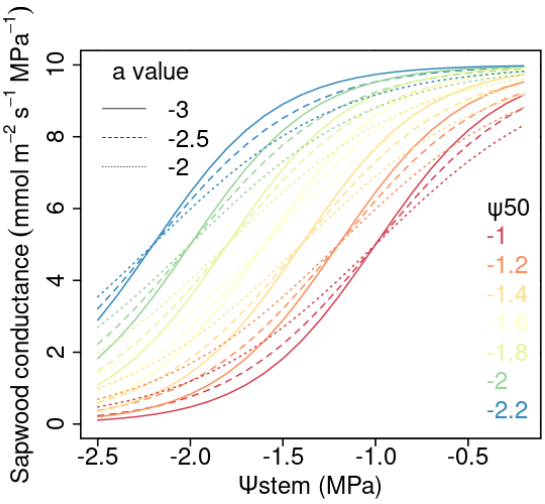

Figure 3.2 Sigmoidal relationship between stem sapwood conductance (normalized by total leaf area) and stem water potential. Line colors correspond to different Ψ_{50} values. The line types (continuous, dashed and dotted line) denote different curvature parameters (a_{stem}).

Water transport pathway simulation

We assume that for leaves, transpiration supply is based on the water input transported from the stem minus the water charge/discharge from the leaf water storage pool (Eq. 16).

$$T_{supply} = J_{leaf,t+1} - W_{leaf,t+1} \quad (16)$$

Where $J_{leaf,t+1}$ is the flux of water transported vertically to leaf from stem sapwood (unit: mmol) and $W_{leaf,t+1}$ the change in leaf water storage. A positive value of $W_{leaf,\,t+1}$ means that the leaf was charged with water during hydraulic recovery, and negative means it was reduced by evapotranspiration. At leaf level, the target is to solve for the leaf water potentials that minimize the difference between

water demand and supply (Eq. 17).

$$\Delta = (J_{leaf,t+1} - W_{leaf,t+1}) - T_{demand} \quad (17)$$

Similarly, at stem level, the target is to minimize the difference between water demand at stem and water supply to the stem (Eq. 18).

$$\Delta = (J_{stem,t+1} - W_{stem,t+1}) - J_{leaf,t+1} \quad (18)$$

$J_{stem,t+1}$ is the water transported vertically from root to stem. $W_{stem,t+1}$ the change in stem water storage. After solving leaf-level target, $J_{leaf,t+1}$ is known, which is the water demand at stem.

At root level, the target is to minimize the difference between water demand at root and water supply to root (Eq. 19)

$$\Delta = (J_{root,t+1} - W_{root,t+1}) - J_{stem,t+1} \quad (19)$$

$J_{root,t+1}$ is the water transported from soil in root zone to root. $W_{root,t+1}$ is the change in root water storage. After solving stem-level target, $J_{stem,t+1}$ is known, which is the water demand at root. The detailed calculations of these water flow variables are explained below in the order of leaf, stem and root.

a. Leaf transport

The water movement into the leaf through the hydraulic pathway is calculated as

$$J_{leaf,t+1} = (\psi_{stem,t} - \psi_{leaf,t+1} - \psi_{h/2}) k_{upper,t+1} LA \quad (20)$$

$$W_{leaf,t+1} = c_{leaf}(\psi_{leaf,t+1} - \psi_{leaf,t}) LA \quad (21)$$

A positive $W_{leaf,t+1}$ means an increase in leaf water storage and vice versa.

$\Psi_{h/2}$ indicates how much water potential gradient is needed to pull water against gravity up to the height (h) of the tree from position of 1/2 tree height (middle of stem).

We calculate $J_{leaf,t+1}$ and $W_{leaf,t+1}$ using an optimization procedure i.e. we start by assuming $\psi_{leaf,t+1} = \psi_{stem,t}$ and progressively decrease $\psi_{leaf,t+1}$ until the difference between leaf water supply and demand is close to zero (Eq. 22).

$$\Delta = T_{supply} - T_{demand} \quad (22)$$

T_{demand} is related to stomatal conductance, VPD and total leaf area (Eq. 23), where stomatal conductance varies with Ψ_{leaf} (Eq. 24).

$$T_{demand} = g_s \frac{VPD}{atm} LA \quad (23)$$

$$g_s = \frac{g_{max} \frac{L \times Rad}{L \times Rad + L_k}}{1 + e^{a_{gs}(\psi_{leaf,t} - \psi_{50,gs})}} + g_{min} \quad (24)$$

g_s, g_{max} and g_{min} are in unit of mmol m^{-2} s^{-1}. VPD is in unit of kPa. LA is total leaf area.

atm is standard atmospheric pressure (101.3 kPa). $\frac{L \times Rad}{L \times Rad + L_k}$ is the function of short-wave radiation (*Rad*), which is used to ensure g_s at night is close to zero. Minimum leaf water potential in this study is set to -3.0 MPa to avoid unrealistic value (Fisher *et al.*, 2006).

We verified that our simulated g_s with the parameters values from Table A1 are of similar magnitude than in the SPA model of Fisher *et al* (2007) at Caxiuana, which was developed independently from ORCHIDEE (Figure S1). Further, in order to show that our model parameters can be used to simulate g_s at other rainforest sites, we collected g_s observations (at leaf scale) from two rainforests in French Guiana and Peru from Lin *et al* (2015) and tested our model against these observations. Figure S2 shows that our simulated g_s values fall in the range observed at these two sites.

b. Stem transport

Next, we know that the water demand at stem is the amount of water transported from stem to leaf, $J_{leaf,t+1}$. We can now use the same procedure to calculate the $\Psi_{stem,\ t+1}$ that produces the expected $J_{leaf,t+1}$, and how much of that transport is from storage and from the roots through the vertical hydraulic pathway.

$$J_{stem,t+1} = \left(\psi_{root,t} - \psi_{stem,t+1} - \psi_{h/2}\right) k_{trunk,t+1} LA \qquad (25)$$

$$W_{stem,t+1} = c_{stem}\left(\psi_{stem,t+1} - \psi_{stem,t}\right) v_{stem} \qquad (26)$$

$$S_{stem,t+1} = J_{stem,t+1} - W_{stem,t+1} \qquad (27)$$

$$\Delta = S_{stem,t+1} - J_{leaf,t+1} \qquad (28)$$

$S_{stem,t+1}$ is the water supply to stem. $J_{leaf,\ t+1}$ is the water demand at stem. Then we try to solve the $\Psi_{stem,t+1}$ to minimize the difference between $J_{leaf,t+1}$ and $S_{stem,t+1}$ (Eqs. 27-28).

c. Root transport

The same procedure is also carried out for root. The total flow out of the root is equal to $J_{stem,t+1}$. We calculate root water transport according to the following equations:

$$J_{root,t+1} = \left(\psi_{soil-root,t} - \psi_{root,t+1}\right) 2 k_{root,t+1} LA \quad (29)$$

$$W_{root,t+1} = c_{root}\left(\psi_{root,t+1} - \psi_{root,t}\right) v_{root} \qquad (30)$$

$$S_{root,t+1} = J_{root,t+1} - W_{root,t+1} \qquad (31)$$

$$\Delta = S_{root,t+1} - J_{stem,t+1} \qquad (32)$$

$J_{stem,\ t+1}$ is the water demand at root. $S_{root,t+1}$ is the water supply to root. Then we try to solve the $\Psi_{root,t+1}$ to minimize the difference between $J_{stem,t+1}$ and $S_{root,t+1}$ (Eq. 31-32). The '2' in Eq. 29 means half of the root is accounted ($\frac{1}{\frac{1}{2 \times k_{root}}}$) here since the other half of the root is considered in $k_{trunk,\ t}$.

We assume that water does not travel in reverse, leaving the roots and going into the soil. We also impose a limit on vertical water flow to non-negative values.

Update water storage pools

After the simulation of water transport, we use the W_{t+1} values to update the water storage in each organ.

$$m_{leaf,t+1} = m_{leaf,t} + W_{leaf,t+1} \quad (33)$$

$$m_{stem,t+1} = m_{stem,t} + W_{stem,t+1} \quad (34)$$

$$m_{root,t+1} = m_{root,t} + W_{root,t+1} \quad (35)$$

All above calculation processes are carried out for 20 circumference classes, separately. The parameters used in the new hydraulic architecture are summarized in Table A1.

Parameterization of tree mortality related to drought

Since trees can endure drought conditions and do not die after one or two days of low stem water potential or water shortage (Brodribb *et al*., 2020), we defined an exposure threshold dessiccation time to trigger mortality. Continuous exposure to a high percentage loss of conductance forebodes tree mortality, therefore a decision rule was set with two empirical parameters, a drought mortality exposure threshold (in days) and a mortality fraction of trees each time (in % of all trees that die). When PLC > 50% condition lasts for more than 15 continuous days, we assume that a fraction of 0.6 % of all the trees in each size cohort are killed. These two parameters are tuned according to the observed annual mortality rates. It should be noted that a cohort model represents all the trees in a grid cell as one average individual, thus an absolute mortality threshold would kill them all on the same day. Hence we impose a fractional mortality to capture the variability in mortality drivers and processes within each cohort. We also consider that a very short wetting break during a drought condition would not necessarily act to reverse embolism and thus the tree's exposure to mortality. Here the minimum threshold for a continuous wetting break (PLC<50%) to reset the exposure to zero is set to 5 days. The annual mortality rate equals to the number of dead trees per year divided by the number of trees alive in the beginning of this year.

Finally, following ORCHIDEE-CAN-RS, the recruitment rate is determined by LAI (Joetzjer *et al*., under review). When LAI decreases during drought, the recruitment rate will increase correspondingly since recruitment is parameterized as function of LAI. The new outputs from ORCHIDEE-CAN-NHA are listed in Table A2.

Biomass growth and loss

Δbiomass = growth – loss (36)

As ORCHIDEE does not account for BVOC emissions, root exudation and C-subsidies to mycorrhizae, biomass growth is simulated as the residual of GPP minus autotrophic respiration. Biomass loss comes from three processes in ORCHIDEE: turnover (loss of leaves and fine roots), self-thinning and climate-induced morality, that is, drought for this study. It should be noted that, in ORCHIDEE-CAN, when the number of individuals falls below a parameterized threshold, self-thinning does not happen and individuals grow without competing with each other.

3.4.2 Site description

The study site is a tropical lowland rainforest located in the Caxiuanã National forest, state of Para, north-east of Brazil (1°43'S, 51°27'W). Annual rainfall in this site is 2000-2500mm with dry season spanning from July to November (monthly rainfall < 100mm). A throughfall exclusion experiment (TFE) started in the end of dry season in 2001, where 50% of canopy throughfall is excluded

by plastic roof at the height of 1-2m above the ground (Fisher *et al*., 2007;Meir *et al*., 2018). At the same time, a 1-ha control plot is also set without any manipulation.

From published literature (Carswell *et al*., 2002;da Costa *et al*., 2010;Fisher *et al*., 2007;Rowland *et al*., 2015), we collected observation data as validation for model simulation, including transpiration data, soil moisture data, annual mortality rate, annual biomass density, GPP and respiration components (Table 3.1). We also used output from the SPA (soil-plant-atmosphere) model with parameters measured for the Caxiuanã experiment. SPA is a multilayer soil-vegetation-atmosphere transfer model, which has been parameterized upon such drought affected ecosystems (Fisher *et al*., 2007). We included simulated GPP output from SPA for model evaluation under TFE since eddy covariance flux measurements can only be used in model-data comparison under CTL.

Table 3.1 Collected observation data used for validation of process-based model simulation.

Variables	Period	Time step	References
Transpiration	2001-2003	Daily	Fisher *et al* (2007)
Soil moisture	2001-2004	Monthly	Fisher *et al* (2007)
Biomass density	2001-2008	Annual	Observation from Rowland *et al* (2015) and da Costa *et al* (2010)
GPP	2001-2003	Daily	SPA model : Fisher *et al* (2007), flux data: Carswell *et al*. (2002)
Mortality rate	2001-2008	Annual	da Costa *et al* (2010); Rowland *et al* (2015)

3.4.3 Simulation protocols

We performed three simulations at site-level for Caxiuanã to compare the hydraulic architecture from each model version. Specifically, we tested the model performance under two setups, the control (CTL) and the throughfall exclusion experiments (TFE). In the model, TFE is reproduced by keeping only 50% of the rainfall of CTL with all else being the same as CTL (Fisher *et al*., 2007). It should be noted that such rainfall cut is a simplification since in reality, a plastic panel is used to exclude 50% of throughfall. We run 250yr spin-up by cycling over climate forcing data over 2001 to 2008 with constant CO_2 concentration of 380 ppm to get the preliminary state of carbon pools and water flow at the beginning of 2001. Two former model versions, and our new developments are integrated as below. We compare ORCHIDEE-CAN-RS and ORCHIDEE-CAN-NHA to see the improvements brought by the new hydraulic architecture. It should be noted that all these three simulations are realized through several flags to switch on/off some functionality.

(1) ORCHIDEE-CAN with the original simple hydraulic module setup.

(2) ORCHIDEE-CAN-RS, which adds new dynamic soil-root scheme on top of (1)

(3) ORCHIDEE-CAN-NHA, with the new mechanistic hydraulics on top of (2).

3.4.4 Statistical tools

We used the R programming environment and statistical packages (version 3.5.0; R Core Team 2019) for all data processing and analysis. Package ncdf4 v1.17 (Pierce, 2019) is used to handle files in NetCDF format from model outputs. Package fields v10.3 (Nychka D, 2020) is used in water potential plotting.

3.5 RESULTS

3.5.1 Model evaluation against observation

Evapotranspiration and soil moisture

Under the control (CTL) condition, the model developed here (ORCHIDEE-CAN-NHA) agreed well with the sap flow observations from well-watered periods but underestimated sap flow in the dry season. The dry season points in Figure 3.3 are those with a water deficit of up to -3 mm day^{-1} (monthly precipitation below evapotranspiration). Regressing modeled transpiration with sap flow observations, we found that the model better represents the month-to-month seasonal variability under CTL than TFE (R=0.73 in CTL v.s. R=0.51 in TFE). Under the TFE condition, the model overestimated transpiration in both the wet and dry seasons, with a positive bias increasing at water deficits typically below -2mm/d (Figure 3.3). Simulation by ORCHIDEE-CAN-RS also showed such a positive bias (Figure S3). This positive model bias was mainly contributed by the simulation in 2002 when the TFE experiment was installed by the end of 2001. The transpiration supply did not show water limitation on transpiration under TFE until the end of the dry season in 2002 (Figure S4).

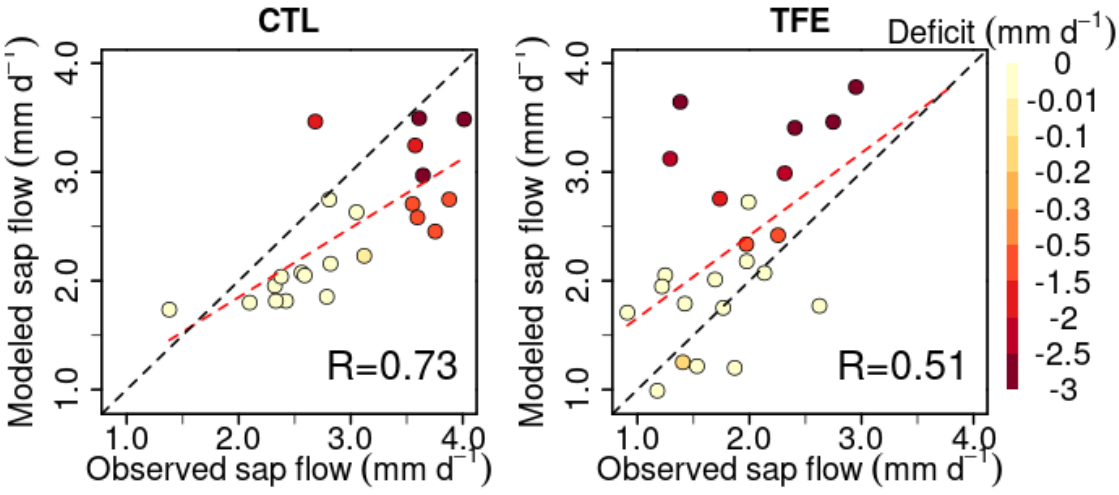

Figure 3.3 Modeled (ORCHIDEE-CAN-NHA) versus observed sap flow (monthly average values are displayed). The color of points indicates water deficit (negative difference between precipitation and evapotranspiration) with darker color meaning more severe water deficit. The black dashed line is the 1:1 line. The red dashed line is the best fit between modeled and observed sap flow.

The partitioning of evapotranspiration (ET) was compared between CTL and TFE. Under the CTL condition, the modeled partition of evapotranspiration (ET) into transpiration (T), intercepted

canopy water or dew re-evaporation (CE), and bare soil evaporation (E) is shown in Figure S5, with the ratio (T/ET) being around 0.62 in the wet season, and 0.75 in the dry season. Under TFE, the difference of T/ET between the dry and the wet season increased (wet: 0.63 vs. dry: 0.84). Specifically, under CTL, the daily mean transpiration can reach more than 4 mm/d and soil evaporation accounted for 31% of total ET in the wet season. The magnitude of transpiration increased by 46% in the dry season (range: 17%-67%) compared to that in wet season under CTL, which is consistent with observations (+44% in Fisher *et al.*, 2007), due to higher energy supply and non-water limiting conditions. This indicated that normal conditions at this site are not very strongly limited by soil moisture during the dry season, despite recurrent deficits, as shown by the red bars on the top of Figure 3.4. Nevertheless, under TFE, the transpiration was lower than in CTL and encountered emerging water supply induced limitation in the dry season, with T_{dry}/T_{wet} of 1.13 over 2002-2008 (minimum T_{dry}/T_{wet} can be 0.62 in 2005) (Figure 3.4). Soil evaporation also decreased a lot under TFE from wet to dry season, and the ratio (E/ET) was halved from the wet to the dry season, especially in the year 2005, 2006 and 2007, when annual rainfall was relatively lower.

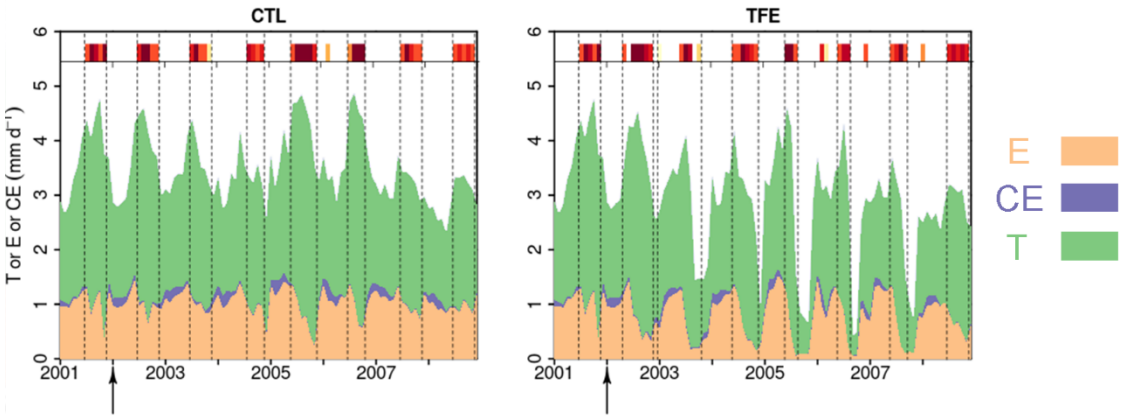

Figure 3.4 Modeled (ORCHIDEE-CAN-NHA) daily soil evaporation (E), canopy evaporation (CE) and transpiration (T) during 2001-2008. The arrows point to the start of TFE in the beginning of 2002. The inserted red shaded bars denote the periods with water deficits during the simulation period, following the same color scale as Fig. 3.

We next examined the model performance (ORCHIDEE-CAN-NHA) for reproducing the soil moisture dynamics during the observation period between 2001 and 2004. Soil moisture content (SMC) featured a pronounced seasonal decrease between wet and dry periods under CTL and TFE (Figure 3.5). Under CTL, in the surface soil, the model produced a small underestimation of SMC in both wet and dry seasons compared to observation. With increasing depth in the soil, this negative difference between modeled and observed SMC became more pronounced in the dry season (Figure 3.5). Under TFE, a similar negative difference also appeared in the dry season only, while a positive difference appeared in the wet period. Besides, under TFE, the modeled SMC was however always lower than for CTL in the surface layer, and got even more depleted in the deeper layer with the dynamic soil-root scheme, even in wet season (Figure 3.6), because this scheme shifts root uptake from surface to deep layers when the surface dries out compared to simulation of ORCHIDEE-CAN (Figure S6).

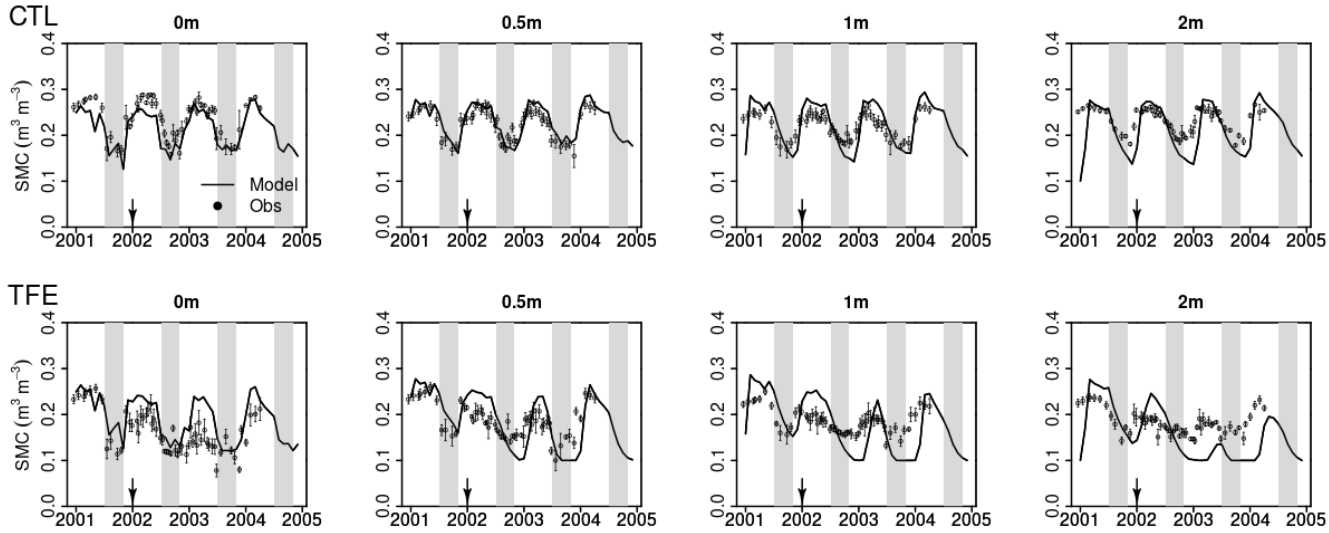

Figure 3.5 Modeled (ORCHIDEE-CAN-NHA, black line) versus observed (black dots) volumetric soil moisture content (SMC) at different depth. Due to the limited time duration of observation data, we only show the modeled SMC during 2001 to 2004. The grey shaded vertical area indicates the dry seasons from July to November.

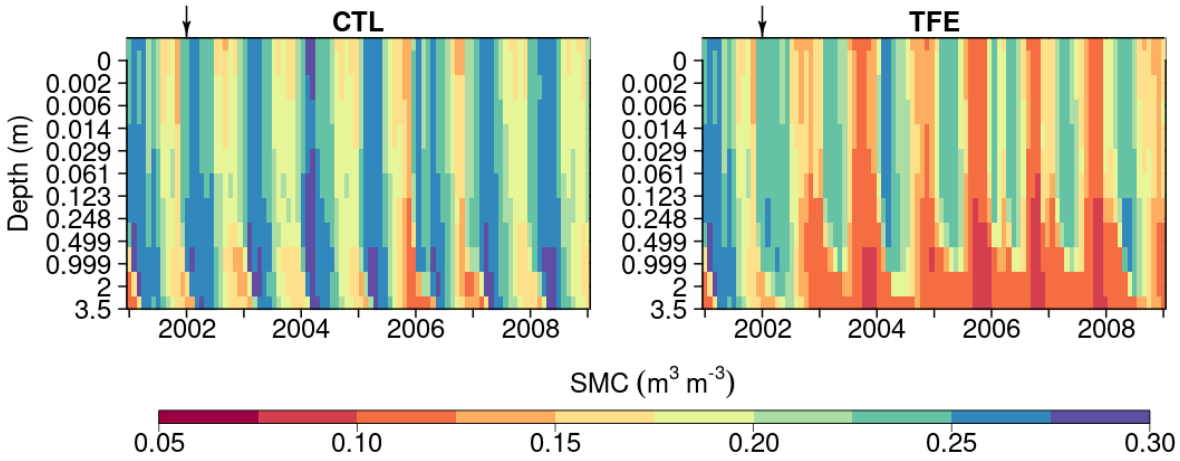

Figure 3.6 Soil moisture content simulated by ORCHIDEE-CAN-NHA during 2001 to 2008 under CTL and TFE. It should be noted the 12 soil layers have different thicknesses and here we show the SMC in same depth interval to present the change in SMC in top layers clearly.

Carbon fluxes

GPP simulation outputs had a similar seasonality under CTL among all model versions (Figure S7). All simulations showed higher GPP in the dry season compared to the wet season under CTL (also in eddy covariance Carswell *et al*., 2002). When we compared GPP against the SPA model results from Fisher et al (2007) that were calibrated to best fit site-level observations, and against flux observation, we found that modeled GPP in ORCHIDEE-CAN-NHA showed a larger seasonal amplitude than that of SPA but with a similar phase (Figure 3.7). GPP seasonality from eddy covariance data was also in agreement with the simulation from ORCHIDEE-CAN-NHA, with a peak in the middle of the dry season. In contrast, the SPA modeled GPP decreased right from the start of the dry season. We found that the impact of TFE condition on modeled GPP was relatively small during the wet season, with a difference less than 10% in comparison with CTL (see Figure S7 for the two other

versions). On the other hand, the impact of TFE during the dry season led to a pronounced decrease of GPP, like in the SPA model. In ORCHIDEE-CAN-NHA, GPP decreased only in the end of the dry season under TFE while in SPA it decreased from the beginning (Figure 3.7). Only after two years of drought, ORCHIDEE-CAN-NHA simulated an early decrease of GPP at the beginning of the dry season, and thus became consistent with SPA (Figure 3.7).

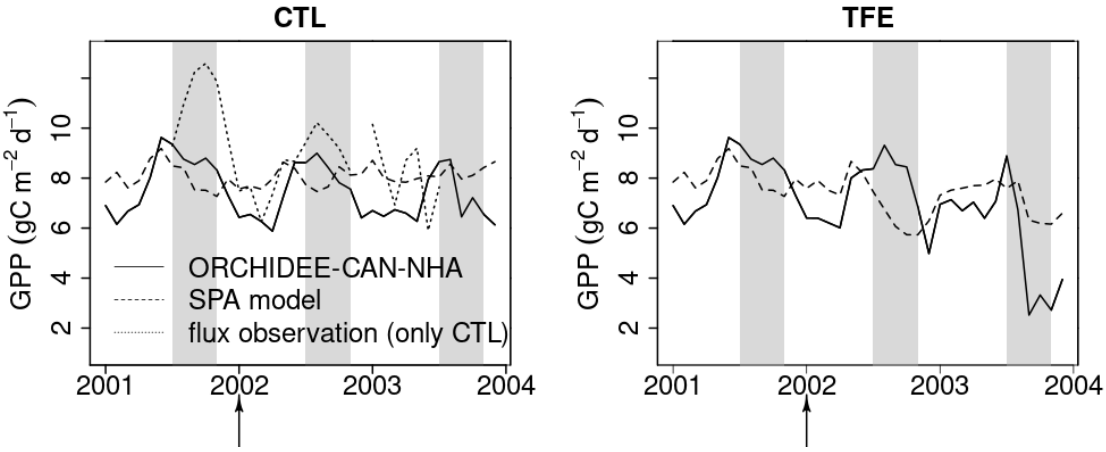

Figure 3.7 Modeled (ORCHIDEE-CAN-NHA) versus observed / modeled monthly mean GPP. The control model is compared to flux tower observations (Carswell *et al.*, 2002). In the case of TFE, as no observation is available, the locally calibrated model SPA is used. Due to GPP flux observation is unrealistically low in the start of 2001 (<5 gC m^{-2} d^{-1}), we only keep flux data after the mid of 2001. The grey shaded vertical area indicates the dry seasons from July to November.

3.5.2 Simulated water potential gradients along the soil to leaf continuum

With the mechanistic hydraulic architecture of ORCHIDEE-CAN-NHA, the dynamic water potential at leaf, stem and root levels were modeled and compared with observations (Figure S8). Diurnal cycle of Ψ_{leaf} was comparable between model and observations although the modeled Ψ_{leaf} was less negative than the observation in the noon (Figure S8). The lowest water potential was simulated in the leaf, followed by stem, as expected. There was clear seasonal variability between wet and dry periods especially under TFE conditions (Figure 3.8). Under CTL, the water potential vertical negative gradient between leaf and root was similar between the wet and the dry season (-0.82 MPa in wet season, -0.86 MPa in dry season for tree cohort #10, that is in diameter of 1.15 m; for the cohorts description see Methods); the minimum monthly mean Ψ_{leaf}, Ψ_{stem} and Ψ_{root} were -1.4 MPa, -1.0 MPa and -0.9 MPa in the dry season, respectively. Under TFE, Ψ_{leaf}, Ψ_{stem} and Ψ_{root} were prominently more negative during the dry season (-2.5 MPa, -1.8 MPa, -1.6 MPa, respectively) and the range of water potential gradients between stem and root in the dry season became a bit narrower than that in the wet season, which reflected the fact that the water flow from vertical transport is limited. With regard to the change of water storage, leaf water storage decreased continuously from wet to dry season but did not approach depletion of water storage (Figure S9). Ψ_{leaf} in the dry season in year 2005 (dry season rainfall is minimum) reached its minimum during the whole simulation period under TFE. We can see that at leaf and stem levels, Ψ_{leaf} and Ψ_{stem} decreased slightly with the size of cohorts and they were a bit more negative in larger (taller) cohorts correspondingly (Figure 3.8, Figure S10). Taller trees have a longer water transport path, which means greater gravitational potential energy is needed to pull water upward (Eq. 20).Thus more negative Ψ values were expected in the cicumference classes with higher trees.

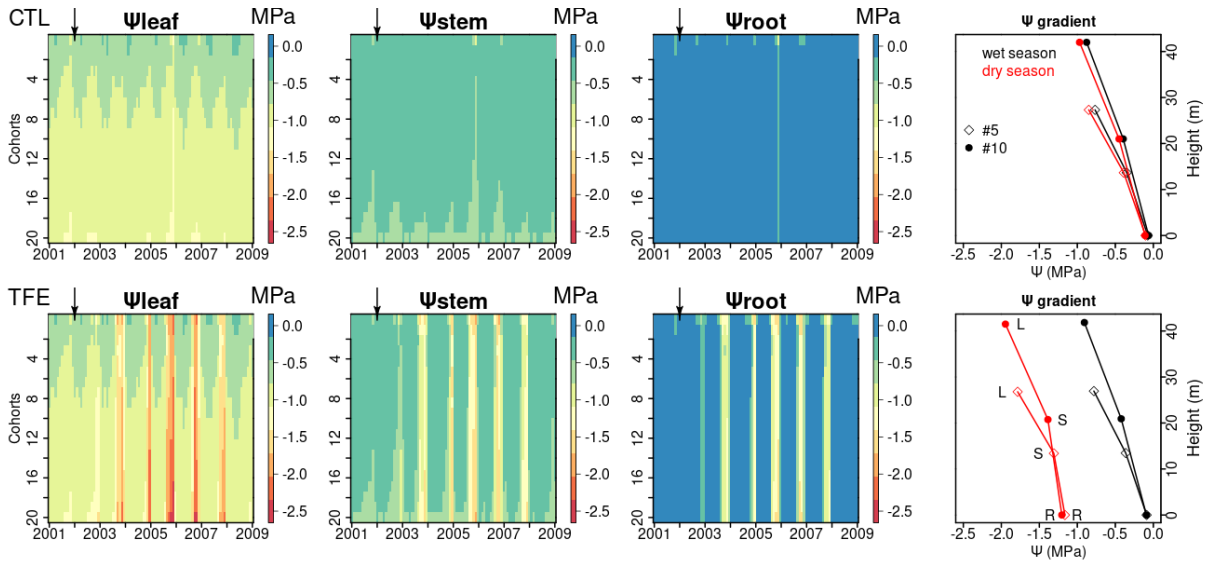

Figure 3.8 Ψ_{leaf}, Ψ_{stem}, and Ψ_{root} simulated by ORCHIDEE-CAN-NHA. Water potential gradients of two cohorts (#5, #10) are shown as an example (May 2005 as wet season, Nov 2005 as dry season). Here the cohort refers to circumference class (mean height of #5 and #10 are 19m, and 35m, respectively). The water potential gradient is composed by Ψ_{leaf} (labeled as L), Ψ_{stem} (labeled as S) and Ψ_{root} (labeled as R). The heights of Ψ_{leaf} and Ψ_{stem} correspond to tree height and half of tree height, respectively.

3.5.3 Simulated hydraulic failure

Here, we used the simulated Percentage Loss of Conductance (PLC) in stem sapwood as an indicator of tree hydraulic failure. Under CTL, the PLC remained lower than 50% even in dry seasons, due to weak water limitation (see soil moisture deficits in Figure 3.5 and water potential gradients in Figure 3.8). Under TFE, the PLC did not reach above 50% in wet seasons, but in dry seasons, it increased to more than 80% especially in the (abnormally dry) year 2005 (Figure 3.9). Under TFE, the number of days with PLC above 50% were 8 days, 52 days in years 2002 and 2003 respectively, and reached up to 73 days in year 2005 (cohort #10). Besides its seasonal variability, PLC also moderately increased with the size of cohorts, denoting more severe water stress in larger / taller cohorts (Figure S11).

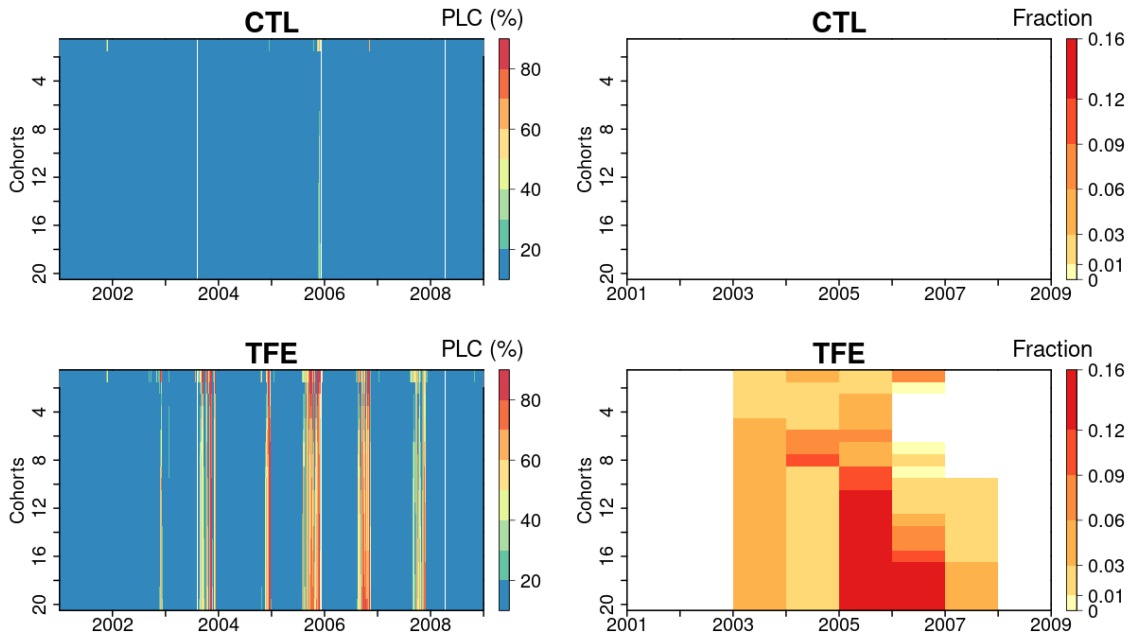

Figure 3.9 Percentage loss of daily stem conductance (PLC) (left) and tree mortality fraction simulated by ORCHIDEE-CAN-NHA (right). The vertical axis is for the index of 20 tree cohorts represented in the model, a larger index indicating taller trees (see Table S1 for tree height and diameter in each cohort). Tree mortality fraction per year is calculated by totaling the number of dead trees in each year and dividing it by the tree density in the first day of each year.

Next, we looked at the two variables defined to link PLC with mortality in the model: the PLC mortality exposure threshold and the mortality fraction per day of exposure (see Methods). The mortality exposure threshold represents a maximum tolerable drought duration for trees before a fraction of them die. In this study, this mortality threshold is set to consecutive 15 days when PLC stays above 50%. The mortality fraction is set to a death rate of 0.6% during each day of the exposure period (no preferential rule is imposed for small or large trees). In absence of any measurement, the values of these two mortality-triggering variables were calibrated to reproduce the observed mortality in the TFE experiment. We estimated the mortality fraction by totaling the dead trees in each year and dividing this number by the initial tree density in each year. With this scheme, estimated drought-induced tree mortality rates were shown in Figure 3.9. The model simulated that more than 10% of trees in larger cohorts (#12 to #20) would be killed by the dry conditions in 2005 (Figure 3.9), which was a bit larger than the 7% of mortality observed in the experiment. The model simulation produced a reasonable (but slightly too large) biomass mortality under TFE during 2002 to 2008 (Figure 3.10, Figure S12), with a modeled biomass loss (~ 56 MgC/ha, ~16% of biomass in 2001) being a bit larger than observation (~30 MgC/ha, ~12% of biomass in 2001). Figure 3.11 showed that under CTL, the biomass loss due to self-thinning and turnover is almost compensated by the biomass growth and recruitment. Under TFE, self-thinning only existed in the years before 2004 according to the model, because a drop of tree density was induced by preceding drought mortality in 2003, which suppressed the competition between trees in the model afterwards. The gain of biomass (labeled as 'growth' in green in Figure 3.11) also decreased under TFE in comparison with CTL. Moreover, when we grouped the mortality rate simulated for 20 cohorts into three classes according to their DBH (<20cm, 20-40cm and >40cm) we can further evaluate the model performance (Figure 3.12). Under CTL, the model produced higher mortality rate (2.0%) than the observation (2001:2008 mean: 1.1%-1.3%) in three classes. In other words, the modeled self-thinning rate was probably higher than that in reality since the mortality rate observed was only 0.4% in year 2001. Under TFE, the model performed differently for each size class. For the small-sized class with DBH<20cm, the model underestimated the mortality rate compared to observations after 2006. For the medium-sized class (DBH: 20-40cm),

the modeled mortality rate was comparable with observation until 2004. For the large-sized class group, the model can estimate successfully the large mortality observed in-situ from 2004-2005. Overall, the averaged mortality rate was comparable between observation and model simulation. The model-observation gap in year 2005, 2.7% in model simulation vs. 4.8% in observation, may be due to modeled underestimation in group of DBH<20cm and larger modeled individual density of this group than the reality (Figure 3.12).

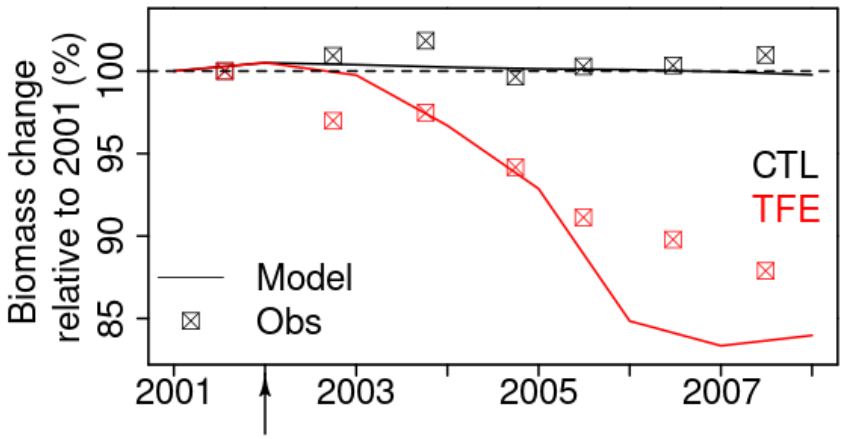

Figure 3.10 Tree biomass change simulated by model after mortality being triggered. The squares in the plot denote the observation. Biomass change relative to 2001 is calculated by dividing biomass during 2002-2008 by biomass in 2001.

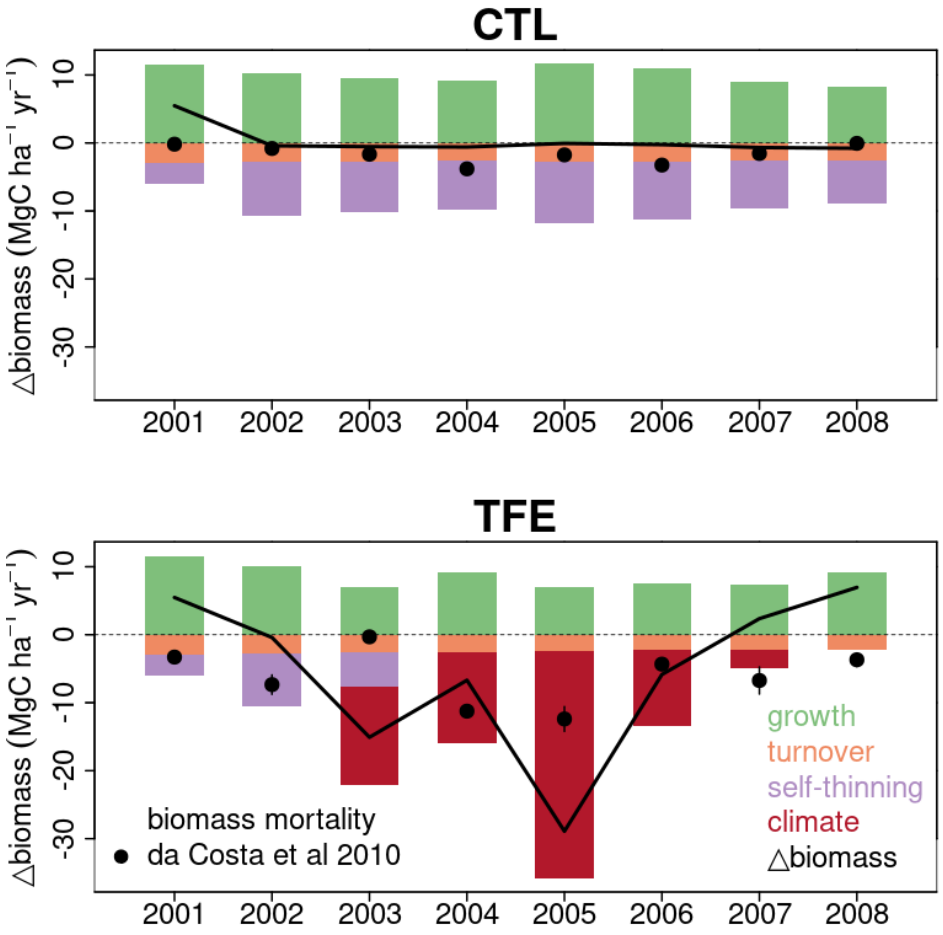

Figure 3.11 Simulated components of biomass change and observed net biomass change during 2001 to 2008. The observed net biomass change data in each year from da Costa et al (2010) is plotted as black dot. The black line shows the net change of simulated biomass by ORCHIDEE-CAN-NHA.

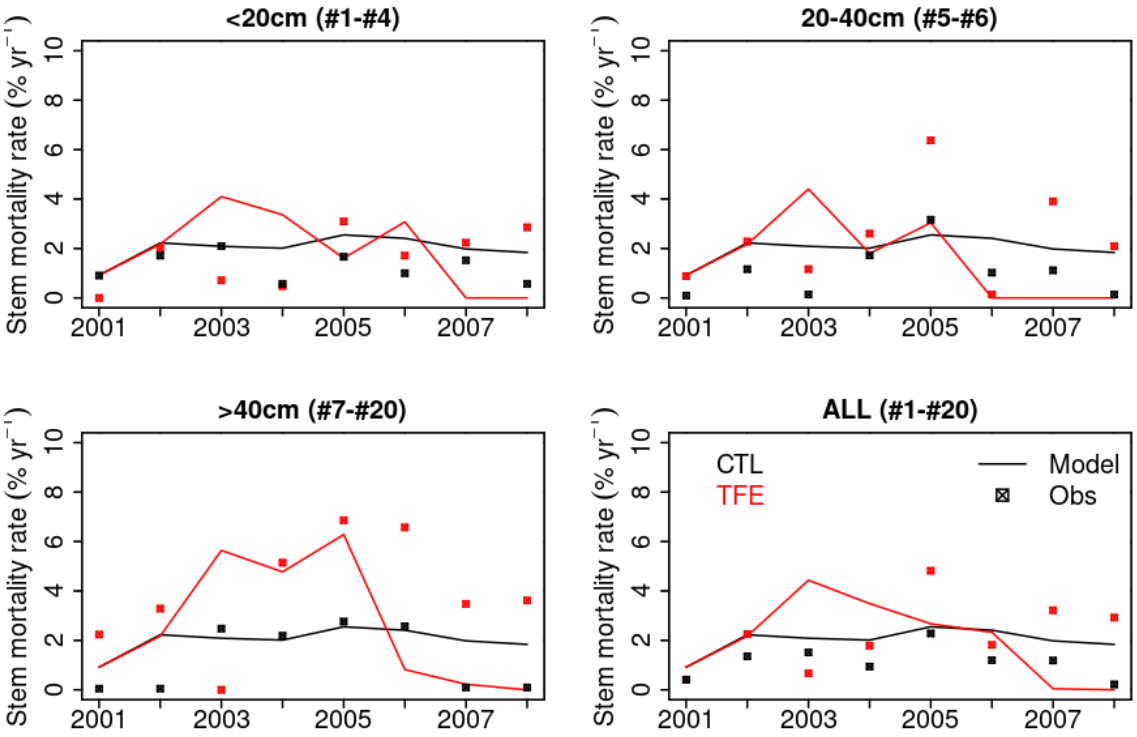

Figure 3.12 Annual stem mortality rates during the study period (2001 - 2008). All 20 cohorts have been aggregated to three classes according to DBH (<20cm, 20-40cm, >40cm). The value in bracket in title of each panel corresponds to the No. of cohorts falling in the class.

Finally, we tested the performance of our hydraulic failure – mortality sub-model at another Throughfall Exclusion Experiment in the Amazon, from the Tapajos site (Nepstad *et al.*, 2007). At this site, TFE only happened in the wet season between 2000 and 2003, with an exclusion of almost 50% rainfall. Figure S13 shows that our model can capture the observed phenomenon of a higher mortality rate found at Tapajos especially in trees with diameter > 30 cm although the modeled mortality rate is lower than that in the field measurement. Our model also simulates the net biomass increase at Tapajos under CTL and the great biomass loss under TFE. The two parameters of our hydraulic failure – mortality model (drought exposure threshold and mortality fraction each day upon exceeding the threshold), which are not directly observable, were effectively calibrated at Caxiuana but the model is also successfully evaluated at Tapajos site. Given the complexity of drought-mortality relationships which lack a unified theory, this shows high performances for the new parameterization we proposed in the study.

3.6 Discussion

3.6.1 Model improvements by new parameterizations of hydraulic transport

The original ORCHIDEE-CAN model included a limit from transpiration supply based on water transport and resistances along a water potential gradient (Naudts *et al.*, 2015). Nonetheless, the constant value assumed for Ψ_{leaf}, the lack of a dynamic simulation of Ψ_{stem} and Ψ_{root} and conductivities limit the mechanistic basis of the approach. To make a step forward, the new hydraulic module

presented here tracks the water flow continuum from the soil to the atmosphere. The water potentials Ψ_{leaf}, Ψ_{stem}, Ψ_{root} are updated at each half-hour time step, based upon a Supply-Demand framework of minimization of difference between water demand and water supply at organ-level. Besides improvements in modeling the processes of vertical water transport, our hydraulic module also considers the tissue water storage and the dynamics of water flow between different organs, both of which are bounded by the capacitance and water volume. The water storage capacity, can affect the water potential and determine the tolerable duration of desiccation before severe water potentials are reached (Gleason *et al*., 2014). For example, in the model, stem sapwood water storage can be discharged under CTL during both wet and dry periods, and this contribution can be larger than that from vertical water flow. In contrast, under TFE, the stem sapwood water pool is not always refilled overnight in the dry season (Figure S14). Martinez-Vilalta *et al*. (2019) also found that a more explicit consideration of water pools helps advance the monitoring and prediction of mortality risk, although more experimental evidence is required for verifying the relationship between relative water content and mortality probability.

Besides the capacity of each organ, stem hydraulic safety indicators like water potential at which 50% of stem conductance lost (Ψ_{50}) can be modeled directly, and used as an indicator of tree responses to drought events. This variable influences the maximum drought exposure threshold proposed in our model, which varies among specific tree species, tree size and different growth conditions (Blackman *et al*., 2016). In a previous study at this site, Rowland *et al*. (2015) found vulnerable and resistant genera have contrasting vulnerability to hydraulic deterioration. Vulnerable trees with larger DBH displayed higher conductivity loss under experimental drought and less negative Ψ_{50}. However, in a more recent study with much more field data in Bittencourt *et al*. (2020), the variability of hydraulic traits among species is also evident and the importance of particular hyper-dominant species becomes notable too in affecting the overall species and size patterns. Naudts *et al* (2015) related stem conductivity to $\Psi_{soil\text{-}root}$ with Ψ_{50} and another shape parameter as an adjustment. In our model, we built sigmoidal relationships between conductance and Ψ_{stem}, of which the slope parameter assesses the sensitivity of conductance loss to decline in water potential that can correspond to different plants water regulation strategies. Through involving trait-related parameters, our model could be used to reflect isohydric or anisohydric patterns although these two parameters are challenging to calibrate for highly diverse tropical forests (e.g Maréchaux *et al*. (2015)).

Recently, there is expansion in the availability of the hydraulic parameters for tropics, but mainly for xylem and leaves. Although the sensitivity analysis of Supply-Demand theory in Sperry *et al*. (2016) suggested that the usage of single stem vulnerability curve would not bring more error to transpiration than the true segmented mode (that is, separate leaf, stem and root curves) as long as the leaf/stem Ψ_{50} and root/stem Ψ_{50} closer to 1, our study included vulnerability segmentation of leaf, stem and root to facilitate the coherent representation of the soil-root-stem-leaf continuum. Besides, the possible context-dependent trait coordination also needs to be noticed in parameterizing models (Maréchaux *et al*., 2020), e.g. the relationship between leaf turgor loss point and leaf area, which will benefit the diversity in vegetation models.

With water transport from vertical gradient of potentials and changes in water storage, OR-CHIDEE-CAN-NHA produced dynamic and reasonable water potentials (Figure S8) and conductance at leaf, stem and root levels. Based on the improved hydraulic architecture, we implemented an empirical algorithm that assumes a fixed fraction of trees will die after 15 days of continuous sustained drought exposure with PLC>50%. Combinations of these two parameters of drought exposure threshold and mortality fraction each time could also be adapted to diverse plants traits to match mortality rates across different sites, coping with adverse conditions, e.g. tree size, different isohydric and anisohydric behaviors of stomatal regulation upon varying water status (McDowell *et al*., 2008). Therefore, these two parameters would need to be calibrated upon data suited to different conditions. For example, Esquivel-Muelbert *et al*. (2017) found that wet-affiliated genera tends to show higher

drought-induced mortality than dry-affiliated ones. Assigning higher mortality fraction for wet-affiliated genera upon such condition can be a solution to test different levels of mortality fraction parameters.

The Supply-Demand framework in our model also draws on Sperry *et al*. (2016) that empirical expression of each continuum component, e.g. stomatal conductance, hydraulic conductivities from vulnerability curve is applied. There are also similarities between our hydraulic structure and Xu *et al*. (2016), in aspects that both vertical water flow and water storage capacity in leaf and stem are accounted in modelling process of water supply and demand. The major differences from Xu et al. (2016) are that our model uses transpiration supply as the leaf-level demand instead and also refines the water transport from soil-root-stem thus water potential of each organ in continuum is solved.

3.6.2 Possible factors affecting tree mortality

Our model simulations showed that larger trees suffer more severe water stress with higher PLC (Figure 3.9) and that the mortality fraction is consequently the highest in groups with DBH>40cm. This uses the theory that longer vertical water transport pathway in taller trees can intensify the height-dependent hydraulic limitation (Grote *et al*., 2016) and site-level experimental evidence (Rowland *et al*., 2015). Such size-regulated mortality has also been corroborated by Bennett *et al*. (2015). Hendrik and Maxime (2017) summarized that drought can be more detrimental on growth and mortality rates of larger trees. Klos *et al*. (2009) also found that older and denser stands are more susceptible to drought damage, but that the mortality-height relationship can also be relaxed by species diversity, for example, the taxonomic identity also controls the traits-size relationship (Bittencourt *et al*., 2020). Environmental gradients of climate conditions and concurrent competition can also affect the height-mortality risk relationship (Stovall *et al*., 2019), and co-explain the forest mortality patterns (Young *et al*., 2017). Conversely, the benefits of deeper root systems potentially may allow tall trees to avoid drought stress (Trugman *et al*., 2021). Simulated water content in bottom soil layers did not counteract the embolism under dry season in our study, so we captured the positive height-mortality relationship observed at this site. Nevertheless, in the Caxiuanã field measurements of Rowland *et al* (2015), trees of similar size also showed different vulnerability (Ψ_{50}), which suggests the influence of other anatomical traits, for instance, wood density, which is already prescribed as PFT-based parameter in simulation setup. Such kind of within PFT variation cannot yet be accounted for in model. Wood density with intra-individual variability is intimately linked with tree mortality, and has been found to explain variation in tropical mortality rate across sites through a hierarchical Bayesian approach (Kraft *et al*., 2010). Plant functional traits like xylem, leaf specific conductivities and capacitances are inversely related to the wood density (Meinzer *et al*., 2008). On the one hand, taller trees with lower wood density (Rozendaal et al., 2020), would be expected to present higher sapwood conductivity although the overall effect would depend on the forest type, and growth conditions (Fajardo, 2018;Meinzer *et al*., 2008). On the other hand, height-dependent water limitation weakens the stem hydraulic conductivity. Such tradeoffs co-determine the resistance to hydraulic failure.

Under extreme drought, hydraulic traits are also highly important factors for mortality risk. Trees with high cavitation resistance and wide hydraulic safety margin can endure longer desiccation (Blackman *et al*., 2019). Although xylem anatomical traits directly related to conductivity better reflect the whole-tree performance (Fan *et al*., 2012), the relative importance of climate conditions, plant functional and hydraulic traits in determining forest mortality risk encountering drought needs further validation with large amount of experimental observations (Aleixo *et al*., 2019).

3.6.3 Model limitations and directions for future development

Several potentially important ecological processes related to plant hydraulics and mortality warrant further consideration. First, tree mortality risk, in the simulations, is mainly triggered by drought-

induced water stress, but soil water limitation can also be alleviated by enhanced tree survival through increasing nutrients uptake, to increase water use efficiency and reduce negative effects of droughts (Wang *et al*., 2012). Fast growth rate, however, is associated with higher mortality probability (see Rozendaal *et al*. (2020) for spatial relationship between basal area growth, diameter and possibility of mortality in Amazonia tropical forest). Discounting the demographic association between tree growth and mortality rate could lead to underestimation of mortality in model simulations. Representations of these interactions should be further incorporated to increase model credibility under various environments. Secondly, the plant functional type classification used in ORCHIDEE-CAN-NHA does not capture hydraulic variation. Some researchers proposed hydraulic trait-based classifications (Anderegg, 2015) or hydraulic functional types (Liu *et al.*, 2021b), which may better represent isohydric and anisohydric behaviors affecting water potential and stomatal regulation. Accounting for the variability in hydraulic traits would be important to properly model in future ecosystem-atmosphere feedback effects (Anderegg *et al*., 2018;Powell *et al*., 2018). More specifically, some traits are also but not always found to vary with tree size, like Ψ_{50}, conductivity and the number of days of exposure to severe drought that a tree can tolerate. Our assumption of fixed Ψ_{50} values for all 20 cohorts may lead to miscalculation of mortality rates in different classes, e.g. overestimation for PLC in smaller cohorts and underestimation for PLC in larger cohorts. Therefore, future research should focus on discerning the empirical connection between species-specific hydraulic strategies toward mortality by distinguishing vegetation functional groups. Thirdly, legacy or memory effects are not fully accounted here. The impacts of drought on increasing tree mortality can last for at least two years after an extreme climatic event (Aleixo *et al*., 2019). Some cumulated or memory indicators may help tackle such problems. For example, we can consider the effects of past drought events on current tree growth by multiplying the drought intensity with the inverse of time passed (Franklin *et al*., 1987). Finally, different threshold indicators like relative water content and turgor loss point can also be tested in mortality triggering process (Sapes *et al*., 2019;Zhu *et al*., 2018).

Besides future developments of the hydraulic module, more calibration and understanding of the lethal threshold required for hydraulic failure is clearly necessary. We call for that more observed hydraulic traits data for tropical trees, including detailed vulnerability, to support more reasonable and appropriate parameterization scheme in mortality risk modeling. For example, the point of no return from drought-induced xylem embolism in aspects of water potential (turgor loss point), conductivity and relative water content. Remote sensing products of vegetation optical depth (VOD), proportional to the vegetation water content, may help benchmark the capacitance dynamics. In addition, in this study we have only calibrated the new hydraulic architecture against observations from one experimentally droughted site. Expanding this method to other drought experiment sites to generalize the model performance is required. For example, this future work could address to what extent the 2005 and 2010 drought affected forest dynamics in western Amazonia. Large-scale mortality observations and more comprehensive mortality benchmarking datasets are also required to evaluate the hydraulic architecture in process-based model (Adams et al., 2013;Allen et al., 2010).

3.7 CONCLUSION

Our study proposes a new mechanistic hydraulic architecture module, ORCHIDEE-CAN-NHA, which simulates dynamic xylem cavitation indicator of percentage loss of conductance (PLC) through modeling the water flow in soil-root-stem-leaf continuum and water charge from storage. The model was calibrated against observations from the Caxiuanã throughfall exclusion field experiment in the eastern Amazon, during 2001 to 2008, with regard to the seasonal variability in transpiration, soil moisture and productivity. Besides the improvement of hydraulic architecture, we also built a relationship between PLC and tree mortality rate via two empirical parameters, drought exposure duration, which determines the mortality frequency and the mortality fraction in each day once exceeding the exposure. Our model produces comparable annual tree mortality rates with observations over the

study period. Introduction of mechanistic hydraulic architecture in land surface models can help provide a window through which we can enable prediction for mortality under future possible drought events. We also call for more available hydraulic traits and vulnerability data for testing the generalization of model performance.

3.8 APPENDIX

Table A1 Parameters used in new hydraulic architecture model. These parameters are selected from the range recorded by literature that we have analyzed.

Symbol	Description	Unit	Value	Source
c_{leaf}	Leaf capacitance	• mmol m^{-2} MPa^{-1}	670	De Kauwe *et al.* (2020)
c_{stem}	Stem capacitance	kg m^{-3} MPa^{-1}	130	Xu *et al*. (2016)
c_{root}	Root capacitance	kg m^{-3} MPa^{-1}	150	Modified from C_{stem}
SLA	Specific leaf area	m^2 kg^{-1}	16.6	Kattge *et al*. (2011)
LDMC	Leaf dry matter content	g g^{-1}	0.2	Kattge *et al*. (2011)
WC	mass of water per unit of sapwood volume	mol m^{-3}	25000	Suzuki (1999)
WD	Wood density	g cm^{-3}	0.645	Chave *et al*. (2006)
$ratio_{root:shoot}$	Root shoot ratio	g g^{-1}	0.25	Mokany *et al*. (2006)
$root_{wc}$	root water content	mmol g^{-1}	35	Markesteijn and Poorter (2009)
ρ_{root}	Root density	g cm^{-3}	0.503	Schuldt *et al*. (2013)
$k_{leaf,\ max}$	Maximum leaf hydraulic conductance per unit leaf area	• mmol m^{-2} s^{-1} MPa^{-1}	15	Sack (2006)

$k_{stem,\ max}$	Maximum sapwood hydraulic conductance per unit leaf area	mmol m^{-2} s^{-1} MPa^{-1}	15*	Hickler *et al*. (2006)
$k_{root,\ max}$	Maximum root hydraulic conductance per unit leaf area	mmol m^{-2} s^{-1} MPa^{-1}	10	Modified from $k_{stem,\ max}$
a_{leaf}	Shape parameter for k_{leaf} vs. Ψ_{leaf} curve	-	-2.5	[-3.8, -0.5] in Bartlett *et al* (2019)
a_{stem}	Shape parameter for k_{stem} vs. Ψ_{stem} curve	-	-2.3	[-3.8, -0.5] in Bartlett *et al* (2019)
a_{root}	Shape parameter for k_{root} vs. Ψ_{root} curve	-	-3.0	[-3.8, -0.5] in Bartlett *et al* (2019)
$\Psi_{50,\ leaf}$	Ψ_{leaf} at 50% loss of leaf conductance	MPa	-1.1	[-3, -0.75] in Bartlett *et al* (2019)
$\Psi_{50,\ stem}$	Ψ_{stem} at 50% loss of stem sapwood conductance	MPa	-1.3	[-3, -0.75] in Bartlett *et al* (2019)
$\Psi_{50,\ root}$	Ψ_{root} at 50% loss of root conductance	MPa	-1.1	[-3, -0.75] in Bartlett *et al* (2019)
g_{max}	Maximum stomatal conductance in Eq. 24	mmol m^{-2} s^{-1}	700	Franks and Brodribb (2005)
g_{min}	Mininum stomatal conductance	mmol m^{-2} s^{-1}	10	Franks and Brodribb (2005)
$\Psi_{50,gs}$	Ψ_{leaf} at 50% decline in stomatal conductance	MPa	-1.7	Bartlett *et al* (2016)
a_{gs}	Shape parameter for g_s vs. Ψ_{leaf} curve	-	-2.3	Bartlett *et al* (2016)
$\frac{L \times Rad}{L \times Rad + L_k}$	In this term, the function of short-wave radiation, is used to ensure the g_s at night to be	-	-	--

close to 0

* In Hickler *et al* (2006), the maximum sapwood conductivity of $50*10^{-4}$ m^2 s^{-1} MPa^{-1} can be converted to ~15 mmol m^{-2} s^{-1} MPa^{-1} if we assume sapwood area/leaf area of 0.0016 (value falls in (Gotsch *et al*., 2010), and tree height of 30m.

Table A2 Outputs variables calculated by ORCHIDEE-CAN-NHA.

Category	Symbol	Description	Unit
Water potentials	$\psi_{soil-root}$	soil water potential in root zone	MPa
	ψ_{root}	Root water potential	MPa
	ψ_{stem}	Stem water potential	MPa
	ψ_{leaf}	Leaf water potential	MPa
Hydraulic conductances	k_{root}	Root hydraulic conductance	mmol m^{-2} s^{-1} MPa^{-1}
	k_{stem}	Stem sapwood hydraulic conductance	mmol m^{-2} s^{-1} MPa^{-1}
	k_{leaf}	Leaf hydraulic conductance	mmol m^{-2} s^{-1} MPa^{-1}
Water storage	m_{root}	Water volume in the root	mmol
	m_{stem}	Water volume in the stem	mmol
	m_{leaf}	Water volume in the leaf	mmol
Cavitation	PLC	Percentage loss of stem conductance	%
Mortality	$counter_{PLC50}$	Number of continuous days with $PLC > 50\%$ (exposure)	days

circ_class_mor	Tree mortality for each circumference class due to exposure to *PLC* > 50%	1 m^{-2}

3.9 REFERENCES

Adams, H. D., Williams, A. P., Xu, C., Rauscher, S. A., Jiang, X., and McDowell, N. G.: Empirical and process-based approaches to climate-induced forest mortality models, Frontiers in plant science, 4, 438, 2013.

Adams, H. D., Zeppel, M. J., Anderegg, W. R., Hartmann, H., Landhäusser, S. M., Tissue, D. T., Huxman, T. E., Hudson, P. J., Franz, T. E., and Allen, C. D.: A multi-species synthesis of physiological mechanisms in drought-induced tree mortality, Nature ecology & evolution, 1, 1285-1291, 2017.

Aleixo, I., Norris, D., Hemerik, L., Barbosa, A., Prata, E., Costa, F., and Poorter, L.: Amazonian rainforest tree mortality driven by climate and functional traits, Nature Climate Change, 9, 384-388, 2019.

Allen, C. D., Macalady, A. K., Chenchouni, H., Bachelet, D., McDowell, N., Vennetier, M., Kitzberger, T., Rigling, A., Breshears, D. D., and Hogg, E. T.: A global overview of drought and heat-induced tree mortality reveals emerging climate change risks for forests, Forest ecology and management, 259, 660-684, 2010.

Allen, C. D., Breshears, D. D., and McDowell, N. G.: On underestimation of global vulnerability to tree mortality and forest die-off from hotter drought in the Anthropocene, Ecosphere, 6, 1-55, 2015.

Anderegg, W. R.: Spatial and temporal variation in plant hydraulic traits and their relevance for climate change impacts on vegetation, New Phytologist, 205, 1008-1014, 2015.

Anderegg, W. R., Flint, A., Huang, C.-y., Flint, L., Berry, J. A., Davis, F. W., Sperry, J. S., and Field, C. B.: Tree mortality predicted from drought-induced vascular damage, Nature Geoscience, 8, 367-371, 2015.

Anderegg, W. R., Konings, A. G., Trugman, A. T., Yu, K., Bowling, D. R., Gabbitas, R., Karp, D. S., Pacala, S., Sperry, J. S., and Sulman, B. N.: Hydraulic diversity of forests regulates ecosystem resilience during drought, Nature, 561, 538-541, 2018.

Bartlett, M. K., Klein, T., Jansen, S., Choat, B., and Sack, L.: The correlations and sequence of plant stomatal, hydraulic, and wilting responses to drought, Proceedings of the National Academy of Sciences, 113, 13098-13103, 2016.

Bartlett, M. K., Detto, M., and Pacala, S. W.: Predicting shifts in the functional composition of tropical forests under increased drought and CO 2 from trade-offs among plant hydraulic traits, Ecology letters, 22, 67-77, 2019.

Bittencourt, P. R., Oliveira, R. S., da Costa, A. C., Giles, A. L., Coughlin, I., Costa, P. B., Bartholomew, D. C., Ferreira, L. V., Vasconcelos, S. S., and Barros, F. V.: Amazonia trees have limited capacity to acclimate plant hydraulic properties in response to long-term drought, Global change biology, 26, 3569-3584, 2020.

Blackman, C. J., Pfautsch, S., Choat, B., Delzon, S., Gleason, S. M., and Duursma, R. A.: Toward an index of desiccation time to tree mortality under drought, Plant, cell & environment, 39, 2342-2345, 2016.

Blackman, C. J., Li, X., Choat, B., Rymer, P. D., De Kauwe, M. G., Duursma, R. A., Tissue, D. T., and Medlyn, B. E.: Desiccation time during drought is highly predictable across species of Eucalyptus from contrasting climates, New Phytologist, 224, 632-643, 2019.

Bonan, G., Williams, M., Fisher, R., and Oleson, K.: Modeling stomatal conductance in the earth system: linking leaf water-use efficiency and water transport along the soil–plant–atmosphere continuum, Geoscientific Model Development, 7, 2193-2222, 2014.

Brienen, R. J., Phillips, O. L., Feldpausch, T. R., Gloor, E., Baker, T. R., Lloyd, J., Lopez-Gonzalez, G., Monteagudo-Mendoza, A., Malhi, Y., and Lewis, S. L.: Long-term decline of the Amazon carbon sink, Nature, 519, 344-348, 2015.

Brodribb, T. J., and Cochard, H.: Hydraulic failure defines the recovery and point of death in water-stressed conifers, Plant physiology, 149, 575-584, 2009.

Brodribb, T. J., Powers, J., Cochard, H., and Choat, B.: Hanging by a thread? Forests and drought, Science, 368, 261-266, 2020.

Carswell, F., Costa, A., Palheta, M., Malhi, Y., Meir, P., de Pr Costa, J., Ruivo, M. d. L., do Sm Leal, L., Costa, J., and Clement, R.: Seasonality in CO2 and H2O flux at an eastern Amazonian rain forest, Journal of Geophysical Research: Atmospheres, 107, LBA 43-41-LBA 43-16, 2002.

Chave, J., Muller-Landau, H. C., Baker, T. R., Easdale, T. A., Steege, H. t., and Webb, C. O.: Regional and phylogenetic variation of wood density across 2456 neotropical tree species, Ecological applications, 16, 2356-2367, 2006.

Choat, B.: Predicting thresholds of drought-induced mortality in woody plant species, Tree physiology, 33, 669-671, 2013.

Choat, B., Brodribb, T. J., Brodersen, C. R., Duursma, R. A., López, R., and Medlyn, B. E.: Triggers of tree mortality under drought, Nature, 558, 531-539, 2018.

Cochard, H., and Delzon, S.: Hydraulic failure and repair are not routine in trees, Annals of Forest Science, 70, 659-661, 2013.

da Costa, A. C. L., Galbraith, D., Almeida, S., Portela, B. T. T., da Costa, M., Junior, J. d. A. S., Braga, A. P., de Gonçalves, P. H., de Oliveira, A. A., and Fisher, R.: Effect of 7 yr of experimental drought on vegetation dynamics and biomass storage of an eastern Amazonian rainforest, New Phytologist, 187, 579-591, 2010.

De Kauwe, M. G., Medlyn, B. E., Ukkola, A. M., Mu, M., Sabot, M. E., Pitman, A. J., Meir, P., Cernusak, L., Rifai, S. W., and Choat, B.: Identifying areas at risk of drought-induced tree mortality across South-Eastern Australia, Global Change Biology, 2020.

Delbart, N., Ciais, P., Chave, J., Viovy, N., Malhi, Y., and Le Toan, T.: Mortality as a key driver of the spatial distribution of aboveground biomass in Amazonian forest: results from a dynamic vegetation model, 2010.

Dewar, R., Mauranen, A., Mäkelä, A., Hölttä, T., Medlyn, B., and Vesala, T.: New insights into the

covariation of stomatal, mesophyll and hydraulic conductances from optimization models incorporating nonstomatal limitations to photosynthesis, New Phytologist, 217, 571-585, 2018.

Duffy, P. B., Brando, P., Asner, G. P., and Field, C. B.: Projections of future meteorological drought and wet periods in the Amazon, Proceedings of the National Academy of Sciences, 112, 13172-13177, 2015.

Eller, C. B., Rowland, L., Oliveira, R. S., Bittencourt, P. R., Barros, F. V., da Costa, A. C., Meir, P., Friend, A. D., Mencuccini, M., and Sitch, S.: Modelling tropical forest responses to drought and El Niño with a stomatal optimization model based on xylem hydraulics, Philosophical Transactions of the Royal Society B: Biological Sciences, 373, 20170315, 2018.

Eller, C. B., Rowland, L., Mencuccini, M., Rosas, T., Williams, K., Harper, A., Medlyn, B. E., Wagner, Y., Klein, T., and Teodoro, G. S.: Stomatal optimization based on xylem hydraulics (SOX) improves land surface model simulation of vegetation responses to climate, New Phytologist, 226, 1622-1637, 2020.

Esquivel-Muelbert, A., Galbraith, D., Dexter, K. G., Baker, T. R., Lewis, S. L., Meir, P., Rowland, L., da Costa, A. C. L., Nepstad, D., and Phillips, O. L.: Biogeographic distributions of neotropical trees reflect their directly measured drought tolerances, Scientific reports, 7, 1-11, 2017.

Fajardo, A.: Insights into intraspecific wood density variation and its relationship to growth, height and elevation in a treeline species, Plant Biology, 20, 456-464, 2018.

Fan, Z. X., Zhang, S. B., Hao, G. Y., Ferry Slik, J., and Cao, K. F.: Hydraulic conductivity traits predict growth rates and adult stature of 40 Asian tropical tree species better than wood density, Journal of Ecology, 100, 732-741, 2012.

Fisher, R., Williams, M., Da Costa, A. L., Malhi, Y., Da Costa, R., Almeida, S., and Meir, P.: The response of an Eastern Amazonian rain forest to drought stress: results and modelling analyses from a throughfall exclusion experiment, Global Change Biology, 13, 2361-2378, 2007.

Fisher, R. A., Williams, M., Do Vale, R. L., Da Costa, A. L., and Meir, P.: Evidence from Amazonian forests is consistent with isohydric control of leaf water potential, Plant, Cell & Environment, 29, 151-165, 2006.

Franklin, J. F., Shugart, H. H., and Harmon, M. E.: Tree death as an ecological process, BioScience, 37, 550-556, 1987.

Franks, P., and Brodribb, T. J.: Stomatal control and water transport in the xylem, in: Vascular transport in plants, Elsevier, 69-89, 2005.

Gleason, S. M., Blackman, C. J., Cook, A. M., Laws, C. A., and Westoby, M.: Whole-plant capacitance, embolism resistance and slow transpiration rates all contribute to longer desiccation times in woody angiosperms from arid and wet habitats, Tree Physiology, 34, 275-284, 2014.

Gotsch, S. G., Geiger, E. L., Franco, A. C., Goldstein, G., Meinzer, F. C., and Hoffmann, W. A.: Allocation to leaf area and sapwood area affects water relations of co-occurring savanna and forest trees, Oecologia, 163, 291-301, 2010.

Grote, R., Gessler, A., Hommel, R., Poschenrieder, W., and Priesack, E.: Importance of tree height and social position for drought-related stress on tree growth and mortality, Trees, 30, 1467-1482, 2016.

Gustafson, E. J., and Sturtevant, B. R.: Modeling forest mortality caused by drought stress: implications for climate change, Ecosystems, 16, 60-74, 2013.

Hammond, W. M., Yu, K., Wilson, L. A., Will, R. E., Anderegg, W. R., and Adams, H. D.: Dead or dying? Quantifying the point of no return from hydraulic failure in drought-induced tree mortality, New Phytologist, 223, 1834-1843, 2019.

Hartmann, H.: Carbon starvation during drought-induced tree mortality–are we chasing a myth?, 2015.

Hendrik, D., and Maxime, C.: Assessing drought-driven mortality trees with physiological process-based models, Agricultural and Forest Meteorology, 232, 279-290, 2017.

Hickler, T., Prentice, I. C., Smith, B., Sykes, M. T., and Zaehle, S.: Implementing plant hydraulic architecture within the LPJ Dynamic Global Vegetation Model, Global Ecology and Biogeography, 15, 567-577, 2006.

Joetzjer, E., Maignan, F., Chave, J., Goll, D., Poulter, B., Barichivich, J., Maréchaux, I., Luyssaert, S., Guimberteau, M. and Naudts, K. The importance of tree demography and root water uptake for modelling the carbon and water cycles of Amazonia. under review, 2021.

Kattge, J., Diaz, S., Lavorel, S., Prentice, I. C., Leadley, P., Bönisch, G., Garnier, E., Westoby, M., Reich, P. B., and Wright, I. J.: TRY–a global database of plant traits, Global change biology, 17, 2905-2935, 2011.

Kennedy, D., Swenson, S., Oleson, K. W., Lawrence, D. M., Fisher, R., Lola da Costa, A. C., and Gentine, P.: Implementing plant hydraulics in the community land model, version 5, Journal of Advances in Modeling Earth Systems, 11, 485-513, 2019.

Klos, R. J., Wang, G. G., Bauerle, W. L., and Rieck, J. R.: Drought impact on forest growth and mortality in the southeast USA: an analysis using Forest Health and Monitoring data, Ecological Applications, 19, 699-708, 2009.

Kraft, N. J., Metz, M. R., Condit, R. S., and Chave, J.: The relationship between wood density and mortality in a global tropical forest data set, New Phytologist, 188, 1124-1136, 2010.

Lewis, S. L., Brando, P. M., Phillips, O. L., van der Heijden, G. M., and Nepstad, D.: The 2010 amazon drought, Science, 331, 554-554, 2011.

Lin, Y. S., Medlyn, B. E., Duursma, R. A., Prentice, I. C., Wang, H., Baig, S., Eamus, D., De Dios, V. R., Mitchell, P., and Ellsworth, D. S.: Optimal stomatal behaviour around the world, Nature Climate Change, 5, 459-464, 2015.

Liu, Q., Peng, C., Schneider, R., Cyr, D., Liu, Z., Zhou, X., and Kneeshaw, D.: TRIPLEX-Mortality model for simulating drought-induced tree mortality in boreal forests: Model development and evaluation, Ecological Modelling, 455, 109652, 2021a.

Liu, Y., Holtzman, N. M., and Konings, A. G.: Global ecosystem-scale plant hydraulic traits retrieved using model–data fusion, Hydrology and Earth System Sciences, 25, 2399-2417, 2021b.

Maréchaux, I., Bartlett, M. K., Sack, L., Baraloto, C., Engel, J., Joetzjer, E., and Chave, J.: Drought tolerance as predicted by leaf water potential at turgor loss point varies strongly across species within an Amazonian forest, Functional Ecology, 29, 1268-1277, 2015.

Maréchaux, I., Saint-André, L., Bartlett, M. K., Sack, L., and Chave, J.: Leaf drought tolerance cannot be inferred from classic leaf traits in a tropical rainforest, Journal of Ecology, 108, 1030-1045, 2020.

Maréchaux, I., Langerwisch, F., Huth, A., Bugmann, H., Morin, X., Reyer, C. P., Seidl, R., Collalti, A., Dantas de Paula, M., and Fischer, R.: Tackling unresolved questions in forest ecology: The past and future role of simulation models, Ecology and evolution, 11, 3746-3770, 2021.

Markesteijn, L., and Poorter, L.: Seedling root morphology and biomass allocation of 62 tropical tree species in relation to drought-and shade-tolerance, Journal of Ecology, 97, 311-325, 2009.

Martinez-Vilalta, J., Anderegg, W. R., Sapes, G., and Sala, A.: Greater focus on water pools may improve our ability to understand and anticipate drought-induced mortality in plants, New Phytologist, 223, 22-32, 2019.

McDowell, N., Pockman, W. T., Allen, C. D., Breshears, D. D., Cobb, N., Kolb, T., Plaut, J., Sperry, J., West, A., and Williams, D. G.: Mechanisms of plant survival and mortality during drought: why do some plants survive while others succumb to drought?, New phytologist, 178, 719-739, 2008.

McDowell, N., Allen, C. D., Anderson-Teixeira, K., Brando, P., Brienen, R., Chambers, J., Christoffersen, B., Davies, S., Doughty, C., and Duque, A.: Drivers and mechanisms of tree mortality in moist tropical forests, New Phytologist, 219, 851-869, 2018.

McDowell, N. G., Beerling, D. J., Breshears, D. D., Fisher, R. A., Raffa, K. F., and Stitt, M.: The interdependence of mechanisms underlying climate-driven vegetation mortality, Trends in ecology & evolution, 26, 523-532, 2011.

Meinzer, F. C., Campanello, P. I., Domec, J.-C., Gatti, M. G., Goldstein, G., Villalobos-Vega, R., and Woodruff, D. R.: Constraints on physiological function associated with branch architecture and wood density in tropical forest trees, Tree Physiology, 28, 1609-1617, 2008.

Meir, P., Mencuccini, M., and Dewar, R. C.: Drought-related tree mortality: addressing the gaps in understanding and prediction, New Phytologist, 207, 28-33, 2015.

Meir, P., Mencuccini, M., Binks, O., da Costa, A. L., Ferreira, L., and Rowland, L.: Short-term effects of drought on tropical forest do not fully predict impacts of repeated or long-term drought: gas exchange versus growth, Philosophical Transactions of the Royal Society B: Biological Sciences, 373, 20170311, 2018.

Mokany, K., Raison, R. J., and Prokushkin, A. S.: Critical analysis of root: shoot ratios in terrestrial biomes, Global Change Biology, 12, 84-96, 2006.

Naudts, K., Ryder, J., McGrath, M., Otto, J., Chen, Y., Valade, A., Bellasen, V., Berhongaray, G., Bönisch, G., and Campioli, M.: A vertically discretised canopy description for ORCHIDEE (SVN r2290) and the modifications to the energy, water and carbon fluxes, Geoscientific Model Development, 8, 2035-2065, 2015.

Nepstad, D. C., Tohver, I. M., Ray, D., Moutinho, P., and Cardinot, G.: Mortality of large trees and lianas following experimental drought in an Amazon forest, Ecology, 88, 2259-2269, 2007.

Nobre, C. A., and Borma, L. D. S.: 'Tipping points' for the Amazon forest, Current Opinion in Environmental Sustainability, 1, 28-36, 2009.

Nychka D, F. R., Paige J, Sain S, Gerber F., Iverson M.: Fields: Tools for Spatial Data

University Corporation for Atmospheric Research, Boulder, CO, USA 10.5065/D6W957CT

URL: https://github.com/NCAR/Fields. R package version 10.3, 2020.

Papastefanou, P., Zang, C. S., Pugh, T. A., Liu, D., Grams, T. E., Hickler, T., and Rammig, A.: A dynamic model for strategies and dynamics of plant water-potential regulation under drought conditions, Frontiers in Plant Science, 11, 373, 2020.

Phillips, O. L., Aragão, L. E., Lewis, S. L., Fisher, J. B., Lloyd, J., López-González, G., Malhi, Y., Monteagudo, A., Peacock, J., and Quesada, C. A.: Drought sensitivity of the Amazon rainforest, Science, 323, 1344-1347, 2009.

Powell, T. L., Galbraith, D. R., Christoffersen, B. O., Harper, A., Imbuzeiro, H. M., Rowland, L., Almeida, S., Brando, P. M., da Costa, A. C. L., and Costa, M. H.: Confronting model predictions of carbon fluxes with measurements of Amazon forests subjected to experimental drought, New Phytologist, 200, 350-365, 2013.

Powell, T. L., Koven, C. D., Johnson, D. J., Faybishenko, B., Fisher, R. A., Knox, R. G., McDowell, N. G., Condit, R., Hubbell, S. P., and Wright, S. J.: Variation in hydroclimate sustains tropical forest biomass and promotes functional diversity, New Phytologist, 219, 932-946, 2018.

R Development Core Team. R: A language and environment for statistical computing. Vienna, Austria: R Foundation for Statistical Computing, available at http://www.R-project.org/ 2019.

Rao, K., Anderegg, W. R., Sala, A., Martínez-Vilalta, J., and Konings, A. G.: Satellite-based vegetation optical depth as an indicator of drought-driven tree mortality, Remote sensing of environment, 227, 125-136, 2019.

Rowland, L., da Costa, A. C. L., Galbraith, D. R., Oliveira, R., Binks, O. J., Oliveira, A., Pullen, A., Doughty, C., Metcalfe, D., and Vasconcelos, S.: Death from drought in tropical forests is triggered by hydraulics not carbon starvation, Nature, 528, 119-122, 2015.

Rozendaal, D. M., Phillips, O. L., Lewis, S. L., Affum-Baffoe, K., Alvarez-Davila, E., Andrade, A., Aragão, L. E., Araujo-Murakami, A., Baker, T. R., and Bánki, O.: Competition influences tree growth, but not mortality, across environmental gradients in Amazonia and tropical Africa, Ecology, 101, e03052, 2020.

Sabot, M. E., De Kauwe, M. G., Pitman, A. J., Medlyn, B. E., Verhoef, A., Ukkola, A. M., and Abramowitz, G.: Plant profit maximization improves predictions of European forest responses to drought, New Phytologist, 226, 1638-1655, 2020.

Sack, L., and Holbrook, N. M.: Leaf hydraulics, Annu. Rev. Plant Biol., 57, 361-381, 2006.

Sapes, G., Roskilly, B., Dobrowski, S., Maneta, M., Anderegg, W. R., Martinez-Vilalta, J., and Sala, A.: Plant water content integrates hydraulics and carbon depletion to predict drought-induced seedling mortality, Tree physiology, 39, 1300-1312, 2019.

Schuldt, B., Leuschner, C., Brock, N., and Horna, V.: Changes in wood density, wood anatomy and hydraulic properties of the xylem along the root-to-shoot flow path in tropical rainforest trees, Tree physiology, 33, 161-174, 2013.

Signori-Müller, C., Oliveira, R. S., de Vasconcellos Barros, F., Tavares, J. V., Gilpin, M., Diniz, F. C., Zevallos, M. J. M., Yupayccana, C. A. S., Acosta, M., and Bacca, J.: Non-structural carbohydrates

mediate seasonal water stress across Amazon forests, Nature communications, 12, 1-9, 2021.

Sperry, J. S., Wang, Y., Wolfe, B. T., Mackay, D. S., Anderegg, W. R., McDowell, N. G., and Pockman, W. T.: Pragmatic hydraulic theory predicts stomatal responses to climatic water deficits, New Phytologist, 212, 577-589, 2016.

Sperry, J. S., Venturas, M. D., Anderegg, W. R., Mencuccini, M., Mackay, D. S., Wang, Y., and Love, D. M.: Predicting stomatal responses to the environment from the optimization of photosynthetic gain and hydraulic cost, Plant, cell & environment, 40, 816-830, 2017.

Stovall, A. E., Shugart, H., and Yang, X.: Tree height explains mortality risk during an intense drought, Nature communications, 10, 1-6, 2019.

Suzuki, E.: Diversity in specific gravity and water content of wood among Bornean tropical rainforest trees, Ecological Research, 14, 211-224, 1999.

Trugman, A. T., Anderegg, L. D., Anderegg, W. R., Das, A. J., and Stephenson, N. L.: Why is tree drought mortality so hard to predict?, Trends in Ecology & Evolution, 2021.

Urli, M., Porté, A. J., Cochard, H., Guengant, Y., Burlett, R., and Delzon, S.: Xylem embolism threshold for catastrophic hydraulic failure in angiosperm trees, Tree physiology, 33, 672-683, 2013.

Van Genuchten, M. T.: A closed-form equation for predicting the hydraulic conductivity of unsaturated soils, Soil science society of America journal, 44, 892-898, 1980.

Wang, W., Peng, C., Kneeshaw, D. D., Larocque, G. R., and Luo, Z.: Drought-induced tree mortality: ecological consequences, causes, and modeling, Environmental Reviews, 20, 109-121, 2012.

Xu, X., Medvigy, D., Powers, J. S., Becknell, J. M., and Guan, K.: Diversity in plant hydraulic traits explains seasonal and inter-annual variations of vegetation dynamics in seasonally dry tropical forests, New Phytologist, 212, 80-95, 2016.

Yang, Y., Saatchi, S. S., Xu, L., Yu, Y., Choi, S., Phillips, N., Kennedy, R., Keller, M., Knyazikhin, Y., and Myneni, R. B.: Post-drought decline of the Amazon carbon sink, Nature communications, 9, 1-9, 2018.

Yin, X., & Struik, P. C. C3 and C4 photosynthesis models: An overview from the perspective of crop modelling. NJAS-Wageningen Journal of Life Sciences, 57(1), 27-38, 2009.

Yoshimura, K., Saiki, S.-T., Yazaki, K., Ogasa, M. Y., Shirai, M., Nakano, T., Yoshimura, J., and Ishida, A.: The dynamics of carbon stored in xylem sapwood to drought-induced hydraulic stress in mature trees, Scientific reports, 6, 24513, 2016.

Young, D. J., Stevens, J. T., Earles, J. M., Moore, J., Ellis, A., Jirka, A. L., and Latimer, A. M.: Long-term climate and competition explain forest mortality patterns under extreme drought, Ecology Letters, 20, 78-86, 2017.

Zhu, D., Peng, S., Ciais, P., Viovy, N., Druel, A., Kageyama, M., Krinner, G., Peylin, P., Ottlé, C., and Piao, S.: Improving the dynamics of Northern Hemisphere high-latitude vegetation in the ORCHIDEE ecosystem model, 2015.

Zhu, S.-D., Chen, Y.-J., Ye, Q., He, P.-C., Liu, H., Li, R.-H., Fu, P.-L., Jiang, G.-F., and Cao, K.-F.: Leaf turgor loss point is correlated with drought tolerance and leaf carbon economics traits, Tree

Physiology, 38, 658-663, 2018.

3.10 SUPPLEMENTARY INFORMATION

Forest fluxes and mortality response to drought: model description (ORCHIDEE-CAN-NHA, r7236) and evaluation at the Caxiuanã drought experiment

Yitong Yao[1*], Emilie Joetzjer[2*], Philippe Ciais[1], Nicolas Viovy[1], Fabio Cresto Aleina[1], Jerome Chave[3], Lawren Sack[4], Megan Bartlett[5], Patrick Meir[6], Rosie Fisher[7], Sebastiaan Luyssaert[8]

[1] Laboratoire des Sciences du Climat et de l'Environnement, LSCE/IPSL, CEA-CNRS-UVSQ, Université Paris-Saclay, Gif-sur-Yvette, 91191, France

[2] Centre National de Recherche Meteorologique, Unite mixte de recherche 3589 Meteo-France/CNRS, 42 Avenue Gaspard Coriolis, Toulouse, 31100, France

[3] Laboratoire Evolution et Diversité Biologique UMR 5174 CNRS, IRD, Université Paul Sabatier, Toulouse, 31062, France

[4] Department of Ecology and Evolutionary Biology, University of California Los Angeles, Los Angeles, California, 90095, USA

[5] Department of Viticulture & Enology, University of California, Davis, California, 95616, USA

[6] Research School of Biology, Australian National University, Canberra, ACT 2601 Australia

[7] CICERO Centre for International Climate and Environmental Research, Oslo, Norway

[8] Faculty of Science, Vrije Universiteit Amsterdam, Netherlands

* These authors contributed equally to this work.

Table S1

Figure S1 to S14

Table S1 Tree height and diameter of each cohort (take CTL as example).

# of cohort	tree diameter (m)	tree height (m)
1	0.02	6
2	0.03	8
3	0.18	18
4	0.32	23
5	0.46	27
6	0.60	31
7	0.74	34
8	0.87	37
9	1.01	40
10	1.15	42
11	1.29	44
12	1.43	47
13	1.57	49
14	1.71	51
15	1.86	53
16	2.02	55
17	2.19	57
18	2.38	59
19	2.64	62
20	3.1	67

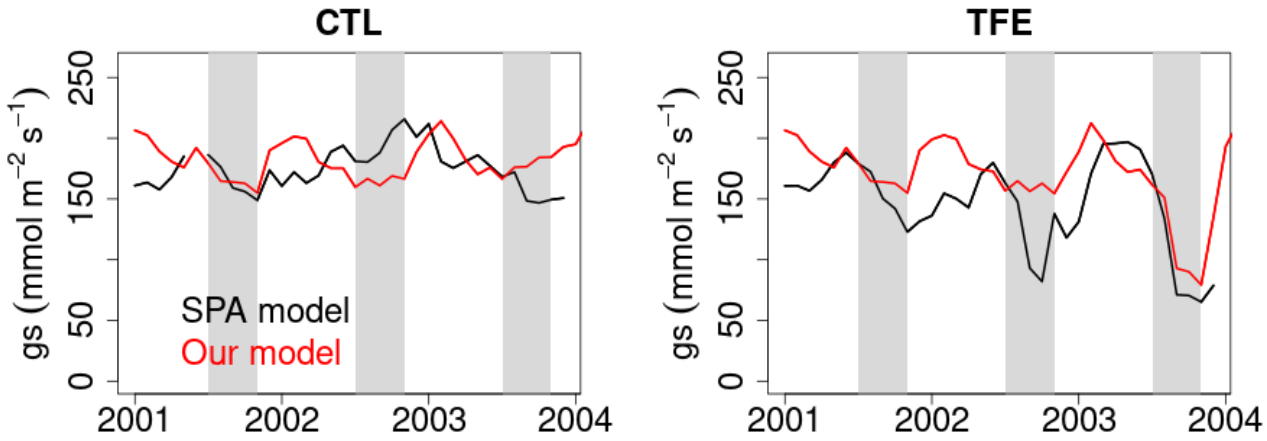

Figure S1 Comparison of our simulated stomatal conductance (gs) with SPA model output in Fisher et al (2007) at Caxiuana site.

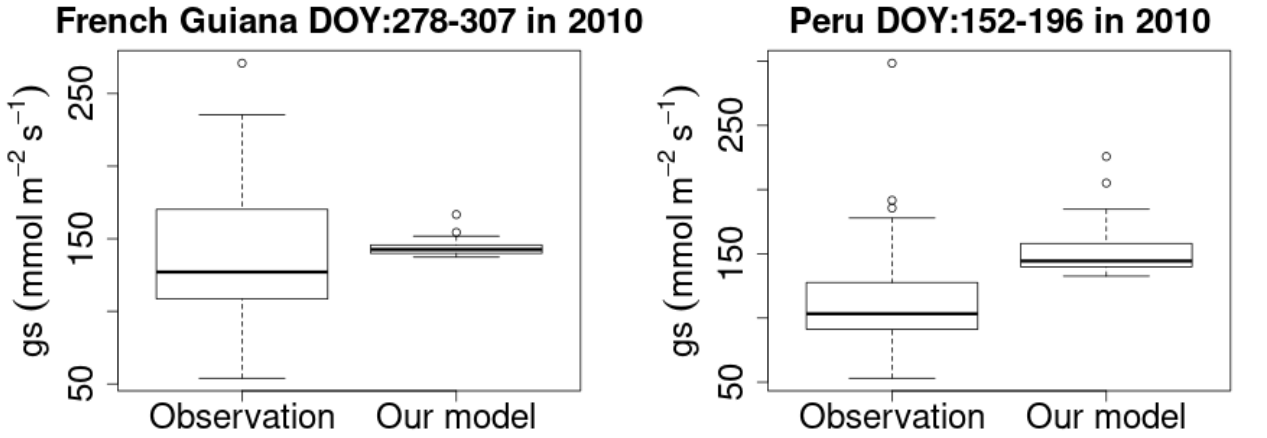

Figure S2 Comparison of our simulated stomatal conductance (gs) at (a) French Guiana and (b) Peru site. The gs observation data at French Guiana and Peru site are from Lin et al (2015).

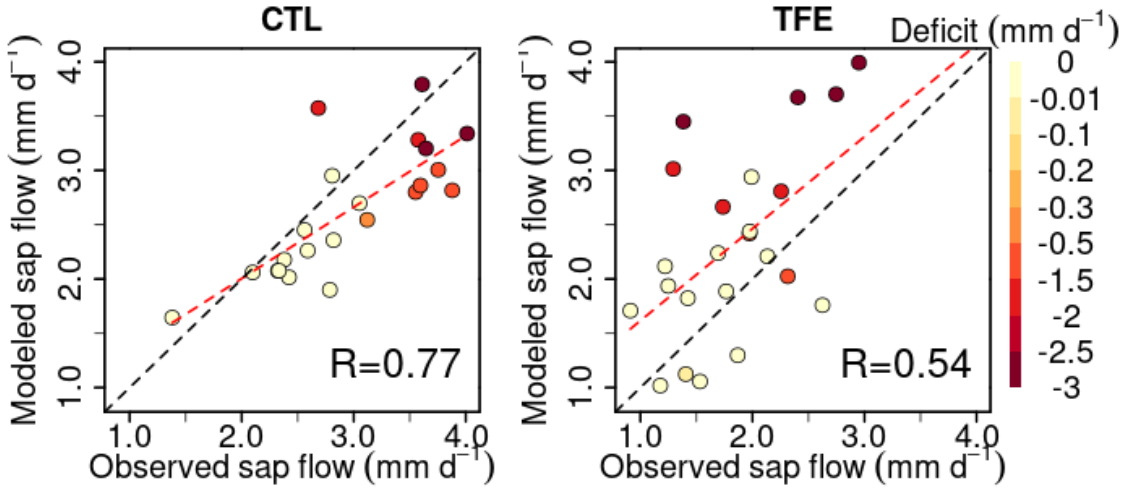

Figure S3 Similar to Figure 3 but for ORCHIDEE-CAN-RS.

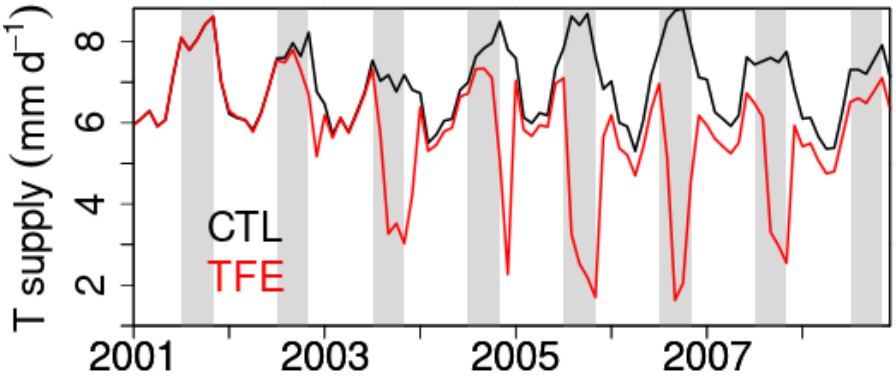

Figure S4 Transpiration supply simulated by ORCHIDEE-CAN-NHA during 2001-2008. In Caxiuanã site, dry season is deemed from July to November.

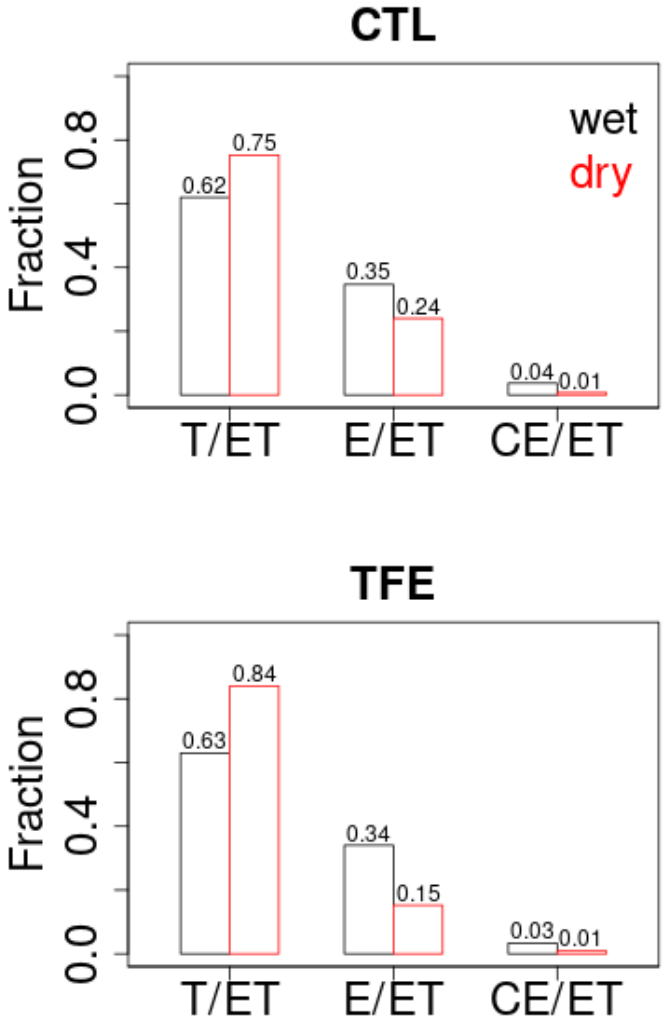

Figure S5 Simulated T/ET, E/ET and CE/ET during 2001 to 2008 under CTL and TFE from ORCHIDEE-CAN-NHA. T, transpiration. ET, evapotranspiration. CE, intercepted canopy water or dew re-evaporation. In Caxiuanã site, dry season is deemed from July to November.

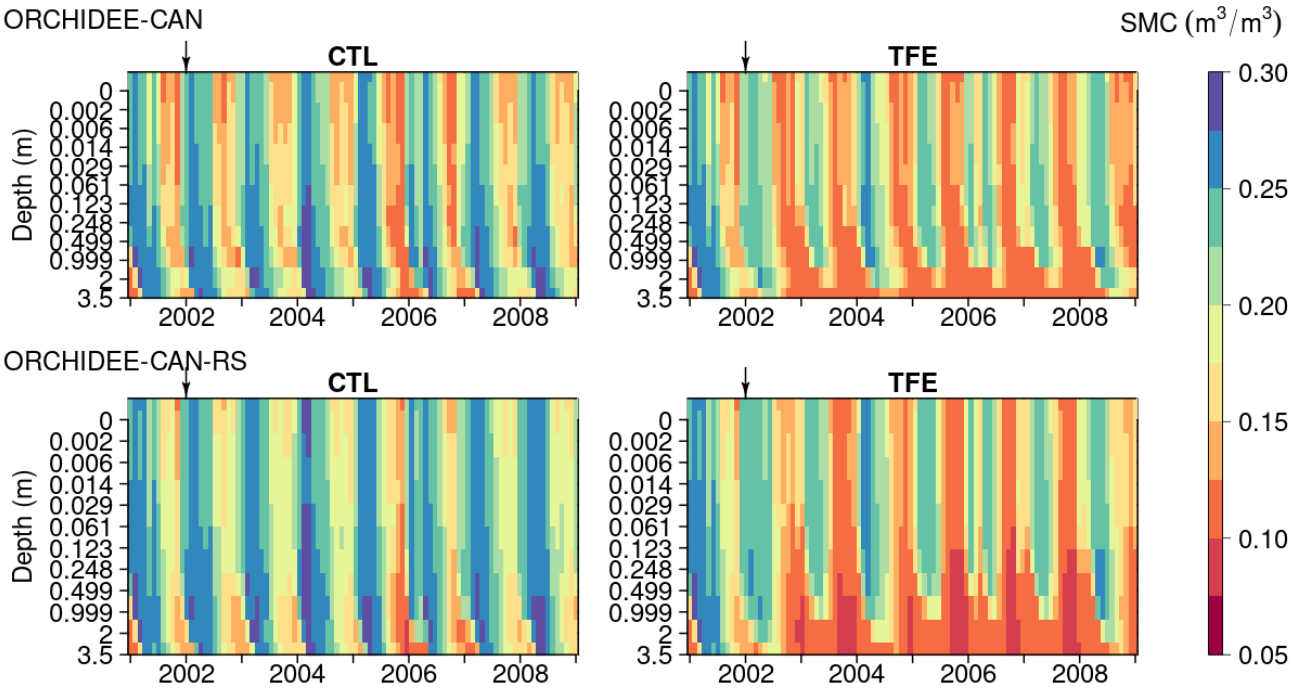

Figure S6 Similar to Figure 6 but for ORCHIDEE-CAN and ORCHIDEE-CAN-RS.

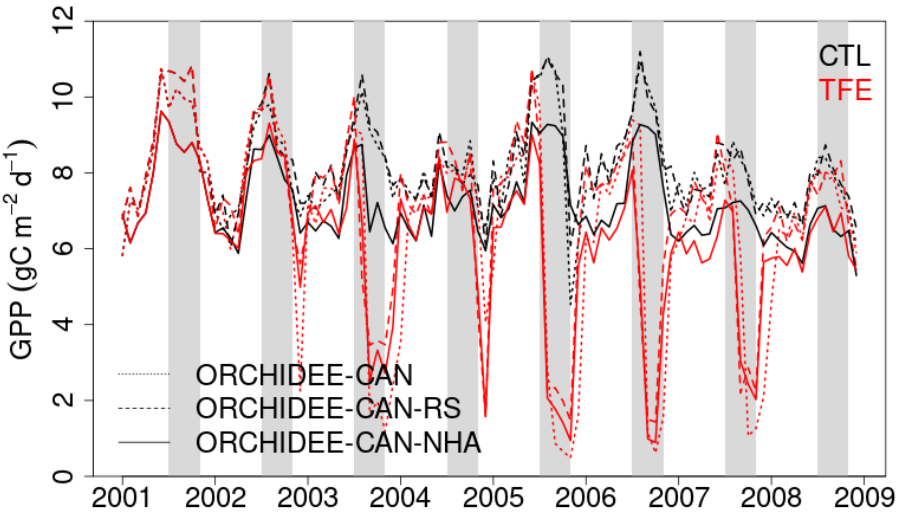

Figure S7 Simulation of GPP dynamics during 2001 to 2008.

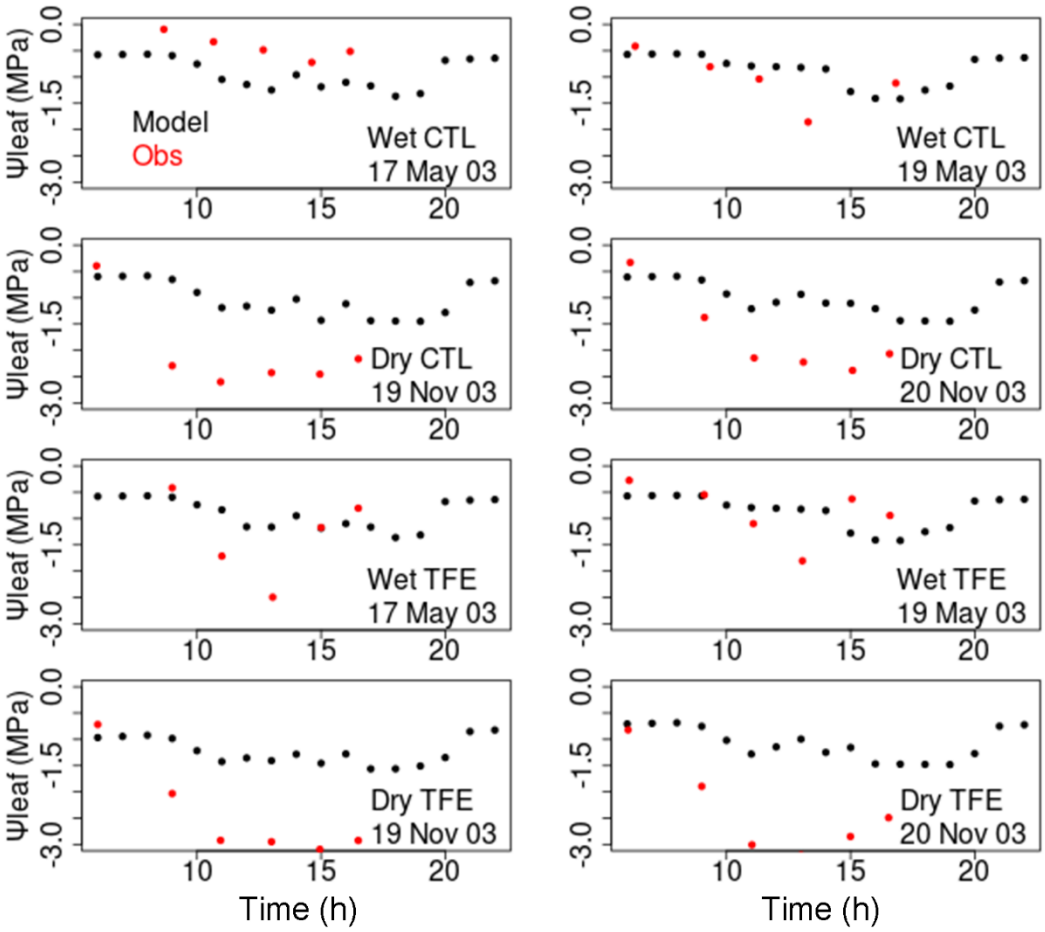

Figure S8 Modeled (black dots) and measured (red dots) leaf water potential in the control (CTL) and throughfall exclusion (TFE) for wet and dry seasons. Measured leaf water potential comes from Fisher et al (2006).

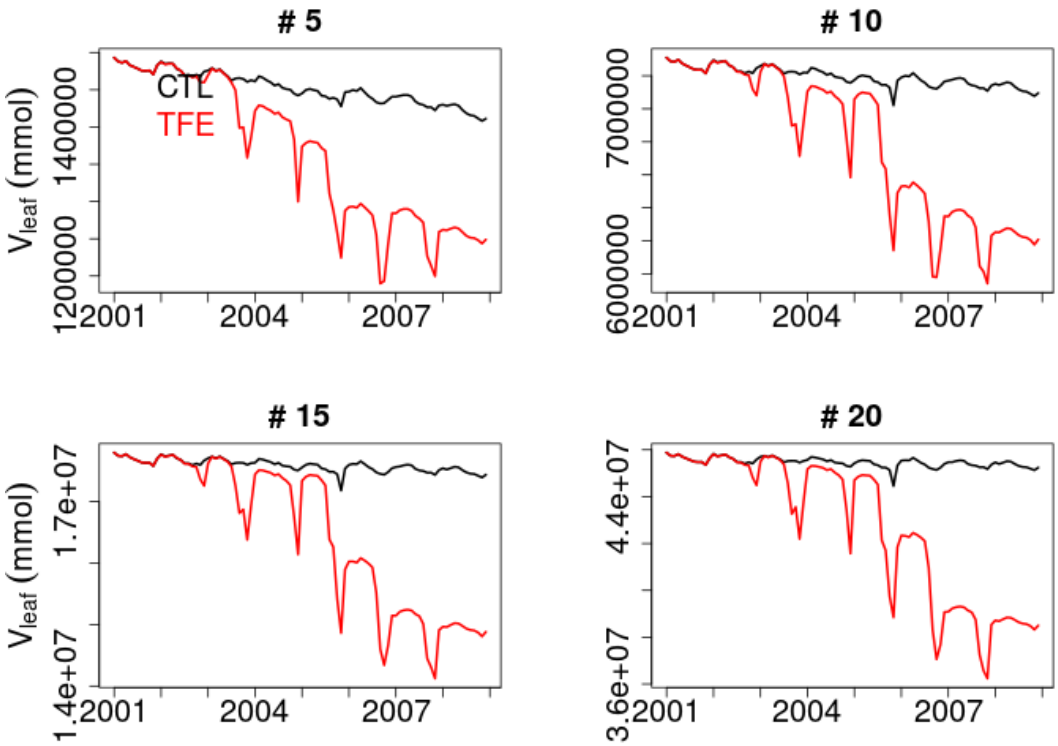

Figure S9 Change in leaf water storage during 2001-2008. Cohorts of #5, #10, #15, and #20 are taken as example here.

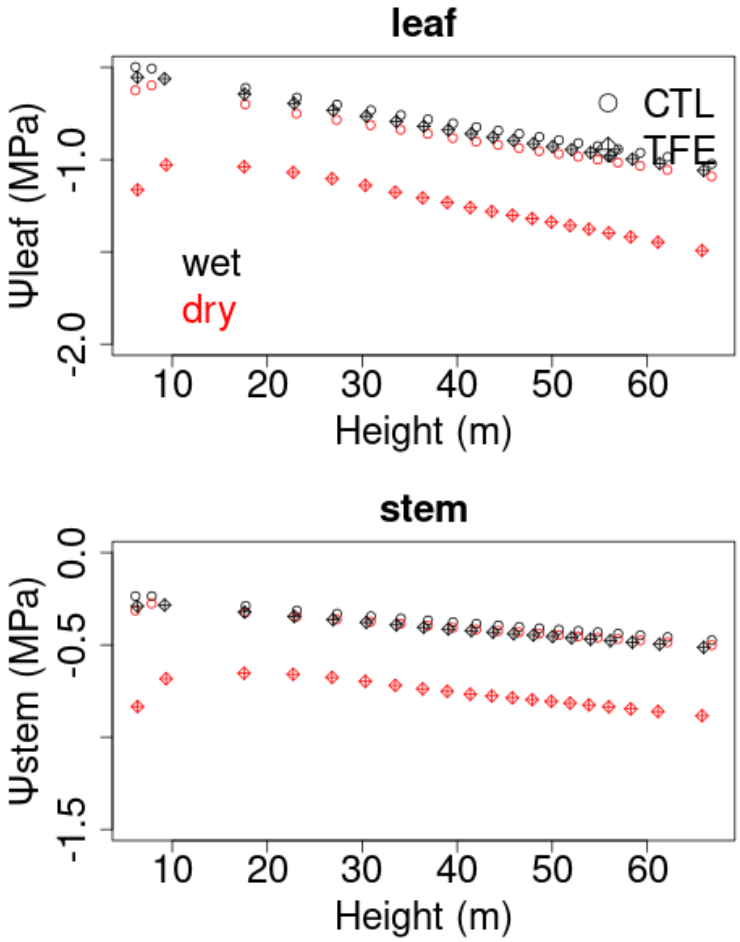

Figure S10 Relationship between Ψ_{leaf}, Ψ_{stem} and tree height.

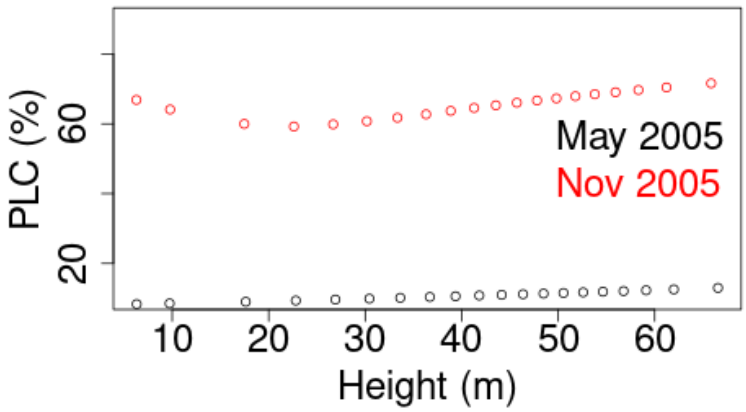

Figure S11 Relationship between percentage loss of conductance (PLC) and tree height.

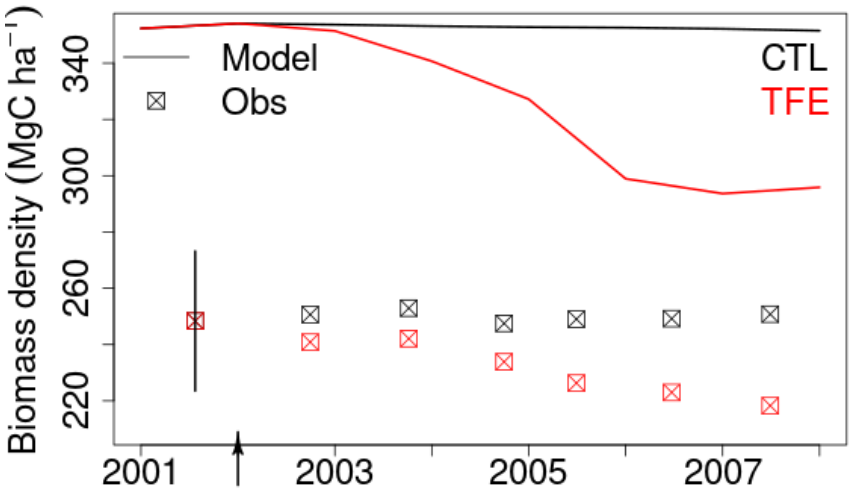

Figure S12 Absolute values of change in biomass simulated by ORCHIDEE-CAN-NHA after mortality being triggered. Since there is a noticeable difference of biomass in 2001 between CTL and TFE observation, we made a shift on CTL biomass to let it to be consistent with TFE in the beginning of experiments (the amount of shift = 25 MgC ha^{-1}).

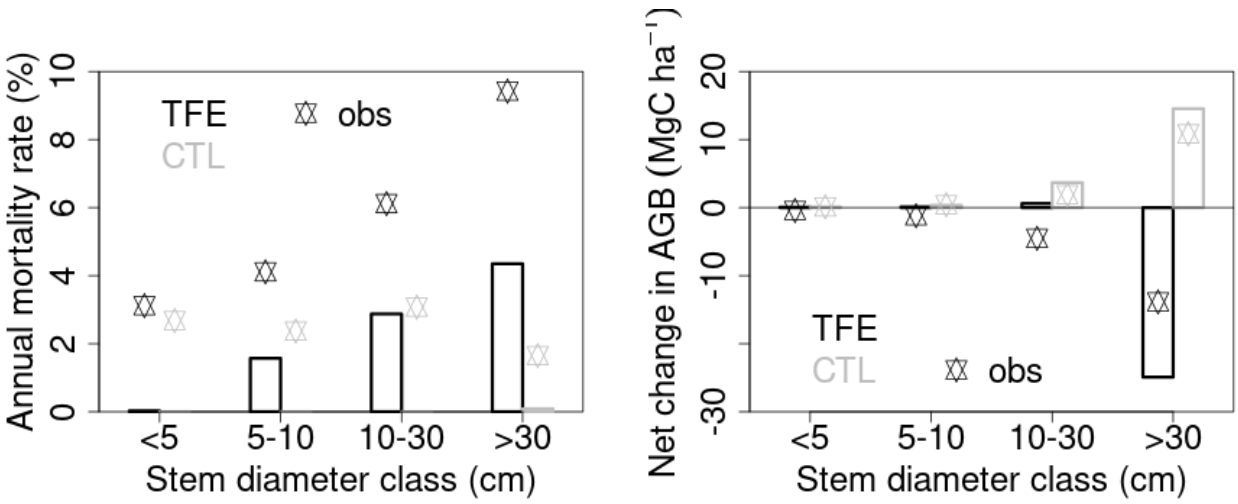

Figure S13 Comparison of (a) annual mortality rates in different diameter size classes and (b) net change in aboveground biomass (AGB) between our model simulation and observation at Tapajos site from 1999 to 2003. CTL: control. TFE: throughfall exclusion experiment. At Tapajos site, TFE only happened in wet season from 2000 to 2003. The net change in AGB accounts for the period from 1999 to 2003.

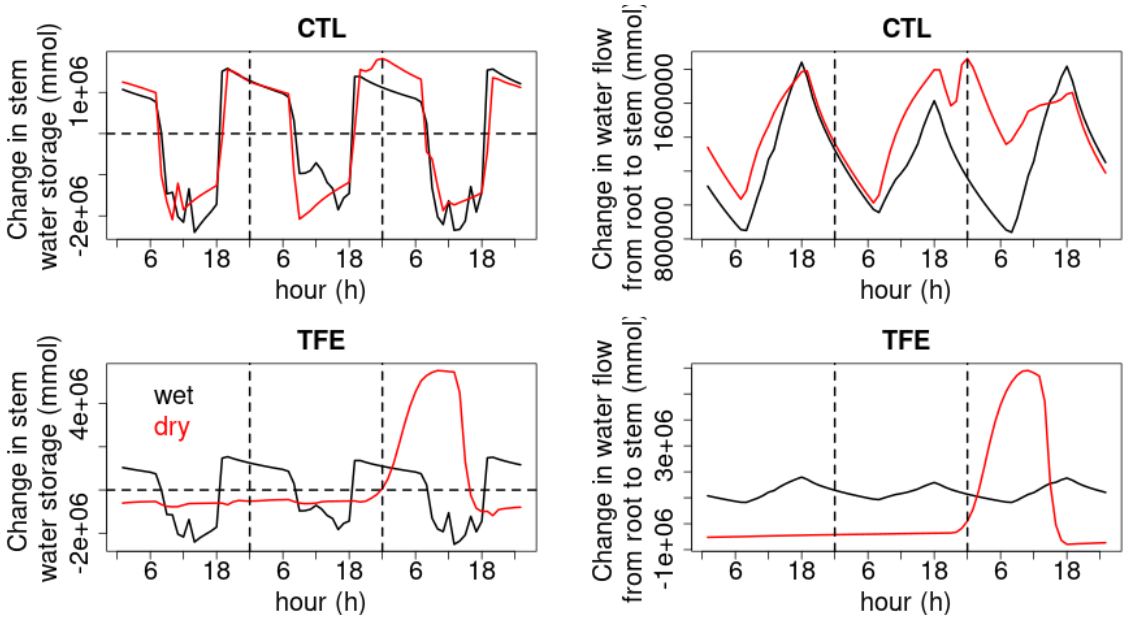

Figure S14 Diurnal cycles of stem water flux and storage change. Here, 'wet' denotes the first three days in May (1-3 May) in 2005, and 'dry' denotes the first three days in November (1-3 Nov) in 2005. Cohort #10 is used here as an example. Positive change in stem water storage means water charge to stem and vice versa.

4 How drought events during the last Century have impacted biomass carbon in Amazonian rainforests

4.1 Summary

Drought events recurrently affected the Amazon rainforest, especially the occurrence of three severe droughts over recent two decades, 2005, 2010 and the 2015/16 El Nino drought, after which the net biomass carbon sink capacity was undermined due to the quicker increase of biomass loss triggered by tree dieback than that of continuing but decelerating productivity increase, as evidenced by the forest inventory measurements. Forest inventory field data and satellite datasets like LiDAR-based tree height changes indeed provide a reference for the drought impacts on forest dynamics, however they are unable to provide an evaluation for earlier droughts. Process-based models, capable of simulating carbon and water cycles at large-scale and over long-time scales struggled to include drought-induced responses of growth and mortality, and have not been evaluated against plot data so far.

In this chapter, we use ORCHIDEE-CAN-NHA, detailed in the previous chapter; which includes modules of forest demography with different tree size cohorts dynamically influenced by growth, self-thinning from light competition and recruitment, a detailed tree hydraulic architecture function of each tree cohort, and drought-driven mortality due to the loss of tree conductance to simulate the impact of drought on biomass dynamics (Chapter 3). Using this model, we simulated the long-term biomass carbon dynamics, composed of carbon gains from stand growth, carbon losses from background and climate mortality and the resulting net carbon balance of biomass carbon stocks. We showed that the model simulates the drought sensitivity for the three severe drought events of the last two decades with results comparable to forest inventory data. Regarding the top eight drought events of the last century, for which no observations exist, we simulated that the 2015/16 El Nino drought is the most severe on record, both from the drought affected area and the area that experienced the most intense biomass loss. Through factorial simulation separating the effects of historical CO_2 concentration increase and climate change, we confirm negative climate change effect but also the alleviation of water stress from higher CO_2 due to higher water use efficiency induced from stomatal closure.

Overall, the model performs well in reproducing the long-term declining trend in net biomass carbon sink, a famous result shown from inventory long-term records by Hubau et al (2020), and a comparable drought sensitivity of biomass gains and loss with forest plots inventory. Further improvement should target a better accounting of fine scale soil texture heterogeneity, hydraulic traits again such as wood density, and root properties to reduce the model-observation misfit in spatial gradients of mortality risk. This study represents a progress from state of the art global models in quantifying the large scale drought effects on tropical rainforest and should increase our confidence for future predictions of climate induced impacts on biomass carbon storage.

This chapter is published in the journal *Global Change Biology*.

Yao, Y., Ciais, P., Viovy, N., Joetzjer, E., & Chave, J. (2022). How drought events during the last Century have impacted biomass carbon in Amazonian rainforests. Global Change Biology. doi : 10.1111/gcb.16504 (see Appendix C)

4.2 ABSTRACT

During the last two decades, droughts have recurrently impacted the Amazon forests, as in the severe drought events of 2005, 2010 and 2015/16. The analysis of forest inventory plots suggests that these droughts have resulted in a reduction of the carbon sink of intact forests by causing mortality to exceed growth. Process-based models have struggled to include drought-induced responses of growth and mortality, and have not been evaluated against plot data. In this study, we use ORCHIDEE-CAN-NHA, a DGVM which includes modules of forest demography with different tree size cohorts dynamically influenced by growth, self-thinning from light competition and recruitment, a detailed tree hydraulic architecture function of each tree cohort, and drought-driven mortality due to the loss of tree conductance to simulate the impact of drought on biomass dynamics. We calibrated the model at a long drought experiment site (Caxiuanã). We then ran the model over Amazonia forests using as an input gridded climate fields and rising atmospheric CO_2 from 1901 to 2019. The model reproduced the drought sensitivity of aboveground biomass (AGB) growth and mortality observed at forest plots across selected Amazon intact forests for 2005 and 2010, and the net balance between these two carbon fluxes. No plot data have been published yet for the recent 2015/16 El Niño, but we predict a more negative sensitivity of the net carbon sink during this event compared to the former 2005 and 2010 droughts. We then ranked all past drought events of the last century based on their maximum cumulated water deficit anomalies, and found that 2015/16 was the most severe drought in terms of both AGB loss and area experiencing a severe carbon loss. Because of the 2015/16 event, together with the 2005 and 2010 droughts, the last 20 years was the period with the largest climate-driven cumulative AGB loss than any other previous 20-years period since 1901. Factorial simulations allowed us to separate the individual contribution of climate change and rising CO_2 concentration on AGB dynamics. We found that even if climate change did increase mortality, increased CO_2 concentration contributed to balance the C loss due to mortality. This is because, in our model, CO_2-induced stomatal closure reduces transpiration and increases soil moisture, offsetting increasing transpiration from CO_2 induced higher foliage area.

4.3 INTRODUCTION

The Amazonian rainforest accounts for 40% of the tropical forest biome area and contains half of its carbon. Changes in the Amazon forest dynamics impact the global water and carbon cycles, and exert key feedbacks on climate change (Jimenez & Takahashi, 2019), leaving open the possibility of crossing 'tipping points' in the form of a regional forest dieback (Ritchie *et al.*, 2021). Both short-term variability and long-term trends in Amazon forest carbon fluxes and stocks are regulated by climate variability. In particular, repeated extreme drought events have the potential to undermine the stability of large parts of the Amazon forest (Zemp *et al.*, 2017). Over the last century, major drought events occurred in Amazonia, generally associated with positive sea surface temperature anomalies in the tropical Atlantic (1916, 1963, 2005, 2010) and with strong El Niño events (1926, 1982/83, 1997/98, 2015/16). El Niño events tend to bring drought in the wet season, whereas Atlantic anomalies exacerbate drought in the dry season (Jimenez et al., 2018).

While the long-term view is crucial to understand the current dynamics of Amazonia, much of our knowledge about the response of Amazonian forests to drought is based on limited field data from the last decades: a slow-down of forest carbon gains from growth and a coincident increase of losses from tree mortality have been observed from successive forest plot inventories, leading to a gradual decline in the strength of the biomass carbon sink (Brienen *et al.*, 2015).

Research focusing on past drought events used different methods, including ground-based observations of carbon fluxes at few sites (Doughty *et al.*, 2015), biomass inventories (Feldpausch *et*

al., 2016; Phillips *et al.*, 2009), drought experiments (Fisher *et al.*, 2007), remote-sensing (Yang *et al.*, 2018), and process-based models (Papastefanou *et al*., 2021). Analyses from the RAINFOR network of forest plots provided net biomass change at selected locations during the 2005 and 2010 droughts (Feldpausch *et al.*, 2016; Hubau *et al.*, 2020), and spatial patterns in variation of mortality rates (Esquivel-Muelbert *et al.*, 2020) and biomass loss (Papastefanou *et al.*, 2020).

Ground-based observations and satellite products only cover climatic anomalies for two decades, a short timescale compared with the natural dynamics of forests. A centennial perspective is needed, as repeated droughts affect decadal-scale carbon processes through legacy effects and slow recovery of forests after disturbances (Lewis *et al.*, 2011). Given the lack of observations, process-based models are useful to explore the effects of drought on the Amazon carbon balance.

Although predicting the risk of mortality from hydraulic failure is challenging given species-specific responses (Rowland *et al.*, 2021), several process-based models have made progress in representing a mechanistic hydraulic architecture simulating the water transport through trees, from the soil to the atmosphere (Kennedy *et al.*, 2019; Li *et al.*, 2021). Leaf-level carbon-water trade-offs, reflecting plant stomatal strategies, are at the foundation of most hydraulic modules, and they are used in models as a target to be optimized, e.g. the product of productivity and water cost (Eller *et al.*, 2020), or the direct and opportunity carbon cost of xylem damage (Lu *et al.*, 2020). Although these studies partly captured changes of plant hydrodynamics, they did not consider the water capacitance of trees (Kennedy *et al*., 2019), or did not model changes in the vertical profile of water potential from soil to leaves, rather focusing on stomatal behavior (Eller *et al*., 2020). A hydraulic architecture model describing explicit water transport process is required to better mimic plant water dynamics in reality. Yao *et al* (2021) simulated half-hourly water potentials at leaf, stem, root and soil levels by minimizing the difference between water demand and supply for each plant organ in the ORCHIDEE-CAN-NHA model, a branch of the ORCHIDEE land surface model (version r7236). In addition to representing changes in water flows and storage on a 30 min time-step in soils and plants, the model includes an empirical parameterization of mortality from hydraulic failure. Namely, when stem water conductance drops below a critical threshold during a certain number of days, a mortality risk function is calculated and trees of each cohort die if this function exceeds a threshold. The advantage of ORCHIDEE-CAN lies in its explicit representation of different tree-size cohorts, which allows us to link realization of simulation of hydrodynamics to forest demography. The model was calibrated against field observations from the Caxiuanã throughfall exclusion (TFE) experiment (Fisher *et al*., 2007) and tested on another TFE experiment site at Tapajos. Yet, it has not been used to assess the carbon impacts of regional drought. Here, we address this challenge by applying the calibrated ORCHIDEE-CAN-NHA model over rainforest in Amazon basin during the last century.

Besides climate change, an important consideration for modelling the Amazonian forest over a century is that CO_2 concentration has increased by more than 120 ppm during this period. There is consensus on the stimulation effects on growth under elevated CO_2, although no field CO_2 enrichment experiment (FACE) is available for Amazonia. A simulated elevated CO_2 forcing predicted an increase in aboveground biomass for an ensemble of models, limited by phosphorus availability (Fleischer *et al.*, 2019). Increased CO_2 concentration also affects initial biomass, carbon allocation, and parameterized self-thinning (Holm *et al.*, 2020), and reduces stomatal conductance, resulting in less transpiration per unit of leaf area, although increased leaf area may act to counteract this effect (Cox *et al.*, 2004; Piao *et al*., 2007). Yet, the effect of elevated CO_2 on stand competition and biomass loss processes is uncertain, especially with a higher drought frequency. Site-level spatial statistical analysis with CO_2 concentration and climatic factors by Hubau *et al.* (2020) suggested significant positive relationships between carbon gains and CO_2 concentration, but not carbon loss. Process-based modelling could be used to design tests to separate the effects of climate change and CO_2, and their interactions. De Almeida Castanho *et al.* (2016) conducted simulations to reproduce the individual and combined effects of climate change and elevated CO_2 but their model included a

simple mortality module and was unable to capture biomass loss from climate extremes. Here again, process-based models incorporating hydraulic architecture and mortality could help resolve the uncertainty in projecting drought-induced mortality in the presence of both elevated CO_2 effects and drought.

In this study, we use a new process-based model with a detailed mechanistic hydraulic architecture and a mortality scheme from hydraulic failure, ORCHIDEE-CAN-NHA (r7236), to reproduce the drought sensitivity and biomass dynamics from drought events of the last century in the Amazon, and *to elucidate* the contribution of climate change and elevated CO_2. Our objectives are: (1) to test the performance of the model for capturing the long-term trend of net carbon sink and its components of gains and losses, (2) to compare simulated patterns of drought-induced changes of growth and mortality against forest plots observations, (3) to compare aboveground biomass (AGB) losses between different drought events, (4) to assess if the extreme drought events of the last 20 years have higher impacts on AGB than previous sequences of drought during the last century; (5) to show the interactions between rising CO_2 and droughts on AGB dynamics.

4.4 Materials & Methods

4.4.1 The land surface model ORCHIDEE-CAN-NHA

In this study, we use a land surface model known as ORCHIDEE-CAN-NHA (r7236), incorporating allometric-based carbon allocation, trees cohorts impacting dynamic canopy structure with different growth of an average tree in each cohort and background mortality induced by self-thinning processes (Naudts *et al.*, 2015) as well as a new mechanistic hydraulic architecture (Yao *et al*, 2021). The hydraulic module includes the dynamic root water uptake scheme proposed by Joetzjer *et al* (under review) and a plant hydraulic model simulating water transport from water potentials gradient between soils and atmosphere, and water capacitance in roots, stems and leaves as described by Yao *et al* (2021). Besides this hydraulic architecture, a cavitation-mortality model was added. Two parameters are used to connect the percentage loss of stem conductance (PLC) simulated by the hydraulic module to mortality. A cumulated drought exposure index when PLC stays above a critical threshold defines a mortality risk. Under this risk, a fraction of trees is killed each day in different cohorts of tree size. The new hydraulic architecture and mortality schemes were calibrated against the world's longest running drought experiments at Caxiuanã (Rowland *et al*., 2015), with overall good performances.

4.4.2 Simulation framework

Climate forcing

The gridded climate forcing used as input to ORCHIDEE-CAN-NHA is the CRUJRA v2.1 dataset (Harris, 2020; Harris *et al.*, 2014; Harris *et al.*, 2020; Kobayashi *et al.*, 2015). CRUJRA v2.1 is constructed by re-gridding data from the Japanese Reanalysis Data (JRA) produced by the Japanese Meteorological Agency (JMA) adjusted to match the monthly observation-based Climatic Research Unit (CRU) TS 4.04 data (Harris *et al.*, 2020). It provides 6-hourly meteorological variables from January 1901 to December 2019 at 0.5×0.5^{o} spatial resolution.

Simulation protocol

To balance the spatial resolution of regional simulations with computing resources, the simulations were carried out at 1×1^{o} horizontal spatial resolution over 1901-2019 (study region see

Figure 4.1). We used a two-step spin-up to bring carbon and water pools in steady-state equilibrium. In the first step, the model is forced by recycling the climate forcing during 1901-1920 with a constant CO_2 concentration of 296 ppm and no climate-induced mortality activated. Then after the end of the first spin-up, we re-ran the model still recycling the climate forcing of 1901-1920 but activating the mortality scheme. At the end of the second stage of spin-up, the model reaches a new equilibrium state, with a lower biomass due to droughts that occur periodically during 1901-1920, with less than 1% variation by the end of second spin-up. This equilibrium state serves as the starting point for three transient simulations during the historical period, as described in Table 4.1. To test the impact of the different drivers of CO_2 and climate we designed a series of factorial experiment S1, S2, S3. In the S1 scenario, the model is forced by recycling the climate forcing data between 1901 and 1920 and the CO_2 concentration increases steadily following the reality. In the S2 scenario, both climate forcing and CO_2 concentration vary. In the S3 scenario, the CO_2 concentration input to model is set constant as 296 ppm but climate forcing data varies.

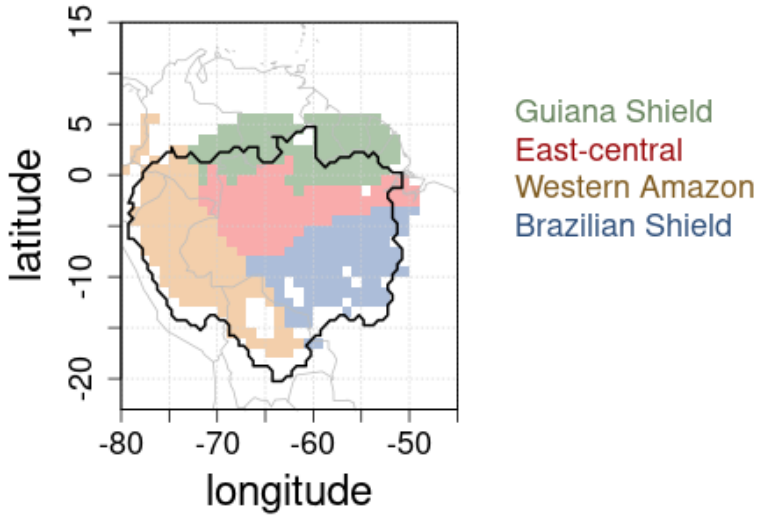

Figure 4.1 Overview of the Amazon basin, which is split into four regions, Guiana Shield, East-Central Amazon, Western Amazon, and Brazilian Shield, shown by different colors, defined after Feldpausch *et al.* (2011). The black line is the border of Amazon basin from Papastefanou *et al* (2020). Only pixels with tree cover more than 80% are shown.

Table 4.1 Description of simulations performed in this study.

	Climate forcing	Atmospheric CO_2	Mortality module	Restart point
spin-up stage 1	1901-1920	Constant (296ppm)	Deactivate	/
spin-up stage 2	1901-1920	Constant (296ppm)	Activate	Stage1
S1	1901-1920	Increasing	Activate	Stage2
S2	1901-2019	Increasing	Activate	Stage2
S3	1901-2019	Constant (296ppm)	Activate	Stage2

4.4.3 Drought characteristics

In this section, we characterized drought events by severity and timing (wet or dry season). In addition, a rainfall seasonality index is used for different regions of the Amazon. The severity and timing indices used are in the results section to compare different events. They are described below.

Drought severity (cumulative water deficit). Following previous research on the evaluation of drought area and extent (Papastefanou *et al.*, 2020), the maximum cumulated water deficit (MCWD) is given by Equations (1) and (2). A fixed value for evapotranspiration (ET) of ~100 mm per month is used. When monthly rainfall is below 100 mm, the forest is under water deficit. The water deficit accumulates over the hydrological year from October in the previous year to September in the next year. MCWD is the most negative value of the cumulative water deficit among all the months. The MCWD anomaly is then derived after subtracting the mean MCWD over a baseline period. For the 2005 drought, the baseline period is set to 2000-2004 to be comparable with plot data from Phillips *et al* (2009). For the 2010 drought, the baseline period is from 2000 to 2010 excluding the years 2005 and 2010. For the 2015/16 El Niño drought, the baseline period is extended to 2016 excluding the three years with drought. When we compare the drought severity and extent of the 8 most severe drought events since 1901, the baseline period is set to 1901-2019 excluding these 8 years with extreme droughts: 1916, 1926, 1963, 1983, 1998, 2005, 2010, 2016.

$CWD_m = CWD_{m-1} + P_m - 100$ if $P_m < 100$, else $CWD_m = 0$

with m being the month 1, …12 (1 = October) (1)

$MCWD = \min(CWD_m)$, m=1, …, 12 (2)

We derived Z-scores of MCWD time series at annual scale following Equation (3) as in Feldpausch *et al* (2016), according to:

$$Z = \frac{MCWD_k - \mu_{MCWD}}{\sigma_{MCWD}}$$ k=1916, 1926, 1963, 1983, 2005, 2010, 2016 (3)

$$Z = \frac{CWD_{k,m} - \mu_{CWD_m}}{\sigma_{CWD_m}}$$ (4)

Where μ and σ are the mean value and standard deviation of MCWD and CWD at month *m* during the baseline period. Drought severity is based on thresholds of Z score distributions, with values of -1.645, -1.96 and -2.576 corresponding to 90%, 95%, and 99% confidence intervals. We defined four classes of severity for droughts, with *small drought* for Z-scores in the range [-1.64, 0], *moderate drought* for [-1.96, -1.64], *severe drought* for [-2.576, -1.96] and *extreme drought* for values below -2.576.

Drought timing in the wet or dry season. To characterize the timing of a drought, being in the wet- or dry-season, we constructed a new index called *DTI*. First, we calculated the monthly rainfall climatology in each pixel during the baseline period excluding drought years, then ranked monthly rainfall from driest to wetter. Then we calculated monthly rainfall anomalies for the drought year by subtracting from each month the monthly rainfall climatology and dividing it by the standard deviation over the baseline period excluding drought years, from which we can rank monthly rainfall anomalies. By locating the month with the most negative precipitation anomaly and its corresponding rainfall climatology interval, we can distinguish between wet-season and dry-season drought. For example, if the most negative rainfall anomaly appears in the driest month, the DTI takes a value of -1 and if it appears in the wettest month, the DTI will equal 1.

Rainfall seasonality. The seasonality index used to compare different regions is defined as the deviation of monthly rainfall distribution from a uniform monthly distribution (Feng *et al.,* 2013). First, a long-term mean monthly rainfall climatology $\acute{R}$was calculated as:

$$\acute{R} = \sum_{m=1}^{12} r_{m}^{'} \qquad \text{with } r_{m}^{'} = \frac{\sum_{m=1}^{12} r_{k,m}}{k} \tag{5}$$

Where m and k represent each month and year. Then, the probability distribution of monthly rainfall was calculated by:

$$p_{m}^{'} = \frac{r_{m}^{'}}{\acute{R}} \tag{6}$$

Equation (7) was then used to calculate the relative entropy $\acute{D}$ which reflects the extent of monthly rainfall concentration, in other words, the deviation from a uniform distribution over 12 months.

$$\acute{D} = \sum_{m=1}^{12} p_{m}^{'} \, log\left(\frac{p_{m}^{'}}{q_m}\right) \tag{7}$$

Here, q_m represents the uniform distribution, of which the value is 1/12 for each month. Finally, the seasonality index is the product of the relative entropy $\acute{D}$ by the mean annual rainfall $\acute{R}$ divided by the maximum mean annual rainfall $R_{max}^{'}$ in the study area:

$$\acute{S} = \acute{D} \frac{\acute{R}}{R_{max}^{'}} \tag{8}$$

The range of $\acute{S}$ values goes from 0.003 to 0.122 in our study region. Smaller $\acute{S}$ indicates less seasonal rainfall distribution, or less contrast between wet and dry season.

4.4.4 How aboveground biomass dynamics was analyzed

From model outputs, net AGB change (△AGB), AGB gain and loss are calculated over the hydrological year from October in previous year to September in the next year. AGB gain is the carbon allocated to growth in aboveground sapwood in cohorts with DBH higher than 10 cm, each year. AGB loss is the biomass mortality of aboveground sapwood and heartwood in cohorts with DBH higher than 10 cm, each year. △AGB is the difference between AGB gain and AGB loss. The anomaly during a drought year k is derived by subtracting the average value (μ) over a multi-year baseline period (see 2.3) by Equations 9 to 11.

$$\Delta AGB_{anomaly} = \Delta AGB_{k} - \mu_{\Delta AGB} \tag{9}$$

$$AGBgain_{anomaly} = AGBgain_{k} - \mu_{AGBgain} \tag{10}$$

$$AGBloss_{anomaly} = AGBloss_{k} - \mu_{AGBloss} \tag{11}$$

Biomass mortality from self-thinning, turnover and droughts are included. In our study, the mortality rate equals the number of dead trees per year divided by the number of trees alive in the beginning of one year.

4.4.5 Model evaluation statistics

We use the R programming environment and statistical packages (version 3.5.0; R Core Team, 2019) for all data processing and analysis. Package 'ncdf4 v1.17' (Pierce, 2019) is used to handle files in NetCDF format from model outputs. Package 'fields v10.3' (Nychka et al, 2020) is used in AGB change and drought indices plotting. We use the least-square linear regression to explore the sensitivity of simulated AGB dynamics to MCWD anomaly. The one-way ANOVA was used to determine the significant differences between four regions and Tukey HSD post-hoc test was used to distinguish which region differed from one another in significance level of $P < 0.05$. We also use package 'simpleboot' (Peng, 2019) to obtain an appropriately conservative estimate on 95% confidence interval for the regression slope.

4.5 RESULTS

4.5.1 Long-term trend of the biomass carbon sink, model vs. inventories

In our simulation S2, we found a mean positive value of ΔAGB equal to 0.21 MgC ha^{-1} yr^{-1} over 1980 - 2019, indicating that the Amazon intact forests accumulate carbon over time. Nevertheless, ΔAGB has a negative trend of 0.006 MgC ha^{-1} yr^{-2} (Figure 4.2). This slowing down of the biomass carbon sink occurs because carbon losses from mortality increase faster than gains from growth and recruitment. The simulated decreasing net carbon sink is similar to inventory data analyzed by Hubau *et al* (2020) and Brienen *et al* (2015). Yet the magnitudes of the simulated growth trend and loss trend are both smaller than in the observations. We simulated an increasing rate of carbon gains of 0.008 MgC ha^{-1} yr^{-2} and of 0.014 MgC ha^{-1} yr^{-2} for carbon losses across the entire basin. In comparison, Hubau *et al* (2020) data from 321 plots gave an increasing gain trend of 0.014 MgC ha^{-1} yr^{-2} and a loss trend of 0.023 MgC ha^{-1} yr^{-2}. This difference can be attributed to limited coverage of inventory sample plots and model limitations, such as non-modeled biotic disturbances. Yet, it is encouraging to see that the essential signal of a decelerating sink from increased mortality is captured by our simulations.

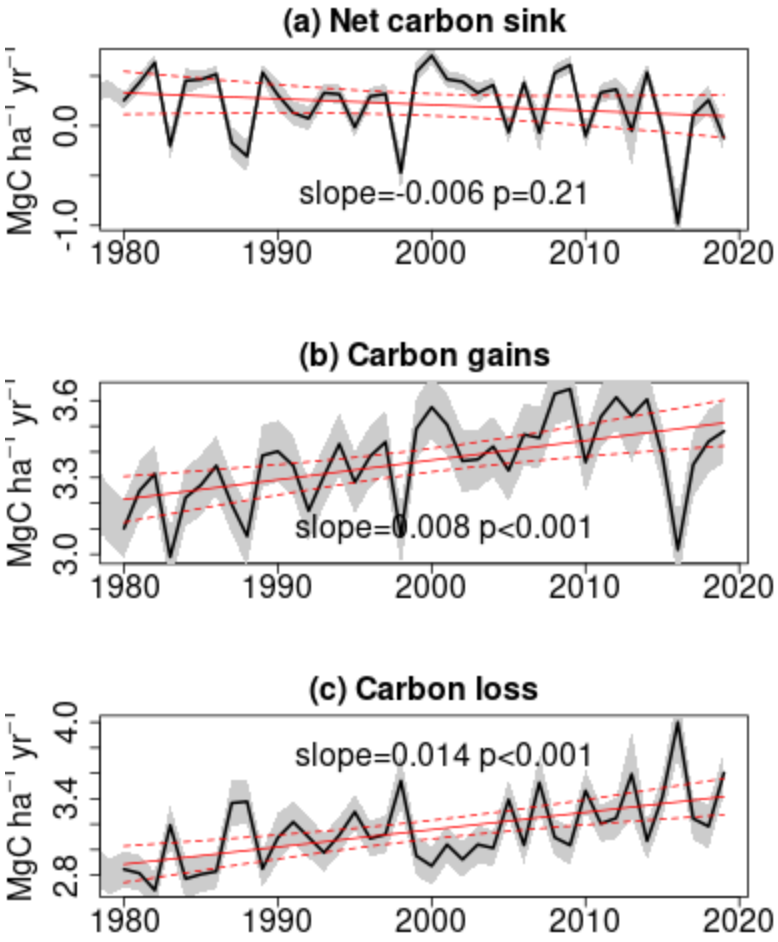

Figure 4.2 Long-term carbon dynamics of rainforest over Amazon basin. a-c, Trends in net aboveground biomass carbon sink (a), carbon gains from tree growth (b), and carbon losses from tree mortality including both self-thinning and drought-induced tree mortality (c). The continuous lines indicate the modelled forest carbon dynamics in Amazonia and the shading area corresponds to the 95% confidence interval. Slopes and P values are from linear regression models.

4.5.2 Biomass growth and mortality for the recent droughts, and sensitivities to water deficits

Mean biomass gain and loss since the year 2000. During the 2000s, excluding the 2005 and 2010 droughts, i.e. focusing on non-drought periods, forests gained AGB, at a rate of +0.42 MgC ha^{-1} yr^{-1} (95% confidence interval 0.37-0.48 MgC ha^{-1} yr^{-1}), i.e. they acted as a carbon sink for the atmosphere. The total carbon sink was 0.21 PgC yr^{-1} over the intact forest area of 500 Mha. There were significant differences among the four regions according to the Tukey HSD post-hoc test (Figure S1) with a higher net AGB sink in the Western Amazon (+0.63 MgC ha^{-1} yr^{-1}), followed by the Guiana Shield (+0.41 MgC ha^{-1} yr^{-1}). The gross gain in AGB, due to growth alone, was 3.5 MgC ha^{-1} yr^{-1}, with the highest gross gain in the Guiana Shield (+4.2 MgC ha^{-1} yr^{-1}). The gross loss in AGB was also highest in the Guiana Shield, and lowest in the Western Amazon. A 'high-gain, high-loss' pattern, thus a larger turnover, was modelled in the Guiana Shield region.

The 2005 drought. This event has a severity epicenter located in the Western Amazon, as seen from Z-transformed MCWD (Figure 4.3). In this epicenter region, we simulated a larger net AGB loss (-0.6 MgC ha^{-1} yr^{-1}) than in the rest of the Amazon. The net loss was driven by a decline in growth and an increase in mortality (Figure 4.3), consistent with forest plots evidence shown by Phillips *et al* (2009). The most severe water deficit matched the largest loss of AGB in our simulations. In the Western Amazon we found a 2.0 MgC ha^{-1} (95% CI: 1.5-2.5) net loss of AGB relative to non-drought

condition. This net loss is composed by a decreased growth gain of 0.2 MgC ha^{-1} (95% CI: 0.1-0.3) and an increased mortality loss of 1.8 MgC ha^{-1} (95% CI: 1.2-2.3). These sensitivities are comparable with plot data analysis by Phillips *et al*. (their Figure 4.2).

The 2010 drought. This event was most severe in the north of the Brazilian Shield. According to our climate forcing data, the drought severity was lower and the affected area smaller than for the 2005 drought, as shown by the magnitude of MCWD anomaly, which spans over -100 to 150 mm (Figure 4.3). Our drought severity and impacted area in 2010 are a bit different than in Lewis *et al* (2011), due to different rainfall forcing data (TRMM satellite rainfall data in Lewis *et al*., 2011 vs. CRUJRA in our study). The drought sensitivity of the AGB net change to MCWD was lower in 2010 than in 2005 (0.73 vs 1.61 MgC ha^{-1} per 100 mm MCWD). Yet, like for the 2005 event, the effect of the drought on net AGB change was dominated by high AGB loss, given the relatively modest reduction of AGB gain. The AGB loss sensitivity of 0.6 MgC ha^{-1} per 100 mm MCWD, was larger than the AGB gain sensitivity of -0.13 MgC ha^{-1} per 100 mm MCWD.

The 2015/16 El Niño drought. This event is centered in the northeastern Amazonia. The simulated response of AGB is shown in Figures 4.3g-4.3i. The magnitude of the MCWD anomaly shows that this drought was more severe than the two previous events. Therefore, we found a higher △AGB sensitivity (Figures 4.3g-4.3i, S2) of -2.43 MgC ha^{-1} per 100 mm MCWD. Further, the AGB gain sensitivity was of -0.52 MgC ha^{-1} per 100 mm MCWD, of same sign but smaller magnitude than the sensitivity of AGB loss of 1.91 MgC ha^{-1} per 100 mm MCWD. In addition, for a 100 mm increase in MCWD, we simulated in 2015/16 an increase of 11 days diagnosed as mortality risk, and a 1.11% increase in the annual mortality rate in the year 2016 compared to the baseline period (Figure S3). In the Brazilian Shield epicenter, we simulated a greater AGB loss and a higher stem mortality rate even in pixels where MCWD anomaly remained below 100 mm. This response likely reflects other stress factors causing an increase of transpiration, followed by loss of conductance and mortality in our model, especially high temperature and elevated vapor pressure deficits (VPD).

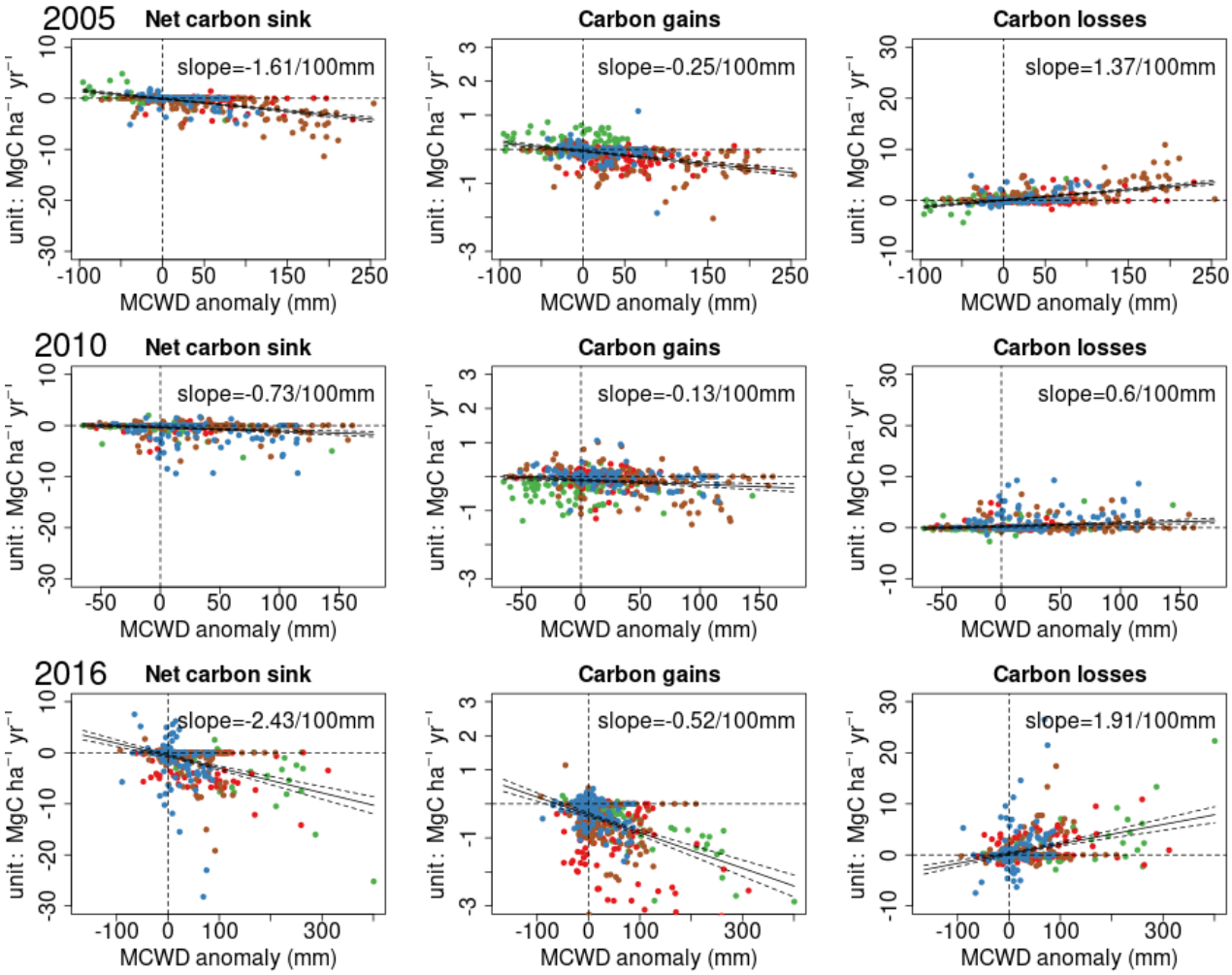

Figure 4.3 AGB versus drought severity in 2005, 2010 and 2016. Severity is defined from MCWD, with higher positive values denoting more acute water stress. The color of the points corresponds to four regions, red: Guiana Shield, green: East-Central Amazon, brown: Western Amazon, and blue: Brazilian Shield. The first column gives the net AGB sink anomaly with MCWD. The second one the AGB growth gain anomaly. The third one the AGB loss (mortality) anomaly.

4.5.3 Drought severity and biomass loss for the most severe drought events of the past century

After having shown that the simulated sensitivities of growth and mortality to MCWD compared well with forest plots data (at least for the 2005 event), we now turn to the analysis of AGB deficits during the most severe droughts of the last century (1916, 1926, 1963, 1983, 1998, 2005, 2010, 2016). Figure 4.4 shows the spatial distribution of the drought intensity, i.e. the Z-score of MCWD anomalies (Section 4.4.3). The epicenter of different droughts varied across events. The northwest Amazon 'ever-wet' region was rarely affected. The northern Brazilian Shield, also an 'ever-wet' region where the dry season even sees a periodical increase of GPP (Green *et al.,* 2020), was particularly affected by the 2015/16 El Niño drought. The southwest regions were hit by the 1983 and 2005 droughts. The East and northeast regions were affected by the 1916, 1983 and 2015/16 droughts. The Southern Amazon was affected by the 1963 and 2010 droughts.

The largest droughts of the Century compared for their area exposed to different drought intensities and area of AGB loss. Figure 4.5 shows the number of 1° pixels for different severity classes (Z-scored CWD). The 2015/16 drought is clearly ranked as the most severe event on record, followed by 1983 and 2005. Both the area under drought (negative Z score), representing 63% of the

evergreen forest area, and the area under *extreme* drought severity, show the largest values during the 2015/16 event. Mirroring mainly the spatial patterns of water deficit, the net AGB dynamics from our simulation is shown in Figure 4.6. Outside the epicenter of each drought, △AGB was small and positive (Figure 4.6) indicating a continuous long-term carbon sink (Figure 4.2). In the drought affected pixels, we found that the AGB net losses always rank with the severity of drought. For instance, △AGB in 2010 was less negative than that during the more extreme events of 2005 and 2016 (Figure 4.6). Among the top 8 drought events, we also found differences in the fraction of area with negative △AGB at a given level (Figure 4.7, S4). The area showing negative △AGB values was the largest in the 2015/16 El Niño, followed by the 1983 one. The area with most negative △AGB (e.g. a loss more than 6 MgC ha^{-1} yr^{-1}) was also the most extensive in 2016, followed by 1983 (Figure 4.6).

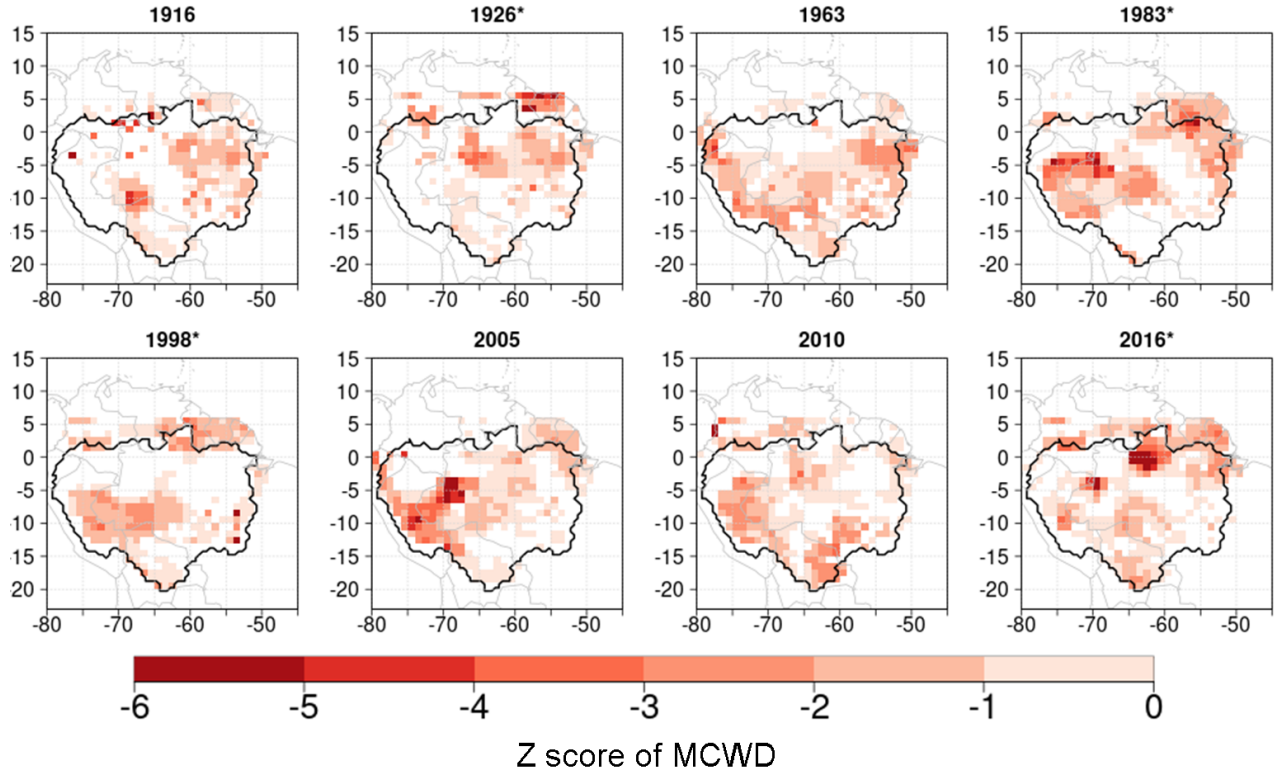

Figure 4.4 Spatial distribution of drought intensity for the top most severe droughts since 1901, which is assessed by Z score values of MCWD anomalies relative to their decadal baseline.

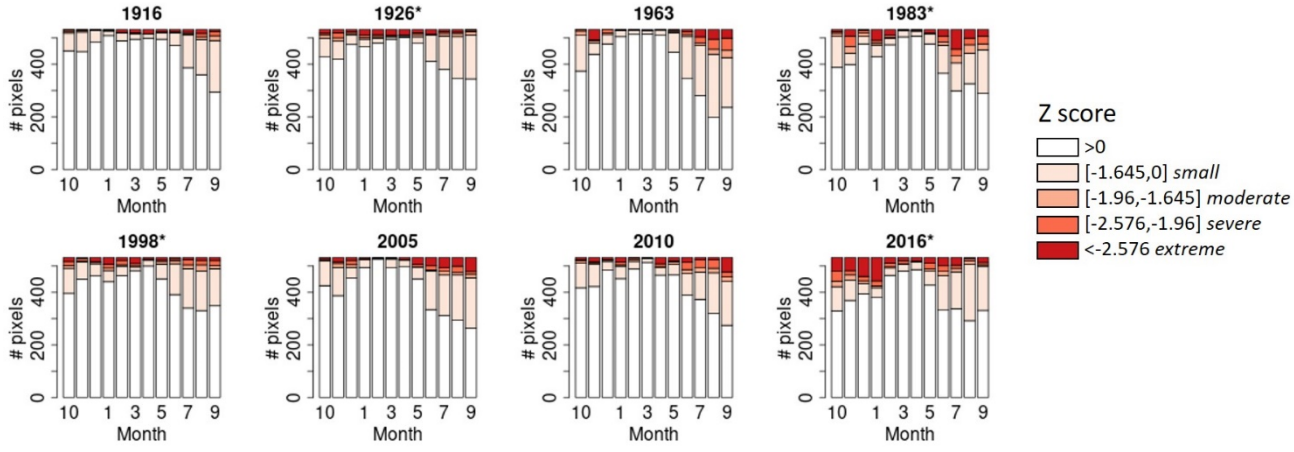

Figure 4.5 Frequency distribution of different drought intensity classes (Z score of monthly CWD corresponding to increasing severity – see text). The thresholds of -1.645, -1.96 and -2.576 correspond to 90%, 95%, and 99% confidence intervals of the distributions, respectively. The asterisks in the title of a panel indicate an El Niño drought. # pixels means the number of pixels underwent CWD in each interval.

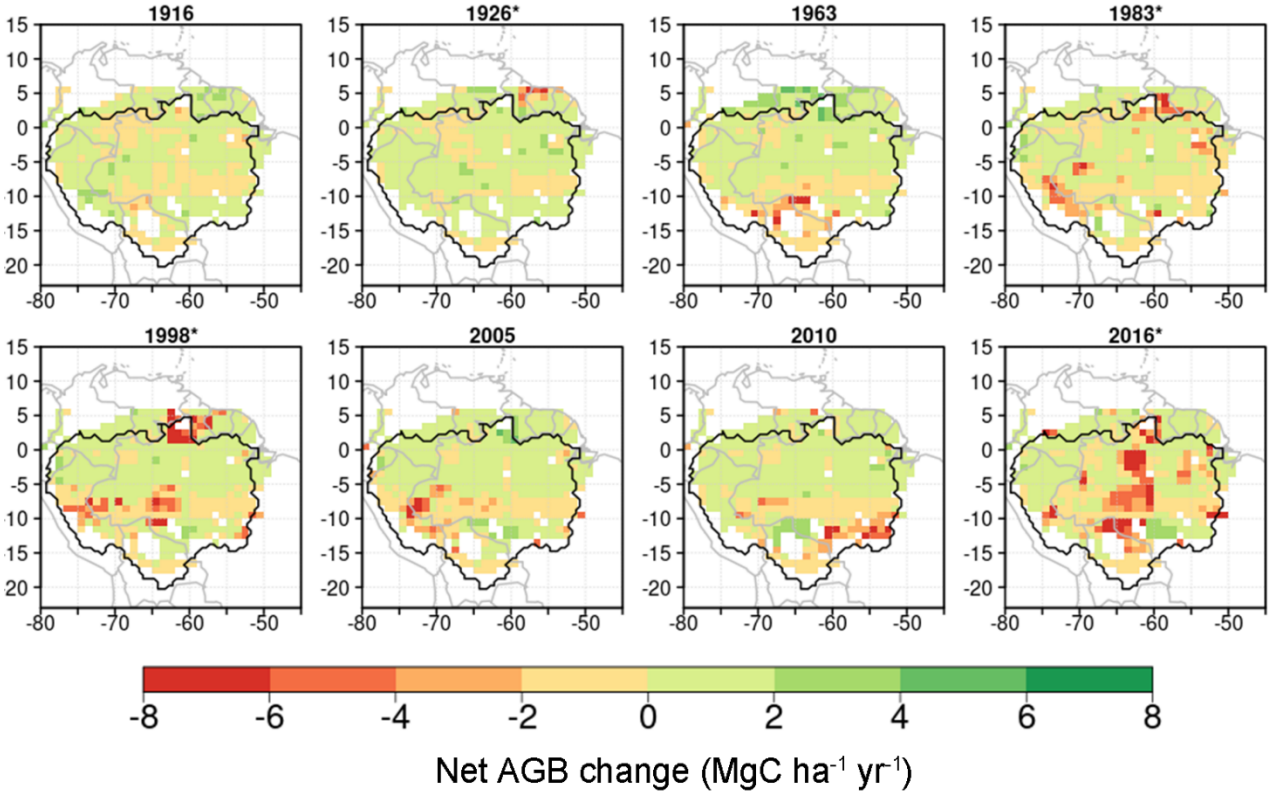

Figure 4.6 Spatial distribution of the simulated net AGB change during the eight largest drought events since 1901. The asterisks in the title of a panel indicates an El Niño drought. Negative value denotes carbon sources and positive value means carbon sink.

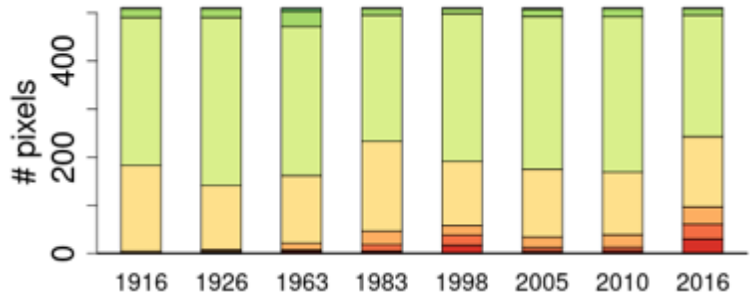

Figure 4.7 Regional extent of net AGB change during 8 drought events. The color corresponds to the different levels of net AGB changes in Figure 4.6. # pixels means the number of pixels underwent net biomass carbon change in each interval.

Wet season drought caused larger AGB loss than dry season drought. We investigated the differences in AGB responses between wet-season and dry-season droughts, distinguished by their

DTI index (see Section 4.4.3). From Figure 4.8 we can see that the east-central region which has a low rainfall seasonality, shows DTI > -0.2 in 1983 and 2016. In other words, these two drought events appeared in the wetter quarter of the year, and can be deemed as wet-season droughts. DTI values close to -1 in the southwest Amazon in 2005, implies that the most negative rainfall anomaly appeared in the dry season. This event was a clear dry-season drought. The epicenters of the 2010 drought are more diffuse and show DTI values between -0.2 and 0.2, which makes this event a composite of dry and wet season drought. As the intensity of wet-season and dry-season droughts differs, so does the corresponding AGB dynamics. Figure 4.5 shows that drought intensity was more severe in the wet-season droughts of 2016 and 1983, and that the drought exposed area was also higher during these two events. Figure 4.7 shows that the AGB loss differs between wet season and dry season droughts. Further, the area undergoing large AGB loss is larger for wet-season droughts like 2016 than for dry-season droughts like 2005 (Figure 4.7). Moreover, if we compute the mean △AGB corresponding to different Z score levels, we found that the mean △AGB is always the most negative during El Niño wet-season droughts, no matter which Z score level is considered. For example, the mean △AGB loss was of -2.96 Mg C ha^{-1} yr^{-1} in *moderate* drought areas during the 1998 El Niño, -2.35 Mg C ha^{-1} yr^{-1} in *severe* drought areas during 1998, and reached -3.9 Mg C ha^{-1} yr^{-1} in the El Niño *extreme* drought of 2016 (Table S1).

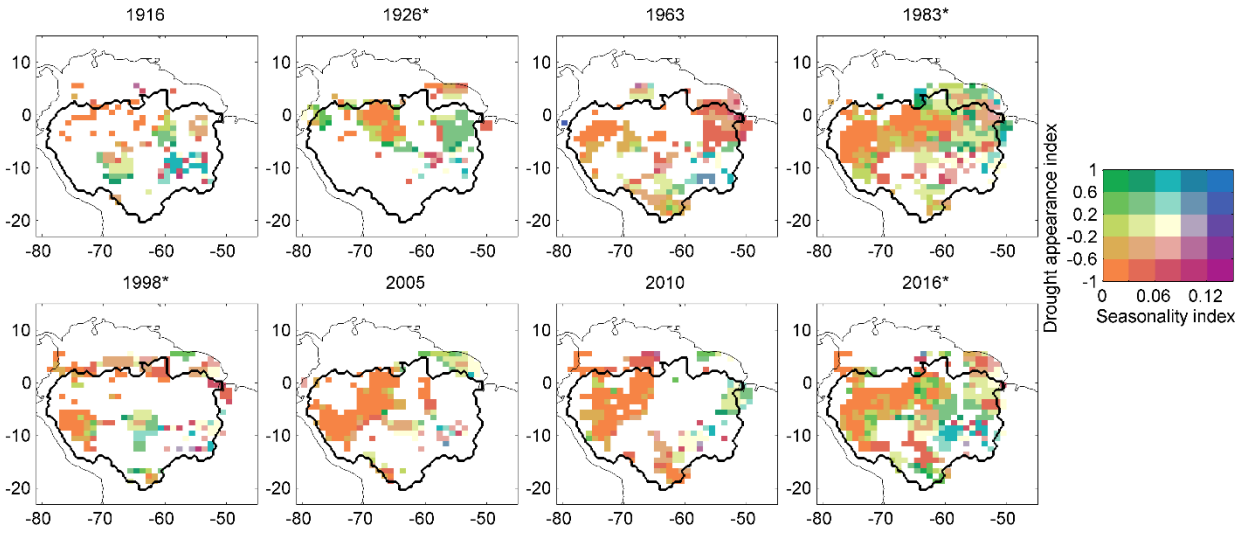

Figure 4.8 Bivariate plots showing the spatial pattern of the rainfall seasonality index and drought timing index (DTI) in the Amazon for the eight largest droughts since 1901. Negative values of DTI mean that drought with the most negative Z score of rainfall anomaly happens in the drier months of the year. Only pixels with a drought Z-score of MCWD below -1.645 is shown, that is at least a *moderate* drought. The asterisks in the title of panel indicates El Niño drought.

The last twenty years has the largest AGB loss caused by droughts. We compared drought effects on AGB on decadal-scale. To do so, we calculated the cumulative AGB loss in successive 20-years intervals since 1901 (Figure 4.9). Looking at the three drought events in the last 20-years, it is clear from our simulations results that the cumulative AGB loss over this period is higher than during any other previous 20-year interval since 1901 (Figure S5). The region which had the higher level of AGB loss (>4 Mg C ha^{-1} per year) during the last 20 years is the East-central Amazon, a region rarely affected by previous droughts.

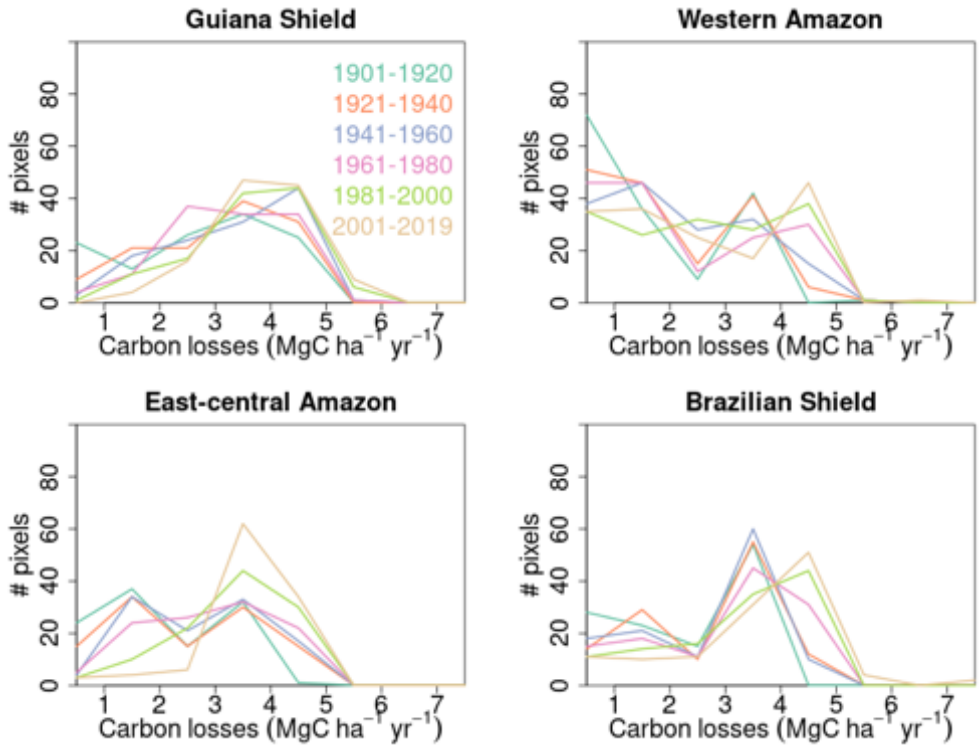

Figure 4.9 Comparison of cumulative AGB loss in 20-year intervals in different regions since 1901. # pixels means the number of pixels underwent carbon loss in each interval.

4.5.4 Interactions between drought and elevated CO2

Elevated CO_2 induces stomatal closure and should partly alleviate the negative effect of drought on AGB. To assess the extent to which the drought effects can be alleviated, we separated the effects of climate change alone vs. increased CO_2 concentration during the last Century through factorial simulations (S1, S2 and S3 see section 4.4.2). The results are shown in Figure 4.10. The simulation S2 was driven by observed historical climate (including the 8 drought events studied above) and atmospheric CO_2 increase, while S1 was driven by recycled 1901-1920 climate (no climate change), and S3 used historical climate but maintained the CO_2 concentration constant at 296 ppm (no CO_2 increase). The comparison between S1 and S2 shows that historical climate since 1901, i.e. mainly droughts, has suppressed plant growth and increased mortality losses. Carbon gains are thus lower in S2 than in S1.

The comparison between S2 and S3 allows us to analyze the effect of rising CO_2 concentration. The AGB gain was significantly higher under S2 than S3 ($P<0.05$), because of the increase of NPP from elevated atmospheric CO_2. AGB density was higher in S2 than S3, reflecting a higher carbon accumulation due to rising CO_2 (Figure S6). Yet, there was also significant difference on AGB loss between S2 and S3 ($P<0.05$). When we look at the mortality risk with and without rising CO_2, in the epicenter of the eight drought events (Z score of MCWD below -1.645), the number of days with mortality risk is significantly higher in S3 than that in S2, with a difference that can reach up to 10 days (Figure S7). This result implies that elevated CO_2 induced a partial alleviation of moisture stress from stomatal closure, offsetting a possible increase of transpiration due to higher foliage area with rising CO_2. During droughts, the modeled evapotranspiration rate confirms a smaller soil moisture stress in S2 (Figure S8) compared to S3 where CO_2 is fixed. Since the model here did not include the downregulation of nutrient limitation, the CO_2 fertilization effects could be overestimated.

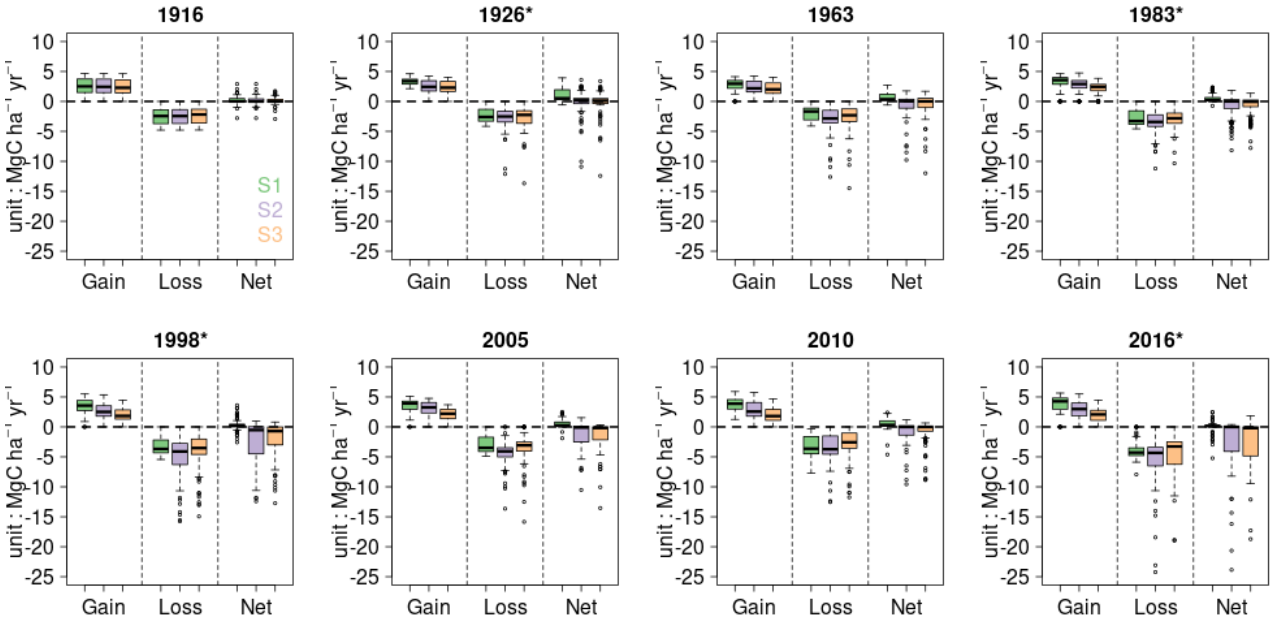

Figure 4.10 AGB gain from growth, loss from mortality and net AGB change in the epicenters of each major drought from the three scenarios. S1: varying CO_2 and recycling climate over 1901-1920, S2: varying CO_2 and historical climate change, S3: historical climate change and constant CO_2 concentration. The epicenter of a drought is defined by pixels with Z scored MCWD below -1.645, corresponding to 90% confidence interval following normal distribution.

4.6 DISCUSSION

4.6.1 Mortality in the model and its sensitivity to water deficits

Mean patterns of mortality and turnover. The frequency of drought events in Amazon is predicted to increase in the future. Therefore, a clearer understanding on the response of this rainforest biome to drought is indispensable for future predictions. We found that our model, despite many generic parameters and no description of the diversity of plant traits, is capable to produce realistic average cross-basin mortality rates, and higher mortality rates and biomass losses in the epicenter of each drought. With our hydraulic failure – mortality module adding up to background tree mortality (self-thinning), the simulations (Figure S9) of the mean spatial pattern of mortality is comparable to inventory data from Esquivel-Muelbert *et al.* (2020) and Johnson *et al.* (2016). Namely, there is a prevalence of higher average mortality in the Brazilian Shield. Nevertheless, the average pattern of 'high-gain, high-loss' observed in the Amazon is not captured by our model. Plot observations suggest a larger turnover (larger gain and loss fluxes) in the Western Amazon, possibly due to different species composition reflecting adaptation to more fertile soils near the Andes (Yang *et al*., 2014). Our model simulates in contrast a pattern of 'high-gain, high-loss' in the Guiana Shield region. This can be related to the fact that our model lacks representations of nutrient dynamics and species trait regional differences, and includes only drought mortality and not the other disturbances modulating forest turnover like windthrow in the Western Amazon (Negrón-Juárez *et al*., 2018).

Drought impacts on demography. The hydraulic architecture and mortality scheme on top of the demography structure through cohorts also permit us to see the tree mortality rate – tree size relationship. Besides the smallest tree size cohort, the annual mortality rate increases with tree size especially regarding the area underwent moderate drought risk (MCWD < -1.645) as shown in Figure S10 no matter in which region, since greater gravitational energy is required to pull water upward along longer transport pathways in bigger trees. The dynamic monitoring in forest plots showed the older or larger trees were disproportionally threatened by El Niño drought (Meakem *et al*., 2018). However, field measurement evidences have not reached consensus as they revealed both vulnerability of bigger trees (Bennett *et al*., 2015), or even counter examples of no such mortality-size relationship (Powers *et al*., 2020), where the size dependence could be superseded by the hydraulic safety traits that can be more prevalent at coarser scales, as well as the agreement regarding whether within-species covariation between tree size and water availability holds at species or landscape level has not been obtained (Trugman *et al*., 2021).

Sensitivity of biomass to droughts compared to observations. The drought sensitivity simulated by our model results from an emerging positive relationship between mortality and water deficit. This result is consistent with forest plot observations. The simulated drought sensitivity is comparable with the one observed in inventory data for the 2005 drought (Phillips *et al*., 2009). Inventory measurements did not sample the epicenter of the 2010 drought. Unlike for the 2005 event, however, selected plots were measured shortly after 2010, thus reducing possible confounding effects of post-drought climate conditions. These scarce data indicate that forest sites that were experiencing a severe drought gained less biomass in 2010 but showed no evidence for a significant mortality co-variation with drought severity (Feldpausch *et al*., 2016). During the 2010 drought, data from other sites with regular measurements of ecosystem-level fluxes (Doughty *et al*., 2015) showed that the AGB gain (foliage and woody NPP) remained unchanged at wet lowland sites, although autotrophic respiration (Ra) decreased. In the 1° grid cells containing the sites of Doughty *et al*., we modeled a decreasing GPP, NPP and Ra with increasing MCWD (Figure S11), which is inconsistent with Doughty *et al* (2015). Our model may over-estimate the negative response of GPP and NPP to drought at these sites, possibly because some of the sites include forests that had access to ground water, a process ignored in the model and also perhaps low resolution description of soil properties. When we combined the three most recent drought events together and divided MCWD anomalies into distinct

severity classes, we found that the negative response of AGB from mortality increases above a threshold of 50 mm MCWD anomaly (Figure S12). Besides, some pixels with a positive MCWD anomaly show only a small △AGB. For such 'insensitive pixels' both plant hydraulic architecture and soil hydraulic properties affect plant water availability, and biomass dynamics. Our model was calibrated against the Caxiuanã experiment with an exclusion of rainfall alone and no coincident manipulation on temperature, and it could underestimate the sensitivity of AGB to compound events with low rain, high temperature and high VPD.

Importance of soil texture for modeling mortality during drought. In the model, a rainfall deficit alone does not always bring severe water stress and mortality. This model behavior is dependent on soil texture parameters. Soils with a higher clay content are closer to their wilting point when rainfall decreases, but have a greater soil water-holding capacity (difference between field capacity and wilting point) (McCulloh *et al.*, 2019). Levine *et al* (2016) found that water stress in soils with higher clay content is likely to influence more negatively plant biomass dynamics. Our simulations used the HWSD soil texture map (Wieder *et al*., 2014) which has loam distributed in the Western Amazon, and silt loam and sandy clay loam soils in the central Amazon. Although this soil texture map produces a reasonable mean mortality rate, there are 'insensitive' pixels where PLC remains below the threshold of 50% (inducing mortality) even under a severe water deficit. Using a more clay rich soil texture could produce a more sensitive response of AGB to water availability, and give results more comparable with inventory observation. For example, when we tested a *sandy clay* texture at one pixel instead of *loam* in the East-Central Amazon, the climate-induced mortality increased a lot in 2005, and AGB was more sensitive to MCWD. The spatial variability of soil properties is high, including at small scale (Marthews *et al*., 2014). Therefore, the mismatch between site-specific soil texture and a 1° model pixel should be considered to understand the model-observation misfit.

Importance of threshold parameters that trigger mortality from hydraulic failure. With regard to the sensitivity of mortality to tree conductance loss (PLC) in each cohort, the drought exposure threshold and the mortality rate applied to kill trees exceeding the exposure are coupled in our model. Adjusting the exposure threshold of PLC causing drought-induced 'cavitation' mortality in the model is difficult, since there is almost no measurement for tropical trees that monitored impairment and mortality risk above a critical PLC threshold. Critical PLC thresholds strongly depend upon species, related to traits like height or wood density. For example, Brodribb *et al* (2020) found that a vulnerable tall tree died in one week after reaching cavitation. We thus need field-based measurement of hydraulic damage in the tropics to better constrain the drought exposure threshold parameterization of the model.

4.6.2 Perspective of future improvements to reduce uncertainty of the biomass drought sensitivity

Variable hydraulic traits. The drought sensitivity of AGB in the real world relates to the diversity of hydraulic traits. Those traits confer regional variations in drought tolerance, and associate with habitat preferences (Kunert *et al.*, 2021), although some traits could be spatially coherent (Powell *et al.*, 2017). Our study used one set of hydraulic parameters for traits, calibrated from the Caxiuanã drought experiment. In reality, there is a broader diversity reflecting plant water use strategies, even at small spatial scale. Highly variable water potentials at which 50% of conductivity is lost (P50) in stem xylem were observed by Oliveira *et al.* (2019). Choat *et al.* (2012) also showed more negative P50 in central Amazonian species. Species traits differences in water deficit *affiliation*, that is how traits leading to hydraulic failure have adapted to local long term frequency and severity of drought, also relates to mortality risk, although a high affiliation to drought does not warrant resistance to the more severe new types of drought emerging in the recent years (Esquivel-Muelbert *et al.*, 2017). Apart from climate affiliation, hydraulic traits also vary with tree size (Bittencourt *et al.*, 2020), soil fertility and topography (Oliveira *et al.*, 2019). Below, a few critical traits that could be given spatial

variability in our model are analyzed.

Tree water potentials safety margin. Hydraulic safety margins calculated as the difference between P50 and the minimum water potential during a drought correlates with mortality risk among species (Powers *et al.*, 2020). Larger hydraulic safety margins protect trees from hydraulic damage (Ziegler *et al.*, 2019). Besides, interspecific heterogeneity in hydraulic performance for xylem safety and efficiency trade-off should induce a possible dominance of drought-tolerant species in the case of more frequent and severe droughts (Zuleta *et al.*, 2017). Species-related hydraulic segmentation between leaf and stem also determines organ-level water regulations and drought resistance (Levionnois *et al.*, 2020). The resistance of trees for small or short-term droughts may be reduced during severe droughts (Guan *et al.*, 2015). To capture these effects, the use of traits maps across the Amazon would improve our simulations. In other words, there is a critical need for incorporating functional diversity in traits that determines vulnerability and water regulation strategies (Anderegg *et al.*, 2019). Liu *et al* (2021) constrained indirectly the distribution of plant hydraulic traits with satellite observations of VOD, evapotranspiration and soil moisture. Although uncertainty of satellite data limits the application of indirect trait variability retrieval, this approach could provide useful insights about hydraulic traits such as water potential safety margin and pre-dawn water potential by calibrating optimal parameters in the model to minimize the difference between satellite observations and simulations.

Wood density. Wood density, partly related to stem water potentials, relates to life history and drought resistance (De Guzman *et al.*, 2021). Species with low wood density are expected to be more vulnerable during droughts. On the contrary, species with high wood density are considered to be more resistant to hydraulic failure, as evidenced by negative effect of wood density on mortality in response to the 2010 drought through generalized linear mixed model (Zuleta *et al.*, 2017). Besides wood density, trade-off in wood volume allocation also relates to xylem efficiency-safety trade-off (Janssen *et al.*, 2020). Site-level evidence showed that easily measured traits like wood density can help to understand drought responses (Santiago *et al.*, 2018). In other words, through the measurement of wood density, and its relationship with plant inherent hydraulic traits, e.g., the negative linear relationship between sapwood turgor loss point and wood density found by De Guzman *et al*. (2021), the variability of hydraulic parameters could be incorporated in our model using new wood density maps.

Effective rooting depth. This important trait, related to the amount of water that can be absorbed from the soil was found to be correlated with the spatial heterogeneity of climate seasonality (dry season length) in the Amazon basin. Shallower rooting depth in 'ever-wet' central Amazon and deeper rooting depth in 'drought prone' southwest and northeast Amazon were showed by Yang *et al*. (2016). Inclusion of the spatial dynamics of this morphological property, combined with other hydraulic traits should be the future model ability to reproduce the large-scale tree mortality pattern and corresponding biomass changes.

Increased drought and elevated CO_2 may cause shifts in functional composition of tropical forests (Bartlett *et al.*, 2019). Observational records suggest that the increase in CO_2 drives a shift to large-statured species (Esquivel-Muelbert *et al.*, 2019). Although taller trees are deemed to be more susceptible to water stress due to their longer and more vulnerable water transport systems, Browne *et al* (2021) found that the mortality rate of drought-sensitive tree seedlings also increased during the 2015/16 El Niño. To compare model results with inventories that only sample trees larger than 10 cm, we only looked at growth in corresponding cohorts. With regard to the recruitment, we found that there would be more new individuals during drought than non-drought period (Figure S13), since the recruitment rate is parameterized in relation to LAI.

4.6.3 Reducing uncertainty on the effect of elevated CO2 to alleviate trees' response to drought

For predicting biomass dynamics in Amazon rainforests, interactions between drought and elevated CO_2 concentration is of key importance. Our model produced a higher AGB gain under elevated CO_2, but this positive effect was overall offset by the negative climate effects, as shown in Figure 4.10. The positive effects on growth from elevated CO_2 in our model is spatially uniform, while there is spatial heterogeneity in the AGB loss response to drought. During drought years, most pixels show a lower mortality risk in S2 with elevated CO_2, compared to S3 (Figure S7), consistent with simulations from (less advanced) terrestrial biosphere models showing that CO_2 fertilization decreased the probability of dieback in eastern Amazon (Zhang *et al.*, 2015). Reduced transpiration due to increased CO_2 (a difference between -0.4 – 0mm/d from S2 minus S3) was modeled in most pixels compared to the simulation S3 where CO_2 was fixed, for example during the 2015/16 event (Figure S8). Yet, the response of transpiration to increasing CO_2 is not spatially uniform and has uncertainties (Mengis *et al.*, 2015). The degree to which water stress can be mitigated by rising CO_2 needs further calibration, e.g. through field-studies of leaf hydraulics adjustment (Cernusak *et al.*, 2013; Zuidema *et al.*, 2020). New data such as the future Amazon Free-Air CO_2 enrichment experiment, should help resolve the optimal stomatal behavior from the trade-off between carbon uptake and water loss. We should also notice that the nutrient cycles are not well characterized in current model version, where the nutrient limitation like N and P deficit can modify the response of vegetation to increasing CO_2.

4.6.4 Legacy mortality and post drought biomass recovery

Legacy mortality. Besides hydraulic transport recovery, legacy effects of drought have an impact on living trees through partial damage. For example, elevated post-drought mortality was shown in the Colombian Amazon (Zuleta *et al.*, 2017) and also central Amazon (Aleixo *et al.*, 2019). Yang *et al* (2018) also found persistent loss of carbon over the next 3 years after 2005 mega drought using spaceborne lidar measurements. Currently, our model only considers cumulative drought exposure through PLC and no legacy mortality effects. Such carryover effects could be further incorporated. For example, we may calibrate the depletion of labile carbon pools and reserves (already included in the model) after a drought to investigate how nonstructural carbohydrates change during the drought and whether less available NSC would affect the following growth trajectory (Signori-Muller *et al.*, 2021). Furthermore, increased mortality during drought is also linked with the appearance of other disturbances, like fire and insect outbreaks (Brando et al., 2014), since droughts concur with peaks of fire activity. Thus, interaction with other disturbances, which can induce a 'death spiral' (Franklin *et al.*, 1987), also needs to be considered. For example, we could adapt the fire module (Yue *et al.*, 2014) of ORCHIDEE to reproduce Amazon fires, through which the effects of droughts and the accompanying higher fire risks can be tracked.

Post-drought resilience. In addition to distinct resistance strategies, possible recovery processes after embolism are also crucial in the simulation of hydraulic efficiency-safety trade-offs (Klein *et al.*, 2018). Recovery from hydraulic damage like embolism repair or vessel refilling can buffer drought mortality. After reaching the cavitation threshold, to what extent the embolism reversal can happen after the re-watering and how much xylem tension can relax are still under debate and require more evidences, like the experiments of the dry-down and re-watering on plant individuals that can permit the detection of the plant tolerance to water stress condition and their recovery abilities, to enable a generalized parameterization into process-based models.

4.7 CONCLUSION

We used a process-based model describing plant hydraulics and both background light competition and drought induced tree mortality, ORCHIDEE-CAN-NHA, to evaluate the drought

sensitivity at regional level and investigate aboveground biomass (AGB) changes in the eight most severe drought events since 1901 over the Amazon. The model can successfully quantify the drought sensitivity of AGB growth and mortality when compared with plot data collected for the 2005 and 2010 droughts. We predict the highest sensitivity of net AGB change in response to water stress during the extreme 2015/16 drought. Besides, comparison of extent and severity of the eight droughts and their AGB anomalies indicates the 2015/16 event was the most severe both for the drought intensity and the area where severe biomass loss occurred. Factorial simulations helped us to discern the contribution of climate change and increased CO_2 concentration: climate change negatively affected AGB gain and loss, whereas moisture stress was reduced to some extent by elevated CO_2. More field-evidences, like hydraulic traits mapping and a better accounting of soil texture heterogeneity, are priorities to fill the model-observation gap and produce more reliable spatial gradients of mortality risk. This study makes an important step forward in quantifying the large scale carbon impacts of tropical forest drought and enhances our ability to make future predictions.

4.8 REFERENCES

Aleixo, I., Norris, D., Hemerik, L., Barbosa, A., Prata, E., Costa, F., & Poorter, L. Amazonian rainforest tree mortality driven by climate and functional traits. Nature Climate Change, 9, 384-388, 2019.

Anderegg, W.R., Anderegg, L.D., Kerr, K.L. & Trugman, A.T. Widespread drought-induced tree mortality at dry range edges indicates that climate stress exceeds species' compensating mechanisms. *Global change biology*, **25**, 3793-3802, 2019.

Arend, M., Link, R.M., Patthey, R., Hoch, G., Schuldt, B. & Kahmen, A. Rapid hydraulic collapse as cause of drought-induced mortality in conifers. *Proceedings of the National Academy of Sciences*, **118**, 2021.

Bartholomew, D.C., Bittencourt, P.R., da Costa, A.C., Banin, L.F., de Britto Costa, P., Coughlin, S.I., Domingues, T.F., Ferreira, L.V., Giles, A. & Mencuccini, M. Small tropical forest trees have a greater capacity to adjust carbon metabolism to long-term drought than large canopy trees. *Plant, Cell & Environment*, **43**, 2380-2393, 2020.

Bartlett, M.K., Detto, M. & Pacala, S.W. Predicting shifts in the functional composition of tropical forests under increased drought and CO 2 from trade-offs among plant hydraulic traits. *Ecology letters*, **22**, 67-77, 2019.

Bennett, A. C., McDowell, N. G., Allen, C. D., & Anderson-Teixeira, K. J. Larger trees suffer most during drought in forests worldwide. Nature Plants, 1, 1-5, 2015.

Bittencourt, P.R., Oliveira, R.S., da Costa, A.C., Giles, A.L., Coughlin, I., Costa, P.B., Bartholomew, D.C., Ferreira, L.V., Vasconcelos, S.S. & Barros, F.V. Amazonia trees have limited capacity to acclimate plant hydraulic properties in response to long-term drought. *Global change biology*, **26**, 3569-3584, 2020.

Brando, P.M., Balch, J.K., Nepstad, D.C., Morton, D.C., Putz, F.E., Coe, M.T., Silvério, D., Macedo, M.N., Davidson, E.A. & Nóbrega, C.C. Abrupt increases in Amazonian tree mortality due to drought–fire interactions. Proceedings of the National Academy of Sciences, 111, 6347-6352, 2014.

Brienen, R.J., Phillips, O.L., Feldpausch, T.R., Gloor, E., Baker, T.R., Lloyd, J., Lopez-Gonzalez, G., Monteagudo-Mendoza, A., Malhi, Y. & Lewis, S.L. Long-term decline of the Amazon carbon

sink. *Nature*, **519**, 344-348, 2015.

Brodribb, T.J., Powers, J., Cochard, H. & Choat, B. Hanging by a thread? Forests and drought. *Science*, **368**, 261-266, 2020.

Browne, L., Markesteijn, L., Engelbrecht, B. M., Jones, F. A., Lewis, O. T., Manzané-Pinzón, E., ... & Comita, L. S. Increased mortality of tropical tree seedlings during the extreme 2015-16 El Niño. Global Change Biology, doi: 10.1111/gcb.15809, 2021.

Cernusak, L.A., Winter, K., Dalling, J.W., Holtum, J.A., Jaramillo, C., Körner, C., Leakey, A.D., Norby, R.J., Poulter, B. & Turner, B.L. Tropical forest responses to increasing atmospheric CO2: current knowledge and opportunities for future research. *Functional Plant Biology*, **40**, 531-551, 2013.

Choat, B., Jansen, S., Brodribb, T.J., Cochard, H., Delzon, S., Bhaskar, R., Bucci, S.J., Feild, T.S., Gleason, S.M. & Hacke, U.G. Global convergence in the vulnerability of forests to drought. *Nature*, **491**, 752-755, 2012.

Cox, P.M., Betts, R., Collins, M., Harris, P.P., Huntingford, C. & Jones, C. Amazonian forest dieback under climate-carbon cycle projections for the 21st century. *Theoretical and applied climatology*, **78**, 137-156, 2004.

de Almeida Castanho, A.D., Galbraith, D., Zhang, K., Coe, M.T., Costa, M.H. & Moorcroft, P. Changing Amazon biomass and the role of atmospheric CO2 concentration, climate, and land use. *Global Biogeochemical Cycles*, **30**, 18-39, 2016.

De Guzman, M.E., Acosta-Rangel, A., Winter, K., Meinzer, F.C., Bonal, D. & Santiago, L.S. Hydraulic traits of Neotropical canopy liana and tree species across a broad range of wood density: implications for predicting drought mortality with models. *Tree Physiology*, **41**, 24-34, 2021.

Doughty, C.E., Metcalfe, D., Girardin, C., Amezquita, F.F., Cabrera, D.G., Huasco, W.H., Silva-Espejo, J., Araujo-Murakami, A., Da Costa, M. & Rocha, W. Drought impact on forest carbon dynamics and fluxes in Amazonia. *Nature*, **519**, 78-82, 2015.

Eller, C.B., Rowland, L., Mencuccini, M., Rosas, T., Williams, K., Harper, A., Medlyn, B.E., Wagner, Y., Klein, T. & Teodoro, G.S. Stomatal optimization based on xylem hydraulics (SOX) improves land surface model simulation of vegetation responses to climate. *New Phytologist*, **226**, 1622-1637, 2020.

Esquivel-Muelbert, A., Galbraith, D., Dexter, K.G., Baker, T.R., Lewis, S.L., Meir, P., Rowland, L., da Costa, A.C.L., Nepstad, D. & Phillips, O.L. Biogeographic distributions of neotropical trees reflect their directly measured drought tolerances. *Scientific reports*, **7**, 1-11, 2017.

Esquivel-Muelbert, A., Phillips, O.L., Brienen, R.J., Fauset, S., Sullivan, M.J., Baker, T.R., Chao, K.-J., Feldpausch, T.R., Gloor, E. & Higuchi, N. Tree mode of death and mortality risk factors across Amazon forests. *Nature communications*, **11**, 1-11, 2020.

Esquivel-Muelbert, A., Baker, T.R., Dexter, K.G., Lewis, S.L., Brienen, R.J., Feldpausch, T.R., Lloyd, J., Monteagudo-Mendoza, A., Arroyo, L. & Álvarez-Dávila, E. Compositional response of Amazon forests to climate change. *Global Change Biology*, **25**, 39-56, 2019.

Feldpausch, T., Phillips, O., Brienen, R., Gloor, E., Lloyd, J., Lopez-Gonzalez, G., Monteagudo-

Mendoza, A., Malhi, Y., Alarcón, A. & Dávila, E.Á. Amazon forest response to repeated droughts. *Global Biogeochemical Cycles*, **30**, 964-982, 2016.

Feldpausch, T.R., Banin, L., Phillips, O.L., Baker, T.R., Lewis, S.L., Quesada, C.A., Affum-Baffoe, K., Arets, E.J., Berry, N.J. & Bird, M. Height-diameter allometry of tropical forest trees. *Biogeosciences*, **8**, 1081-1106, 2011.

Feng, X., Porporato, A. & Rodriguez-Iturbe, I. Changes in rainfall seasonality in the tropics. *Nature Climate Change*, **3**, 811-815, 2013.

Fisher, R., Williams, M., Da Costa, A.L., Malhi, Y., Da Costa, R., Almeida, S. & Meir, P. The response of an Eastern Amazonian rain forest to drought stress: results and modelling analyses from a throughfall exclusion experiment. *Global Change Biology*, **13**, 2361-2378, 2007.

Fleischer, K., Rammig, A., De Kauwe, M.G., Walker, A.P., Domingues, T.F., Fuchslueger, L., Garcia, S., Goll, D.S., Grandis, A. & Jiang, M. Amazon forest response to CO 2 fertilization dependent on plant phosphorus acquisition. *Nature Geoscience*, **12**, 736-741, 2019.

Fontes, C.G., Dawson, T.E., Jardine, K., McDowell, N., Gimenez, B.O., Anderegg, L., Negrón-Juárez, R., Higuchi, N., Fine, P.V. & Araújo, A.C. Dry and hot: the hydraulic consequences of a climate change–type drought for Amazonian trees. *Philosophical Transactions of the Royal Society B: Biological Sciences*, **373**, 20180209, 2018.

Franklin, J.F., Shugart, H.H. & Harmon, M.E. Tree death as an ecological process. *BioScience*, **37**, 550-556, 1987.

Giardina, F., Konings, A.G., Kennedy, D., Alemohammad, S.H., Oliveira, R.S., Uriarte, M. & Gentine, P. Tall Amazonian forests are less sensitive to precipitation variability. *Nature Geoscience*, **11**, 405-409, 2018.

Gora, E.M. & Esquivel-Muelbert, A. Implications of size-dependent tree mortality for tropical forest carbon dynamics. *Nature Plants*, 1-8, 2021.

Green, J. K., Berry, J., Ciais, P., Zhang, Y., & Gentine, P. Amazon rainforest photosynthesis increases in response to atmospheric dryness. Science advances, 6, eabb7232, 2020.

Guan, K., Pan, M., Li, H., Wolf, A., Wu, J., Medvigy, D., Caylor, K.K., Sheffield, J., Wood, E.F. & Malhi, Y. Photosynthetic seasonality of global tropical forests constrained by hydroclimate. *Nature Geoscience*, **8**, 284-289, 2015.

Harris, I., Jones, P.D., Osborn, T.J. & Lister, D.H. Updated high-resolution grids of monthly climatic observations–the CRU TS3. 10 Dataset. *International journal of climatology*, **34**, 623-642, 2014.

Harris, I. CRU JRA v2. 1: A forcings dataset of gridded land surface blend of Climatic Research Unit (CRU) and Japanese reanalysis (JRA) data, January 1901–December 2019, University of East Anglia Climatic Research Unit, Centre for Environmental Data Analysis. *University of East Anglia Climatic Research Unit, Centre for Environmental Data Analysis*, **10**, 2020.

Harris, I., Osborn, T.J., Jones, P. & Lister, D. Version 4 of the CRU TS monthly high-resolution gridded multivariate climate dataset. *Scientific data*, **7**, 1-18, 2020.

Holm, J.A., Knox, R.G., Zhu, Q., Fisher, R.A., Koven, C.D., Nogueira Lima, A.J., Riley, W.J., Longo,

M., Negrón-Juárez, R.I. & de Araujo, A.C. The central Amazon biomass sink under current and future atmospheric CO2: Predictions from big-leaf and demographic vegetation models. *Journal of Geophysical Research: Biogeosciences*, **125**, e2019JG005500, 2020.

Hubau, W., Lewis, S.L., Phillips, O.L., Affum-Baffoe, K., Beeckman, H., Cuní-Sanchez, A., Daniels, A.K., Ewango, C.E., Fauset, S. & Mukinzi, J.M. Asynchronous carbon sink saturation in African and Amazonian tropical forests. *Nature*, **579**, 80-87, 2020.

Janssen, T.A., Hölttä, T., Fleischer, K., Naudts, K. & Dolman, H. Wood allocation trade-offs between fiber wall, fiber lumen, and axial parenchyma drive drought resistance in neotropical trees. *Plant, cell & environment*, **43**, 965-980, 2020.

Jiang, M., Kelly, J.W., Atwell, B.J., Tissue, D.T. & Medlyn, B.E. Drought by CO2 interactions in trees: a test of the water savings mechanism. *New Phytologist*, 2021.

Jiménez-Muñoz, J.C., Mattar, C., Barichivich, J., Santamaría-Artigas, A., Takahashi, K., Malhi, Y., Sobrino, J.A. & Van Der Schrier, G. Record-breaking warming and extreme drought in the Amazon rainforest during the course of El Niño 2015–2016. *Scientific reports*, **6**, 1-7, 2016.

Jimenez, J. C., Libonati, R., & Peres, L. F. Droughts over Amazonia in 2005, 2010, and 2015: a cloud cover perspective. Frontiers in Earth Science, 6, 227, 2018.

Jimenez, J.C. & Takahashi, K. Tropical Climate Variability and Change: Impacts in the Amazon. *Frontiers in Earth Science*, **7**, 215, 2019.

Johnson, M.O., Galbraith, D., Gloor, M., De Deurwaerder, H., Guimberteau, M., Rammig, A., Thonicke, K., Verbeeck, H., Von Randow, C. & Monteagudo, A. Variation in stem mortality rates determines patterns of above-ground biomass in A mazonian forests: implications for dynamic global vegetation models. *Global change biology*, **22**, 3996-4013, 2016.

Kennedy, D., Swenson, S., Oleson, K.W., Lawrence, D.M., Fisher, R., Lola da Costa, A.C. & Gentine, P. Implementing plant hydraulics in the community land model, version 5. *Journal of Advances in Modeling Earth Systems*, **11**, 485-513, 2019.

Klein, T., Zeppel, M.J., Anderegg, W.R., Bloemen, J., De Kauwe, M.G., Hudson, P., Ruehr, N.K., Powell, T.L., von Arx, G. & Nardini, A. Xylem embolism refilling and resilience against drought-induced mortality in woody plants: processes and trade-offs. *Ecological research*, **33**, 839-855, 2018.

Kobayashi, S., Ota, Y., Harada, Y., Ebita, A., Moriya, M., Onoda, H., Onogi, K., Kamahori, H., Kobayashi, C. & Endo, H. The JRA-55 reanalysis: General specifications and basic characteristics. *Journal of the Meteorological Society of Japan. Ser. II*, **93**, 5-48, 2015.

Levine, N. M., Zhang, K., Longo, M., Baccini, A., Phillips, O. L., Lewis, S. L., ... & Moorcroft, P. R. Ecosystem heterogeneity determines the ecological resilience of the Amazon to climate change. Proceedings of the National Academy of Sciences, 113, 793-797, 2016.

Levionnois, S., Ziegler, C., Jansen, S., Calvet, E., Coste, S., Stahl, C., Salmon, C., Delzon, S., Guichard, C. & Heuret, P. Vulnerability and hydraulic segmentations at the stem–leaf transition: coordination across Neotropical trees. *New Phytologist*, **228**, 512-524, 2020.

Lewis, S.L., Brando, P.M., Phillips, O.L., van der Heijden, G.M. & Nepstad, D. The 2010 amazon drought. *Science*, **331**, 554-554, 2011.

Li, L., Yang, Z.L., Matheny, A.M., Zheng, H., Swenson, S.C., Lawrence, D.M., Barlage, M., Yan, B., McDowell, N.G. & Leung, L.R. Representation of Plant Hydraulics in the Noah-MP Land Surface Model: Model Development and Multi-scale Evaluation. *Journal of Advances in Modeling Earth Systems*, **13**, e2020MS002214, 2021.

Liu, Y., Holtzman, N. M., & Konings, A. G. Global ecosystem-scale plant hydraulic traits retrieved using model–data fusion. Hydrology and Earth System Sciences, 25, 2399-2417, 2021.

Lu, Y., Duursma, R.A., Farrior, C.E., Medlyn, B.E. & Feng, X. Optimal stomatal drought response shaped by competition for water and hydraulic risk can explain plant trait covariation. *New Phytologist*, **225**, 1206-1217, 2020.

Marthews, T. R., Quesada, C. A., Galbraith, D. R., Malhi, Y., Mullins, C. E., Hodnett, M. G., & Dharssi, I. High-resolution hydraulic parameter maps for surface soils in tropical South America. Geoscientific Model Development, 7, 711-723, 2014.

McCulloh, K.A., Domec, J.C., Johnson, D.M., Smith, D.D. & Meinzer, F.C. A dynamic yet vulnerable pipeline: Integration and coordination of hydraulic traits across whole plants. *Plant, Cell & Environment*, **42**, 2789-2807, 2019.

Meakem, V., Tepley, A. J., Gonzalez-Akre, E. B., Herrmann, V., Muller-Landau, H. C., Wright, S. J., ... & Anderson-Teixeira, K. J. Role of tree size in moist tropical forest carbon cycling and water deficit responses. New Phytologist, 219, 947-958, 2018.

Mengis, N., Keller, D.P., Eby, M. & Oschlies, A. Uncertainty in the response of transpiration to CO2 and implications for climate change. *Environmental Research Letters*, **10**, 094001, 2015.

Naudts, K., Ryder, J., McGrath, M., Otto, J., Chen, Y., Valade, A., Bellasen, V., Berhongaray, G., Bönisch, G. & Campioli, M. A vertically discretised canopy description for ORCHIDEE (SVN r2290) and the modifications to the energy, water and carbon fluxes. *Geoscientific Model Development*, **8**, 2035-2065, 2015.

Negrón-Juárez, R. I., Holm, J. A., Marra, D. M., Rifai, S. W., Riley, W. J., Chambers, J. Q., ... & Higuchi, N. Vulnerability of Amazon forests to storm-driven tree mortality. Environmental Research Letters, 13, 054021, 2018.

Nepstad, D.C., Tohver, I.M., Ray, D., Moutinho, P. & Cardinot, G. Mortality of large trees and lianas following experimental drought in an Amazon forest. *Ecology*, **88**, 2259-2269, 2007.

Nychka D, F.R., Paige J, Sain S, Gerber F., Iverson M. Fields: Tools for Spatial Data, University Corporation for Atmospheric Research, Boulder, CO, USA *10.5065/D6W957CT,* R package version 10.3, 2020.

Oliveira, R.S., Costa, F.R., van Baalen, E., de Jonge, A., Bittencourt, P.R., Almanza, Y., Barros, F.d.V., Cordoba, E.C., Fagundes, M.V. & Garcia, S. Embolism resistance drives the distribution of Amazonian rainforest tree species along hydro-topographic gradients. *New Phytologist*, **221**, 1457-1465, 2019.

Oliveira, R. S., Eller, C. B., Barros, F. D. V., Hirota, M., Brum, M., & Bittencourt, P. Linking plant hydraulics and the fast–slow continuum to understand resilience to drought in tropical ecosystems. New Phytologist, 230, 904-923, 2021.

Panisset, J.S., Libonati, R., Gouveia, C.M.P., Machado-Silva, F., França, D.A., França, J.R.A. &

Peres, L.F. Contrasting patterns of the extreme drought episodes of 2005, 2010 and 2015 in the Amazon Basin. *International Journal of Climatology*, **38**, 1096-1104, 2018.

Papastefanou, P., Zang, C.S., Angelov, Z., de Castro, A.A., Jimenez, J.C., De Rezende, L.F.C., Ruscica, R., Sakschewski, B., Sörensson, A. & Thonicke, K. Quantifying the spatial extent and intensity of recent extreme drought events in the Amazon rainforest and their impacts on the carbon cycle. *Biogeosciences Discussions*, 1-37, 2020.

Peng, R.D. Package 'simpleboot'. *https://github.com/rdpeng/simpleboot*, 2019.

Phillips, O.L., Aragão, L.E., Lewis, S.L., Fisher, J.B., Lloyd, J., López-González, G., Malhi, Y., Monteagudo, A., Peacock, J. & Quesada, C.A. Drought sensitivity of the Amazon rainforest. *Science*, **323**, 1344-1347, 2009.

Piao, S., Friedlingstein, P., Ciais, P., de Noblet-Ducoudré, N., Labat, D., & Zaehle, S. Changes in climate and land use have a larger direct impact than rising CO2 on global river runoff trends. Proceedings of the National academy of Sciences, 104, 15242-15247, 2007.

Pierce, D. (2019) Package 'ncdf4' http://cirrus.ucsd.edu/~pierce/ncdf.

Powell, T.L., Wheeler, J.K., de Oliveira, A.A., da Costa, A.C.L., Saleska, S.R., Meir, P. & Moorcroft, P.R. Differences in xylem and leaf hydraulic traits explain differences in drought tolerance among mature Amazon rainforest trees. *Global Change Biology*, **23**, 4280-4293, 2017.

Powers, J.S., Vargas G, G., Brodribb, T.J., Schwartz, N.B., Pérez-Aviles, D., Smith-Martin, C.M., Becknell, J.M., Aureli, F., Blanco, R. & Calderón-Morales, E. A catastrophic tropical drought kills hydraulically vulnerable tree species. *Global change biology*, **26**, 3122-3133, 2020.

R Development Core Team. R: A language and environment for statistical computing. Vienna, Austria: R Foundation for Statistical Computing, available at http://www.R-project.org/. 2021.

Ritchie, P., Clarke, J., Cox, P. & Huntingford, C. Overshooting Tipping Point Thresholds in A Changing Climate. *Nature*, **592**, 517-523, 2021.

Rowland, L., Martínez-Vilalta, J. & Mencuccini, M. Hard times for high expectations from hydraulics: predicting drought-induced forest mortality at landscape scales remains a challenge. *New Phytologist*, 2021.

Santiago, L.S., De Guzman, M.E., Baraloto, C., Vogenberg, J.E., Brodie, M., Hérault, B., Fortunel, C. & Bonal, D. Coordination and trade-offs among hydraulic safety, efficiency and drought avoidance traits in Amazonian rainforest canopy tree species. *New Phytologist*, **218**, 1015-1024, 2018.

Signori-Müller, C., Oliveira, R. S., de Vasconcellos Barros, F., Tavares, J. V., Gilpin, M., Diniz, F. C., ... & Galbraith, D. Non-structural carbohydrates mediate seasonal water stress across Amazon forests. Nature communications, 12, 1-9, 2021.

R: A language and environment for statistical computing. Vienna, Austria: R Foundation for Statistical Computing, available at http://www.R-project.org/ 2021.

Trugman, A. T., Anderegg, L. D., Anderegg, W. R., Das, A. J., & Stephenson, N. L. Why is tree drought mortality so hard to predict?. Trends in Ecology & Evolution, **36**, 520-532, 2021.

Van Der Sleen, P., Groenendijk, P., Vlam, M., Anten, N.P., Boom, A., Bongers, F., Pons, T.L., Terburg, G. & Zuidema, P.A. No growth stimulation of tropical trees by 150 years of CO 2 fertilization but water-use efficiency increased. *Nature Geoscience*, **8**, 24-28, 2015.

Wieder, W.R., J. Boehnert, G.B. Bonan, and M. Langseth. Regridded Harmonized World Soil Database v1.2. ORNL DAAC, Oak Ridge, Tennessee, USA. https://doi.org/10.3334/ORNLDAAC/1247, 2014.

Yang, X., W.M. Post, P.E. Thornton, and A. Jain. Global Gridded Soil Phosphorus Distribution Maps at 0.5-degree Resolution. Data set. Available on-line [http://daac.ornl.gov] from Oak Ridge National Laboratory Distributed Active Archive Center, Oak Ridge, Tennessee, USA, 2014. http://dx.doi.org/10.3334/ORNLDAAC/1223

Yang, Y., Donohue, R. J., & McVicar, T. R. Global estimation of effective plant rooting depth: Implications for hydrological modeling. Water Resources Research, 52, 8260-8276, 2016.

Yang, Y., Saatchi, S.S., Xu, L., Yu, Y., Choi, S., Phillips, N., Kennedy, R., Keller, M., Knyazikhin, Y. & Myneni, R.B. Post-drought decline of the Amazon carbon sink. *Nature communications*, **9**, 1-9, 2018.

Yue, C., Ciais, P., Cadule, P., Thonicke, K., Archibald, S., Poulter, B., ... & Viovy, N. Modelling the role of fires in the terrestrial carbon balance by incorporating SPITFIRE into the global vegetation model ORCHIDEE–Part 1: simulating historical global burned area and fire regimes. Geoscientific Model Development, 7, 2747-2767, 2014.

Zemp, D.C., Schleussner, C.-F., Barbosa, H.M., Hirota, M., Montade, V., Sampaio, G., Staal, A., Wang-Erlandsson, L. & Rammig, A. Self-amplified Amazon forest loss due to vegetation-atmosphere feedbacks. *Nature communications*, **8**, 1-10, 2017.

Zhang, K., de Almeida Castanho, A.D., Galbraith, D.R., Moghim, S., Levine, N.M., Bras, R.L., Coe, M.T., Costa, M.H., Malhi, Y. & Longo, M. The fate of Amazonian ecosystems over the coming century arising from changes in climate, atmospheric CO 2, and land use. *Global change biology*, **21**, 2569-2587, 2015.

Ziegler, C., Coste, S., Stahl, C., Delzon, S., Levionnois, S., Cazal, J., Cochard, H., Esquivel-Muelbert, A., Goret, J.-Y. & Heuret, P. Large hydraulic safety margins protect Neotropical canopy rainforest tree species against hydraulic failure during drought. *Annals of Forest Science*, **76**, 1-18, 2019.

Zuidema, P.A., Heinrich, I., Rahman, M., Vlam, M., Zwartsenberg, S.A. & van der Sleen, P. Recent CO2 rise has modified the sensitivity of tropical tree growth to rainfall and temperature. *Global change biology*, **26**, 4028-4041, 2020.

Zuleta, D., Duque, A., Cardenas, D., Muller-Landau, H.C. & Davies, S.J. Drought-induced mortality patterns and rapid biomass recovery in a terra firme forest in the Colombian Amazon. *Ecology*, **98**, 2538-2546, 2017.

4.9 SUPPLEMENTARY INFORMATION

Contents :

Figure S1-S13

Table S1 Mean △AGB (MgC ha^{-1} yr^{-1}) undergoing different levels of drought intensity (measured as Z score of MCWD).

Z score Year	[-1.96,-1.645]	[-2.576,-1.96]	<-2.576
1916	0.29	0.54	-0.24
1926	0.94	0.42	-2.06
1963	-0.24	-0.66	-0.74
1983	-0.39	-0.46	-1.04
1998	-2.96	-2.35	-1.59
2005	-0.45	-1.01	-1.98
2010	-0.77	-0.51	-1.69
2016	-1.45	-1.85	-3.86

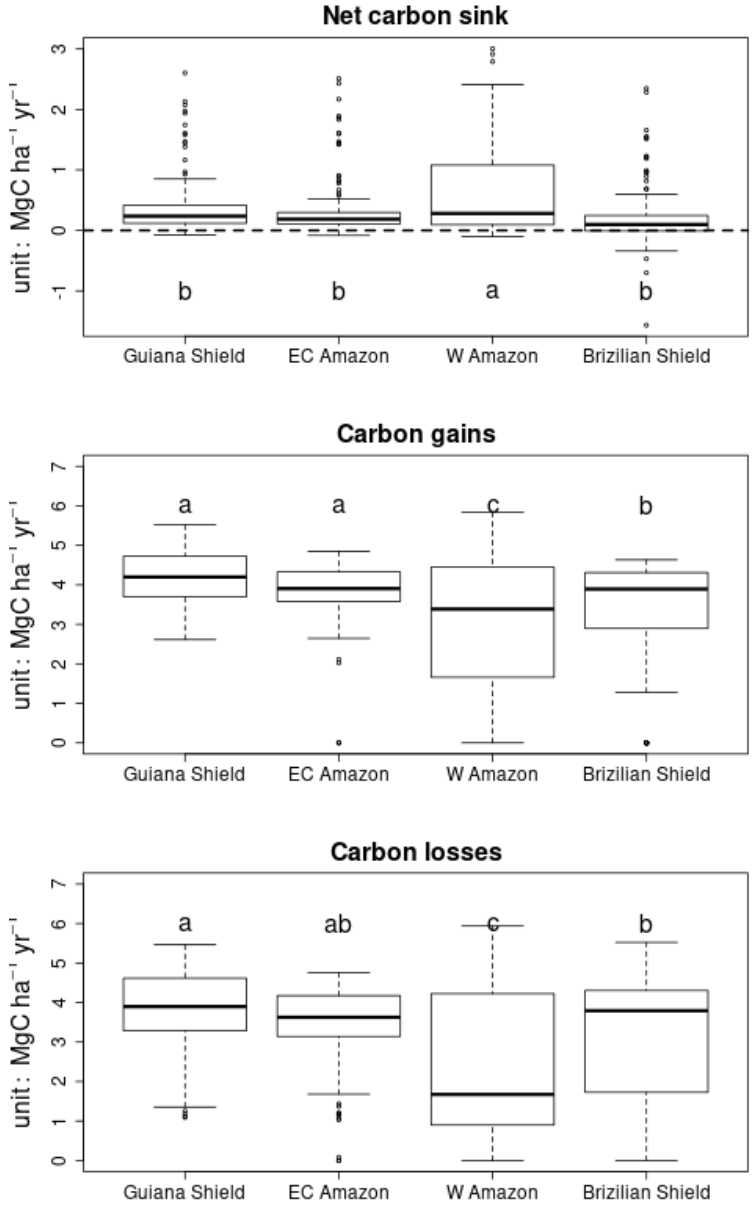

Figure S1 Regional difference on long-term AGB dynamics during 2000s excluding 2005 and 2010. Labels with different letter indicate significant differences between regions.

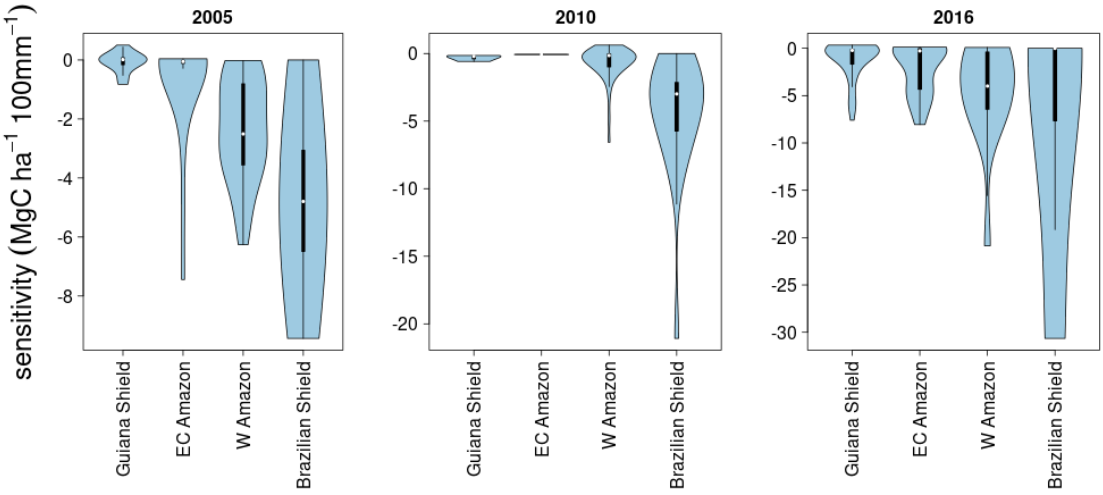

Figure S2 Whisker plot for sensitivity to 100mm increase in MCWD in each region and each drought.

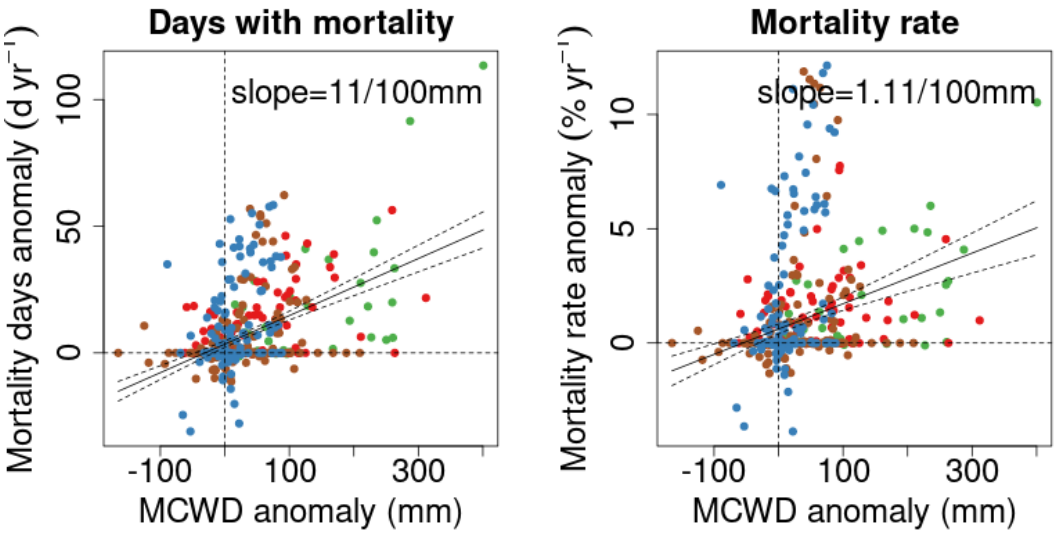

Figure S3 Simulated number of days with mortality and mortality rate during 2015//16 drought.

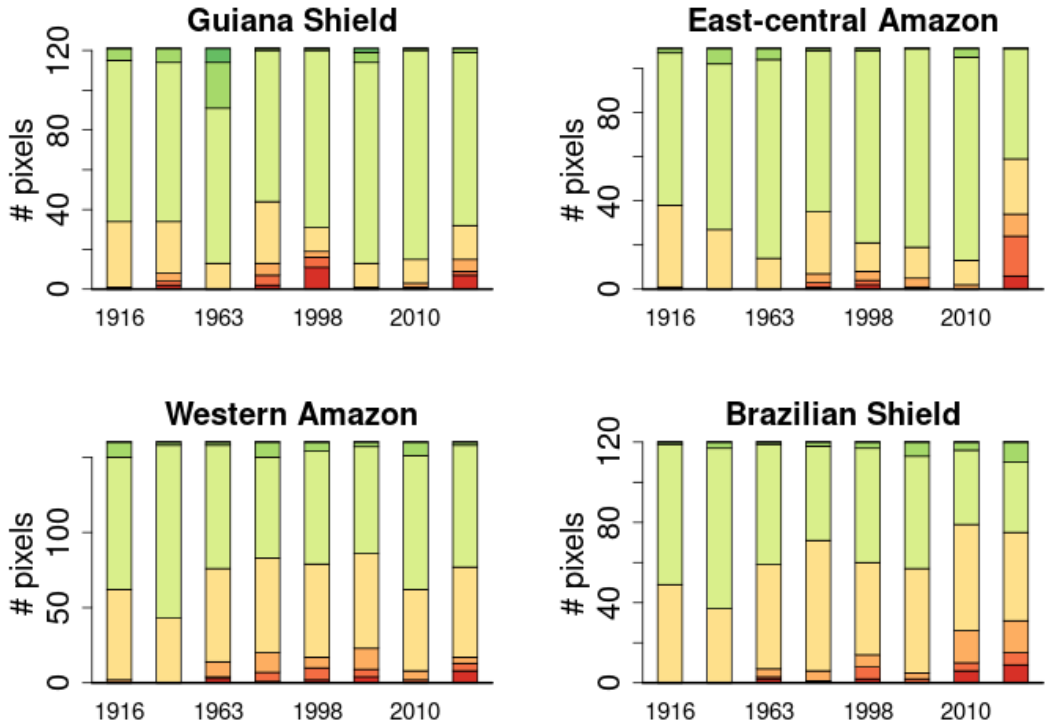

Figure S4 Similar to Figure 7 but for four separate regions.

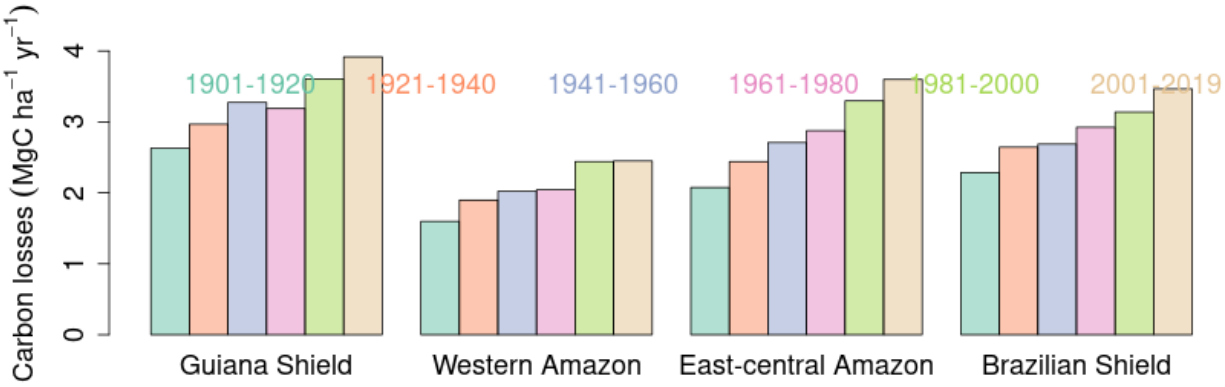

Figure S5 Simulation of carbon loss in each time period and each region.

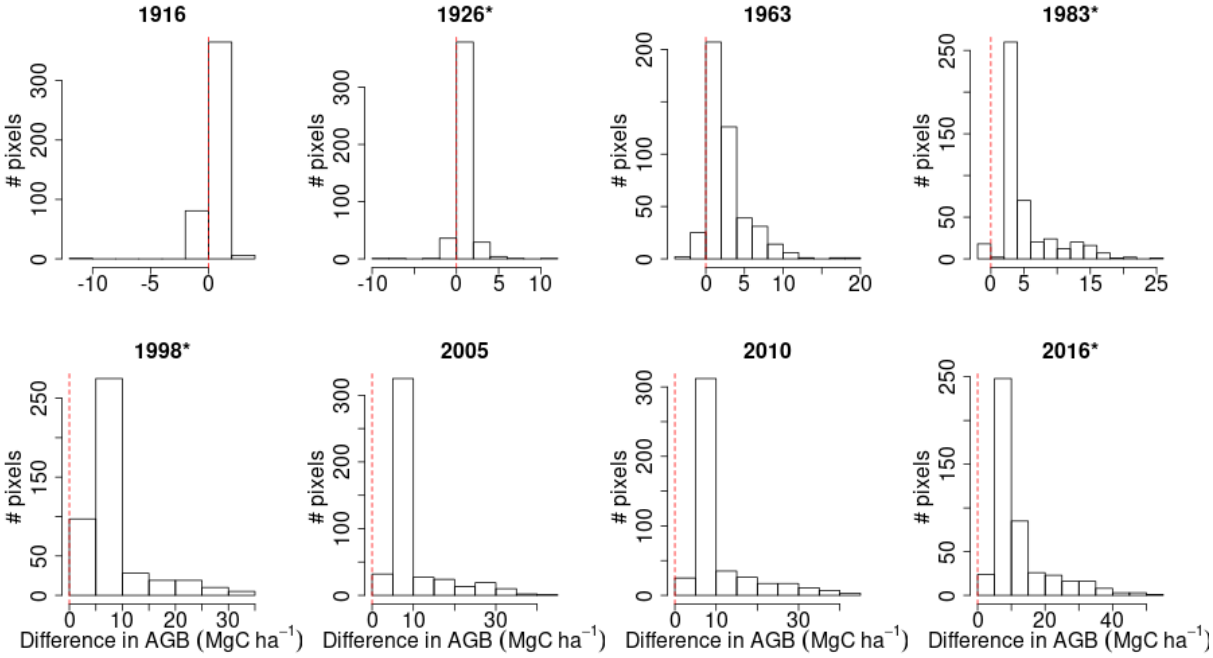

Figure S6 Difference in background AGB density between S2 and S3.

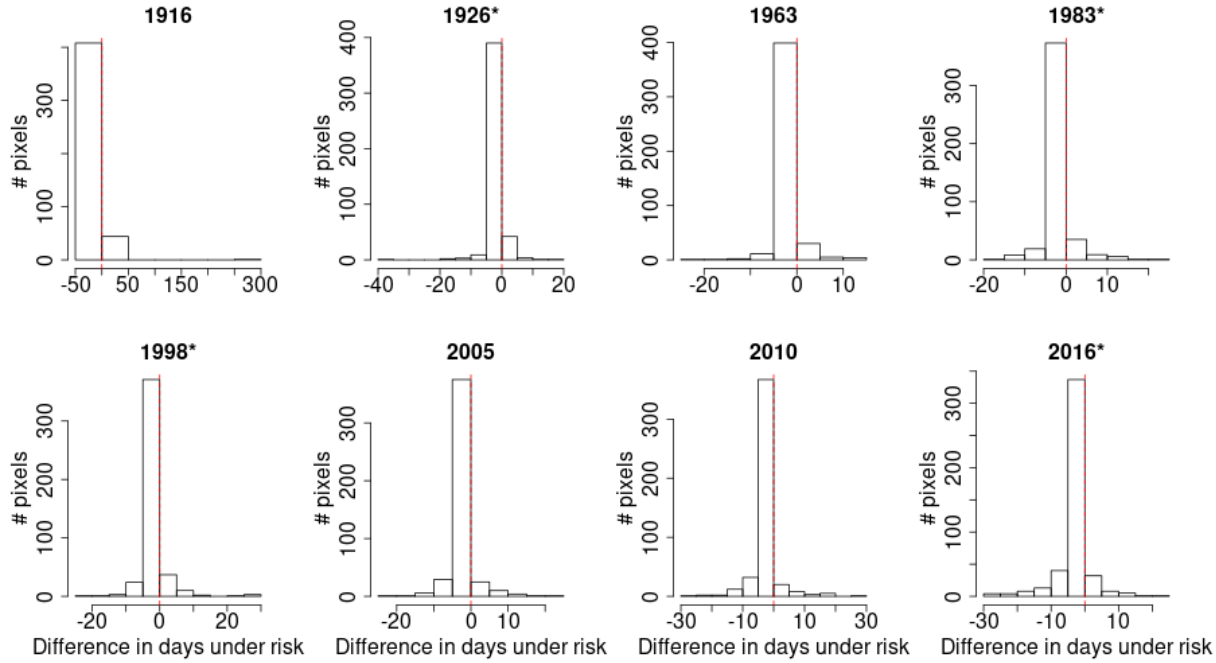

Figure S7 Difference in number of days under mortality risk between S2 and S3.

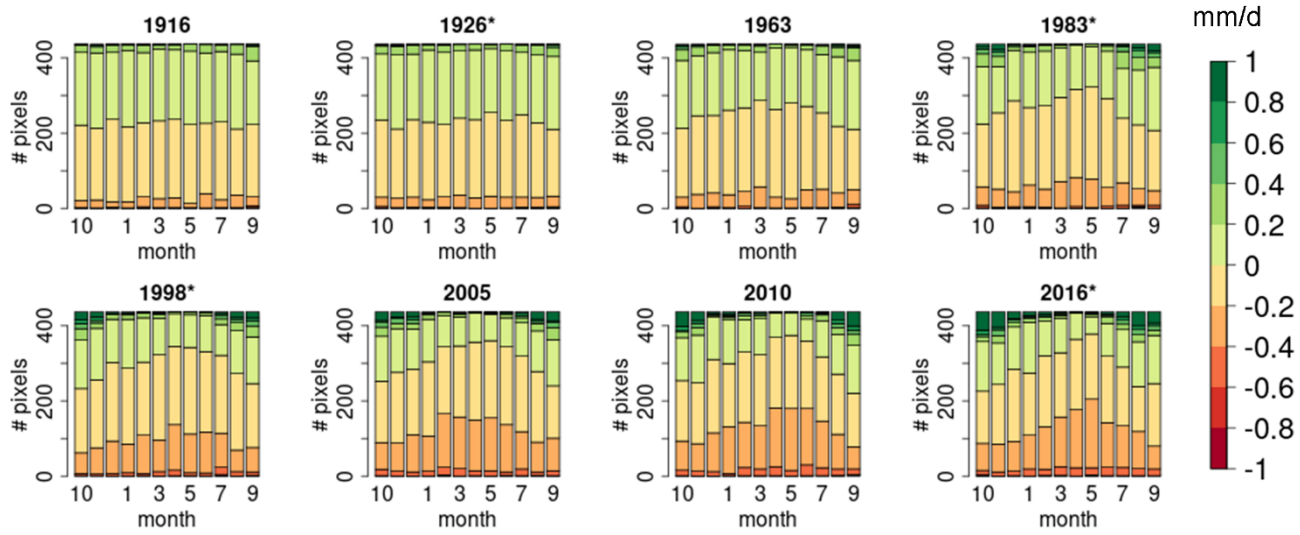

Figure S8 Difference in evapotranspiration between S2 and S3.

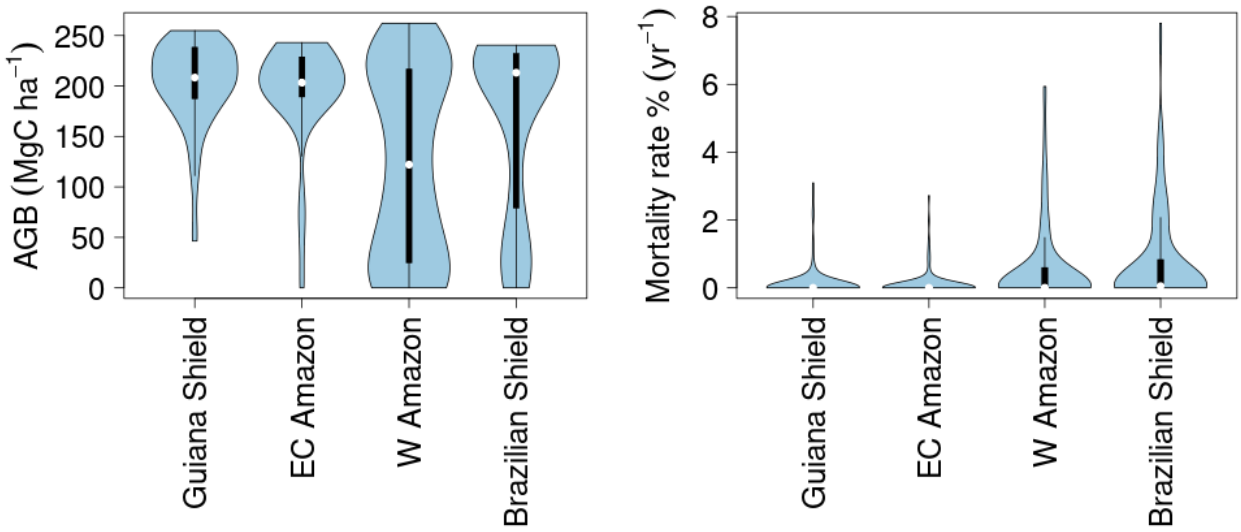

Figure S9 Modeled AGB and mortality rate during 2000s excluding 2005 and 2010.

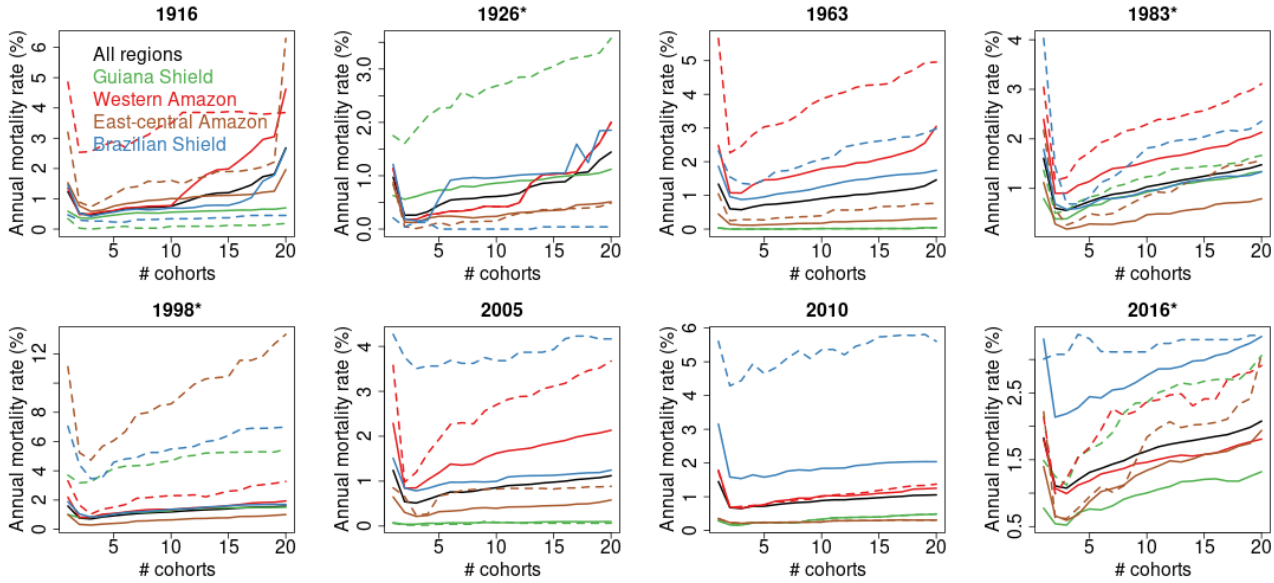

Figure S10 Annual tree mortality rate during 8 top drought events. Continuous lines denote the value averaged over Amazon basin and dashed lines the mean value over area with MCWD below -1.645, corresponding to 90% confidence interval and at least moderate drought. # cohorts represents the continuum of circumference class from the smallest one to the biggest one.

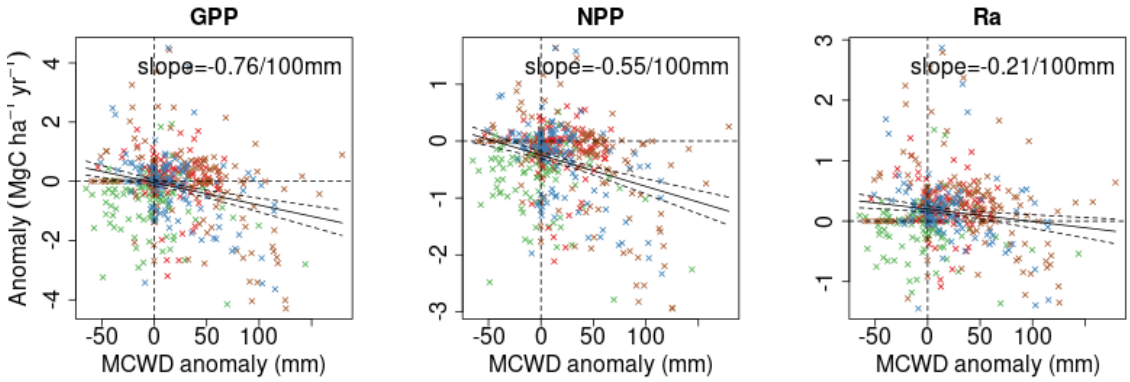

Figure S11 The relationship between annual GPP, NPP and Ra anomalies with MCWD anomaly during 2010 drought.

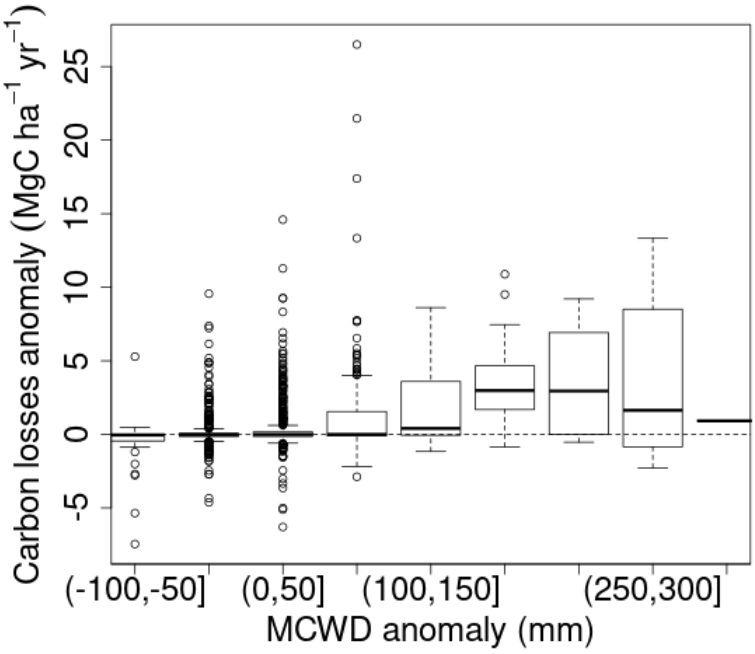

Figure S12 Carbon losses in binned MCWD anomalies.

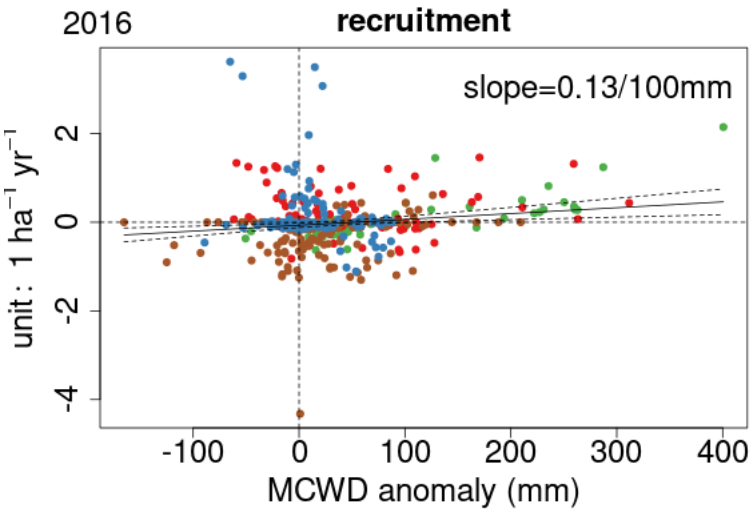

Figure S13 Response of recruitment rate to the relative drought intensity in 2015/16.

5 FUTURE DROUGHT-INDUCED TREE MORTALITY RISK IN AMAZON RAINFORESTS

5.1 SUMMARY

The carbon sink capacity of the Amazon rainforest is believed to be threatened by recurrent drought events that could lead to massive tree dieback and biomass loss. For the future, global climate models predicted that warming and drying trend induce more frequent drought events, of comparable severity with 2015/16 El Nino event, albeit with large uncertainties remain among their projections. In particular Earth System models from CMIP5 do not show any consensus about the sign of precipitation change over Amazon sub-regions. Given the possible large threat from future drought events, the evolution of Amazon rainforest carbon balance is both of great concern and highly uncertain due to uncertain climate projections and poorly understood tree mortality and recovery processes. Most process-based land carbon models part of Earth System Models assume constant tree mortality rate from turnover, or use carbon balance base 'tree vigor' metrics, and lack mechanistic tree mortality modules as well as forest demography modules. Therefore, to address the problem of simulating the future fate of biomass carbon storage in the Amazon rainforest, it is necessary to account for at least these two key processes.

In this chapter, the ORCHIDEE-CAN-NHA model developed in Chapter 3 and applied to historical droughts with reconstructed climate as an input in Chapter 4, was forced by historical climate and bias-corrected future climate forcing data from CMIP5 climate models. The bias correction of the interannual variability of climate is based on a quasi-emergent constraint method. The forcing data come from the ISIMIP-2 program, considering two scenarios (RCP2.6, RCP8.5) and four different climate models (GFDL, IPSL, MIROC, HadGEM). The goal is to simulate future biomass changes in the Amazon rainforest from 2015 to 2100, including uncertainties from the spread of climate projections. The future evolution of the climate of the Amazon shows a widespread warming trend, although its magnitude varies among climate models. There is also a pronounced increase in the maximum cumulated water deficit (MCWD), but with different regional patterns between the four climate models. The only consistent MCWD pattern is a drier trend in the northeastern Amazon. Compared to the historical drought in 2005, the MCWD anomalies during future drought years can be larger, thus a more severe water stress is anticipated. The sensitivity of net biomass change to drought also becomes more negative in the future, compared to what was simulated for the 2005 drought in Chapter 4. These conditions give rise to a reduction / suppression of the net biomass sink in the face of continuous warming and higher water deficits. The simulation forced by the HadGEM climate model in RCP8.5 scenario, showed the most pronounced Amazon drying, especially in the eastern Amazon and northeastern Amazon, with cross-over point at which the regional carbon sinks turn to carbon sources in Guiana Shield and East-central Amazon. This cross over point is passed in the middle of the 21st century.

This study offers an opportunity 'window for the future' for predicting the evolution of future Amazon rainforest net carbon balance, through a well-calibrated model that incorporates tree mortality triggered impaired hydraulic transport pipeline, and subsequent recovery of drought-affected forests from demographic processes, including recruitment and growth of survivor trees. Differences in projection of climate models contribute a large uncertainty to the projected future fate of the Amazon rainforest biomass carbon stocks. Therefore, further work should target on reducing the uncertainty in climate models besides the constraint applied already on climate projections to reduce the spread of climate data as well as uncertainty in tree mortality process to benefit a more comprehensive knowledge on fate of Amazon rainforest.

This chapter will be submitted for publication as: Yao, Y., Ciais, P., Viovy, N., Joetzjer, E., *et al*. Future drought-induced tree mortality risk in Amazon rainforests.

5.2 ABSTRACT

The carbon sink capacity in Amazon rainforest is under threat due to repeated and severe drought events that strongly increase biomass mortality. Global climate models projected that warming and drying trend would lead to more frequent drought events of comparable intensity with 2015/16 El Nino events but their projections are uncertain, even for the sign of precipitation changes in Amazon sub-regions. The future evolution of the Amazon rainforest carbon balance is uncertain not only from this climate uncertainty, but also because the balance between tree growth and mortality is still poorly understood. Most Earth System Models assume for instance that mortality rates are constant and independent of climate. Previous assessment studies used land carbon models forced by future climate forcing data not always bias corrected, and those models did not consider drought-induced tree mortality nor forest demography (Zhang *et al.*, 2015). In this study, the ORCHIDEE-CAN-NHA, a land surface model with a mechanistic hydraulic architecture, a tree mortality sub-model linked to the occurrence of hydraulic failure from loss of stem conductance, and a representation of stand-level recruitment and demography, was forced by historical climate reconstruction and bias-corrected future climate forcing data from the ISIMIP-2 program, considering two scenarios and four different climate models, in order to project biomass changes in the Amazon rainforest from 2015 to 2100. Changes in the maximum cumulated water deficit (MCWD) indicate that climate models present different patterns but most of them consistently predict drier trend in northeastern Amazon. Compared to the historical drought in 2005 taken as a reference, MCWD during future drought years becomes more intense. The negative sensitivity of net biomass change to drought can also be more negative, as evidenced by a more negative net biomass sink anomaly corresponding to temperature increase and higher water deficit. One simulation forced by the HadGEM climate model, the one with the most pronounced Amazon drying, showed a cross-over point of carbon sink turning to a carbon source in Guiana Shield and East-central Amazon since the middle of the 21st century. This study sheds light on uncertainties in the future of the Amazon forest carbon sink, through a well-calibrated model that incorporates tree mortality triggered by hydraulic damage and the subsequent recovery of drought-affected forests from demographic processes. Climate forcing data and our hypothesis about implementing only one set of hydraulic traits constitute the uncertainty underlying our understanding of future fate of Amazon rainforest biomass dynamics.

5.3 INTRODUCTION

Given its huge but vulnerable carbon and biodiversity stores, the evolution of the Amazon rainforest biome is of great concern. The remaining intact Amazon forests host more than 20% of terrestrial species, contain 100 billion tons of carbon (Feldpausch *et al.*, 2012), remove atmospheric CO_2 from the atmosphere, and maintain the inland regional and continental climate wetter through moisture cycling (Werth & Avissar, 2004; Zemp *et al.*, 2017). However, the occurrence of climate extreme events such as droughts and storms, large scale deforestation in the South, East, and South-West and along the rivers that does not seem to stop, and forest degradation over a wide area in the vicinity of deforestation jeopardize the stability and spatial continuity of the forest. Hence the risk of crossing a tipping point, when intact forests will turn to carbon sources and could even collapse in a few decades deserves great focus.

Increasing biomass mortality triggered by recent drought events, which seem to be more frequent and severe than in the early 20th Century was suggested to explain the decline in net biomass carbon sink during past three decades, in spite of a continuing but decelerating increase of tree growth (Brienen *et al.*, 2015). The carbon sink strength thus weakens in the Amazon intact forests (Phillips & Brienen, 2017). When added to degradation, fires and deforestation losses, the Brazilian Amazon biome, and certainly its South-east part, appears to be losing carbon to the atmosphere (Gatti *et al.*,

2021). Given likely more severe climate condition by the end of the 21st century, e.g. hotpot of hot and dry clusters in the northeastern Amazon (Vogel *et al.*, 2020), it is important to predict the future trajectory of the intact rainforest, and anticipate the degree beyond which its structure and function would be highly threatened, with a loss of carbon sink and the appearance of massive biomass carbon losses in some regions. Such knowledge is fundamental to provide early warning information, and help policies to protect this biome.

Since the beginning of 21st century, several big drought events hit large regions of the intact Amazon rainforest. Among them, the 2005, and 2010 drought events have been evaluated for their impact on growth and mortality through forest inventory plot data like the RAINFOR network (Doughty *et al.*, 2015; Feldpausch *et al.*, 2016; Phillips *et al.*, 2009). Besides laborious but precious field measurements, satellite data were also used to investigate the drought effects and occurrence signal. Temporal autocorrelation with long-time series of remote sensing data reflecting ecosystem response has been used to detect early warning signals of reduced resilience or inadequate recovery (Liu *et al.*, 2019; Saatchi *et al.*, 2021). LiDAR-based tree height collected after the severe drought of 2005 was also used to show post-drought mortality in the epicenter region of that drought (Yang *et al.*, 2018). However, both forest inventory data and satellite products can only be useful in evaluating past drought effects and cannot be used to inform future projections, given that the future will bring new conditions that have no past analogue like elevated CO_2, drought in regions that merely experienced them before, and emerging nutrient limitations. For the future, considering the likelihood of more frequent, warmer, and severe droughts over 21st century (Parsons, 2020), process-based models that incorporate key mechanisms of ecosystem-level physiological response offer us an opportunity to project changes in forest dynamics and in their carbon balance.

Process-based model has been used to investigate the Mid-Holocene drought in Amazon due to less human intervention and drier climate over this period than the present, in aspects of tree cover resilience (Kukla *et al.*, 2021) and possible tree die-back (Smith *et al.*, 2022). Smith *et al.* (2022) focused on mid-Holocene drying as an analogue to the drier future and used model vs. paleo-data comparisons to assess the risk of future Amazon rainforest dieback, from the higher vulnerability and sensitivity to mid-Holocene drought reconstructed in transitional area of the southern Amazon. The rainforest in central Amazon largely remained intact in response to drier climate condition in that study. Nevertheless, we still lack spatially explicit simulations of the Amazon forest dynamics based on trees demography, droughts mortality, drought recovery, and interactions between climate change and rising CO_2, which will altogether determine biomass changes in the future. Therefore, a critical need has emerged to predict the response of Amazon rainforest with more realistic process-based models.

Tree mortality constitutes one of the most uncertain processes that challengingly affects the simulation of the Amazon forest's sensitivity to climate change, due to insufficiency in our knowledge on plant hydraulics physiology (Trugman *et al.*, 2021), large variations of the response across different species, insufficient understanding of the mechanistic linkages between plant stress and tree mortality. This has resulted in multiple tentative empirical mortality parameterizations by modelers therein (Liu *et al.*, 2021b; Xu *et al.*, 2021). To improve models' performance on reproducing the climate-induced mortality pattern, possible physiological mechanisms underlying tree dieback were encapsulated in models and examined against field evidence. Water demand down-regulation by an insufficient xylem supply serves as an indispensable process for modeling plant hydraulic architecture in ecosystem-level or individual-based demography models with Darcy's law as approximation of plant hydrodynamics and the calculation of water potentials coupled to water supply to upper organs and water demand and changes in water holding capacitance (Kennedy *et al.*, 2019; Xu *et al.*, 2016). Safety-efficiency trade-off is also a valuable theory to optimize the response of stomatal conductance during drought, although it may not occur as strong as we expected (Gleason *et al.*, 2016). Such configurations of models help to refine the simulation of water flow from soil-root-stem-leaf

continuum, water potential and water conductance of each organ, so that hydraulic-failure related loss of tree vitality can be predicted, which is a condition for being able to model mortality due to cavitation. Hence, the mechanistic hydraulic architecture of a model allows to connect environmental water stress and tree mortality through modeling plant hydrodynamics.

Yet, little is known about how trees die and thus how mortality can be modeled. Different formulations of tree mortality have been attempted including theoretical formula, empirical or statistical basis (related to tree growth), and mechanistic one stemming from physiological mechanisms (Bugmann *et al.*, 2019), among which the mechanistic one should be prioritized. Nonetheless, full plant hydraulics process-based models have rarely been used to predict future mortality risk at regional spatial scales (Trugman, 2021). In this study, we used the recently developed and calibrated process-based model ORCHIDEE-CAN-NHA (Yao *et al.*, 2021), where mechanistic hydraulic architecture simulates plant hydrodynamics from soil to atmosphere, with a mortality sub-model based on the persistent loss of tree conductance and empirical equations to determine the size class of trees that are killed. This model of hydraulic failure induced tree mortality was demonstrated to perform well against experimental drought studies at Caxiuanã in eastern Amazon and Tapajos in east-central Brazilian Amazon. At larger scale for simulations across all intact forests of the Amazon, the model was also able to reproduce the decelerating net carbon sink trend over the last three decades, and the observed drought sensitivity of trees growth and mortality during recent severe drought events (Yao *et al.*, in prep). In this study, we aim to predict the future biomass carbon sink trajectory and investigate the possible mortality risk over intact rainforests in the Amazon basin. To account for the source of uncertainty in climate forcing data, the simulations were performed using four different climate models. Because climate models have huge biases over the Amazon, especially of precipitation, the climate models fields were bias corrected using the harmonized procedure of the Inter-Sectoral Impact Model Inter-comparison Project (ISIMIP). The climate models are IPSL-CM5A, GFDL-ESM2M, HadGEM, and MIROC. The specific aims of this study are:

(1) What are the spatiotemporal features of future droughts projected by the climate models, and are those future droughts more severe / frequent than past ones?
(2) Does the sensitivity of net biomass change during future drought events differ from the one of recent past events?
(3) What is the uncertainty of regional biomass carbon change caused by differences in climate projections?
(4) Which part of the Amazon rainforest are consistently most vulnerable or closer to reach a point where carbon sources appear?

5.4 Materials & Methods

5.4.1 The land surface model ORCHIDEE-CAN-NHA

ORCHIDEE-CAN-NHA (Yao *et al.*, 2021) added a new mechanistic hydraulic architecture and a hydraulic-failure induced mortality sub model to the process-based model ORCHIDEE. In this new version, dynamic ½ hourly water potentials, water flows along the water potential gradient, and change in water transport conductance and plant organs capacitance can be simulated. The key plant water stress indicator is the percentage loss of stem conductance (PLC), which is assumed to relate to tree mortality through two empirical parameters, a cumulated drought exposure threshold, and a tree mortality fraction for each tree size cohort each time step exceeding the threshold. There is no field measurement for these two parameters in tropical rainforest, so they were calibrated at the world's longest running through-fall exclusion (TFE) manipulation experiment of Caxiuanã (Rowland *et al.*, 2015) and the model results for biomass mortality were evaluated against data from another TFE site, at Tapajos.

5.4.2 Treatment of ISIMIP (Inter-Sectoral Impact Model Intercomparison Project) forcing data

Four ISIMIP models (GFDL-ESM2M, HadGEM-2ES, IPSL-CM5A-LR, MIROC5) and two emission scenarios (RCP2.6, RCP8.5) contributing to eight gridded climate fields for the future are used in our simulation work. Due to a strict climate input data policy, only four GCMs were selected (Frieler *et al.*, 2017). Since bias in precipitation is huge and influences the mean aboveground biomass bias (Ahlström *et al.*, 2017), ISIMIP forcing, in addition to downscale climate forcing to 0.5° also uses a bias correction, we used the bias correction of ISIMIP, of which the spatial and seasonal patterns of the climate models were essentially corrected upon the CRU fields for the period 1960-1990. This bias correction removes for instance mean precipitation biases, but the inter-annual variability of climate models is not bias corrected. This means that the ISIMIP models are likely to have either too many or too severe droughts, or the opposite, during the current period, and this bias can persist in the future. Correction for the mean value could be sufficient to evaluate the mean productivity but not for investigating the tree mortality that largely related to extreme events. Therefore, we used an emergent constraint to resample the future inter-annual variability so that the models' present-day variability is realistic when compared to observations from CRUJRA2.1 (Cox *et al.*, 2013), where the correction also allows to keep the change in climate variability in the future.

We find that the climate models have a larger than observed inter-annual standard deviation (SD) of rainfall over the historical period, and also a larger standard deviation in the future as well (Figure 5.1), although all models seem to over-estimate the observed SD. Therefore, we designed a new quasi-emergent constraint method by constraining the future expected SD based on the relationship between present and future across the models, shown in Figure 5.1. The constraint is the observed SD from CRUJRA2.1 over 1901-2005. We first calculate the annual rainfall over Amazon basin (basin map in Figure 5.2). We then do a bias correction of mean value and SD of rainfall over the historical and future periods. For calibrating SD, we define an initial threshold of $M \pm x*SD$, where M is the mean value of each ISIMIP model, SD is the inter-annual standard deviation of individual ISIMIP model, and x is a parameter adjusted for four ISIMIP models individually. If the annual precipitation is above the upper bound (or below the lower bound) defined by $M \pm x*SD$, the annual precipitation is set to be equal to the upper (or lower) limit. This process is performed iteratively until the corrected SD is closer to the constrained one, where the expected SD is constrained as shown in Figure 5.1. Then the correction ratio can be derived as the 'corrected' annual precipitation dividing the 'uncorrected' one. For the mean value correction, we refer to the multiplicative method used in Hempel *et al.* (2013) on top of precipitation data by a ratio derived from the mean annual rainfall from the baseline one (CRUJRA) divided by that from four ISIMIP forcing. In total, the precipitation forcing data was corrected by two ratio values, one for SD, and one for the mean value. The corrected precipitation forcing was used in model simulation.

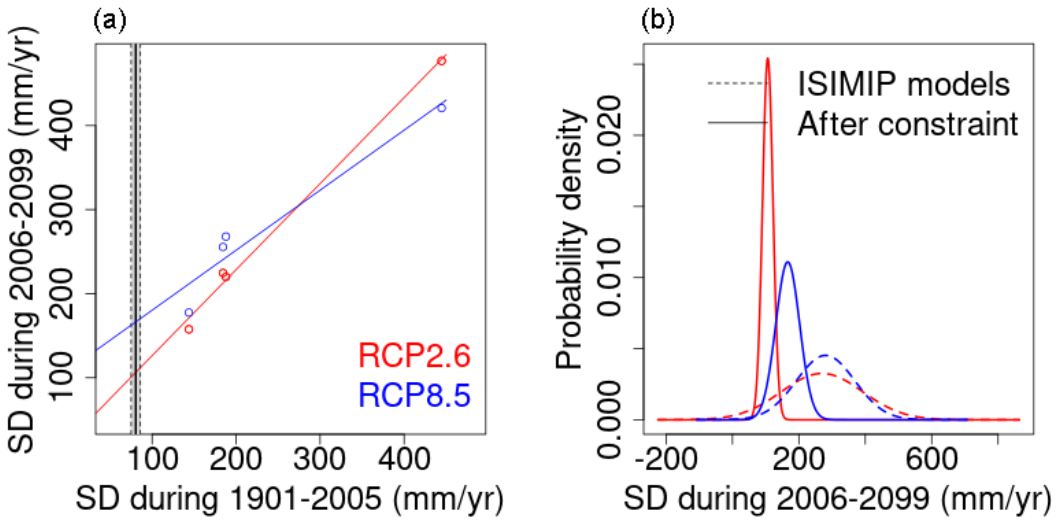

Figure 5.1 Quasi-emergent constraint on the model-simulated Amazon rainfall. (a) Amazon rainfall inter-annual standard deviation (sd) in the past (1901-2005) versus that in the future (2006-2099) among four models. The black vertical dashed line denotes the sd of the past from CRUJRA, ~ 80 mm yr^{-1}. The SD of each ISIMIP model seems to be overestimated compared to that of CRUJRA. (b) PDF for the SD over 2006-2099. The continuous lines were derived by applying the SD constraint from CRUJRA to the across-model relationship shown in (a). The dashed lines show the Gaussian distribution of original SD assuming that all the ISIMIP models' results are equally correct.

5.4.3 Simulation protocol

To initialize carbon pools from the ORCHIDEE CAN NHA model simulations, we designed a two-steps spin-up. During the first spin-up, the model recycles the climate forcing data of the period 1861-1880 with constant CO_2 concentration of 286 ppm and a constant mortality, which points to a longevity-inversed metric and also self-thinning. At the end of this first spin-up stage, biomass carbon storage reaches an equilibrium. Then, a second spin-up takes the end of the first one as starting point. During the second spin-up stage, the model still recycles the climate forcing data during 1861-1880 with constant CO_2 concentration of 286ppm but the mortality scheme is activated. The drought events during 1861-1880 then lead the model to reach another dynamic equilibrium, with less biomass caused by recurrent drought mortality. After the spin up, the historical and future simulations followed the protocols shown in Table 5.1.

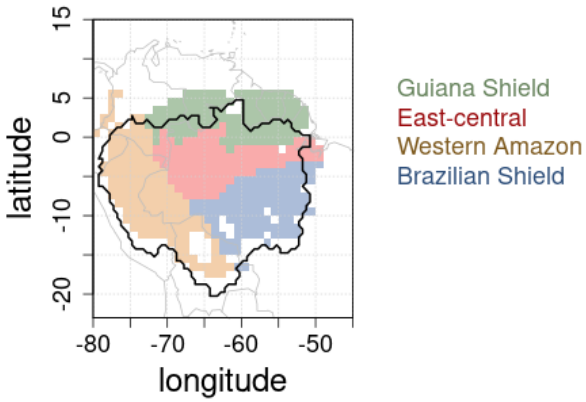

Figure 5.2 Overview of the rainforest area over Amazon basin, which is split into four regions, Guiana Shield, East-Central Amazon, Western Amazon, and Brazilian Shield, shown by different colors, defined after Feldpausch *et al.* (2011). The black line is the border of Amazon basin from Papastefanou *et al.* (2020). Only pixels with tree cover more than 80% are shown, where tree cover

data come from (Hansen *et al.*, 2013).

Table 5.1 Description of simulations performed in this study.

	Climate forcing	Atmospheric CO_2	Mortality module	Restart point	
spin-up stage 1	1861-1880	Constant (286ppm)	Deactivated	/	/
spin-up stage 2	1861-1880	Constant (286ppm)	Activated	Stage1	/
S – historical	1861-2005	Increasing	Activated	Stage2	Historical
S – future	2006-2099	Increasing	Activated	End of S2 - historical	RCP2.6, RCP8.5

5.4.4 Drought severity (cumulative water deficit)

Following previous research on the evaluation of drought area and severity (Papastefanou *et al.*, 2020), the maximum cumulated water deficit (MCWD) was used to compare droughts, as given by Equations (1) and (2). A fixed value for evapotranspiration (ET) of ~100 mm per month is used. When monthly rainfall is below 100 mm, the forest undergoes water deficit. The water deficit accumulates over the hydrological year from October in the previous year to September in the current one. MCWD is the most negative value of the cumulative water deficit among all 12 months. Then decadal mean of MCWD over baseline period was subtracted from the MCWD of year with drought and MCWD anomaly was derived. For drought 2005, the decadal mean is the average of MCWD over 2000s excluding 2005.

$CWD_m = CWD_{m-1} + P_m\text{-}100$ if $P_m < 100$, else $CWD_m=0$

with m being the month 1, …12 (1 = October) (1)

$MCWD = \min(CWD_m)$, m=1, …, 12 (2)

5.4.5 How aboveground biomass dynamics was analyzed ?

From model outputs, the net aboveground biomass change (△AGB), AGB gain and loss are calculated over each hydrological year. AGB gain is the carbon allocated to the growth of aboveground sapwood in cohorts with DBH above 10 cm, each year. Note that the model includes a conversion of sapwood to heartwood. AGB loss is the biomass mortality of aboveground sapwood and heartwood in cohorts with DBH above 10 cm, each year. △AGB is the difference between AGB gain and AGB loss. The anomaly during a drought year *k* is derived by subtracting the average value (μ) over a multi-year baseline period by Equations 3 to 5. The recruitment constitutes also a part of growth, however, here to be comparable with the inventories that only sample the plant individuals with DBH above 10cm, growth of samplings below 10cm is not accounted.

$$\Delta AGB_{anomaly} = \Delta AGB_k - \mu_{\Delta AGB} \quad (3)$$

$$AGBgain_{anomaly} = AGBgain_k - \mu_{AGBgain} \quad (4)$$

$$AGBloss_{anomaly} = AGBloss_k - \mu_{AGBloss} \quad (5)$$

5.4.6 Drought sensitivity

With water deficit anomaly and carbon flux anomaly, the drought sensitivity is derived through the linear regression between these two variables spatially.

5.4.7 Model evaluation statistics

We use the R programming environment and statistical packages (version 3.5.0; R Core Team, 2019) for all data processing and analysis. Package 'ncdf4 v1.17' (Pierce, 2019) is used to handle files in NetCDF format from model outputs. Package 'fields v10.3' (Nychka D, 2020) is used in AGB change and climate metrics mapping. We use the least-square linear regression to fit the modeled long-term trend of the net carbon sink, and also carbon gain and carbon loss. We also use package 'simpleboot' (Peng, 2019) to obtain an appropriately conservative estimate on 95% confidence interval for the regression slope.

5.5 RESULTS

5.5.1 Quantification of future climate evolution

Warming is widespread across the whole Amazon basin by the end of this century, yet with heterogeneous pattern and different hotpots, as given by the ISIMIP forcing data (Figure 5.3). In RCP2.6 scenario, IPSL and MIROC show a warming of higher magnitude than the other climate models, especially in southern Amazon for MIROC and western Amazon for IPSL. The mean warming across models is of 1.3±0.3 °C in 2080-2099 compared to the current period 1986-2005. The geographic extent of the warming trend expands and intensifies in the RCP8.5 scenario, with an average warming of 4.9±1.4 °C. As shown in Figure 5.3, two models (GFDL and MIROC) show a lower warming especially in the southern Amazon (less than 5°C), while one model (HadGEM) shows the largest warming, mainly in eastern Amazon (about 7°C).

The vapor pressure deficit (VPD) is a key driver of the evaporative demand, and thus of the potential water stress on plants. In the model, a higher VPD increases the transpiration demand (which initially acts to increase transpiration but can reduce it later when soil moisture is limiting), and reduces stomatal conductance thus photosynthesis. Figure 5.4 shows the change of VPD between the end of this century (2080-2099) and the recent historical period (1986-2005). Similar to the pattern of temperature change, in both RCP2.6 and RCP8.5 scenarios, the IPSL climate model predicts the VPD increase in western Amazon. MIROC climate model predicts the VPD increase in southern Amazon and eastern Amazon. HadGEM climate model predicts greater VPD increase in eastern Amazon especially. VPD increase estimated by GFDL forcing is less obvious than that in other models in both RCP2.6 and RCP8.5 scenarios (Figure 5.4). VPD largely follows the pattern of temperature change (Figure 5.3 and 5.4).

With regard to rainfall changes, the climate models simulate both drying and wetting trends across different sub-regions of the Amazon basin as shown in Figure 5.5. There is less agreement among the four climate models than for MAT and VPD changes. In the RCP2.6 scenario, MIROC and HadGEM show a wetting trend in the western Amazon and a drying trend in the northeastern Amazon, more extensive in HadGEM. The IPSL model shows a wetting trend from the central Amazon to the east side but GFDL model shows extensive drying trend over the similar geographic span. The wetting-drying dipole is similar between RCP2.6 and RCP8.5 scenario but more contrast in RCP8.5 scenario, with rainfall difference reaching as large as 1000mm yr^{-1} (note the different color scales for each scenario in Figure 5.5). Climate model predictions still exhibit less agreement on the area with greater drying trend. Nevertheless, drought events in northeastern Amazon occur more frequently in all the models given higher temperature, higher VPD and a decline of precipitation.

MCWD as a water deficit metric, shows a drying trend spatially consistent with the pattern of precipitation reductions as shown in Figure 5.6. MCWD reflects the accumulation of water deficit especially in the dry season with monthly rainfall below 100 mm. The MIROC climate model is the only one that shows different pattern between MAP and MCWD change, as the change of MCWD difference reveals greater water stress in central and eastern Amazon (Figure 5.6). Three models including GFDL, IPSL and HadGEM present similar pattern between MAP and MCWD, like more water stress in southern Amazon as found by GFDL climate model, drier trend in western Amazon detected from IPSL climate model, and more severe water stress mainly in northeastern Amazon from HadGEM forcing.

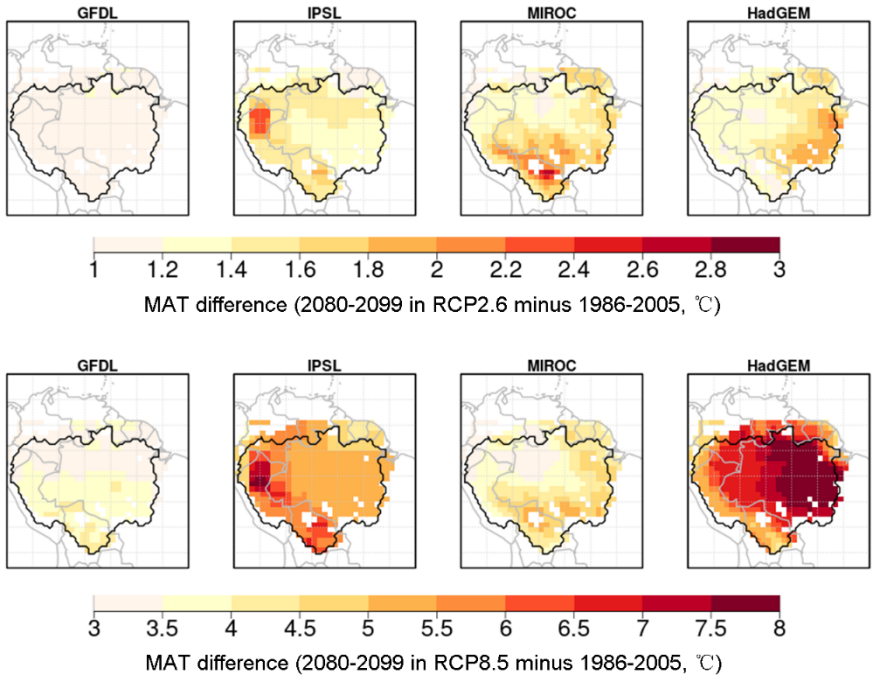

Figure 5.3 Evolution of future temperature change shown as the difference between MAT (mean annual temperature) during last 20 years by the end of the 21st century (2080-2099) and MAT during 1986-2005. Top panels: RCP2.6, bottom panels: RCP8.5.

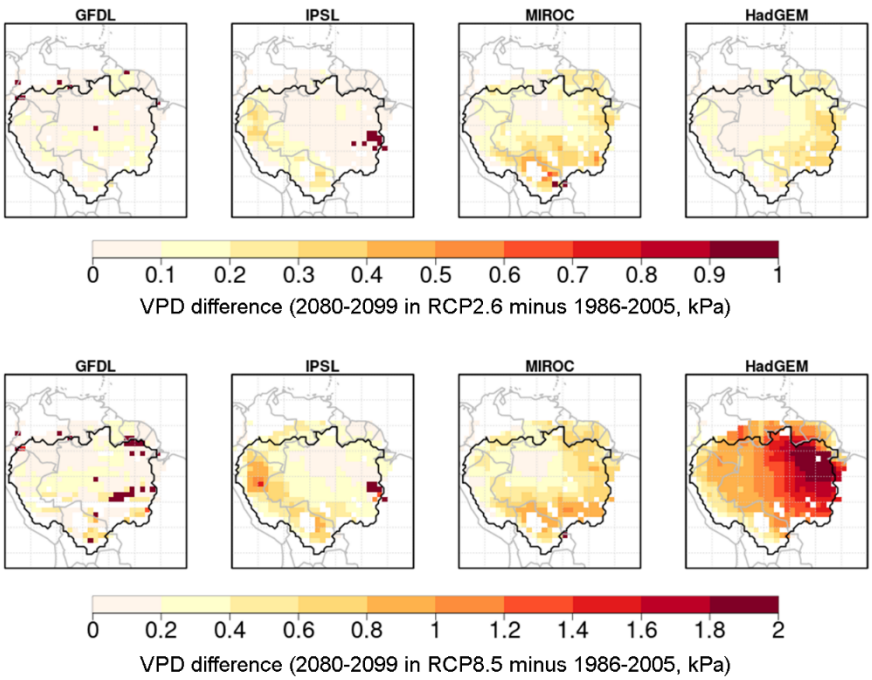

Figure 5.4 Similar to Figure 5.3 but for vapor pressure deficit (VPD).

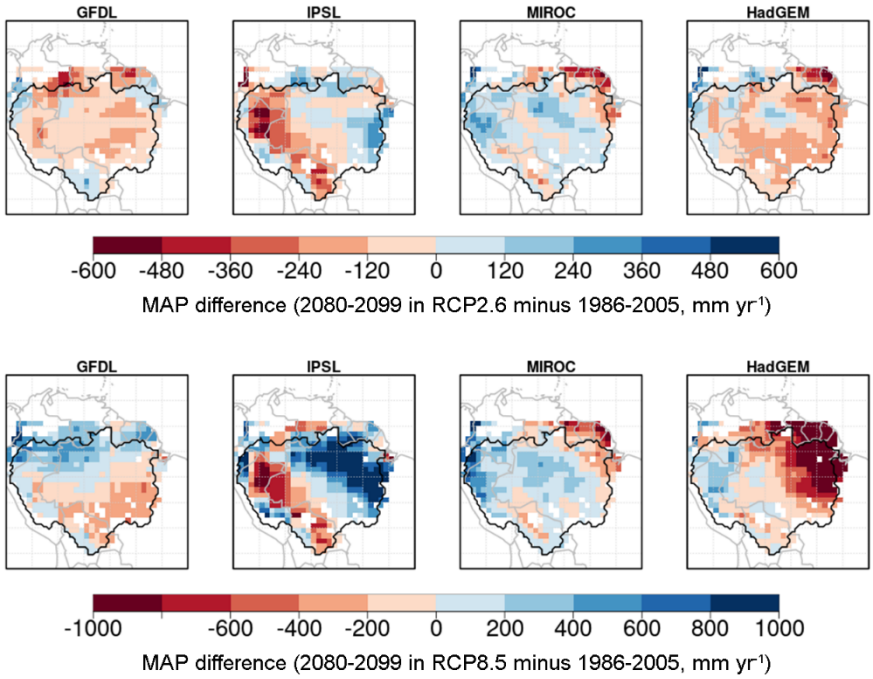

Figure 5.5 Similar to Figure 5.3 but for mean annual precipitation (MAP).

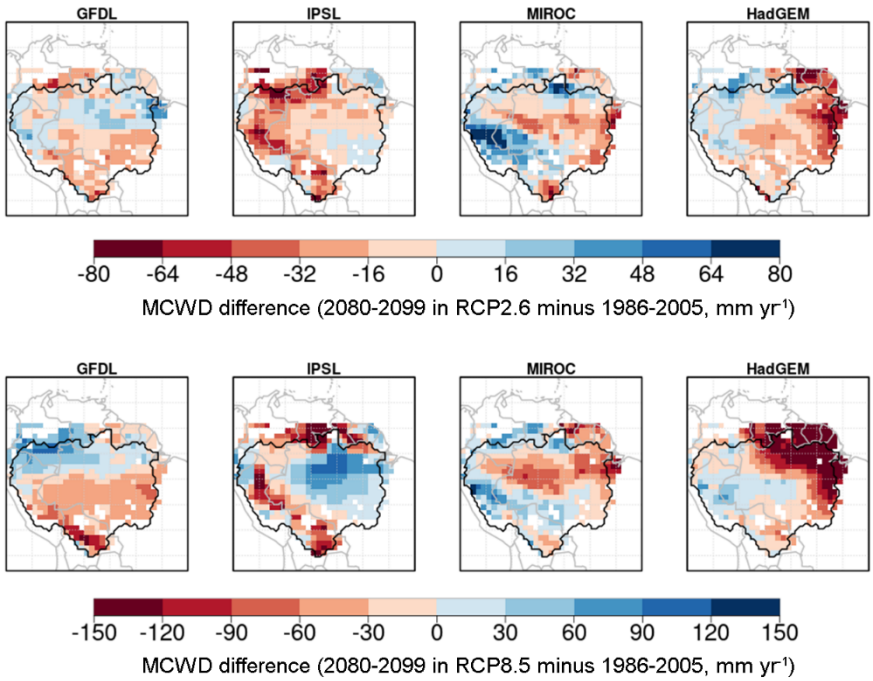

Figure 5.6 Similar to Figure 5.3 but for maximum cumulated water deficit (MCWD) after the bias correction.

5.5.2 Change of the biomass carbon sink

Figure 5.7 presents the distribution of △AGB in 20-yr period in historical period and the future, as shown by the area undergoing different magnitude of △AGB. By the end of the 21st century in RCP2.6 scenario, the area where the forest is a net carbon source is a bit more extensive in the GFDL simulation than the area remaining a carbon sink. For the net Amazon carbon balance, the source is almost equal to the sink in the period 2080-2099 (source: -0.7 PgC yr^{-1} v.s. sink: 0.8 PgC yr^{-1}). In comparison, the area being a carbon source is smaller than the one being a sink in MIROC, IPSL and HadGEM. In the IPSL and HadGEM models, regional sinks exceed sources and the Amazon remains a net carbon sink, comparable in magnitude to the historical period. In MIROC, the model gives a net carbon sink in the future but it is a carbon source in the historical period (unlike in the RAINFOR observations). In the RCP8.5 scenario, regional carbon sinks and sources both intensify, in wetting and drying regions respectively. HadGEM simulates a net carbon source across the whole Amazon of -0.26 PgC yr^{-1}, which is composed of a -0.37 PgC yr^{-1} carbon source mainly located in northeastern Amazon, which outweighs a 0.11 PgC yr^{-1} carbon sink in other regions (Figure 5.7). With regard to simulations forced by other three climate models (GFDL, IPSL and MIROC), they all predicts more carbon sink and less carbon source relative to that in historical period and their source area shrinks.

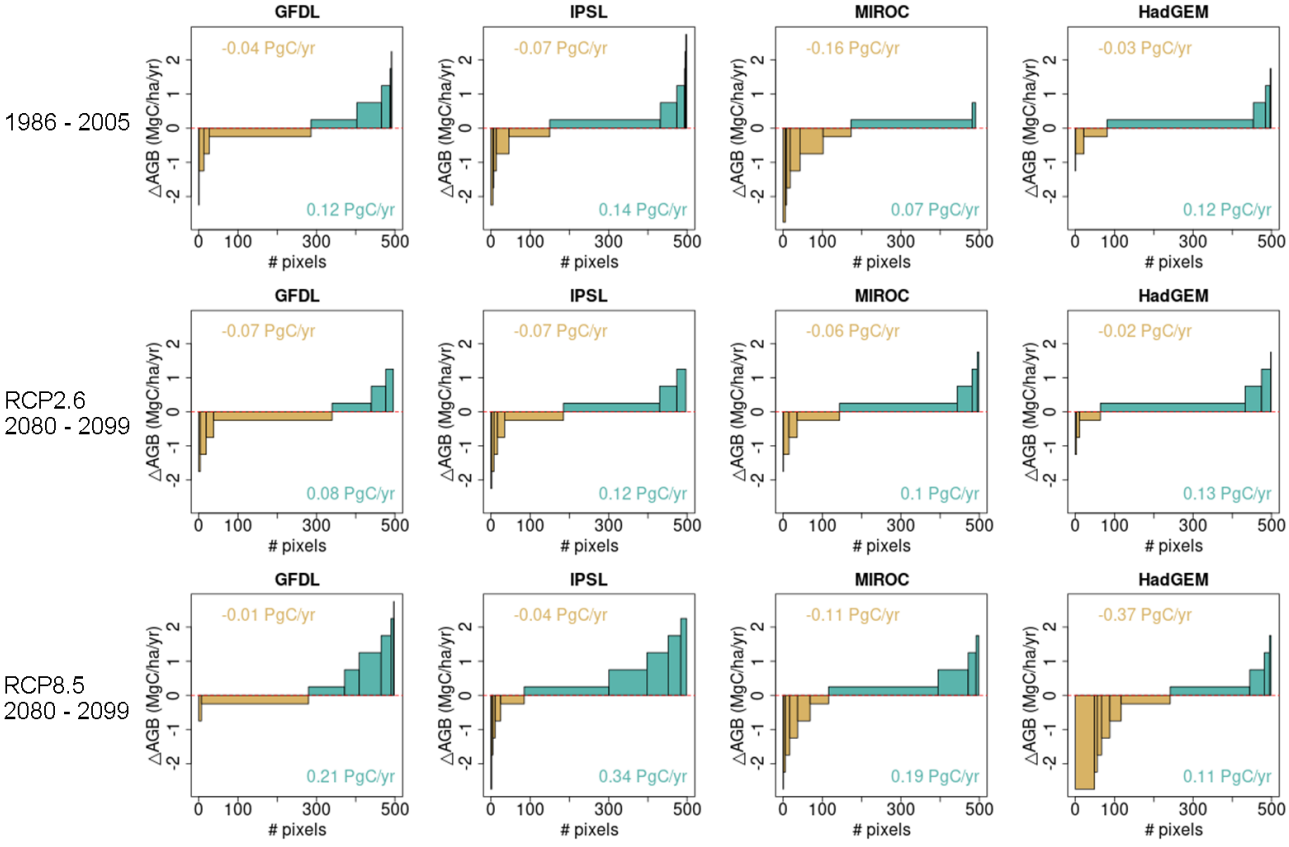

Figure 5.7 Net biomass carbon sink intensities during 2080-2099 and 1986-2005 (height of each rectangle) and the area (width of each rectangle) of different intensity categories, presenting as descending order of net carbon sink. Total carbon budget is labeled in the panel, separated by carbon source (dark-yellow color) and carbon sink (cyan).

Besides the comparison between two time periods, from Figure 5.8 we can see that there is large inter-annual variation of net biomass change over both the historical period and the future. By the end of the 21st century, years with positive and negative net biomass change appear alternatively in RCP2.6 scenario. The frequency distribution of carbon source and sinks in last 20 years in historical period and last 20 years in future is shown in Figure 5.9. In RCP2.6 scenario, the number of years in

source state does not increase relative to the historical period. In RCP8.5 scenario, the number of years in source state increases and the magnitude of carbon source also increases in Guiana Shield and East-central Amazon forced by HadGEM forcing. However, in RCP8.5 scenario, HadGEM forcing shows that since around 2045, Guiana Shield and East-Central Amazon turn to be net carbon sources. The western Amazon also becomes a carbon source in this model (which has a regional drying trend, Figure S1) after the middle of the 21st century, which will last for long time until the time around 2085, after which a weak carbon sink appears when carbon loss drops due to regional wetting trend (Figure S1). Although we only find such 'cross-over' in one simulation forced by HadGEM climate forcing, separating the contribution of climate change and CO_2 increase (with simulations forced by fix CO_2) should help to understand these "tipping points".

Then we look at model agreement on the prediction of net biomass change in detail. Figure 5.10 shows that in RCP2.6 scenario, simulations forced by the four climate models tend to agree on the sign of net biomass change in East-central Amazon and Guiana Shield, but diverge in the Western Amazon. In the RCP8.5 scenario, all simulations agree on weaker net biomass carbon sink in Western Amazon but disagree on the sign of the carbon balance of the Guiana Shield. Three models (GFDL, IPSL, and MIROC) predict same sign of positive on net biomass change in East-central Amazon and Brazilian Shield.

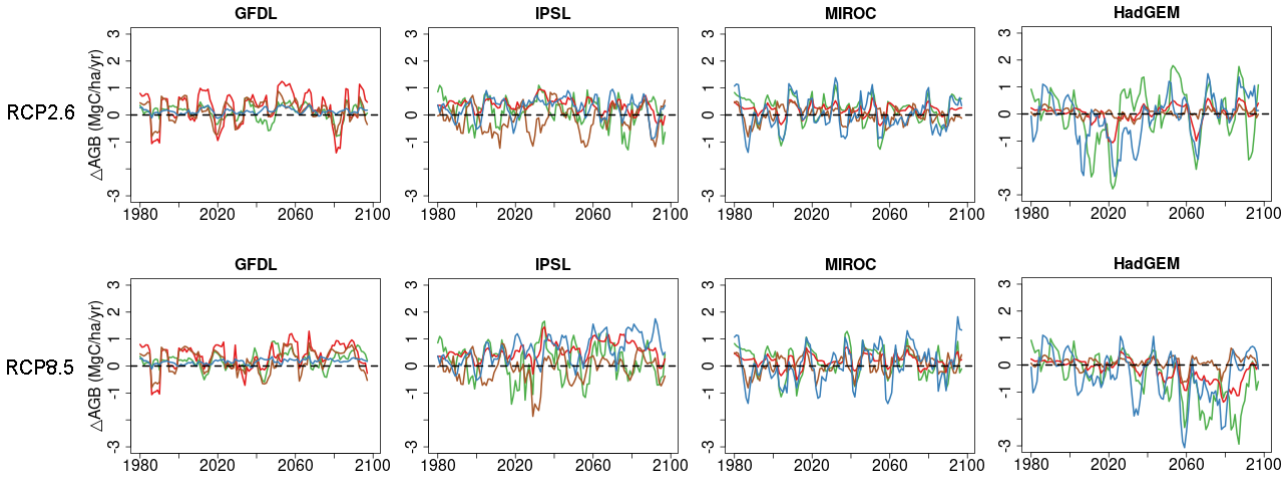

Figure 5.8 The rolling mean of net biomass change since 1980. The width of rolling window is 5yr. The color of lines in each panel denote four regions, Guiana Shield (green), East-central Amazon (red), Western Amazon (brown), and Brazilian Shield (blue).

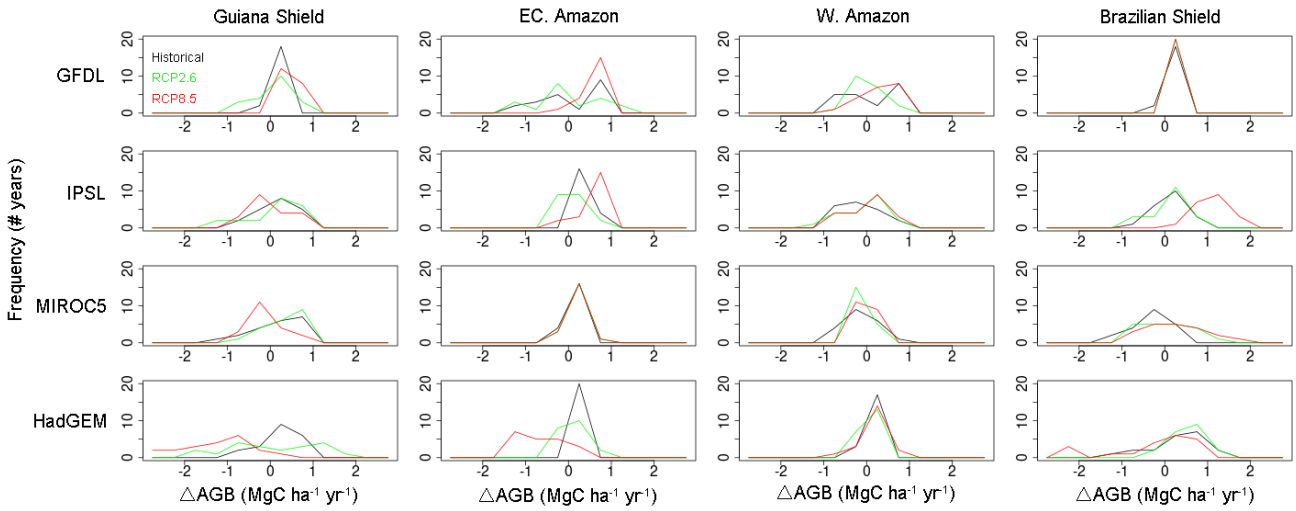

Figure 5.9 The frequency distribution of carbon source years and carbon sinks years. The comparison is made between last 20 years in historical period (1986-2005) and future (2080-2099).

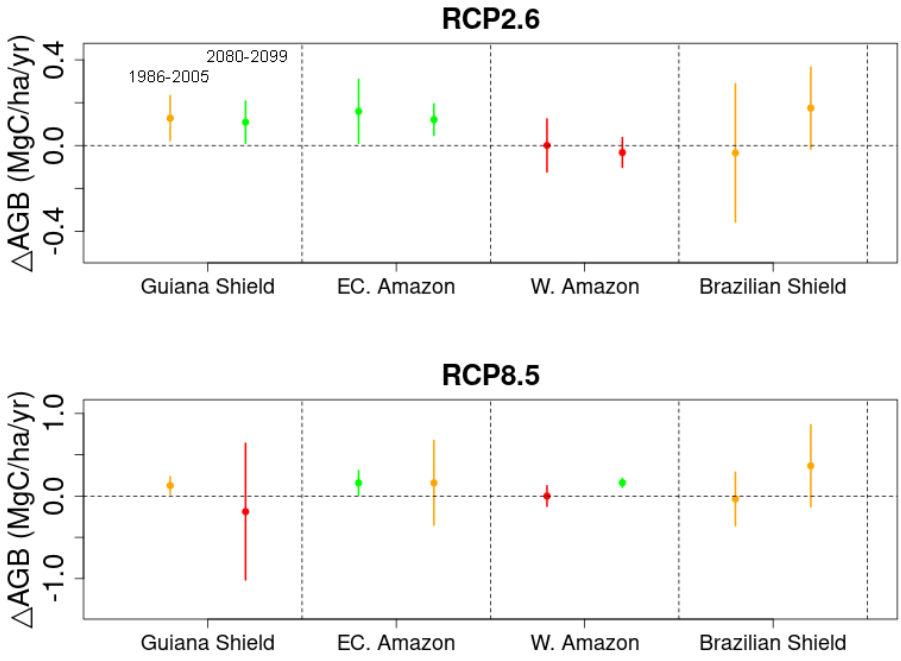

Figure 5.10 △AGB between the historical period (1986-2005) and future (2080-2099). The color of dots denote the agreement among models, where green means four models agree on the sign, orange means three models agree on the sign and red means two models agree on the sign.

5.5.3 Comparison of drought sensitivity between the past and the future

Model simulation forced by the ISIMIP historical forcing captured the negative relationship between net biomass change anomaly and MCWD anomaly as shown in Figure 5.11, where the drought sensitivity was derived from 2005 drought. The drought sensitivity simulated by CRUJRA forcing is about 2.0 MgC ha^{-1} of net carbon loss corresponding to 100mm increase in MCWD (Yao *et al.*, in prep). Here only three climate models captured the 2005 drought in the epicenter of western Amazon since droughts emerged from ISIMIP models are not synchronized with the real world. Model-derived drought sensitivity in the epicenter of western Amazon (-0.49 ~ -3.04 MgC ha^{-1} per 100mm increase in MCWD) is also comparable with the forest inventory plot analysis from Phillips *et al.* (2009), with more contribution from carbon loss than that of biomass growth (Figure 5.12).

However, since ISIMIP climate model also estimates severe water deficit in northeastern Amazon and southern Amazon, a highly negative sensitivity was also found in Guiana Shield and Brazilian Shield given their larger magnitude of MCWD anomaly (Figure 5.11).

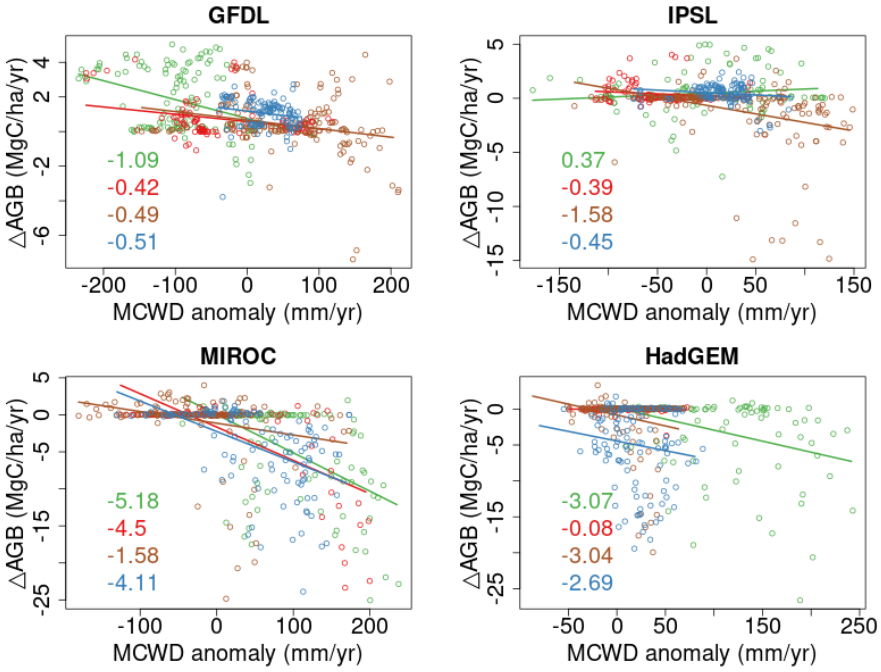

Figure 5.11 Net biomass change versus drought severity in 2005. Severity is defined from MCWD, with higher positive values denoting more acute water stress. The color of the points corresponds to four regions, green: Guiana Shield, red: East-Central Amazon, brown: Western Amazon, and blue: Brazilian Shield. The continuous lines denote the best model-fit for each region. Here, to be comparable with the plot in Phillips *et al.* (2009), positive MCWD anomaly means more severe water stress as an exception.

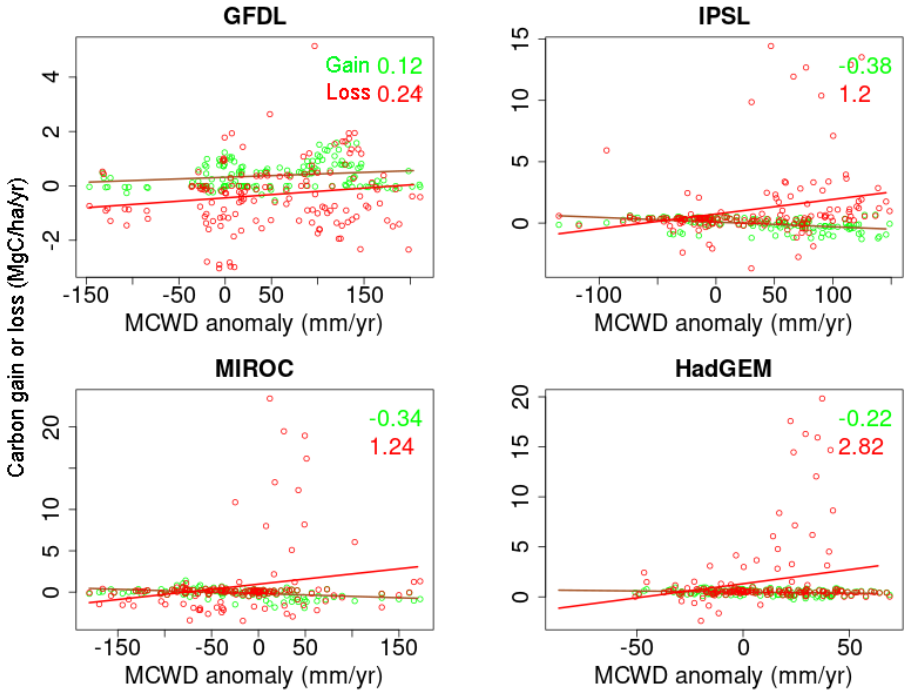

Figure 5.12 Biomass growth (green) and loss (red) versus drought severity in 2005 in epicenter of

western Amazon. The continuous lines denote the best model-fit for each carbon flux component. The drought sensitivity per 100mm increase in MCWD is labeled. Similar to Figure 5.11, to be comparable with the plot in Phillips *et al.* (2009), positive MCWD anomaly means more severe water stress as an exception.

For the future, given the large divergence of regional rainfall prediction among the four climate models, we still lack agreement on the occurrence of possible extreme events if we use Z score transformed MCWD as metrics. Here we take the simulation forced by HadGEM climate data as an example to show a shift of drought sensitivity in the future relative to that in the historical period. Figure 5.13 shows the change in △AGB corresponding to change in temperature and MCWD. It can be seen clearly that less water deficit (positive MCWD anomaly) and colder condition (negative temperature anomaly) benefits positive △AGB anomaly or more biomass carbon accumulation, for example, during the wet extremes in RCP2.6 scenario, as expected. When temperate anomalies turns to be higher and water deficit anomaly is more negative, negative △AGB anomaly appears in the bottom-right corner in panels presenting the dry extremes. As shown in Figure 5.13, it is an interesting phenomenon that the sensitivity of △AGB anomaly is not asymmetrical between the wet and dry extreme events no matter which period is considered (historical or future). Warmer-drier trend corresponds to more AGB loss than the AGB increase under colder-wetter condition.

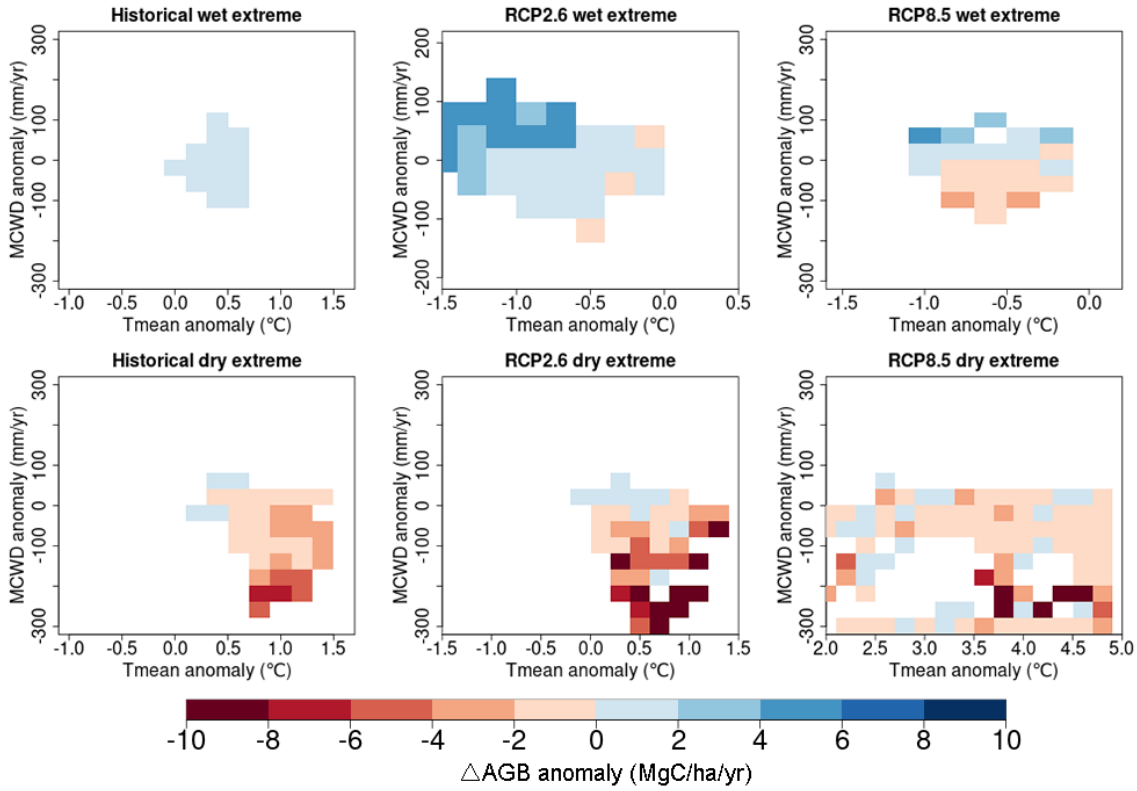

Figure 5.13 Composite maps showing △AGB anomaly corresponding to MCWD anomaly and temperature anomaly. Historical wet extreme refers to year 2003 and 2004. Historical dry extreme refers to year 1998 and 2005. RCP2.6 wet extreme refers to year 2096 and 2097. RCP2.6 dry extreme refers to year 2093 and 2094. RCP8.5 wet extreme refers to year 2048 and 2057. RCP8.5 dry extreme refers to year 2098 and 2099. Historical baseline period is 1862-2005. Baseline period for the future is 2006-2099. Negative MCWD anomaly denotes more severe water stress. Positive temperature anomaly denotes warmer condition. Blue box means the positive △AGB anomaly relative to the

baseline period, and red box the negative △AGB anomaly. The results shown in this figure is taken from simulation forced by HadGEM climate forcing.

5.6 DISCUSSION

5.6.1 Future drought risk

Future climate change over the Amazon shows a large uncertainty as evidenced by the spread among the four climate models we used from ISIMIP2b program (Frieler *et al.*, 2017), where the number of models is restricted by the strict climate data selection criterion. There seems to be however some agreement between models of the larger CMIP5 ensemble on an average rainfall decrease in the Amazon basin in the future. In the four models used, a warmer and drier tendency diagnosed from the air temperature and water deficit variables prevails in the future. This means a higher drought-induced tree mortality risk over this rainforest. To the best of our knowledge, this study is one of the first that predicts future changes in the Amazon rainforest biomass and tree dieback in response to drought with a process-based model incorporating a mechanistic hydraulic architecture coupled to an empirical tree mortality model, whose results compared well with forest inventory data for two recent droughts (Yao *et al.*, in prep). Without plant hydraulics related mortality, many process-based models did not reproduce the observed biomass loss and decrease of individual density with regard to observed field data at drought manipulation experiments (Powell *et al.*, 2013).

When forced by HadGEM climate forcing, we predict a higher tree mortality and correspondingly a greater biomass loss in northeastern and eastern Amazon, especially in the RCP8.5 scenario. This simulation shows a cross-over transition from carbon sink to source in the Guiana Shield and East-central Amazon by the middle of the 21st century. Such transition suggests a possible vulnerability in these regions of the Amazon. It is not unreasonable since eastern Amazonia tends to experience larger dry-season water stress (Duffy *et al.*, 2015; Malhi *et al.*, 2009), and also a faster warming trend and a greater water deficit reflected by MCWD. Several researches have investigated the future fate of Amazon basin. An earlier study by Poulter *et al.* (2010) used LPJml forced by 8 GCMs and found that both HadCM3 and HadGEM predicted large biomass loss over most Amazon basin by the end of the 21st century, where the competition-induced biomass carbon loss was considered. Huntingford *et al.* (2013) using the MOSES-TRIFFID land surface scheme forced by 22 climate models, predicted that Amazon intact rainforest carbon sinks will keep some resistance to climate change, where only one climate forcing (HadCM3) predicts the biomass loss till the end of the 21st century although this land surface model did not account for drought-induced tree mortality process. A more recent study by Shi *et al.* (2021) combined 5 process-based models and also 4 climate projections from ISIMIP2b, and found that high-emission end scenario would face carbon sink saturation whereas low-emission pathway would induce decline in carbon sink strength over almost whole Amazon basin in 2080-2099 relative to 1986-2005, where only one land surface model (improved LPJml) considered tree mortality depending on climate stress, tree density and growth vigor and other models resorted to constant metrics like turnover. The climate projections, their corresponding emission pathway and model structure all contribute to the uncertainty underlying the predictions of carbon sink strength evolution in Amazon rainforest.

Our prediction of possible loss in northeastern Amazon deserves further attention since the maximum tree height therein is the highest (Gorgens *et al.*, 2021) and taller trees importantly affect the local ecosystem functioning given their dominance in global carbon budget (Gora & Esquivel-Muelbert, 2021). The sensitivity of carbon dynamics related to tree height still has not reached consensus. On the one hand, the photosynthesis of tall trees in Amazonia was found to be less sensitive to rainfall inter-annual variability than the shorter one as evidenced by solar-induced fluorescence data, the mechanism proposed being that deeper root system of taller trees give them access to ground water (Giardina *et al.*, 2018). On the other hand, the narrower hydraulic safety

margin of taller trees suggested more vulnerable response to drought-induced water stress (Liu *et al.*, 2021a). From a drought manipulation experiment at Caxiuanã site, taller trees were found to have less negative Ψ_{50} and could die first (Rowland *et al.*, 2015). Therefore, the availability of deep soil water source and also the possible shift of intrinsic hydraulic characteristics co-determine the response of tall trees to future drought risks. Further efforts on analyzing the RAINFOR data to see if taller trees also die first during these mega droughts are required to fill the knowledge gap in identifying the relative importance of these two factors in shaping taller trees performance.

In this study, we find that warmer-drier trend appears in most of the Amazon basin although its intensity and geographic span vary among the four ISIMIP2b climate model projections and emission pathways. Since our model (ORCHIDEE-CAN-NHA) was calibrated against a drought experiment with only exclusion of rainfall, our 'calibrated' sensitivity to rain-out condition may be an underestimation relative to the reality since the field data did not consider combined effects of higher temperature and VPD with soil moisture deficits. Compound precipitation deficits and aridity events are largely co-occurring (Zhou *et al.*, 2019), in which mortality thresholds could be more rapidly reached than by soil water stress alone. The indirect effect of drought on stomatal closure was found to outweigh the direct negative biochemical response to high temperature as deduced from an experimental drought study (Smith *et al.*, 2020), which suggests that several degrees of temperature increase may still be tolerated by trees before the photosynthesis limitation occurs, although it is VPD rather than the high temperature that drives the photosynthesis decline in response to drought. Huntingford *et al.* (2013) used sensitivity simulations by perturbing only one factor of temperature, rainfall and atmospheric CO_2 to demonstrate that the predictions of the change in forest carbon across Amazon by the end of the 21st century were more sensitive to variation in temperature and atmospheric CO_2 concentration than to alteration in rainfall. Shi *et al.* (2021) found more negative sensitivity of carbon sink strength to temperature increase facing higher CO_2 levels in Amazon basin except the southwestern region but less distinct effect on precipitation sensitivity through factorial simulations. Besides the CO_2 fertilization effect on photosynthesis presented in models, Yao *et al.* (in prep) confirmed an alleviation of drought risk under current CO_2 concentration through a decline in the number of days with exposure to a mortality risk. However, manipulations on seedlings found that the time for plants to reach a water stress threshold during drought was not modified by the elevated CO_2 levels (Gattmann *et al.*, 2021). Nutrient limitations like phosphorus in tropics may inhibit the response of growth to elevated CO_2 although such limitation can also cause the decrease in water consumption in wet season thus benefit the productivity later in dry season to some extent (Goll *et al.*, 2018). Therefore, whether the stress alleviation of tree dieback from elevated CO_2 effect would persist or not remains to be tested through longer observation treatment or ongoing Amazon FACE.

The tree mortality risk can also be modulated by soil texture, where sandy soil tends to show greater resilience than that of clayed soil (Longo *et al.*, 2018). Yet, in reality soil texture also affects the nutrient availability, drainage state, and thus the biomass accumulation. For example, sand-rich soil performs poor in retaining nutrients, but such soil can be naturally selected for slow-growing trees that may invest more carbon into preservation of hydraulic safety (Oliveira *et al.*, 2019). With regard to the anticipation of the future drought sensitivity, plant water use strategies determined by hydraulic traits and soil texture should be greatly emphasized on improving the knowledge on forest response since soil hydraulics can also determine the degree of isohydricity (Javaux & Carminati, 2021). The further improvement of our model can therefore focus on such interactions between soil texture, nutrients and hydraulic safety.

5.6.2 Asymmetry of net biomass change between wet and dry years

In this study, the drought sensitivity of tree biomass in the future is found to be more negative than that in the past. This result suggests that taking past drought sensitivity to predict future drought

risk can underestimate negative impacts. Therefore, early warning signals referring to past drought sensitivity that can be used to presage the possible following tree dieback events should be treated with caution. Besides a trend of sensitivity over time, the contrast of sensitivity between wet and dry years is also found in our simulations, as evidenced by the net biomass change in wet extremes versus dry extremes as shown in Figure 5.11. Such nonlinear relationship between net biomass change and climate anomalies implies that carbon loss induced by a drought year is hardly compensated by gains from wet extremes, namely, a negative asymmetry. Not to mention the possible negative effects from wet events of unexpected flood that can trigger carbon source as well. Theoretically both dry and wet extremes impose negative effects on tree growth and tree mortality rate can thus be elevated in both cases. However, the sequential occurrence of wet and dry extremes can buffer their respective adverse effects, which is modulated by the water table depth or namely local soil hydrologic condition (Esteban *et al.*, 2021). Drought events lead to tree dieback and recovery can be slowed down whereas wet years without disturbances would contribute to more growth without too much positive legacy effect. Such nonlinear response to precipitation anomalies can also be modulated by the duration of events (Felton *et al.*, 2021) and also nutrient limitation (Goll *et al.*, 2018). Whether the legacy effects or compensatory effects dominates the forest response still requires further evidence of either field measurements or satellite detection, which can then be incorporated into process-based model.

5.6.3 Perspective for improving our projections

Post-extreme legacy. Legacy effects have not been captured by earth system models (Anderegg *et al.*, 2015), although satellite products confirmed their existence in the Amazon, like a decline in carbon sink several years after the drought (Yang *et al.*, 2018). Accumulative metrics or variables denoting memory effect should be analyzed to understand legacy tree growth in model simulation. Besides, acclimation to warmer or drier condition should be also considered as another aspect of legacy. Ignoring the adaptation mechanism would underestimate the ecosystem resilience (Singh *et al.*, 2022), which is the characteristic with the lowest recovery pace after disturbance (Poorter *et al.*, 2021).

Hydraulic traits. In the present paper, uncertainty of the predicted drought-induced mortality risk also lies in our setup of constant hydraulic traits for one PFT describing all intact rainforests, so that plant water regulation does not embody spatial or temporal variation. Both intra- and inter-species variation of hydraulic traits exist and temporal shift of trait also occurs depending on surrounding hydric condition. The Caxiuanã study found that resistant species had more negative Ψ_{50} value and were less vulnerable to the water stress (Rowland *et al.*, 2015). The growth of hydraulic-stressed trees was more affected by their hydraulic traits rather than by their allocation-related traits (Rowland *et al.*, 2021). Variation of hydraulic traits is also linked to ecosystem community composition (Lourenço Junior *et al.*, 2022). Therefore, more comprehensive plant trait data could be assimilated into a model like ORCHIDEE-CAN-NHA to define a more realistic hydraulic response, for example, starting with isohydric or anisohydric characteristics.

We acknowledge that uncertainties associated with future climate signals and in the sensitivity of forest response both affect the spread of projections. Huntingford *et al.* (2013) found that it is the physiological processes of DGVMs, or namely the implicitly-formulated sensitivity, rather than uncertainties among climate projections, that dominated the uncertainties in future carbon storage trajectory. To further clarify the impact of drought on Amazon intact forests, more collaboration between experimentalists and modelers remains necessary, with ground-based truth of field campaigns, and inventories data collected during and after droughts. Considering the projected increase in the intensity and frequency of drought events in the 21st century and possible corresponding tree mortality, strategies should be developed and implemented to manage risks and improve the ecosystem adaption capacity.

5.7 CONCLUSION

A process-based model incoporating plant hydraulics and both self-thinning and drought induced tree mortality, ORCHIDEE-CAN-NHA, was forced by historical climate reconstruction and bias-corrected future climtae forcing from ISIMIP-2 program to predict the future biomass carbon dynamics and tree mortality risk over the Amazon rainforest from 2015-2100. The future climate evolution in Amazon shows a widespread warming trend, although its magnitude varies among climate models. A pronounced increase in the maximum cumulated water deficit (MCWD) is also found, but different regional patterns emerged from the four climate models. The only consistent signal in MCWD pattern is a drier trend in the northeastern Amazon. Compared to the historical drought in 2005, the MCWD anomalies during future drought years can be more negative. The sensitivity of net biomass change to drought also becomes more negative in the future, corresponding to a reduction in the net biomass sink facing continuous warming and higher water deficits. The simulation forced by the HadGEM climate model in RCP8.5 scenario, showed the most pronounced Amazon drying, especially in the eastern Amazon and northeastern Amazon, with cross-over point at which the regional carbon sinks turn to carbon sources in Guiana Shield and East-central Amazon that could be reached in the middle of the 21st century. This study makes an important step forward by providing a spatial image of the likelihood of drought risks and predicting the evolution of future Amazon rainforest net carbon balance, by resorting to a well-calibrated model that incorporates hydraulic failure induced tree mortality, and subsequent recovery from demographic processes, including recruitment and growth of survivor trees. The predicted possible vulnerability state of Amazon rainforest required further investigation and concerns on mitigation policies.

5.8 REFERENCES

Ahlström, A., Canadell, J.G., Schurgers, G., Wu, M., Berry, J.A., Guan, K. & Jackson, R.B. Hydrologic resilience and Amazon productivity. *Nature communications*, **8**, 1-9, 2017.

Anderegg, W.R., Schwalm, C., Biondi, F., Camarero, J.J., Koch, G., Litvak, M., Ogle, K., Shaw, J.D., Shevliakova, E. & Williams, A. Pervasive drought legacies in forest ecosystems and their implications for carbon cycle models. *Science*, **349**, 528-532, 2015.

Brienen, R.J., Phillips, O.L., Feldpausch, T.R., Gloor, E., Baker, T.R., Lloyd, J., Lopez-Gonzalez, G., Monteagudo-Mendoza, A., Malhi, Y. & Lewis, S.L. Long-term decline of the Amazon carbon sink. *Nature*, **519**, 344-348, 2015.

Bugmann, H., Seidl, R., Hartig, F., Bohn, F., Brůna, J., Cailleret, M., François, L., Heinke, J., Henrot, A.J. & Hickler, T. Tree mortality submodels drive simulated long-term forest dynamics: assessing 15 models from the stand to global scale. *Ecosphere*, **10**, e02616, 2019.

Cox, P.M., Pearson, D., Booth, B.B., Friedlingstein, P., Huntingford, C., Jones, C.D. & Luke, C.M. Sensitivity of tropical carbon to climate change constrained by carbon dioxide variability. *Nature*, **494**, 341-344, 2013.

Doughty, C.E., Metcalfe, D., Girardin, C., Amezquita, F.F., Cabrera, D.G., Huasco, W.H., Silva-Espejo, J., Araujo-Murakami, A., Da Costa, M. & Rocha, W. Drought impact on forest carbon dynamics and fluxes in Amazonia. *Nature*, **519**, 78-82, 2015.

Duffy, P.B., Brando, P., Asner, G.P. & Field, C.B. Projections of future meteorological drought and wet periods in the Amazon. *Proceedings of the National Academy of Sciences*, **112**, 13172-13177, 2015.

Esteban, E.J., Castilho, C.V., Melgaço, K.L. & Costa, F.R. The other side of droughts: wet extremes and topography as buffers of negative drought effects in an Amazonian forest. *New Phytologist*, **229**, 1995-2006, 2021.

Feldpausch, T., Phillips, O., Brienen, R., Gloor, E., Lloyd, J., Lopez-Gonzalez, G., Monteagudo-Mendoza, A., Malhi, Y., Alarcón, A. & Dávila, E.Á. Amazon forest response to repeated droughts. *Global Biogeochemical Cycles*, **30**, 964-982, 2016.

Feldpausch, T.R., Banin, L., Phillips, O.L., Baker, T.R., Lewis, S.L., Quesada, C.A., Affum-Baffoe, K., Arets, E.J., Berry, N.J. & Bird, M. Height-diameter allometry of tropical forest trees. *Biogeosciences*, **8**, 1081-1106, 2011.

Feldpausch, T.R., Lloyd, J., Lewis, S.L., Brienen, R.J., Gloor, M., Monteagudo Mendoza, A., Lopez-Gonzalez, G., Banin, L., Abu Salim, K. & Affum-Baffoe, K. Tree height integrated into pantropical forest biomass estimates. *Biogeosciences*, **9**, 3381-3403, 2012.

Felton, A.J., Knapp, A.K. & Smith, M.D. Precipitation–productivity relationships and the duration of precipitation anomalies: An underappreciated dimension of climate change. *Global Change Biology*, **27**, 1127-1140, 2021.

Frieler, K., Lange, S., Piontek, F., Reyer, C.P., Schewe, J., Warszawski, L., Zhao, F., Chini, L., Denvil, S. & Emanuel, K. Assessing the impacts of 1.5 C global warming–simulation protocol of the Inter-Sectoral Impact Model Intercomparison Project (ISIMIP2b). *Geoscientific Model Development*, **10**, 4321-4345, 2017.

Gatti, L.V., Basso, L.S., Miller, J.B., Gloor, M., Domingues, L.G., Cassol, H.L., Tejada, G., Aragão, L.E., Nobre, C. & Peters, W. Amazonia as a carbon source linked to deforestation and climate change. *Nature*, **595**, 388-393, 2021.

Gattmann, M., Birami, B., Nadal Sala, D. & Ruehr, N.K. Dying by drying: timing of physiological stress thresholds related to tree death is not significantly altered by highly elevated CO2. *Plant, cell & environment*, **44**, 356-370, 2021.

Giardina, F., Konings, A.G., Kennedy, D., Alemohammad, S.H., Oliveira, R.S., Uriarte, M. & Gentine, P. Tall Amazonian forests are less sensitive to precipitation variability. *Nature Geoscience*, **11**, 405-409, 2018.

Gleason, S.M., Westoby, M., Jansen, S., Choat, B., Hacke, U.G., Pratt, R.B., Bhaskar, R., Brodribb, T.J., Bucci, S.J. & Cao, K.F. Weak tradeoff between xylem safety and xylem-specific hydraulic efficiency across the world's woody plant species. *New Phytologist*, **209**, 123-136, 2016.

Goll, D.S., Joetzjer, E., Huang, M. & Ciais, P. Low phosphorus availability decreases susceptibility of tropical primary productivity to droughts. *Geophysical Research Letters*, **45**, 8231-8240, 2018.

Gora, E.M. & Esquivel-Muelbert, A. Implications of size-dependent tree mortality for tropical forest carbon dynamics. *Nature Plants*, 1-8, 2021.

Gorgens, E.B., Nunes, M.H., Jackson, T., Coomes, D., Keller, M., Reis, C.R., Valbuena, R., Rosette, J., de Almeida, D.R. & Gimenez, B. Resource availability and disturbance shape maximum tree height across the Amazon. *Global Change Biology*, **27**, 177-189, 2021.

Hansen, M.C., Potapov, P.V., Moore, R., Hancher, M., Turubanova, S.A., Tyukavina, A., Thau, D.,

Stehman, S.V., Goetz, S.J. & Loveland, T.R. High-resolution global maps of 21st-century forest cover change. *science*, **342**, 850-853, 2013.

Hempel, S., Frieler, K., Warszawski, L., Schewe, J. & Piontek, F. A trend-preserving bias correction–the ISI-MIP approach. *Earth System Dynamics*, **4**, 219-236, 2013.

Huntingford, C., Zelazowski, P., Galbraith, D., Mercado, L.M., Sitch, S., Fisher, R., Lomas, M., Walker, A.P., Jones, C.D. & Booth, B.B. Simulated resilience of tropical rainforests to CO 2-induced climate change. *Nature Geoscience*, **6**, 268-273, 2013.

Javaux, M. & Carminati, A. Soil hydraulics affect the degree of isohydricity. *Plant Physiology*, **186**, 1378-1381, 2021.

Kennedy, D., Swenson, S., Oleson, K.W., Lawrence, D.M., Fisher, R., Lola da Costa, A.C. & Gentine, P. Implementing plant hydraulics in the community land model, version 5. *Journal of Advances in Modeling Earth Systems*, **11**, 485-513, 2019.

Kukla, T., Ahlström, A., Maezumi, S.Y., Chevalier, M., Lu, Z., Winnick, M.J. & Chamberlain, C.P. The resilience of Amazon tree cover to past and present drying. *Global and Planetary Change*, **202**, 103520, 2021.

Liu, L., Chen, X., Ciais, P., Yuan, W., Maignan, F., Wu, J., Piao, S., Wang, Y.P., Wigneron, J.P. & Fan, L. Tropical tall forests are more sensitive and vulnerable to drought than short forests. *Global change biology*, 2021a.

Liu, Q., Peng, C., Schneider, R., Cyr, D., Liu, Z., Zhou, X. & Kneeshaw, D. TRIPLEX-Mortality model for simulating drought-induced tree mortality in boreal forests: Model development and evaluation. *Ecological Modelling*, **455**, 109652, 2021b.

Liu, Y., Kumar, M., Katul, G.G. & Porporato, A. Reduced resilience as an early warning signal of forest mortality. *Nature Climate Change*, **9**, 880-885, 2019.

Longo, M., Knox, R.G., Levine, N.M., Alves, L.F., Bonal, D., Camargo, P.B., Fitzjarrald, D.R., Hayek, M.N., Restrepo-Coupe, N. & Saleska, S.R. Ecosystem heterogeneity and diversity mitigate Amazon forest resilience to frequent extreme droughts. *New Phytologist*, **219**, 914-931, 2018.

Lourenço Junior, J., Enquist, B.J., von Arx, G., Sonsin-Oliveira, J., Morino, K., Thomaz, L.D. & Milanez, C.R.D. Hydraulic tradeoffs underlie local variation in tropical forest functional diversity and sensitivity to drought. *New Phytologist*, **n/a**, https://doi.org/10.1111/nph.17944, 2022.

Malhi, Y., Aragão, L.E., Galbraith, D., Huntingford, C., Fisher, R., Zelazowski, P., Sitch, S., McSweeney, C. & Meir, P. Exploring the likelihood and mechanism of a climate-change-induced dieback of the Amazon rainforest. *Proceedings of the National Academy of Sciences*, **106**, 20610-20615, 2009.

Nychka D, F.R., Paige J, Sain S, Gerber F., Iverson M. Fields: Tools for Spatial Data

University Corporation for Atmospheric Research, Boulder, CO, USA *10.5065/D6W957CT*

URL: https://github.com/NCAR/Fields. R package version 10.3, 2020.

Oliveira, R.S., Costa, F.R., van Baalen, E., de Jonge, A., Bittencourt, P.R., Almanza, Y., Barros, F.d.V., Cordoba, E.C., Fagundes, M.V. & Garcia, S. Embolism resistance drives the distribution of Amazonian rainforest tree species along hydro-topographic gradients. *New Phytologist*, **221**, 1457-1465, 2019.

Papastefanou, P., Zang, C.S., Angelov, Z., de Castro, A.A., Jimenez, J.C., De Rezende, L.F.C., Ruscica, R., Sakschewski, B., Sörensson, A. & Thonicke, K. Quantifying the spatial extent and intensity of recent extreme drought events in the Amazon rainforest and their impacts on the carbon cycle. *Biogeosciences Discussions*, 1-37, 2020.

Parsons, L. Implications of CMIP6 projected drying trends for 21st century Amazonian drought risk. *Earth's Future*, **8**, e2020EF001608, 2020.

Peng, R.D. Package 'simpleboot'. *https://github.com/rdpeng/simpleboot*, 2019.

Phillips, O.L., Aragão, L.E., Lewis, S.L., Fisher, J.B., Lloyd, J., López-González, G., Malhi, Y., Monteagudo, A., Peacock, J. & Quesada, C.A. Drought sensitivity of the Amazon rainforest. *Science*, **323**, 1344-1347, 2009.

Phillips, O.L. & Brienen, R.J. Carbon uptake by mature Amazon forests has mitigated Amazon nations' carbon emissions. *Carbon balance and management*, **12**, 1-9, 2017.

Pierce, D. (2019) Package 'ncdf4' http://cirrus.ucsd.edu/~pierce/ncdf. In:

Poorter, L., Craven, D., Jakovac, C.C., van der Sande, M.T., Amissah, L., Bongers, F., Chazdon, R.L., Farrior, C.E., Kambach, S. & Meave, J.A. Multidimensional tropical forest recovery. *Science*, **374**, 1370-1376, 2021.

Poulter, B., Hattermann, F., Hawkins, E., Zaehle, S., Sitch, S., RESTREPO-COUPE, N., Heyder, U. & Cramer, W. Robust dynamics of Amazon dieback to climate change with perturbed ecosystem model parameters. *Global Change Biology*, **16**, 2476-2495, 2010.

Powell, T.L., Galbraith, D.R., Christoffersen, B.O., Harper, A., Imbuzeiro, H.M., Rowland, L., Almeida, S., Brando, P.M., da Costa, A.C.L. & Costa, M.H. Confronting model predictions of carbon fluxes with measurements of Amazon forests subjected to experimental drought. *New Phytologist*, **200**, 350-365, 2013.

Rowland, L., da Costa, A.C.L., Galbraith, D.R., Oliveira, R., Binks, O.J., Oliveira, A., Pullen, A., Doughty, C., Metcalfe, D. & Vasconcelos, S. Death from drought in tropical forests is triggered by hydraulics not carbon starvation. *Nature*, **528**, 119-122, 2015.

Rowland, L., Oliveira, R.S., Bittencourt, P.R., Giles, A.L., Coughlin, I., Costa, P.d.B., Domingues, T., Ferreira, L.V., Vasconcelos, S.S. & Junior, J.A. Plant traits controlling growth change in response to a drier climate. *New Phytologist*, **229**, 1363-1374, 2021.

Saatchi, S., Longo, M., Xu, L., Yang, Y., Abe, H., Andre, M., Aukema, J.E., Carvalhais, N., Cadillo-Quiroz, H. & Cerbu, G.A. Detecting vulnerability of humid tropical forests to multiple stressors. *One Earth*, **4**, 988-1003, 2021.

Shi, H., Tian, H., Pan, N., Reyer, C.P., Ciais, P., Chang, J., Forrest, M., Frieler, K., Fu, B. & Gädeke, A. Saturation of global terrestrial carbon sink under a high warming scenario. *Global Biogeochemical Cycles*, **35**, e2020GB006800, 2021.

Singh, C., van der Ent, R., Wang-Erlandsson, L. & Fetzer, I. Hydroclimatic adaptation critical to the resilience of tropical forests. *Global Change Biology*, **n/a**, https://doi.org/10.1111/gcb.16115, 2022.

Smith, M.N., Taylor, T.C., van Haren, J., Rosolem, R., Restrepo-Coupe, N., Adams, J., Wu, J., de Oliveira, R.C., da Silva, R. & de Araujo, A.C. Empirical evidence for resilience of tropical forest photosynthesis in a warmer world. *Nature plants*, **6**, 1225-1230, 2020.

Smith, R.J., Singarayer, J.S. & Mayle, F.E. Response of Amazonian forests to mid-Holocene drought: A model-data comparison. *Global Change Biology*, **28**, 201-226, 2022.

Trugman, A.T. Integrating plant physiology and community ecology across scales through trait-based models to predict drought mortality. *New Phytologist*, 2021.

Trugman, A.T., Anderegg, L.D., Anderegg, W.R., Das, A.J. & Stephenson, N.L. Why is tree drought mortality so hard to predict? *Trends in Ecology & Evolution*, 2021.

Vogel, M.M., Hauser, M. & Seneviratne, S.I. Projected changes in hot, dry and wet extreme events' clusters in CMIP6 multi-model ensemble. *Environmental Research Letters*, **15**, 094021, 2020.

Werth, D. & Avissar, R. The regional evapotranspiration of the Amazon. *Journal of Hydrometeorology*, **5**, 100-109, 2004.

Xu, X., Medvigy, D., Powers, J.S., Becknell, J.M. & Guan, K. Diversity in plant hydraulic traits explains seasonal and inter-annual variations of vegetation dynamics in seasonally dry tropical forests. *New Phytologist*, **212**, 80-95, 2016.

Xu, X., Konings, A.G., Longo, M., Feldman, A., Xu, L., Saatchi, S., Wu, D., Wu, J. & Moorcroft, P. Leaf surface water, not plant water stress, drives diurnal variation in tropical forest canopy water content. *New Phytologist*, 2021.

Yang, Y., Saatchi, S.S., Xu, L., Yu, Y., Choi, S., Phillips, N., Kennedy, R., Keller, M., Knyazikhin, Y. & Myneni, R.B. Post-drought decline of the Amazon carbon sink. *Nature communications*, **9**, 1-9, 2018.

Yao, Y., Joetzjer, E., Ciais, P., Viovy, N., Cresto Aleina, F., Chave, J., Sack, L., Bartlett, M., Meir, P. & Fisher, R. Forest fluxes and mortality response to drought: model description (ORCHIDEE-CAN-NHA, r7236) and evaluation at the Caxiuanã drought experiment. *Geoscientific Model Development Discussions*, 1-38, 2021.

Yao, Y., Ciais, P., Viovy, N. & Joetzjer, E. How drought events during the last Century have impacted biomass carbon in Amazonian rainforests. in prep.

Zemp, D.C., Schleussner, C.-F., Barbosa, H.M., Hirota, M., Montade, V., Sampaio, G., Staal, A., Wang-Erlandsson, L. & Rammig, A. Self-amplified Amazon forest loss due to vegetation-atmosphere feedbacks. *Nature communications*, **8**, 1-10, 2017.

Zhang, K., de Almeida Castanho, A.D., Galbraith, D.R., Moghim, S., Levine, N.M., Bras, R.L., Coe, M.T., Costa, M.H., Malhi, Y. & Longo, M. The fate of Amazonian ecosystems over the coming century arising from changes in climate, atmospheric CO 2, and land use. *Global change biology*, **21**, 2569-2587, 2015.

Zhou, S., Williams, A.P., Berg, A.M., Cook, B.I., Zhang, Y., Hagemann, S., Lorenz, R., Seneviratne,

S.I. & Gentine, P. Land–atmosphere feedbacks exacerbate concurrent soil drought and atmospheric aridity. *Proceedings of the National Academy of Sciences*, **116**, 18848-18853, 2019.

5.9 SUPPLEMENTARY INFORMATION

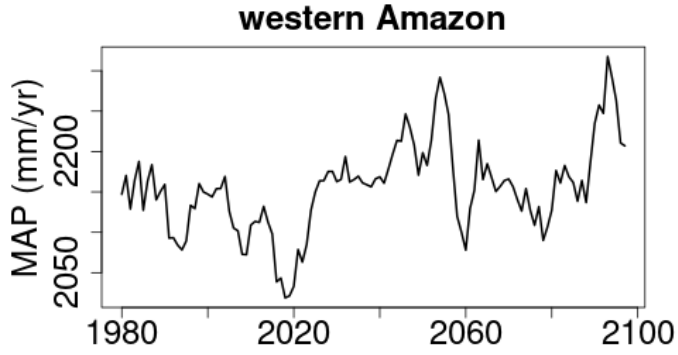

Figure S1 Mean annual precipitation (MAP) in western Amazon since 1980. Here only HadGEM climate model is shown.

6 CONCLUSIONS AND PERSPECTIVES

6.1 CONCLUSIONS

In summary, the motivation behind this research was that large uncertainty exists in the simulation behavior of soil carbon and biomass dynamics and net carbon fluxes with process-based models over the Amazon intact forests regarding their response to drought. The absence of hydraulic water transport processes in trees and tree mortality is hypothesized to be a major gap of most current models. Further the response of soil carbon decomposition to water and temperature is parametric, often calibrated based on data from temperate and boreal systems. This thesis improved our knowledge on soil heterotrophic respiration (SHR), a critical flux component of soil-atmosphere carbon exchange, and improved the process-based model ORCHIDEE-CAN by implementing a new mechanistic tree hydraulic architecture coupled to stand demography, and a tree mortality sub-model linked to the xylem dysfunction. This model was applied over the Amazon basin for intact forests to evaluate the long-term net biomass carbon sink trends and drivers, the drought sensitivity of biomass, and to identify the areas with greater mortality risk that may push those intact forests to reach a "tipping point", namely, when carbon sink turns to carbon source in the face of droughts. Gridded SHR estimates were established through upscaling of site-level SHR observation with Random Forest algorithm and multiple environmental predictors (Chapter 2). For the implementation of the mechanistic hydraulic architecture and tree mortality scheme, I calibrated the ORCHIDEE-CAN-NHA model (short for New Hydraulic Architecture) against the world's longest-running drought manipulation experiment at Caxiuana in the eastern Brazilian Amazon. The model after calibration was integrated to evaluate the long-term change in net carbon fluxes across the basin, ignoring land use change and degradation and thus focusing on the response of intact forests to climate (Chapter 3). Through the application of the calibrated model ORCHIDEE-CAN-NHA over the intact rainforest, I evaluated the long-term net forest biomass carbon balance, the drought sensitivity of biomass, the impacts of past severe drought events and separated the effects of climate change and elevated CO_2 based on historical factorial simulation since 1901 (Chapter 4). Following, this chapter the ORCHIDEE-CAN-NHA model was further applied to predict the evolution of future forest biomass net carbon balance and detect vulnerable regions a with more extensive tree mortality risk (Chapter 5).

In answer to the first question posed in the introduction, **how does the tropical soil heterotrophic respiration (SHR) respond to climate variability?** Since the net carbon flux is the balance between change in soil carbon storage and biomass dynamics, we tried to improve our knowledge on soil carbon dynamics in tropical rainforest. I upscaled site-level SHR observation to regional scale and further investigated the drivers for the inter-annual variability (IAV) of annual SHR, particularly for tropical forests. Temperature dominates the SHR IAV in tropical forest, opposite to the results of the TRENDYv6 global dynamic vegetation models, whose ensemble mean has a higher importance of water availability. The positive temperature sensitivity and the negative precipitation sensitivity of SHR in the Amazon basin imply that future warming and local drying would induce more soil carbon loss if the current observation-based sensitivity can be assumed to prevail in the future. The overall carbon sink capacity would thus be highly threatened if there is no significant enhancement in productivity. To reduce the SHR uncertainty and strengthen our ability to investigate the current patterns of SHR and its future evolution in the Amazon forests, where few SHR observations are available until now, more site-level observations, including measurement of temporal changes during droughts (Werner *et al.*, 2021) is indispensable and deep learning that can maximize the usage of available observations should be encouraged.

In answer to the second question: **how to simulate the plant hydraulics and estimate the tree**

mortality rate in process-based models? I implemented a new mechanistic hydraulic architecture in the process-based model ORCHIDEE-CAN-NHA and calibrated it against the field measurements of the drought manipulation experiment of Caxiuanã, in eastern Amazon, with both a control (CTL) and a throughfall exclusion experiment setup (TFE). The mechanistic hydraulic architecture deterministic model tracks the vertical water flow along the water potential gradient from soil to the atmosphere following Darcy's law with node at leaf, stem and root, as well as water in / out plant water storage pools regulated by water capacitances and water potential changes between two consecutive time steps. The hydraulic conductance is not constant but it varies following changes in water potential. The model approximates the occurrence of xylem cavitation through a percentage loss of stem conductance above a given threshold (PLC). A simpler tree mortality sub-model was added by including two empirical parameters, a drought exposure threshold that defines the time period experiencing high PLC as a condition to trigger tree die-back, and a tree mortality fraction under drought exposure function of tree diameter classes. These two parameters are tuned against the observed mortality rate in Caxiuanã site for different tree size cohorts, and the mortality scheme was validated against another TFE experiment (Tapajos), which demonstrated the robustness of the approach. Our model can reproduce the biomass loss under the TFE conditions, especially the large biomass drop and the death of the largest trees that was observed after 4 years of rain-out in 2005. There is still a model-observation misfit in estimation of annual mortality rate, and the underestimation of mortality rate in small trees (DBH < 20cm) contributes the most to this uncertainty since this group contains most plant individuals in stand. Only one set of hydraulic traits parameters was tested at Caxiuanã in our model simulation. Inclusion of spatially variable hydraulic traits, reflecting different tree species and resistance / resilience strategies to drought would improve the generalization of model performance, especially to reproduce finer-scale response from isohydric to anisohydric behaviors, which can now be inferred from satellite microwave measurements (Konings & Gentine, 2017).

In answer to the third question: **to what extent the model that I developed can capture the long-term net forest biomass carbon trends over Amazon basin and how drought impacts biomass growth and mortality**? I applied ORCHIDEE-CAN-NHA incorporating mechanistic hydraulic architecture and tree mortality sub-model over intact rainforest in Amazon basin, to simulate the long-term trend of forest biomass carbon gains, carbon losses and net carbon balance, drought sensitivities and separate the effects of climate change and rising CO_2 concentration. Model simulation shows a decline in net forest biomass carbon sink caused by quicker rise of biomass mortality loss than the decelerating tree growth, which matches the fundamental observation from 30 years of forest plots monitoring, a slow-down of the carbon sink that very few DGVM models can reproduce. The modeled drought sensitivity of the net biomass change (growth minus mortality) to cumulated water deficit is also shown to be comparable with forest plot observations from the RAINFOR network sampled around the 2005 drought. Among the top eight drought events during the last century, 2015/16 is the most severe event regarding either the area that underwent the most intense drought risk or the area that suffered the largest biomass mortality. Based on factorial simulation that separates the contribution of climate change and elevated CO_2 on forest biomass dynamics, alleviation of water stress is indeed found from elevated CO_2, manifested as a shorter time period experiencing mortality risk when CO_2 concentration increases. To our knowledge, our model is one of the first DGVMs that can capture the essential signal of decelerating net forest biomass carbon sink over Amazon basin, which opens a "window for future" for exploring the future fate of the carbon sink capacity in intact rainforests.

In answer to the fourth questions, **is there a tipping point of net forest biomass carbon sink and when would it occur over the Amazonian intact rainforest?** The ORCHIDEE-CAN-NHA was forced by historical climate reconstruction and bias-corrected future climate forcing data from the ISIMIP-2 program, considering two scenarios and four different climate models, in order to project biomass changes in the Amazon rainforest from 2015 to 2100. Future warming is

unambiguous and widespread, although its regional magnitude varies among climate models. Changes in the maximum cumulated water deficit (MCWD) indicate that climate models present different wetting-drying patterns, but that most of them consistently predict drier trend in northeastern Amazon. Compared to the historical drought in 2005 taken as a reference, the MCWD during future drought years is simulated to be more intense. The sensitivity of net biomass change to drought also becomes more negative, as evidenced by more negative net biomass sink anomalies corresponding to warming and higher water stress. The simulation forced by the HadGEM climate model in the RCP8.5 scenario had the most distinct drying in eastern and northeastern Amazon. Especially, it showed a cross-over point of carbon sink turning to a carbon source in the Guiana Shield and East-central Amazon by the middle of the 21st century. This chapter brings new information about the future evolution of Amazon rainforest, where uncertainties in both climate model projections and model structure require further amelioration to better understand drought-induced risks of positive carbon climate feedbacks from rainforests.

6.2 PERSPECTIVES

Our results highlight the value of incorporating the eco-hydrological processes in process-based models to reduce uncertainty in reproducing the forest responses to drought, especially tree mortality and biomass loss events. It further points out possibilities for refining the drought response simulation by considering the variability in hydraulic traits that can be extended from my PhD work. Perspectives in that direction are discussed as below.

(1) Incorporation of variation in hydraulic traits

It is unclear whether - and if so, to what extent – plant hydraulic traits spatial heterogeneity affect the spatial distribution of biomass dynamics. Xylem anatomical traits determine the forest response to change in water availability and also affect species habitat preference along water availability gradients (Lourenço Junior *et al.*, 2022). This observation suggests that vulnerability or higher sensitivity to water stress in some forest regions could be predicted more efficiently. Field measurements already present genus-to-genus difference in ψ_{50} values of either resistant or vulnerable trees (Rowland *et al.*, 2015). Both time and spatial scales in plant hydraulics matter in water transport simulation (Mayr, 2021). Variation over time can be reflected as plasticity in hydraulic traits that affects plant adaptation to change in water condition, particularly to water stress. Variation over spatial scales is manifested as segmentation and capacitance protecting plant from embolism, like inter-adapted behavior of distal and proximal branches, or even trunks (Hoffmann *et al.*, 2021). Finer differentiation of tree structure would help us to a more explicit simulation of hydraulic segmentation through leaf xylem, branch xylem and trunk xylem (Wang *et al.*, 2021).

One important limitation in ORCHIDEE-CAN-NHA is that the variability of hydraulic traits was not considered since both inter-species and intra-species differences vary a lot across trait axis. Distinct water use strategies e.g. from isohydric to anisohydric behaviors determine the plant response to extreme drought events, like whether they are vulnerable or not. In order to generalize the performance of our model, potential solutions include prescribing an interpolated trait map from the TRY database version 5 (Kattge *et al.*, 2020). For example, Ψ_{50} and sensitivity of water conductance to water potential variations. Currently, these two trait parameters are prescribed as constants without variation over temporal- and spatial scales. Besides, hydraulic traits like Ψ_{50} could be optimized through constraining the model behavior by observed vegetation optical depth (VOD), soil moisture and evapotranspiration (ET) e.g. through Markov Chain Monte Carlo on top of a hydrology model (Liu *et al.*, 2021b). However, in our framework, the forward process that can be used to calculate the likelihood of the retrieved parameter is time-consuming given the complicated format of ORCHIDEE-CAN-NHA. ORCHIDAS, a data assimilation system that can retrieve the parameters in either gradient-descent way or global search way in harnessing many data streams like remote sensing,

ground-based or inventory data (MacBean *et al.*, 2015), can be used to retrieve the hydraulic traits with constraints from remotely-sensed VOD or ET, and a spatial map can be obtained as inputs to the model correspondingly. Alternatively, a simpler way is to build relationship between traits and climate data to incorporate both temporal- and spatial-scale variation, like dynamic Ψ_{50} during the development of drought. Among these three solutions, the choice 1 and 3 can be less time-consuming but may be unable to provide the range of hydraulic parameters like choice 2 does, but choice 1 and 3 can still be quick means to give a glance on the spread in water regulation strategies.

(2) Possible post-drought legacy and recovery

After extreme drought events, re-watering and xylem reparation and regrowth contribute to the recovery of hydraulic transport system. New recruited individuals would appear in the gaps created by big tree loss, and legacy in tree mortality may also occur (Yang *et al.*, 2018). This legacy process of either recovery or mortality has not been clearly represented in models. Progressive partial recovery of xylem function could be incorporated into model by changing the hydraulic conductance theoretically. The tree cohorts model used in my PhD simulates the hydraulic conductance for each tree size group, thus the separation of trees with xylem recovery or persistent embolism cavitation can only be realized by resorting to conception of 'fraction' since there is no distinction of individuals. Nevertheless, we could choose a water stress threshold for the occurrence of recovery, beyond which the recovery would not occur and mortality legacy would take place, and persist for a while. Such a threshold can be obtained empirically from the results of dry-down experiments, and also the regrowth speed can be measured, which can help to define new empirical parameters in our process-based model. Besides modulation at xylem scale, recruitment, depending on the surrounding environmental condition, could be modified to reflect the recovery at macroscopic scale, which constitutes a more efficient and parsimonious way to simulate the recovery of integral forest structure. For example, recruitment rate at Caxiuana site was well recorded, and could be used to model a signal. In addition, legacy can also be reflected in aspects of allocation, namely, the priority of carbon investment, although the tree adaptation may not respond strongly. Post-drought *in-situ* observation on carbon allocated to leaf, trunk and root would be helpful to ascertain this issue. Therefore, the water stress threshold under which the xylem regrowth would occur, a more realistic recruitment formulation and post-drought carbon allocation variation can be attempted in model to imply the ecosystem inherent resistance, the possibility of the recovery as well as the strength of legacy.

(3) Representation of trade-off from individual to community scale

In simulations of plant water transport, hydraulic safety-efficiency trade-offs can mediate drought sensitivity and serve as constraint on the relationship among hydraulic traits. Yet such trade-offs may be not as strong as we expected and regulated by climate seasonality (Liu *et al.*, 2021a). Practically, since stomatal conductance is formulated as a logistic function of leaf water potential in our current model, we could set a safety-efficiency trade-off as a first attempt at leaf-level, like the definition of two parameters of stomatal conductance under high water availability – the leaf water potential when 50% of stomatal conductance is lost (Henry *et al.*, 2019). Optimization-based approaches especially for stomatal conductance have been formulated with various targets, e.g. maximizing the difference between leaf carbon gain and risk related to leaf hydraulics (Wang *et al.*, 2021), or maximizing the product of leaf photosynthesis and xylem hydraulic conductance (Eller *et al.*, 2020). Although instantaneous optimization may not always prevail over long time scales, incorporating such trade-off would really benefit to the simulation of carbon-water coupling instead of current empirical representation that could be poorly constrained. Maximizing the difference between leaf carbon gain and leaf carbon loss triggered by embolism could be a reasonable solution. Other available relationship like growth-risk trade-off at individual level, or even stature-recruitment trade-off (large stature could exhibit low recruitment, (Rüger *et al.*, 2020)) at community scale can all behave as constraint on the simulation of vegetation structure, composition as well as carbon and water budgets.

Our model can be used to test the performance of different optimization paradigms.

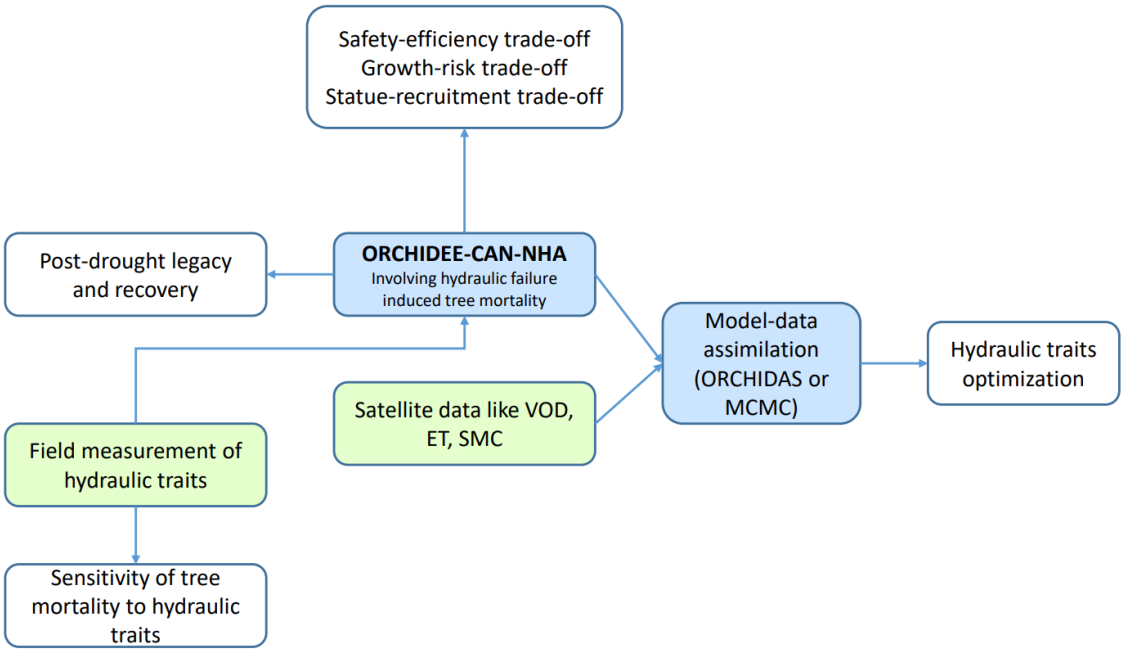

Figure 6.1 Perspective application of ORCHIDEE-CAN-NHA. Frame with blue shade means model or method, green one denotes the data sources, and white one the target.

6.3 REFERENCES

Anderegg, L.D., Griffith, D.M., Cavender-Bares, J., Riley, W.J., Berry, J.A., Dawson, T.E. & Still, C.J. Representing plant diversity in land models: An evolutionary approach to make 'Functional Types' more functional. *Global Change Biology*, 2021.

Eller, C.B., Rowland, L., Mencuccini, M., Rosas, T., Williams, K., Harper, A., Medlyn, B.E., Wagner, Y., Klein, T. & Teodoro, G.S. Stomatal optimization based on xylem hydraulics (SOX) improves land surface model simulation of vegetation responses to climate. *New Phytologist*, **226**, 1622-1637, 2020.

Giles, A., Rowland, L., Bittencourt, P., Bartholomew, D., Coughlin, I., Costa, P., Domingues, T., Miatto, R., Barros, F. & Ferreira, L. Small understorey trees have greater capacity than canopy trees to adjust hydraulic traits following prolonged experimental drought in a tropical forest. *Tree Physiology*, 2021.

Henry, C., John, G.P., Pan, R., Bartlett, M.K., Fletcher, L.R., Scoffoni, C. & Sack, L. A stomatal safety-efficiency trade-off constrains responses to leaf dehydration. *Nature communications*, **10**, 1-9, 2019.

Hoffmann, W.A., Rodrigues, A.C., Uncles, N. & Rossi, L. Hydraulic segmentation does not protect stems from acute water loss during fire. *Tree Physiology*, 2021.

Kattge, J., Bönisch, G., Díaz, S., Lavorel, S., Prentice, I.C., Leadley, P., Tautenhahn, S., Werner, G.D., Aakala, T. & Abedi, M. TRY plant trait database–enhanced coverage and open access.

Global change biology, **26**, 119-188, 2020.

Konings, A.G. & Gentine, P. Global variations in ecosystem-scale isohydricity. Global change biology, 23, 891-905, 2017.

Liu, H., Ye, Q., Gleason, S.M., He, P. & Yin, D. Weak tradeoff between xylem hydraulic efficiency and safety: climatic seasonality matters. *New Phytologist*, **229**, 1440-1452, 2021a.

Liu, Y., Holtzman, N.M. & Konings, A.G. Global ecosystem-scale plant hydraulic traits retrieved using model–data fusion. *Hydrology and Earth System Sciences*, **25**, 2399-2417, 2021b.

Lourenço Junior, J., Enquist, B.J., von Arx, G., Sonsin-Oliveira, J., Morino, K., Thomaz, L.D. & Milanez, C.R.D. Hydraulic tradeoffs underlie local variation in tropical forest functional diversity and sensitivity to drought. *New Phytologist*, **n/a**, https://doi.org/10.1111/nph.17944, 2022.

MacBean, N., Maignan, F., Peylin, P., Bacour, C., Bréon, F.-M. & Ciais, P. Using satellite data to improve the leaf phenology of a global terrestrial biosphere model. *Biogeosciences*, **12**, 7185-7208, 2015.

Mayr, S. Relevance of time and spatial scales in plant hydraulics. *Tree Physiology*, **41**, 1781-1784, 2021.

Rowland, L., da Costa, A.C.L., Galbraith, D.R., Oliveira, R., Binks, O.J., Oliveira, A., Pullen, A., Doughty, C., Metcalfe, D. & Vasconcelos, S. Death from drought in tropical forests is triggered by hydraulics not carbon starvation. *Nature*, **528**, 119-122, 2015.

Rüger, N., Condit, R., Dent, D.H., DeWalt, S.J., Hubbell, S.P., Lichstein, J.W., Lopez, O.R., Wirth, C. & Farrior, C.E. Demographic trade-offs predict tropical forest dynamics. Science, 368, 165-168, 2020.

Wang, Y., Köhler, P., He, L., Doughty, R., Braghiere, R.K., Wood, J.D. & Frankenberg, C. Testing stomatal models at stand level in deciduous angiosperm and evergreen gymnosperm forests using CliMA Land (v0. 1). *Geoscientific Model Development Discussions*, 1-35, 2021.

Werner, C., Meredith, L.K., Ladd, S.N., Ingrisch, J., Kübert, A., van Haren, J., Bahn, M., Bamberger, I., Beyer, M. & Blomdahl, D. Ecosystem fluxes during drought and recovery in an experimental forest. *Science*, **374**, 1514-1518, 2021.

Yang, Y., Saatchi, S.S., Xu, L., Yu, Y., Choi, S., Phillips, N., Kennedy, R., Keller, M., Knyazikhin, Y. & Myneni, R.B. Post-drought decline of the Amazon carbon sink. *Nature communications*, **9**, 1-9, 20

7 APPENDIX

7.1 APPENDIX A

Published version of Yao et al (2021)

7.2 APPENDIX B

Published version of Yao et al (2022a)

7.3 APPENDIX C

Published version of Yao et al (2022b)

Global Biogeochemical Cycles

RESEARCH ARTICLE
10.1029/2020GB006918

Key Points:

- A new data-driven global soil heterotrophic respiration (SHR) product benefits our understanding of its spatiotemporal dynamics
- Water availability plays an important role in driving inter-annual fluctuation of SHR
- Ecosystem-level drivers for SHR anomalies vary between water-limiting and non-water-limiting regions

Supporting Information:

Supporting Information may be found in the online version of this article.

Correspondence to:

Y. Yao,
yitong.yao@lsce.ipsl.fr

Citation:

Yao, Y., Ciais, P., Viovy, N., Li, W., Cresto-Aleina, F., Yang, H., et al. (2021). A data-driven global soil heterotrophic respiration dataset and the drivers of its inter-annual variability. *Global Biogeochemical Cycles*, *35*, e2020GB006918. https://doi.org/10.1029/2020GB006918

Received 14 DEC 2020
Accepted 23 JUL 2021

A Data-Driven Global Soil Heterotrophic Respiration Dataset and the Drivers of Its Inter-Annual Variability

Yitong Yao[1], Philippe Ciais[1], Nicolas Viovy[1], Wei Li[2], Fabio Cresto-Aleina[1], Hui Yang[1], Emilie Joetzjer[3], and Ben Bond-Lamberty[4]

[1]LSCE/IPSL, CEA-CNRS-UVSQ, Laboratoire des Sciences du Climat et de l'Environnement, Université Paris-Saclay, Gif-sur-Yvette, France, [2]Department of Earth System Science, Tsinghua University, Beijing, China, [3]CNRS, CNRM, Université de Toulouse, Météo-France, Toulouse, France, [4]Pacific Northwest National Laboratory, Joint Global Change Research Institute at the University of Maryland-College Park, College Park, MD, USA

Abstract Soil heterotrophic respiration (SHR) is important for carbon-climate feedbacks because of its sensitivity to soil carbon, climatic conditions and nutrient availability. However, available global SHR estimates have either a coarse spatial resolution or rely on simple upscaling formulations. To better quantify the global distribution of SHR and its response to climate variability, we produced a new global SHR data set using Random Forest, up-scaling 455 point data from the Global Soil Respiration Database (SRDB 4.0) with gridded fields of climatic, edaphic and productivity. We estimated a global total SHR of $46.8^{56.3}_{38.6}$ Pg C yr^{-1} over 1985–2013 with a significant increasing trend of 0.03 Pg C yr^{-2}. Among the inputs to generate SHR products, the choice of soil moisture datasets contributes more to the difference among SHR ensemble. Water availability dominates SHR inter-annual variability (IAV) at the global scale; more precisely, temperature strongly controls the SHR IAV in tropical forests, while water availability dominates in extra-tropical forest and semi-arid regions. Our machine-learning SHR ensemble of data-driven gridded estimates and outputs from process-based models (TRENDYv6) shows agreement for a strong association between water variability and SHR IAV at the global scale, but ensemble members exhibit different ecosystem-level SHR IAV controllers. The important role of water availability in driving SHR suggests both a direct effect limiting decomposition and an indirect effect on litter available from productivity. Considering potential uncertainties remaining in our data-driven SHR datasets, we call for more scientifically designed SHR observation network and deep-learning methods making maximum use of observation data.

1. Introduction

Soil heterotrophic respiration (SHR), the CO_2 flux produced by free-living microbial heterotrophs and soil fauna feeding on soil organic matter (Carbone et al., 2016; Hanson et al., 2000), constitutes a key ecosystem-to-atmosphere carbon flux that affects soil carbon storage and carbon-climate feedbacks. Since the magnitude of SHR is roughly four times of global annual anthropogenic fossil fuel emission (Le Quéré et al., 2018) and SHR can regulate the net ecosystem carbon exchange variability in some regions (Liu, Ballantyne, et al., 2018), even small changes in this flux can cause carbon redistribution between soil and atmosphere, and modify the carbon sink. Enhanced microbial dynamics in soil organic matter decomposition have been detected as the dominant factor in an increasing imbalance between higher CO_2 loss rate and CO_2 uptake by plants (Bond-Lamberty et al., 2018). Therefore, a detailed understanding of the SHR spatial and temporal dynamics under changing climate conditions is pivotal to improve projections of the carbon–climate feedback (Ballantyne et al., 2017; Bradford et al., 2019).

However, unlike other components of the terrestrial carbon cycle like gross primary productivity (GPP) that can be measured through eddy covariance flux tower at plot scale, SHR observations mainly come from small-scale chambers, combined with intrusive methods (trenching, root exclusion, root extraction), or non-intrusive methods of isotope labeling with uncertainty in ^{14}C measurements (Bond-Lamberty et al., 2004; Hanson et al., 2000) to partition the heterotrophic and autotrophic soil fluxes. Due to the considerable uncertainty underlying these measurements, SHR is the most poorly constrained ecosystem and global carbon flux (Ciais et al., 2020; Konings et al., 2019).

Table 1
Comparison With Previously Published Respiration Datasets

Data type	Reference	Target variable	Number of site data	Method	Period	Spatial resolution	Uncertainty
Site-level data	Bond-Lamberty and Thomson (2010)	Rs, SHR	3,379 records of Rs; 333 records of SHR (if we use same filtering criterion)	Collecting published studies	1961–2007	-	-
Global map	Hashimoto et al. (2015)	Rs, SHR	1,638 records of Rs	Monthly Rs = f(monthly temperature, monthly precipitation, precipitation of the previous month) A globally constant coarse ratio is used to transform Rs to SHR: ln(annual SHR) = 1.22 + 0.73*ln(annual Rs)	1965–2012	0.5° × 0.5°	-
	Tang et al. (2020)	SHR	504 records of SHR (with update from Chinese publications)	Random Forest	1980–2016	0.5° × 0.5°	-
	Warner et al. (2019)	Rs; SHR	2,657 records of Rs	Quantile regression forest on Rs, and empirical equation on SHR.	-	1 km	Sampling bias uncertainty
	Adachi et al. (2017)	Rs	Only five sites were used in validation	Empirical equation	2001–2009	4 km	-
	Konings et al. (2019) – top-down	SHR	-	Inverting land surface carbon balance	2010–2012	4° × 5°	Inversion uncertainty
	This study	SHR	455 records of SHR (after filtering)	Random Forest	1985-2013 (overlapped period affected by the explanatory variables)	0.5° × 0.5°	Extrapolation uncertainty and uncertainty from alternative gridded input datasets

Note. Rs: soil respiration.
Abbreviation: SHR, soil heterotrophic respiration.

Most existing SHR-related research has focused on testing the sensitivities of SHR to environmental variations through multi-factorial manipulation experiments at small scales like soil warming (Noh et al., 2016; Schindlbacher et al., 2009), rainfall exclusion (Hinko-Najera et al., 2015; S. Huang et al., 2018), water addition (Liu, Lü, et al., 2018; Zou et al., 2018), and nitrogen fertilization experiments (Z. Chen et al., 2018; Peng et al., 2018). Although these studies enable us to understand local SHR responses under different environmental conditions, large-scale spatial information of SHR is still limited, and contains large uncertainty. For example, global SHR estimates from Earth System Models (ESMs) range from 40 to 70 PgC yr^{-1} during 1965–2004 (Hashimoto et al., 2015; Shao et al., 2013) with large inter-model differences. Apart from these ESM estimates, we know of only four global SHR maps available at present (Table 1). The first data-driven SHR map was generated by Hashimoto et al. (2015) who upscaled *in situ* measurements of soil respiration with a modified version of functional relations from Raich and Potter (1995) and Raich et al. (2002) to calculate total soil respiration using monthly temperature and precipitation, and then used a constant partitioning ratio to scale down total soil respiration to SHR. One limitation acknowledged by this study is that only 53 sites from Bond-Lamberty et al. (2004) were used to derive that coarse ratio. Warner et al. (2019) used a

similar approach, first computing total soil respiration and then SHR from a partitioning ratio, to generate a static high resolution global SHR map. Tang et al. (2020) used Random Forest model to produce a data-driven global SHR data set but this lacked uncertainty evaluation. Finally, Konings et al. (2019) employed a constrained carbon balance framework using atmospheric inversion based on net ecosystem productivity (NEP), solar-induced fluorescence based GPP, and modeled carbon use efficiency to produce a top-down global SHR estimation; this is available at relatively coarse spatial resolution (4° × 5°) and for a short time period (2010–2012), which limits its validation against *in situ* measurements. Considering the limitations of the above-mentioned datasets, there is a clear need for spatially explicit data-driven global-scale SHR maps at a finer resolution and for a longer time period with full uncertainty accounting, which can be used for evaluation and optimization of process-based models (N. Huang et al., 2020; J. Li et al., 2016).

A decade ago, Bond-Lamberty and Thomson (2010) compiled a large soil respiration database — the Global Soil Respiration Database (SRDB), with soil respiration observations from peer-reviewed literature studies. The number of soil respiration records has reached 6,634 (4,111 valid values) in the latest SRDB 4.0 (Bond-Lamberty & Thomson, 2018) although SHR observations are far fewer (674 valid values before filtering); very recently, the SRDB 5.0 (Jian et al., 2021, not used here) was released with 1,147 annual SHR values. A data-driven SHR estimate from site to regional even global scale is thereby becoming feasible now, and Bond-Lamberty et al. (2016) suggested that machine learning could be an ideal tool toward the large-scale data-driven SHR estimation. Machine learning algorithms are powerful tools for data-driven up-scaling estimation of a target variable in ecological studies (Jung et al., 2011; Steidinger et al., 2019; Yao et al., 2018). Research on predictions of carbon or water flux (Jung et al., 2010; Z. Zeng et al., 2014) and crop yield (Cai et al., 2019; Feng et al., 2019) have affirmed the utility of those algorithms. Estimation with such data-oriented techniques gives us a new opportunity to evaluate SHR and its dynamics in response to environmental variations globally.

In this study, we apply Random Forest (RF) algorithms to estimate global annual SHR at 0.5° × 0.5° spatial resolution over the period 1985–2013 with meteorological, edaphic factors and GPP as explanatory variables. With this method, we can produce an ensemble of different data-driven SHR gridded data set at global scale over last three decades, and we are also able to examine the contribution of dynamic climate drivers to SHR inter-annual variability (IAV), including annual temperature, precipitation or soil moisture, and radiation.

2. Materials and Methods

2.1. Soil Respiration Database

The Global SRDB, is composed of soil respiration measurements from peer-reviewed studies. It was first released in Bond-Lamberty and Thomson (2010) and updated in Bond-Lamberty and Thomson (2018) as SRDB version 4.0. We used 455 site-year observations after data filtering. There are 290 sites in total and most sites have records less than 3. Our data filtering criteria included: (a) removing records without detailed temporal, coordinates and annual SHR information, and (b) excluding observations from manipulation experiments and soda lime measurements, which tend to underestimate soil CO_2 fluxes (Haynes & Gower, 1995). Records using isotope, gas chromatography or other measurements were retained. Figure 1 shows that current SHR observations after filtering mainly distributed in temperate zones, with higher sample density in East Asia, Europe and North America. These available observations belong to seven ecosystem types (Friedl et al., 2010).

Here we introduce different climatic, soil moisture and GPP datasets that are used to produce large ensemble global SHR datasets by upscaling SRDB point data, which improves on previous studies with only few available SHR members resulting in incomplete uncertainty accounting.

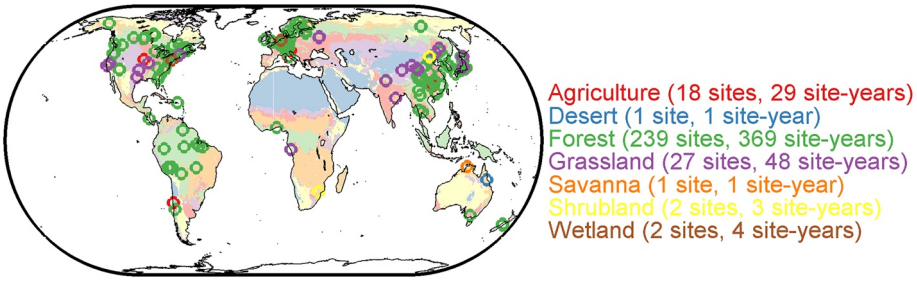

Figure 1. The spatial distribution of selected soil heterotrophic respiration observation sites (bold circles) by ecosystem type. The land cover used to define ecosystems from MCD12Q1 is shown in a color lighter than the circles in same category. Numbers in brackets denote the available sites and records for a given ecosystem.

2.2. Climatic Datasets

2.2.1. Temperature, Precipitation and Radiation

2.2.1.1. CRUNCEP

The climatic variables of annual temperature, annual precipitation and annual short-wave radiation used in this study are obtained from the CRUNCEP v6.1 (Viovy, 2015) covering the period 1901 to 2015. CRUNCEP is a combination of two existing datasets: the Climate Research Unit (CRU) TS3.2 observation-based monthly climatological data in spatial resolution of 0.5° × 0.5°, and the National Center for Environmental Prediction (NCEP) reanalysis product in 2.5° × 2.5° and 6-hour temporal step. The latter is used to define the diurnal and daily variation of the climate forcing.

2.2.1.2. CRUJRA

CRUJRA v1.1 is based on the same methodology as CRUNCEP but uses the Japanese Reanalysis Data (JRA) produced by the Japanese Meteorological Agency (JMA) with a spatial resolution of 0.5° × 0.5°adjusted to match the CRU TS 3.26 data (Harris et al., 2014; Kobayashi et al., 2015). These data are available at a 6-hour time-step from 01/1901 to 12/2017. The annual temperature, annual precipitation and annual short-wave radiation from CRUJRA are also used in this study.

2.2.1.3. Princeton Climate Data Set

This global meteorological forcing data set is a blend of NCEP/NCAR reanalysis data and a series of global observations to form global 0.25°×0.25° daily temperature and precipitation datasets from 1948 to 2016 (Sheffield et al., 2006). We aggregate daily data to annual values first.

2.2.1.4. WFDEI Meteorological Forcing Data Set

This WFDEI meteorological forcing data set is a combination of ERA-interim re-analysis data with daily variability and monthly in-situ observation. There are two precipitation products available from WFDEI: one is corrected using CRU observations, and the other using the Global Precipitation Climatology Centre (GPCC) data set (Weedon et al., 2014). WFDEI-CRU and WFDEI-GPCC are both used in this study. These two datasets span from 1979 to 2016 and are provided at 0.5°×0.5° spatial resolution.

2.2.1.5. Climate Prediction Center (CPC)

This CPC climatological data set includes daily maximum and minimum temperature (t_{max} and t_{min}) and daily precipitation. Daily average temperature is generated by averaging t_{max} and t_{min}. Then the daily temperature and daily precipitation are aggregated to annual values. This data set starts from 1979, has been updated through 2021, and is available at 0.5° × 0.5°.

2.2.2. Soil Moisture Datasets

2.2.2.1. CPC Soil Moisture

The CPC monthly soil moisture data set is estimated by a one-layer leaky-bucket model (J. Huang et al., 1996; Van den Dool et al., 2003). The driving fields for the model include temperature and precipitation from CPC

precipitation reconstruction over Land (M. Chen et al., 2002) and CPC Global Land Surface Air Temperature Analysis (Fan & Van den Dool, 2008). This data set starts from 1948 and updates in real time (currently to 2021), with a spatial resolution of 0.5° × 0.5° (Fan & van den Dool, 2004). The CPC moisture is calculated with a soil depth of 1.6 m.

2.2.2.2. Gravity Recovery and Climate Experiment Terrestrial Water Storage Reconstruction (GRACE-Rec TWS)

Humphrey et al. (2017) constructed a statistical model by linking the anomalies of the main meteorological drivers to the terrestrial water storage (TWS) anomalies observed by the GRACE satellite after 2002. The pre-2002 TWS anomalies are reconstructed based on this calibrated statistical model, driven by precipitation and temperature. This reconstructed TWS data set covers 1985–2015 and is provided at a spatial resolution of 0.5° × 0.5°. It should be noted that this variable is not equal to soil moisture but also includes change in land ice, and free water (Humphrey et al., 2017). In the results section below, "GRACE-rec" is used as an abbreviation for GRACE reconstruction.

2.2.2.3. Global Land Data Assimilation System (GLDAS) Version 2

GLDAS version 2 data is composed by GLDAS 2.0, which uses the Princeton meteorological data as forcing data for 1948–2010, and GLDAS 2.1, which is forced by a combination of model and observation based datasets from 2000 to present (Beaudoing & Rodell, 2016; Rodell et al., 2004). The output soil moisture is at 0.25° × 0.25° and has four soil layers, 0–0.1 m, 0.1–0.4 m, 0.4–1.0 m, and 1.0–2.0 m. We take the sum of soil moisture in these four layers.

2.3. Soil Properties Datasets

2.3.1. Soil Carbon Content

Soil carbon content is extracted from Harmonized World Soil Database (HWSD), which is produced by FAO and IIASA by combining existing global regional and national inventories for soil information in over 15,000 different soil mapping units (Nachtergaele et al., 2010; Wieder et al., 2014). Top-soil (0–0.3 m) and sub-soil (0.3–1.0 m) organic carbon content are provided and employed.

2.3.2. Soil Nitrogen Density

We also used a soil nitrogen density data set (unit: g N m^{-2}) from Global Gridded Surfaces of Selected Soil Characteristics developed by the International Geosphere-Biosphere Program Data and Information System (IGBP-DIS). A statistical bootstrapping approach is applied by the SoilData System to link the global pedon records to the FAO/UNCESCO digital soil map. The total soil nitrogen content is for a soil depth of 0–1.0 m. Soil nitrogen density was treated as explanatory variable for SHR estimate.

2.4. Land Cover Data Set

The MODIS land cover type product (MCD12Q1) is derived using a supervised decision tree classification algorithm (Friedl et al., 2010). We group land cover types in the MODIS product to correspond with the classification in SRDB following Table S1. In this study, we do not consider the effect of land use/cover change (cf. N. Huang et al., 2020), and we use a static land cover map in 2001 as input for the estimation model.

2.5. Gross Primary Productivity Datasets

2.5.1. FLUXCOM

GPP drives net primary production and litterfall, thus it is used as a predictor of SHR. We used an ensemble of gridded GPP products generated by training three machine learning algorithms (Random Forest, Multivariate Adaptive Regression Spline, and Artificial Neural Network) on daily GPP estimates from 224 flux towers (Jung et al., 2017; Tramontana et al., 2016). The combinations between three available algorithms and two GPP estimates (due to two partitioning methods) produce 6 GPP ensembles spanning 1980–2013 in monthly intervals. Each GPP member is used as one GPP data source for SHR estimation.

2.5.2. P-Model GPP

P-model is a Light Use Efficiency (LUE) model (Wang et al., 2017), in which monthly LUE is predicted on the basis of changing environmental conditions and an optimality criterion with respect to stomatal behaviors and other related traits (Prentice et al., 2014). Daily GPP, which is then calculated by monthly LUE and daily varying absorbed photosynthetically active radiation, can be further aggregated to annual time step. This product is released at a spatial resolution of 0.25×0.25°and over a time span of 1982–2016 (Stocker et al., 2019). This GPP data set includes the soil moisture effects on LUE.

2.6. Random Forest Algorithm and Its Performance

To generate a data-driven SHR estimation, we implemented a Random Forest ensemble machine learning algorithm, as in former carbon research studies (Baccini et al., 2012; Buermann et al., 2018; Jung et al., 2017; Schwalm et al., 2017; Zhu et al., 2017). Random Forest, as one of the widely used and fast running algorithms, is suited for handling non-linear relationship between the target and the corresponded independent variables, without requiring predefined functional forms or a normal sample distribution (Breiman, 2001). A RF model consists of multiple uncorrelated regression trees, each of which uses a subset of all the training samples with replacement (~63%) to reach the same total sample size and random subset of explanatory variables (Breiman, 2001). This bootstrapping procedure can decrease the influence of noise and outliers, and raise the stability of model predictions, by averaging over all constructed trees. In our study, the number of trees is set to be 1,000. In addition to the mean value output from 1,000 trees, we also obtain 95% confidence interval of outputs from these trees. The feature importance is provided by assessing the difference in prediction error (Mean Squared Error for this study) on out-of-bag data before and after variable permutation.

To get a robust evaluation of model performance, we use Leave-One-Out Cross Validation (hereinafter LOOCV). The goal of cross-validation is to test the model's ability to work on independent samples, in order to identify problems like over-fitting. Each time a sample is excluded and the remaining samples are used to train a RF model, the predicted value of the excluded one is estimated by that fitted model. Instead of taking average of out-of-bag R^2 from all trained RF models, we use the LOOCV-based predicted value of each observation to get R^2 as metric. LOOCV is used both at the sample and site levels.

Since the observed SHR data are provided at annual timescale, we need to aggregate the high temporal resolution to coarser time scale (annual) as inputs to the RF model. The RF model was first fitted on our filtered 455 site-year observation data set, and then applied to predict annual SHR for each 0.5° × 0.5° grid cell driven by meteorological factors and other environmental indicators (Table 2). We obtain 126 (6*7*3 = 126) global SHR members in total derived from crossing combinations of six climate datasets, seven GPP datasets (six members from FLUXCOM and one member from P-model) and three soil moisture/ TWS datasets (CPC, GRACE-rec and GLDAS) used as gridded inputs to RF model. Considering that different climate datasets (temperature and precipitation), soil moisture datasets, and GPP datasets served as our efficient explanatory variables and their different time period coverage, we choose 1985–2013 as the common time length for estimation.

2.7. Soil Heterotrophic Respiration Datasets Used for Comparison

2.7.1. Soil Respiration Data Set From Hashimoto et al. (2015)

Hashimoto et al. (2015) applied climate-driven functions modified from Raich et al. (2002) to fit soil respiration from 1,638 data points. The soil respiration was solely driven by temperature and precipitation, and the partitioning between its autotrophic and heterotrophic part followed two fixed parameters summarized from the data in Bond-Lamberty et al. (2004) (an approach also used by Warner et al., 2019). Two parameters in the model were assumed to be globally constant, so that the spatial heterogeneity in the Hashimoto et al. (2015) data set is provided only by variations in climatic drivers. This data-driven model was extrapolated to 1901–2012. We downloaded this data set from http://cse.ffpri.affrc.go.jp/shojih/data/index.html.

Table 2
Explanatory Variables Used for Soil Heterotrophic Respiration Upscaling and Their Data Access

Variable name	Variable variability state	Data access
Annual temperature	Inter-annual	CPC: https://www.esrl.noaa.gov/psd/data/gridded/data.cpc.globaltemp.html
Annual precipitation	Inter-annual	https://www.esrl.noaa.gov/psd/data/gridded/data.cpc.globalprecip.html
Annual short-wave radiation	Inter-annual	CRUNCEP: http://dods.extra.cea.fr/store/p529viov/cruncep/ CRUJRA: http://dx.doi.org/10.5285/13f3635174794bb98cf8ac4b0ee8f4ed Princeton: http://hydrology.princeton.edu/data.pgf.php WFDEI: http://www.eu-watch.org/data_availability
Annual soil moisture	Inter-annual	CPC: https://www.esrl.noaa.gov/psd/data/gridded/data.cpcsoil.html GRACE reconstruction: http://doi.org/10.5905/ethz-1007-85 GLDAS: https://disc.gsfc.nasa.gov/datasets/GLDAS_NOAH025_M_V2.1/summary
Annual gross primary productivity	Inter-annual	FLUXCOM: https://www.bgc-jena.mpg.de/geodb/projects/Home.php P-model: https://doi.org/10.5281/zenodo.1423484
Annual nitrogen deposition	Inter-annual	https://daac.ornl.gov/NACP/guides/NACP_MsTMIP_Model_Driver.html
Soil carbon content	Static	https://daac.ornl.gov/cgi-bin/dsviewer.pl?ds_id=1247
Total nitrogen density	Static	https://daac.ornl.gov/SOILS/guides/igbp-surfaces.html
Land cover classification	Static	https://modis.gsfc.nasa.gov/data/dataprod/mod12.php

Abbreviations: CPC, climate prediction center; GLDAS, global land data assimilation system; GRACE, gravity recovery and climate experiment.

2.7.2. Soil Heterotrophic Respiration Data From Tang et al. (2020)

Tang et al. (2020) upscaled site-level observations in SRDB4.0 using Random Forest model to produce an annual global SHR data set spanning 1980–2016 in spatial resolution of 0.5° × 0.5°. The explanatory variables include mean annual temperature, mean annual precipitation, diurnal temperature range, nitrogen deposition, Palmer Drought Severity Index, shortwave radiation, soil carbon content, soil nitrogen content and soil water content. We downloaded this data set from https://doi.org/10.6084/m9.figshare.8882567.

2.7.3. Top-Down SHR Data Set From Konings et al., (2019)

Konings et al., (2019) produced a top-down SHR estimate from 2010 to 2012 in spatial resolution of 4° × 5°. Total ecosystem respiration was first derived from carbon balance method by the difference between GPP and NEP and carbon use efficiency from model-data fusion framework was used to partition the autotrophic and heterotrophic respiration. NEP is from atmospheric inversion of NASA Carbon Monitoring System-Flux. GPP is based on satellite-observed solar-induced fluorescence. Monthly top-down SHR data was aggregated to an annual time step.

2.7.4. TRENDY Global Models

We use simulations of 12 dynamic global vegetation models from the project "Trends and drivers of the regional scale sources and sinks of carbon dioxide" (TRENDY) v6 for the period of 1985–2013. These models used a common set of observed climate, atmospheric CO_2 concentration, land-use change, and experimental protocols. Our analysis uses model SHR outputs (named as Rh in models) under the TRENDY "S3" experiment (which included the effects of time-varying CO_2 concentrations, climate change, and land use change). The 12 models are CABLE (Haverd et al., 2018), CLASS-CTEM (Melton & Arora, 2016), CLM4.5

(Oleson et al., 2013), ISAM (Jain et al., 2013), JSBACH (Reick et al., 2013), JULES (Clark et al., 2011), LPX (Keller et al., 2017), OCN (Zaehle & Friend, 2010), ORCHIDEE-MICT (Guimberteau et al., 2018), ORCHIDEE (Krinner et al., 2005), VEGAS (N. Zeng et al., 2005) and VISIT (Kato et al., 2013).

2.8. Attribution Analysis for SHR Inter-Annual Variability (IAV)

We apply the carbon flux anomaly decomposition approach proposed in Jung et al. (2017) to diagnose the contribution of different climate variables on SHR IAV, including annual temperature (TEMP), annual water availability proxies (precipitation or soil moisture, PREC or SMC) and annual short-wave radiation (RAD). We first obtain detrended annual SHR anomalies and climate indicators anomalies in each pixel by removing their linear trend on annual basis (least-squares fitting). Then we implement multiple linear regressions with zero-intercept between anomalies in SHR and all variables to separate their contribution. The estimated SHR sensitivity to climate anomaly (shown as the linear regression slopes a_s^{var} in Equation 1) multiplied by the corresponding forcing anomaly (shown as $\Delta \mathrm{var}_{s,y}$ in Equation 1) defines the SHR anomaly component $\Delta \mathrm{SHR}_{s,y}^{\mathrm{var}}$ driven by each forcing variable. These components can be added together to form a reconstructed SHR anomaly ($\Delta \mathrm{SHR}_{s,y}^{*}$ in Equation 2). A correlation coefficient is calculated to demonstrate the consistency between the climate-reconstructed SHR anomalies ($\Delta \mathrm{SHR}_{s,y}^{*}$) and the detrended estimates ($\Delta \mathrm{SHR}_{s,y}$). We also implement similar procedures on SHR from the Hashimoto and Tang datasets and TRENDY models. In all attribution analyses (except Hashimoto), both precipitation and soil moisture are considered as water-related proxies in the regression processes (Equations 1–4).

$$\Delta \mathrm{SHR}_{s,y,e} = a_{s,e}^{\mathrm{TEMP}} \times \Delta \mathrm{TEMP}_{s,y,e} + a_{s,e}^{\mathrm{PREC}} \times \Delta \mathrm{PREC}_{s,y,e} + a_{s,e}^{\mathrm{RAD}} \times \Delta \mathrm{RAD}_{s,y,e} + \in_{s,y,e} \quad (1)$$

$$\Delta \mathrm{SHR}^{*}{}_{s,y,e} = \Delta \mathrm{SHR}_{s,y,e}^{\mathrm{TEMP}} + \Delta \mathrm{SHR}_{s,y,e}^{\mathrm{PREC}} + \Delta \mathrm{SHR}_{s,y,e}^{\mathrm{RAD}} \quad (2)$$

$$\Delta \mathrm{SHR}_{s,y,e} = a_{s,e}^{\mathrm{TEMP}} \times \Delta \mathrm{TEMP}_{s,y,e} + a_{s,e}^{\mathrm{SMC}} \times \Delta \mathrm{SMC}_{s,y,e} + a_{s,e}^{\mathrm{RAD}} \times \Delta \mathrm{RAD}_{s,y,e} + \in_{s,y,e} \quad (3)$$

$$\Delta \mathrm{SHR}^{*}{}_{s,y,e} = \Delta \mathrm{SHR}_{s,y,e}^{\mathrm{TEMP}} + \Delta \mathrm{SHR}_{s,y,e}^{\mathrm{SMC}} + \Delta \mathrm{SHR}_{s,y,e}^{\mathrm{RAD}} \quad (4)$$

Subscripts *s*, *y,* and *e* refer to index of grid cells, every year from 1985 to 2013, and one member from the SHR ensemble, respectively.

2.9. Factorial Analysis for SHR Trend

To understand the controlling variables for the regional variation in SHR trend map, we performed factorial estimation by removing the inter-annual variation of each dynamic explanatory variable, that is, keeping each variable static during 1985–2013. Dynamic explanatory variables of annual temperature, annual precipitation, annual radiation, annual GPP, annual soil moisture and annual nitrogen deposition were tested.

2.10. Statistical Software

All data processing and statistical analysis were performed in R statistical software (R Development Core Team, 2019) version 3.5.0 using packages "randomForest" version 4.6–14 (Liaw & Wiener, 2018), "raster" version 3.0–7 (Hijmans et al., 2019), "pracma" version 2.2.5 (Borchers, 2019).

3. Results

3.1. Performance of Random Forest Via Cross Validation

After testing on all combinations of these temperature and precipitation datasets, soil moisture and GPP choices, we derived the LOOCV R^2 of these RF models, which is 0.57 ± 0.01 (0.01 is the standard deviation of LOOCV R^2 from all combinations). We can see that at least at site-level, different climate datasets sources, soil moisture and GPP variable choices do not result in any R^2 or RMSE difference (Figure 2a). We

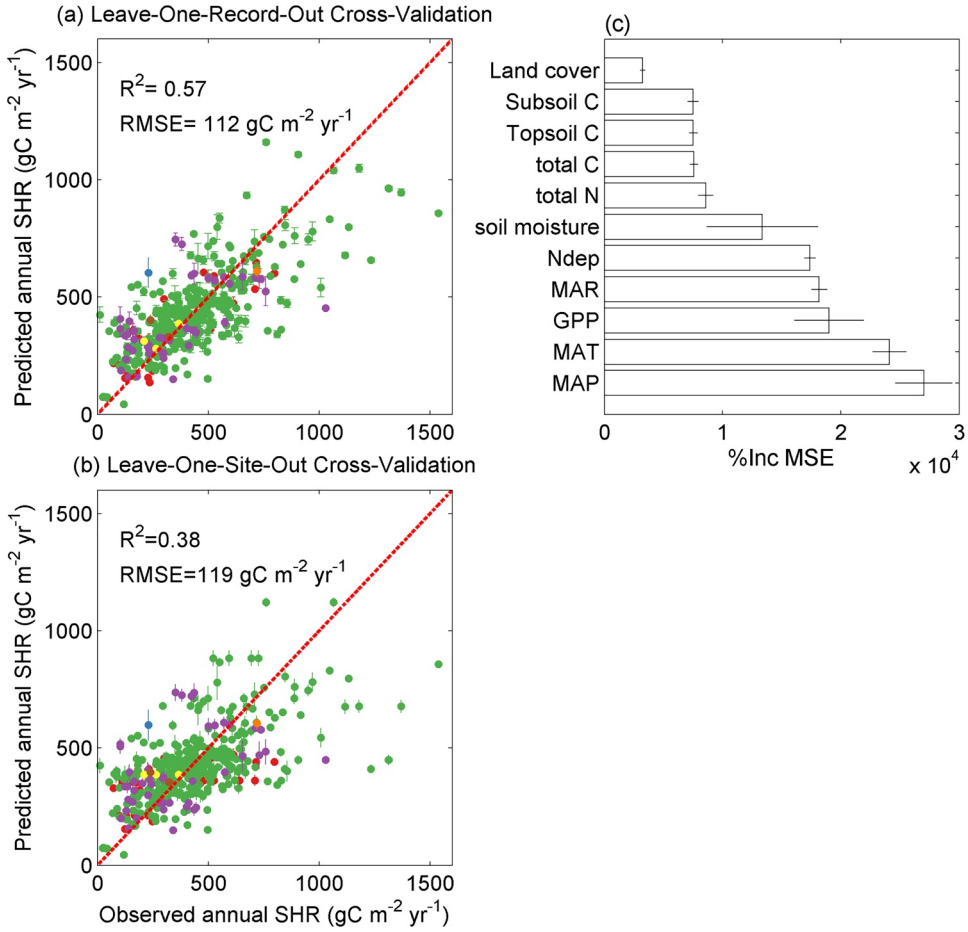

Figure 2. The performance of Random Forest evaluated by (a) Leave-One-Record-Out Cross Validation and (b) Leave-One-Site-Out Cross Validation. The error bar on each point denotes the standard deviation of soil heterotrophic respiration predictions estimated on the basis of different temperature and precipitation, soil moisture and gross primary productivity (GPP) datasets combinations. Different colors show the land cover types of the observation data (same color setting as Figure 1). (c) Feature importance scores ranking deduced from increase of mean squared error (MSE) after permuting variable. MAT (annual temperature), MAP (annual precipitation), MAR (annual radiation), Ndep (nitrogen deposition), GPP, soil moisture are time specific values depending on the observation year.

also try leave-one-site-out evaluation, which resulted in a lower R^2 (Figure 2b). Tests of model performance with more input explanatory variables are shown in Figures S1–S3. We show the importance of different variables in Figure 2c. Annual precipitation and annual temperature are the two most important variables, whereas static variables such as land cover type, soil carbon and nitrogen content contribute relatively less to model performance.

3.2. Spatiotemporal Pattern of Global SHR

The spatial pattern of mean annual SHR at 0.5°×0.5° spatial resolution during 1985–2013 is shown in Figure 3a, and follows the geographic GPP variations to a large degree (see Figure S4). Annual SHR decreases from tropics to high-latitude area, with the highest values in wet tropics of exceeding 800 gC m^{-2} yr^{-1} and the lowest in northern boreal area including Alaska, northern Canada and Siberia area (less than 200 gC m^{-2} yr^{-1}). Such a latitudinal SHR gradient particularly appears in Australia (from coastal area to inland), Africa and South America. Similar spatial gradients appear among all members of our data-driven SHR estimates.

The global mean of our data-driven SHR is 46.8 Pg C yr^{-1} over 1985–2013, (95% confidence interval: 38.6–56.3 Pg C yr^{-1} based on the estimates of 1,000 Random Forest model trees), with an increasing trend of

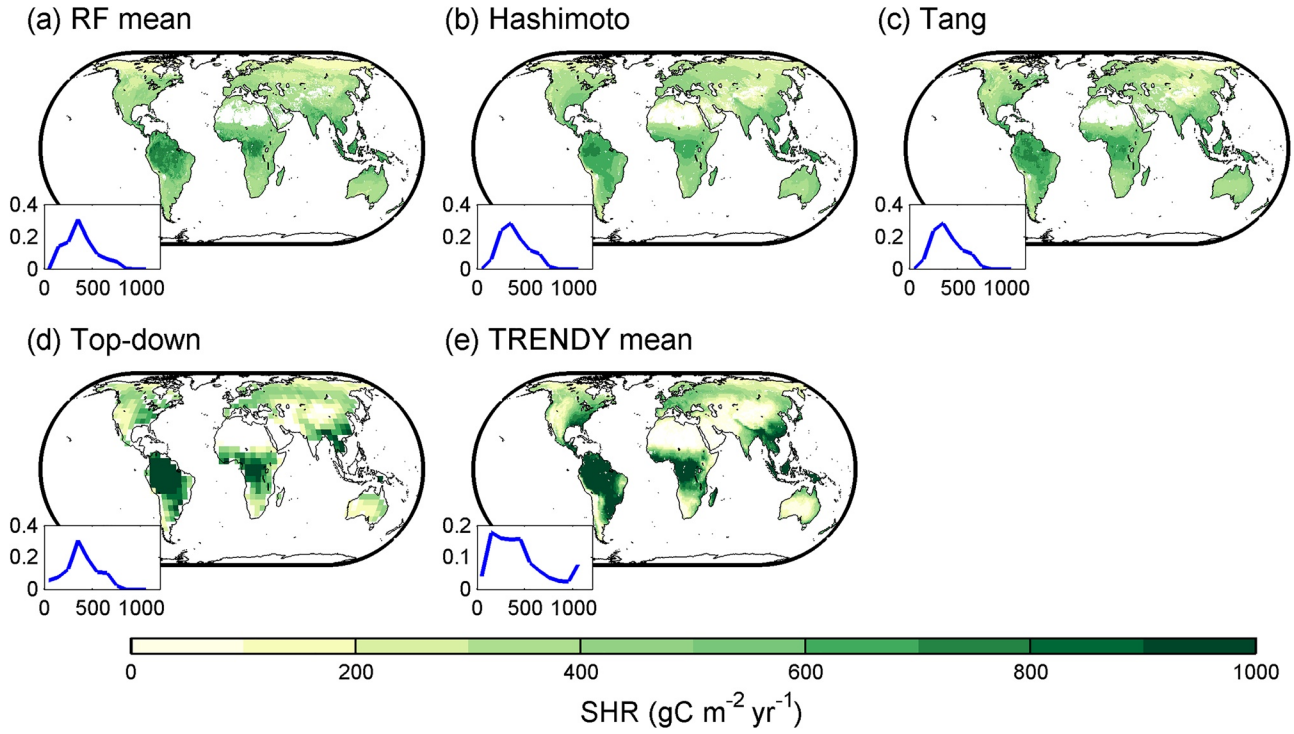

Figure 3. Spatial pattern of (a) ensemble mean of our data-driven soil heterotrophic respiration (SHR) members, (b) Hashimoto et al. (2015), (c) Tang et al. (2020), (d) top-down and (e) TRENDY model ensemble mean. Frequency distribution of SHR in different levels for each SHR data set is shown in the bottom left of each panel. It should be noted that the studied period of Hashimoto product is up to 2012 and the studied period of top-down SHR data set is between 2010 and 2012.

0.03 Pg C yr^{-2} (0.015–0.044 Pg C yr^{-2}, $P < 0.01$), which is similar to the 1.2% increase of SHR detected in Bond-Lamberty et al. (2018) over a similar timespan. The global total SHR is close to global total NPP (48.8 Pg C yr^{-1} during 2001–2015, Table S2) when we applied the same spatial mask. We do expect SHR to be globally smaller than NPP, because of lateral export by ecosystems that reduce considerably the fraction of NPP given to soil as litter for SHR (Ciais et al., 2020).

The choice of soil moisture variables contributes more to the difference among these data-driven SHR members rather than that of GPP, temperature and precipitation data sources (Figure S5). For example, using CPC soil moisture data produces an almost 1 Pg C yr^{-1} lower global SHR value than other data-driven estimates using GLDAS soil moisture (Figure S5c). In spite of these differences, the total amount of all our data-driven SHR members consistently displays a drop in 1992 and a peak in 2010 across all members (Figure S5).

3.3. Comparison With Previous Data Products and Models

Our data-driven SHR estimation is close to that of Hashimoto et al. (2015), who predicted a global flux of 46.5 Pg C yr^{-1} and temporal trend of 0.05 Pg C yr^{-2} (Figure 4). These two sets of gridded SHR products also show similar frequency distributions, although the spatial variation of Hashimoto et al. (2015) as smoother, as SHR in that data set depends only on climate (Figure 3b). Compared to our data-driven estimate, Hashimoto et al. (2015) presented higher SHR values in boreal area and lower values in tropics (Figures S6a, S6b and S7). Conversely, Tang et al. (2020) found lower values in Amazon and central Africa and higher values in temperate areas; their global total SHR amount of 46.9 Pg C yr^{-1} after applying same land mask was similar (Figures S6c and S6d). Global total amount of top-down SHR was about 40.8 Pg C yr^{-1} during 2010–2012 (Konings et al., 2019). The top-down SHR shows more distinct spatial gradients (Figure 3d) and larger values than this study in both tropics and boreal area (Figures S6e and S6f).

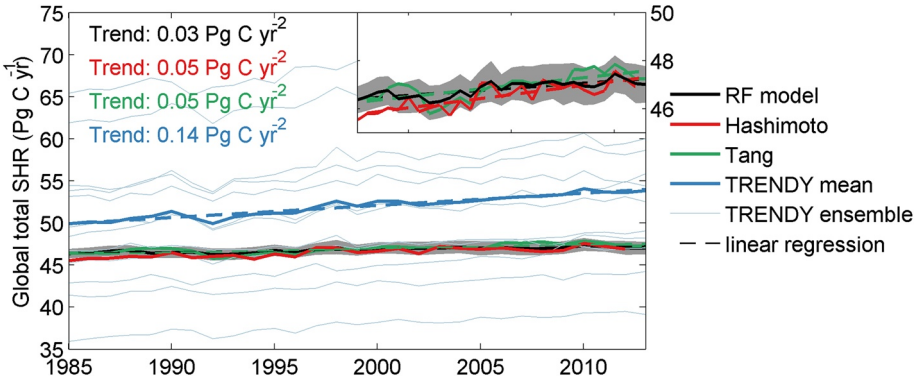

Figure 4. Global total amount of soil heterotrophic respiration (SHR) over 1985–2013. The shaded area in gray indicates the spread over all members from Random Forest models (RF). The zoomed plot in the top right shows the global mean of our data-driven ("RF"), Tang and Hashimoto SHR estimates more clearly. The dashed lines refer to fitted global total SHR time series against time. The global total amount of SHR in each TRENDY model is shown as thin blue line.

The ensemble mean SHR over all TRENDY models is larger than empirically estimated SHR products, increasing from 49.9 Pg C yr^{-1} to 53.8 Pg C yr^{-1} during our studied period, due to a four times larger temporal trend (0.14 Pg C yr^{-2} vs. 0.03 Pg C yr^{-2} in our data-driven products) (Figure 4). The TRENDY multi-model ensemble mean shows more drastic geographic contrasts across the globe (Figure 3e), with a different frequency distribution of SHR from our data-oriented estimate (Figures 3a and 3e). Large inter-model discrepancies are present among TRENDY models both for global totals and spatial details; the standard deviation can be as high as 8–9 Pg C yr^{-1} in each year and both underestimation and overestimation of SHR appear in different models in comparison to our data-oriented products (Figures S6g, S6h and s8–s9).

With respect to the spatial distribution of temporal trend of SHR, we can find that there is no uniform trend in our data-driven products (Figure S10a). To understand the controlling variables for the regional variation in SHR trend map, here we ran factorial estimation for one SHR member only for efficiency (see Section 2.9). Through comparison between Figures S11 and S12 we can see that change in soil moisture dominates the negative SHR trend in South America and central Africa, as well as the positive trend in Arctic tundra, and the increase in atmospheric nitrogen deposition contributes to patterns of positive SHR trend in Asia near urbanized areas. Tang et al. (2020) found clearly positive SHR trends in Arctic tundra areas (Figure S10c). Hashimoto et al. (2015) and TRENDY ensemble mean also produced positive trends in most areas, matching their increasing global trends (Figures 4, S10b, and S10d).

3.4. SHR Anomalies in Relation to Meteorological Factors

We attribute the factors contributing to SHR IAV using a linear decomposition approach described in Section 2.8. We first verified that the SHR anomaly reconstructed with climate factors can correctly reproduce the detrended SHR time series spatially (evaluated by the correlation coefficients as shown in Figure S13). It should be noted that both soil moisture and precipitation are used in upscaling of SHR but only one water proxy is used in the reconstruction of SHR anomalies. The quality of the reconstruction is impacted by the choice of water-related variables in linear decomposition process. For example, when CPC soil moisture is employed in the up-scaling of SHR, including it allows for better reconstruction of the SHR IAV than when using precipitation (Figure S13). Conversely, when using GLDAS soil moisture as input, precipitation has better performance in reconstructing SHR anomaly than the soil moisture variable. When the reconstructed anomalies are integrated to the global scale, we find that the correlation coefficient between reconstructed and detrended SHR anomalies can reach 0.9 when annual precipitation is used as a predictor, and 0.94 when soil moisture is used.

In general, we can see from Figure 5 that the globally integrated SHR IAV is mainly controlled by water availability, with higher correlation coefficients between reconstructed SHR and the water related SHR anomalies (SHR^{PREC} or SHR^{SMC}). However, the strength of this control varies depending on the water

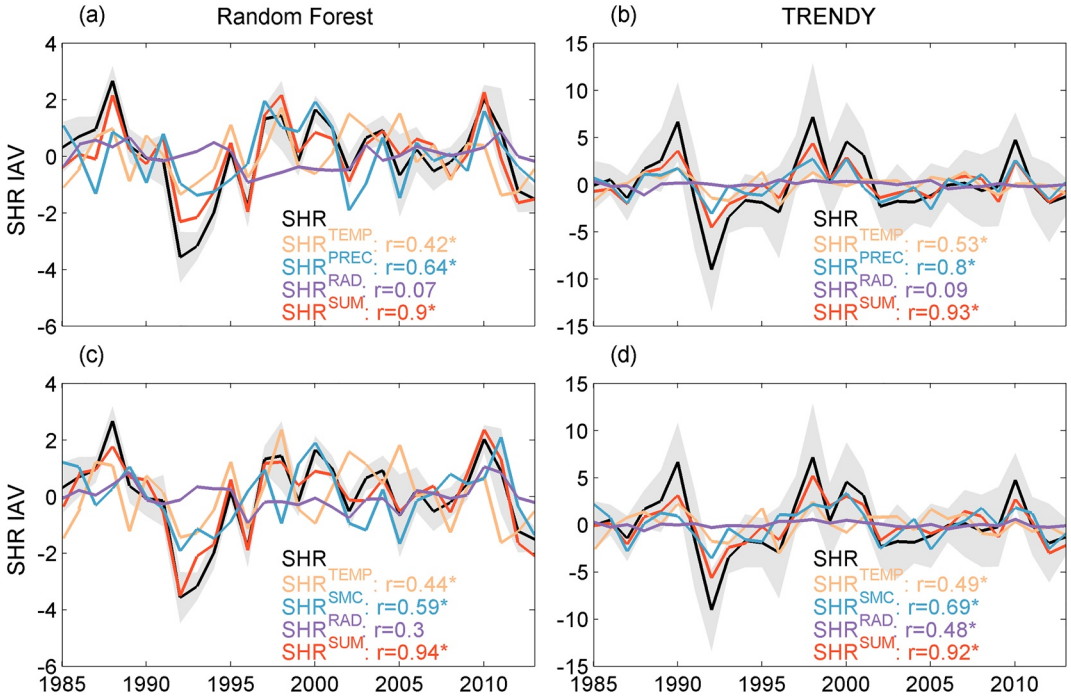

Figure 5. Climatic variables controls on soil heterotrophic respiration (SHR) inter-annual variability (IAV) at global scale. The black lines indicate detrended SHR anomalies. The colored lines indicate SHR anomalies driven by different climate factors. 'SUM' means the sum of SHR IAV driven by three climatic factors. The top panels include regressions using precipitation as a water proxy; in the bottom panels, the water proxy is soil moisture. The correlation coefficient between SHR anomaly and the component driven by a forcing is labeled. An asterisk denotes the significance of the corresponding correlation coefficient ($P < 0.05$). Shaded areas represent the spread among ensembles of Random Forest or TRENDY products. Due to the difference between soil moisture and water storage variables, only SHR estimated using soil moisture (CPC and GLDAS) is shown here. Regression for SHR estimated from GRACE-rec TWS is shown in Figure S14.

availability variables that are used in the SHR estimation and subsequent regression. For SHR up-scaled using GRACE-rec TWS, the correlation coefficient between SHR^{SMC} and SHR IAV is two times higher than when using precipitation as a regressor, although the overall reconstruction efficiency does not differ greatly (Figure S14). This should be expected since TWS anomaly is not always comparable to soil moisture and precipitation. Specifically, there are two most prominent anomalies in all data-driven SHR estimation members in 1992 and 2010 consistently (Figure S15). According to the similarity between SHR IAV driven by each climatic factor and the detrended series locally, we found that the negative SHR anomaly in 1992 is particularly driven by water-related proxies under cooler and drier climate after the Mount Pinatubo eruption (Figures S16–S18). The contribution of precipitation variability to the positive SHR anomaly in 2010 is larger than the one from temperature anomaly (Figure 5). We also identified the climatic drivers for the Tang et al. (2020) SHR product, and found that, similarly, precipitation or soil moisture anomaly dominate its SHR IAV (Figure S19).

We analyzed the drivers for SHR IAV from TRENDY model ensembles using the same approach. For TRENDY models, their simulated soil moisture is also used in the regression. In general, climate variables had a good capacity for reconstructing TRENDY SHR anomalies (Figures S20 and S21). SHR IAV from TRENDY ensemble mean displays dominance by water availability at global scale (Figures 5b and 5d). The driving factors for SHR IAV differ widely among TRENDY models (Figure S22), with six models showing dominance of water availability fluctuation on SHR IAV at the global scale, and five exhibiting dominance by temperature. The TRENDY models capture the negative SHR anomaly in 1992 and precipitation variability can better account for that. With regard to the distinctly positive anomaly in 2010, TRENDY ensemble mean also shows an apparent dominance of precipitation variability (Figure 5b). We repeated the analysis

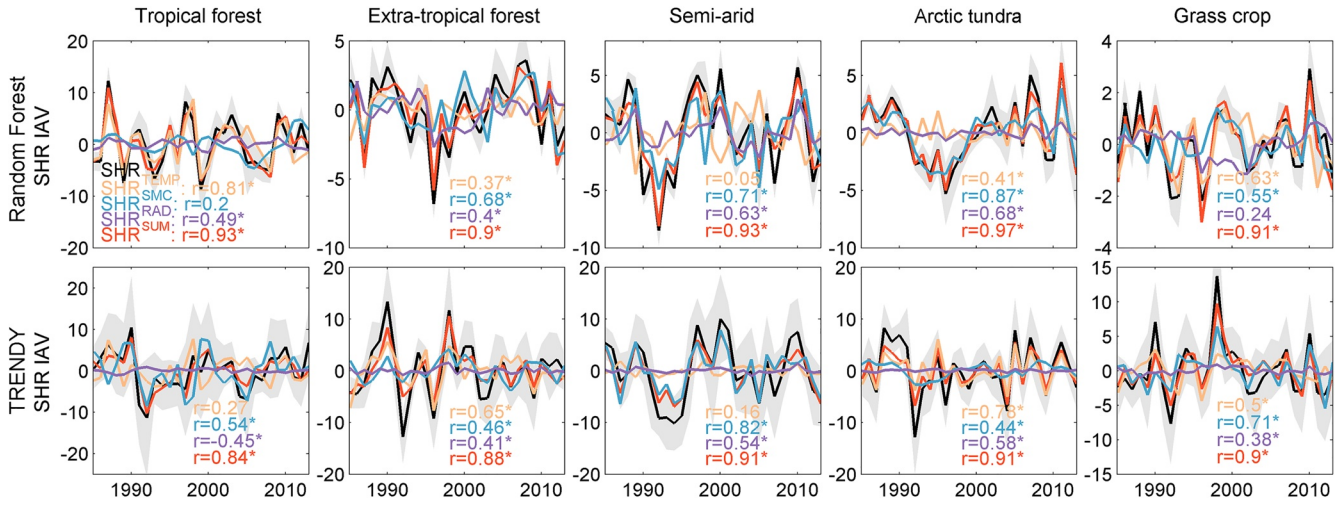

Figure 6. Environmental controls on soil heterotrophic respiration (SHR) inter-annual variability (IAV) in different ecosystems. Panels in top row are derived using our data-driven SHR products. Panels in the bottom row are derived using TRENDY multi-ensemble mean. The correlation coefficients between SHR IAV and SHR anomalies driven by a given factor are labeled in each panel. An asterisk denotes the significance of the corresponding correlation coefficient ($P < 0.05$). The decomposition using precipitation anomaly is shown in Figure S25.

on the Hashimoto data set and we show the result in the supporting information section of this paper (Text S1).

3.5. Biome-Scale SHR Anomalies Attribution

To check whether the dominance of water availability on SHR IAV differs between biome types and regions, we aggregate SHR anomalies to tropical forest, extra-tropical forest, semi-arid region, Arctic tundra, grass and crop area (Figure S23, adapted from Ahlström et al. (2015)). To confirm whether the uncertainty affects the relationship between SHR and climatic factors, here we show the pattern of correlation between SHR anomaly driven by each climatic factor and SHR anomaly in Figure S24. We can find that precipitation and soil moisture significantly control the SHR IAV in Arctic tundra, semi-arid regions and extra-tropical forests. In tropical forests, as well as grass and cropland, fluctuations in both temperature and precipitation show significant effects on SHR IAV in more than half of our SHR ensembles (63 of 126 members). Such a statistically significant response to climatic factors across multiple members allows us to analyze the regional drivers of SHR IAV.

In tropical forests, SHR IAV is mainly driven by temperature variability, whereas in extra-tropical forests and semi-arid areas, precipitation variability plays a dominant role (Figure S25). Precipitation variability is comparable to temperature in driving SHR anomalies in grass and crop areas. In Arctic tundra, the dominant factor for SHR IAV is the fluctuation in soil water content, regardless of the moisture variable being used, while fluctuation in temperature seems to be less important (Figures 6, S25, and S26). When considering regression against soil moisture, we notice that the ranking of factors is shuffled to some extent (Figures 6 and S25), which may be due to the difference between variability in precipitation and soil moisture regionally (Figures S17 and S18). For example, in extra-tropical areas, the importance of water availability increases greatly when regression is carried out against soil moisture (CPC or GLDAS, Figures 6 and S25). For the Tang data set, we found that a dominance of precipitation or soil moisture also appears in tropical and extra-tropical forests, semi-arid areas, and Arctic tundra (Figure S27). In grass and cropland, temperature is also important for SHR IAV regionally (Figure S27). Our attribution of climatic drivers for SHR IAV differs from Tang et al. (2020) mainly in tropical forests (temperature is dominant in our study vs. precipitation in Tang et al., 2020).

Attribution of the TRENDY ensemble shows consistent water-driven estimation in semi-arid areas but differs from our data-driven results mainly in the tropical forest (Figure 6): in these regions, TRENDY SHR IAV is mainly driven by precipitation or soil moisture variability rather than temperature variability (Figures 6

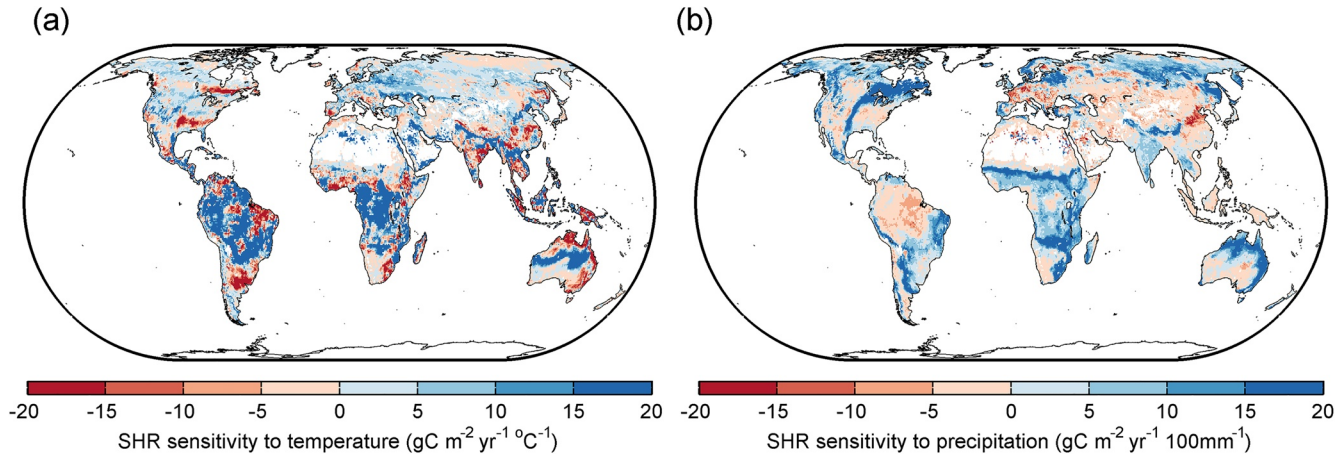

Figure 7. Spatial distribution of the sensitivities of our data-oriented soil heterotrophic respiration (SHR) to anomalies in (a) temperature and (b) precipitation. A negative temperature sensitivity means that when temperature increases, SHR decreases.

and S28). In extra-tropical forest and Arctic tundra, the controlling effect of temperature on TRENDY SHR anomaly is also non-negligible compared to that of water availability (Figure 6). In grass and crop area, TRENDY ensemble mean shows that both precipitation and soil water effects outbalance temperature effects, which does not perfectly match our estimation. Furthermore, it also should be noted that the different TRENDY models disagree on the attribution of SHR anomalies between water versus temperature across different ecosystems (Figures S28 and S29).

During the reconstruction process, we also computed the distinct sensitivities of SHR to climate factors, especially temperature and water availability (Figures 7 and S30). Regional heterogeneity of the sensitivity of SHR to temperature and precipitation/ soil moisture may alter the overall trajectory of SHR because of coexistence of regional deceleration and acceleration of SHR and/or compensatory effects of temperature and precipitation. For our data-driven SHR members, for example, in the tropics, positive temperature sensitivity in Amazon, central Africa, as well as negative sensitivity to precipitation in these areas lead to opposite temperature and precipitation driven SHR anomalies in the cooler and drier year of 1992. In Siberia, negative SHR sensitivity to temperature and positive sensitivity to precipitation contribute to additive climate driven sub-components in IAV under warm but dry condition. The sensitivity of SHR to soil moisture depends on the data set used, especially in boreal regions and central Africa (Figure S30). More negative sensitivity to soil moisture availability was found in wet tropics areas when using GLDAS soil moisture (0–2.0 m) as a predictor than when using CPC (0–1.6 m), indicating that soil moisture increases in deeper layers can be more negatively related to SHR than changes in shallow layers if we assume little difference of soil moisture in their common depth intervals.

4. Discussion

4.1. Implications and Future Directions of Data-Driven SHR estimation

In this study, we generated a newly up-scaled SHR data set using a Random Forest algorithm and explanatory variables of climatological indicators, GPP as well as soil properties. We carefully evaluated the model performance with cross-validation and assessed the estimated uncertainty, which has generally not been done in previous studies. Our products can be utilized to evaluate the sensitivities of process-based models and constrain their performances in both spatial and temporal scales (Ichii et al., 2017).

Our results exhibited both similarities and differences compared to results from previous analyses. The similarities in spatial distribution with Hashimoto et al. (2015) could be due to two reasons. First, both studies used observation records from SRDB, which ensured their similar SHR range (although a more recent version of SRDB, with much more data, was used here). Second, both two studies are vulnerable to uneven sampling and potential extrapolation problem to some extent. In terms of the Tang SHR data, both differences in explanatory variables selection and sample data set affect regional SHR variation between Tang

et al. (2020) and our SHR datasets, and the inclusion of records with annual SHR above 1,100 gC m^{-2} yr^{-1} influences the magnitude of SHR in tropical regions (Figures S31a and S31d). When we exclude GPP from explanatory variables sets, SHR differs especially in central Africa and India, where inclusion of GPP helps produce higher SHR in central Africa and lower SHR in India (Figures S31a and S31c). It also should be noted that Tang et al. (2020) included more sample data in China, which also contributes to the difference of their SHR estimation in temperate climate regions like China and Europe. RMSE from LOOCV was 20% smaller in our study (112 gC m^{-2} yr^{-1}) compared to Tang et al. (2020), with RMSE of 143 gC m^{-2} yr^{-1}.

We found that TRENDY models underestimate boreal region SHR, and overestimate SHR especially in tropics, with a conspicuous spatial contrast along latitudes (Figure S8). A misrepresentation of nitrogen constraints, and oversimplified treatment of processes like microbial dynamics and the climatological dependence of decomposition in different soil texture types, may be responsible for this tendency to produce unrealistic SHR values compared to observations, in turn suggesting areas for focused model research and improvement (Shao et al., 2013; Yan et al., 2018). Our newly derived estimation can thus help improve model ability to accurately predict response of soil carbon to future climate change scenarios.

Nevertheless, limitations undoubtedly remain in our data-driven products, which we suggest can be split into uncertainties in the (a) underlying soil respiration observation data, (b) the driving climate and GPP gridded data, and (c) the up-scaling process. First of all, the uncertainty introduced by partitioning of autotrophic and heterotrophic (i.e., SHR) components of the measured soil respiration flux is poorly understood but potentially large. Approaches such as isotope labeling bring less disturbance to the root-soil system, but introduce their own uncertainties from for example, mixing model assumptions. Root extraction methods neglect the contribution of priming mechanism (Kuzyakov & Larionova, 2005), the amplified effect of which is ~12% in permafrost ecosystem (Keuper et al., 2020). Trenching approaches feature significant disturbance but subsequent simpler inference. Better partitioning will reduce uncertainties entered into the estimation model (Carbone et al., 2016), and we suggest that it is the right time for a meta-analysis examining the potential biases of these different approaches.

Second, observation data of SHR is provided at coarse temporal resolution of a year. Our upscaled SHR data set thus incorporates responses to environmental variations only annually, which mask different sensitivities (possibly different signs of sensitivities as well) at the seasonal scales (Shao et al., 2013). More SHR observations at daily, monthly, and seasonal measurements will help us understand more of its responses to varying environmental conditions like seasonal lagged responses (Vargas et al., 2010) and also benefit model evaluations.

Third, the biased sampling of observations at the global scale (Schimel et al., 2015; Xu & Shang, 2016) forces up-scaling approaches to extrapolate to under-sampled area, affecting the accuracy of model prediction. For example, the tropics are predicted to have the largest SHR fluxes, but are greatly under-sampled, leading to the largest uncertainty in our data-driven SHR data set. The climate space sampled by all filtered observations ranges from 11.5 to 5,302 mm in mean annual precipitation and from −10 to 31.5°C in mean annual temperature. Relatively few reported data exist from cold areas, warm dry areas, and warm humid areas (Figure S32). The space of GPP, soil moisture, soil carbon content and annual nitrogen deposition under-sampled by measurement records are shown in Figure S33. The spread of 1,000 trees in Random Forest can reflect the uncertainty from such extrapolation to under-sampled domain, from which the 95% CI is 38.6–56.3 Pg C yr^{-1}. This uncertainty measure has also been used in J. Zeng et al. (2020) for net ecosystem productivity and Warner et al. (2019) as well as Stell et al. (2021) for soil respiration. Through the comparison of two sources of uncertainties (alternative gridded explanatory data and uncertainty from extrapolation to under-sampled domain by spread of trees), we find that uncertainty from individual trees in Random Forest model is far larger than that from different explanatory variables datasets. Our similarity with Hashimoto data set in spatial gradient could also be partly explained by the under-sampling issue in both studies. In the Hashimoto work, the two globally fixed parameters to derive SHR from soil respiration can possibly narrow the real range of SHR compared to broader coverage of soil respiration point data in climate space. Therefore, the priority should be more data collection in under-sampled areas to constrain the current wider prediction distributions, as an optimized network design has been demonstrated to decrease uncertainty in global estimates (Stell et al., 2021).

In addition, unlike eddy-covariance records extending more than 20 years, most available SHR observations are of short duration (the longest continuous observation lasted 6 years in SRDB 4.0). The "space substitution for time" concept is common under such circumstances but should be treated with caution since the prediction accuracy of such substitution requires consistency between temporal and spatial variation in climate space (Blois et al., 2013). Therefore, we call for more valid sub-sampling, which can be indispensable to fill the gap between spatial and temporal climatic gradients. Further data compilation and integration are extremely valuable for upscaling and improving performances of SHR estimation models (Bond-Lamberty, 2018; Harden et al., 2018).

With regard to uncertainty emerged during the up-scaling process, it is worth noting that some variables are poorly represented within our procedure. For example, land cover is found to contribute the least to change in model error as shown in Figure 2c. Although our way of handling this categorical variable, one-hot encoding (Lantz, 2013), is good at tackling discrete variables, land cover's effect may covary with other environmental gradients and climatic proxies. In addition, climatological and other physiological inputs are less certain, especially in the tropics. Besides, some key explanatory variables remain unavailable currently, for example, other nutrients like phosphorus availability, microbial activity, mycorrhizal types (Crowther et al., 2019), as well as disturbance information including land use/ cover change (LUCC). The uncertainties in inputs and the lack of consideration of other potential factors can be responsible for the underestimation in prediction for observed SHR exceeding 1000 gC m^{-2} yr^{-1} in tropics (Figure 2a). Disturbances affect how SHR varies over vegetation succession and then lead to changes of ecosystem soil carbon pools (Harmon et al., 2011), but limited mapping of this information, and the highly uncertain consequences of SHR responses to LUCC, impede our careful consideration of its effect. The treatment of disturbance history has been attempted in the case of taking stand age to account for disturbance effects on forest carbon dynamics (Xiao et al., 2014), and a similar approach could be used to extend our estimation framework toward better SHR prediction.

Recently, scientists have started to explore the application of deep-learning in data-driven earth system science (Reichstein et al., 2019). Recurrent Neural Network (RNN) may have great potential in modeling dynamic time series like net ecosystem productivity, with advantages over other regression methods in considering legacy effects or lagged indicators (Reichstein et al., 2018). Considering that time-lag responses of SHR to climate anomalies are important in evaluating terrestrial carbon cycle feedbacks to climate warming (X. Zhou et al., 2010), and photosynthesis can also influence soil respiration with hysteresis regionally (Kuzyakov & Gavrichkova, 2010), deep learning frameworks like RNN are ideal tools for improving our SHR estimation. Given the large demand for observation samples in deep learning neural networks, we highlight again that more SHR observations should be implemented and compiled. Since eddy covariance data provides ecosystem respiration records (auto-plus heterotrophic respiration) as well, a reasonable model as partition tool from autotrophic parts can also be an ideal solution for collecting more available SHR data (Koerber et al., 2016).

4.2. Climatic Drivers of SHR Anomalies

Since many studies emphasize the controls of water availability on ecosystem carbon fluxes (Humphrey et al., 2018; Jung et al., 2017), it is not surprising that we found that global SHR IAV is mainly controlled by the fluctuation in water condition. The dominance of water variation exists, yet the sensitivity of SHR IAV to water depends on the choice of proxy for water content (using soil moisture or precipitation in linear decomposition of SHR anomalies). Similar findings have been identified in Ballantyne et al. (2017) and Yan et al. (2018). This can be expected since SHR depends on soil water content (Skopp et al., 1990), although this relationship can be influenced by soil property (Moyano et al., 2012, 2013), microbial diversity (Zhang & Zhang, 2016), historical rainfall condition (Hawkes et al., 2017), and background water condition (Hinko-Najera et al., 2015; Matteucci et al., 2015). In addition, water content also affects the microbial community composition (Zhao et al., 2016), substrates availability, activities of extracellular enzymes (Schindlbacher et al., 2012), and even temperature sensitivity to SHR (Suseela et al., 2012).

Regionally speaking, our result of dominant water controls of SHR in extra-tropical forest and semi-arid regions are consistent with plot-scale experimental tests (Hursh et al., 2017; W. Liu et al., 2009). In semi-arid areas, a small response to temperature fluctuation is possibly restrained by soil moisture and substrate

availability (N. Zhang et al., 2013). As for Arctic tundra, such colder high-latitude areas can be more responsive to warming (Carey et al., 2016) and warmer temperature can cause shifts from heterotrophic to autotrophic respiration (Hicks Pries et al., 2015). Nevertheless, our diagnosed soil moisture control on tundra SHR IAV is not unrealistic, as some researchers have also reported that soil moisture affects ground thaw and the magnitudes of carbon loss is driven by soil moisture (Natali et al., 2015). There are also few records from Arctic tundra, meaning that incorrect spatial extrapolation might explain this particular positive response of tundra SHR to water availability.

Given that large-scale droughts will likely to happen by the end of the 21st century (Lu et al., 2019), our examined response of SHR to variability in water condition is a first step toward making reliable projections of soil carbon loss. However, we only consider the nonlag (yearly) response of SHR to environmental variability in current year; in the real world, lagged or adapted responses are non-negligible (Arnone Iii et al., 2008; de Nijs et al., 2019; Göransson et al., 2013). As noted above, applying deep learning techniques such as RNN (Kraft et al., 2019) hold great promise to robustly deal with such dynamics.

Despite the prevalent positive water controlling effects of SHR in most ecosystems, we also note that our ecosystem-level IAV attribution found that temperature anomalies dominate tropical forest SHR variability. Warming stimulating soil respiration has been demonstrated in many previous studies (Hursh et al., 2017; O'Connell et al., 2018), although thermal acclimation of heterotrophic microbes occurs (Carey et al., 2016; Crowther & Bradford, 2013). Since warming could also lead to soil water loss, primary positive effects of temperature mainly distribute in non-water-limited areas. Tropical forests account for the largest fraction of global SHR, and current tropical temperatures seem still lower than the physiological optima for respiration (M. Huang et al., 2019; Liu, He, et al., 2018). In other words, a stimulation effect from warming to SHR still exists, which may greatly affect the local soil-atmospheric carbon fluxes fluctuations and place tropical soil carbon storage at risk given the positive sensitivity to temperature. In addition, any interplay among different factors is not accounted for in our multiple linear regression formula. Therefore, further research is required to clarify the interaction effects between two associated factors of temperature and water availability.

The responses of SHR from TRENDY models to climatic variability differ among models at biome and global scales (Figures S22 and S28). This could be due to different specific formula forms of SHR parameterizations with climatic factors among models, like Arrhenius, hill or monotonic type (Todd-Brown et al., 2013) and to different degrees of couplings between productivity and respiration. For example, CABLE, ISAM and VEGAS exhibit dominant temperature controls on SHR IAV, which are different from the water effects identified in nearly all data-driven products in our study. The underestimation of water effects on year-to-year fluctuations of net carbon fluxes in process-based models has already been highlighted (Green et al., 2017; Humphrey et al., 2018; Liu, Ballantyne, et al., 2018). Therefore, the internal parameterization schemes should be rigorously constrained and improved with the aid of causal perspectives in sensitivities of SHR to climate variability from our data-driven estimation. Using such causal statistics as a benchmark can better constrain the modeled carbon cycle feedback (Claessen et al., 2019), reducing the uncertainties in climate projections (Friedlingstein et al., 2014).

4.3. Effects of Other Environmental Factors on SHR

Apart from the climate variables that have been used in our attribution analyses, other explanatory variables like GPP (affected by climate) and nitrogen availability are non-negligible factors affecting SHR through substrate availability and/ or microbial activity (Figure 2c). The spatial gradient reflected in our data-driven SHR resembles that of GPP. This is expected, as decomposition of fresh or recent organic matter like leaves and fine roots contributes to the main component of SHR (Janssens et al., 2001). However, the association between productivity and substrate availability is not constant or always predictable (Peterson & Lajtha, 2013), and the dependence of SHR on productivity can be confounded by temperature effects (P. Li et al., 2013).

We also found that nitrogen deposition influences the change in mean squared error of predicted SHR (Figure 2c). Nitrogen content may exert a major control on soil microbial activity (Janssens et al., 2010), indirectly expressed as soil acidification (Wang et al., 2019), limitation on substrate sources supply through harm on specific enzymes (Y. Li et al., 2015), and functional changes in the microbial community (Allison

et al., 2008). Higher carbon to nitrogen ratio in soil organic matter decreases decomposer carbon use efficiency and often impedes decomposition (Manzoni et al., 2017; H. Zhang et al., 2018), but not always (Bowden et al., 2004; Guo et al., 2017; Olsson et al., 2005). Controversy still exists on the stimulatory or suppressive effects of nitrogen addition on SHR (Z. Chen et al., 2018), which also vary depending on original nitrogen availability (X. Liu et al., 2017; Sun et al., 2014), the amount of addition (Gao et al., 2014) and even ecosystem types (Cusack et al., 2010; Maaroufi et al., 2019; Mo et al., 2008; L. Zhou et al., 2014). Since any SHR reduction caused by nitrogen addition could reach the same order of magnitude of forest carbon sink (Janssens et al., 2010), further fundamental research is needed to understand how SHR responds to nitrogen deposition in different ecosystems, and whether possible negative effect on SHR could offset the warming induced increase in carbon loss, to better predict SHR changes given increasing nitrogen deposition in the future.

5. Conclusion

Our study integrates a large number of in-situ SHR measurements, satellite and meteorological observations using Random Forest models to produce an ensemble of data-driven global SHR products. This ensemble data set is independent of process-based model outputs and is expected to be beneficial for the model sensitivity parameter calibration. Our attribution analysis provides evidence for an important role of water availability in impacting year-to-year fluctuations of carbon fluxes, although of which can be mediated to some extent by choice of water content proxies in attribution process. To reduce SHR uncertainty and advance our ability to diagnose the state of SHR, we argue that more evenly distributed SHR observations—especially from cold, warm dry and warm humid areas—and more powerful deep learning methods should be considered in further global SHR mapping tasks.

Data Availability Statement

The detailed R codes for producing the soil heterotrophic respiration data can be obtained from http://doi.org/10.5281/zenodo.4321758. Soil heterotrophic respiration data from 1985 to 2013 (all 126 combinations using Random Forest) are available at https://doi.org/10.6084/m9.figshare.11340770.

Acknowledgments
This work was financially supported by the CLAND Convergence Institute funded by ANR (16-CONV-0003). Y. Yao also acknowledges support from Make Our Planet Great Again (MOPGA) Scholarship.

References

Adachi, M., Ito, A., Yonemura, S., & Takeuchi, W. (2017). Estimation of global soil respiration by accounting for land-use changes derived from remote sensing data. *Journal of Environmental Management*, *200*, 97–104. https://doi.org/10.1016/j.jenvman.2017.05.076

Ahlström, A., Raupach, M. R., Schurgers, G., Smith, B., Arneth, A., Jung, M., et al. (2015). The dominant role of semi-arid ecosystems in the trend and variability of the land CO_2 sink. *Science*, *348*, 895–899. https://doi.org/10.1126/science.aaa1668

Allison, S. D., Czimczik, C. I., & Treseder, K. K. (2008). Microbial activity and soil respiration under nitrogen addition in Alaskan boreal forest. *Global Change Biology*, *14*, 1156–1168. https://doi.org/10.1111/j.1365-2486.2008.01549.x

Arnone Iii, J. A., Verburg, P. S., Johnson, D. W., Larsen, J. D., Jasoni, R. L., Lucchesi, A. J., et al. (2008). Prolonged suppression of ecosystem carbon dioxide uptake after an anomalously warm year. *Nature*, *455*, 383–386. https://doi.org/10.1038/nature07296

Baccini, A., Goetz, S., Walker, W., Laporte, N. T., Sun, M., Sulla-Menashe, D., et al. (2012). Estimated carbon dioxide emissions from tropical deforestation improved by carbon-density maps. *Nature Climate Change*, *2*, 182–185. https://doi.org/10.1038/nclimate1354

Ballantyne, A., Smith, W., Anderegg, W., Kauppi, P., Sarmiento, J., Tans, P., et al. (2017). Accelerating net terrestrial carbon uptake during the warming hiatus due to reduced respiration. *Nature Climate Change*, *7*, 148–152. https://doi.org/10.1038/nclimate3204

Beaudoing, H., & Rodell, M. (2016). GLDAS Noah Land Surface Model L4 monthly 0.25 x 0.25 degree V2. 1. In *NASA/GSFC/HSL: Greenbelt, Maryland, USA*. Goddard Earth Sciences Data and Information Services Center (GES DISC).

Blois, J. L., Williams, J. W., Fitzpatrick, M. C., Jackson, S. T., & Ferrier, S. (2013). Space can substitute for time in predicting climate-change effects on biodiversity. *Proceedings of the National Academy of Science of the United States of America*, *110*, 9374–9379. https://doi.org/10.1073/pnas.1220228110

Bond-Lamberty, B. (2018). New techniques and data for understanding the global soil respiration flux. *Earth's Future*, *6*, 1176–1180. https://doi.org/10.1029/2018EF000866

Bond-Lamberty, B., Bailey, V. L., Chen, M., Gough, C. M., & Vargas, R. (2018). Globally rising soil heterotrophic respiration over recent decades. *Nature*, *560*, 80–83. https://doi.org/10.1038/s41586-018-0358-x

Bond-Lamberty, B., Epron, D., Harden, J., Harmon, M. E., Hoffman, F., Kumar, J., et al. (2016). Estimating heterotrophic respiration at large scales: Challenges, approaches, and next steps. *Ecosphere*, *7*, e01380. https://doi.org/10.1002/ecs2.1380

Bond-Lamberty, B., & Thomson, A. (2010). A global database of soil respiration data. *Biogeosciences*, *7*, 1915–1926. https://doi.org/10.5194/bg-7-1915-2010

Bond-Lamberty, B., & Thomson, A. (2018). *A Global Database of Soil Respiration Data*. Version 4.0. ORNL DAAC.

Bond-Lamberty, B., Wang, C., & Gower, S. T. (2004). A global relationship between the heterotrophic and autotrophic components of soil respiration? *Global Change Biology*, *10*, 1756–1766.

Borchers, H. W. (2019). *Pracma: Practical numerical math functions*. R package version 2.2.5. 8 April 2019. Retrieved from https://cran.r-project.org/web/packages/pracma/

Bowden, R. D., Davidson, E., Savage, K., Arabia, C., & Steudler, P. (2004). Chronic nitrogen additions reduce total soil respiration and microbial respiration in temperate forest soils at the Harvard Forest. *Forest Ecology and Management*, *196*, 43–56. https://doi.org/10.1016/j.foreco.2004.03.011

Bradford, M. A., McCulley, R. L., Crowther, T. W., Oldfield, E. E., Wood, S. A., & Fierer, N. (2019). Cross-biome patterns in soil microbial respiration predictable from evolutionary theory on thermal adaptation. *Nature Ecology & Evolution*, *3*, 223–231. https://doi.org/10.1038/s41559-018-0771-4

Breiman, L. (2001). Random forests. *Machine learning*, *45*, 5–32. https://doi.org/10.1023/a:1010933404324

Buermann, W., Forkel, M., O'Sullivan, M., Sitch, S., Friedlingstein, P., Haverd, V., et al. (2018). Widespread seasonal compensation effects of spring warming on northern plant productivity. *Nature*, *562*, 110–114. https://doi.org/10.1038/s41586-018-0555-7

Cai, Y., Guan, K., Lobell, D., Potgieter, A. B., Wang, S., Peng, J., et al. (2019). Integrating satellite and climate data to predict wheat yield in Australia using machine learning approaches. *Agricutural and Forest Meteorology*, *274*, 144–159. https://doi.org/10.1016/j.agrformet.2019.03.010

Carbone, M. S., Richardson, A. D., Chen, M., Davidson, E. A., Hughes, H., Savage, K. E., & Hollinger, D. Y. (2016). Constrained partitioning of autotrophic and heterotrophic respiration reduces model uncertainties of forest ecosystem carbon fluxes but not stocks. *Journal of Geophysical Research: Biogeosciences*, *121*, 2476–2492. https://doi.org/10.1002/2016jg003386

Carey, J. C., Tang, J., Templer, P. H., Kroeger, K. D., Crowther, T. W., Burton, A. J., et al. (2016). Temperature response of soil respiration largely unaltered with experimental warming. *Proceedings of the National Academy of Science of the United States of America*, *113*, 13797–13802. https://doi.org/10.1073/pnas.1605365113

Chen, M., Xie, P., Janowiak, J. E., & Arkin, P. A. (2002). Global land precipitation: A 50-yr monthly analysis based on gauge observations. *Journal of Hydrometeorology*, *3*, 249–266. https://doi.org/10.1175/1525-7541(2002)003<0249:GLPAYM>2.0.CO;2

Chen, Z., Xu, Y., He, Y., Zhou, X., Fan, J., Yu, H., & Ding, W. (2018). Nitrogen fertilization stimulated soil heterotrophic but not autotrophic respiration in cropland soils: A greater role of organic over inorganic fertilizer. *Soil Biology and Biochemistry*, *116*, 253–264. https://doi.org/10.1016/j.soilbio.2017.10.029

Ciais, P., Yao, Y., Gasser, T., Alessandro, B., Yilong, W., Ronny, L., et al. (2020). Empirical estimates of regional carbon budgets imply reduced global soil heterotrophic respiration. *National Science Review*, *8*. https://doi.org/10.1093/nsr/nwaa145

Claessen, J., Molini, A., Martens, B., Detto, M., Demuzere, M., & Miralles, D. (2019). Global biosphere–climate interaction: A multi-scale appraisal of observations and models. *Biogeosciences Discussions*. https://doi.org/10.5194/bg-2019-212

Clark, D. B., Mercado, L. M., Sitch, S., Jones, C. D., Gedney, N., Best, M. J., et al. (2011). The Joint UK Land Environment Simulator (JULES), model description–Part 2: Carbon fluxes and vegetation dynamics. *Geoscientific Model Development*, *4*, 701–722. https://doi.org/10.5194/gmd-4-701-2011

Crowther, T., Van Den Hoogen, J., Wan, J., Mayes, M. A., Keiser, A. D., Mo, L., et al. (2019). The global soil community and its influence on biogeochemistry. *Science*, *365*, eaav0550. https://doi.org/10.1126/science.aav0550

Crowther, T. W., & Bradford, M. A. (2013). Thermal acclimation in widespread heterotrophic soil microbes. *Ecology Letters*, *16*, 469–477. https://doi.org/10.1111/ele.12069

Cusack, D. F., Torn, M. S., McDOWELL, W. H., & Silver, W. L. (2010). The response of heterotrophic activity and carbon cycling to nitrogen additions and warming in two tropical soils. *Global Change Biology*, *16*, 2555–2572. https://doi.org/10.1111/j.1365-2486.2009.02131.x

de Nijs, E. A., Hicks, L. C., Leizeaga, A., Tietema, A., & Rousk, J. (2019). Soil microbial moisture dependences and responses to drying–rewetting: The legacy of 18 years drought. *Global Change Biology*, *25*, 1005–1015. https://doi.org/10.1111/gcb.14508

Fan, Y., & van den Dool, H. (2004). Climate Prediction Center global monthly soil moisture data set at 0.5 resolution for 1948 to present. *Journal of Geophysical Research*, *109*, D10102. https://doi.org/10.1029/2003JD004345

Fan, Y., & Van den Dool, H. (2008). A global monthly land surface air temperature analysis for 1948–present. *Journal of Geophysical Research*, *113*, D01103. https://doi.org/10.1029/2007JD008470

Feng, P., Wang, B., Li Liu, D., Waters, C., & Yu, Q. (2019). Incorporating machine learning with biophysical model can improve the evaluation of climate extremes impacts on wheat yield in south-eastern Australia. *Agricultural and Forest Meteorology*, *275*, 100–113. https://doi.org/10.1016/j.agrformet.2019.05.018

Friedl, M. A., Sulla-Menashe, P., Tan, B., Schneider, A., Ramankutty, N., Sibley, A., & Huang, X. (2010). MODIS Collection 5 global land cover: Algorithm refinements and characterization of new datasets. *Remote Sensing of Environment*, *114*, 168–182. https://doi.org/10.1016/j.rse.2009.08.016

Friedlingstein, P., Meinshausen, M., Arora, V. K., Jones, C. D., Anav, A., Liddicoat, S. K., & Knutti, R. (2014). Uncertainties in CMIP5 climate projections due to carbon cycle feedbacks. *Journal of Climate*, *27*, 511–526. https://doi.org/10.1175/jcli-d-12-00579.1

Gao, Q., Hasselquist, N. J., Palmroth, S., Zheng, Z., & You, W. (2014). Short-term response of soil respiration to nitrogen fertilization in a subtropical evergreen forest. *Soil Biology and Biochemistry*, *76*, 297–300. https://doi.org/10.1016/j.soilbio.2014.04.020

Göransson, H., Godbold, D. L., Jones, D. L., & Rousk, J. (2013). Bacterial growth and respiration responses upon rewetting dry forest soils: Impact of drought-legacy. *Soil Biology and Biochemistry*, *57*, 477–486. https://doi.org/10.1016/j.soilbio.2012.08.031

Green, J. K., Konings, A. G., Alemohammad, S. H., Berry, J., Entekhabi, D., Kolassa, J., et al. (2017). Regionally strong feedbacks between the atmosphere and terrestrial biosphere. *Nature Geoscience*, *10*, 410–414. https://doi.org/10.1038/ngeo2957

Guimberteau, M., Zhu, D., Maignan, F., Huang, Y., Yue, C., Dantec-Nédélec, S., et al. (2018). ORCHIDEE-MICT (v8. 4.1), a land surface model for the high latitudes: Model description and validation. *Geoscientific Model Development*, *11*, 121–163. https://doi.org/10.5194/gmd-11-121-2018

Guo, H., Ye, C., Zhang, H., Pan, S., Ji, Y., Li, Z., et al. (2017). Long-term nitrogen & phosphorus additions reduce soil microbial respiration but increase its temperature sensitivity in a Tibetan alpine meadow. *Soil Biology and Biochemistry*, *113*, 26–34. https://doi.org/10.1016/j.soilbio.2017.05.024

Hanson, P., Edwards, N., Garten, C. T., & Andrews, J. A. (2000). Separating root and soil microbial contributions to soil respiration: A review of methods and observations. *Biogeochemistry*, *48*, 115–146. https://doi.org/10.1023/a:1006244819642

Harden, J. W., Hugelius, G., Ahlström, A., Blankinship, J. C., Bond-Lamberty, B., Lawrence, C. R., et al. (2018). Networking our science to characterize the state, vulnerabilities, and management opportunities of soil organic matter. *Global Change Biology*, *24*, e705–e718. https://doi.org/10.1111/gcb.13896

Harmon, M. E., Bond-Lamberty, B., Tang, J., & Vargas, R. (2011). Heterotrophic respiration in disturbed forests: A review with examples from North America. *Journal of Geophysical Research*, *116*, G00K04. https://doi.org/10.1029/2010JG001495

Harris, I., Jones, P. D., Osborn, T. J., & Lister, D. H. (2014). Updated high-resolution grids of monthly climatic observations–the CRU TS3. 10 Dataset. *International Journal of Climatology*, *34*, 623–642. https://doi.org/10.1002/joc.3711

Hashimoto, S., Carvalhais, N., Ito, A., Nishina, K., & Reichstein, M. (2015). Global spatiotemporal distribution of soil respiration modeled using a global database. *Biogeosciences*, *12*, 4121–4132. https://doi.org/10.5194/bg-12-4121-2015

Haverd, V., Smith, B., Nieradzik, L., Briggs, P. R., Woodgate, W., Trudinger, C. M., et al. (2018). A new version of the CABLE land surface model (Subversion revision r4601) incorporating land use and land cover change, woody vegetation demography, and a novel optimisation-based approach to plant coordination of photosynthesis. *Geoscientific Model Development*, *11*, 2995–3026. https://doi.org/10.5194/gmd-11-2995-2018

Hawkes, C. V., Waring, B. G., Rocca, J. D., & Kivlin, S. N. (2017). Historical climate controls soil respiration responses to current soil moisture. *Proceedings of the National Academy of Science of the United States of America*, *114*, 6322–6327. https://doi.org/10.1073/pnas.1620811114

Haynes, B. E., & Gower, S. T. (1995). Belowground carbon allocation in unfertilized and fertilized red pine plantations in northern Wisconsin. *Tree Physiology*, *15*, 317–325. https://doi.org/10.1093/treephys/15.5.317

Hicks Pries, C. E., van Logtestijn, R. S., Schuur, E. A., Natali, S. M., Cornelissen, J. H., Aerts, R., & Dorrepaal, E. (2015). Decadal warming causes a consistent and persistent shift from heterotrophic to autotrophic respiration in contrasting permafrost ecosystems. *Global Change Biology*, *21*, 4508–4519. https://doi.org/10.1111/gcb.13032

Hijmans, R. J., van Etten, J., Sumner, M., Cheng, J., Baston, D., Bevan, A., et al. (2019). *raster: Geographic Data Analysis and Modeling*. R package version 3.0-7. 22 September 2019. Retrieved from https://CRAN.R-project.org/package=raster

Hinko-Najera, N., Fest, B., Livesley, S. J., & Arndt, S. K. (2015). Reduced throughfall decreases autotrophic respiration, but not heterotrophic respiration in a dry temperate broadleaved evergreen forest. *Agricultural and Forest Meteorology*, *200*, 66–77. https://doi.org/10.1016/j.agrformet.2014.09.013

Huang, J., van den Dool, H. M., & Georgarakos, K. P. (1996). Analysis of model-calculated soil moisture over the United States (1931–1993) and applications to long-range temperature forecasts. *Journal of Climate*, *9*, 1350–1362. https://doi.org/10.1175/1520-0442(1996)009<1350:AOMCSM>2.0.CO;2

Huang, M., Piao, S., Ciais, P., Peñuelas, J., Wang, X., Keenan, T. F., et al. (2019). Air temperature optima of vegetation productivity across global biomes. *Nature Ecology & Evolution*, *3*, 772–779. https://doi.org/10.1038/s41559-019-0838-x

Huang, N., Wang, L., Song, X. P., Black, T. A., Jassal, R. S., Myneni, R. B., et al. (2020). Spatial and temporal variations in global soil respiration and their relationships with climate and land cover. *Science advances*, *6*, eabb8508. https://doi.org/10.1126/sciadv.abb8508

Huang, S., Ye, G., Lin, J., Chen, K., Xu, X., Ruan, J. H., et al. (2018). Autotrophic and heterotrophic soil respiration responds asymmetrically to drought in a subtropical forest in the Southeast China. *Soil Biology and Biochemistry*, *123*, 242–249. https://doi.org/10.1016/j.soilbio.2018.04.029

Humphrey, V., Gudmundsson, L., & Seneviratne, S. I. (2017). A global reconstruction of climate-driven subdecadal water storage variability. *Geophysical Research Letters*, *44*, 2300–2309. https://doi.org/10.1002/2017gl072564

Humphrey, V., Zscheischler, J., Ciais, P., Gudmundsson, L., Sitch, S., & Seneviratne, S. I. (2018). Sensitivity of atmospheric CO_2 growth rate to observed changes in terrestrial water storage. *Nature*, *560*, 628–631. https://doi.org/10.1038/s41586-018-0424-4

Hursh, A., Ballantyne, A., Cooper, L., Maneta, M., Kimball, J., & Watts, J. (2017). The sensitivity of soil respiration to soil temperature, moisture, and carbon supply at the global scale. *Global Change Biology*, *23*, 2090–2103. https://doi.org/10.1111/gcb.13489

Ichii, K., Ueyama, M., Kondo, M., Saigusa, N., Kim, J., Alberto, M. C., et al. (2017). New data-driven estimation of terrestrial CO_2 fluxes in Asia using a standardized database of eddy covariance measurements, remote sensing data, and support vector regression. *Journal of Geophysical Research: Biogeosciences*, *122*, 767–795. https://doi.org/10.1002/2016jg003640

Jain, A. K., Meiyappan, P., Song, Y., & House, J. I. (2013). CO_2 emissions from land-use change affected more by nitrogen cycle, than by the choice of land-cover data. *Global Change Biology*, *19*, 2893–2906. https://doi.org/10.1111/gcb.12207

Janssens, I., Dieleman, W., Luyssaert, S., Subke, J. A., Reichstein, M., Ceulemans, R., et al. (2010). Reduction of forest soil respiration in response to nitrogen deposition. *Nature Geoscience*, *3*, 315–322. https://doi.org/10.1038/ngeo844

Janssens, I., Lankreijer, H., Matteucci, G., Kowalski, A. S., Buchmann, N., Epron, D., et al. (2001). Productivity overshadows temperature in determining soil and ecosystem respiration across European forests. *Global Change Biology*, *7*, 269–278. https://doi.org/10.1046/j.1365-2486.2001.00412.x

Jian, J., Vargas, R., Anderson-Teixeira, K., Stell, E., Herrmann, V., Horn, M., et al. (2021). A restructured and updated global soil respiration database (SRDB-V5). *Earth System Science Data*, *13*, 255–267. https://doi.org/10.5194/essd-13-255-2021

Jung, M., Reichstein, M., Ciais, P., Seneviratne, S. I., Sheffield, J., Goulden, M. L., et al. (2010). Recent decline in the global land evapotranspiration trend due to limited moisture supply. *Nature*, *467*, 951–954. https://doi.org/10.1038/nature09396

Jung, M., Reichstein, M., Margolis, H. A., Cescatti, A., Richardson, A. D., Arain, M. A., et al. (2011). Global patterns of land-atmosphere fluxes of carbon dioxide, latent heat, and sensible heat derived from eddy covariance, satellite, and meteorological observations. *Journal of Geophysical Research*, *116*, G00J07. https://doi.org/10.1029/2010JG001566

Jung, M., Reichstein, M., Schwalm, C. R., Huntingford, C., Sitch, S., Ahlström, A., et al. (2017). Compensatory water effects link yearly global land CO_2 sink changes to temperature. *Nature*, *541*, 516–520. https://doi.org/10.1038/nature20780

Kato, E., Kinoshita, T., Ito, A., Huntingford, C., Sitch, S., Ahlström, A., et al. (2013). Evaluation of spatially explicit emission scenario of land-use change and biomass burning using a process-based biogeochemical model. *Journal of Land Use Science*, *8*, 104–122. https://doi.org/10.1080/1747423x.2011.628705

Keller, K., Lienert, S., Bozbiyik, A., Stocker, T. F., Frank, D. C., Klesse, S., et al. (2017). 20th century changes in carbon isotopes and water-use efficiency: Tree-ring-based evaluation of the CLM4. 5 and LPX-Bern models. *Biogeosciences*, *14*, 2641–2673. https://doi.org/10.5194/bg-14-2641-2017

Keuper, F., Wild, B., Kummu, M., Beer, C., Blume-Werry, G., Fontaine, S., et al. (2020). Carbon loss from northern circumpolar permafrost soils amplified by rhizosphere priming. *Nature Geoscience*, *13*, 560–565. https://doi.org/10.1038/s41561-020-0607-0

Kobayashi, S., Ota, Y., Harada, Y., Beer, C., Blume-Werry, G., Fontaine, S., et al. (2015). The JRA-55 reanalysis: General specifications and basic characteristics. *Journal of the Meteorological Society of Japan Ser. II*, *93*, 5–48. https://doi.org/10.2151/jmsj.2015-001

Koerber, G. R., Meyer, W. S., SUN, Q, Cale, P., & Ewenz, C. M. (2016). Under a new light: Validation of eddy covariance flux with light response functions of assimilation and estimates of heterotrophic soil respiration. *Biogeosciences Discussions*, 1–28. https://doi.org/10.5194/bg-2016-182

Konings, A. G., Bloom, A. A., Liu, J., Parazoo, N. C., Schimel, D. S., & Bowman, K. W. (2019). Global satellite-driven estimates of heterotrophic respiration. *Biogeosciences*, *16*, 2269–2284. https://doi.org/10.5194/bg-16-2269-2019

Kraft, B., Jung, M., Körner, M., Requena, M. C., Cortés, J., & Reichstein, M. (2019). Identifying Dynamic Memory Effects on Vegetation State Using Recurrent Neural Networks. *Frontiers in Big Data*, *2*, 31. https://doi.org/10.3389/fdata.2019.0003

Krinner, G., Viovy, N., de Noblet-Ducoudré, N., Ogée, J., Polcher, J., Friedlingstein, P., et al. (2005). A dynamic global vegetation model for studies of the coupled atmosphere-biosphere system. *Global Biogeochemical Cycles*, *19*, GB1015. https://doi.org/10.1029/2003GB002199

Kuzyakov, Y., & Gavrichkova, O. (2010). Time lag between photosynthesis and carbon dioxide efflux from soil: A review of mechanisms and controls. *Global Change Biology*, *16*, 3386–3406. https://doi.org/10.1111/j.1365-2486.2010.02179.x

Kuzyakov, Y., & Larionova, A. A. (2005). Root and rhizomicrobial respiration: A review of approaches to estimate respiration by autotrophic and heterotrophic organisms in soil. *Journal of Plant Nutrition and Soil Science*, *168*, 503–520. https://doi.org/10.1002/jpln.200421703

Lantz, B. (2013). *Machine learning with R*. Packt Publishing Ltd.

Le Quéré, C., Andrew, R. M., Friedlingstein, P., Sitch, S., Hauck, J., Pongratz, J., et al. (2018). Global carbon budget 2018. *Earth System Science Data*, *10*, 2141–2194.

Li, J., Wang, Y. P., Duan, Q., Lu, X., Pak, B., Wiltshire, A., et al. (2016). Quantification and attribution of errors in the simulated annual gross primary production and latent heat fluxes by two global land surface models. *Journal of Advances in Modeling Earth Systems*, *8*, 1270–1288. https://doi.org/10.1002/2015ms000583

Li, P., Yang, Y., & Fang, J. (2013). Variations of root and heterotrophic respiration along environmental gradients in China's forests. *Journal of Plant Ecology*, *6*, 358–367. https://doi.org/10.1093/jpe/rtt009

Li, Y., Liu, Y., Wu, S., Niu, L., & Tian, Y. (2015). Microbial properties explain temporal variation in soil respiration in a grassland subjected to nitrogen addition. *Scientific Reports*, *5*, 18496. https://doi.org/10.1038/srep18496

Liaw, A., & Wiener, M. (2018). *Classification and regression based on a forest of trees using random inputs, based on Breiman (2001) R package version 4* (pp. 6–14). 22 March 2018. Retrieved from https://www.stat.berkeley.edu/~breiman/RandomForests/

Liu, W., Lü, X., Xu, W., Shi, H., Hou, L., Li, L., & Yuan, W. (2018). Effects of water and nitrogen addition on ecosystem respiration across three types of steppe: The role of plant and microbial biomass. *Science of the Total Environment*, *619*, 103–111. https://doi.org/10.1016/j.scitotenv.2017.11.119

Liu, W., Zhang, Z., & Wan, S. (2009). Predominant role of water in regulating soil and microbial respiration and their responses to climate change in a semiarid grassland. *Global Change Biology*, *15*, 184–195. https://doi.org/10.1111/j.1365-2486.2008.01728.x

Liu, X., Yang, Z., Lin, C., Giardina, C. P., Xiong, D., Lin, W, et al. (2017). Will nitrogen deposition mitigate warming-increased soil respiration in a young subtropical plantation? *Agricultural and Forest Meteorology*, *246*, 78–85. https://doi.org/10.1016/j.agrformet.2017.06.010

Liu, Y., He, N., Wen, X., Xu, L., Sun, X., Yu, G., et al. (2018). The optimum temperature of soil microbial respiration: Patterns and controls. *Soil Biology and Biochemistry*, *121*, 35–42. https://doi.org/10.1016/j.soilbio.2018.02.019

Liu, Z., Ballantyne, A. P., Poulter, B., Anderegg, W. R., Li, W., Bastos, A., & Ciais, P. (2018). Precipitation thresholds regulate net carbon exchange at the continental scale. *Nature Communications*, *9*, 3596. https://doi.org/10.1038/s41467-018-05948-1

Lu, J., Carbone, G. J., & Grego, J. M. (2019). Uncertainty and hotspots in 21st century projections of agricultural drought from CMIP5 models. *Scientific Reports*, *9*, 4922. https://doi.org/10.1038/s41598-019-41196-z

Maaroufi, N. I., Nordin, A., Palmqvist, K., Hasselquist, N. J., Forsmark, B., Rosenstock, N. P., et al. (2019). Anthropogenic nitrogen enrichment enhances soil carbon accumulation by impacting saprotrophs rather than ectomycorrhizal fungal activity. *Global Change Biology*. https://doi.org/10.1111/gcb.14722

Manzoni, S., Čapek, P., Mooshammer, M., Lindahl, B. D., Richter, A., & Šantrůčková, H. (2017). Optimal metabolic regulation along resource stoichiometry gradients. *Ecology Letters*, *20*, 1182–1191. https://doi.org/10.1111/ele.12815

Matteucci, M., Gruening, C., Ballarin, I. G., Seufert, G., & Cescatti, A. (2015). Components, drivers and temporal dynamics of ecosystem respiration in a Mediterranean pine forest. *Soil Biology and Biochemistry*, *88*, 224–235. https://doi.org/10.1016/j.soilbio.2015.05.017

Melton, J. R., & Arora, V. K. (2016). Competition between plant functional types in the Canadian Terrestrial Ecosystem Model (CTEM) v. 2.0. *Geoscientific Model Development*, *9*, 323–361. https://doi.org/10.5194/gmd-9-323-2016

Mo, J., Zhang, W., Zhu, W., Gundersen, P. E. R., Fang, Y., Li, D., & Wang, H. U. I. (2008). Nitrogen addition reduces soil respiration in a mature tropical forest in southern China. *Global Change Biology*, *14*, 403–412. https://doi.org/10.1111/j.1365-2486.2007.01503.x

Moyano, F. E., Manzoni, S., & Chenu, C. (2013). Responses of soil heterotrophic respiration to moisture availability: An exploration of processes and models. *Soil Biology and Biochemistry*, *59*, 72–85. https://doi.org/10.1016/j.soilbio.2013.01.002

Moyano, F. E., Vasilyeva, N. A., Bouckaert, L., Cook, F., Craine, J., Curiel Yuste, J., et al. (2012). The moisture response of soil heterotrophic respiration: Interaction with soil properties. *Biogeosciences*, *9*, 1173–1182. https://doi.org/10.5194/bg-9-1173-2012

Nachtergaele, F., van Velthuizen, H., Verelst, L., Batjes, N. H., Dijkshoorn, K., van Engelen, V. W. P., et al. (2010). The harmonized world soil database. In *Proceedings of the 19th World Congress of Soil Science, Soil Solutions for a Changing World*, Brisbane, Australia, 1–6 August 2010 (pp. 34–37).

Natali, S. M., Schuur, E. A., Mauritz, M., Schade, J. D., Celis, G., Crummer, K. G., et al. (2015). Permafrost thaw and soil moisture driving CO_2 and CH4 release from upland tundra. *Journal of Geophysical Research: Biogeosciences*, *120*, 525–537. https://doi.org/10.1002/2014jg002872

Noh, N.-J., Kuribayashi, M., Saitoh, T. M., Nakaji, T., Nakamura, M., Hiura, T., & Muraoka, H. (2016). Responses of soil, heterotrophic, and autotrophic respiration to experimental open-field soil warming in a cool-temperate deciduous forest. *Ecosystems*, *19*, 504–520. https://doi.org/10.1007/s10021-015-9948-8

O'Connell, C. S., Ruan, L., & Silver, W. L. (2018). Drought drives rapid shifts in tropical rainforest soil biogeochemistry and greenhouse gas emissions. *Nature Communications*, *9*, 1348. https://doi.org/10.1038/s41467-018-03352-3

Oleson, K., Lawrence, D. M., Bonan, G. B., & Drewniak, B. (2013). *Technical description of version 4.5 of the Community Land Model (CLM)*. Boulder, CO. NCAR.

Olsson, P., Linder, S., Giesler, R., & Högberg, P. (2005). Fertilization of boreal forest reduces both autotrophic and heterotrophic soil respiration. *Global Change Biology*, *11*, 1745–1753. https://doi.org/10.1111/j.1365-2486.2005.001033.x

Peng, Y., Chen, G., Li, S., Hu, H. L., Hu, T. X., Liu, L., et al. (2018). Nitrogen additions reduce rhizospheric and heterotrophic respiration in a subtropical evergreen broad-leaved forest. *Plant and Soil*, *431*, 449–463. https://doi.org/10.1007/s11104-018-3751-1

Peterson, F. S., & Lajtha, K. J. (2013). Linking aboveground net primary productivity to soil carbon and dissolved organic carbon in complex terrain. *Journal of Geophysical Research: Biogeosciences*, *118*, 1225–1236. https://doi.org/10.1002/jgrg.20097

Prentice, I. C., Dong, N., Gleason, S. M., Maire, V., & Wright, I. (2014). Balancing the costs of carbon gain and water transport: Testing a new theoretical framework for plant functional ecology. *Ecology Letters*, *17*, 82–91. https://doi.org/10.1111/ele.12211

Raich, J. W., & Potter, C. S. (1995). Global patterns of carbon dioxide emissions from soils. *Global Biogeochemical Cycles*, *9*, 23–36. https://doi.org/10.1029/94gb02723

Raich, J. W., Potter, C. S., & Bhagawati, D. (2002). Interannual variability in global soil respiration, 1980–94. *Global Change Biology*, *8*, 800–812. https://doi.org/10.1046/j.1365-2486.2002.00511.x

R Development Core Team (2019). *R: A language and environment for statistical computing*. Vienna, Austria. R Foundation for Statistical Computing. Retrieved from http://www.R-project.org/

Reichstein, M., Besnard, S., Carvalhais, N., Gans, F., Jung, M., Kraft, B., & Mahecha, M. (2018). Modelling Landsurface Time-Series with Recurrent Neural Nets. In *IGARSS 2018-2018 IEEE International Geoscience and Remote Sensing Symposium* (pp. 7640–7643).

Reichstein, M., Camps-Valls, G., Stevens, B., Jung, M., Denzler, J., & Carvalhais, N., et al. (2019). Deep learning and process understanding for data-driven Earth system science. *Nature*, *566*, 195–204. https://doi.org/10.1038/s41586-019-0912-1

Reick, C. H., Raddatz, T., Brovkin, V., & Gayler, V. (2013). Representation of natural and anthropogenic land cover change in MPI-ESM. *Journal of Advances in Modeling Earth Systems*, *5*, 459–482. https://doi.org/10.1002/jame.20022

Rodell, M., Houser, P., Jambor, U., Gottschalck, J., Mitchell, K., Meng, C. J., et al. (2004). The global land data assimilation system. *Bulletin of the American Meteorological Society*, *85*, 381–394. https://doi.org/10.1175/bams-85-3-381

Schimel, D., Stephens, B. B., & Fisher, J. B. (2015). Effect of increasing CO_2 on the terrestrial carbon cycle. *Proceedings of the National Academy of Science of the United States of America*, *112*, 436–441. https://doi.org/10.1073/pnas.1407302112

Schindlbacher, A., Wunderlich, S., Borken, W., Kitzler, B., Zechmeister-Boltenstern, S., & Jandl, R. (2012). Soil respiration under climate change: Prolonged summer drought offsets soil warming effects. *Global Change Biology*, *18*, 2270–2279. https://doi.org/10.1111/j.1365-2486.2012.02696.x

Schindlbacher, A., ZECHMEISTER-BOLTENSTERN, S., & Jandl, R. (2009). Carbon losses due to soil warming: Do autotrophic and heterotrophic soil respiration respond equally? *Global Change Biology*, *15*, 901–913. https://doi.org/10.1111/j.1365-2486.2008.01757.x

Schwalm, C. R., Anderegg, W. R., Michalak, A. M., Fisher, J. B., Biondi, F., Koch, G., et al. (2017). Global patterns of drought recovery. *Nature*, *548*, 202–205. https://doi.org/10.1038/nature23021

Shao, P., Zeng, X., Moore, D. J., & Zeng, X. (2013). Soil microbial respiration from observations and Earth System Models. *Environmental Research Letters*, *8*, 034034. https://doi.org/10.1088/1748-9326/8/3/034034

Sheffield, J., Goteti, G., & Wood, E. F. (2006). Development of a 50-year high-resolution global dataset of meteorological forcings for land surface modeling. *Journal of Climate*, *19*, 3088–3111. https://doi.org/10.1175/jcli3790.1

Skopp, J., Jawson, M., & Doran, J. (1990). Steady-state aerobic microbial activity as a function of soil water content. *Soil Science Society of America Journal*, *54*, 1619–1625. https://doi.org/10.2136/sssaj1990.03615995005400060018x

Steidinger, B. S., Crowther, T. W., Liang, J., Van Nuland, M. E., Werner, G. D., Reich, P. B., et al. (2019). Climatic controls of decomposition drive the global biogeography of forest-tree symbioses. *Nature*, *569*, 404–408. https://doi.org/10.1038/s41586-019-1128-0

Stell, E., Warner, D., Jian, J., Bond-Lamberty, B., & Vargas, R. (2021). Spatial biases of information influence global estimates of soil respiration: How can we improve global predictions? *Global Change Biology*. https://doi.org/10.1111/GCB.15666

Stocker, B. D., Zscheischler, J., Keenan, T. F., Prentice, I. C., Seneviratne, S. I., & Peñuelas, J. (2019). Drought impacts on terrestrial primary production underestimated by satellite monitoring. *Nature Geoscience*, *12*, 264–270. https://doi.org/10.1038/s41561-019-0318-6

Sun, Z., Liu, L., Ma, Y., Yin, G., Zhao, C., Zhang, Y., & Piao, S. (2014). The effect of nitrogen addition on soil respiration from a nitrogen-limited forest soil. *Agricultural and Forest Meteorology*, *197*, 103–110. https://doi.org/10.1016/j.agrformet.2014.06.010

Suseela, V., Conant, R. T., Wallenstein, M. D, & Dukes, J. S. (2012). Effects of soil moisture on the temperature sensitivity of heterotrophic respiration vary seasonally in an old-field climate change experiment. *Global Change Biology*, *18*, 336–348. https://doi.org/10.1111/j.1365-2486.2011.02516.x

Tang, X., Fan, S., Du, M., Zhang, W., Gao, S., Liu, S., et al. (2020). Spatial and temporal patterns of global soil heterotrophic respiration in terrestrial ecosystems. *Earth System Science Data*, *12*, 1037–1051. https://doi.org/10.5194/essd-12-1037-2020

Todd-Brown, K., Randerson, J., Post, W., Hoffman, F. M., Tarnocai, C., Schuur, E. A. G., & Allison, S. D. (2013). Causes of variation in soil carbon simulations from CMIP5 Earth system models and comparison with observations. *Biogeosciences*, *10*, 1717–1736. https://doi.org/10.5194/bg-10-1717-2013

Tramontana, G., Jung, M., Camps-Valls, G., Schwalm, C. R., Ichii, K., Ráduly, B., et al. (2016). Predicting carbon dioxide and energy fluxes across global FLUXNET sites with regression algorithms. *Biogeosciences Discussions*. https://doi.org/10.5194/bg-2015-661

Van den Dool, H., Huang, J., & Fan, Y. (2003). Performance and analysis of the constructed analogue method applied to US soil moisture over 1981–2001. *Journal of Geophysical Research*, *108*(D16), 8617. https://doi.org/10.1029/2002JD003114

Vargas, R., Baldocchi, D. D., Allen, M. F., Bahn, M., Black, T. A., Collins, S. L., et al. (2010). Looking deeper into the soil: Biophysical controls and seasonal lags of soil CO_2 production and efflux. *Ecological Applications*, *20*, 1569–1582. https://doi.org/10.1890/09-0693.1

Viovy, N. (2015). *CRU-NCEP v6.1 Dataset*. Retrieved from http://dods.extra.cea.fr/store/p529viov/cruncep/

Wang, H., Prentice, I. C., Keenan, T. F., Davis, T. W., Wright, I. J., Cornwell, W. K., et al. (2017). Towards a universal model for carbon dioxide uptake by plants. *Nature Plants*, *3*, 734–741. https://doi.org/10.1038/s41477-017-0006-8

Wang, J., Fu, X., Zhang, Z., Li, M., Cao, H., Zhou, X., & Ni, H. (2019). Responses of soil respiration to nitrogen addition in the Sanjiang Plain wetland, northeastern China. *PloS One*, *14*, e0211456. https://doi.org/10.1371/journal.pone.0211456

Warner, D. L., Bond-Lamberty, B., Jian, J., Stell, E., & Vargas, R. (2019). Spatial predictions and associated uncertainty of annual soil respiration at the global scale. *Global Biogeochemical Cycles*, *33*, 1733–1745. https://doi.org/10.1029/2019gb006264

Weedon, G. P., Balsamo, G., Bellouin, N., Gomes, S., Best, M. J., & Viterbo, P. (2014). The WFDEI meteorological forcing data set: WATCH Forcing Data methodology applied to ERA-Interim reanalysis data. *Water Resources Research*, *50*, 7505–7514. https://doi.org/10.1002/2014wr015638

Wieder, W., Boehnert, J., Bonan, G., & Langseth, M. (2014). *Regridded harmonized world soil database v1. 2*. ORNL DAAC.

Xiao, J., Ollinger, S. V., Frolking, S., Hurtt, G. C., Hollinger, D. Y., Davis, K. J., et al. (2014). Data-driven diagnostics of terrestrial carbon dynamics over North America. *Agricultural and Forest Meteorology*, *197*, 142–157. https://doi.org/10.1016/j.agrformet.2014.06.013

Xu, M., & Shang, H. (2016). Contribution of soil respiration to the global carbon equation. *Journal of Plant Physiology*, *203*, 16–28. https://doi.org/10.1016/j.jplph.2016.08.007

Yan, Z., Bond-Lamberty, B., Todd-Brown, K. E., Bailey, V. L., Li, S., Liu, C., & Liu, C. (2018). A moisture function of soil heterotrophic respiration that incorporates microscale processes. *Nature Communications*, *9*, 2562. https://doi.org/10.1038/s41467-018-04971-6

Yao, Y., Wang, X., Li, Y., Wang, T., Shen, M., Du, M., et al. (2018). Spatiotemporal pattern of gross primary productivity and its covariation with climate in China over the last thirty years. *Global Change Biology*, *24*, 184–196. https://doi.org/10.1111/gcb.13830

Zaehle, S., & Friend, A. D. (2010). Carbon and nitrogen cycle dynamics in the O-CN land surface model: 1. Model description, site-scale evaluation, and sensitivity to parameter estimates. *Global Biogeochemical Cycles*, *24*. https://doi.org/10.1029/2009GB003522

Zeng, J., Matsunaga, T., Tan, Z. H., Saigusa, N., Shirai, T., Tang, Y., et al. (2020). Global terrestrial carbon fluxes of 1999–2019 estimated by upscaling eddy covariance data with a random forest. *Scientific data*, *7*, 1–11. https://doi.org/10.1038/s41597-020-00653-5

Zeng, N., Mariotti, A., & Wetzel, P. (2005). Terrestrial mechanisms of interannual CO_2 variability. *Global Biogeochemical Cycles*, *19*, GB1016. https://doi.org/10.1029/2004GB002273

Zeng, Z., Wang, T., Zhou, F., Ciais, P., Mao, J., Shi, X., & Piao, S. (2014). A worldwide analysis of spatiotemporal changes in water balance-based evapotranspiration from 1982 to 2009. *Journal of Geophysical Research: Atmospheres*, *119*, 1186–1202. https://doi.org/10.1002/2013jd020941

Zhang, F. G., & Zhang, Q. G. (2016). Microbial diversity limits soil heterotrophic respiration and mitigates the respiration response to moisture increase. *Soil Biology and Biochemistry*, *98*, 180–185. https://doi.org/10.1016/j.soilbio.2016.04.017

Zhang, H., Goll, D. S., Manzoni, S., Ciais, P., Guenet, B., & Huang, Y. (2018). Modeling the effects of litter stoichiometry and soil mineral N availability on soil organic matter formation using CENTURY-CUE (v1. 0). *Geoscientific Model Development*, *11*, 4779–4796. https://doi.org/10.5194/gmd-11-4779-2018

Zhang, N., Liu, W., Yang, H., Yu, X., Gutknecht, J. L., Zhang, Z., et al. (2013). Soil microbial responses to warming and increased precipitation and their implications for ecosystem C cycling. *Oecologia*, *173*, 1125–1142. https://doi.org/10.1007/s00442-013-2685-9

Zhao, C., Miao, Y., Yu, C., Zhu, L., Wang, F., Jiang, L., et al. (2016). Soil microbial community composition and respiration along an experimental precipitation gradient in a semiarid steppe. *Scientific Reports*, *6*, 24317. https://doi.org/10.1038/srep24317

Zhou, L., Zhou, X., Zhang, B., Lu, M., Luo, Y., Liu, L., & Li, B. (2014). Different responses of soil respiration and its components to nitrogen addition among biomes: A meta-analysis. *Global Change Biology*, *20*, 2332–2343. https://doi.org/10.1111/gcb.12490

Zhou, X., Luo, Y., Gao, C., Verburg, P. S., Arnone, J. A. III, Darrouzet-Nardi, A., & Schimel, D. S. (2010). Concurrent and lagged impacts of an anomalously warm year on autotrophic and heterotrophic components of soil respiration: A deconvolution analysis. *New Phytology*, *187*, 184–198. https://doi.org/10.1111/j.1469-8137.2010.03256.x

Zhu, J., Hu, H., Tao, S., Chi, X., Li, P., Jiang, L., et al. (2017). Carbon stocks and changes of dead organic matter in China's forests. *Nature Communications*, *8*, 151. https://doi.org/10.1038/s41467-017-00207-1

Zou, J., Tobin, B., Luo, Y., & Osborne, B. (2018). Response of soil respiration and its components to experimental warming and water addition in a temperate Sitka spruce forest ecosystem. *Agricultural and Forest Meteorology*, *260*, 204–215. https://doi.org/10.1016/j.agrformet.2018.06.020

Geosci. Model Dev., 15, 7809–7833, 2022
https://doi.org/10.5194/gmd-15-7809-2022

Geoscientific Model Development
Open Access
EGU

Forest fluxes and mortality response to drought: model description (ORCHIDEE-CAN-NHA r7236) and evaluation at the Caxiuanã drought experiment

Yitong Yao[1,★], Emilie Joetzjer[2,★], Philippe Ciais[1], Nicolas Viovy[1], Fabio Cresto Aleina[1], Jerome Chave[3], Lawren Sack[4], Megan Bartlett[5], Patrick Meir[6], Rosie Fisher[7], and Sebastiaan Luyssaert[8]

[1]Laboratoire des Sciences du Climat et de l'Environnement, LSCE/IPSL, CEA-CNRS-UVSQ, Université Paris-Saclay, Gif-sur-Yvette, 91191, France
[2]Centre National de Recherche Meteorologique, Unite mixte de recherche 3589 Meteo-France/CNRS, 42 Avenue Gaspard Coriolis, Toulouse, 31100, France
[3]Laboratoire Evolution et Diversité Biologique UMR 5174 CNRS, IRD, Université Paul Sabatier, Toulouse, 31062, France
[4]Department of Ecology and Evolutionary Biology, University of California Los Angeles, Los Angeles, California 90095, USA
[5]Department of Viticulture & Enology, University of California, Davis, California 95616, USA
[6]Research School of Biology, Australian National University, Canberra, ACT 2601 Australia
[7]CICERO Center for International Climate and Environmental Research, Oslo, Norway
[8]Faculty of Science, Vrije Universiteit Amsterdam, the Netherlands
★These authors contributed equally to this work.

Correspondence: Yitong Yao (yitong.yao@lsce.ipsl.fr)

Received: 1 November 2021 – Discussion started: 20 December 2021
Revised: 28 September 2022 – Accepted: 2 October 2022 – Published: 24 October 2022

Abstract. Extreme drought events in Amazon forests are expected to become more frequent and more intense with climate change, threatening ecosystem function and carbon balance. Yet large uncertainties exist on the resilience of this ecosystem to drought. A better quantification of tree hydraulics and mortality processes is needed to anticipate future drought effects on Amazon forests. Most state-of-the-art dynamic global vegetation models are relatively poor in their mechanistic description of these complex processes. Here, we implement a mechanistic plant hydraulic module within the ORCHIDEE-CAN-NHA r7236 land surface model to simulate the percentage loss of conductance (PLC) and changes in water storage among organs via a representation of the water potentials and vertical water flows along the continuum from soil to roots, stems and leaves. The model was evaluated against observed seasonal variability in stand-scale sap flow, soil moisture and productivity under both control and drought setups at the Caxiuanã throughfall exclusion field experiment in eastern Amazonia between 2001 and 2008. A relationship between PLC and tree mortality is built in the model from two empirical parameters, the cumulated duration of drought exposure that triggers mortality, and the mortality fraction in each day exceeding the exposure. Our model captures the large biomass drop in the year 2005 observed 4 years after throughfall reduction, and produces comparable annual tree mortality rates with observation over the study period. Our hydraulic architecture module provides promising avenues for future research in assimilating experimental data to parameterize mortality due to drought-induced xylem dysfunction. We also highlight that species-based (isohydric or anisohydric) hydraulic traits should be further tested to generalize the model performance in predicting the drought risks.

Published by Copernicus Publications on behalf of the European Geosciences Union.

1 Introduction

Drought-induced forest mortality events are projected to become more frequent and intense under current climate trends (Allen et al., 2015) and may threaten vegetation carbon sinks, as well as biophysical climate regulation by forests (Allen et al., 2010; McDowell et al., 2018). Amazonian rainforests hold the largest forest biomass carbon stock on Earth as one of the most important components of the global carbon balance. In the last 15–20 years, Amazonia has been heavily affected by concurrent drought at intervals of 5–6 years (Lewis et al., 2011; Phillips et al., 2009; Yang et al., 2018). A persistent increase of biomass mortality and leveling-off of stand-level growth rate from forest inventory plots suggest a decrease of net biomass accumulation rate over the past 30 years (Brienen et al., 2015). The predicted intensification of droughts for future climate change scenarios may continue to cause increased tree mortality across large areas (Duffy et al., 2015) and exacerbate the likelihood of exceeding a tipping point for regional carbon stocks (Nobre and Borma, 2009). Yet, great uncertainties prevent understanding and quantification of tree mortality, given the high diversity of tree species with different resistance and resilience to drought. Ecosystem models are especially challenged to simulate climate-induced mortality at individual and stand level, given the lack of field studies providing long-term data for both biometric measurements and observations of soil and canopy physical climate variables leading to water stress and impairment of tree function. Local ecosystem models with a simulation of individual tree growth and death are computationally expensive, require a large number of parameters per species, and are generally less developed for simulating the soil water dynamics and surface energy budget. Upscaling of these models is also challenging (Maréchaux et al., 2021), and to our knowledge, few land surface models have included climate-induced mortality beyond that arising from crowding and tree-longevity-related mortality for large regions (Adams et al., 2017; Delbart et al., 2010; Powell et al., 2013). On the other hand, land surface models, part of Earth system models (ESMs), have advanced capabilities to simulate water and energy fluxes between forests and the atmosphere, but usually have rather simple representations of biomass carbon dynamics, and many of them do not explicitly resolve climate-induced mortality processes. A mechanistic representation and prediction of the Amazon forest response to drought in global land surface models is thus an important priority for research.

Early vegetation models parameterized mortality through indicators of competition-induced self-thinning and/or threshold of growth vigor (Adams et al., 2013; Zhu et al., 2015; McDowell et al., 2011), which ignored the mortality related to extreme events such as drought. Improving mortality representation requires more robust physiological processes embedded in models that couple water, carbon and energy fluxes (Gustafson and Sturtevant, 2013). Recent advances have been made for improved resolution of the mechanisms by which trees die from drought. Two non-exclusive physiological mechanisms have been proposed: hydraulic failure and carbon starvation (Choat et al., 2018; McDowell et al., 2018; Meir et al., 2015). Hydraulic failure occurs when the tension within the xylem vessels is so high that it causes air-seeded embolism, which impedes water transport. If embolism exceeds a tree-dependent survival threshold (Cochard and Delzon, 2013), individual tree dieback may occur, possibly with some lag in case of insufficient repair capabilities to restore upward water transport. Carbon starvation during drought is expected to occur from prolonged stomatal closure causing reduced photosynthetic assimilation, resulting in a drawdown and possible exhaustion of nonstructural carbohydrate reserves (NSC) (Hartmann, 2015; Signori-Müller et al., 2021). Additionally, embolized vessels may be detrimental to the carbon-assimilation processes, so that hydraulic failure and carbon starvation are coupled together (McDowell et al., 2018). Many studies have tried to discern the respective contributions of the two mechanisms in tree wilting during drought (Rowland et al., 2015; Yoshimura et al., 2016). After 15 years of experimental throughfall exclusion in a forest in the Amazon, Rowland et al. (2015) found that hydraulic failure was most closely associated with tree mortality under the drier condition, and that there was no distinct difference in NSC concentration between droughted and non-droughted trees, although seasonal differences were observed. Here, we will build on this early understanding of drought-induced impacts in the Amazon and present a model where hydraulic failure is considered to be the dominant risk factor for tree mortality, but we recognize the importance of carbon starvation and also investigate primary production and labile carbon changes in the simulations.

Efforts have been made toward accounting for physically based water transport in land surface models, implemented through regulation of stomatal behavior, and the explicit simulation of water transport across the soil, root, stem, leaves and atmosphere continuum following a gradient of water potential and organ-specific conductivity parameters (see summary in Table A1). The Ecosystem Demography model optimized the marginal increase of net carbon assimilation per unit of water loss within the soil–plant–atmosphere continuum to simulate a realistic stomatal conductance (Xu et al., 2016). Given the benefit-cost tradeoff between photosynthetic carbon gain and hydraulic uplift of water, Sperry et al. (2017) modeled stomatal behavior by maximizing the instantaneous difference between photosynthetic gain and the proximity to hydraulic failure. The target of such stomatal optimization schemes varies from carbon gains (Dewar et al., 2018), water-use efficiency (Bonan et al., 2014) to profit maximization of the difference between carbon gain and hydraulic cost (Sabot et al., 2020), or optimization was performed using a linear function of water potential (Eller et al., 2018) or xylem conductance (Eller et al., 2020). In addition to the optimization of stomatal control, key features of

water potential along the soil–plant–atmosphere continuum are also introduced in some models to describe plant hydraulic responses. Papastefanou et al. (2020) modeled plant hydraulics starting from leaf water potential in consideration of isohydricity among different hydraulic strategies. De Kauwe et al. (2020) incorporated the plant hydraulic module "'Desica" into the CABLE land surface model, which simulated water flows and water potential through the soil–plant–atmosphere continuum following Xu et al. (2016). Kennedy et al. (2019) generated new configurations of prognostic vegetation water potential at the root, stem and leaf levels and based plant water stress on the metrics of leaf water potential in the Community Land Model (CLM) version 5a. Explicit representations of plant hydraulics in process-based models advance our knowledge of the plant responses to drought (Hendrik and Maxime, 2017). However, in terms of how tree mortality responds to future climate scenarios, research gaps still remain in the specific thresholds of hydraulic failure beyond which drought stress induces tree mortality (Anderegg, 2015; Choat, 2013; Hammond et al., 2019), which limits the development and testing of hydraulic failure mechanisms coupled to mortality in Amazonian rainforests.

Identifying a specific threshold for hydraulic failure associated with a given mortality likelihood remains challenging (Choat et al., 2018). Drought indices related to climate have already been tested in this context and were found to be species- and trait-dependent. Anderegg et al. (2015) found that hydraulic conductivity of aspen dropped rapidly when accumulated climatic water deficit from 2000–2013 exceeds almost 5300 mm from break-point regression analysis. Relative water content derived from vegetation optical depth (VOD) also contains the signal of such a threshold relationship with drought-driven mortality rates (Rao et al., 2019). The percentage of loss in conductance (PLC) has also been found to be an appropriate metric for assessment of hydraulic dysfunction (Adams et al., 2017), and has been linked experimentally to plant mortality (Brodribb and Cochard, 2009; Q. Liu et al., 2021; Urli et al., 2013). Q. Liu et al. (2021) fitted relationships between simulated PLC and observed mortality rate across investigated sites via multiple regression, and used this formula for the prediction of mortality. Brodribb and Cochard (2009) found that the maximum survivable water stress in conifer species was a 95 % loss in leaf conductance. For five angiosperm tree species in Europe, Urli et al. (2013) found that the embolism threshold was closer to the water potential at 88 % of conductance loss. Plant volumetric water content also shows a threshold-type response empirically related to mortality risk, with an inflection point at 47 % of volumetric content (Sapes et al., 2019). Thus, the lethal point can differ among tree species, and presumably strongly in tropical forests in which different species vary widely over hydraulic traits (Bittencourt et al., 2020; Rowland et al., 2015). This variation needs to be considered in hydraulic modeling.

Currently, only a few studies have integrated plant hydraulic failure as a process in a global land surface model and parameterized mortality as a consequence. In this study, we implement a mechanistic hydraulic architecture modeling of the water transport in the continuum from soil to atmosphere in the ORCHIDEE-CAN model. We refer to this New Hydraulic Architecture module as "NHA" that is, ORCHIDEE-CAN-NHA. We describe three developments and their evaluation against field measurements for control and experimental throughfall conditions, in aspects of soil and plant water variables, and biometric variables such as tree growth and mortality, at the Amazon tropical forest site of Caxiuanã (Fisher et al., 2006; Meir et al., 2018). Firstly, we describe the development of the new hydraulic architecture model. We then carry out site-level simulations and evaluate the model performance in aspects of seasonal variability in transpiration, soil moisture and productivity against experimental control and drought observations. Thirdly, with the simulation of dynamic water potential, water transport, and conductance, the model is extended to define a mortality risk from continuous high loss of stem conductance from cavitation. In this part, we bridge the gap between reaching a stem conductance threshold corresponding to a high loss of conductance and mortality risk. Finally, we compare the modeled mortality in different circumference classes to verify whether our improved model can capture the observed size-related mortality distribution, with trees initially being rather insensitive to drought during the first years, after which larger trees are affected by dieback.

2 Methods

2.1 Model description and simulation protocols

2.1.1 The starting point: ORCHIDEE-CAN r2290

The model version taken as the starting point for development in this study is ORCHIDEE-CAN (r2290), a branch of the ORCHIDEE land surface model. ORCHIDEE is a physical process-based model, which can simulate the energy, water and carbon fluxes between land surfaces and the atmosphere. The SECHIBA module corresponds to faster processes, such as the exchange of water and energy as well as photosynthesis between land and the atmosphere in time intervals of 30 min. The carbon module (STOMATE) simulates soil processes (soil decomposition, heterotrophic respiration, soil organic carbon dynamics) at the 30 min time step and vegetation carbon cycle processes at daily intervals, including carbon allocation, vegetation mortality and recruitment, phenology and litter fall. The development of this branch of the ORCHIDEE model focuses on improving the capability of the ORCHIDEE model to simulate the biogeochemical and biophysical effects of forest management and includes allometric-based allocations of carbon to different

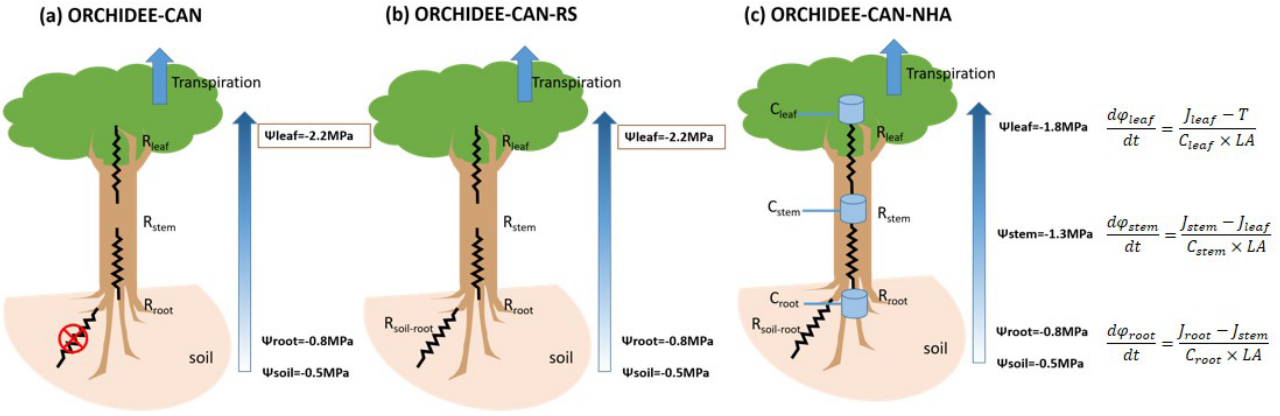

Figure 1. Schematic framework for hydraulic architecture in **(a)** ORCHIDEE-CAN, **(b)** ORCHIDEE-CAN-RS and **(c)** ORCHIDEE-CAN-NHA. The framed rectangles represent fixed values during the simulation. In ORCHIDEE-CAN and ORCHIDEE-CAN-RS, R_{leaf} is related to leaf conductivity and leaf area. R_{stem} is related to sapwood conductivity that can vary with cavitation and sapwood area. R_{root} is related to fine root conductivity and root biomass. In ORCHIDEE-CAN-NHA, transport conductance of each organ is a function of their organ-specific water potential, maximum conductance and water potential when loss of 50 % conductance occurred. C_{leaf}, C_{stem} and C_{root} represent water storage capacitance. J_{leaf}, J_{stem} and J_{root} are vertical water transport to leaf, stem and root, respectively. LA is total leaf area.

pools, a simple plant hydraulic structure (see below) as well as an albedo scheme that in part depends on canopy structure (Naudts et al., 2015). One of its new features is the way the vegetation is discretized; a dynamic canopy structure is simulated by considering a user-defined number of circumference classes ($n = 20$ in this study) and an empirical rule reflecting intra-tree competition that downscales canopy level gross primary productivity (GPP) into the different circumference classes, providing feedback on light interception and mortality through self-thinning. Background mortality comes from the reciprocal of a constant residence time. Climate-based mortality, e.g., from drought, has not been modeled yet using this system.

2.1.2 Hydraulic architecture representation in ORCHIDEE-CAN

In ORCHIDEE-CAN r2290 (Naudts et al., 2015), the representation of water stress is realized through a constraint based on the amount of water that plants can transport from soil to their leaves. This constrained transpiration supply equals the quotient between the water potential gradient from soil to leaves, and a total hydraulic resistance of leaf, stem and root. In this framework, the leaf water potential is fixed to a constant value for each plant functional type (PFT), with a specific minimum value (−2.2 MPa for tropical evergreen forests, Hickler et al., 2006). The soil water potential in the root zone is calculated by adding a tuned scaling factor, accounting for soil–root resistance and other missing processes, to the sum of the soil water potential (calculated from soil moisture and van Genuchten parameters, Van Genuchten, 1980) weighted by a proportion of root mass in each soil layer. Such hard a modulator can sometimes lead to unrealistic soil water potential in the root zone (Joetzjer et al., 2022). The prescribed vegetation distribution is used to constrain this modulator to minimize model bias (Naudts et al., 2015). During the simulation, transpiration is co-limited by the energy budget providing a transpiration demand, and the transpiration water supply limited by transport from soil to leaves. When the potential transpiration constrained by the energy budget is higher than the transpiration supply, real transpiration is limited to the physically plausible water supply. Then the energy budget and photosynthesis-related processes are recalculated. It should be noted that the root- and leaf-resistance parameters in ORCHIDEE-CAN depend only on conductivity and biomass (root mass for root, leaf area index (LAI) for leaf) and do not respond to hydrological conditions directly. Only the stem resistance related to xylem conductivity is dynamic and changes as a function of the soil water potential in the root zone. The schematic framework of the ORCHIDEE-CAN model is illustrated in Fig. 1a. This architecture is not completely mechanistic, given the tuned factor on top of soil water potential, the fixed leaf water potential values and the conductivities affected solely by organ mass. Therefore, further developments of the hydraulic architecture scheme were performed and presented here.

2.1.3 Dynamic root scheme in ORCHIDEE-CAN-RS

To increase the reliability of soil water potential simulations in root zone ($\Psi_{\text{soil-root}}$), Joetzjer et al. (2022) improved this part of the model (flowchart in Fig. 1b, ORCHIDEE-CAN-RS); $\Psi_{\text{soil-root}}$integrated Ψ_{soil} in the root zone vertically, i.e., Ψ_{soil} in the root zone is now weighted by the maximum amount of water that can be absorbed by roots in each soil layer (E_{max}), which depends on a soil-to-root

resistance and on a prescribed minimum root water potential (−3 MPa in this study) below which no more water in a given soil layer can be drawn into the plant. The soil-to-root resistance accounts for the water transport path from soil to root surface. With this scheme, the plant will dynamically use deep-layer soil moisture when the surface soil desiccates, so that this process allows the sustenance of more transpiration from deeper layers during the dry periods. Although Joetzjer et al. (2022) solved the problem of tuned modulator imposed on $\Psi_{\text{soil-root}}$ by adding a parameterization of the soil-to-root resistance, a more integral mechanistic structure of water transport from soil to leaf remains to be done to enable a dynamic connection between soil and leaf as well as corresponded simulations during drought events. For different cohorts, $\Psi_{\text{soil-root}}$ is calculated separately, since we assume taller trees have deeper roots and can reach water stored in deeper layers. For example, we assume that the largest cohort can take water from all 12 soil layers while the smallest cohort can only take water in the shallow layers.

2.1.4 Hydraulic scheme development and implementation in ORCHIDEE-CAN-NHA r7236

Figure 1c presents the schematic diagram of the new hydraulic architecture in ORCHIDEE-CAN-NHA. Besides the water transport driven by vertical water pressure difference, the water flow to/from organ-specific water storage at time t is explicitly modeled based on capacitances and water potential differences between time t and $t-1$. For each organ, the water supply should meet its water demand. For example, water demand at leaf level is parameterized as the transpiration supply. Water supply to leaf is composed by water transport from stem minus the water charge or plus the discharge from the leaf water storage pool. The water budget of the leaves is calculated first, in order to determine how much water has to be drawn up from the other connected upstream organs. It should be noted that the new hydraulic mechanism is imposed on 20 circumference classes, separately. The detailed description of new mechanistic hydraulic processes is given below.

Water storage calculation

The supply–demand framework is solved at leaf, stem and root, separately. We assume that during the first time step, all water potentials in different organs are the same (Eq. 1). Here, "the first time step" points to the very first 30 min of the simulation. At the first time step, the initial value of Ψ_{l}, Ψ_{s}, and Ψ_{r} are all equal to $\Psi_{\text{soil-root}}$, which is the weighted sum of soil water potential:

$$\Psi_{\text{leaf},t} = \Psi_{\text{stem},t} = \Psi_{\text{root},t} = \Psi_{\text{soil-root,t}}. \quad (1)$$

Water storage in the different organs is calculated with organ-specific capacitance values (water storage unit: mmol):

$$M_{\text{leaf,max}} = \frac{B_{\text{leaf}}}{L} - B_{\text{leaf}}, \quad (2)$$

$$M_{\text{leaf},t} = M_{\text{leaf,max}} + C_{\text{leaf}} \times \Psi_{\text{leaf},t} \times \text{LA}, \quad (3)$$

where C_{leaf} is relative leaf capacitance in unit of $\text{mmol m}^{-2}\,\text{MPa}^{-1}$, L is the leaf dry matter content, B_{leaf} is the dry leaf biomass and LA is total leaf area. Maximum water storage in leaf ($M_{\text{leaf,max}}$) is generated by leaf fresh mass minus dry mass; $M_{\text{leaf},t}$ is leaf water storage at time t.

$$M_{\text{sap,max}} = V_{\text{stem}} \times \gamma, \quad (4)$$

$$M_{\text{sap},t} = M_{\text{sap,max}} + C_{\text{stem}} \times \Psi_{\text{stem},t} \times V_{\text{stem}}, \quad (5)$$

$$V_{\text{stem}} = \pi \left(\frac{D}{2}\right)^2 h, \quad (6)$$

where C_{stem} is sapwood capacitance (unit: $\text{kg m}^{-3}\,\text{MPa}^{-1}$), h is tree height in m, V_{stem} is proportional to the volume of tree stem in m^3, γ is the amount of water (mmol) per unit stem volume, which corresponds to the maximum mass of water per stem volume and $M_{\text{sap,max}}$ and $M_{\text{sap},t}$ are maximum sapwood water storage and sapwood water storage at time t, respectively. The diameter at breast height (DBH) is D. In the model, we also did a unit transform from kg to mmol:

$$M_{\text{root,max}} = B_{\text{root}} \times \varepsilon, \quad (7)$$

$$B_{\text{root}} = V_{\text{stem}} \times \delta \times \theta, \quad (8)$$

$$V_{\text{root}} = \frac{B_{\text{root}}}{\rho_{\text{root}}}, \quad (9)$$

$$M_{\text{root},t} = M_{\text{root,max}} + C_{\text{root}} \times \Psi_{\text{root},t} \times V_{\text{root}}, \quad (10)$$

where ε indicates the amount of water (mmol) stored in per gram of root mass, δ is aboveground wood density, V_{root} is root volume, θ is root-to-shoot ratio, B_{root} is root mass and ρ_{root} is root density. The maximum root water storage and root water storage at time t are $M_{\text{root,max}}$ and $M_{\text{root},t}$, respectively and C_{root} is root capacitance (unit: $\text{kg m}^{-3}\,\text{MPa}^{-1}$).

Hydraulic conductance calculation

Hydraulic conductance per unit of leaf area in leaf, sapwood and root at time t ($k_{\text{leaf},t}$, $k_{\text{stem},t}$, $k_{\text{root},t}$) are calculated with sigmoidal relationships (Pammenter and Van der Willigen, 1998), based on their real-time water potential and a maximum conductance. Water potential is denoted by $\Psi_{50,\text{organ}}$ when 50 % conductance lost, and $e^{a_{\text{organ}}}$ describes the sensitivity of conductance to changes in water potential around $\Psi_{50,\text{organ}}$. An example for how these two shape parameters affect sapwood conductance is shown in Fig. S1 in the Supplement.

$$k_{\text{leaf},t} = \frac{k_{\text{leaf,max}}}{1 + \exp\left(a_{\text{leaf}} \times \left(\varphi_{\text{leaf},t} - \varphi_{50,\text{leaf}}\right)\right)}, \quad (11)$$

where $k_{\mathrm{leaf},t}$ and $k_{\mathrm{leaf,max}}$ are leaf conductance at time t and maximum leaf conductance, respectively.

$$k_{\mathrm{stem},t} = \frac{k_{\mathrm{stem,max}}}{1+\exp\left(a_{\mathrm{stem}} \times \left(\varphi_{\mathrm{stem},t} - \varphi_{50,\mathrm{stem}}\right)\right)}, \quad (12)$$

where $k_{\mathrm{stem},t}$ and $k_{\mathrm{stem,max}}$ are stem sapwood conductance at time t and maximum stem sapwood conductance, respectively.

$$k_{\mathrm{root},t} = \frac{k_{\mathrm{root,max}}}{1+\exp\left(a_{\mathrm{root}} \times \left(\varphi_{\mathrm{root},t} - \varphi_{50,\mathrm{root}}\right)\right)}, \quad (13)$$

where $k_{\mathrm{root},t}$ and $k_{\mathrm{root,max}}$ are root conductance at time t and maximum root conductance, respectively.

The conductance of the upper part of the tree (leaf plus upper part of stem) and lower part of the tree (lower part of stem plus root) are calculated following Eqs. (14) and (15). These two conductances will be used to calculate the water flow from stem to leaf, and root to stem later, separately. The value 2 in front of $k_{\mathrm{stem},t}$ in each equation denotes that only half of the stem is accounted for in the upper part and trunk part separately. Half of the root length is considered in the trunk part as well. The water transport process is assumed to be similar to electric current, of which the resistance (the reciprocal of hydraulic conductance) should be added up along the water transport path:

$$k_{\mathrm{upper},t} = \frac{1}{\frac{1}{k_{\mathrm{leaf},t}} + \frac{1}{2k_{\mathrm{stem},t}}}, \quad (14)$$

$$k_{\mathrm{trunk},t} = \frac{1}{\frac{1}{2k_{\mathrm{root},t}} + \frac{1}{2k_{\mathrm{stem},t}}}. \quad (15)$$

Water transport pathway simulation

We assume that for leaves, transpiration supply is based on the water input transported from the stem minus the water charge/discharge from the leaf water storage pool (Eq. 16):

$$T_{\mathrm{supply}} = J_{\mathrm{leaf},t+1} - W_{\mathrm{leaf},t+1}, \quad (16)$$

where $J_{\mathrm{leaf},t+1}$ is the flux of water transported vertically to leaf from stem sapwood (unit: mmol) and $W_{\mathrm{leaf},t+1}$ is the change in leaf water storage. A positive value of $W_{\mathrm{leaf},t+1}$ means that the leaf was charged with water during hydraulic recovery, and negative means it was reduced by evapotranspiration (ET). At leaf level, the target is to solve for the leaf water potentials that minimize the difference between potential transpiration demand and supply (Eq. 17):

$$\Delta = (J_{\mathrm{leaf},t+1} - W_{\mathrm{leaf},t+1}) - \mathrm{PT}_{\mathrm{demand}}. \quad (17)$$

Similarly, at stem level, the target is to minimize the difference between water demand at stem and water supply to the stem (Eq. 18):

$$\Delta = (J_{\mathrm{stem},t+1} - W_{\mathrm{stem},t+1}) - J_{\mathrm{leaf},t+1}, \quad (18)$$

where $J_{\mathrm{stem},t+1}$ is the water transported vertically from root to stem and $W_{\mathrm{stem},t+1}$ is the change in stem water storage. After solving leaf-level target, $J_{\mathrm{leaf},t+1}$ is known, which is the water demand at stem.

At root level, the target is to minimize the difference between water demand at root and water supply to root (Eq. 19):

$$\Delta = (J_{\mathrm{root},t+1} - W_{\mathrm{root},t+1}) - J_{\mathrm{stem},t+1}, \quad (19)$$

where $J_{\mathrm{root},t+1}$ is the water transported from soil in root zone to root and $W_{\mathrm{root},t+1}$ is the change in root water storage. After solving stem-level target, $J_{\mathrm{stem},t+1}$ is known, which is the water demand at root. The detailed calculations of these water flow variables are explained below in the order of leaf, stem and root.

Thus, water potentials are solved to let the water supply be equal to water demand at each organ. In the model, the HYBRD1 function from Minpack package in Fortran is used, which seeks a zero of N nonlinear equations in N variables. The evaluated function is the difference between water supply and water demand at each organ level. This function iteratively minimizes the absolute value of the evaluated function. The initial estimate of the solution vector is quite important and comes from the water potential at the last time step. For example, the initial estimate for leaf water potential at time step t that will be used in the formula is the stem water potential at time step $t-1$.

a. Leaf transport

The water movement into the leaf through the hydraulic pathway is calculated as follows:

$$J_{\mathrm{leaf},t+1} = (\Psi_{\mathrm{stem},t} - \Psi_{\mathrm{leaf},t+1} - \Psi_{h/2}) \times k_{\mathrm{upper},t+1} \times \mathrm{LA}, \quad (20)$$

$$W_{\mathrm{leaf},t+1} = C_{\mathrm{leaf}} \times (\Psi_{\mathrm{leaf},t+1} - \Psi_{\mathrm{leaf},t}) \times \mathrm{LA}, \quad (21)$$

where a positive $W_{\mathrm{leaf},t+1}$ means an increase in leaf water storage and vice versa and $\Psi_{h/2}$ indicates how much water potential gradient is needed to pull water against gravity up to the height (h) of the tree from the position of 1/2 tree height (middle of stem).

We calculate $J_{\mathrm{leaf},t+1}$ and $W_{\mathrm{leaf},t+1}$ using an optimization procedure, i.e., we start by assuming $\Psi_{\mathrm{leaf},t+1} = \Psi_{\mathrm{stem},t}$ and progressively decrease $\Psi_{\mathrm{leaf},t+1}$ until the difference between leaf water supply and demand is close to zero (Eq. 22). Leaf water potential is solved using the HYBRD1 function (see above). The tolerance is 0.00001 MPa. When the relative error between two consecutive iterates is below the tolerance, the calculation routine is terminated:

$$\Delta = T_{\mathrm{supply}} - \mathrm{PT}_{\mathrm{demand}}, \quad (22)$$

where $\mathrm{PT}_{\mathrm{demand}}$ (potential transpiration demand) is related to stomatal conductance, vapor pressure deficit (VPD) and total

leaf area (Eq. 23), where stomatal conductance varies with Ψ_{leaf} (Eq. 24):

$$\text{PT}_{\text{demand}} = g_{\text{s}} \times \frac{\text{VPD}}{P} \times \text{LA}, \tag{23}$$

$$g_{\text{s}} = \frac{g_{\max} \frac{L \times \text{Rad}}{L \times \text{Rad} + L_{\text{k}}}}{1 + e^{a_{\text{gs}}(\Psi_{\text{leaf},t} - \Psi_{50,\text{gs}})}} + g_{\min}, \tag{24}$$

where g_{s}, $g_{\max}$ and $g_{\min}$ are in the unit of $\text{mmol}\,\text{m}^{-2}\,\text{s}^{-1}$, VPD is in the unit of kPa and LA is the total leaf area.

The standard atmospheric pressure is denoted by P (101.3 kPa). The aim of this g_{s} model is to let g_{s} vary, following dynamics of leaf water potential in the sigmoidal function, then g_{s} can be coupled into the plant water transport system via the transpiration supply. Meanwhile, the g_{s} is assured to be close to 0 in the night, mediated by the radiation-related variable ($\frac{L \times \text{Rad}}{L \times \text{Rad} + L_{\text{k}}}$) and L and L_{k} are parameters specifying the strength of short-wave radiation limitation on stomatal conductance. Minimum leaf water potential in this study is set to −3.0 MPa to avoid unrealistic values (Fisher et al., 2006).

We verified that our simulated g_{s} with the parameter values from Table A2 are of similar magnitude than in the soil–plant–atmosphere (SPA) model of Fisher et al. (2007) at Caxiuanã, which was developed independently from ORCHIDEE (Fig. S2). The g_{s} in the SPA model is obtained by maximizing the marginal carbon gain of stomatal openness (intrinsic water use efficiency). Further, in order to show that our model parameters can be used to simulate g_{s} at other rainforest sites, we collected g_{s} observations (at leaf scale) from two rainforests in French Guiana and Peru from Lin et al. (2015) and tested our model against these observations. Figure S3 shows that our simulated g_{s} values fall in the range observed at these two sites.

b. Stem transport

Next, we know that the water demand at stem is the amount of water transported from stem to leaf, $J_{\text{leaf},t+1}$. We can now use the same procedure to calculate the $\Psi_{\text{stem},t+1}$ that produces the expected $J_{\text{leaf},t+1}$, and how much of that transport is from storage and from the roots through the vertical hydraulic pathway:

$$J_{\text{stem},t+1} = (\Psi_{\text{root},t} - \Psi_{\text{stem},t+1} - \Psi_{h/2}) \times k_{\text{trunk},t+1} \times \text{LA}, \tag{25}$$

$$W_{\text{stem},t+1} = c_{\text{stem}} \times (\Psi_{\text{stem},t+1} - \Psi_{\text{stem},t}) \times V_{\text{stem}}, \tag{26}$$

$$S_{\text{stem},t+1} = J_{\text{stem},t+1} - W_{\text{stem},t+1}, \tag{27}$$

$$\Delta = S_{\text{stem},t+1} - J_{\text{leaf},t+1}, \tag{28}$$

where $S_{\text{stem},t+1}$ is the water supply to stem and $J_{\text{leaf},t+1}$ is the water demand at stem. We then solved the $\Psi_{\text{stem},t+1}$ to minimize the difference between $J_{\text{leaf},t+1}$ and $S_{\text{stem},t+1}$ (Eqs. 27 and 28).

c. Root transport

The same procedure is also carried out for root. The total flow out of the root is equal to $J_{\text{stem},t+1}$. We calculate root water transport according to the following equations:

$$J_{\text{root},t+1} = (\Psi_{\text{soil-root},t} - \Psi_{\text{root},t+1}) \times 2 \times k_{\text{root},t+1} \times \text{LA}, \tag{29}$$

$$W_{\text{root},t+1} = C_{\text{root}} \times (\Psi_{\text{root},t+1} - \Psi_{\text{root},t}) \times V_{\text{root}}, \tag{30}$$

$$S_{\text{root},t+1} = J_{\text{root},t+1} - W_{\text{root},t+1}, \tag{31}$$

$$\Delta = \text{S}_{\text{root},t+1} - J_{\text{stem},t+1}, \tag{32}$$

where $J_{\text{stem},t+1}$ is the water demand at root and $S_{\text{root},t+1}$ is the water supply to root. We then solved the $\Psi_{\text{root},t+1}$ to minimize the difference between $J_{\text{stem},t+1}$ and $S_{\text{root},t+1}$ (Eqs. 31 and 32). The "2" in Eq. (29) means half of the root is accounted for ($\frac{1}{\frac{1}{2 \times k_{\text{root}}}}$) here since the other half of the root is considered in $k_{\text{trunk},t}$.

We assume that water does not travel in reverse, leaving the roots and going into the soil. We also impose a limit on vertical water flow to non-negative values.

Update water storage pools

After the simulation of water transport, we use the W_{t+1} values to update the water storage in each organ:

$$M_{\text{leaf},t+1} = M_{\text{leaf},t} + W_{\text{leaf},t+1}, \tag{33}$$

$$M_{\text{stem},t+1} = M_{\text{stem},t} + W_{\text{stem},t+1}, \tag{34}$$

$$M_{\text{root},t+1} = M_{\text{root},t} + W_{\text{root},t+1}. \tag{35}$$

All of the above calculation processes are carried out for 20 circumference classes, separately. The parameters used in the new hydraulic architecture are summarized in Table A2. We did some sensitivity tests by attempting different value combinations of parameters within a range of records in literature, such as degree of vulnerability, Ψ_{50} and degree of sensitivity, a (shape parameter), as shown in Fig. S4. Parameters set that can better capture the observed variation of drought-induced tree mortality (especially the higher tree mortality rate in larger cohorts) was chosen. We do not aim for a perfect match between model output and observation to avoid the overfit issue during the generalization of the model.

2.1.5 Parameterization of tree mortality related to drought

Since trees can endure drought conditions and do not die after 1 or 2 d of low stem water potential or water shortage (Brodribb et al., 2020), we defined an exposure threshold desiccation time to trigger mortality. Continuous exposure to a high percentage loss of conductance (PLC) forebodes tree mortality, therefore a decision rule was set with two empirical parameters, a drought mortality exposure threshold (in days) and a mortality fraction of trees each time (in % of all trees

that die). When the PLC > 50 % condition lasts for more than 15 continuous days, we assume that a fraction of 0.3 % of all the trees in each size cohort are killed. These two parameters are tuned according to the observed annual mortality rates. It should be noted that a cohort model represents all the trees in a grid cell as one average individual, thus an absolute mortality threshold would kill them all on the same day. Hence we impose a fractional mortality to capture the variability in mortality drivers and processes within each cohort. We also consider that a very short wetting break during a drought condition would not necessarily act to reverse embolism and thus the tree's exposure to mortality. Here, the minimum threshold for a continuous wetting break (PLC < 50 %) to reset the exposure to zero is set to 5 d. The annual mortality rate equals to the number of dead trees per year divided by the number of trees alive in the beginning of this year.

Finally, following ORCHIDEE-CAN-RS, the recruitment rate is determined by LAI (Joetzjer et al., 2022). LAI is determined by leaf mass, which is regulated by the leaf growth, leaf turnover and leaf loss due to drought-induced tree mortality. When LAI decreases during drought, the recruitment rate will increase correspondingly since recruitment is parameterized as a function of LAI. The new outputs from ORCHIDEE-CAN-NHA are listed in Table A3.

2.2 Biomass growth and loss calculation

$$\Delta \text{ biomass} = \text{growth} - \text{loss}. \quad (36)$$

As ORCHIDEE does not account for biogenic volatile organic compound (BVOC) emissions, root exudation and C-subsidies to mycorrhizae, biomass growth is simulated as the residual of GPP minus autotrophic respiration. Biomass loss comes from three processes in ORCHIDEE: turnover (loss of leaves and fine roots), self-thinning and climate-induced mortality, i.e., drought for this study. It should be noted that, in ORCHIDEE-CAN, when the number of individuals falls below a parameterized threshold, self-thinning does not happen and individuals grow without competing with each other. This calculation process is the same among three different model versions.

2.3 Site description

The study site is a tropical lowland rainforest located in the Caxiuanã National forest, state of Para, northeast of Brazil (1°43′ S, 51°27′ W). Annual rainfall in this site is 2000–2500 mm with a dry season spanning from July to November (monthly rainfall < 100 mm). There are two experiments, which were carried out since the beginning of 2001. A throughfall exclusion experiment (TFE) started at the end of the dry season in 2001, where 50 % of canopy throughfall is excluded by plastic roof at the height of 1–2 m above the ground (Fisher et al., 2007; Meir et al., 2018). It is 1 ha in size. Another 1 ha control plot is also set without any manipulation. Here, the observation data we used extend to 2008 at most due to data-access issues, but these experiments are still running.

From published literature (Carswell et al., 2002; da Costa et al., 2010; Fisher et al., 2007; Rowland et al., 2015), we collected observation data as validation for model simulation, including transpiration data, soil moisture data, annual mortality rate, annual biomass density, and GPP (Table 1). We also used output from the SPA (soil–plant–atmosphere) model with parameters measured for the Caxiuanã experiment. The SPA model is a multilayer soil–plant–atmosphere transfer model, which has been parameterized upon such drought-affected ecosystems (Fisher et al., 2007). We included simulated GPP output from SPA for model comparison under TFE since eddy covariance flux measurements can only be used in model–data comparison under control (CTL).

2.4 Simulation protocols

We performed three simulations at site-level for Caxiuanã to compare the hydraulic architecture from each model version. Specifically, we tested the model performance under two setups, the control (CTL) and the throughfall exclusion experiment (TFE). In the model, TFE is reproduced by keeping only 50 % of the rainfall of CTL with all else being the same as CTL (Fisher et al., 2007). It should be noted that such a rainfall cut is a simplification, since in reality, a plastic panel is used to exclude 50 % of throughfall. We ran 250 year spin-ups by cycling climate-forcing data over 2001 to 2008 with constant CO_2 concentration of 380 ppm to get the preliminary state of carbon pools and water flow at the beginning of 2001. The meteorological forcing is at 30 min time steps. The meteorological data every 30 min are measured using an automatic weather station located at the top (51.5 m) of a tower 1 km from the experimental plot. The simulation was run offline without coupling with a climate model. Two former model versions and our new developments are integrated as below. We compared ORCHIDEE-CAN-RS and ORCHIDEE-CAN-NHA to see the improvements brought by the new hydraulic architecture. It should be noted that all three of these simulations are realized through several flags to switch on/off some functionality:

1. ORCHIDEE-CAN with the original simple hydraulic module setup,
2. ORCHIDEE-CAN-RS, which adds a new dynamic soil–root scheme on top of (1),
3. ORCHIDEE-CAN-NHA, with the new mechanistic hydraulics on top of (2).

2.5 Statistical tools

We used the R programming environment and statistical packages (version 3.5.0; R Core Team, 2019) for all data processing and analysis. Package ncdf4 v1.17 (Pierce, 2019) is used to handle files in NetCDF format from model outputs.

Table 1. Collected observation data used for validation of process-based model simulation.

Variables	Period	Time step	References
Transpiration	2001–2003	Daily	Fisher et al. (2007)
Soil moisture	2001–2004	Monthly	Fisher et al. (2007)
Biomass density	2001–2008	Annual	Observation from Rowland et al. (2015) and da Costa et al. (2010)
GPP	2001–2003	Daily	SPA model : Fisher et al. (2007), flux data: Carswell et al. (2002)
Mortality rate	2001–2008	Annual	da Costa et al. (2010); Rowland et al. (2015)

Package fields v10.3 (Nychka D, 2020) is used in water potential plotting.

3 Results

3.1 Model evaluation against observation

3.1.1 Evapotranspiration and soil moisture

Under the CTL condition, the model developed here (ORCHIDEE-CAN-NHA) agreed well with the sap-flow observations from well-watered periods but underestimated sap flow in the dry season. The dry-season points in Fig. 2 are those with a water deficit of up to $-3\,\mathrm{mm\,d^{-1}}$ (monthly precipitation below evapotranspiration). Regressing modeled transpiration with sap-flow observations, we found that the model better represents the month-to-month seasonal variability under CTL than TFE ($R = 0.76$ in CTL v.s. $R = 0.48$ in TFE). Under the TFE condition, the model overestimated transpiration in both the wet and dry seasons, with a positive bias increasing at water deficits typically below $-2\,\mathrm{mm\,d^{-1}}$ (Fig. 2). Simulation by ORCHIDEE-CAN-RS also showed such a positive bias (Fig. S5). This positive model bias was mainly contributed by the simulation in 2002 when the TFE experiment was installed by the end of 2001. The transpiration supply did not show water limitation on transpiration under TFE until the end of the dry season in 2002 (Fig. S6). The simulated transpiration could be limited by water supply (water limitation) or water demand (energy limitation). Under CTL, there is almost no water limitation, even in the dry season. The underestimated sap flow can be due to the fact that the model tends to underestimate the sensitivity to VPD increase in the dry season. Under TFE, there is water supply limitation. The possible reasons for such overestimation under TFE can be that the sensitivity of water supply to drop in soil moisture is underestimated or the too-slow soil water drainage in our model setup is relative to that in reality (Kennedy et al., 2019).

In terms of comparison on transpiration (Table S1 in the Supplement), under CTL, the correlation coefficient with the observation is similar among the three model versions (0.71–0.76), although there is indeed a bit increase in other error metrics in ORCHIDEE-CAN-NHA, like the root mean square error (RMSE) and mean absolute percentage error (MAPE). The ORCHIDEE-CAN-NHA performs better in water-stress conditions (under TFE) in aspects of these error metrics, but shows a bit lower correlation with observation than the other two versions.

The partitioning of evapotranspiration (ET) was compared between CTL and TFE. Under the CTL condition, the modeled partitioning of ET into transpiration (T), intercepted canopy water or dew re-evaporation (CE), and bare soil evaporation (E) is shown in Fig. S7, with the ratio (T/ET) being around 0.57 in the wet season, and 0.74 in the dry season. Under TFE, the difference of T/ET between the dry and the wet seasons increased (wet: 0.58 vs. dry: 0.82). Specifically, under CTL, the daily mean transpiration can reach more than $4\,\mathrm{mm\,d^{-1}}$ and soil evaporation accounted for 29 % of the total ET in the wet season. The magnitude of transpiration increased by 51 % in the dry season (range: 22 %–71 %) compared to that in the wet season under CTL, which is similar to the observations (+44 % in Fisher et al., 2007), due to higher energy supply and non-water limiting conditions. This indicated that normal conditions at this site are not very strongly limited by soil moisture during the dry season, despite recurrent deficits, as shown by the red bars on the top of Fig. 3. Nevertheless, under TFE, the transpiration was lower than in CTL and encountered emerging water-supply-induced limitation in the dry season, with $T_{\mathrm{dry}}/T_{\mathrm{wet}}$ of 1.12 over 2002–2008 (minimum $T_{\mathrm{dry}}/T_{\mathrm{wet}}$ can be 0.60 in 2005) (Fig. 3). Soil evaporation also decreased a lot under TFE from the wet to the dry season, and the ratio (E/ET) was halved from the wet to the dry season, especially in the years 2005, 2006 and 2007, when annual rainfall was relatively lower.

We next examined the model performance (ORCHIDEE-CAN-NHA) for reproducing the soil moisture dynamics during the observation period between 2001 and 2004. Soil moisture content (SMC) featured a pronounced seasonal decrease between the wet and dry periods under CTL and TFE (Fig. 4). Under CTL, in the surface soil, the model produced a small underestimation of SMC in both wet and dry seasons compared to observation. With increasing depth in the soil, this negative difference between modeled and observed SMC became more pronounced in the dry season (Fig. 4). Under TFE, a similar negative difference also appeared in the dry season only, while a positive difference appeared in the wet period. Besides, under TFE, the modeled SMC was however always lower than for CTL in the surface layer, and

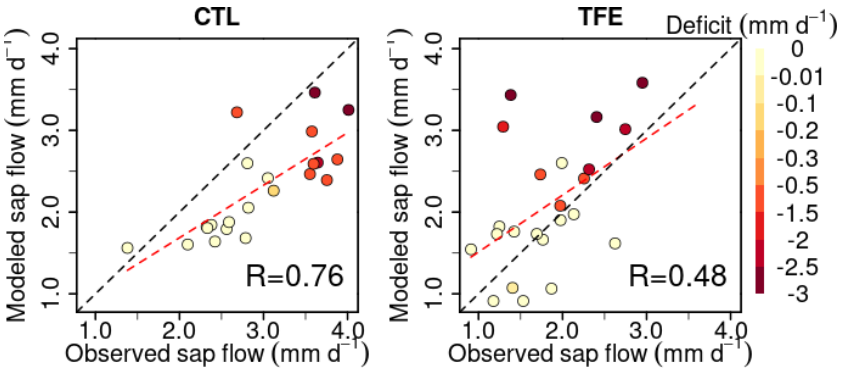

Figure 2. Modeled (ORCHIDEE-CAN-NHA) vs. observed sap flow (monthly average values are displayed). The color of points indicates water deficit (negative difference between precipitation and evapotranspiration) with darker color meaning more severe water deficit. The dashed black line is the 1 : 1 line. The dashed red line is the best fit between modeled and observed sap flow.

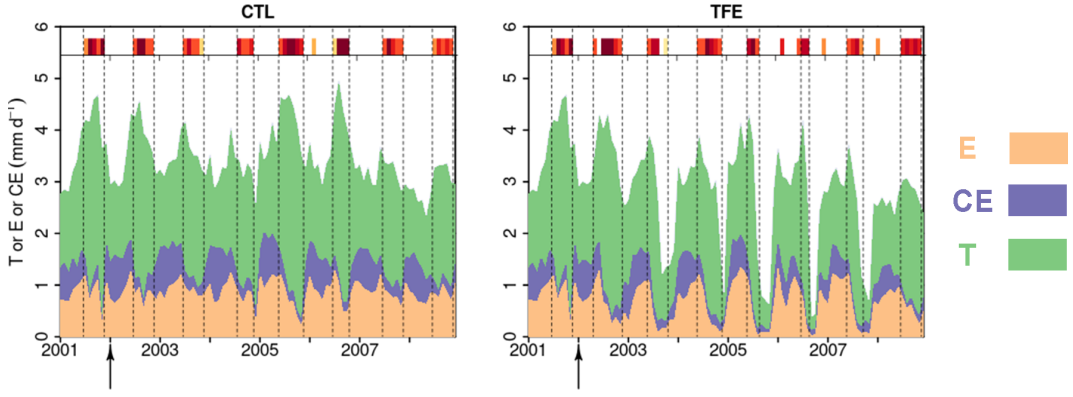

Figure 3. Modeled (ORCHIDEE-CAN-NHA) daily soil evaporation (E), canopy evaporation (CE) and transpiration (T) during 2001–2008. The arrows point to the start of TFE at the beginning of 2002. The inserted shaded red bars denote the periods with water deficits during the simulation period, following the same color scale as Fig. 2.

became even more depleted in the deeper layer with the dynamic soil–root scheme, even in the wet season (Fig. 5), because this scheme shifts root uptake from surface to deep layers when the surface dries out compared to the simulation of ORCHIDEE-CAN (Fig. S8). The SMC at each layer is influenced by infiltration, evaporation, transpiration and drainage. The amount of water that can be absorbed from each layer (η) is determined by its water potential and also soil–root resistance. Soil water potential decreases with soil depth while soil–root resistance becomes much smaller with soil depth as well. Therefore, η does not change monotonically with soil depth. For example, during the wet season in 2005 under TFE, η in the deeper soil layer is higher than that in the top layer, while in the dry season, η in the deeper soil layer can decrease to almost 0 when the water supply mainly comes from the shallower layer. In year 2004, even in the dry season, lower soil layers can contribute a lot to water uptake (Fig. S9).

3.1.2 Carbon fluxes

The GPP simulation outputs had a similar seasonality under CTL among all model versions (Fig. S10 in the Supplement). All simulations showed higher GPP in the dry season compared to the wet season under CTL (also in eddy covariance, Carswell et al., 2002) (Table S2). When we compared GPP against the SPA model results from Fisher et al. (2007) that were calibrated to best-fit site-level observations, and against flux observation, we found that modeled GPP in ORCHIDEE-CAN-NHA showed a larger seasonal amplitude than that of SPA but with a similar phase (Fig. 6). The GPP from ORCHIDEE-CAN-NHA presents a 1.1 g C m^{-2} d^{-1} difference between wet and dry seasons, which is similar to the two previous versions. The GPP seasonality from eddy covariance data was also in agreement with the simulation from ORCHIDEE-CAN-NHA, with a peak in the middle of the dry season. In contrast, the SPA-modeled GPP decreased right from the start of the dry season. We found that the impact of the TFE condition on modeled GPP was relatively small during the wet season, with

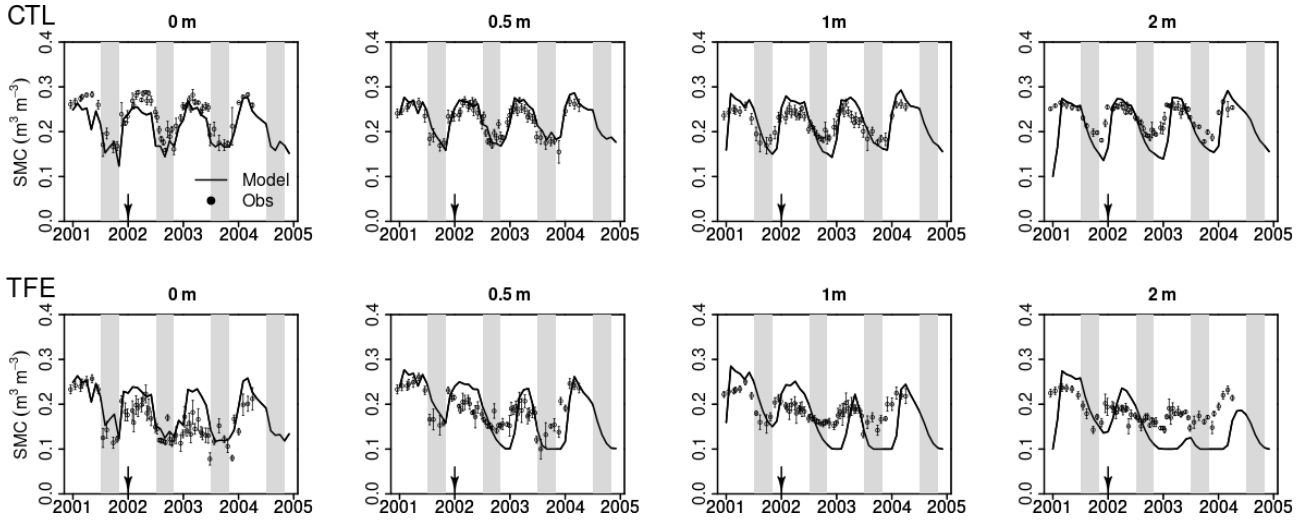

Figure 4. Modeled (ORCHIDEE-CAN-NHA, black line) vs. observed (black dots) volumetric soil moisture content (SMC) at different depths. Due to the limited time duration of observation data, we only show the modeled SMC during 2001–2004. The shaded gray vertical area indicates the dry seasons from July to November.

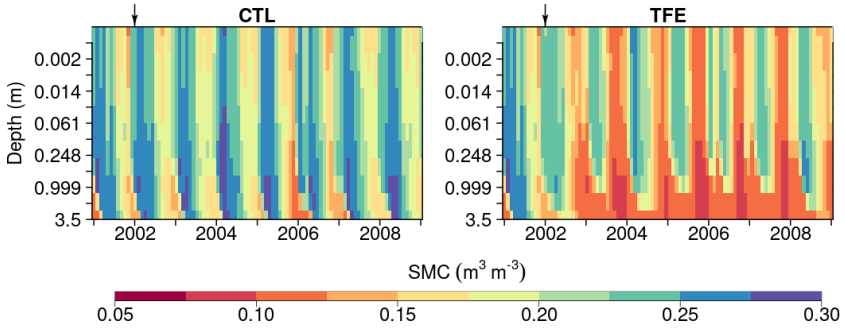

Figure 5. Soil moisture content (SMC) simulated by ORCHIDEE-CAN-NHA during 2001–2008 under CTL and TFE. It should be noted that the 12 soil layers have different thicknesses and here we show the SMC in the same depth interval to present the change in SMC in top layers clearly.

a difference less than 10 % in comparison with CTL (see Fig. S10 for the two other versions). On the other hand, the impact of TFE during the dry season led to a pronounced decrease of GPP, like in the SPA model. In ORCHIDEE-CAN-NHA, GPP decreased only at the end of the dry season under TFE while in SPA, it decreased from the beginning (Fig. 6). Only after 2 years of drought, ORCHIDEE-CAN-NHA simulated an early decrease of GPP at the beginning of the dry season, and thus became consistent with SPA (Fig. 6). The dry season GPP increase is also found in the other two model versions, despite a bit difference in the magnitude. In the SPA model, GPP is simulated using the FvCB model regulated by optimization of intrinsic water use efficiency, in which the optimization target is $\frac{\partial A}{\partial g_s}$ (A is assimilation, g_s is stomatal conductance), not accounting for VPD. So the magnitude of the GPP variation would not be too high. In ORCHIDEE-CAN-NHA that we used here, larger seasonal amplitude of the modeled GPP, especially the low GPP in the dry season under TFE, is due to higher water limitation imposed from our hydraulic architecture.

3.2 Simulated water potential gradients along the soil-to-leaf continuum

With the mechanistic hydraulic architecture of ORCHIDEE-CAN-NHA, the dynamic water potential at leaf, stem and root levels were modeled and compared with observations (Fig. S11 in the Supplement). The diurnal cycle of Ψ_{leaf} was comparable between model and observations, although the modeled Ψ_{leaf} was less negative than the observation at noon (Fig. S11). The lowest water potential was simulated in the leaf, followed by the stem, as expected. There was clear seasonal variability between the wet and dry periods, especially under TFE conditions (Fig. 7). Under CTL, the water potential vertical negative gradient between leaf and root was similar between the wet and the dry seasons (−0.79 MPa in the

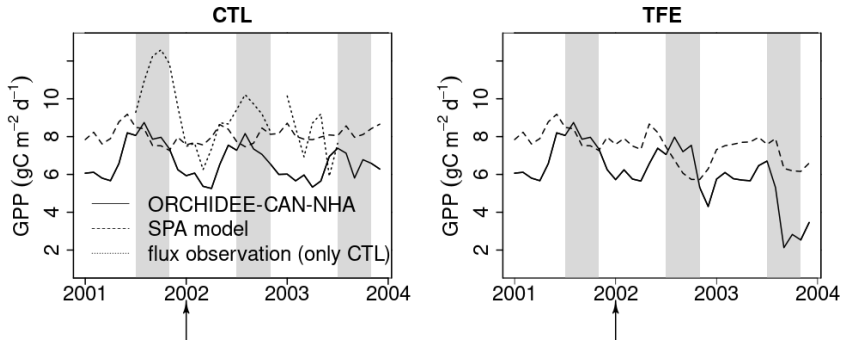

Figure 6. Modeled (ORCHIDEE-CAN-NHA) vs. observed/modeled monthly mean GPP. The control model is compared to flux-tower observations (Carswell et al., 2002). In the case of TFE, as no observation is available, the locally calibrated SPA model is used. Due to GPP, flux observation is unrealistically low at the start of 2001 ($< 5\,\mathrm{g\,C\,m^{-2}\,d^{-1}}$), we only keep flux data after mid-2001. The shaded gray vertical area indicates the dry season from July to November.

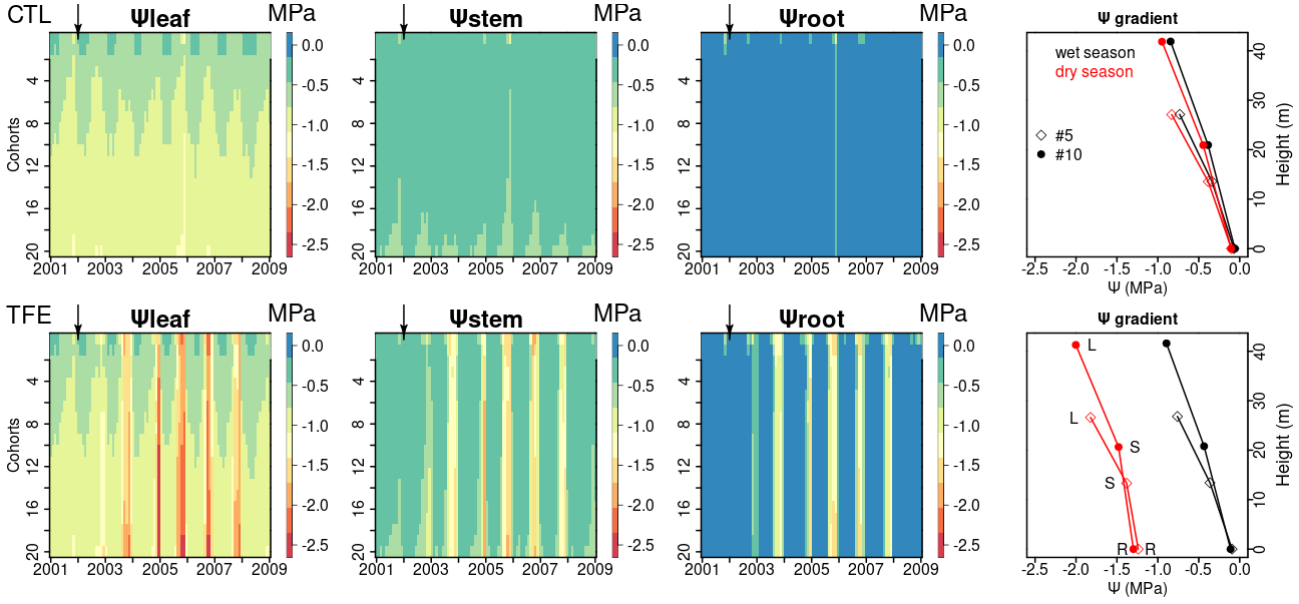

Figure 7. Ψ_{leaf}, Ψ_{stem}, and Ψ_{root} simulated by ORCHIDEE-CAN-NHA. Water potential gradients of two cohorts (#5, #10) are shown as an example (May 2005 as the wet season and November 2005 as the dry season). Here, the cohort refers to the circumference class (mean height of #5 and #10 are 19 and 35 m, respectively). The water potential gradient is composed by Ψ_{leaf} (labeled as L), Ψ_{stem} (labeled as S) and Ψ_{root} (labeled as R). The heights of Ψ_{leaf} and Ψ_{stem} correspond to tree height and half of tree height, respectively.

wet season and −0.84 MPa in the dry season for tree cohort #10 that is in diameter of 1.15 m; for the cohorts description see the Methods section); the minimum monthly mean Ψ_{leaf}, Ψ_{stem} and Ψ_{root} were −1.3, −1.0 and −0.8 MPa in the dry season, respectively. Under TFE, Ψ_{leaf}, Ψ_{stem} and Ψ_{root} were prominently more negative during the dry season (−2.5, −1.9, −1.7 MPa, respectively) and the range of water potential gradients between stem and root in the dry season became a bit narrower than that in the wet season, which reflected the fact that the water flow from vertical transport is limited. With regard to the change of water storage, leaf water storage decreased continuously from the wet to dry seasons but did not approach depletion of water storage (Fig. S12 in the Supplement). In year 2005, Ψ_{leaf} in the dry season (dry season rainfall is minimum) reached its minimum during the entire simulation period under TFE. We can see that at leaf and stem levels, Ψ_{leaf} and Ψ_{stem} decreased slightly with the size of cohorts and they were a bit more negative in larger (taller) cohorts correspondingly (Figs. 7 and S13 in the Supplement). Taller trees have a longer water transport path, which means greater gravitational potential energy is needed to pull water upward (Eq. 20). Thus, more negative Ψ values were expected in the circumference classes with higher trees; $\Psi_{soil\text{-}root}$ did not show too much variation among different cohorts (Fig. S14 in the Supplement). Then the leaf water

potential difference among cohorts is mainly contributed by the height effect, which is about $-0.1\,\mathrm{MPa}\,10\,\mathrm{m}^{-1}$.

3.3 Simulated hydraulic failure

Here, we used the simulated PLC in stem sapwood as an indicator of tree hydraulic failure. Under CTL, the PLC remained lower than 50 %, even in dry seasons, due to weak water limitation (see soil moisture deficits in Fig. 4 and water potential gradients in Fig. 7). Under TFE, the PLC did not reach above 50 % in wet seasons, but in dry seasons, it increased to more than 80 %, especially in the (abnormally dry) year 2005 (Fig. 8). Under TFE, the number of days with a PLC above 50 % were 12 d, 63 d in years 2002 and 2003, respectively, and reached up to 84 d in year 2005 (cohort #10). Besides its seasonal variability, the PLC also moderately increased with the size of cohorts, denoting more severe water stress in larger/taller cohorts (Fig. S15 in the Supplement).

Next, we looked at the two variables defined to link PLC with mortality in the model: the PLC mortality exposure threshold and the mortality fraction per day of exposure (see Methods section). The mortality exposure threshold represents a maximum tolerable drought duration for trees before a fraction of them die. In this study, this mortality threshold is set to consecutive 15 d when the PLC stays above 50 %. The mortality fraction is set to a death rate of 0.3 % during each day of the exposure period (no preferential rule is imposed for small or large trees). In the absence of any measurement, the values of these two mortality-triggering variables were calibrated to reproduce the observed mortality in the TFE experiment. We estimated the mortality fraction by totaling the dead trees in each year and dividing this number by the initial tree density in each year. With this scheme, estimated drought-induced tree mortality rates were shown in Fig. 8. The model simulated that more than 10 % of trees in larger cohorts (#12 to #20) would be killed by the dry conditions in 2005 (Fig. 8), which was a bit higher than the 7 % of mortality observed in the experiment. Figures S16 and S17 in the Supplement present that a smaller cohort (#5 here) shows somewhat larger variation in water potential dynamics and corresponding PLC, which indicates that an adequate cumulated drought exposure occurs less frequently than in larger cohorts (#20 here). Thus, the higher annual tree mortality rate is found in larger cohorts (Fig. 8).

The model simulation (ORCHIDEE-CAN-NHA) produced a reasonable (but slightly too large) biomass mortality under TFE during 2002–2008 (Figs. 9 and S18 in the Supplement), with a modeled biomass loss ($\sim 67\,\mathrm{Mg\,C\,ha}^{-1}$, ~ 19 % of biomass in 2001) being a bit larger than the observation ($\sim 30\,\mathrm{Mg\,C\,ha}^{-1}$, ~ 12 % of biomass in 2001). The other two previous model versions cannot reproduce the comparable drought-induced biomass loss (Table S3). Figure 10 showed that under CTL, the biomass loss due to self-thinning and turnover is almost compensated by the biomass growth and recruitment. Under TFE, self-thinning only existed in the years before 2004 according to the model, because a drop of tree density was induced by preceding drought mortality in 2003, which suppressed the competition between trees in the model afterwards. The gain of biomass (labeled as "growth" in green in Fig. 10) also decreased under TFE in comparison with CTL. Moreover, when we grouped the mortality rate simulated for 20 cohorts into three classes according to their DBH (< 20, 20–40 and > 40 cm), we can further evaluate the model performance (Fig. 11). Under CTL, the model produced a higher mortality rate (1.7 %) than the observation (2001:2008 mean: 1.1 %–1.3 %) in three classes. In other words, the modeled self-thinning rate was probably higher than that in reality since the mortality rate observed was only 0.4 % in year 2001. Under TFE, the model performed differently for each size class. For the small-sized class with DBH < 20 cm, the model underestimated the mortality rate compared to observations after 2006. For the medium-sized class (DBH: 20–40 cm), the modeled mortality rate was comparable with observations in year 2001, 2002 and 2006. For the large-sized class group, the model can successfully estimate the large mortality observed in situ from 2004 to 2005. Overall, the averaged mortality rate was comparable between observation and model simulation. The model–observation gap in year 2005, 3.7 % in model simulation vs. 4.8 % in observation, may be due to modeled underestimation in a medium-sized group and large-sized group (Fig. 11).

Finally, we tested the performance of our hydraulic failure–mortality submodel at another TFE site in the Amazon, from the Tapajos site (Nepstad et al., 2007). At this site, TFE only happened in the wet season between 2000 and 2003, with an exclusion of almost 50 % rainfall. Figure S19 in the Supplement shows that our model can capture the observed phenomenon of a higher mortality rate found at Tapajos, especially in trees with a diameter > 30 cm, although the modeled mortality rate is lower than that in the field measurement. Our model also simulates the net biomass increase at Tapajos under CTL and the great biomass loss under TFE. The two parameters of our hydraulic failure–mortality model (drought exposure threshold and mortality fraction each day upon exceeding the threshold), which are not directly observable, were effectively calibrated at Caxiuanã, but the model is also successfully evaluated at Tapajos site. Given the complexity of drought–mortality relationships which lack a unified theory, this shows high performances for the new parameterization we proposed in the study.

4 Discussion

4.1 Model improvements by new parameterizations of hydraulic transport

The original ORCHIDEE-CAN model included a limit from transpiration supply based on water transport and resis-

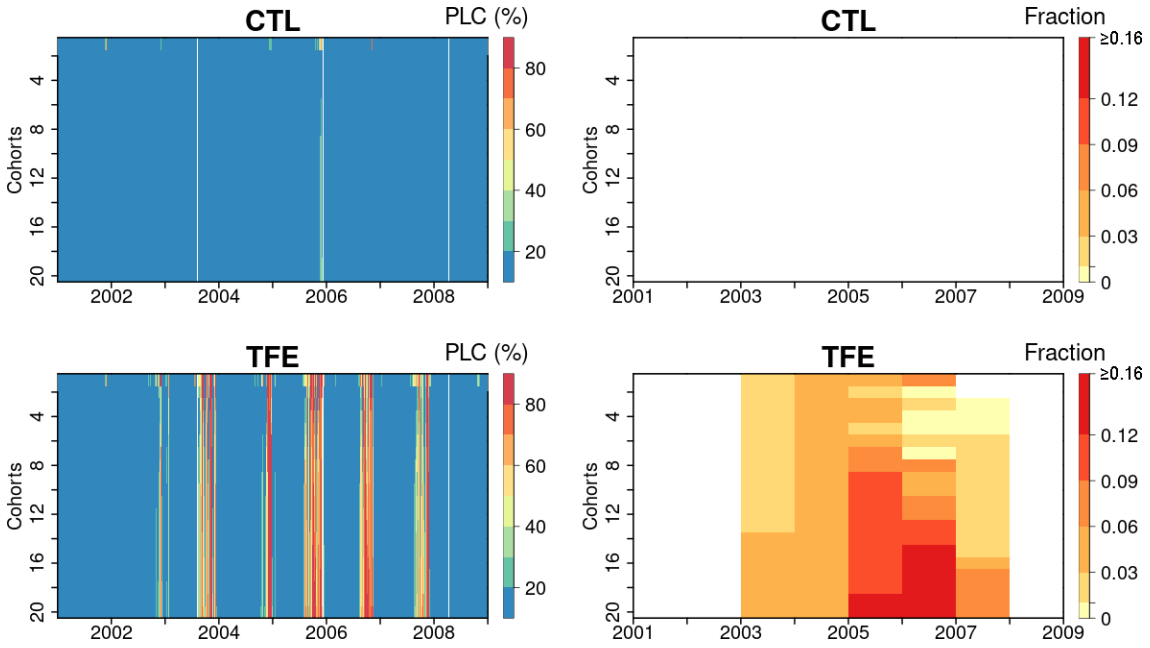

Figure 8. Percentage loss of daily stem conductance (PLC) (left) and tree mortality fraction simulated by ORCHIDEE-CAN-NHA (right). The vertical axis is for the index of 20 tree cohorts represented in the model, a larger index indicating taller trees (see Table S4 for tree height and diameter in each cohort). Tree mortality fraction per year is calculated by totaling the number of dead trees in each year and dividing it by the tree density on the first day of each year.

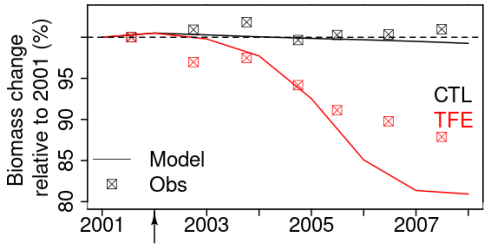

Figure 9. Tree biomass change simulated by model after mortality being triggered. The squares in the plot denote the observation. Biomass change relative to 2001 is calculated by dividing biomass during 2002–2008 by biomass in 2001.

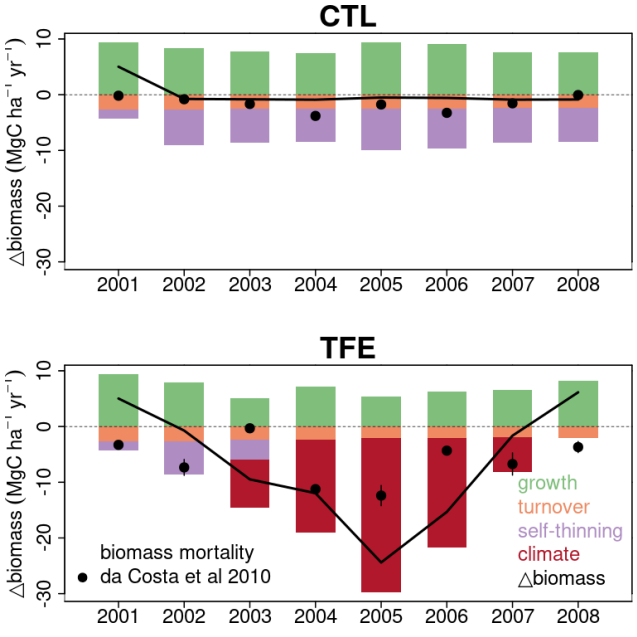

Figure 10. Simulated components of biomass change and observed net biomass change during 2001–2008. The observed net biomass change data in each year from da Costa et al. (2010) are plotted as black dot. The black line shows the net change of simulated biomass by ORCHIDEE-CAN-NHA.

tances along a water potential gradient (Naudts et al., 2015). Nonetheless, the constant value assumed for Ψ_{leaf}, the lack of a dynamic simulation of Ψ_{stem} and Ψ_{root} and conductivities limit the mechanistic basis of the approach. To make a step forward, the new hydraulic module presented here tracks the water flow continuum from the soil to the atmosphere. The water potentials Ψ_{leaf}, Ψ_{stem} and Ψ_{root} are updated at each 30 min time step, based upon a supply–demand framework of minimization of the difference between water demand and water supply at organ level. Besides improvements in modeling the processes of vertical water transport, our hydraulic module also considers the tissue water storage and the dynamics of water flow between different organs, both of which are bounded by the capacitance and water volume. The water

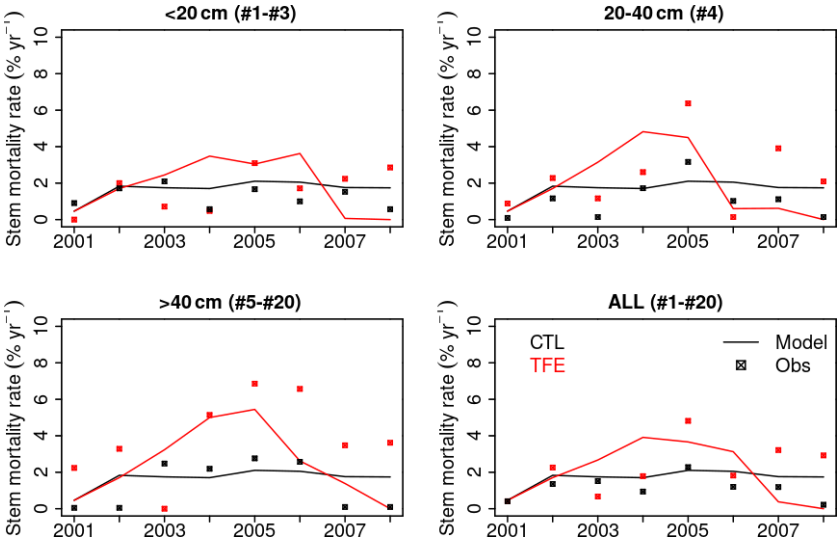

Figure 11. Annual stem mortality rates during the study period (2001–2008). All 20 cohorts have been aggregated to three classes according to DBH (< 20, 20–40, > 40 cm). The value in brackets in the title of each panel corresponds to the cohort numbers falling in the class.

storage capacity can affect the water potential and determine the tolerable duration of desiccation before severe water potentials are reached (Gleason et al., 2014). For example, in the model, stem sapwood water storage can be discharged under CTL during both the wet and dry periods, and this contribution can be larger than that from vertical water flow. In contrast, under TFE, the stem sapwood water pool is not always refilled overnight in the dry season (Fig. S20 in the Supplement). Martinez-Vilalta et al. (2019) also found that a more explicit consideration of water pools helps advance the monitoring and prediction of mortality risk, although more experimental evidence is required for verifying the relationship between relative water content and mortality probability.

Besides the capacity of each organ, stem hydraulic safety indicators like water potential, at which 50 % of stem conductance is lost (Ψ_{50}), can be modeled directly and used as an indicator of tree responses to drought events. This variable influences the maximum drought exposure threshold proposed in our model, which varies among specific tree species, tree size and different growth conditions (Blackman et al., 2016). In a previous study at this site, Rowland et al. (2015) found that vulnerable and resistant genera have contrasting vulnerability to hydraulic deterioration. Vulnerable trees with larger DBH displayed higher conductivity loss under experimental drought and less negative Ψ_{50}. However, in a more recent study with much more field data in Bittencourt et al. (2020), the variability of hydraulic traits among species is also evident and the importance of particular hyper-dominant species also becomes notable in affecting the overall species and size patterns. Naudts et al. (2015) related stem conductivity to $\Psi_{\text{soil-root}}$ with Ψ_{50} and another shape parameter as an adjustment. In our model, we built sigmoidal relationships between conductance and Ψ_{stem}, of which the slope parameter assesses the sensitivity of conductance loss to decline in water potential that can correspond to different plant water-regulation strategies. Through involving trait-related parameters, our model could be used to reflect isohydric or anisohydric patterns, although these two parameters are challenging to calibrate for highly diverse tropical forests (e.g., Maréchaux et al., 2015).

Recently, there has been expansion in the availability of the hydraulic parameters for tropics, but mainly for xylem and leaves. Although the sensitivity analysis of the supply–demand theory in Sperry et al. (2016) suggested that the usage of the single-stem vulnerability curve would not bring more error to transpiration than the true segmented mode (i.e., separate leaf, stem and root curves) as long as the leaf/stem Ψ_{50} and root/stem Ψ_{50} is closer to 1, our study included vulnerability segmentation of leaf, stem and root to facilitate the coherent representation of the soil–root–stem–leaf continuum. Besides, the possible context-dependent trait coordination also needs to be noticed in parameterizing models (Maréchaux et al., 2020), e.g., the relationship between leaf turgor loss point and leaf area, which will benefit the diversity in vegetation models.

With water transport from the vertical gradient of potentials and changes in water storage, ORCHIDEE-CAN-NHA produced dynamic and reasonable water potentials (Fig. S11) and conductance at leaf, stem and root levels. Based on the improved hydraulic architecture, we implemented an empirical algorithm that assumes that a fixed fraction of trees will die after 15 d of continuous sustained drought exposure with PLC > 50 %. Combinations of these two parameters of drought exposure threshold and mortality fraction each time could also be adapted to diverse plant traits to match mortality rates across different sites, coping with ad-

verse conditions, e.g., tree size, different isohydric and anisohydric behaviors of stomatal regulation upon varying water status (McDowell et al., 2008). Therefore, these two parameters would need to be calibrated upon data suited to different conditions. For example, Esquivel-Muelbert et al. (2017) found that wet-affiliated genera tend to show higher drought-induced mortality than dry-affiliated ones. Assigning higher mortality fraction for wet-affiliated genera under such conditions can be a solution to test different levels of mortality fraction parameters.

The supply–demand framework in our model also draws on Sperry et al. (2016) that the empirical expression of each continuum component, e.g., stomatal conductance and hydraulic conductivities from the vulnerability curve, is applied. There are also similarities between our hydraulic structure and that of Xu et al. (2016) in aspects that both vertical water flow and water storage capacity in leaf and stem are accounted for in the modeling process of water supply and demand. The major differences from the model of Xu et al. (2016) are that our model uses potential water demand (rather than the real transpiration) as the leaf-level demand instead and also refines the water transport from soil–root–stem, thus the water potential of each organ in the continuum is solved.

The earlier hydraulic models like SPA and that of Xu et al. (2016) indeed proposed the simulation framework of water flow and water potential following Darcy's law; however, a full segmentation of the hydraulic system including water flow and water storage change of leaves, stem and root are still not completely solved (i.e., the root part was missing in Xu et al., 2016). Our hydraulic architecture refines the segmentation of plant hydraulics of leaves, stem and root, separately, of which the hydraulic conductance varies with water potential value following the sigmoidal relationship. Meanwhile, the water capacitance is considered as well to account for the variation in water storage. The hydraulic models like SPA and that of Xu et al. (2016), lack either the full segmentation or the consideration of contribution of each water storage pool (SPA model only used canopy capacitance). Our model also extends one step further to link the hydraulic failure measured by PLC to the tree mortality rate via an empirical model composed of two parameters: drought exposure threshold (number of continuous days under water stress), and tree mortality fraction upon each tree mortality event. This tree mortality submodel accounts for the cumulative drought effects, which can adapt to different drought strengths and drought frequencies. Therefore, our hydraulic model with tree mortality scheme improves the hydraulic segmentation simulation and also paves a new way of linking hydraulic failure to tree mortality. Admittedly, weakness does exist in our model, e.g., parameter retrieval can be further realized through data assimilation that use more benchmarking (see below). More optimization paradigms can be integrated into our model, which would benefit the parameterization process.

4.2 Possible factors affecting tree mortality

Our model simulations showed that larger trees suffer more severe water stress with higher PLC (Fig. 8) and that the mortality fraction is consequently the highest in groups with DBH > 40 cm. This uses the theory that longer, vertical water transport pathways in taller trees can intensify the height-dependent hydraulic limitation (Grote et al., 2016) and site-level experimental evidence (Rowland et al., 2015). Such size-regulated mortality has also been corroborated by Bennett et al. (2015). Hendrik and Maxime (2017) summarized that drought can be more detrimental to growth and mortality rates of larger trees. Klos et al. (2009) also found that older and denser stands are more susceptible to drought damage, but that the mortality–height relationship can also be relaxed by species diversity, e.g., the taxonomic identity also controls the trait–size relationship (Bittencourt et al., 2020). Environmental gradients of climate conditions and concurrent competition can also affect the mortality–height risk relationship (Stovall et al., 2019) and co-explain the forest mortality patterns (Young et al., 2017). Conversely, the benefits of deeper root systems may potentially allow tall trees to avoid drought stress (Trugman et al., 2021). Simulated water content in bottom soil layers did not counteract the embolism during the dry season in our study, so we captured the positive mortality–height relationship observed at this site. Nevertheless, in the Caxiuanã field measurements of Rowland et al. (2015), trees of similar size also showed different vulnerability (Ψ_{50}), which suggests the influence of other anatomical traits, e.g., wood density, which is already prescribed as a PFT-based parameter in simulation setup. Such a kind of within-PFT variation cannot yet be accounted for in the model. Wood density with intra-individual variability is intimately linked with tree mortality, and has been found to explain variation in the tropical mortality rate across sites through a hierarchical Bayesian approach (Kraft et al., 2010). Plant functional traits like xylem, leaf specific conductivities and capacitances are inversely related to the wood density (Meinzer et al., 2008). On the one hand, taller trees with lower wood density (Rozendaal et al., 2020) would be expected to present higher sapwood conductivity although the overall effect would depend on the forest type and growth conditions (Fajardo, 2018; Meinzer et al., 2008). On the other hand, height-dependent water limitation weakens the stem hydraulic conductivity. Such tradeoffs co-determine the resistance to hydraulic failure.

Under extreme drought conditions, hydraulic traits are also highly important factors for mortality risk. Trees with high cavitation resistance and wide hydraulic safety margins can endure longer desiccation (Blackman et al., 2019). Although xylem anatomical traits directly related to conductivity better reflect the whole-tree performance (Fan et al., 2012), the relative importance of climate conditions, plant functional and hydraulic traits in determining forest mortality risk en-

countering drought needs further the validation with a large amount of experimental observations (Aleixo et al., 2019).

4.3 Model limitations and directions for future development

Several potentially important ecological processes related to plant hydraulics and mortality warrant further consideration. Firstly, tree mortality risk, in the simulations, is mainly triggered by drought-induced water stress, but soil water limitation can also be alleviated by enhanced tree survival through increasing nutrient uptake, to increase water use efficiency and reduce negative effects of droughts (Wang et al., 2012). Fast growth rate, however, is associated with higher mortality probability (see Rozendaal et al. (2020) for a spatial relationship between basal area growth, diameter and the possibility of mortality in the Amazonia tropical forest). Discounting the demographic association between tree growth and mortality rate could lead to underestimation of mortality in model simulations. Representations of these interactions should be further incorporated to increase model credibility under various environments. Secondly, the PFT classification used in ORCHIDEE-CAN-NHA does not capture hydraulic variation. Some researchers proposed hydraulic trait-based classifications (Anderegg, 2015) or hydraulic functional types (Y. Liu et al., 2021), which may better represent isohydric and anisohydric behaviors affecting water potential and stomatal regulation. Accounting for the variability in hydraulic traits would be important to properly model ecosystem–atmosphere feedback effects (Anderegg et al., 2018; Powell et al., 2018) in future. More specifically, some traits are also but not always found to vary with tree size, like Ψ_{50}, conductivity and the number of days of exposure to severe drought that a tree can tolerate. Our assumption of fixed Ψ_{50} values for all 20 cohorts may lead to the miscalculation of mortality rates in different classes, e.g., overestimation for the PLC in smaller cohorts and underestimation for the PLC in larger cohorts. Therefore, future research should focus on discerning the empirical connection between species-specific hydraulic strategies toward mortality by distinguishing vegetation functional groups. Thirdly, legacy or memory effects are not fully accounted for here. The impacts of drought on increasing tree mortality can last for at least 2 years after an extreme climatic event (Aleixo et al., 2019). Some cumulated or memory indicators may help tackle such problems. For example, we can consider the effects of past drought events on current tree growth by multiplying the drought intensity with the inverse of time passed (Franklin et al., 1987). Finally, different threshold indicators like relative water content and turgor loss point can also be tested in the mortality triggering process (Sapes et al., 2019; Zhu et al., 2018).

Besides future developments of the hydraulic module, more calibration and understanding of the lethal threshold required for hydraulic failure is clearly necessary. We call for data of more observed hydraulic traits for tropical trees, including detailed vulnerability, to support more reasonable and appropriate parameterization schemes in mortality risk modeling, e.g., the point of no return from drought-induced xylem embolism in aspects of water potential (turgor loss point), conductivity and relative water content. Remote-sensing products of vegetation optical depth (VOD), proportional to the vegetation water content, may help benchmark the capacitance dynamics. Additionally, in this study we have only calibrated the new hydraulic architecture against observations from one drought experiment site. It should be noted that the hydrological parameters are quite sensitive in aspect of drought response and are also uncertain. Expanding this method to other drought experiment sites is required to generalize the model performance. For example, this future work could address the extent to which the drought of 2005 and 2010 affected forest dynamics in western Amazonia. Large-scale mortality observations and more comprehensive mortality benchmarking datasets are also required to evaluate the hydraulic architecture in the process-based model (Adams et al., 2013; Allen et al., 2010). Regarding the parameterization of the model at the regional and global scales, here we focus on the tree mortality submodel to clarify the issue of parameter uncertainties. In our tree mortality empirical submodel, the two parameters, drought exposure threshold and tree mortality fraction upon each stress event, are related to each other, given a target tree mortality rate. We derive a parameter space composed of these two empirical parameters in the tree mortality scheme that can produce a similar tree mortality rate for cohort #20 in the Caxiuanã TFE experiment in 2005 (cohort #20 is taken as an example here). That is to say, higher drought exposure threshold should be combined with a higher tree mortality rate in each event, and vice versa (Fig. S21 in the Supplement). Specifying a higher drought exposure threshold, such a parameterization scheme would underestimate the impact of drought with high intensity but short period since a higher drought exposure threshold would lead to the detection of less frequent tree mortality events in model perspective.

After the derivation of a parameter space, we did a regional simulation focusing on the 2005 drought in western Amazon using parameters specified in the main text (named as default simulation). To reduce the computation load, we just use the PLC output in the default simulation to calculate the number of tree mortality events with varying drought exposure threshold in order to test the range of parameters values. Figure S22 shows that the tree mortality rate (cohort #20) below 20 % can become lower if the model was fed with a higher drought exposure threshold (DT = 25 or 30). And the tree mortality rate below 20 % tends to be higher with a lower drought exposure threshold (DT = 10). Although all these parameter combinations can produce a similar tree mortality phenomenon (cohort #20) for the Caxiuanã TFE setup in 2005, they will perform differently regarding drought with different intensities and durations regionally. Therefore, more experiment data manifesting the tree

tolerance should be well included to constrain the drought exposure threshold uncertainties in our model framework.

Towards the enrichment of parameters for the regional simulation, generally, three means can be resorted to for the benefit of such realizations. The first one can be embedding the plant trait database like TRY (Kattge et al., 2020) into our process-based model, although the records are still limited in aspect of hydraulic traits. The second solution can be the optimization of hydraulic parameters using e.g., Markov chain Monte Carlo methodology with measurements or remote-sensing products as constraints like the retrieval of traits in Y. Liu et al. (2021) or other data-assimilation systems like ORCHIDAS. Here, the data quality of constraint is highly important as the error can be accumulated. The third method can be to build a simple regression formula between plant traits and the climatology in which the plants reside. In a next step, these solutions will be attempted to test the generalization of process-based model performance at large scale.

5 Conclusion

Our study proposes a new mechanistic hydraulic architecture module, ORCHIDEE-CAN-NHA, which simulates a dynamic xylem cavitation indicator of percentage loss of conductance (PLC) through modeling the water flow in the soil–root–stem–leaf continuum and water charge from storage. The model was calibrated against observations from the Caxiuanã throughfall exclusion field experiment in the eastern Amazon, during 2001–2008, with regard to the seasonal variability in transpiration, soil moisture and productivity. Besides the improvement of hydraulic architecture, we also built a relationship between PLC and tree mortality rate via two empirical parameters, drought exposure duration, which determines the mortality frequency and the mortality fraction in each day once exceeding the exposure. Our model produces comparable annual tree mortality rates with observations over the study period. The introduction of mechanistic hydraulic architecture in land surface models can help to provide a window through which we can enable the prediction of mortality under future possible drought events. We also call for more available hydraulic traits and vulnerability data for testing the generalization of model performance.

Appendix A

Table A1. Plant hydraulics in major vegetation models. The column of validation indicates how the model performance is validated against observation.

Model	Framework for modeling hydrodynamics	Validation	Reference
CLM v5	Stomata optimization and supply–demand theory	Caxiuanã site	Kennedy et al. (2019)
JULES-SOX	Optimization of stomatal conductance by maximizing the product of leaf photosynthesis and xylem hydraulic conductance	70 global eddy flux sites	Eller et al. (2020)
CliMA	Optimization-based stomatal model by maximizing the difference between leaf-level carbon gain and risk	Two flux sites in USA	Wang et al. (2021)
CABLE	Supply–demand theory	Garden dry-down experiment across southeast Australia	De Kauwe et al. (2020)
ORCHIDEE-CAN	Water supply via Darcy's law without dynamics in stem water potential	Europe	Naudts et al. (2015)
Ecosystem demography model 2	Stomata optimization and supply–demand theory	Costa Rican field	Xu et al. (2016)
TRIPLEX	Loss of stem conductivity is related to soil water potential	Canadian boreal forests	Q. Liu et al. (2021)
SPAC	Stomata optimization and supply–demand theory	13 temperate and tropical forest biomes across the globe	Liu et al. (2017)
One hydraulic module	Two parameters: isohydricity factor and well-watered forcing pressure	Leaf and soil water potentials of 66 species under drought and non-drought conditions	Papastefanou et al. (2020)
SurEau	Water mass conservation law	One forest site in east France	Cochard et al. (2021)
TFS v.1-Hydro	Continuous porous approach with pressure–volume formula	Caxiuanã site	Christoffersen et al. (2016)
SPA	Stomata optimization and supply–demand theory	Caxiuanã site	Fisher et al. (2007)

Table A2. Parameters used in the new hydraulic architecture model. These parameters are selected from the range recorded by literature that we have analyzed.

Symbol	Description	Unit	Value	Source
C_{leaf}	Leaf capacitance	$mmol\,m^{-2}\,MPa^{-1}$	670	De Kauwe et al. (2020)
C_{stem}	Stem capacitance	$kg\,m^{-3}\,MPa^{-1}$	130	Xu et al. (2016)
C_{root}	Root capacitance	$kg\,m^{-3}\,MPa^{-1}$	150	Modified from C_{stem}
S	Specific leaf area	$m^2\,kg^{-1}$	16.6	Kattge et al. (2011)
L	Leaf dry matter content	$g\,g^{-1}$	0.2	Kattge et al. (2011)
γ	Mass of water per unit of sapwood volume	$mol\,m^{-3}$	25 000	Suzuki (1999)
δ	Wood density	gcm^{-3}	0.645	Chave et al. (2006)
θ	Root shoot ratio	$g\,g^{-1}$	0.25	Mokany et al. (2006)
ε	Root water content	$mmol\,g^{-1}$	35	Markesteijn and Poorter (2009)
ρ_{root}	Root density	$g\,cm^{-3}$	0.503	Schuldt et al. (2013)
$k_{leaf,max}$	Maximum leaf hydraulic conductance per unit leaf area	$mmol\,m^{-2}\,s^{-1}\,MPa^{-1}$	15	Sack and Holbrook (2006)
$k_{stem,max}$	Maximum sapwood hydraulic conductance per unit leaf area	$mmol\,m^{-2}\,s^{-1}\,MPa^{-1}$	15*	Hickler et al. (2006)
$k_{root,max}$	Maximum root hydraulic conductance per unit leaf area	$mmol\,m^{-2}\,s^{-1}\,MPa^{-1}$	10	Modified from $k_{stem,max}$
a_{leaf}	Shape parameter for k_{leaf} vs. Ψ_{leaf} curve	–	−2.5	[−3.8, −0.5] in Bartlett et al. (2019)
a_{stem}	Shape parameter for k_{stem} vs. Ψ_{stem} curve	–	−2.3	[−3.8, −0.5] in Bartlett et al. (2019)
a_{root}	Shape parameter for k_{root} vs. Ψ_{root} curve	–	−3.0	[−3.8, −0.5] in Bartlett et al. (2019)
$\Psi_{50,leaf}$	Ψ_{leaf} at 50 % loss of leaf conductance	MPa	−1.1	[−3, −0.75] in Bartlett et al. (2019)
$\Psi_{50,stem}$	Ψ_{stem} at 50 % loss of stem sapwood conductance	MPa	−1.2	[−3, −0.75] in Bartlett et al. (2019)
$\Psi_{50,root}$	Ψ_{root} at 50 % loss of root conductance	MPa	−1.1	[−3, −0.75] in Bartlett et al. (2019)
g_{max}	Maximum stomatal conductance in Eq. (24)	$mmol\,m^{-2}\,s^{-1}$	700	Franks and Brodribb (2005)
g_{min}	Mininum stomatal conductance	$mmol\,m^{-2}\,s^{-1}$	10	Franks and Brodribb (2005)
$\Psi_{50,gs}$	Ψ_{leaf} at 50 % decline in stomatal conductance	MPa	−1.2	Bartlett et al. (2016)
a_{gs}	Shape parameter for g_s vs. Ψ_{leaf} curve	–	−2.3	Bartlett et al. (2016)
$\frac{L\times Rad}{L\times Rad+L_k}$	In this term, the function of short-wave radiation is used to ensure the g_s at night to be close to 0	–	–	–

* In Hickler et al. (2006), the maximum sapwood conductivity of $50\times10^{-4}\,m^2\,s^{-1}\,MPa^{-1}$ can be converted to $\sim 15\,mmol\,m^{-2}\,s^{-1}\,MPa^{-1}$ if we assume sapwood area/leaf area of 0.0016 (value falls in Gotsch et al., 2010), and tree height of 30 m.

Table A3. Outputs variables calculated by ORCHIDEE-CAN-NHA.

Category	Symbol	Description	Unit
Water potentials	$\Psi_{soil\text{-}root}$	Soil water potential in root zone	MPa
	Ψ_{root}	Root water potential	MPa
	Ψ_{stem}	Stem water potential	MPa
	Ψ_{leaf}	Leaf water potential	MPa
Hydraulic conductances	k_{root}	Root hydraulic conductance	$mmol\,m^{-2}\,s^{-1}\,MPa^{-1}$
	k_{stem}	Stem sapwood hydraulic conductance	$mmol\,m^{-2}\,s^{-1}\,MPa^{-1}$
	k_{leaf}	Leaf hydraulic conductance	$mmol\,m^{-2}\,s^{-1}\,MPa^{-1}$
Water storage	m_{root}	Water volume in the root	mmol
	m_{stem}	Water volume in the stem	mmol
	m_{leaf}	Water volume in the leaf	mmol
Cavitation	PLC	Percentage loss of stem conductance	%
Mortality	NK	Number of continuous days with PLC > 50 % (exposure)	days
	CM	Tree mortality for each circumference class due to exposure to PLC > 50 %	$1\,m^{-2}$

Code availability. The ORCHIDEE-CAN-NHA model (r7236) code used in this study is deposited at https://forge.ipsl.jussieu.fr/orchidee/browser/branches/publications/ORCHIDEE_CAN_NHA (last access: 17 June 2021) and archived at https://doi.org/10.14768/8C2D06FB-0020-4BC5-A831-C876F5FBBFE9 (Yao, 2021a). The detailed code used to reproduce the analysis and figures is publicly available at https://doi.org/10.5281/zenodo.5721245 (Yao, 2021b).

Supplement. The supplement related to this article is available online at: https://doi.org/10.5194/gmd-15-7809-2022-supplement.

Author contributions. YY, EJ, PC and NV designed the study. YY and EJ developed the code. YY conducted the analysis. YY wrote the manuscript. All authors provided comments and contributed to the final version of the paper.

Competing interests. The contact author has declared that none of the authors has any competing interests.

Disclaimer. Publisher's note: Copernicus Publications remains neutral with regard to jurisdictional claims in published maps and institutional affiliations.

Financial support. This research has been supported by the Centre National de la Recherche Scientifique, Institut écologie et environnement (grant no. 16-CONV-0003 and "Make Our Planet Great Again Scholarship" grant).

Review statement. This paper was edited by Jinkyu Hong and reviewed by two anonymous referees.

References

Adams, H. D., Williams, A. P., Xu, C., Rauscher, S. A., Jiang, X., and McDowell, N. G.: Empirical and process-based approaches to climate-induced forest mortality models, Front. Plant Sci., 4, 438, https://doi.org/10.3389/fpls.2013.00438, 2013.

Adams, H. D., Zeppel, M. J., Anderegg, W. R., Hartmann, H., Landhäusser, S. M., Tissue, D. T., Huxman, T. E., Hudson, P. J., Franz, T. E., and Allen, C. D.: A multi-species synthesis of physiological mechanisms in drought-induced tree mortality, Nature Ecology & Evolution, 1, 1285–1291, 2017.

Aleixo, I., Norris, D., Hemerik, L., Barbosa, A., Prata, E., Costa, F., and Poorter, L.: Amazonian rainforest tree mortality driven by climate and functional traits, Nat. Clim. Change, 9, 384–388, 2019.

Allen, C. D., Macalady, A. K., Chenchouni, H., Bachelet, D., McDowell, N., Vennetier, M., Kitzberger, T., Rigling, A., Breshears, D. D., and Hogg, E. T.: A global overview of drought and heat-induced tree mortality reveals emerging climate change risks for forests, Forest Ecol. Manag., 259, 660–684, 2010.

Allen, C. D., Breshears, D. D., and McDowell, N. G.: On underestimation of global vulnerability to tree mortality and forest die-off from hotter drought in the Anthropocene, Ecosphere, 6, 1–55, 2015.

Anderegg, W. R.: Spatial and temporal variation in plant hydraulic traits and their relevance for climate change impacts on vegetation, New Phytol., 205, 1008–1014, 2015.

Anderegg, W. R., Flint, A., Huang, C.-y., Flint, L., Berry, J. A., Davis, F. W., Sperry, J. S., and Field, C. B.: Tree mortality predicted from drought-induced vascular damage, Nat. Geosci., 8, 367–371, 2015.

Anderegg, W. R., Konings, A. G., Trugman, A. T., Yu, K., Bowling, D. R., Gabbitas, R., Karp, D. S., Pacala, S., Sperry, J. S., and Sulman, B. N.: Hydraulic diversity of forests regulates ecosystem resilience during drought, Nature, 561, 538–541, 2018.

Bartlett, M. K., Klein, T., Jansen, S., Choat, B., and Sack, L.: The correlations and sequence of plant stomatal, hydraulic, and wilting responses to drought, P. Natl. Acad. Sci. USA, 113, 13098–13103, 2016.

Bartlett, M. K., Detto, M., and Pacala, S. W.: Predicting shifts in the functional composition of tropical forests under increased drought and CO_2 from trade-offs among plant hydraulic traits, Ecol. Lett., 22, 67–77, 2019.

Bennett, A., McDowell, N., Allen, C., and Anderson-Teixeira, K. J.: Larger trees suffer most during drought in forests worldwide, Nature Plants, 1, 15139, https://doi.org/10.1038/nplants.2015.139, 2015.

Bittencourt, P. R., Oliveira, R. S., da Costa, A. C., Giles, A. L., Coughlin, I., Costa, P. B., Bartholomew, D. C., Ferreira, L. V., Vasconcelos, S. S., and Barros, F. V.: Amazonia trees have limited capacity to acclimate plant hydraulic properties in response to long-term drought, Glob. Change Biol., 26, 3569–3584, 2020.

Blackman, C. J., Pfautsch, S., Choat, B., Delzon, S., Gleason, S. M., and Duursma, R. A.: Toward an index of desiccation time to tree mortality under drought, Plant Cell Environ., 39, 2342–2345, 2016.

Blackman, C. J., Li, X., Choat, B., Rymer, P. D., De Kauwe, M. G., Duursma, R. A., Tissue, D. T., and Medlyn, B. E.: Desiccation time during drought is highly predictable across species of Eucalyptus from contrasting climates, New Phytol., 224, 632–643, 2019.

Bonan, G. B., Williams, M., Fisher, R. A., and Oleson, K. W.: Modeling stomatal conductance in the earth system: linking leaf water-use efficiency and water transport along the soil–plant–atmosphere continuum, Geosci. Model Dev., 7, 2193–2222, https://doi.org/10.5194/gmd-7-2193-2014, 2014.

Brienen, R. J., Phillips, O. L., Feldpausch, T. R., Gloor, E., Baker, T. R., Lloyd, J., Lopez-Gonzalez, G., Monteagudo-Mendoza, A., Malhi, Y., and Lewis, S. L.: Long-term decline of the Amazon carbon sink, Nature, 519, 344–348, 2015.

Brodribb, T. J., and Cochard, H.: Hydraulic failure defines the recovery and point of death in water-stressed conifers, Plant Physiol., 149, 575–584, 2009.

Brodribb, T. J., Powers, J., Cochard, H., and Choat, B.: Hanging by a thread? Forests and drought, Science, 368, 261–266, 2020.

Carswell, F., Costa, A., Palheta, M., Malhi, Y., Meir, P., de Pr Costa, J., Ruivo, M. d. L., do Sm Leal, L., Costa, J., and Clement, R.:

Seasonality in CO2 and H2O flux at an eastern Amazonian rain forest, J. Geophys. Res.-Atmos., 107, LBA 43-41–LBA 43-16, 2002.

Chave, J., Muller-Landau, H. C., Baker, T. R., Easdale, T. A., Steege, H. T., and Webb, C. O.: Regional and phylogenetic variation of wood density across 2456 neotropical tree species, Ecol. Appl., 16, 2356–2367, 2006.

Choat, B.: Predicting thresholds of drought-induced mortality in woody plant species, Tree Physiol., 33, 669–671, 2013.

Choat, B., Brodribb, T. J., Brodersen, C. R., Duursma, R. A., López, R., and Medlyn, B. E.: Triggers of tree mortality under drought, Nature, 558, 531–539, 2018.

Christoffersen, B. O., Gloor, M., Fauset, S., Fyllas, N. M., Galbraith, D. R., Baker, T. R., Kruijt, B., Rowland, L., Fisher, R. A., Binks, O. J., Sevanto, S., Xu, C., Jansen, S., Choat, B., Mencuccini, M., McDowell, N. G., and Meir, P.: Linking hydraulic traits to tropical forest function in a size-structured and trait-driven model (TFS v.1-Hydro), Geosci. Model Dev., 9, 4227–4255, https://doi.org/10.5194/gmd-9-4227-2016, 2016.

Cochard, H. and Delzon, S.: Hydraulic failure and repair are not routine in trees, Ann. For. Sci., 70, 659–661, 2013.

Cochard, H., Pimont, F., Ruffault, J., and Martin-StPaul, N.: SurEau: a mechanistic model of plant water relations under extreme drought, Ann. For. Sci., 78, 1–23, 2021.

da Costa, A. C. L., Galbraith, D., Almeida, S., Portela, B. T. T., da Costa, M., Junior, J. d. A. S., Braga, A. P., de Gonçalves, P. H., de Oliveira, A. A., and Fisher, R.: Effect of 7 yr of experimental drought on vegetation dynamics and biomass storage of an eastern Amazonian rainforest, New Phytol., 187, 579–591, 2010.

De Kauwe, M. G., Medlyn, B. E., Ukkola, A. M., Mu, M., Sabot, M. E., Pitman, A. J., Meir, P., Cernusak, L., Rifai, S. W., and Choat, B.: Identifying areas at risk of drought-induced tree mortality across South-Eastern Australia, Glob. Change Biol., 26, 5716–5733, 2020.

Delbart, N., Ciais, P., Chave, J., Viovy, N., Malhi, Y., and Le Toan, T.: Mortality as a key driver of the spatial distribution of aboveground biomass in Amazonian forest: results from a dynamic vegetation model, Biogeosciences, 7, 3027–3039, https://doi.org/10.5194/bg-7-3027-2010, 2010.

Dewar, R., Mauranen, A., Mäkelä, A., Hölttä, T., Medlyn, B., and Vesala, T.: New insights into the covariation of stomatal, mesophyll and hydraulic conductances from optimization models incorporating nonstomatal limitations to photosynthesis, New Phytol., 217, 571–585, 2018.

Duffy, P. B., Brando, P., Asner, G. P., and Field, C. B.: Projections of future meteorological drought and wet periods in the Amazon, P. Natl. Acad. Sci. USA, 112, 13172–13177, 2015.

Eller, C. B., Rowland, L., Oliveira, R. S., Bittencourt, P. R., Barros, F. V., da Costa, A. C., Meir, P., Friend, A. D., Mencuccini, M., and Sitch, S.: Modelling tropical forest responses to drought and El Niño with a stomatal optimization model based on xylem hydraulics, Philos. T. R. Soc. B, 373, 20170315, https://doi.org/10.1098/rstb.2017.0315, 2018.

Eller, C. B., Rowland, L., Mencuccini, M., Rosas, T., Williams, K., Harper, A., Medlyn, B. E., Wagner, Y., Klein, T., and Teodoro, G. S.: Stomatal optimization based on xylem hydraulics (SOX) improves land surface model simulation of vegetation responses to climate, New Phytol., 226, 1622–1637, 2020.

Esquivel-Muelbert, A., Galbraith, D., Dexter, K. G., Baker, T. R., Lewis, S. L., Meir, P., Rowland, L., da Costa, A. C. L., Nepstad, D., and Phillips, O. L.: Biogeographic distributions of neotropical trees reflect their directly measured drought tolerances, Sci. Rep.-UK, 7, 1–11, 2017.

Fajardo, A.: Insights into intraspecific wood density variation and its relationship to growth, height and elevation in a treeline species, Plant Biol., 20, 456–464, 2018.

Fan, Z. X., Zhang, S. B., Hao, G. Y., Ferry Slik, J., and Cao, K. F.: Hydraulic conductivity traits predict growth rates and adult stature of 40 Asian tropical tree species better than wood density, J. Ecol., 100, 732–741, 2012.

Fisher, R., Williams, M., Da Costa, A. L., Malhi, Y., Da Costa, R., Almeida, S., and Meir, P.: The response of an Eastern Amazonian rain forest to drought stress: results and modelling analyses from a throughfall exclusion experiment, Glob. Change Biol., 13, 2361–2378, 2007.

Fisher, R. A., Williams, M., Do Vale, R. L., Da Costa, A. L., and Meir, P.: Evidence from Amazonian forests is consistent with isohydric control of leaf water potential, Plant Cell Environ., 29, 151–165, 2006.

Franklin, J. F., Shugart, H. H., and Harmon, M. E.: Tree death as an ecological process, BioScience, 37, 550–556, 1987.

Franks, P., and Brodribb, T. J.: Stomatal control and water transport in the xylem. In: Holbrook NM, Zwieniecki MA, eds, Vascular transport in plants, New York, NY, USA: Academic Press, 69–89, https://doi.org/10.1016/B978-012088457-5/50006-X, 2005.

Gleason, S. M., Blackman, C. J., Cook, A. M., Laws, C. A., and Westoby, M.: Whole-plant capacitance, embolism resistance and slow transpiration rates all contribute to longer desiccation times in woody angiosperms from arid and wet habitats, Tree Physiol., 34, 275–284, 2014.

Gotsch, S. G., Geiger, E. L., Franco, A. C., Goldstein, G., Meinzer, F. C., and Hoffmann, W. A.: Allocation to leaf area and sapwood area affects water relations of co-occurring savanna and forest trees, Oecologia, 163, 291–301, 2010.

Grote, R., Gessler, A., Hommel, R., Poschenrieder, W., and Priesack, E.: Importance of tree height and social position for drought-related stress on tree growth and mortality, Trees, 30, 1467–1482, 2016.

Gustafson, E. J. and Sturtevant, B. R.: Modeling forest mortality caused by drought stress: implications for climate change, Ecosystems, 16, 60–74, 2013.

Hammond, W. M., Yu, K., Wilson, L. A., Will, R. E., Anderegg, W. R., and Adams, H. D.: Dead or dying? Quantifying the point of no return from hydraulic failure in drought-induced tree mortality, New Phytol., 223, 1834–1843, 2019.

Hartmann, H.: Carbon starvation during drought-induced tree mortality – are we chasing a myth?, J. Plant Hydraul., 2, e005, https://doi.org/10.20870/jph.2015.e005, 2015.

Hendrik, D. and Maxime, C.: Assessing drought-driven mortality trees with physiological process-based models, Agr. Forest Meteorol., 232, 279–290, 2017.

Hickler, T., Prentice, I. C., Smith, B., Sykes, M. T., and Zaehle, S.: Implementing plant hydraulic architecture within the LPJ Dynamic Global Vegetation Model, Global Ecol. Biogeogr., 15, 567–577, 2006.

Joetzjer, E., Maignan, F., Chave, J., Goll, D., Poulter, B., Barichivich, J., Maréchaux, I., Luyssaert, S., Guimberteau, M.,

Naudts, K., Bonal, D., and Ciais, P.: Effect of tree demography and flexible root water uptake for modeling the carbon and water cycles of Amazonia, Ecol. Modell., 469, 109969, https://doi.org/10.1016/j.ecolmodel.2022.109969, 2022.

Kattge, J., Diaz, S., Lavorel, S., Prentice, I. C., Leadley, P., Bönisch, G., Garnier, E., Westoby, M., Reich, P. B., and Wright, I. J.: TRY–a global database of plant traits, Glob. Change Biol., 17, 2905–2935, 2011.

Kattge, J., Bönisch, G., Díaz, S., et al.: TRY plant trait database-enhanced coverage and open access, Glob. Change Biol., 26, 119–188, 2020.

Kennedy, D., Swenson, S., Oleson, K. W., Lawrence, D. M., Fisher, R., Lola da Costa, A. C., and Gentine, P.: Implementing plant hydraulics in the community land model, version 5, J. Adv. Model. Earth Sy., 11, 485–513, 2019.

Klos, R. J., Wang, G. G., Bauerle, W. L., and Rieck, J. R.: Drought impact on forest growth and mortality in the southeast USA: an analysis using Forest Health and Monitoring data, Ecol. Appl., 19, 699–708, 2009.

Kraft, N. J., Metz, M. R., Condit, R. S., and Chave, J.: The relationship between wood density and mortality in a global tropical forest data set, New Phytol., 188, 1124–1136, 2010.

Lewis, S. L., Brando, P. M., Phillips, O. L., van der Heijden, G. M., and Nepstad, D.: The 2010 amazon drought, Science, 331, 554–554, 2011.

Lin, Y. S., Medlyn, B. E., Duursma, R. A., Prentice, I. C., Wang, H., Baig, S., Eamus, D., De Dios, V. R., Mitchell, P., and Ellsworth, D. S.: Optimal stomatal behaviour around the world, Nat. Clim. Change, 5, 459–464, 2015.

Liu, Q., Peng, C., Schneider, R., Cyr, D., Liu, Z., Zhou, X., and Kneeshaw, D.: TRIPLEX-Mortality model for simulating drought-induced tree mortality in boreal forests: Model development and evaluation, Ecol. Model., 455, 109652, https://doi.org/10.1016/j.ecolmodel.2021.109652, 2021.

Liu, Y., Parolari, A. J., Kumar, M., Huang, C.-W., Katul, G. G., and Porporato, A.: Increasing atmospheric humidity and CO_2 concentration alleviate forest mortality risk, P. Natl. Acad. Sci. USA, 114, 9918–9923, 2017.

Liu, Y., Holtzman, N. M., and Konings, A. G.: Global ecosystem-scale plant hydraulic traits retrieved using model–data fusion, Hydrol. Earth Syst. Sci., 25, 2399–2417, https://doi.org/10.5194/hess-25-2399-2021, 2021.

Maréchaux, I., Bartlett, M. K., Sack, L., Baraloto, C., Engel, J., Joetzjer, E., and Chave, J.: Drought tolerance as predicted by leaf water potential at turgor loss point varies strongly across species within an Amazonian forest, Funct. Ecol., 29, 1268–1277, 2015.

Maréchaux, I., Saint-André, L., Bartlett, M. K., Sack, L., and Chave, J.: Leaf drought tolerance cannot be inferred from classic leaf traits in a tropical rainforest, J. Ecol., 108, 1030–1045, 2020.

Maréchaux, I., Langerwisch, F., Huth, A., Bugmann, H., Morin, X., Reyer, C. P., Seidl, R., Collalti, A., Dantas de Paula, M., and Fischer, R.: Tackling unresolved questions in forest ecology: The past and future role of simulation models, Ecol. Evol., 11, 3746–3770, 2021.

Markesteijn, L. and Poorter, L.: Seedling root morphology and biomass allocation of 62 tropical tree species in relation to drought-and shade-tolerance, J. Ecol., 97, 311–325, 2009.

Martinez-Vilalta, J., Anderegg, W. R., Sapes, G., and Sala, A.: Greater focus on water pools may improve our ability to understand and anticipate drought-induced mortality in plants, New Phytol., 223, 22–32, 2019.

McDowell, N., Pockman, W. T., Allen, C. D., Breshears, D. D., Cobb, N., Kolb, T., Plaut, J., Sperry, J., West, A., and Williams, D. G.: Mechanisms of plant survival and mortality during drought: why do some plants survive while others succumb to drought?, New Phytol., 178, 719–739, 2008.

McDowell, N., Allen, C. D., Anderson-Teixeira, K., Brando, P., Brienen, R., Chambers, J., Christoffersen, B., Davies, S., Doughty, C., and Duque, A.: Drivers and mechanisms of tree mortality in moist tropical forests, New Phytol., 219, 851–869, 2018.

McDowell, N. G., Beerling, D. J., Breshears, D. D., Fisher, R. A., Raffa, K. F., and Stitt, M.: The interdependence of mechanisms underlying climate-driven vegetation mortality, Trends Ecol. Evol., 26, 523–532, 2011.

Meinzer, F. C., Campanello, P. I., Domec, J.-C., Gatti, M. G., Goldstein, G., Villalobos-Vega, R., and Woodruff, D. R.: Constraints on physiological function associated with branch architecture and wood density in tropical forest trees, Tree Physiol., 28, 1609–1617, 2008.

Meir, P., Mencuccini, M., and Dewar, R. C.: Drought-related tree mortality: addressing the gaps in understanding and prediction, New Phytol., 207, 28–33, 2015.

Meir, P., Mencuccini, M., Binks, O., da Costa, A. L., Ferreira, L., and Rowland, L.: Short-term effects of drought on tropical forest do not fully predict impacts of repeated or long-term drought: gas exchange versus growth, Philos. T. R. Soc. B, 373, 20170311, https://doi.org/10.1098/rstb.2017.0311, 2018.

Mokany, K., Raison, R. J., and Prokushkin, A. S.: Critical analysis of root: shoot ratios in terrestrial biomes, Glob. Change Biol., 12, 84–96, 2006.

Naudts, K., Ryder, J., McGrath, M. J., Otto, J., Chen, Y., Valade, A., Bellasen, V., Berhongaray, G., Bönisch, G., Campioli, M., Ghattas, J., De Groote, T., Haverd, V., Kattge, J., MacBean, N., Maignan, F., Merilä, P., Penuelas, J., Peylin, P., Pinty, B., Pretzsch, H., Schulze, E. D., Solyga, D., Vuichard, N., Yan, Y., and Luyssaert, S.: A vertically discretised canopy description for ORCHIDEE (SVN r2290) and the modifications to the energy, water and carbon fluxes, Geosci. Model Dev., 8, 2035–2065, https://doi.org/10.5194/gmd-8-2035-2015, 2015.

Nepstad, D. C., Tohver, I. M., Ray, D., Moutinho, P., and Cardinot, G.: Mortality of large trees and lianas following experimental drought in an Amazon forest, Ecology, 88, 2259–2269, 2007.

Nobre, C. A. and Borma, L. D. S.: 'Tipping points' for the Amazon forest, Curr. Opin. Env. Sust., 1, 28–36, 2009.

Nychka D, F. R., Paige J, Sain S, Gerber F., and Iverson M.: Fields: Tools for Spatial Data, University Corporation for Atmospheric Research, Boulder, CO, USA, https://doi.org/10.5065/D6W957CT, R package version 10.3, 2020.

Pammenter, N. W. and Van der Willigen, C.: A mathematical and statistical analysis of the curves illustrating vulnerability of xylem to cavitation, Tree Physiol., 18, 589–593, 1998.

Papastefanou, P., Zang, C. S., Pugh, T. A., Liu, D., Grams, T. E., Hickler, T., and Rammig, A.: A dynamic model for strategies and dynamics of plant water-potential regulation under drought conditions, Front. Plant Sci., 11, 373, https://doi.org/10.3389/fpls.2020.00373, 2020.

Phillips, O. L., Aragão, L. E., Lewis, S. L., Fisher, J. B., Lloyd, J., López-González, G., Malhi, Y., Monteagudo, A., Peacock, J., and Quesada, C. A.: Drought sensitivity of the Amazon rainforest, Science, 323, 1344–1347, 2009.

Pierce, D.: Interface to Unidata netCDF (Version 4 or Earlier) Format Data, https://cran.r-project.org/web/packages/ncdf4/ (last access: 1 February 2019), 2019.

Powell, T. L., Galbraith, D. R., Christoffersen, B. O., Harper, A., Imbuzeiro, H. M., Rowland, L., Almeida, S., Brando, P. M., da Costa, A. C. L., and Costa, M. H.: Confronting model predictions of carbon fluxes with measurements of Amazon forests subjected to experimental drought, New Phytol., 200, 350–365, 2013.

Powell, T. L., Koven, C. D., Johnson, D. J., Faybishenko, B., Fisher, R. A., Knox, R. G., McDowell, N. G., Condit, R., Hubbell, S. P., and Wright, S. J.: Variation in hydroclimate sustains tropical forest biomass and promotes functional diversity, New Phytol., 219, 932–946, 2018.

R Development Core Team: R: A language and environment for statistical computing, R Foundation for Statistical Computing, Vienna, Austria, http://www.R-project.org/ (last access: 1 February 2019), 2019.

Rao, K., Anderegg, W. R., Sala, A., Martínez-Vilalta, J., and Konings, A. G.: Satellite-based vegetation optical depth as an indicator of drought-driven tree mortality, Remote Sens. Environ., 227, 125–136, 2019.

Rowland, L., da Costa, A. C. L., Galbraith, D. R., Oliveira, R., Binks, O. J., Oliveira, A., Pullen, A., Doughty, C., Metcalfe, D., and Vasconcelos, S.: Death from drought in tropical forests is triggered by hydraulics not carbon starvation, Nature, 528, 119–122, 2015.

Rozendaal, D. M., Phillips, O. L., Lewis, S. L., Affum-Baffoe, K., Alvarez-Davila, E., Andrade, A., Aragão, L. E., Araujo-Murakami, A., Baker, T. R., and Bánki, O.: Competition influences tree growth, but not mortality, across environmental gradients in Amazonia and tropical Africa, Ecology, 101, e03052, https://doi.org/10.1002/ecy.3052, 2020.

Sabot, M. E., De Kauwe, M. G., Pitman, A. J., Medlyn, B. E., Verhoef, A., Ukkola, A. M., and Abramowitz, G.: Plant profit maximization improves predictions of European forest responses to drought, New Phytol., 226, 1638–1655, 2020.

Sack, L. and Holbrook, N. M.: Leaf hydraulics, Annu. Rev. Plant Biol., 57, 361–381, 2006.

Sapes, G., Roskilly, B., Dobrowski, S., Maneta, M., Anderegg, W. R., Martinez-Vilalta, J., and Sala, A.: Plant water content integrates hydraulics and carbon depletion to predict drought-induced seedling mortality, Tree Physiol., 39, 1300–1312, 2019.

Schuldt, B., Leuschner, C., Brock, N., and Horna, V.: Changes in wood density, wood anatomy and hydraulic properties of the xylem along the root-to-shoot flow path in tropical rainforest trees, Tree Physiol., 33, 161–174, 2013.

Signori-Müller, C., Oliveira, R. S., de Vasconcellos Barros, F., Tavares, J. V., Gilpin, M., Diniz, F. C., Zevallos, M. J. M., Yupayccana, C. A. S., Acosta, M., and Bacca, J.: Non-structural carbohydrates mediate seasonal water stress across Amazon forests, Nat. Commun., 12, 1–9, 2021.

Sperry, J. S., Wang, Y., Wolfe, B. T., Mackay, D. S., Anderegg, W. R., McDowell, N. G., and Pockman, W. T.: Pragmatic hydraulic theory predicts stomatal responses to climatic water deficits, New Phytol., 212, 577–589, 2016.

Sperry, J. S., Venturas, M. D., Anderegg, W. R., Mencuccini, M., Mackay, D. S., Wang, Y., and Love, D. M.: Predicting stomatal responses to the environment from the optimization of photosynthetic gain and hydraulic cost, Plant Cell Environ., 40, 816–830, 2017.

Stovall, A. E., Shugart, H., and Yang, X.: Tree height explains mortality risk during an intense drought, Nat. Commun., 10, 1–6, 2019.

Suzuki, E.: Diversity in specific gravity and water content of wood among Bornean tropical rainforest trees, Ecol. Res., 14, 211–224, 1999.

Trugman, A. T., Anderegg, L. D., Anderegg, W. R., Das, A. J., and Stephenson, N. L.: Why is tree drought mortality so hard to predict?, Trends Ecol. Evol., 36, 520–532, https://doi.org/10.1016/j.tree.2021.02.001, 2021.

Urli, M., Porté, A. J., Cochard, H., Guengant, Y., Burlett, R., and Delzon, S.: Xylem embolism threshold for catastrophic hydraulic failure in angiosperm trees, Tree Physiol., 33, 672–683, 2013.

Van Genuchten, M. T.: A closed-form equation for predicting the hydraulic conductivity of unsaturated soils, Soil Sci. Soc. Am. J., 44, 892–898, 1980.

Wang, W., Peng, C., Kneeshaw, D. D., Larocque, G. R., and Luo, Z.: Drought-induced tree mortality: ecological consequences, causes, and modeling, Environ. Rev., 20, 109–121, 2012.

Wang, Y., Köhler, P., He, L., Doughty, R., Braghiere, R. K., Wood, J. D., and Frankenberg, C.: Testing stomatal models at the stand level in deciduous angiosperm and evergreen gymnosperm forests using CliMA Land (v0.1), Geosci. Model Dev., 14, 6741–6763, https://doi.org/10.5194/gmd-14-6741-2021, 2021.

Xu, X., Medvigy, D., Powers, J. S., Becknell, J. M., and Guan, K.: Diversity in plant hydraulic traits explains seasonal and inter-annual variations of vegetation dynamics in seasonally dry tropical forests, New Phytol., 212, 80–95, 2016.

Yang, Y., Saatchi, S. S., Xu, L., Yu, Y., Choi, S., Phillips, N., Kennedy, R., Keller, M., Knyazikhin, Y., and Myneni, R. B.: Post-drought decline of the Amazon carbon sink, Nat. Commun., 9, 1–9, 2018.

Yao, Y.: ORCHIDEE-CAN-NHA model (r7236), IPSL Data Catalog [code], https://doi.org/10.14768/8C2D06FB-0020-4BC5-A831-C876F5FBBFE9, 2021a.

Yao, Y.: yitongyao56/ORCHIDEE-CAN-NHA: Data analysis code, Zenodo [code], https://doi.org/10.5281/zenodo.5721245, 2021b.

Yoshimura, K., Saiki, S.-T., Yazaki, K., Ogasa, M. Y., Shirai, M., Nakano, T., Yoshimura, J., and Ishida, A.: The dynamics of carbon stored in xylem sapwood to drought-induced hydraulic stress in mature trees, Sci. Rep.-UK, 6, 24513, https://doi.org/10.1038/srep24513, 2016.

Young, D. J., Stevens, J. T., Earles, J. M., Moore, J., Ellis, A., Jirka, A. L., and Latimer, A. M.: Long-term climate and competition explain forest mortality patterns under extreme drought, Ecol. Lett., 20, 78–86, 2017.

Zhu, D., Peng, S. S., Ciais, P., Viovy, N., Druel, A., Kageyama, M., Krinner, G., Peylin, P., Ottlé, C., Piao, S. L., Poulter, B., Schepaschenko, D., and Shvidenko, A.: Improving the dynamics of Northern Hemisphere high-latitude vegetation in the ORCHIDEE ecosystem model, Geosci. Model Dev., 8, 2263–2283, https://doi.org/10.5194/gmd-8-2263-2015, 2015.

Zhu, S.-D., Chen, Y.-J., Ye, Q., He, P.-C., Liu, H., Li, R.-H., Fu, P.-L., Jiang, G.-F., and Cao, K.-F.: Leaf turgor loss point is cor-

related with drought tolerance and leaf carbon economics traits, Tree Physiol., 38, 658–663, 2018.

YAO YITONG (Orcid ID: 0000-0002-1713-6719)
Chave Jerome (Orcid ID: 0000-0002-7766-1347)

How drought events during the last Century have impacted biomass carbon in Amazonian rainforests

Running title : drought impacts in Amazon rainforest

Yitong Yao[1], Philippe Ciais[1], Nicolas Viovy[1], Emilie Joetzjer[2], Jerome Chave[3]

[1] Laboratoire des Sciences du Climat et de l'Environnement, LSCE/IPSL, CEA-CNRS-UVSQ, Université Paris-Saclay, Gif-sur-Yvette, 91191, France

[2] INRAE, Universite de Lorraine, AgroParisTech, UMR Silva, Nancy, 54280, France

[3] Laboratoire Evolution et Diversité Biologique UMR 5174 CNRS, IRD, Université Paul Sabatier, Toulouse, 31062, France

Corresponding author: Yitong Yao

Email: yitong.yao@lsce.ipsl.fr

ORCID list:

Yitong Yao https://orcid.org/0000-0002-1713-6719

Philippe Ciais https://orcid.org/0000-0001-8560-4943

Nicolas Viovy https://orcid.org/0000-0002-9197-6417

Emilie Joetzjer https://orcid.org/0000-0001-6781-1535

Jerome Chave https://orcid.org/0000-0002-7766-1347

This article has been accepted for publication and undergone full peer review but has not been through the copyediting, typesetting, pagination and proofreading process which may lead to differences between this version and the Version of Record. Please cite this article as doi: 10.1111/gcb.16504

Abstract

During the last two decades, inventory data show that droughts have reduced biomass carbon sink of the Amazon forest by causing mortality to exceed growth. However, process-based models have struggled to include drought-induced responses of growth and mortality, and have not been evaluated against plot data. A process-based model, ORCHIDEE-CAN-NHA, including forest demography with tree cohorts, plant hydraulic architecture and drought-induced tree mortality, was applied over Amazonia rainforests forced by gridded climate fields and rising CO_2 from 1901 to 2019. The model reproduced the decelerating signal of net carbon sink and drought sensitivity of aboveground biomass (AGB) growth and mortality observed at forest plots across selected Amazon intact forests for 2005 and 2010. We predicted a larger mortality rate and a more negative sensitivity of the net carbon sink during the 2015/16 El Niño compared to the former droughts. 2015/16 was indeed the most severe drought since 1901 regarding both AGB loss and area experiencing a severe carbon loss. We found that even if climate change did increase mortality, elevated CO_2 contributed to balance the biomass mortality, since CO_2-induced stomatal closure reduces transpiration thus offsets increased transpiration from CO_2-induced higher foliage area.

Keywords:

Amazon rainforest; drought sensitivity; process-based model; tree mortality; net forest carbon sink

1 Introduction

The Amazonian rainforest accounts for 40% of the tropical forest biome area and contains half of its carbon. Changes in the Amazon forest dynamics impact the global water and carbon cycles, and

exert key feedbacks on climate change (Jimenez & Takahashi, 2019), leaving open the possibility of crossing 'tipping points' in the form of a regional forest dieback (Ritchie *et al.*, 2021). Both short-term variability and long-term trends in the carbon fluxes and stocks of the forest are regulated by climate variability. In particular, repeated extreme drought events have the potential to undermine the stability of large parts of the Amazon forest (Zemp *et al.*, 2017). Over the last century, major drought events occurred in Amazonia, generally associated with positive sea surface temperature anomalies in the tropical Atlantic (1916, 1963, 2005, 2010) and with strong El Niño events (1926, 1982/83, 1997/98, 2015/16). El Niño events tend to bring drought in the wet season, whereas Atlantic anomalies exacerbate drought in the dry season (Jimenez *et al.*, 2018).

While the long-term view is crucial to understand the current dynamics of Amazonia, much of our knowledge about the response of Amazonian forests to drought is based on limited field data from the last decades: a slow-down of forest carbon gains from growth and a coincident increase of losses from tree mortality have been observed from successive forest plot inventories, leading to a gradual decline in the strength of the biomass carbon sink (Brienen *et al.*, 2015).

Research focusing on past drought events used different methods, including ground-based observations of carbon fluxes at few sites (Doughty *et al.*, 2015), biomass inventories (Phillips *et al.*, 2009; Feldpausch *et al.*, 2016), drought experiments (Fisher *et al.*, 2007), remote-sensing (Yang *et al.*, 2018), and process-based models (Papastefanou *et al.*, 2021). Analyses from the RAINFOR network of forest plots provided net biomass change at selected locations during the 2005 and 2010 droughts (Feldpausch *et al.*, 2016; Hubau *et al.*, 2020), and spatial patterns in variation of mortality rates (Esquivel-Muelbert *et al.*, 2020) and biomass loss (Papastefanou *et al.*, 2022).

Ground-based observations and satellite products only cover climatic anomalies for two decades,

a short timescale compared with the natural dynamics of forests. A centennial perspective is needed, as repeated droughts affect decadal-scale carbon processes through legacy effects and slow recovery of forests after disturbances (Lewis *et al.*, 2011). Given the lack of observations, process-based models are useful to explore the effects of drought on the Amazon carbon balance.

Although predicting the risk of mortality from hydraulic failure is challenging given species-specific responses (Rowland *et al.*, 2021), several process-based models have made progress in representing a mechanistic hydraulic architecture simulating the water transport through trees, from the soil to the atmosphere (Kennedy *et al.*, 2019; Li *et al.*, 2021). Leaf-level carbon-water trade-offs, reflecting plant stomatal strategies, are at the foundation of most hydraulic modules, and they are used in models as a target to be optimized, e.g., the product of productivity and water cost (Eller *et al.*, 2020), or the direct and opportunity carbon cost of xylem damage (Lu *et al.*, 2020). Although these studies partly captured changes of plant hydrodynamics, they did not consider the water capacitance of trees (Kennedy *et al.*, 2019), or did not model changes in the vertical profile of water potential from soil to leaves, rather focusing on stomatal behavior (Eller *et al.*, 2020). A hydraulic architecture model describing explicit water transport process is required to better mimic plant water dynamics in reality. Yao *et al.* (2022) simulated half-hourly water potentials at leaf, stem, root and soil levels by minimizing the difference between water demand and supply for each plant organ in the ORCHIDEE-CAN-NHA model, a branch of the ORCHIDEE land surface model (version r7236). In addition to representing changes in water flows and storage on a 30 min time-step in soils and plants, this model includes an empirical parameterization of mortality from hydraulic failure. Namely, when stem water conductance drops below a critical threshold during a certain number of days, a mortality risk function is calculated and trees of each cohort die if this function exceeds a threshold. The advantage of ORCHIDEE-CAN

lies in its explicit representation of different tree-size cohorts, which allows us to link realization of simulation of hydrodynamics to forest demography. The model was calibrated against field observations from the Caxiuanã throughfall exclusion (TFE) experiment (Fisher *et al.*, 2007) and tested on another TFE experiment site at Tapajos. Yet, it has not been used to assess the carbon impacts of regional drought. Here, we address this challenge by applying this model over rainforest in Amazon basin during the last century.

Besides climate change, an important consideration for modelling the carbon balance of the Amazon over a century is that CO_2 concentration has increased by more than 120 ppm during this period. There is consensus on the stimulation effects on growth under elevated CO_2, although no field CO_2 enrichment experiment (FACE) is available for Amazonia. A simulated elevated CO_2 forcing predicted an increase in aboveground biomass for an ensemble of models, but limited by phosphorus availability (Fleischer *et al.*, 2019). Increased CO_2 concentration also affects carbon allocation, and self-thinning (Holm *et al.*, 2020), and reduces stomatal conductance, resulting in less transpiration per unit of leaf area, although increased leaf area may act to counteract this effect (Cox *et al.*, 2004; Piao *et al.*, 2007). Yet, the effect of elevated CO_2 on stand competition and biomass loss processes is uncertain, especially with a higher drought frequency. Site-level spatial statistical analysis with CO_2 concentration and climatic factors by Hubau *et al.* (2020) suggested significant positive relationships of carbon gains with CO_2 concentration, but not of carbon loss. Process-based models can thus be used to tests to separate the effects of climate change and CO_2, and their interactions. de Almeida Castanho *et al.* (2016) conducted simulations to reproduce the individual and combined effects of climate change and elevated CO_2 but their model included a simple mortality module and was unable to capture the biomass loss from climate extremes.

In this study, we use a new process-based model with a detailed mechanistic hydraulic architecture and mortality arising from hydraulic failure, ORCHIDEE-CAN-NHA (r7236), to understand the sensitivity of biomass growth and mortality to drought events of the last century in the Amazon, and *to elucidate* the contribution of climate change and elevated CO_2. Our objectives are: (1) to test the performance of the model for simulating the long-term trend of net carbon sink and its component gains and losses, (2) to compare simulated patterns of drought-induced changes of growth and mortality against forest plots observations, (3) to compare aboveground biomass (AGB) losses between different drought events, (4) to assess if the recent extreme drought events of the last 20 years had higher impacts on AGB than during previous droughts of the early part of the century; (5) to understand the interactions between rising CO_2 and droughts on AGB dynamics.

2 Materials and Methods

2.1 The land surface model ORCHIDEE-CAN-NHA

In this study, we use the ORCHIDEE-CAN-NHA (r7236) land surface model, incorporating allometric-based carbon allocation, trees cohorts making the canopy structure with different growth of an average tree in each cohort and background mortality induced by self-thinning processes (Naudts *et al.*, 2015) as well as a new mechanistic hydraulic architecture (Yao *et al.*, 2022). The hydraulic module includes the dynamic root water uptake scheme proposed by Joetzjer *et al.* (2022) and a plant hydraulic model simulating water transport from water potentials gradient between soils and atmosphere, and water capacitance in roots, stems and leaves. Besides this hydraulic architecture, a cavitation-induced mortality model was added. Two parameters are used to translate the percentage loss of stem conductance (PLC) simulated by the hydraulic module to mortality. A cumulated drought exposure index when PLC stays above a critical threshold defines a mortality risk. Under this risk, a fraction of trees is killed each day in the different cohorts of tree size. The new hydraulic architecture and mortality schemes were calibrated against the world's longest running drought experiments at Caxiuanã (Rowland *et al.*, 2015), with overall good performances.

2.2 Simulation framework

2.2.1 Climate forcing

The gridded climate forcing used as input to ORCHIDEE-CAN-NHA is the CRUJRA v2.1 dataset (Harris *et al.*, 2014; Kobayashi *et al.*, 2015; Harris, 2020; Harris *et al.*, 2020). CRUJRA v2.1 was constructed by re-gridding data from the Japanese Reanalysis Data (JRA) produced by the Japanese Meteorological Agency (JMA) adjusted to match the monthly observation-based Climatic Research

Unit (CRU) TS 4.04 data (Harris *et al.*, 2020). It provides 6-hourly meteorological variables from January 1901 to December 2019 at 0.5×0.5° spatial resolution.

2.2.2 Simulation protocol

To balance the spatial resolution of our regional simulations with computing resources, the simulations were carried out at 1×1° horizontal spatial resolution over 1901-2019 (study region see Fig. 1). We used a two-step spin-up to bring carbon and water pools in steady-state equilibrium. In the first step, the model is forced by recycling the climate forcing during 1901-1920 with a constant CO_2 concentration of 296 ppm and no climate-induced mortality activated. Then after the end of the first spin-up, we re-ran the model still recycling the climate forcing of 1901-1920 but activating the mortality scheme. At the end of the second stage of spin-up, the model reaches a new equilibrium state, with a lower biomass due to droughts that occur periodically during 1901-1920, with less than 1% variation by the end of second spin-up. This equilibrium state serves as the starting point for three transient simulations during the historical period. To test the impact of the different drivers of CO_2 and climate we designed a series of factorial experiment S1, S2, S3, as described in Table 1.

2.3 Drought characteristics

The maximum climatological water deficit (MCWD) is the most negative value of the difference between monthly precipitation and a fixed value for evapotranspiration of ~100mm among all the months (Eq.1 and 2). MCWD anomaly is derived after subtracting the mean MCWD over a baseline period. By locating the month with the most negative precipitation anomaly and its corresponding rainfall climatology interval, we distinguish between wet-season and dry-season drought by using a new drought timing index (DTI). A second index for the rain seasonality is defined as the deviation of

monthly rainfall distribution from a uniform monthly distribution (Feng *et al.*, 2013). Detailed description of these indices can be found in SI Notes S1.

$CWD_m = CWD_{m-1} + P_m - 100$ if $P_m < 100$, else $CWD_m = 0$

with m being the month 1, …12 (1 = October) (1)

$MCWD = \min(CWD_m)$, m=1, …, 12 (2)

2.4 How aboveground biomass dynamics was analyzed

From model outputs, net AGB change (△AGB), AGB gain and loss are calculated over the hydrological year from October in previous year to September in the next year. AGB gain is the carbon allocated to growth in aboveground sapwood in cohorts with DBH higher than 10 cm, each year. AGB loss is the biomass mortality of aboveground sapwood and heartwood in cohorts with DBH higher than 10 cm, each year. △AGB is the difference between AGB gain and AGB loss. The anomaly during a drought year k is derived by subtracting the average value (μ) over a multi-year baseline period by Equations 3 to 5.

$$\Delta AGB_{anomaly} = \Delta AGB_k - \mu_{\Delta AGB} \quad (3)$$

$$AGBgain_{anomaly} = AGBgain_k - \mu_{AGBgain} \quad (4)$$

$$AGBloss_{anomaly} = AGBloss_k - \mu_{AGBloss} \quad (5)$$

Biomass mortality from self-thinning and droughts are included. In our study, the mortality rate equals the number of dead trees per year divided by the number of trees alive in the beginning of one year.

3 Results

3.1 Long-term trend of the biomass carbon sink, model vs. inventories

In our simulation S2 with variable CO_2 and climate, we found a mean positive value of ΔAGB equal to 0.22 MgC ha^{-1} yr^{-1} over 1980 - 2019, indicating that the Amazon intact forests accumulate carbon over time. Nevertheless, this increase of ΔAGB has a negative trend of 0.006 MgC ha^{-1} yr^{-2} (Fig. 2). This slowing down of the biomass carbon sink occurs because carbon losses from mortality increase faster than gains from growth and recruitment. Our finding of a decreasing biomass sink is consistent with inventory data analyzed by Hubau *et al.* (2020) and Brienen *et al.* (2015). Yet the magnitudes of the simulated growth trend and loss trend are both smaller than in the observations. We simulated an increasing trend of carbon gains of 0.008 MgC ha^{-1} yr^{-2} against 0.014 MgC ha^{-1} yr^{-2} for carbon losses across the entire basin. In comparison, Hubau *et al* (2020) from 321 plots found an increasing trend of gain of 0.014 MgC ha^{-1} yr^{-2} and a trend of loss of 0.023 MgC ha^{-1} yr^{-2}. This difference can be attributed to limited coverage of inventory sample plots and model limitations, such as non-modeled biotic disturbances. Yet, it is encouraging to see that the essential signal of a decelerating biomass sink from increased mortality is captured by our simulations.

3.2 Biomass growth and mortality for the recent droughts, and sensitivities to water deficits

Mean biomass gains and losses during normal years. During the 2000s, excluding the 2005 and 2010 droughts to focus on non-drought periods, forests gained AGB, at a rate of +0.44 MgC ha^{-1} yr^{-1} (95% confidence interval 0.39-0.50 MgC ha^{-1} yr^{-1}), i.e., they acted as a carbon sink in biomass. The total carbon sink was 0.22 PgC yr^{-1} over our intact forest area of 500 Mha. There were significant differences among the four regions (tested from the Tukey HSD post-hoc test; Fig. S1). We found a higher net AGB sink density in the Western Amazon (+0.69 MgC ha^{-1} yr^{-1}), followed by the Guiana

Shield (+0.41 MgC ha^{-1} yr^{-1}). The gross gain in AGB, due to growth alone, was 3.6 MgC ha^{-1} yr^{-1}, with the highest gross gain in the Guiana Shield (+4.2 MgC ha^{-1} yr^{-1}). The gross loss in AGB was also highest in the Guiana Shield, and lowest in the Western Amazon. A 'high-gain, high-loss' pattern, thus a larger turnover, was modelled in the Guiana Shield region.

The 2005 drought. This event has its severity epicenter located in the Western Amazon, as seen from Z-transformed MCWD (Fig. 3). In this epicenter, we simulated a larger net AGB loss (-0.6 MgC ha^{-1} yr^{-1}) than for the rest of the Amazon. The net annual loss from October 2004 to September 2005 was driven by a decline in growth and an increase in mortality (Fig. 3), consistent with forest plots evidence shown by Phillips *et al* (2009). The most severe water deficit matched the largest loss of AGB in our simulations. In the Western Amazon we found a 2.0 MgC ha^{-1} (95% CI: 1.5-2.5) net loss of AGB relative to non-drought condition (Table S1). This net loss is composed by a modest decrease of growth gain of 0.2 MgC ha^{-1} (95% CI: 0.1-0.3) and a large increase of mortality loss of 1.8 MgC ha^{-1} (95% CI: 1.2-2.3). These figures are comparable with plot data analysis by Phillips *et al*. (their Fig. 2).

The 2010 drought. This event was most severe in the north of the Brazilian Shield. According to our climate forcing data (CRUJRA). The drought severity, however, was lower and the affected area was smaller than for the 2005 drought, as shown by the magnitude of MCWD anomaly, which spans over -100 to 150 mm (Fig. 3). The drought severity and impacted area in 2010 are a bit different than in Lewis *et al* (2011), due to different rainfall forcing data (TRMM satellite rainfall data in Lewis *et al*., 2011 vs. CRUJRA in our study). The drought sensitivity of the AGB net change to MCWD was lower in 2010 than in 2005 (0.83 vs 1.64 MgC ha^{-1} per 100 mm MCWD) over whole basin but

comparable in their epicenters (Table S1). Yet, like for the 2005 event, the effect of the drought on net AGB change was dominated by higher AGB loss and a relatively modest reduction of AGB gain.

The 2015/16 El Niño drought. This event is mainly centered in northeastern Amazonia (Guiana Shield). The simulated response of AGB is shown in Fig. 3g-3i. The magnitude of the MCWD anomaly shows that this drought was more severe than the two previous events. Therefore, we found a higher △AGB sensitivity (Fig. 3g-3i, S2) of -2.63 MgC ha^{-1} per 100 mm MCWD than in the former two droughts. Further, the AGB gain sensitivity was of -0.57 MgC ha^{-1} per 100 mm MCWD, in smaller magnitude than the sensitivity of AGB loss of 2.06 MgC ha^{-1} per 100 mm MCWD. In addition, for a 100 mm increase in MCWD, we simulated in 2015/16 an increase of 12 days as 'mortality risk', and a 1.2% increase in the annual mortality rate compared to the baseline period (Fig. S3). In the northern Brazilian Shield epicenter, we simulated a greater AGB loss and a higher stem mortality rate even in pixels where MCWD anomaly remained below 100 mm. This response likely reflects other stress factors causing an increase of transpiration, followed by loss of conductance and mortality in our model, especially high temperature and elevated vapor pressure deficits (VPD).

3.3 Drought severity and biomass loss for the most severe drought events of the past century

After having shown that the simulated sensitivities of growth and mortality to MCWD compared well with forest plots data (at least for the 2005 event that was extensively measured across many plots), we now turn to the analysis of AGB deficits during the most severe droughts of the last century (1916, 1926, 1963, 1983, 1998, 2005, 2010, 2016). Fig. 4 shows the spatial distribution of the drought intensity, i.e. the Z-score of MCWD anomalies (Section 2.3). The epicenter of different droughts varied

across events. The northwest Amazon 'ever-wet' region was rarely affected. The northern Brazilian Shield, also an 'ever-wet' region where the dry season even sees a periodical increase of GPP (Green *et al.,* 2020), was particularly affected by the 2015/16 El Niño drought. The southwest regions were hit by the 1983 and 2005 droughts. The East and northeast regions were affected by the 1916, 1983 and 2015/16 droughts. The Southern Amazon was affected by the 1963 and 2010 droughts.

The largest droughts of the Century compared for their area exposed to different drought intensities and area of AGB loss. Fig. 5 shows the number of 1° pixels for different severity classes (Z-scored CWD). The 2015/16 drought is clearly ranked as the most severe event on record, followed by 1983 and 2005. Both the area under drought (negative Z score), representing 63% of the evergreen forest area, and the area under *extreme* drought, show the largest values during the 2015/16 event. Mirroring mainly the spatial patterns of water deficit, the net AGB dynamics from our simulation is shown in Fig. 6. Outside the epicenter of each drought, △AGB was small and positive (Fig. 6) indicating a continuous long-term carbon sink (Fig. 2). In the drought affected pixels, we found that the AGB net losses always ranked with the severity of drought. For instance, △AGB in 2010 was less negative than that during the more extreme droughts of 2005 and 2016 (Fig. 6). Among the top 8 drought events of the last century, we found differences in the fraction of area with negative △AGB at a given level (Fig. 7, S4). The area showing negative △AGB values was the largest in the 2015/16 El Niño, followed by the 1983 one. The area with the most negative △AGB per unit area (e.g. a loss more than 6 MgC ha^{-1} yr^{-1}) was the most extensive in 2016, followed by 1983 (Fig. 6).

Wet season droughts caused larger AGB loss than dry season ones. We investigated the differences in AGB responses between wet-season and dry-season droughts, distinguished by their DTI index (see Section 2.3 and SI Notes S1). It should be noted that the 'wet season' drought actually happened during the period that was normally the wet season but encountered a severe water deficit, which can be regarded as the extension of dry season length or severity. From Fig. 8 we can see that the east-central Amazon region which has a low rainfall seasonality, shows DTI > -0.2 in 1983 and 2016. In other words, these two drought events appeared in the wetter quarter of the year, and can be deemed as wet-season droughts. DTI values close to -1 in the southwest Amazon in 2005, implies this event was a clear dry-season drought. The epicenters of the 2010 drought are more diffuse and show DTI values between -0.2 and 0.2, which makes this event a composite of dry and wet season drought. As the intensity of wet-season and dry-season droughts differs, so does the corresponding AGB dynamics. Fig. 5 shows that the drought severity was higher in the wet-season droughts of 2016 and 1983, and that the drought exposed area was also higher during these two events. Fig. 7 shows that the AGB loss differs between wet and dry season droughts. Namely, the area undergoing large AGB loss is larger for wet-season droughts like 2016 than for dry-season droughts like 2005 (Fig. 7). Moreover, if we compute the mean △AGB corresponding to different Z score levels, we found that the mean △AGB is always the most negative during (El Niño) wet-season droughts, no matter which Z score level is considered (Table S2).

The last twenty years show the largest AGB loss caused by droughts. We then compared

drought effects on AGB on decadal-scale. To do so, we calculated the cumulative AGB loss in successive 20-year intervals since 1901 (Fig. 9). Looking at the three extreme drought events in the last 20-year, it is clear from our simulations results that the cumulative AGB loss over this period was higher than during any other previous 20-year interval since 1901 (Fig. S5). The region which had the higher level of AGB loss (>4 Mg C ha^{-1} yr^{-1}) during the last 20 years is the East-central Amazon, even though this region was rarely affected by previous droughts.

3.4 Interactions between drought and elevated CO_2

We make the reasonable hypothesis that (in the model) elevated CO_2 induces stomatal closure and should thus partly alleviate the negative effect of drought on AGB. To assess the extent to which the drought effects can be alleviated, we separated the effects of climate change alone vs. increased CO_2 concentration during the major droughts of the last Century through factorial simulations (S1, S2 and S3 see Section 2.2). The results are shown in Fig. 10. The simulation S2 driven by observed historical climate (including the 8 drought events studied above) and atmospheric CO_2 increase, while S1 was driven by recycled 1901-1920 climate (no climate change), and S3 used historical climate but maintained the CO_2 concentration constant at 296 ppm (no CO_2 increase). The comparison between S1 and S2 shows that historical climate change since 1901, i.e., mainly droughts, has suppressed plant growth and increased mortality losses. The net biomass carbon gains during each drought year are thus lower in S2 than in S1.

The comparison between S2 and S3 allows us to isolate the effect of rising CO_2 concentration. The AGB gain was significantly higher under S2 than S3 ($P<0.05$), because of the increase of NPP from elevated atmospheric CO_2. The AGB density was higher in S2 than in S3, reflecting a higher

carbon accumulation due to the historical increase of CO_2 (Fig. S6). Yet, there was also significant difference of AGB loss between S2 and S3 ($P<0.05$). When we look at the mortality risk with and without rising CO_2, in the epicenter of the eight drought events (Z score of MCWD below -1.645), the number of days with mortality risk was significantly higher in S3 than that in S2, with a difference that can reach up to 10 days (Fig. S7). This result implies that, in our model, elevated CO_2 induced a partial alleviation of moisture stress from stomatal closure and reduced transpiration, offsetting a possible increase of transpiration due to higher foliage area. During droughts, the modeled evapotranspiration rate confirms a smaller soil moisture stress in S2 (Fig. S8) compared to S3 where CO_2 is fixed. Since the model here did not include the downregulation of nutrient limitation, the CO_2 fertilization effects could be overestimated.

4 Discussion

4.1 Mortality in the model and its sensitivity to water deficits

Mean patterns of mortality and turnover. A clearer understanding on the response of the Amazon rainforest to drought is indispensable for future predictions. We found that our model, despite having its parameters calibrated only for the Caxiuanã throughfall experiment, and lacking a description of the diversity of plant traits, is capable to produce realistic average cross-basin mortality rates, and higher mortality rates and biomass losses in the epicenter of each drought. With our hydraulic failure – mortality module adding up to background tree mortality (from self-thinning), our simulations (Fig. S9) of the mean spatial pattern of mortality are comparable to mortality rates from inventory data shown by Esquivel-Muelbert *et al.* (2020). Namely, there is a prevalence of higher average mortality in the Brazilian Shield. Nevertheless, the average pattern of 'high-gain, high-loss' observed in the Amazon e.g. by (Hubau *et al.*, 2020) is not captured by our model. Plot observations suggest a larger turnover (larger gain and loss fluxes) in the Western Amazon, possibly due to different species composition reflecting adaptation to more fertile soils near the Andes (Yang *et al.*, 2014). Our model simulates in contrast a pattern of 'high-gain, high-loss' in the Guiana Shield region. This can be related to the fact that our model lacks representations of nutrient dynamics (higher phosphorus content of soils promoting growth in the Western forests) and species traits regional differences, and that it includes only drought mortality and not the other disturbances modulating forest turnover, like windthrown in the Western Amazon (Negrón-Juárez *et al.*, 2018).

Drought impacts on demography. The hydraulic architecture and drought induced mortality scheme on top of the demography structure permit us to analyze the tree mortality rate per tree size.

Besides the smallest tree size cohort, the annual mortality rate increases with tree size in our simulations, especially in area with a moderate drought risk (Z-score MCWD < -1.645) as shown in Fig. S10. A larger mortality of taller trees is independent of the region considered, since greater gravitational energy is required to pull water upward along longer transport pathways in bigger trees in the model. Monitoring of forest plots showed that older or larger trees were disproportionally threatened by El Niño drought (Meakem *et al.*, 2018). However, field measurement evidences have not reached consensus as they showed vulnerability of bigger trees (Bennett *et al.*, 2015) or no mortality-size relationship (Powers *et al.*, 2020), where the size dependence could be superseded by hydraulic safety traits that can be more prevalent at coarser scales, as well as the agreement regarding whether within-species covariation between tree size and water availability holds at species or landscape level has not been obtained (Trugman *et al.*, 2021). To compare model results with inventories that only sample trees larger than 10 cm, we only looked in the model at growth in corresponding cohorts. With regard to the recruitment, we simulated more new individuals recruited during drought than non-drought period (Fig. S11), since the recruitment rate is parameterized in relation to LAI (Joetzjer *et al.*, 2022). In other words, a decrease of LAI promoted recruitment during drought in our simulations.

Sensitivity of biomass to droughts compared to observations. The drought sensitivity simulated by our model shows an emerging positive relationship between mortality and water deficit. This result is consistent with forest plot observations. The simulated drought sensitivity is comparable with the one observed in inventory data for the 2005 drought (Phillips *et al.*, 2009). Inventory measurements did not sample the epicenter of the 2010 drought. Unlike for the 2005 event, however, selected plots

were measured shortly after 2010, thus reducing possible confounding effects of post-drought climate conditions. These scarce data indicate that forest sites that were experiencing a severe drought gained less biomass in 2010 but showed no evidence for a significant mortality co-variation with drought severity (Feldpausch *et al.*, 2016). During the 2010 drought, data from other sites with regular measurements of ecosystem-level fluxes (Doughty *et al.*, 2015) showed that foliage and woody NPP remained unchanged at wet lowland sites, although autotrophic respiration (Ra) decreased. In the 1° grid cells containing the sites of Doughty *et al.*, we modeled a decreasing GPP, NPP and Ra with increasing MCWD (Fig. S12), which is inconsistent with Doughty *et al* (2015), excepted for Ra. Our model may over-estimate the negative response of GPP and NPP to drought at these sites, possibly because some of the sites include forests that had access to ground water, a process ignored in the model. It is also possible that soil properties in the 1° grid cells do not correspond to those observed at the sites. When we combined the three most recent drought events together and divided MCWD anomalies into distinct severity classes, we found that the negative response of AGB from mortality increases above a threshold of 50 mm MCWD anomaly (Fig. S13). Besides, several pixels with a positive MCWD anomaly show only a small $\triangle$AGB. For such 'insensitive pixels' both plant hydraulic architecture and soil hydraulic properties seemed to control plant water availability and biomass dynamics. We note here that our model was calibrated against the Caxiuanã experiment with a half-exclusion of rainfall alone and no coincident manipulation of temperature, and it could underestimate the sensitivity of AGB to compound events with low rain, high temperature and high VPD.

Importance of soil texture for modeling mortality during drought. In the model, a rainfall

deficit alone does not always bring severe water stress and mortality as shown in the previous paragraph. This model behavior is dependent on soil texture parameters. Soils with a higher clay content are closer to their wilting point when rainfall decreases, but have a greater soil water-holding capacity (difference between field capacity and wilting point) (McCulloh *et al.*, 2019). Levine *et al.* (2016) found that water stress in soils with higher clay content is likely to influence more negatively plant biomass dynamics. Our simulations used the HWSD soil texture map (Wieder *et al.*, 2014) which has loam distributed in the Western Amazon, and silt loam and sandy clay loam soils in the central Amazon. Although this soil texture map produces a reasonable mean mortality rate, there are 'insensitive' pixels where PLC remains below the threshold of 50% (inducing mortality) even under a severe water deficit (see Fig. S14). Using a more clay rich soil texture in the model could produce a more sensitive response of AGB to water availability, and give results more comparable with local inventory observation. As a test of this hypothesis, at one pixel in the East-Central Amazon, we prescribed a *sandy clay* texture instead of *loam*, and found that climate-induced mortality increased a lot in 2005, and AGB became more sensitive to MCWD with sandy clay. The spatial variability of soil properties is high, including at small scale (Marthews *et al.*, 2014). Therefore, the mismatch between site-specific soil texture and our 1° model pixels should be considered to understand the model-observation misfit.

Importance of threshold parameters that trigger mortality from hydraulic failure. With regard to the sensitivity of mortality to tree conductance loss (PLC) in each cohort, the drought exposure threshold and the mortality rate applied to kill trees exceeding the exposure as defined for simulating mortality by Yao *et al.* (2022) are coupled in our model. Adjusting the exposure threshold of PLC causing drought-induced 'cavitation' mortality in the model is difficult, since there is almost

no measurement for tropical trees that monitored impairment and mortality risk above a critical PLC threshold. Critical PLC thresholds strongly depend upon species, related to traits like height or wood density. For example, Brodribb *et al.* (2020) found that a vulnerable tall tree died in one week after reaching cavitation. We thus would need field-based measurement of hydraulic damage in the tropics to better constrain the drought exposure threshold parameterization of the model.

4.2 Perspective to reduce uncertainty of the biomass drought sensitivity

Variable hydraulic traits. The drought sensitivity of AGB in the real world relates to the diversity of hydraulic traits. Those traits confer regional variations in drought tolerance, and associate with habitat preferences (Kunert *et al.*, 2021), although some traits could be spatially coherent (Powell *et al.*, 2017). Our study used a set of hydraulic parameters for traits calibrated from the Caxiuanã drought experiment. In reality, there is a broader diversity reflecting plant water use strategies, even at small spatial scale. Highly variable water potentials at which 50% of conductivity is lost (Ψ_{50}) in stem xylem were observed by Oliveira *et al.* (2019). Species traits spatial differences in water deficit *affiliation*, that is how traits leading to hydraulic failure have adapted to local long-term frequency and severity of drought at a given place, also relate to mortality risk. But a high *affiliation* to drought does not warrant resistance to the more severe 'new types' of drought emerging in the recent years (Esquivel-Muelbert *et al.*, 2017). Apart from background climate affiliation, hydraulic traits also vary with tree size (Bittencourt *et al.*, 2020), soil fertility and topography (Oliveira *et al.*, 2019). Below, we discuss a few critical traits that could be given spatial variability in our model.

Tree water potentials safety margin. Hydraulic safety margins calculated as the difference between Ψ_{50} and the minimum water potential during a drought correlates with mortality risk among

species (Powers *et al.*, 2020). Larger hydraulic safety margins protect trees from hydraulic damage (Ziegler *et al.*, 2019). Interspecific heterogeneity in hydraulic performance for xylem safety and efficiency trade-off should give the possibility to see a possible dominance of drought-tolerant species in the case of more frequent and severe droughts (Zuleta *et al.*, 2017). To capture these effects in models, we see a critical need for incorporating functional diversity in the traits that determine vulnerability and water regulation strategies (Anderegg *et al.*, 2019). Liu *et al.* (2021) proposed to constrain indirectly the distribution of plant hydraulic traits with satellite observations of VOD, evapotranspiration and soil moisture. This approach could provide useful insights about hydraulic traits such as water potential safety margin and pre-dawn water potential by calibrating optimal parameters in the model to minimize the difference between satellite observations and simulations.

Wood density. Wood density is partly related to stem water potentials, life history and drought resistance (De Guzman *et al.*, 2021). Species with low wood density are expected to be more vulnerable to droughts. On the contrary, species with high wood density are considered to be more resistant to hydraulic failure, as evidenced by negative effect of wood density on mortality in response to the 2010 drought through generalized linear mixed model (Zuleta *et al.*, 2017). Besides wood density, trade-off in wood volume allocation also relates to xylem efficiency-safety trade-off (Janssen *et al.*, 2020). Site-level evidence showed that easily measured traits like wood density can help to understand drought responses (Santiago *et al.*, 2018). In other words, through the measurement of wood density, and its relationship with plant inherent hydraulic traits, e.g., the negative linear relationship between sapwood turgor loss point and wood density found by De Guzman *et al.* (2021), variability of hydraulic parameters could be incorporated into our model using new wood density maps (Mitchard *et al.*, 2014).

4.3 Reducing uncertainty on the effect of elevated CO_2 to alleviate trees' response to drought

For predicting biomass dynamics in Amazon rainforests, interactions between drought and elevated CO_2 are of key importance. Our model produced a higher AGB gain under elevated CO_2 during droughts but this positive effect was overall offset by negative climate effects, as shown in Fig. 10. The positive effects on growth from elevated CO_2 in our model is spatially uniform, while there is spatial heterogeneity in the AGB loss response to drought. During drought years, most pixels show a lower mortality risk in S2 with elevated CO_2, compared to S3 with fixed CO_2 (Fig. S7), consistent with simulations from (less advanced) terrestrial biosphere models showing that CO_2 fertilization decreased the probability of dieback in eastern Amazon (Zhang *et al.*, 2015). Reduced transpiration due to increased CO_2 (a difference between -0.4 – 0mm/d from S2 minus S3) was modeled in most pixels, for example during the 2015/16 event (Fig. S8). Yet, this response of transpiration to increasing CO_2 is not spatially uniform and has uncertainties (Mengis *et al.*, 2015). The degree to which water stress can be mitigated by rising CO_2 needs further calibration, e.g. through field-studies of leaf hydraulics adjustment (Cernusak *et al.*, 2013; Zuidema *et al.*, 2020). New data such as the future Amazon Free-Air CO_2 enrichment experiment, should also help resolve the optimal stomatal behavior from the trade-off between carbon uptake and water loss. We should also notice that the nutrient cycles are not well characterized in current model version, where the nutrient limitation like N and P deficit can modify the response of vegetation to increasing CO_2.

4.4 Legacy mortality and post drought biomass recovery

Legacy mortality. Besides hydraulic transport recovery, legacy effects of drought have an impact on living trees through partial damage. For example, elevated post-drought mortality was shown in the

Colombian Amazon (Zuleta *et al.*, 2017) and also central Amazon (Aleixo *et al.*, 2019). Currently, our model only considers cumulative drought exposure through PLC and has no legacy mortality effects. Such carryover effects could be further incorporated. For example, we may calibrate the depletion of labile carbon pools and reserves (already included in the model) after a drought to investigate how nonstructural carbohydrates (NSC) change during the drought and whether less available NSC would affect the following growth trajectory (Signori-Müller *et al.*, 2021). Furthermore, increased mortality during drought is also linked with the appearance of other disturbances, like fire and insect outbreaks (Brando *et al.*, 2014), since droughts concur with peaks of fire activity. Thus, interaction with other disturbances, which can induce a 'death spiral' (Franklin *et al.*, 1987), also needs to be considered. For example, we could adapt the fire module (Yue *et al.*, 2014) of ORCHIDEE to reproduce Amazon fires, through which the effects of droughts and the accompanying higher fire risks can be tracked.

Post-drought resilience. In addition to distinct resistance strategies, possible recovery processes after embolism are also crucial in the simulation of hydraulic efficiency-safety trade-offs (Klein *et al.*, 2018). Recovery from hydraulic damage like embolism repair or vessel refilling can buffer drought mortality. After reaching the cavitation threshold, to what extent the embolism reversal can happen after the re-watering and how much xylem tension can relax are still under debate and require more evidences, like the experiments of the dry-down and re-watering on plant individuals that can permit the detection of the plant tolerance to water stress condition and their recovery abilities, to enable a generalized parameterization into process-based models.

5 Conclusion

We used a process-based model describing plant hydraulics, background light competition and drought induced tree mortality, ORCHIDEE-CAN-NHA, to evaluate the drought sensitivity at regional level and investigate aboveground biomass (AGB) changes for the eight most severe drought events since 1901 over the Amazon. The model can successfully quantify the drought sensitivity of AGB growth and mortality to cumulative water deficits when compared with plot data collected for the 2005 and 2010 droughts. We assessed a higher sensitivity of net AGB change in response to water stress during the extreme 2015/16 drought. Comparison of extent and severity of the eight droughts and their AGB anomalies indicates that the 2015/16 event was the most severe both in terms of drought intensity in its epicenter and the area where severe biomass loss occurred. Factorial simulations helped us to discern the contribution of climate change and increased CO_2 concentration: climate change negatively affected AGB gain and loss, whereas moisture stress was reduced to some extent by elevated CO_2. More field-evidence, like hydraulic traits distributions and a better accounting of soil texture heterogeneity, are priorities to fill the model-observation gap and produce more reliable spatial gradients of mortality risk. We hope that this study makes an important step forward in quantifying the large-scale carbon impacts of tropical forest drought and enhances our ability to make future predictions.

Acknowledgements

This work was financially supported by the CLAND Convergence Institute funded by ANR (16-CONV-0003). YY also acknowledges support from Make Our Planet Great Again (MOPGA) Scholarship.

Author contribution

PC and YY designed the study. YY ran the simulation, analyzed the outputs and drafted the manuscript. All authors contributed to manuscript drafts, where PC substantially contributed to the final manuscript.

Data Availability

Code and dataset supporting the results are available in Zenodo at doi: 10.5281/zenodo.6529664 and 10.5281/zenodo.6668376.

References

Aleixo I, Norris D, Hemerik L, Barbosa A, Prata E, Costa F, Poorter L. 2019. Amazonian rainforest tree mortality driven by climate and functional traits. *Nature Climate Change* 9(5): 384-388.

Anderegg WR, Anderegg LD, Kerr KL, Trugman AT. 2019. Widespread drought-induced tree mortality at dry range edges indicates that climate stress exceeds species' compensating mechanisms. *Global Change Biology* 25(11): 3793-3802.

Bennett AC, McDowell NG, Allen CD, Anderson-Teixeira KJ. 2015. Larger trees suffer most during drought in forests worldwide. *Nature Plants* 1(10): 15139, doi: 10.1038/nplants.2015.139

Bittencourt PR, Oliveira RS, da Costa AC, Giles AL, Coughlin I, Costa PB, Bartholomew DC, Ferreira LV, Vasconcelos SS, Barros FV. 2020. Amazonia trees have limited capacity to acclimate plant hydraulic properties in response to long-term drought. *Global Change Biology* 26(6): 3569-3584.

Brando PM, Balch JK, Nepstad DC, Morton DC, Putz FE, Coe MT, Silvério D, Macedo MN, Davidson EA, Nóbrega CC. 2014. Abrupt increases in Amazonian tree mortality due to drought–fire interactions. *Proceedings of the National Academy of Sciences* 111(17): 6347-6352.

Brienen RJ, Phillips OL, Feldpausch TR, Gloor E, Baker TR, Lloyd J, Lopez-Gonzalez G, Monteagudo-Mendoza A, Malhi Y, Lewis SL. 2015. Long-term decline of the Amazon carbon sink. *Nature* 519(7543): 344-348.

Brodribb TJ, Powers J, Cochard H, Choat B. 2020. Hanging by a thread? Forests and drought. *Science* 368(6488): 261-266.

Cernusak LA, Winter K, Dalling JW, Holtum JA, Jaramillo C, Körner C, Leakey AD, Norby RJ, Poulter B, Turner BL. 2013. Tropical forest responses to increasing atmospheric CO2: current

knowledge and opportunities for future research. *Functional Plant Biology* 40(6): 531-551.

Cox PM, Betts R, Collins M, Harris PP, Huntingford C, Jones C. 2004. Amazonian forest dieback under climate-carbon cycle projections for the 21st century. *Theoretical and applied climatology* 78(1): 137-156.

de Almeida Castanho AD, Galbraith D, Zhang K, Coe MT, Costa MH, Moorcroft P. 2016. Changing Amazon biomass and the role of atmospheric CO2 concentration, climate, and land use. *Global Biogeochemical Cycles* 30(1): 18-39.

De Guzman ME, Acosta-Rangel A, Winter K, Meinzer FC, Bonal D, Santiago LS. 2021. Hydraulic traits of Neotropical canopy liana and tree species across a broad range of wood density: implications for predicting drought mortality with models. *Tree physiology* 41(1): 24-34.

Doughty CE, Metcalfe D, Girardin C, Amezquita FF, Cabrera DG, Huasco WH, Silva-Espejo J, Araujo-Murakami A, Da Costa M, Rocha W. 2015. Drought impact on forest carbon dynamics and fluxes in Amazonia. *Nature* 519(7541): 78-82.

Eller CB, Rowland L, Mencuccini M, Rosas T, Williams K, Harper A, Medlyn BE, Wagner Y, Klein T, Teodoro GS. 2020. Stomatal optimization based on xylem hydraulics (SOX) improves land surface model simulation of vegetation responses to climate. *New Phytologist* 226(6): 1622-1637.

Esquivel-Muelbert A, Galbraith D, Dexter KG, Baker TR, Lewis SL, Meir P, Rowland L, da Costa ACL, Nepstad D, Phillips OL. 2017. Biogeographic distributions of neotropical trees reflect their directly measured drought tolerances. *Scientific reports* 7, 8334, doi: 10.1038/s41598-017-08105-8

Esquivel-Muelbert A, Phillips OL, Brienen RJ, Fauset S, Sullivan MJ, Baker TR, Chao K-J,

Feldpausch TR, Gloor E, Higuchi N. 2020. Tree mode of death and mortality risk factors across Amazon forests. *Nature communications* 11, 5515, doi: 10.1038/s41467-020-18996-3

Feldpausch T, Phillips O, Brienen R, Gloor E, Lloyd J, Lopez-Gonzalez G, Monteagudo-Mendoza A, Malhi Y, Alarcón A, Dávila EÁ. 2016. Amazon forest response to repeated droughts. *Global Biogeochemical Cycles* 30(7): 964-982.

Feng X, Porporato A, Rodriguez-Iturbe I. 2013. Changes in rainfall seasonality in the tropics. *Nature Climate Change* 3(9): 811-815.

Fisher R, Williams M, Da Costa AL, Malhi Y, Da Costa R, Almeida S, Meir P. 2007. The response of an Eastern Amazonian rain forest to drought stress: results and modelling analyses from a throughfall exclusion experiment. *Global Change Biology* 13(11): 2361-2378.

Fleischer K, Rammig A, De Kauwe MG, Walker AP, Domingues TF, Fuchslueger L, Garcia S, Goll DS, Grandis A, Jiang M. 2019. Amazon forest response to CO 2 fertilization dependent on plant phosphorus acquisition. *Nature Geoscience* 12(9): 736-741.

Franklin JF, Shugart HH, Harmon ME. 1987. Tree death as an ecological process. *BioScience* 37(8): 550-556.

Harris I. 2020. CRU JRA v2. 1: A forcings dataset of gridded land surface blend of Climatic Research Unit (CRU) and Japanese reanalysis (JRA) data, January 1901–December 2019, University of East Anglia Climatic Research Unit, Centre for Environmental Data Analysis. *University of East Anglia Climatic Research Unit, Centre for Environmental Data Analysis* 10.

Harris I, Jones PD, Osborn TJ, Lister DH. 2014. Updated high-resolution grids of monthly climatic observations–the CRU TS3. 10 Dataset. *International Journal of Climatology* 34(3): 623-642.

Harris I, Osborn TJ, Jones P, Lister D. 2020. Version 4 of the CRU TS monthly high-resolution gridded

multivariate climate dataset. *Scientific data* 7, 109, doi: 10.1038/s41597-020-0453-3

Holm JA, Knox RG, Zhu Q, Fisher RA, Koven CD, Nogueira Lima AJ, Riley WJ, Longo M, Negrón-Juárez RI, de Araujo AC. 2020. The central Amazon biomass sink under current and future atmospheric CO2: Predictions from big-leaf and demographic vegetation models. *Journal of Geophysical Research: Biogeosciences* 125(3): e2019JG005500, doi: 10.1029/2019JG005500

Hubau W, Lewis SL, Phillips OL, Affum-Baffoe K, Beeckman H, Cuní-Sanchez A, Daniels AK, Ewango CE, Fauset S, Mukinzi JM. 2020. Asynchronous carbon sink saturation in African and Amazonian tropical forests. *Nature* 579(7797): 80-87.

Janssen TA, Hölttä T, Fleischer K, Naudts K, Dolman H. 2020. Wood allocation trade-offs between fiber wall, fiber lumen, and axial parenchyma drive drought resistance in neotropical trees. *Plant, Cell & Environment* 43(4): 965-980.

Jimenez JC, Libonati R, Peres LF. 2018. Droughts over Amazonia in 2005, 2010, and 2015: a cloud cover perspective. *Frontiers in Earth Science* 6: 227, doi: 10.3389/feart.2018.00227

Jimenez JC, Takahashi K. 2019. Tropical Climate Variability and Change: Impacts in the Amazon. *Frontiers in Earth Science* 7: 215, doi: 10.3389/feart.2019.00215

Joetzjer E, Maignan F, Chave J, Goll D, Poulter B, Barichivich J, Maréchaux I, Luyssaert S, Guimberteau M, Naudts K. 2022. Effect of tree demography and flexible root water uptake for modeling the carbon and water cycles of Amazonia. *Ecological modelling* 469: 109969, doi: 10.1016/j.ecolmodel.2022.109969

Kennedy D, Swenson S, Oleson KW, Lawrence DM, Fisher R, Lola da Costa AC, Gentine P. 2019. Implementing plant hydraulics in the community land model, version 5. *Journal of Advances in Modeling Earth Systems* 11(2): 485-513.

Klein T, Zeppel MJ, Anderegg WR, Bloemen J, De Kauwe MG, Hudson P, Ruehr NK, Powell TL, von Arx G, Nardini A. 2018. Xylem embolism refilling and resilience against drought-induced mortality in woody plants: processes and trade-offs. *Ecological research* 33(5): 839-855.

Kobayashi S, Ota Y, Harada Y, Ebita A, Moriya M, Onoda H, Onogi K, Kamahori H, Kobayashi C, Endo H. 2015. The JRA-55 reanalysis: General specifications and basic characteristics. *Journal of the Meteorological Society of Japan. Ser. II* 93(1): 5-48.

Kunert N, Zailaa J, Herrmann V, Muller-Landau HC, Wright SJ, Pérez R, McMahon SM, Condit RC, Hubbell SP, Sack L. 2021. Leaf turgor loss point shapes local and regional distributions of evergreen but not deciduous tropical trees. *New Phytologist* 230(2): 485-496.

Levine NM, Zhang K, Longo M, Baccini A, Phillips OL, Lewis SL, Alvarez-Dávila E, de Andrade ACS, Brienen RJ, Erwin TL. 2016. Ecosystem heterogeneity determines the ecological resilience of the Amazon to climate change. *Proceedings of the National Academy of Sciences* 113(3): 793-797.

Lewis SL, Brando PM, Phillips OL, van der Heijden GM, Nepstad D. 2011. The 2010 amazon drought. *Science* 331(6017): 554-554.

Li L, Yang ZL, Matheny AM, Zheng H, Swenson SC, Lawrence DM, Barlage M, Yan B, McDowell NG, Leung LR. 2021. Representation of Plant Hydraulics in the Noah-MP Land Surface Model: Model Development and Multi-scale Evaluation. *Journal of Advances in Modeling Earth Systems* 13: e2020MS002214, doi: 10.1029/2020MS002214

Liu Y, Holtzman NM, Konings AG. 2021. Global ecosystem-scale plant hydraulic traits retrieved using model–data fusion. *Hydrology and Earth System Sciences* 25(5): 2399-2417.

Lu Y, Duursma RA, Farrior CE, Medlyn BE, Feng X. 2020. Optimal stomatal drought response shaped

by competition for water and hydraulic risk can explain plant trait covariation. *New Phytologist* 225(3): 1206-1217.

Marthews TR, Quesada CA, Galbraith DR, Malhi Y, Mullins CE, Hodnett MG, Dharssi I. 2014. High-resolution hydraulic parameter maps for surface soils in tropical South America. *Geoscientific Model Development* 7(3): 711-723.

McCulloh KA, Domec JC, Johnson DM, Smith DD, Meinzer FC. 2019. A dynamic yet vulnerable pipeline: Integration and coordination of hydraulic traits across whole plants. *Plant, Cell & Environment* 42(10): 2789-2807.

Meakem V, Tepley AJ, Gonzalez-Akre EB, Herrmann V, Muller-Landau HC, Wright SJ, Hubbell SP, Condit R, Anderson-Teixeira KJ. 2018. Role of tree size in moist tropical forest carbon cycling and water deficit responses. *New Phytologist* 219(3): 947-958.

Mengis N, Keller DP, Eby M, Oschlies A. 2015. Uncertainty in the response of transpiration to CO2 and implications for climate change. *Environmental Research Letters* 10(9): 094001, doi: 10.1088/1748-9326/10/9/094001

Mitchard ET, Feldpausch TR, Brienen RJ, Lopez‐Gonzalez G, Monteagudo A, Baker TR, Lewis SL, Lloyd J, Quesada CA, Gloor M. 2014. Markedly divergent estimates of Amazon forest carbon density from ground plots and satellites. *Global Ecology and Biogeography* 23(8): 935-946.

Naudts K, Ryder J, McGrath M, Otto J, Chen Y, Valade A, Bellasen V, Berhongaray G, Bönisch G, Campioli M. 2015. A vertically discretised canopy description for ORCHIDEE (SVN r2290) and the modifications to the energy, water and carbon fluxes. *Geoscientific Model Development* 8: 2035-2065.

Negrón-Juárez RI, Holm JA, Marra DM, Rifai SW, Riley WJ, Chambers JQ, Koven CD, Knox RG,

McGroddy ME, Di Vittorio AV. 2018. Vulnerability of Amazon forests to storm-driven tree mortality. *Environmental Research Letters* 13(5): 054021, doi: 10.1088/1748-9326/aabe9f

Oliveira RS, Costa FR, van Baalen E, de Jonge A, Bittencourt PR, Almanza Y, Barros FdV, Cordoba EC, Fagundes MV, Garcia S. 2019. Embolism resistance drives the distribution of Amazonian rainforest tree species along hydro-topographic gradients. *New Phytologist* 221(3): 1457-1465.

Papastefanou P, Zang C, Pugh T, Liu D, Lapola D, Fleischer K, Grams T, Hickler T, Rammig A. 2021. New plant hydraulic architecture reproduces impacts of droughts in the Amazon rainforest: Copernicus Meetings.

Papastefanou P, Zang CS, Angelov Z, de Castro AA, Jimenez JC, De Rezende LFC, Ruscica R, Sakschewski B, Sörensson A, Thonicke K. 2022. Recent extreme drought events in the Amazon rainforest: assessment of different precipitation and evapotranspiration datasets and drought indicators, Biogeosciences, 19, 3843–3861, doi: 10.5194/bg-19-3843-2022.

Phillips OL, Aragão LE, Lewis SL, Fisher JB, Lloyd J, López-González G, Malhi Y, Monteagudo A, Peacock J, Quesada CA. 2009. Drought sensitivity of the Amazon rainforest. *Science* 323(5919): 1344-1347.

Piao S, Friedlingstein P, Ciais P, de Noblet-Ducoudré N, Labat D, Zaehle S. 2007. Changes in climate and land use have a larger direct impact than rising CO2 on global river runoff trends. *Proceedings of the National Academy of Sciences* 104(39): 15242-15247.

Powell TL, Wheeler JK, de Oliveira AA, da Costa ACL, Saleska SR, Meir P, Moorcroft PR. 2017. Differences in xylem and leaf hydraulic traits explain differences in drought tolerance among mature Amazon rainforest trees. *Global Change Biology* 23(10): 4280-4293.

Powers JS, Vargas G G, Brodribb TJ, Schwartz NB, Pérez-Aviles D, Smith-Martin CM, Becknell JM,

Aureli F, Blanco R, Calderón-Morales E. 2020. A catastrophic tropical drought kills hydraulically vulnerable tree species. *Global Change Biology* 26(5): 3122-3133.

Ritchie P, Clarke J, Cox P, Huntingford C. 2021. Overshooting Tipping Point Thresholds in A Changing Climate. *Nature* 592: 517-523.

Rowland L, da Costa ACL, Galbraith DR, Oliveira R, Binks OJ, Oliveira A, Pullen A, Doughty C, Metcalfe D, Vasconcelos S. 2015. Death from drought in tropical forests is triggered by hydraulics not carbon starvation. *Nature* 528(7580): 119-122.

Rowland L, Martínez-Vilalta J, Mencuccini M. 2021. Hard times for high expectations from hydraulics: predicting drought-induced forest mortality at landscape scales remains a challenge. *New Phytologist,* 230, 1685-1687.

Santiago LS, De Guzman ME, Baraloto C, Vogenberg JE, Brodie M, Hérault B, Fortunel C, Bonal D. 2018. Coordination and trade-offs among hydraulic safety, efficiency and drought avoidance traits in Amazonian rainforest canopy tree species. *New Phytologist* 218(3): 1015-1024.

Signori-Müller C, Oliveira RS, de Vasconcellos Barros F, Tavares JV, Gilpin M, Diniz FC, Zevallos MJM, Yupayccana CAS, Acosta M, Bacca J. 2021. Non-structural carbohydrates mediate seasonal water stress across Amazon forests. *Nature Communications* 12, 2310, doi: 10.1038/s41467-021-22378-8.

Trugman AT, Anderegg LD, Anderegg WR, Das AJ, Stephenson NL. 2021. Why is tree drought mortality so hard to predict? *Trends in Ecology & Evolution*, 36(6), 520-532.

Wieder W, Boehnert J, Bonan G, Langseth M. 2014. Regridded harmonized world soil database v1. 2. *ORNL DAAC*.

Yang X, Post W, Thornton P, Jain A. 2014. Global gridded soil phosphorus distribution maps at 0.5-

degree resolution. *ORNL DAAC*.

Yang Y, Saatchi SS, Xu L, Yu Y, Choi S, Phillips N, Kennedy R, Keller M, Knyazikhin Y, Myneni RB. 2018. Post-drought decline of the Amazon carbon sink. *Nature Communications* 9, 3172, doi: 10.1038/s41467-018-05668-6

Yao, Y., Joetzjer, E., Ciais, P., Viovy, N., Cresto Aleina, F., Chave, J., Sack, L., Bartlett, M., Meir, P., Fisher, R., and Luyssaert, S. 2022. Forest fluxes and mortality response to drought: model description (ORCHIDEE-CAN-NHA r7236) and evaluation at the Caxiuanã drought experiment, Geosci. Model Dev., 15, 7809–7833, doi: 10.5194/gmd-15-7809-2022.

Yue C, Ciais P, Cadule P, Thonicke K, Archibald S, Poulter B, Hao W, Hantson S, Mouillot F, Friedlingstein P. 2014. Modelling the role of fires in the terrestrial carbon balance by incorporating SPITFIRE into the global vegetation model ORCHIDEE–Part 1: simulating historical global burned area and fire regimes. *Geoscientific Model Development* 7(6): 2747-2767.

Zemp DC, Schleussner C-F, Barbosa HM, Hirota M, Montade V, Sampaio G, Staal A, Wang-Erlandsson L, Rammig A. 2017. Self-amplified Amazon forest loss due to vegetation-atmosphere feedbacks. *Nature communications* 8, 14681, doi: 10.1038/ncomms14681.

Zhang K, de Almeida Castanho AD, Galbraith DR, Moghim S, Levine NM, Bras RL, Coe MT, Costa MH, Malhi Y, Longo M. 2015. The fate of Amazonian ecosystems over the coming century arising from changes in climate, atmospheric CO 2, and land use. *Global Change Biology* 21(7): 2569-2587.

Ziegler C, Coste S, Stahl C, Delzon S, Levionnois S, Cazal J, Cochard H, Esquivel-Muelbert A, Goret J-Y, Heuret P. 2019. Large hydraulic safety margins protect Neotropical canopy rainforest tree

species against hydraulic failure during drought. *Annals of Forest Science* 76, 115, 10.1007/s13595-019-0905-0.

Zuidema PA, Heinrich I, Rahman M, Vlam M, Zwartsenberg SA, van der Sleen P. 2020. Recent CO2 rise has modified the sensitivity of tropical tree growth to rainfall and temperature. *Global Change Biology* 26(7): 4028-4041.

Zuleta D, Duque A, Cardenas D, Muller-Landau HC, Davies SJ. 2017. Drought-induced mortality patterns and rapid biomass recovery in a terra firme forest in the Colombian Amazon. *Ecology* 98(10): 2538-2546.

Table 1 Description of simulations performed in this study. In the S1 scenario, the model is forced by recycling the climate forcing data between 1901 and 1920 and the CO_2 concentration increases following the reality. In the S2 scenario, both climate forcing and CO_2 concentration vary. In the S3 scenario, the CO_2 concentration input to model is set constant as 296 ppm but climate forcing data varies.

	Climate forcing	Atmospheric CO_2	Mortality module	Restart point
spin-up stage 1	1901-1920	Constant (296ppm)	Deactivate	/
spin-up stage 2	1901-1920	Constant (296ppm)	Activate	Stage1
S1	1901-1920	Increasing	Activate	Stage2
S2	1901-2019	Increasing	Activate	Stage2
S3	1901-2019	Constant (296ppm)	Activate	Stage2

Figure legends

Fig. 1 Overview of the Amazon basin, which is split into four regions, Guiana Shield, East-Central Amazon, Western Amazon, and Brazilian Shield, shown by different colors, defined after Feldpausch *et al.* (2011). The black line is the border of Amazon basin from Papastefanou *et al* (2022). Only pixels with tree cover more than 80% are shown. Map lines delineate study areas and do not necessarily depict accepted national boundaries.

Fig. 2 Long-term carbon dynamics of rainforest over Amazon basin. a-c, Trends in net aboveground biomass carbon sink (a), carbon gains from tree growth (b), and carbon losses from tree mortality including both self-thinning and drought-induced tree mortality (c). The continuous lines indicate the modelled forest carbon dynamics in Amazonia and the shading area corresponds to the 95% confidence interval. Slopes and P values are from linear regression models.

Fig. 3 AGB versus drought severity in 2005, 2010 and 2016. Severity is defined from MCWD, with higher positive values denoting more acute water stress. The color of the points corresponds to four regions, red: Guiana Shield, green: East-Central Amazon, brown: Western Amazon, and blue: Brazilian Shield. The first column gives the net AGB sink anomaly with MCWD. The second one the AGB growth gain anomaly. The third one the AGB loss (mortality) anomaly. Map lines delineate study areas and do not necessarily depict accepted national boundaries.

Fig. 4 Spatial distribution of the drought intensity of the top most severe droughts since 1901, is assessed by Z score values of MCWD anomalies relative to their decadal baseline.

Fig. 5 Frequency distribution of different drought intensity classes (Z score of monthly CWD corresponding to increasing severity). The thresholds of -1.645, -1.96 and -2.576 correspond to 90%, 95%, and 99% confidence intervals of the distributions, respectively. The asterisks in the title of a panel indicate an El Niño drought (wet season drought). The # pixels on the vertical axis means the number of 1° model pixels with CWD values in each interval.

Fig. 6 Spatial distribution of the simulated net AGB change during the eight largest drought events since 1901. Such change is calculated on yearly interval, from the October in the previous year to September in the current year. The asterisks in the title of a panel indicates an El Niño drought. Negative value denotes carbon sources and positive value means carbon sink. Map lines delineate study areas and do not necessarily depict accepted national boundaries.

Fig. 7 Regional extent of net AGB change during 8 drought events. The colors correspond to the different levels of net AGB changes with the same color palette than in Fig. 6. # pixels means the number of 1° model pixels that underwent net biomass carbon change in each interval.

Fig. 8 Bivariate plots showing the spatial pattern of the rainfall seasonality index and drought timing index (DTI) in the Amazon for the eight largest droughts since 1901. Negative values of DTI mean that drought with the most negative Z score of rainfall anomaly happens in the drier months of the year. Only pixels with a drought Z-score of MCWD below -1.645 are shown, which is at least a *moderate*

drought (see definition of drought intensities in SI). The asterisks in the title of each panel indicates an El Niño drought. Map lines delineate study areas and do not necessarily depict accepted national boundaries.

Fig. 9 Comparison of cumulative AGB loss in 20-year intervals in different regions since 1901. # pixels means the number of pixels underwent carbon loss in each interval. The last 20-year period is highlighted as the thick red line.

Fig. 10 AGB gain from growth, loss from mortality and net AGB change in the epicenters of each major drought from the three scenarios. S1: varying CO_2 and recycling climate over 1901-1920, S2: varying CO_2 and historical climate change, S3: historical climate change and constant CO_2 concentration. The epicenter of a drought is defined by pixels with Z scored MCWD below -1.645, corresponding to 90% confidence interval following normal distribution.

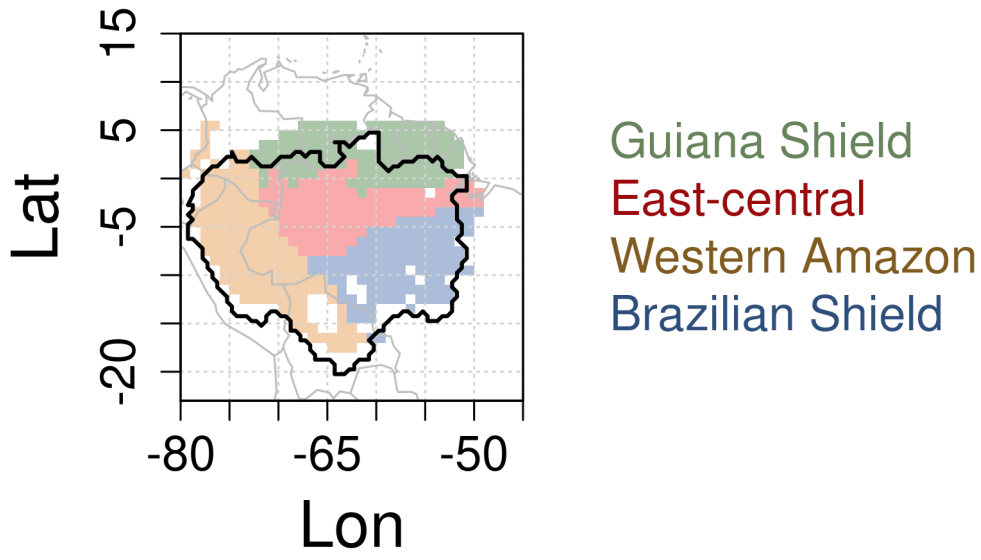

GCB_16504_Figure 1.tiff

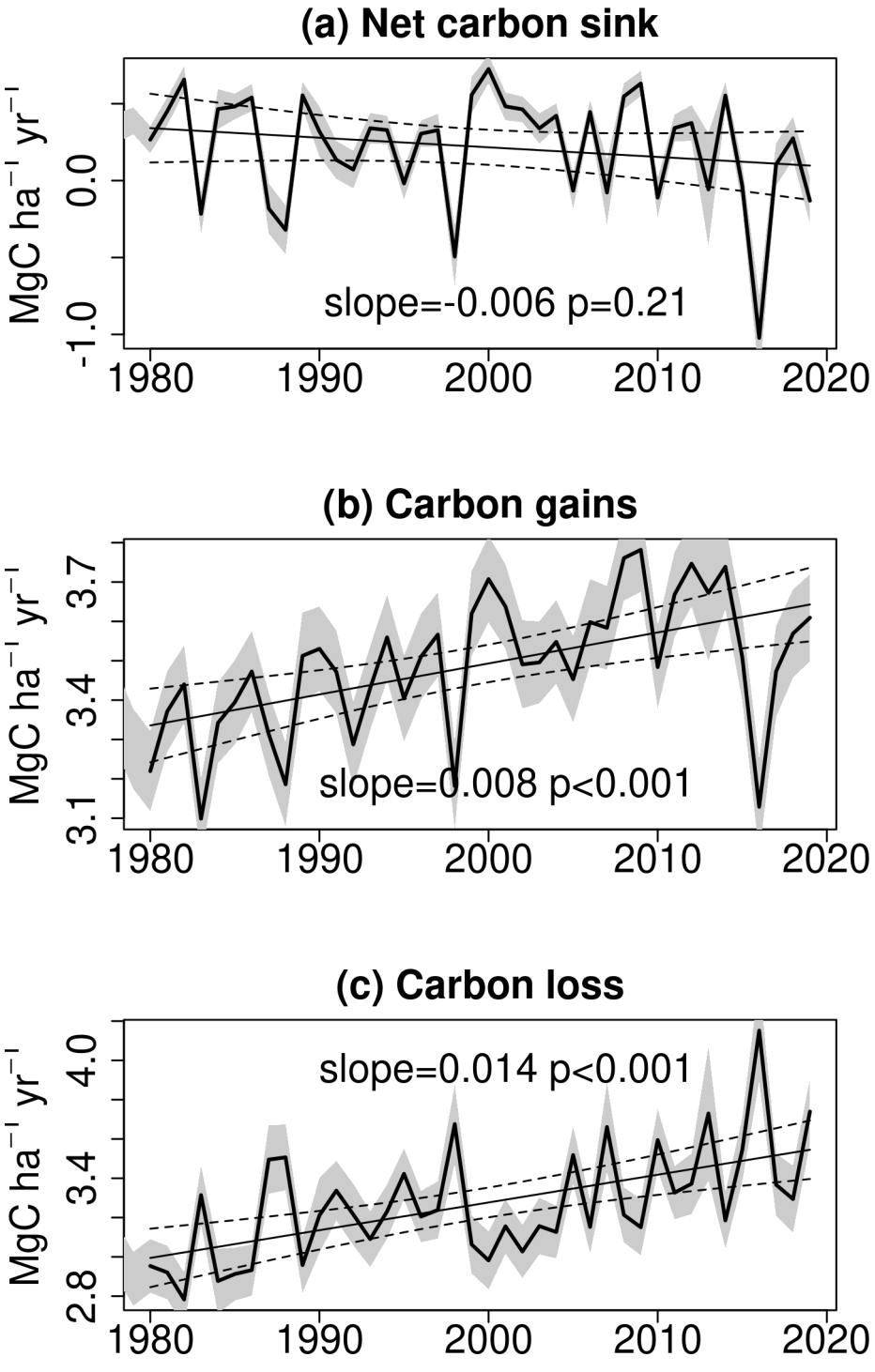

GCB_16504_Figure 2.tiff

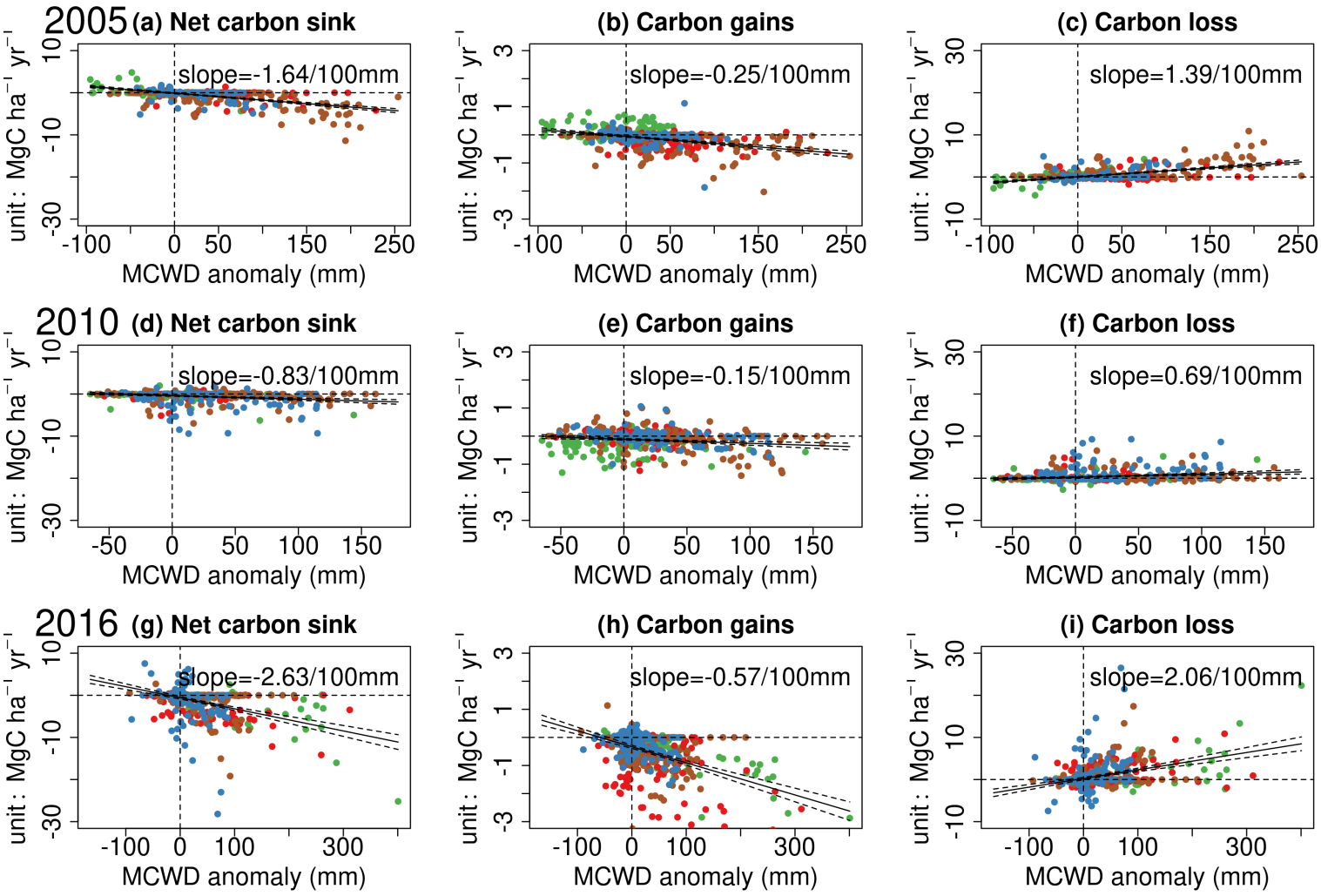

GCB_16504_Figure 3.tiff

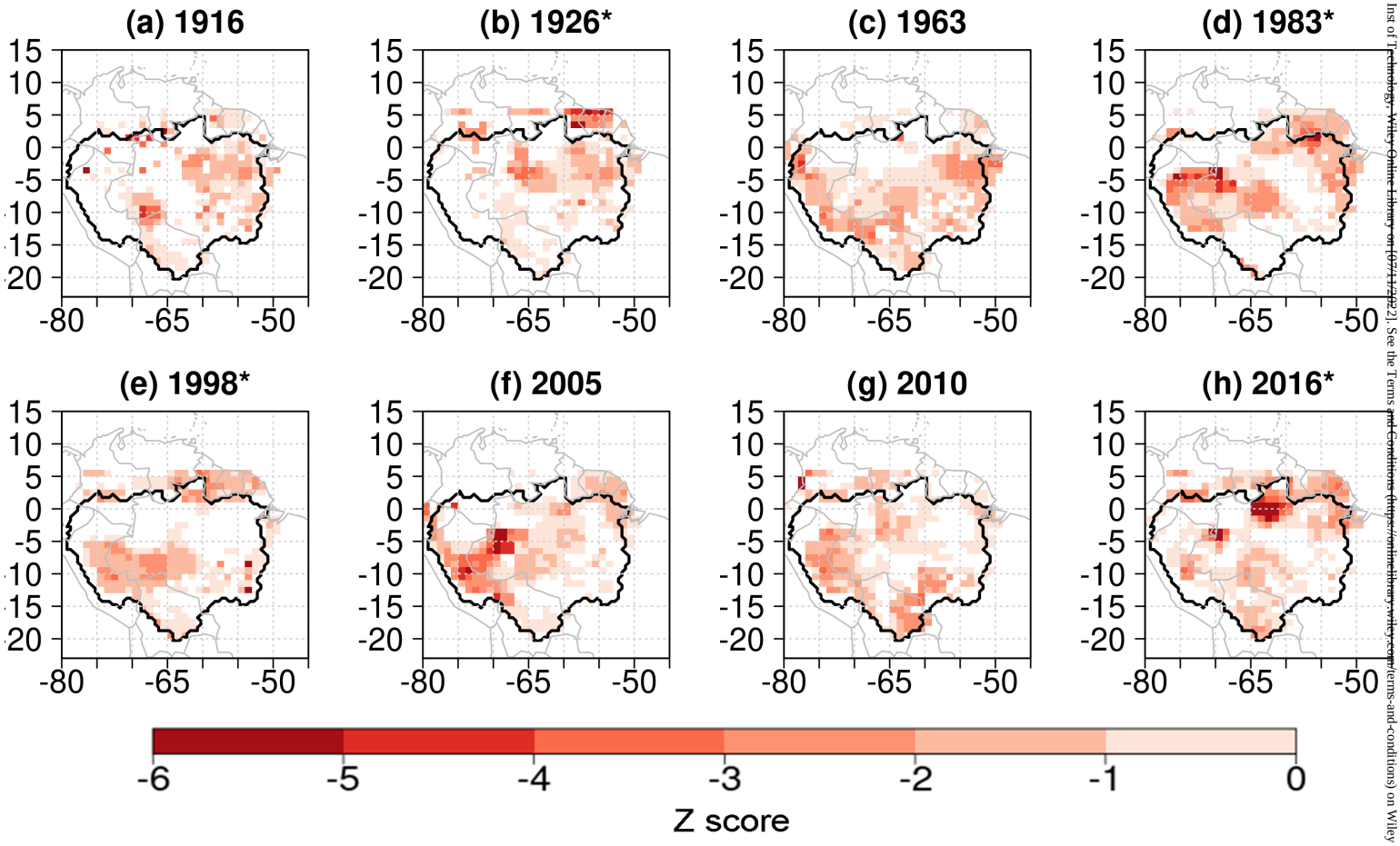

GCB_16504_Figure 4.tif

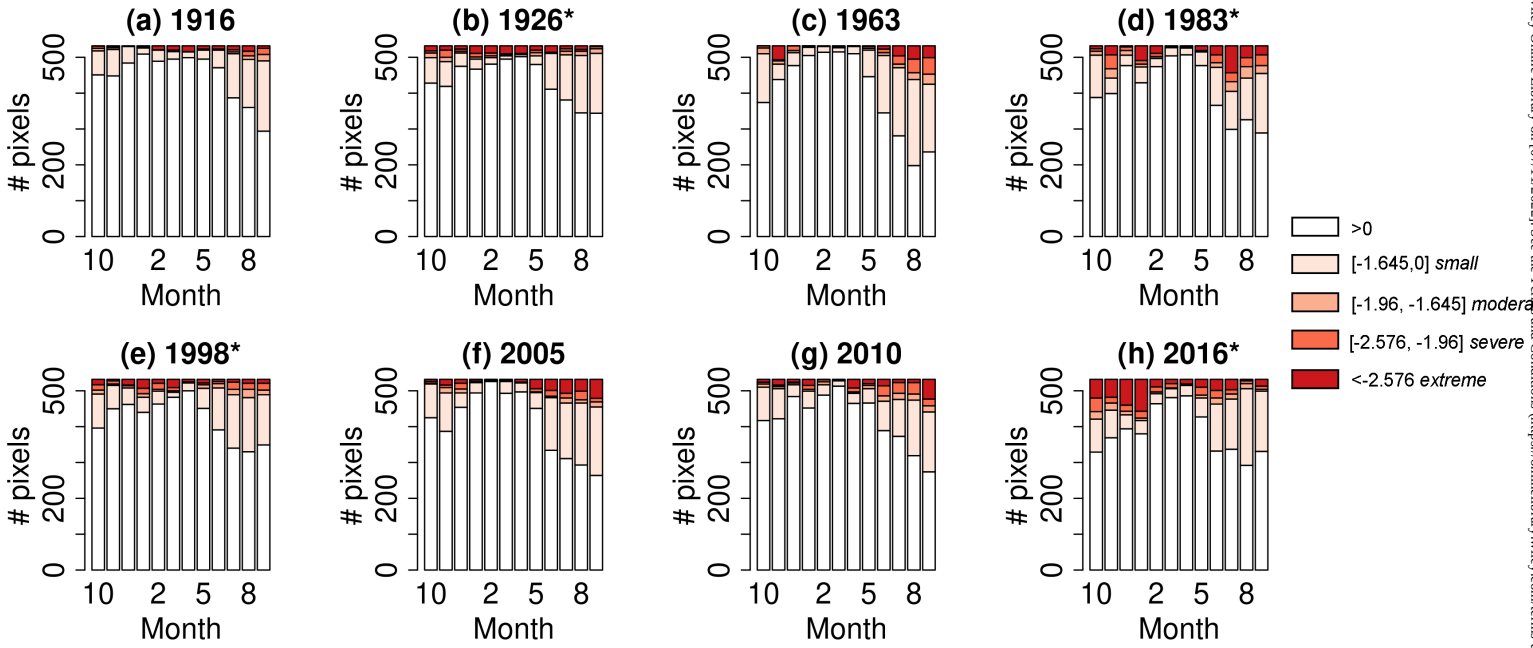

GCB_16504_Figure 5.tif

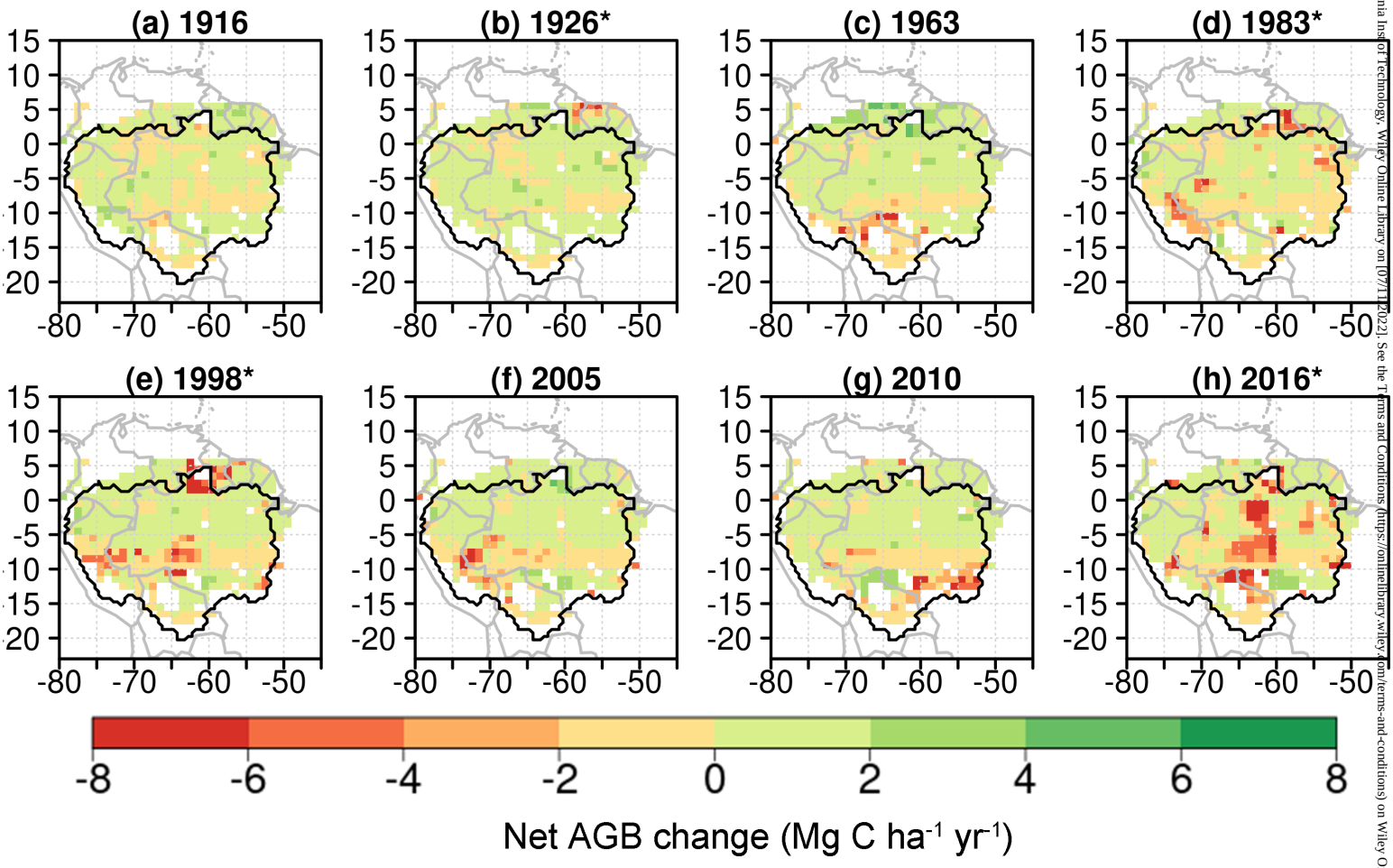

GCB_16504_Figure 6.tif

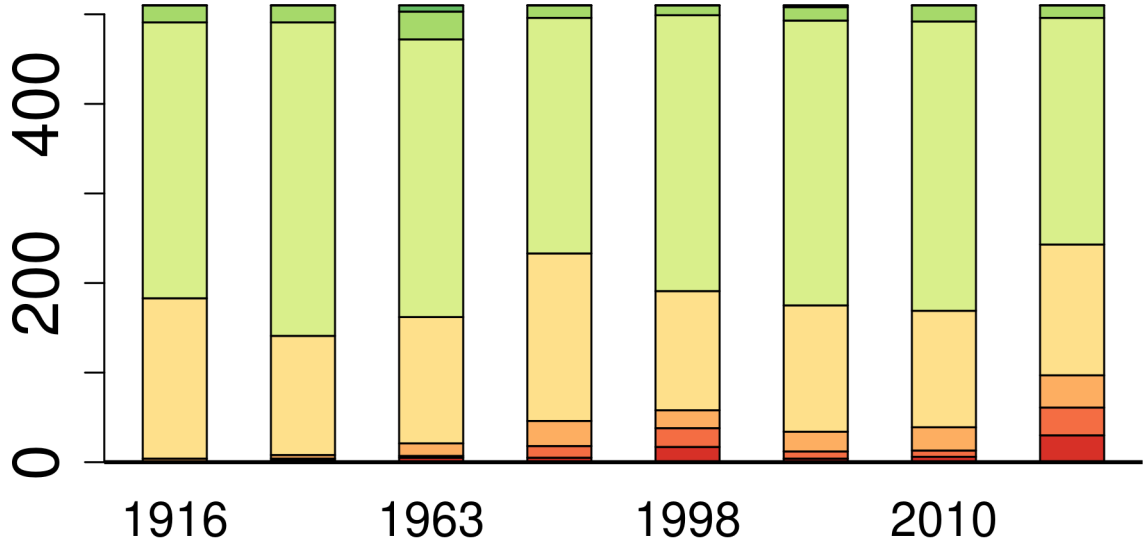

GCB_16504_Figure 7.tiff

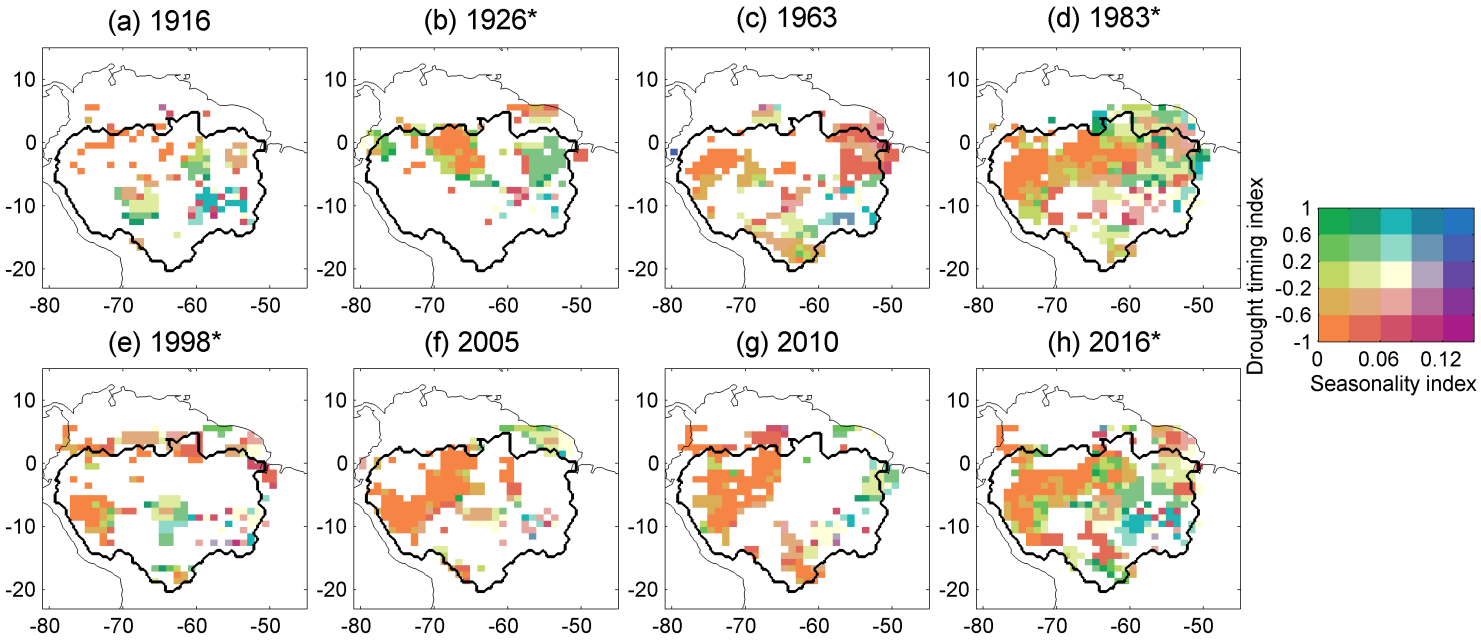

GCB_16504_Figure 8.tif

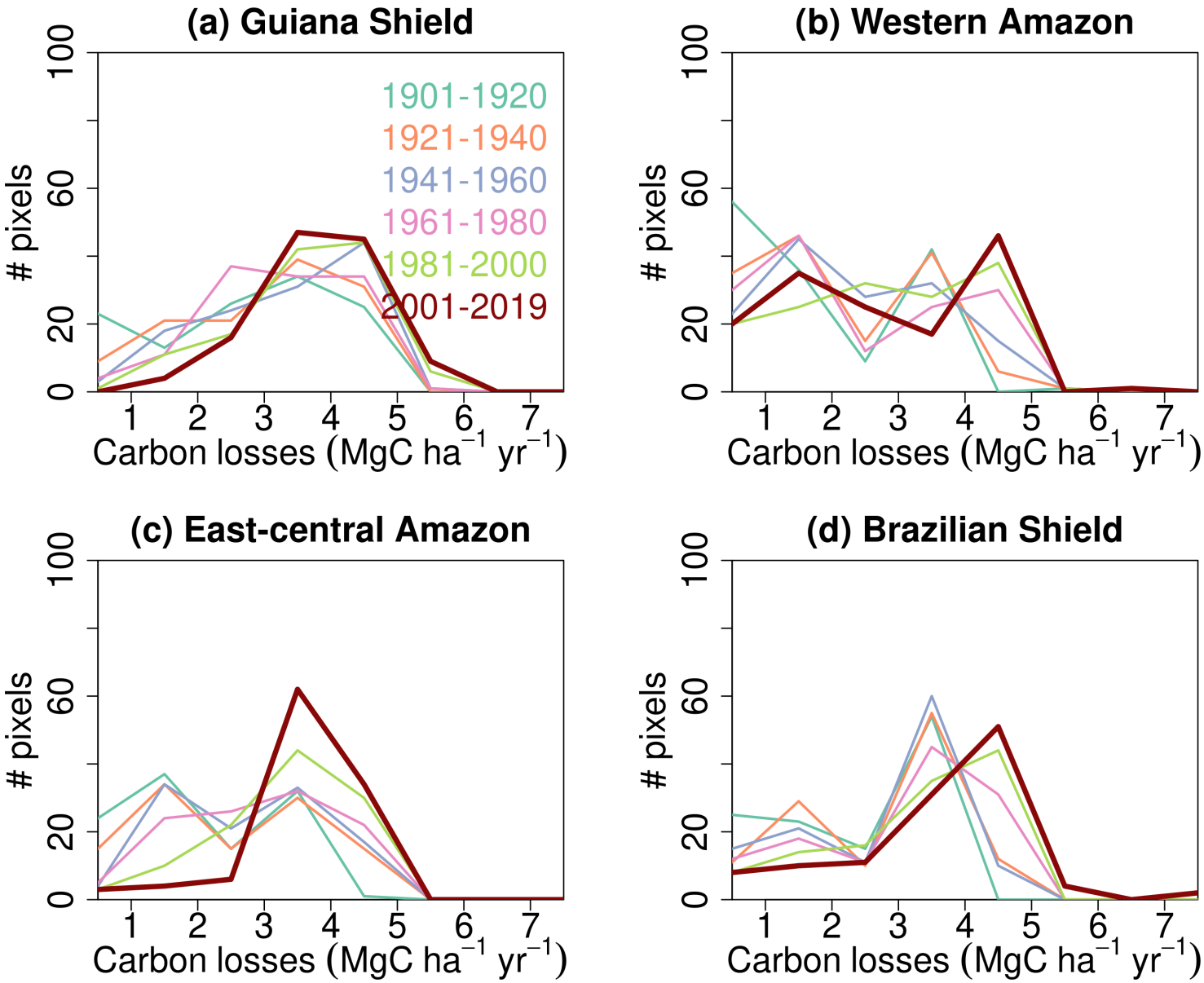

GCB_16504_Figure 9.tiff

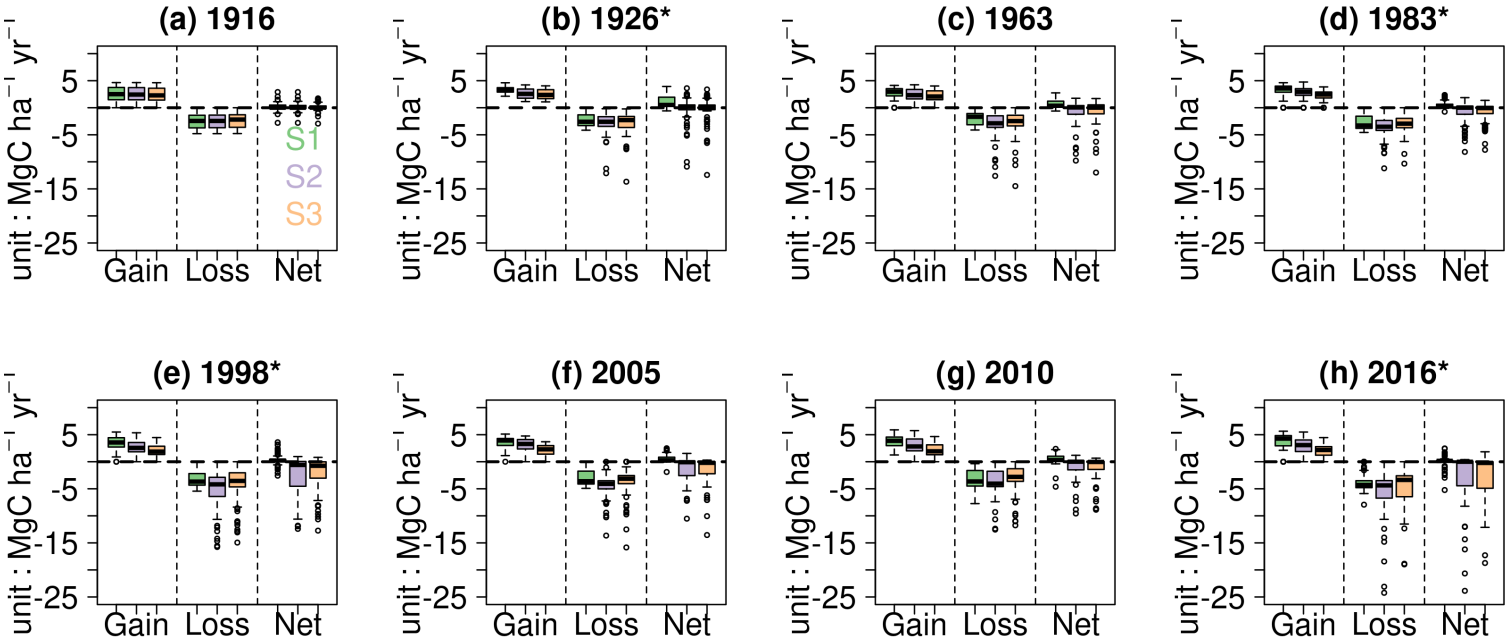

GCB_16504_Figure 10.tiff